PolyPublie
Polytechnique Montréal

POLYTECHNIQUE MONTRÉAL
UNIVERSITÉ D'INGÉNIERIE

Titre: Title:	Development of a Thermodynamic Database for Copper Smelting and Converting
Auteur: Author:	Denis Shishin
Date:	2013
Type:	Mémoire ou thèse / Dissertation or Thesis
Référence: Citation:	Shishin, D. (2013). Development of a Thermodynamic Database for Copper Smelting and Converting [Thèse de doctorat, École Polytechnique de Montréal]. PolyPublie. https://publications.polymtl.ca/1248/

Document en libre accès dans PolyPublie
Open Access document in PolyPublie

URL de PolyPublie: PolyPublie URL:	https://publications.polymtl.ca/1248/
Directeurs de recherche: Advisors:	Sergei Decterov, & Christopher Bale
Programme: Program:	Génie métallurgique

Ce fichier a été téléchargé à partir de PolyPublie, le dépôt institutionnel de Polytechnique Montréal
This file has been downloaded from PolyPublie, the institutional repository of Polytechnique Montréal

https://publications.polymtl.ca

UNIVERSITÉ DE MONTRÉAL

DEVELOPMENT OF A THERMODYNAMIC DATABASE FOR COPPER SMELTING AND CONVERTING

DENIS SHISHIN

DÉPARTEMENT DE GÉNIE CHIMIQUE

ÉCOLE POLYTECHNIQUE DE MONTRÉAL

THÈSE PRÉSENTÉE EN VUE DE L'OBTENTION

DU DIPLÔME DE PHILOSOPHIAE DOCTOR

(GÉNIE MÉTALLURGIQUE)

OCTOBRE 2013

© Denis Shishin, 2013.

UNIVERSITÉ DE MONTRÉAL

ÉCOLE POLYTECHNIQUE DE MONTRÉAL

Cette thèse intitulée:

DEVELOPMENT OF A THERMODYNAMIC DATABASE FOR COPPER SMELTING AND CONVERTING

présentée par : SHISHIN Denis

en vue de l'obtention du diplôme de : Philosophiae Doctor

a été dûment acceptée par le jury d'examen constitué de :

M. PELTON Arthur, Ph.D., président

M. DECTEROV Sergei, Chercheur, membre et directeur de recherche

M. BALE Christopher, Ph. D., membre et codirecteur de recherche

M. CHARTRAND Patrice, Ph. D., membre

M. MACKEY Phillip, Ph. D., membre

DEDICATION

Measure what is measurable, and make measurable what is not so

Galileo Galilei

I wish to dedicate this thesis to my parents and my family

ACKNOWLEDGEMENTS

I would like to express my deep appreciation to my research director Dr. Sergei A. Decterov for the opportunity to do research in the field of computational thermochemistry. His guidance and support kept me inspired and motivated. I especially appreciate his attention to the minor details that provided me with discipline required to complete a valuable scientific project.

I owe great thanks to my co-director Dr. Christopher Bale for his introduction to the genius FactSage software and his patience that helped me to cope with computational problems.

I am grateful to the members of the members of the jury Dr. Arthur D. Pelton, Dr. Phillip Mackey and Dr. Patrice Chartrand for their critical review and constructive comments. The brilliant course “The thermodynamics of solutions” given by Dr. Arthur D. Pelton provided me with necessary background to start the project. Dr. Patrice Chartrand has always had a minute to give an independent view on some my problems.

I express gratitude to Dr. Eugene Jak from the Pyrometallurgy Research Center for the financial support and collaboration. The experimental data and modeling part provided by Dr. Taufiq Hidayat were essential for the quality of this thesis.

I am thankful to my wife and colleague Viktoria Prostakova, who helped me to correct the text of this thesis. We both struggle with English articles and prepositions and it was certainly easier to share this burden.

Many thanks to our colleagues Evguenia Sokolenko, Dr. Jacques Melançon, Dr. Christian Robelin and Eve Belisle. Evguenia helped enormously with the organization of thousands of articles and references. Jacques provided the technical support to the office facilities. Christian Robelin kindly agreed to correct the French translation of the introduction to this thesis. Eve Belisle organized great Christmas parties for the laboratory.

I appreciate the friendship of the fellow graduate students: Guillaume Lambotte, Wan-Yi Kim, Adarsh Shukla, Liling Jin, Jean-Philippe Harvey and others.

RÉSUMÉ

L'introduction de la modélisation thermodynamique dans la pratique de la production pyrométallurgique du cuivre pourrait augmenter significativement l'efficacité économique et le respect de l'environnement par l'industrie. Une base de données thermodynamiques fiable, en combinaison avec le logiciel de minimisation de l'énergie de Gibbs, est capable de prédire le bilan énergétique, la distribution des éléments, les transformations de phases au cours du procédé chimique. Mis en œuvre dans le couplage contrôle/simulation, la base de données thermodynamiques et le logiciel pourront réhausser l'automatisation du procédé à un nouveau niveau.

L'objectif de cette thèse est le développement de la base de données capable de prédire les propriétés thermodynamiques et les équilibres de phases dans le système chimique de base pour la production pyrométallurgique du cuivre, à savoir le système Al–Ca–**Cu**–Fe–Mg–O–S–Si. Cela implique l'évaluation critique et l'optimisation thermodynamique des données expérimentales disponibles pour toutes les phases. La base de données est auto-cohérente, c'est-à-dire que les phases solides, liquides et gazeuses sont évaluées simultanément. 4 systèmes binaires, 5 systèmes ternaires, 7 systèmes quaternaires, 2 systèmes quinaires et 1 système à six composants ont été évalués ou réévalués. Le projet est réalisé en étroite collaboration avec le groupe Pyrosearch (Université de Queensland, Australie), qui a effectué des expériences cruciales. Certains des systèmes mentionnés ci-dessus ont été optimisés avec T. Hidayat. En outre, 4 systèmes ternaires et 5 systèmes quaternaires ont été optimisés par T. Hidayat en collaboration avec le présent auteur et ont été rapportés dans une autre thèse de doctorat [1].

En particulier, les phases du métal liquide et de la matte ont été décrites comme une solution unique en utilisant le Formalisme Quasichimique Modifié dans l'approximation des paires. La solution a été construite en utilisant un sous-réseau et les espèces non chargées: (Cu^{I}, Cu^{II}, Fe^{II}, Fe^{III}, O, S). De cette façon, le modèle est capable de décrire un large écart à la stoechiométrie de la phase sulfurée en direction de l'excès de métal ou de l'excès de soufre et d'oxygène. La solubilité de l'oxygène dans la phase sulfurée est correctement décrite. Le modèle prend en compte l'existence de compositions d'ordonnancement maximal à courte distance entre premiers voisins au voisinage de Cu_2O, CuO, FeO, Fe_2O_3, Cu_2S et FeS et il prédit les changements drastiques de $P(O_2)$ et $P(S_2)$ à ces compositions. Il évalue précisément les solubilités du soufre et

de l'oxygène dans la zone métallique de la solution. Il peut être utilisé pour prédire les équilibres solides-liquides dans les systèmes chimiques contenant les phases d'oxyde et de sulfure à des pressions partielles d'oxygène faibles et élevées.

La solution de laitier est modélisée à l'aide du Formalisme Quasichimique Modifié dans l'approximation des quadruplets. Les cations sont chargés et placés sur un sous-réseau séparé de celui des anions : (Al^{3+}; Ca^{2+}, Cu^{1+}, Fe^{2+}, Fe^{3+}, Mg^{2+}, Si^{+4})(O^{2-}, S^{2-}). Ce modèle tient compte de l'ordre à courte distance entre les cations seconds voisins {cations basiques (Ca^{2+}, Fe^{2+}, etc.) et acides (Si^{4+})}, tandis que l'ordre à courte distance entre les premiers voisins est supposé être complet. Les bases de données pour les sous-systèmes d'oxydes optimisées auparavant, ré-optimisées et récemment obtenues ont été combinées et complétées avec les composants à base de soufre. La base de données de laitier résultante est capable de décrire les relations de phases dans les systèmes d'oxydes, ainsi que les capacités du soufre. L'effet du soufre sur la solubilité du cuivre dans les scories est démontré et modélisé. Ceci est d'une importance primordiale pour l'industrie qui s'efforce d'éviter les pertes de cuivre dans les scories. L'effet du calcium sur la solubilité du cuivre et du soufre dans le laitier de fayalite est modélisé quantitativement pour la première fois.

Le cuivre et le calcium sont ajoutés dans la base de données de la spinelle d'une manière thermodynamiquement compatible. La base de données de la spinelle peut être utilisée pour estimer l'usure des matériaux réfractaires et pour surveiller les conditions permettant d'éviter la précipitation de spinelle ; cette dernière pouvant provoquer l'occlusion des réacteurs. Cette base de données est capable de prédire la distribution des cations entre les sous-réseaux ; ce qui est important pour les applications électroniques.

La capacité prédictive de la base de données est testée au cours de la simulation d'un four de fusion. Les résultats des calculs sont comparés aux données d'usine. Un très bon accord est démontré lors de l'estimation des bilans d'énergie et de matière et lors de la prédiction des distributions d'éléments entre les sorties du four.

Ainsi, la base de données thermodynamiques pour les applications dans la production pyrométallurgique du cuivre que nous avons développée dans le cadre de ce projet est la plus précise et la plus complète au monde. Elle est destinée à être utilisée avec le logiciel FactSage™. En utilisant les méthodes affinées dans cette étude, d'autres éléments peuvent être facilement

ajoutés à la base de données. Les travaux se poursuivent actuellement par l'ajout de Co, Pb, Ni et Zn.

ABSTRACT

Introduction of thermodynamic modeling into the practice of the pyrometallurgical copper production may significantly increase the economic efficiency and environmental friendliness of the industry. A reliable thermodynamic database in combination with the Gibbs energy minimizing software is able to predict the energy balance, distribution of elements, phase transformations during the chemical process. Implemented in the control/simulation package, such thermodynamic database and software will be able to raise the process automation to a new level.

The goal of this thesis is the development of the database able to predict the thermodynamic properties and phase equilibria in the basic chemical system for the pyrometallurgical copper production, which is the Al–Ca–**Cu**–Fe–Mg–O–S–Si system. This involves the critical evaluation and thermodynamic optimization of available experimental data for all phases. The database is self-consistent, i.e. solid, liquid and gas phases are assessed simultaneously. 4 binary, 5 ternary, 7 quaternary, 2 quinary and 1 six-component system were evaluated or re-evaluated. The project is performed in close collaboration with the Pyrosearch group (University of Queensland, Australia), who performed some crucial experiments. Some of the above-mentioned systems were optimized together with T. Hidayat. In addition, 4 ternary and 5 quaternary systems were optimized by T. Hidayat in co-operation with the present author and reported in another Ph.D. thesis [1].

In particular, liquid metal and matte phases were described as one solution using the Modified Quasichemical Formalism in the pair approximation. The solution was built using one sublattice and uncharged species: (Cu^{I}, Cu^{II}, Fe^{II}, Fe^{III}, O, S). In this way, the model is able to describe wide deviations from stoichiometry in the sulfide phase towards excess metal or excess sulfur and oxygen. The oxygen solubility in the sulfide phase is correctly described. The model takes into account the existence of compositions of maximum first nearest neighbor short-range ordering near Cu_2O, CuO, FeO, Fe_2O_3, Cu_2S and FeS and predicts the drastic changes in $P(O_2)$ and $P(S_2)$ at these compositions. It accurately estimates the solubilities of sulfur and oxygen in metal region of the solution. It can be used to predict solid-liquid equilibria in chemical systems containing sulfide and oxide phases at low and high oxygen partial pressures.

The slag solution was modeled within the Quasichemical Formalism in quadruplet approximation. Cations are charged and placed in a separate sublattice from anions: (Al^{3+}, Ca^{2+}, Cu^{1+}, Fe^{2+}, Fe^{3+}, Mg^{2+}, Si^{+4})(O^{2-}, S^{2-}). The model of this type takes into account the second nearest neighbor short-range ordering between basic (Ca^{2+}, Fe^{2+}, etc.) and acidic (Si^{4+}) cations, while the first nearest neighbor short range ordering between metals and non-metals is assumed to be complete. Previously optimized, re-optimized and newly obtained databases for oxide subsystems were combined together and complemented with sulfide components. The resulting slag database is able to describe phase relations in oxide systems, as well as sulfide capacities. The effect of sulfur on the solubility of copper in slag is demonstrated and modeled. This is of primary importance for the industry which is trying to avoid copper losses into slag. The effect of calcium on the solubility of copper and sulfur in fayalite slag is modeled quantitatively for the first time.

Copper and calcium were added into the spinel database in a thermodynamically consistent way. The spinel database may be used to estimate the wearing of refractory materials and to monitor the conditions to prevent the spinel precipitation, which might cause occlusions of reactors. It is able to predict cation distribution between sublattices, which is important for electronic applications.

The predictive ability of the database was tested during the simulation of a smelting furnace. The calculation results are compared with the plant data. Very good agreement is demonstrated in the estimation of energy and mass balance and in the prediction of element distributions between outputs of the furnace.

Thus, the thermodynamic database for the applications in the pyrometallurgical production of copper, developed during the course of this project, is the most accurate and complete in the world. It is intended to be used with the FactSage^{TM} software. Using the methods, refined in this study, more elements can be easily added to the database. The work currently continues on the addition of Co, Pb, Ni and Zn to the database.

CONDENSÉ

Contexte

Le cuivre joue un rôle considérable dans la technologie moderne. Cependant, l'industrie de la production du cuivre est influencée par la volatilité du marché de même que toute autre sphère de l'économie. Une fois rentable, une usine pourrait se trouver être préjudiciable pour l'entreprise après le changement drastique des prix des matières premières et des produits ou après de nouvelles réglementations environnementales. Afin de restaurer la rentabilité, une réponse rapide du service de marketing est nécessaire pour estimer les coûts, et les paramètres du procédé alternatifs devraient être rapidement mis en œuvre par les opérateurs de l'usine. Idéalement, les paramètres du procédé devraient changer constamment en fonction des prix du marché pour donner le meilleur rendement économique. Il existe des entreprises qui mènent une telle surveillance en essayant d'atteindre la façon «constamment optimisée» de la production. Malheureusement, leur connaissance des processus physico-chimiques au cours de la production du cuivre n'a pas le même degré de précision que le marketing ou les modèles logistiques. Souvent, des réactions simplistes sont utilisées pour justifier un changement dans le procédé. Alternativement, des modèles empiriques basés sur des années d'expérience en exploitation d'une usine sont créés, et le changement majeur dans le procédé repose sur l'extrapolation de ces modèles. Les extrapolations ne fonctionnent pas toujours, sauf si elles sont basées sur des études fondamentales.

Ainsi, il existe une demande des entreprises métallurgiques pour la recherche dans un domaine de la thermodynamique chimique, qui prédit le résultat final des réactions chimiques et des transitions de phases si un temps suffisant est donné au système pour atteindre l'équilibre. Ces travaux commencent généralement en même temps que l'étude expérimentale. Jusqu'à récemment les expériences n'étaient complétées que par des corrélations empiriques. Avec le développement de la thermodynamique chimique, les lois fondamentales ont été utilisées pour vérifier la cohérence des résultats expérimentaux et pour donner des interpolations et des extrapolations correctes. Les capacités de calcul accrues ont permis la création de bases de données thermodynamiques électroniques. Ces bases de données stockent des paramètres de modelés thermodynamiques de toutes les phases possibles dans le système en fonction de la composition,

de la température et de la pression et, associées à un logiciel de minimisation de l'énergie de Gibbs, elles permettent de calculer l'équilibre physico-chimique du système complexe.

Cette thèse présente les résultats du projet consistant en la création de la base de données thermodynamiques destinée à modéliser la production pyrométallurgique du cuivre. Le projet est réalisé en collaboration avec le groupe Pyrosearch de l'Université de Queensland, en Australie. Les données expérimentales importantes manquantes sont fournies par ce groupe.

Énoncé du problème

Les phases les plus importantes au cours de la production pyrométallurgique du cuivre sont le laitier liquide, la matte et le cuivre brut. Le laitier est essentiellement un liquide d'oxydes, la matte est basée sur les sulfures liquides et le cuivre brut est un liquide métallique. Ces trois liquides sont capables de se mélanger dans une certaine mesure. Il est souhaitable de connaître la répartition de tous les éléments entre ces phases et la façon dont elle est régie par les paramètres du procédé.

Les propriétés thermodynamiques des phases solides, des sulfures, des oxydes et des métaux sont nécessaires pour prédire une précipitation possible à partir des phases liquides, pour calculer l'énergie nécessaire à la fonte des intrants du four et pour estimer la corrosion des matériaux réfractaires des parois du four. La solution solide de spinelle est une phase solide très importante et la phase solide la plus difficile à modéliser.

Les bases de données pour les phases solides et liquides doivent être compatibles les unes avec les autres et avec la base de données pour la phase gazeuse pour calculer la composition des gaz de sortie.

Objectifs

L'objectif principal de ce projet est de modéliser les propriétés thermodynamiques des solutions liquides, des solutions solides et des composés en cohérence avec la phase gazeuse pour le système chimique représentant le procédé de production pyrométallurgique du cuivre. Ce système se compose des sulfures, des oxydes et des métaux du système chimique Al–Ca–Cu–Fe–Mg–O–S–Si. Les défauts de la base de données précédente [2] doivent être corrigés. Par exemple, la solubilité de l'oxygène dans la matte et celle du soufre dans le cuivre brut doivent être prises en compte. Le cuivre et le calcium devraient être introduits dans la base de données de la spinelle.

L'effet du soufre sur la solubilité du cuivre dans le laitier doit être modélisé. Les phases liquides doivent être compatibles avec les sulfures solides ainsi que les oxydes solides. La base de données contient les paramètres du modèle, qui sont obtenus par la procédure d'optimisation thermodynamique décrite plus loin.

L'objectif principal comprend les objectifs secondaires, tels que la possibilité de calculer les solubilités et les activités des composants dans les phases, les températures et les compositions de solidification, le bilan énergétique lors de la fusion et lors du brûlage des intrants du four. Ces calculs sont possibles en intégrant les paramètres du modèle à partir de la base de données thermodynamiques à l'aide du logiciel thermodynamique FactSage^{TM} [3].

Méthodologie

Lors de la modélisation thermodynamique (ou l'optimisation thermodynamique) du système, les fonctions d'énergie de Gibbs sont affectées à chaque phase possible. Les énergies de Gibbs sont des fonctions de la température, de la pression et de la composition, et certaines approximations du modèle sont utilisées pour chaque phase du système. L'hypothèse principale sur laquelle se fonde ce projet est la suivante : aux fins de la production pyrométallurgique du cuivre, il est possible de modéliser la phase de laitier avec le Modèle Quasichimique Modifié (MQM) dans l'approximation des quadruplets, la phase matte - avec le MQM dans l'approximation des paires, et la phase de spinelle - avec le modèle basé sur le « Compound Energy Formalism » (CEF). Une fois que les fonctions d'énergie de Gibbs sont obtenues, toutes les autres propriétés peuvent être dérivées de manière analytique. Des hypothèses secondaires sont également nécessaires, telles que l'existence des équilibres $Cu^{I} \leftrightarrow Cu^{II}$ et $Fe^{II} \leftrightarrow Fe^{III}$ dans la phase de matte, l'occupation sélective par Ca^{2+} des sites octaédriques seuls dans la phase de spinelle, etc.

Une approche systématique a été utilisée dans cette étude pour obtenir les valeurs des paramètres du modèle. Dans l'optimisation thermodynamique, ou l'optimisation de type CALPHAD ("CALculation of PHAse Diagrams"), toutes les données thermodynamiques et données de diagrammes de phases disponibles sont évaluées simultanément afin d'obtenir un ensemble d'équations du modèle pour les énergies de Gibbs de toutes les phases en fonction de la température et de la composition. A partir de ces équations, toutes les propriétés thermodynamiques et les diagrammes de phases peuvent être calculés en retour. De cette façon,

toutes les données sont rendues auto-cohérentes et conformes aux principes de la thermodynamique. Des données sur les propriétés thermodynamiques, telles que les données d'activité, peuvent aider à l'évaluation du diagramme de phases, et les mesures du diagramme de phases peuvent être utilisées pour déduire les propriétés thermodynamiques. Les écarts dans les données disponibles peuvent souvent être résolus, et des interpolations et extrapolations peuvent être faites de manière thermodynamiquement correcte. On obtient un petit ensemble de paramètres du modèle; ce qui est idéal pour le stockage informatique et le calcul des propriétés et des diagrammes de phases. La méthodologie peut être représentée par les étapes suivantes :

• Étape 1. Revue de la littérature pour toutes les données expérimentales disponibles nécessaires à l'optimisation thermodynamique : diagrammes de phases, mesures calorimétriques et mesures d'activité, pression partielle, distribution des éléments entre les phases, etc.

• Étape 2. Construction de modèles thermodynamiques en définissant les taux d'occupation des cations ou les valences possibles des espèces.

• Étape 3. Estimation des paramètres du modèle, en commençant par les composés solides, puis les solutions solides et, enfin, les solutions liquides. Calculs initiaux et comparaisons avec les données expérimentales. Identification des zones avec des données expérimentales manquantes ou contradictoires.

• Étape 4. Demande d'informations expérimentales spécifiques à nos collaborateurs de Pyrosearch. Choix des conditions expérimentales en utilisant les calculs thermodynamiques initiaux. Retour à l'Étape 1.

• Étape 5. Obtention d'un dernier ensemble de paramètres du modèle. Justification des modèles dans le cas où toutes les données expérimentales sont reproduites dans les limites de l'erreur expérimentale.

La base de données obtenue sera transmise au groupe Pyrosearch, qui à son tour va l'utiliser pour la consultation de ses sponsors et clients industriels (BHP Billiton, Outotec et Xstrata Copper pour n'en nommer que quelques-uns). De cette façon, les résultats de la présente étude auront un impact sur les grandes entreprises internationales produisant le cuivre.

Organisation de la thèse

La thèse commence par un bref aperçu de la production pyrométallurgique du cuivre dans le Chapitre 1. La description mathématique des modèles thermodynamiques utilisés dans cette étude est ensuite donnée dans le Chapitre 2.

La prochaine partie est principalement consacrée à l'élaboration de la base de données de la matte; ce qui comprend l'examen des systèmes Cu–S, Fe–S et Cu–Fe–S précédemment optimisés suivi des corrections nécessaires (Chapitre 3), l'ajout de l'oxygène aux systèmes Cu–S et Fe–S (Chapitre 4 et Chapitre 5, respectivement), et la fusion des bases de données résultantes pour décrire les systèmes Cu–Fe–O (Chapitre 6) et Cu–Fe–O–S (Chapitre 7). Simultanément, les composés existants et les solutions solides sont modélisés et inclus dans la base de données thermodynamiques « fusionnée ».

Le Chapitre 6 commence par le développement de la solution solide de spinelle avec l'ajout de Cu à la spinelle Fe_3O_4. Cela se poursuit dans le Chapitre 8 par l'addition de Ca et l'évaluation de l'ensemble des systèmes connexes.

Dans le Chapitre 9, l'effet du soufre sur la solubilité du cuivre dans la phase de laitier du système Cu–Fe–O–S–Si est évalué. Dans le Chapitre 10, le calcium est ajouté au laitier et son influence est modélisée.

Enfin, la capacité prédictive de la base de données thermodynamiques est vérifiée par la simulation d'un véritable procédé industriel (Chapitre 11). Les prédictions du modèle sont comparées aux données d’usine.

Conclusions

Une base de données thermodynamiques pour la fonte et la conversion du cuivre a été développée. Elle inclut toutes les phases importantes du système chimique Al–Ca–Cu–Fe–Mg–O–S–Si. Les phases de sulfure solide, d’oxyde et de métal sont compatibles les unes avec les autres, avec le laitier liquide et la matte/métal, et avec la phase gazeuse. Les modèles thermodynamiques proposés sont basés sur les structures des phases correspondantes.

Les paramètres du modèle nouvellement optimisés pour les phases ont été intégrés dans les bases de données de FactSage.

Les phases, qui ont été étendues, et les systèmes chimiques évalués et optimisés dans la présente étude sont résumés ci-dessous.

Phases :

Matte/métal liquide: $\left(Cu^{I},\ Cu^{II},\ Fe^{II},\ Fe^{III},\ O,\ S\right)$

Laitier liquide: $\left(Al^{3+},\ Ca^{2+},\ Cu^{1+},\ Fe^{2+},\ Fe^{3+},\ Mg^{2+},\ Si^{4+}\right)\left(O^{2-},\ S^{2-}\right)$

Spinelle: $(Al^{+3},Cu^{+2},Fe^{+2},Fe^{+3},\ Mg^{+2})^{tetr}[Al^{+3},Ca^{+2},Cu^{+2},Fe^{+2},Fe^{+3},Mg^{+2},Va]_2^{oct}O_4^{-2}$

Monoxyde: ($AlO_{1.5}$, CaO, CuO, FeO, $FeO_{1.5}$, MgO)

Composés stœchiométriques: $CuSO_4$, Cu_2SO_4, $(CuO)(CuSO_4)$, $CuFeO_2$, $FeSO_4$, $Fe_2(SO_4)_3$, $CaFe_2O_4$, $Ca_2Fe_2O_5$, $CaFe_3O_5$, $CaFe_4O_7$, $CaFe_5O_7$, $Ca_4Fe_9O_{17}$, $Ca_4Fe_{17}O_{29}$, $CuAlO_2$.

Systèmes:

(1) Cu–O–S (Chapitre 4)

Une évaluation critique complète et l'optimisation des systèmes Cu–O et Cu–O–S ont été effectuées. Un modèle pour la phase liquide a été développé dans le cadre du formalisme quasichimique. Ce modèle décrit simultanément un liquide métallique, un liquide sulfuré (matte) et un liquide d'oxydes. Pour le système Cu–O, le modèle reflète l'existence de deux domaines d'ordre à courte distance à peu près aux compositions Cu_2O et CuO. Toutes les données thermodynamiques et données d'équilibre de phases disponibles ont été évaluées de manière critique afin d'obtenir un ensemble de paramètres du modèle optimisés pour les énergies de Gibbs de toutes les phases, permettant de reproduire les données expérimentales dans les limites de l'erreur expérimentale.

(2) Fe–O–S (Chapitre 5)

Une évaluation critique complète et l'optimisation des systèmes Fe–O et Fe–O–S ont été réalisées. Un modèle pour la phase liquide a été développé dans le cadre du formalisme quasichimique. Ce modèle décrit simultanément un liquide métallique, un liquide sulfuré (matte) et un liquide d'oxydes. Pour le système Fe–O, le modèle reflète l'existence de deux domaines d'ordre à courte distance à peu près aux compositions FeO et Fe_2O_3. Toutes les données thermodynamiques et données d'équilibre de phases disponibles ont été évaluées de manière critique afin d'obtenir un ensemble de paramètres du modèle optimisés pour les énergies de Gibbs

de toutes les phases, permettant de reproduire la majorité des données expérimentales dans les limites de l'erreur expérimentale. La lacune de miscibilité Fe–S–O entre les phases métallique et d'oxysulfure à haute température est décrite semi-quantitativement.

(3) Cu–Fe–O (Chapitre 6)

Une évaluation critique complète de tous les diagrammes de phases et données thermodynamiques disponibles pour le système Cu–Fe–O à une pression totale de 1 atm a été faite, et les paramètres des modèles thermodynamiques ont été optimisés afin de reproduire toutes les données expérimentales dans les limites de l'erreur expérimentale.

Un modèle pour la phase liquide a été développé dans le cadre du formalisme quasichimique. Il est applicable sur l'ensemble du domaine de compositions du métal liquide jusqu'à l'oxyde liquide. Le modèle de spinelle a été développé dans le cadre du « Compound Energy Formalism ». La formation de Cu^{+1} par sauts d'électrons suivant la réaction $Cu^{+2} + Fe^{+2} \rightarrow Cu^{+1} + Fe^{+3}$ a été prise en compte indirectement par l'introduction d'un paramètre en excès du modèle.

(4) Cu–Fe–O–S (Chapitre 7)

La base de données thermodynamiques, combinée à partir des bases de données obtenues antérieurement pour les systèmes Cu–O–S, Fe–O–S, Cu–Fe–O et Cu–Fe–S, s'est avérée capable de prédire les équilibres de phases chimiques dans le système Cu–Fe–O–S. Le paramètre ternaire $q^{001}_{Fe^{III}Cu^{I}(S)}$ a été optimisé pour mieux décrire les données expérimentales dans le système Cu–Fe–O–S. Ce paramètre ne peut être obtenue à partir des données de système ternaire Cu–Fe–S et n'a aucune influence sur il.

(5) Ca–Fe–O, Ca–Cu–Fe–O, Al–Cu–O, Al–Cu–Fe–O, Al–Ca–Fe–O, Ca–Fe–Mg–O (Chapitre 8)

La solution de spinelle a été étendue par l'ajout de Ca et Cu. Dans ce modèle, les cations Ca^{+2} occupent seulement le sous-réseau octaédrique, tandis que les cations Cu^{+2} occupent les deux sous-réseaux tétraédrique et octaédrique. La base de données de spinelle a été combinée avec des phases solides et liquides préalablement optimisées dans le système. Les calculs ont été effectués en utilisant la base de données combinée et ont été comparés avec les données expérimentales disponibles. Un très bon accord a été démontré.

(6) Fe–O–S–Si, Cu–Fe–O–S–Si (Chapitre 9)

Une évaluation critique complète de toutes les données thermodynamiques et données de diagrammes de phases disponibles pour les systèmes Fe–O–S–Si et Cu–Fe–O–S–Si à une pression totale de 1 atm a été faite. Un modèle pour la phase de laitier a été développé dans le cadre du formalisme quasichimique dans l'approximation des quadruplets. La base de données du laitier a été combinée avec des bases de données précédemment obtenues pour les phases solides et liquides dans ce système et a été utilisée pour prédire les équilibres laitier–matte dans des conditions proches de la production pyrométallurgique du cuivre. Un très bon accord avec les données expérimentales a été obtenu, en particulier pour la solubilité du cuivre dans la phase de laitier. Ceci est d'une importance primordiale pour l'industrie du cuivre, qui tente d'empêcher les pertes de cuivre dans les scories.

(7) Ca–Fe–O–S, Ca–O–S–Si et Ca–Cu–Fe–O–S–Si (Chapitre 10)

L'effet du calcium sur la solubilité du cuivre et du soufre dans le laitier est évalué. Les paramètres du modèle sont optimisés pour décrire quantitativement la solubilité du soufre et du cuivre pendant l'équilibre laitier-matte-métal et les capacités du soufre dans les laitiers sans cuivre.

L'application de la base de données est illustrée dans le Chapitre 11. Le procédé d'extraction du cuivre est simulé, en utilisant uniquement deux paramètres du procédé. Le bilan d'énergie et le bilan de matière calculés, ainsi que la distribution des éléments entre les sorties du four de fusion sont en bon accord avec les données d'usine.

La poursuite du développement de la base de données thermodynamiques présentée dans cette étude comprendra l'ajout de Ni, Co, Pb et Zn, qui sont des éléments mineurs mais importants au cours de l'extraction du cuivre pyrométallurgique. La base de données résultante pour le système chimique Al–Ca–Co–Cu–Fe–Mg–Ni–O–Pb–S–Si–Zn sera également applicable pour la simulation des procédés de production du nickel, du plomb et du zinc. La plupart des sous-systèmes de ce grand système ont déjà été optimisés, de sorte que le travail futur consistera à combler les lacunes.

TABLE OF CONTENTS

DEDICATION III

ACKNOWLEDGEMENTS IV

RÉSUMÉ V

ABSTRACT VIII

CONDENSÉ X

TABLE OF CONTENTS XVIII

LIST OF TABLES XXIV

LIST OF FIGURES XXV

INTRODUCTION 1

CHAPTER 1 PYROMETALLURGICAL PRODUCTION OF COPPER 6

CHAPTER 2 THERMODYNAMIC APPROACH TO THE MODELING OF PYROMETALLURGICAL COPPER PRODUCTION 10

2.1 Bragg-Williams formalism and geometric models 11

2.2 Matte (oxysulfide) and liquid metal 14

2.3 Slag 17

2.4 Spinel 19

CHAPTER 3 EVALUATION OF PREVIOUSLY MODELED SYSTEMS 26

3.1 Fe–S system 26

3.2 Cu–S system 34

3.3 Cu–Fe–S system 38

CHAPTER 4 ARTICLE 1: CRITICAL ASSESSMENT AND THERMODYNAMIC MODELING OF THE Cu–O AND Cu–O–S SYSTEMS 51

4.1 Introduction 51

4.2 Thermodynamic models 53

4.2.1 Liquid solution 53
4.2.2 Solid FCC copper 55
4.2.3 Digenite 56
4.3 The Cu–S system 56
4.4 The Cu–O system 57
4.4.1 Phase diagrams 57
4.4.2 Solid Cu_2O and CuO 59
4.4.3 Liquid phase 59
4.4.4 FCC solid solution 64
4.5 The Cu–O–S system 65
4.5.1 Phase diagrams 65
4.5.2 Solubility of oxygen in liquid copper and matte 70
4.5.3 Results of optimization 73
4.6 Conclusions 77
4.7 Acknowledgements 78
CHAPTER 5 CRITICAL ASSESSMENT AND THERMODYNAMIC MODELING OF THE Fe–O AND Fe–O–S SYSTEMS 83
5.1 Thermodynamic models 84
5.1.1 Liquid solution 85
5.1.2 Solid FCC and BCC iron 89
5.1.3 Monoxide 90
5.2 The Fe–S system 90
5.3 The Fe–O system 91
5.3.1 Phase diagram 91
5.3.2 Monoxide and spinel 92

5.3.3 Liquid phase 93
5.3.4 FCC and BCC solid solutions 97
5.4 The Fe–O–S system 98
5.4.1 Phase diagrams 98
5.4.2 Solubility of oxygen and sulfur in matte 105
5.4.3 Solubility of oxygen and sulfur in liquid iron 110
5.4.4 Optimization 112
5.5 Summary of results 114
CHAPTER 6 ARTICLE 2: CRITICAL ASSESSMENT AND THERMODYNAMIC MODELING OF THE Cu–Fe–O SYSTEM 120
6.1 Introduction 120
6.2 Binary systems 121
6.3 Thermodynamic models 124
6.3.1 fcc and bcc 124
6.3.2 Liquid solution 125
6.3.3 Monoxide 126
6.3.4 Spinel 127
6.4 Assessment of experimental data 134
6.4.1 Subsolidus phase equilibria 134
6.4.2 Equilibrium oxygen partial pressure 139
6.4.3 Solubility of copper in monoxide 142
6.4.4 Liquid phase 144
6.4.5 Oxygen non-stoichiometry of spinel 151
6.4.6 Solubility of oxygen in liquid Cu–Fe alloys 153
6.4.7 $CuFeO_2$ (Delafossite) 155

6.4.8 $CuFe_2O_4$ (Spinel) 158
6.5 Results of optimization 161
6.6 Conclusions 163
6.7 Acknowledgements 164
CHAPTER 7 EQUILIBRIA IN THE Cu–Fe–O–S SYSTEM 169
7.1 Thermodynamic models 170
7.1.1 Liquid solution 170
7.1.2 Solid FCC and BCC metal 171
7.1.3 Pyrrhotite, pyrite, ISS, covellite, digenite-bornite 172
7.2 Phase equilibria 173
7.2.1 Subsolidus equilibria at $P(SO_2)$ = 1 atm 181
7.2.2 Oxygen and sulfur content of single-phase matte 185
7.2.3 Matte–spinel equilibrium 200
7.3 Optimization of parameters 203
7.4 Summary of results 205
CHAPTER 8 DEVELOPMENT OF THE SPINEL DATABASE IN THE Al–Ca–Cu–Fe–Mg–O SYSTEM 211
8.1 Ca–Fe–O system 211
8.1.1 Thermodynamic model for spinel 211
8.1.2 Results of optimization 213
8.2 Ca–Cu–Fe–O system 216
8.2.1 Thermodynamic model for spinel 216
8.2.2 Results of optimization 216
8.3 Al–Cu–O and Al–Cu–Fe–O systems 220
8.3.1 Thermodynamic model for spinel 220

8.3.2 Results of optimization....221
8.4 Al–Ca–Fe–O system....226
8.4.1 Thermodynamic model for spinel....226
8.4.2 Results of optimization....227
8.5 Ca–Fe–Mg–O system....230
8.5.1 Thermodynamic model for spinel....230
8.5.2 Results of optimization....230
8.6 Summary of results....232
CHAPTER 9 DEVELOPMENT OF THE THERMODYNAMIC DATABASE FOR COPPER SMELTING AND CONVERTING. THE Cu–Fe–O–S–Si SYSTEM....245
9.1 Fe–O–S–Si system....248
9.2 Experimental studies of slag–matte equilibrium....251
9.2.1 Slag–matte–SiO_2–metal equilibrium....252
9.2.2 Slag–matte–SiO_2–SO_2 equilibrium....259
9.3 Optimization of parameters and results....266
CHAPTER 10 EFFECT OF Ca ON MATTE–SLAG EQUILIBRIA DURING COPPER SMELTING AND CONVERTING....272
10.1 Ca–Fe–O–S and Ca–O–S–Si systems....272
10.2 Ca–Cu–Fe–O–Si system....274
10.3 Ca–Cu–Fe–O–S system....276
10.4 Ca–Cu–Fe–O–S–Si system....280
10.5 Optimization of parameters and results....283
10.5.1 Alternative optimization attempts and long range parameter....284
CHAPTER 11 SIMULATION OF THE ISASMELT™ FURNACE....288
11.1 The ISASMELT™ process....290

11.1.1 Mount Isa Copper ISASMELT™ Plant 291
11.1.2 Southern Peru Ilo Smelter 294
11.1.3 Smelting mechanism 299
11.2 Modeling 301
11.2.1 Thermodynamic database 301
11.2.2 Equilibrium approximation 301
11.2.3 Operating FactSage streams 302
11.3 Discussion 304
11.4 Summary of results 309
GENERAL DISCUSSIONS AND CONCLUSIONS 310
LIST OF REFERENCES 314

LIST OF TABLES

Table 4-1. Calculated invariant points in the Cu–O–S system. 77

Table 4-2. Optimized properties of stoichiometric compounds and model parameters for the liquid, fcc and digenite solid solutions in the Cu–O–S system ($J \cdot mol^{-1}$ and $J\ mol^{-1} \cdot K^{-1}$) 79

Table 5-1. Calculated invariant points in the Fe–O–S system. 114

Table 5-2. Optimized properties of stoichiometric compounds and model parameters for liquid and solid solutions in the Fe–O–S system ($J \cdot mol^{-1}$ and $J\ mol^{-1} \cdot K^{-1}$) 116

Table 6-1. Optimized properties of stoichiometric compounds in the Cu–Fe–O system 165

Table 6-2. Optimized model parameters for liquid and solid solutions in the Cu–Fe–O system 165

Table 7-1. Calculated four-phase invariant equilibria in the Cu–Fe–O–S system at 700, 900 and 1200 °C and P = 1 atm 174

Table 7-2. Optimized properties of stoichiometric compounds and model parameters for liquid and solid solutions in the Cu–Fe–O–S system ($J \cdot mol^{-1}$ and $J \cdot mol^{-1} \cdot K^{-1}$) 206

Table 8–1. Optimized thermodynamic properties of stoichiometric compounds and model parameters for liquid and solid solutions in the Al–Ca–Cu–Fe–Mg–O system ($J \cdot mol^{-1}$ and $J \cdot mol^{-1} \cdot K^{-1}$) 233

Table 9-1. Optimized properties of stoichiometric compounds and solutions in the Cu–Fe–O–S–Si system 269

Table 10-1. Optimized properties of stoichiometric compounds and model parameters in the Ca-Cu-Fe-O-S-Si system ($J\ mol^{-1}$ and $J\ mol^{-1} \cdot K^{-1}$).....287

Table 11-1. Concentrate, Flux and Reverts flows for simulation of the Player [400] results.....304

Table 11-2. Coke flow for simulation of the Player [400] results.....305

Table 11-3. Blow and Ingress air* flow for simulation of the Player [400] results.....305

Table 11-4. Moisture flow for simulation of the Player [400] results.....305

Table 11-5. Equilibrium simulation results.....306

Table 11-6. Material balance: simulation results and plant assays [400].....306

LIST OF FIGURES

Figure 1.1. World export of refined copper and copper alloys in 2010. 6

Figure 1.2. Principal processes for extracting copper from sulfide ores [5]. Parallel lines indicate alternative processes. 7

Figure 2.1. Geometric models for estimating ternary thermodynamic properties from optimizaed binary data. 13

Figure 2.2. The 3D model of $MgAl_2O_4$ completely normal spinel. Mg (green) occupy 1/8 of the tetrahedral interstices, Al (grey) occupy half of the octahedral interstices. 20

Figure 3.1. Phase diagram of the Fe–S system and S_2-isobar at 1 atm. Experimental points [28-54] and calculated lines: thin red lines – [26], black lines – this study. 28

Figure 3.2. Activity of sulfur in the Fe–S system expressed as $P(S_2)$, (a) – the overview (b) – metal region (c) – sulfide region. Experimental points [33, 34, 36, 53-63] and calculated lines: thin solid – [26], thick dashed – this study. 30

Figure 3.3. Enthalpy of mixing of ½ S_2(gas) and either Fe(fcc) at 1200 °C or liquid iron at other temperatures. Experimental points [64-67] and calculated lines: thick dashed – this study, thin solid lines – [26]. 31

Figure 3.4. Phase diagram of the Fe–S system in the metal region. Experimental points [68-73] and calculated lines: thin red lines – [26], black lines – this study. 31

Figure 3.5. Potential phase diagram of the Fe–S system. Experimental points [33-36, 41, 47, 60, 69, 71-77] and calculated lines: solid – this study, dashed red line – [26]. 32

Figure 3.6. Activity coefficient of sulfur in Fe–O–S liquid in the metal region at 1500 °C. Experimental points [27, 57] and calculated lines: solid – this study, dotted line – [26]. 32

Figure 3.7. Activity coefficient of sulfur in Fe–O–S liquid in the metal region at 1550 °C. Experimental points [27, 56, 57, 61-63] and calculated lines: solid – this study, dotted line – [26]. 33

Figure 3.8. Activity coefficient of sulfur in Fe–O–S liquid in the metal region at 1600 °C. Experimental points [27, 55-57] and calculated lines: solid – this study, dotted line – [26]. 33

Figure 3.9. Value of the main excess parameter $\Delta g^{\circ}_{Fe^{I}S}$ in the present study and in the optimization of Waldner and Pelton [26]. 34

Figure 3.10. Phase diagram of the Cu–S system. Gas phase is suppressed. Experimental points [36, 79-91] and calculated lines: thin red lines – [92], black solid lines – phase boundaries in this study, dashed lines – sulfur isobars in this study. 35

Figure 3.11. Activity of sulfur in the Cu–S system expressed as $P(S_2)$, (a) – the overview (b,c) – metal region (d) – sulfide region. Experimental points [36, 80, 81, 85, 93, 94] and calculated lines: dashed – [92], solid – this study. 37

Figure 3.12. Excess parameter $g^{90}_{Cu^{I}S}$ in the Cu–S system. 38

Figure 3.13. Metal region of the Cu–S phase diagram. Experimental points [95, 96] and calculated lines: thin red lines – [92], black lines – this study. 38

Figure 3.14. $CuFeS_2$–$FeS_{1.08}$ section of the phase diagram of the Cu–Fe–S system. Experimental points [97, 98, 104] and calculated lines: thin red lines – [92], black lines – this study. Formation of gas phase is suppressed. 41

Figure 3.15. Cu_5FeS_4–S section of the phase diagram of the Cu–Fe–S system. Experimental points [99] and calculated lines: thin red lines – [92], black lines – this study. Formation of gas phase is suppressed. 41

Figure 3.16. Cu–$Fe_{0.4950}S_{0.5049}$ (Fe/S = 1/1.02) section of the phase diagram of the Cu–Fe–S system. Experimental points [97] and calculated lines: thin red lines – [92], black lines – this study. Formation of gas phase is suppressed. 42

Figure 3.17. Cu_2S–$FeS_{1.08}$ section of the phase diagram of the Cu–Fe–S system. Experimental points [97, 105-109] and calculated lines: thin red lines – [92], black lines – this study. Formation of gas phase is suppressed. 42

Figure 3.18. Isothermal section of the Cu–Fe–S phase diagram at 1350 °C. Experimental points [97, 102] and calculated lines: thin red lines – [92], black lines – this study. Formation of gas phase is suppressed. 43

Figure 3.19. Isothermal section of the Cu–Fe–S phase diagram at 1250 °C. Experimental points [60, 97, 102] and calculated lines: thin red lines – [92], black lines – this study. Formation of gas phase is suppressed. 43

Figure 3.20. Isothermal section of the Cu–Fe–S phase diagram at 1200 °C. Experimental points [36, 97, 110, 111] and calculated lines: thin red lines – [92], black lines – this study. Formation of gas phase is suppressed. 44

Figure 3.21. Isothermal section of the Cu–Fe–S phase diagram at 1150 °C. Experimental points [102, 105] and calculated lines: thin red lines – [92], black lines – this study. Formation of gas phase is suppressed. 44

Figure 3.22. Isothermal section of the Cu–Fe–S phase diagram at 1000 °C. Calculated lines: thin red lines – [92], black lines – this study. Formation of gas phase is suppressed. 45

Figure 3.23. Isothermal section of the Cu–Fe–S phase diagram at 800 °C. Calculated lines: thin red lines – [92], black lines – this study. Formation of gas phase is suppressed. 45

Figure 3.24. Isothermal section of the Cu–Fe–S phase diagram at 700 °C. Experimental points [109] and calculated lines: thin red lines – [92], black lines – this study. Formation of gas phase is suppressed.....46

Figure 3.25. Isothermal section of the Cu–Fe–S phase diagram at 600 °C. Experimental points [112] and calculated lines: thin red lines – [92], black lines – this study. Formation of gas phase is suppressed.....46

Figure 3.26. Sulfur potential (expressed as equilibrium partial pressure of S_2) in the Cu–Fe–S system at 1200 °C. Experimental points [36, 111] and calculated lines: thin solid line – [92], thick dashed line – this study. Calculated lines correspond to experimental conditions. 47

Figure 3.27. Sulfur potential (expressed as equilibrium partial pressure of S_2) in the Cu–Fe–S system. Experimental points [102] and calculated lines: thin solid line – [92], thick dashed line – this study. Calculated lines correspond to experimental conditions. 47

Figure 3.28. Sulfur potential (expressed as equilibrium partial pressure of S_2) in the Cu–Fe–S system. Experimental points [102] and calculated lines: thin solid line – [92], thick dashed line – this study. Calculated lines correspond to experimental conditions. 48

Figure 3.29. Sulfur potential (expressed as equilibrium partial pressure of S_2) in the Cu–Fe–S system at 1250 °C. Experimental points [60] and calculated lines: thin solid line – [92], thick dashed line – this study. Calculated lines correspond to experimental conditions. 48

Figure 3.30. $CuFeS_2$–Cu_2S section of the phase diagram of the Cu–Fe–S system. Experimental points [97, 98, 113] and calculated lines: thin red lines – [92], black lines – this study. Formation of gas phase is suppressed. 49

Figure 3.31. $Cu_{0.5}Fe_{0.5}$–S section of the phase diagram of the Cu–Fe–S system. Experimental points [98, 103, 109, 112] and calculated lines: thin red lines – [92], black lines – this study. Formation of gas phase is suppressed. 50

Figure 3.32. $Cu_{0.556}S_{0.444}$–Fe (Cu/S = 5/4) section of the phase diagram of the Cu–Fe–S system. Experimental points [97] and calculated lines: thin red lines – [92], black lines – this study. Formation of gas phase is suppressed. 50

Figure 4.1. Calculated entropy of mixing in Cu–O liquid at 1200 °C. 54

Figure 4.2. Calculated distribution of copper between Cu^{I} and Cu^{II} in Cu–O liquid at 1200 °C. .54

Figure 4.3. Calculated phase diagram of the Cu–O system along with experimental points [121-136] and special points from assessment [120]. Dashed lines are calculated oxygen isobars. The scatter of the experimental data collected by Hallstedt *et al*. [118] for each special point is shown by red rectangles. Gas phase is suppressed. 58

Figure 4.4. Calculated potential phase diagram of the Cu–O system along with experimental points [124, 125, 127, 129, 130, 135-140] and invariant points from assessment [120]. The scatter of the experimental data collected by Hallstedt *et al*. [118] for each invariant point is shown by bars. The gas phase is suppressed. 58

Figure 4.5. Calculated oxygen potential in Cu–O liquid expressed as isotherms along with experimental points [125, 127, 132, 137].....59

Figure 4.6. Gibbs energy of dissolution of oxygen in liquid Cu at infinite dilution with 1 mole % O liquid and 1 atm O_2 gas as reference states. Dotted and dashed lines represent the experimental data [125, 132, 141] and the assessment of Hallstedt *et al.* [118]. Thin solid lines show other series of experimental data reviewed by Hallstedt *et al.* [118]. Thick black line is calculated using the model parameters of the present study. 61

Figure 4.7. First-order interaction coefficient for O in liquid Cu. Dotted and dashed lines represent the experimental data [125, 127, 132] and the assessment of Hallstedt *et al.* [118]. Thin solid lines show other series of experimental data reviewed by Hallstedt *et al.* [118]. Thick black line is calculated using the model parameters of the present study. 61

Figure 4.8. Gibbs energy of formation of liquid Cu_2O from liquid copper and O_2 gas at 1 atm. The solid line is calculated from the model parameters for the liquid phase optimized in the present study. The other lines were derived by Taskinen [132] from EMF measurements [127, 129, 132, 144]. 62

Figure 4.9. Heat content of Cu_2O: experimental points [142, 143] and calculated lines indicating optimizations of the present study and of Hallstedt *et al.* [118]. 62

Figure 4.10. Solubility of oxygen in fcc (solid Cu) phase: experimental points [147-154] and calculated lines. 64

Figure 4.11. Calculated isothermal section of the Cu–O–S phase diagram at 1250 °C and P = 1 atm. 65

Figure 4.12. Liquid metal + matte region on the Cu–O–S isothermal sections at P = 1 atm: experimental points [155] and calculated lines. The corresponding $P(SO_2)$ is indicated for each metal – matte tie-line. (a) 1100 °C, (b) 1250 °C. 66

Figure 4.13. (a) Equilibrium $P(SO_2)$ over liquid metal + matte tie-lines in the Cu–S–O system. (b) Solubility of oxygen in Cu–S–O matte in equilibrium with liquid copper and SO_2/N_2 gas mixtures. Experimental points [155, 156] and calculated lines. 67

Figure 4.14. $P(S_2)$ vs $P(O_2)$ dependence in the liquid metal + matte region of the Cu–O–S system: experimental points [157, 158] and calculated lines. 68

Figure 4.15. Cu_2O–Cu_2S isopleth. Formation of the gas phase is suppressed. Circles represent the phase diagram estimated by Oelsen [159], lines are calculated from the model parameters optimized in the present study. 69

Figure 4.16. $P(SO_2)$ over tie-lines between metallic Cu phases and oxysulfide phases located approximately along the Cu_2O–Cu_2S join. Formation of the gas phase is suppressed. Full lines are calculated from the model parameters optimized in the present study, the other lines represent $P(SO_2)$ estimated by Oelsen [159]. 69

Figure 4.17. Liquid copper region of the Cu–O–S phase diagram: experimental points [155, 164, 165] and calculated phase boundaries and $P(SO_2)$ isobars. 71

Figure 4.18. Relationship between $P(O_2)$ and oxygen content of liquid copper in the Cu–O–S system at fixed $P(SO_2)$. Experimental points [165, 166] and calculated lines.....71

Figure 4.19. Activity coefficient of oxygen in Cu–O–S liquid: experimental points [166-168] and calculated lines. The break in the X-axis is introduced to enlarge the liquid metal and matte regions. 73

Figure 4.20. Calculated potential phase diagram of the Cu–O–S system at $P(SO_2)$ = 1 atm. 74

Figure 4.21. Calculated liquidus projection for the Cu–O–S system in the oxysulfide liquid region. Gas phase is suppressed. 76

Figure 5.1. Calculated enthalpy of mixing (solid line) and its derivative (dashed line) in Fe–O liquid at 1600 ° C. 86

Figure 5.2. Calculated distribution of iron between Fe^{II} and Fe^{III} in Fe–O liquid at 1600 °C. 87

Figure 5.3. (a) Calculated phase diagram of the Fe–O system along with experimental points [188-191]. Dashed lines are calculated oxygen isobars. Gas phase is suppressed. (b) Enlarged FeO–Fe_2O_3 part of the same diagram. Grey thin lines are from previous optimization [21]. References for subsolidus experimental points are given in [21]. 92

Figure 5.4. Calculated oxygen potential in Fe–O liquid expressed as isotherms along with experimental points [188, 192-197]. 93

Figure 5.5. Gibbs energy of dissolution of oxygen in liquid Fe at infinite dilution with 1 mole % O liquid and 1 atm O_2 gas as reference states. Experimental data [192-198]. Dotted line is the assessment from [199]. 95

Figure 5.6. First-order interaction coefficient for O in liquid Cu. Experimental data [192-198]. Dotted line is the assessment from [199]. 96

Figure 5.7. Solubility of oxygen in FCC and BCC (solid Fe) phase: experimental points [200, 201] and calculated lines. 97

Figure 5.8. Potential phase diagram of the Fe–O–S system at $P(SO_2)$ = 1 atm. 98

Figure 5.9. Calculated isothermal section of the Fe–O–S phase diagram at 1200 °C and P = 1 atm. 102

Figure 5.10. Liquidus projection of the Fe–O–S system (FeO–FeS region). The formation of the gas phase is suppressed. Experimental invariant points from [186, 208, 212, 214]. 102

Figure 5.11. Isothermal sections of the Fe–S–O phase diagram with superimposed O_2 and S_2 isobars at a) 1000 °C b) 1100 °C and 1120 c) 1200 °C d) 1300 °C e) 1400 °C f) 1450 °C and P = 1 atm. Experimental points from [15, 208-211, 213]. Solid lines – calculated. 104

Figure 5.12. Projection of the Fe–S–O phase diagram in equilibrium with iron on the FeS–FeO section through the Fe corner. Experimental points from [100, 208, 209, 213, 214]. 105

Figure 5.13. Partial pressure of oxygen along the matte-iron border in the Fe–O–S system. Experimental points: [15, 211, 213, 214]. 108

Figure 5.14. Solubility of oxygen and sulfur in Fe–O–S oxysulfide melt at 1200 °C. 109

Figure 5.15. Liquidus projection of the Fe–S–O system near the Fe corner. Experimental points [208] and calculated lines. 110

Figure 5.16. Effect of sulfur on the activity coefficient of oxygen in Fe–O–S metallic liquid: experimental points [27], dashed lines – calculated using parameters from [224], solid lines – calculated in this study. 112

Figure 5.17. Effect of oxygen on the activity coefficient of sulfur in Fe–O–S metallic liquid: experimental points [27], dashed lines – calculated using parameters from [224], solid lines – calculated in this study. 112

Figure 6.1. Phase diagram of the Cu–Fe system. Solid and dashed lines are calculated based on the optimizations of Ansara and Jansson [225] and of Swartzendruber [228], respectively. 122

Figure 6.2. Calculated phase diagram of the Cu–O system [114]. Oxygen isobars are shown by the short-dashed lines. 123

Figure 6.3. Calculated phase diagram of the Fe–O system [227]. Oxygen isobars are shown by the short-dashed lines. 123

Figure 6.4. Degree of inversion of $CuFe_2O_4$ spinel: s is the number of moles of copper on the octahedral sublattice. 129

Figure 6.5. Degree of inversion in Fe_3O_4–$CuFe_2O_4$ spinel: experimental points [249-258] and calculated lines. *s* is the number of moles of Cu on the octahedral sublattice per formula unit of spinel $(Cu_{x-s},Fe_{1-x+s})^{tetr}[Cu_{s/2},Fe_{1-s/2}]_2^{oct}O_4$. 132

Figure 6.6. (a) Calculated isothermal section of the Cu–Fe–O phase diagram at 1000 °C and *P* = 1 atm. (b) Magnification of the oxide part of the Cu–Fe–O diagram. 135

Figure 6.7. (a) Calculated isothermal section of the Cu–Fe–O phase diagram at 800 °C and *P* = 1 atm. (b) Magnification of the oxide part of the Cu–Fe–O diagram. 136

Figure 6.8. Calculated isothermal section of the Cu–Fe–O phase diagram at 600 °C and *P* = 1 atm. 137

Figure 6.9. Fe_3O_4–$CuFe_2O_4$ section of the Cu–Fe–O system at *P* = 1 atm: experimental data [177, 226, 259, 262, 264, 267, 270-272] and calculated lines. 139

Figure 6.10. Equilibrium oxygen partial pressures over three-phase regions in the Cu–Fe–O system: calculated lines and experimental points [231, 264-267, 273-277]. 141

Figure 6.11. Phase diagram of the Cu–Fe–O system at 1000 °C. Equilibrium oxygen partial pressure versus molar metal ratio: points indicate experimental data [267, 271, 272, 279, 280], solid lines are calculated from model parameters optimized in this study and dashed lines represent the optimization of Khvan et *al.* [177]. 142

Figure 6.12. Solubility of CuO in wüstite at 1000 °C in the Cu–Fe–O system: experimental points [231] and calculated lines. Solid and open squares indicate single-phase and two-phase regions, respectively. 143

Figure 6.13. Oxygen partial pressure in the monoxide region of the Cu–Fe–O system at 1000 °C: experimental points [231] and calculated lines. Solid and open squares indicate single-phase and two-phase regions, respectively. The compositions of points are shown in the previous figure. 143

Figure 6.14. Calculated isothermal section of the Cu–Fe–O phase diagram at 1200 °C and P = 1 atm. Calculated and experimental [281] oxygen isoactivity lines are superimposed over the oxide liquid region. 145

Figure 6.15. (a) Calculated isothermal section of the Cu–Fe–O phase diagram at 1500 °C and P = 1 atm. Calculated and experimental [282] tie-lines between liquid oxide and liquid metal. (b) Equilibrium $P(O_2)$ corresponding to these tie-lines. (c) Calculated distribution of iron between the Fe^{II} and Fe^{III} species and of copper between the Cu^{I} and Cu^{II} species in the oxide liquid end of these tie-lines. 146

Figure 6.16. Calculated distribution of iron between the Fe^{II} and Fe^{III} species and of copper between the Cu^{I} and Cu^{II} species in Cu–Fe–O oxide liquid at 1500 °C and fixed oxygen pressure. The formation of solid oxide phases is suppressed.....147

Figure 6.17. Phase diagram of the Fe_3O_4–Cu_2O quasi-binary section. Oxide phases are in equilibrium with solid or liquid metal copper for the majority of compositions and temperatures. Points and thin lines indicate experimental liquidus and invariant temperatures [226, 283, 284, 286]. Thick solid lines and dotted lines are calculated phase boundaries and oxygen isobars, respectively. 149

Figure 6.18. Phase diagram of the Cu–Fe–O system in air. Experimental points are from References [257, 266, 270, 287-295], solid lines are calculated from the model parameters optimized in the present study and dashed lines are calculated from the optimization of Khvan *et al.* [177].....150

Figure 6.19. Phase diagram of the Cu–Fe–O system at $P(O_2)$ = 1 atm. Experimental points are from Gadalla and White [296], solid lines are calculated from the model parameters optimized in the present study and dotted lines are calculated from the optimization of Khvan *et al.* [177].....151

Figure 6.20. Calculated Fe_3O_4–$CuFe_2O_4$–Fe_2O_3 region of the Cu–Fe–O phase diagram at 1250 °C and P = 1 atm. Calculated oxygen isobars are shown by dotted lines and correspond to experimental points [251, 259].....152

Figure 6.21. Gibbs energy of dissolution of oxygen in liquid Cu–Fe alloys at infinite dilution with 1 mole % O liquid and 1 atm O_2 gas as reference states: experimental points [196, 282, 297-301] and calculated lines. 155

Figure 6.22. Heat capacity of $CuFeO_2$. Experimental points [269] and calculated line. 156

Figure 6.23. Heat content of $CuFeO_2$. Experimental points [269] and calculated line. The break in the heat content corresponds to the incongruent melting of $CuFeO_2$. 157

Figure 6.24. Heat capacity of $CuFe_2O_4$. Points indicate experimental data [229, 230, 306]. Calculated solid and dotted lines correspond to cubic spinel with equilibrium and with frozen cation distributions, respectively. 161

Figure 6.25. Heat content of $CuFe_2O_4$. Points are experimental data of Barany *et al.* [269]. Calculated solid and dotted lines correspond to *cubic* spinel with equilibrium and with frozen cation distributions, respectively. 161

Figure 7.1. Isothermal section of the Cu–O–S phase diagram at 700 °C and 900 °C and P = 1 atm. 176

Figure 7.2. Isothermal section of the Cu–Fe–S phase diagram at 700 °C and 900 °C and P = 1 atm. 177

Figure 7.3. Isothermal section of the Cu–Fe–O phase diagram at 700 °C and 900 °C and P = 1 atm. 177

Figure 7.4. Isothermal section of the Fe–O–S phase diagram at 700 °C and 900 °C and P = 1 atm. 178

Figure 7.5. Isothermal section of the Cu–Fe–O–S phase diagram at 700 °C and 900 °C and P = 1 atm. 2-phase equilibria are shown using blue lines, 3-phase – using red lines, 4-phase equilibria – using black lines and facets. The 3-D figure files are available in the supplementary data. They may be opened by the MATLAB® software. 178

Figure 7.6. Isothermal section of the Cu–O–S phase diagram at 1200 °C and P = 1 atm. 179

Figure 7.7. Isothermal section of the Cu–Fe–S phase diagram at 1200 °C and P = 1 atm. 180

Figure 7.8. Isothermal section of the Cu–Fe–O phase diagram at 1200 °C and P = 1 atm. 180

Figure 7.9. Isothermal section of the Fe–O–S phase diagram at 1200 °C and P = 1 atm. 181

Figure 7.10. (a) Isothermal section of the Cu–Fe–O–S phase diagram at 1200 °C and P = 1 atm. Single phase regions are shown using green points, 2-phase equilibria are shown using blue lines and points, 3-phase – using red lines and points, 4-phase equilibria – using black lines and facets. (b) The same, but only the liquid phases are shown. The 3-D figure file is available in the supplementary data. It may be opened with the MATLAB® software. 181

Figure 7.11. Oxygen potential for 1 atm of SO_2 as a function of temperature for assemblages in the Cu–Fe–O–S system: calculated lines and experimental points [101]. 183

Figure 7.12. Oxygen potential for 1 atm of SO_2 as a function of temperature for assemblages in the Cu–Fe–O–S system: calculated lines and experimental points [101]. 183

Figure 7.13. Oxygen potential for 1 atm of SO_2 as a function of temperature for assemblages in the Cu–Fe–O–S system: calculated lines and experimental points [101]. 184

Figure 7.14. Oxygen potential in the Cu–Fe–O–S system at 727 °C and $P(SO_2)$ = 1 atm. Solid lines are model calculations, dashed lines are the assessment of Rosenqvist and Hofseth [101]. 184

Figure 7.15. Oxygen potential in the Cu–Fe–O–S system at 827 °C and $P(SO_2)$ = 1 atm. Solid lines are model calculations, dashed lines are the assessment of Rosenqvist and Hofseth [101]. 185

Figure 7.16. Oxygen potential in the Cu–Fe–O–S system at 977 °C and $P(SO_2)$ = 1 atm. Solid lines are model calculations, dashed lines are the assessment of Rosenqvist and Hofseth [101]. 185

Figure 7.17. Symbol shapes used in the following figures. 188

Figure 7.18. Calculated sulfur and oxygen content of the Cu–Fe–O–S matte as functions of Po, Ps and Fe/(Cu + Fe) ratio. Experimental points (see Figure 7.17) and calculated lines. 190

Figure 7.19. Calculated sulfur and oxygen content of the Cu–Fe–O–S matte as functions of Po, Ps and Fe/(Cu + Fe) ratio. Experimental points (see Figure 7.17) and calculated lines. 191

Figure 7.20. Calculated sulfur and oxygen content of the Cu–Fe–O–S matte as functions of Po, Ps and Fe/(Cu + Fe) ratio. Experimental points (see Figure 7.17) and calculated lines. 192

Figure 7.21. Calculated sulfur and oxygen content of the Cu–Fe–O–S matte as functions of Po, Ps and Fe/(Cu + Fe) ratio. Experimental points (see Figure 7.17) and calculated lines. 193

Figure 7.22. Calculated sulfur and oxygen content of the Cu–Fe–O–S matte as functions of Po, Ps and Fe/(Cu + Fe) ratio. Experimental points (see Figure 7.17) and calculated lines. 194

Figure 7.23. Calculated sulfur and oxygen content of the Cu–Fe–O–S matte as functions of Po, Ps and Fe/(Cu + Fe) ratio. Experimental points (see Figure 7.17) and calculated lines. 195

Figure 7.24. Calculated sulfur and oxygen content of the Cu–Fe–O–S matte as functions of Po, Ps and Fe/(Cu + Fe) ratio. Experimental points (see Figure 7.17) and calculated lines. 196

Figure 7.25. Calculated sulfur and oxygen content of the Cu–Fe–O–S matte as functions of Po, Ps and Fe/(Cu + Fe) ratio. Experimental points (see Figure 7.17) and calculated lines. 197

Figure 7.26. Calculated sulfur and oxygen content of the Cu–Fe–O–S matte as functions of Po, Ps and Fe/(Cu + Fe) ratio. Experimental points (see Figure 7.17) and calculated lines. 198

Figure 7.27. Calculated sulfur and oxygen content of the Cu–Fe–O–S matte as functions of Po, Ps and Fe/(Cu + Fe) ratio. Experimental points (see Figure 7.17) and calculated lines. 199

Figure 7.28. Matte–spinel equilibrium. Weight percent of oxygen in matte. Experimental points [210, 316-318] and calculated lines. 201

Figure 7.29. Matte–spinel equilibrium. Weight percent of sulfur in matte. Experimental points [210, 316, 317] and calculated lines. 202

Figure 7.30. Matte–spinel equilibrium. Weight percent of iron in matte. Experimental points [210, 316] and calculated lines. 202

Figure 7.31. Matte–spinel equilibrium. Partial pressure of sulfur. Experimental points [210, 316] and calculated lines. 203

Figure 7.32. Matte–spinel equilibrium. Partial pressure of oxygen. Experimental points [316] and calculated lines. 203

Figure 8.1. Isothermal section of the CaO–FeO–Fe_2O_3 system at 1200 °C. Experimental points [320] and calculated lines : dashed orange [174], dashed blue [182] and solid lines – this study. 213

Figure 8.2. Isothermal section of the CaO–FeO–Fe_2O_3 system at 1300 °C. Experimental points [320] and calculated lines : dashed orange [174], dashed blue [182] and solid lines – this study. 214

Figure 8.3. Phase diagram of the Ca–Fe–O system in air ($P(O_2)$ = 0.21 atm). Experimental points [272, 320-323] and calculated lines: dashed orange [174], dashed blue [182] and solid – this study. 214

Figure 8.4. Phase diagram of the Ca–Fe–O system in oxygen ($P(O_2)$ = 1 atm). Experimental points [321, 324] and calculated lines: dashed orange [174], dashed blue [182] and solid – this study. 215

Figure 8.5. Calcium content of spinel in the Ca–Fe–O system at equilibria with two other solid phases. Experimental points [272] and calculated lines : dashed [174], solid – this study..215

Figure 8.6. Black lines: Isothermal section of the phase diagram of the Ca–Cu–Fe–O system at 1100 °C and molar ratio Cu/(Cu_2O + Fe_3O_4 + CaO) = 0.1. Experimental points [325] and calculated red lines: composition of phases, projected from the oxygen corner of the Ca–Cu–Fe–O tetrahedron onto the CaO–Cu_2O–Fe_3O_4 plane. Triangles – compositions of spinel in equilibrium with slag and liquid Cu, squares compositions of slag in equilibrium with spinel and liquid Cu, circles – compositions of slag in equilibrium with $Ca_2Fe_2O_5$ and liquid Cu, inversed triangles compositions of slag in equilibrium with Cu_2O and liquid Cu, half-filled diamond compositions of slag in equilibrium with C_4WF_4 and liquid Cu.....217

Figure 8.7. Black lines: Isothermal section of the phase diagram of the Ca–Cu–Fe–O system at 1150 °C and molar ratio Cu/(Cu_2O + Fe_3O_4 + CaO) = 0.1. Experimental points [284, 325, 326] and calculated red lines: composition of phases, projected from the oxygen corner of the Ca–Cu–Fe–O tetrahedron onto the CaO–Cu_2O– Fe_3O_4 plane. Symbols as in Figure 8.7. 218

Figure 8.8. Black lines: Isothermal section of the phase diagram of the Ca–Cu–Fe–O system at 1200 °C and molar ratio Cu/(Cu_2O + Fe_3O_4 + CaO) = 0.1. Experimental points [284, 325, 326] and calculated red lines: composition of phases, projected from the oxygen corner of the Ca–Cu–Fe–O tetrahedron onto the CaO–Cu_2O– Fe_3O_4 plane. Symbols as in Figure 8.7. 218

Figure 8.9. Black lines: Isothermal section of the phase diagram of the Ca–Cu–Fe–O system at 1235 °C and molar ratio Cu/(Cu_2O + Fe_3O_4 + CaO) = 0.1. Experimental points [284] and calculated red lines: composition of phases, projected from the oxygen corner of the Ca–Cu–Fe–O tetrahedron onto the CaO–Cu_2O– Fe_3O_4 plane. Symbols as in Figure 8.7. 219

Figure 8.10. Black lines: Isothermal section of the phase diagram of the Ca–Cu–Fe–O system at 1250 °C and molar ratio Cu/(Cu_2O + Fe_3O_4 + CaO) = 0.1. Experimental points [284, 325, 326] and calculated red lines: composition of phases, projected from the oxygen corner of the Ca–Cu–Fe–O tetrahedron onto the CaO–Cu_2O– Fe_3O_4 plane. Symbols as in Figure 8.7. 219

Figure 8.11. Phase diagram of the Al–Cu–O system at 1000 °C and P = 1 atm. 220

Figure 8.12. Heat capacities of $CuAl_2O_4$ and $CuAlO_2$ in comparison with the corresponding sum of oxides. 222

Figure 8.13. Degree of inversion of $CuAl_2O_4$ spinel : s is the number of moles of copper on the octahedral sublattice. Experimental points [327-333] and calculated line.....223

Figure 8.14. Equilibrium oxygen partial pressures over three-phase regions in the Al–Cu–O system : experimental points [334-337] and calculated lines. 223

Figure 8.15. Phase diagram of Al–Cu–O system in air ($P(O_2)$ = 0.21 atm): experimental points [1, 335, 338-340], solid lines are calculated in the present study, dashed lines show the schematic phase diagram, which cannot be described without adding CuO to the slag components.....224

Figure 8.16. Phase diagram of Al–Cu–O system at copper saturation Cu/(Cu_2O + Al_2O_3) = 0.03: experimental points [1, 126, 341, 342] and calculated lines. 225

Figure 8.17. Reduction of $CuFe_{1.75}Al_{0.25}O_4$ spinel with H_2 at 1000 °C. Experimental points [344] and calculated line. 226

Figure 8.18. Isothermal section of the phase diagram of the Al–Ca–Fe–O system at 1200 °C and molar ratio Fe/(Al_2O_3 + FeO + CaO) = 0.5. 227

Figure 8.19. Isothermal section of the phase diagram of the Al–Ca–Fe–O system at 1400 °C and molar ratio Fe/(Al_2O_3 + FeO + CaO) = 0.5. 228

Figure 8.20. Molar ratio Ca/(Al + Ca + Fe) in spinel for different 4-phase equilibria in the Al–Ca–Fe–O system: experimental points [272] and calculated lines. 228

Figure 8.21. Molar ratio Fe/(Al + Ca + Fe) in the $Ca(Al, Fe)_2O_4$ phase for different 4-phase equilibria in the Al–Ca–Fe–O system: experimental points [272] and calculated lines. 229

Figure 8.22. Molar ratio Fe/(Al + Ca + Fe) in the $Ca(Al, Fe)_4O_7$ phase for different 4-phase equilibria in the Al–Ca–Fe–O system: experimental points [272] and calculated lines. 229

Figure 8.23. Isothermal section of the phase diagram of the Ca–Mg–Fe–O system at 1500 °C in air: experimental points [345] and calculated lines. Red dotted line corresponds to the section shown in the next figure.....231

Figure 8.24. Phase diagram of the $Ca_2Fe_2O_5$-$MgFe_2O_4$ section with excess Fe_2O_3: mass ratio $Fe_2O_3/(Ca_2Fe_2O_5 + MgFe_2O_4) = 0.01$ in air. This section is shown by the red dashed line in the previous figure. Experimental points [346] and calculated lines. 231

Figure 9.1 Activity of ½(Cu_2O) in slag vs. copper content of slag in the Cu–Fe–O–Si system: experimental points [1, 356-363] and calculated lines.....247

Figure 9.2. Phase diagram of the FeO–FeS–SiO_2 system in equilibrium with Fe at 1200 °C: experimental evaluation [364] and calculated lines. 249

Figure 9.3. Slag–matte–SiO_2–Fe equilibrium in the Fe–O–S–Si system with varying temperature and total pressure of 1 atm. (a) Composition of slag; (b) composition of matte. Experimental points [14, 15] and calculated lines.....250

Figure 9.4. Slag–matte–SiO_2–Fe equilibrium in the Fe–O–S–Si system with varying temperature and total pressure of 1 atm. Partial pressures of O_2, S_2 and SO_2: experimental points [15] and calculated lines. 251

Figure 9.5. Sulfide capacity of slag in the Fe–O–S–Si system. Experimental points [366-368]. Calculated lines correspond to $\log_{10}[P(O_2), \text{atm}] = -7$ and $\log_{10}[P(S_2), \text{atm}] = -3$. Dotted lines – [354], solid lines – this study.....251

Figure 9.6. Slag–matte–SiO_2–metal equilibrium in the Cu–Fe–O–S–Si system at fixed temperature and total pressure of 1 atm. a) Copper content of slag. Experimental points [10,

13, 365, 369, 371, 372] and calculated lines: grey – [3], colored – this study. b) Calculated mole fractions of copper-containing quadruplets in the slag phase at 1200 °C. 254

Figure 9.7. Slag–matte–SiO_2–metal equilibrium in the Cu–Fe–O–S–Si system at fixed temperature and total pressure of 1 atm. Sulfur content of slag. Experimental points [10, 13-15, 365, 369-372] and calculated lines: grey – [3], colored – this study. 255

Figure 9.8. Slag–matte–SiO_2–metal equilibrium in the Cu–Fe–O–S–Si system at fixed temperature and total pressure of 1 atm. Oxygen content of matte. Experimental points [10-15] and calculated lines. 255

Figure 9.9. Slag–matte–SiO_2–metal equilibrium in the Cu–Fe–O–S–Si system at fixed temperature and total pressure of 1 atm. Sulfur content of matte. Experimental points [14, 15, 371, 379] and calculated lines. 256

Figure 9.10. Slag–matte–SiO_2–metal equilibrium in the Cu–Fe–O–S–Si system at fixed temperature and total pressure of 1 atm. Iron content of matte. Experimental points [14, 15, 371, 379] and calculated lines. 256

Figure 9.11. Slag–matte–SiO_2–metal equilibrium in the Cu–Fe–O–S–Si system at fixed temperature and total pressure of 1 atm. Partial pressure of SO_2. Experimental points [10, 13] and calculated lines. 257

Figure 9.12. Slag–matte–SiO_2–metal equilibrium in the Cu–Fe–O–S–Si system at fixed temperature and total pressure of 1 atm. Partial pressure of S_2. Experimental points [10, 371] and calculated lines. 257

Figure 9.13. Slag–matte–SiO_2–metal equilibrium in the Cu–Fe–O–S–Si system at fixed temperature and total pressure of 1 atm. Partial pressure of O_2. Experimental points [10, 15, 371] and calculated lines. 258

Figure 9.14. Slag–matte–SiO_2–metal equilibrium in the Cu–Fe–O–S–Si system at fixed temperature and total pressure of 1 atm. Oxygen content of liquid copper. Experimental points [10, 13] and calculated lines. 258

Figure 9.15. Slag–matte–SiO_2–metal equilibrium in the Cu–Fe–O–S–Si system at fixed temperature and total pressure of 1 atm. Sulfur content of liquid copper. Experimental points [10, 13] and calculated lines. 259

Figure 9.16. Slag–matte–SiO_2–$P(SO_2)$ = 0.1 atm equilibrium in the Cu–Fe–O–S–Si system at fixed temperature and total pressure of 1 atm. Copper content of slag. Experimental points [373, 375, 377, 380, 381] and calculated lines.....260

Figure 9.17. Slag–matte–SiO_2–$P(SO_2)$ = 0.1 atm equilibrium in the Cu–Fe–O–S–Si system at fixed temperature and total pressure of 1 atm. Sulfur content of slag. Experimental points [10, 370, 372, 373, 376, 377] and calculated lines.....261

Figure 9.18. Slag–matte–SiO_2–$P(SO_2)$ = 0.1 atm equilibrium in the Cu–Fe–O–S–Si system at fixed temperature and total pressure of 1 atm. Oxygen content of matte. Experimental points [373, 375, 376, 381] and calculated lines.....261

Figure 9.19. Slag–matte–SiO_2–$P(SO_2)$ = 0.1 atm equilibrium in the Cu–Fe–O–S–Si system at fixed temperature and total pressure of 1 atm. Sulfur content of matte. Experimental points [373, 381] and calculated lines.....261

Figure 9.20. Slag–matte–SiO_2–$P(SO_2)$ = 0.1 atm equilibrium in the Cu–Fe–O–S–Si system at fixed temperature and total pressure of 1 atm. Iron content of matte. Experimental points [373, 376, 377, 381] and calculated lines.....262

Figure 9.21. Slag–matte–SiO_2–$P(SO_2)$ = 0.1 atm equilibrium in the Cu–Fe–O–S–Si system at fixed temperature and total pressure of 1 atm. Partial pressure of S_2. Experimental points [15, 376, 380] and calculated lines.....262

Figure 9.22. Slag–matte–SiO_2–$P(SO_2)$ = 0.1 atm equilibrium in the Cu–Fe–O–S–Si system at fixed temperature and total pressure of 1 atm. Partial pressure of O_2. Experimental points [15, 376, 377, 380] and calculated lines.....263

Figure 9.23. Slag–matte–SiO_2–$P(SO_2)$ = 1 atm equilibrium in the Cu–Fe–O–S–Si system at fixed temperature and total pressure of 1 atm. Copper content of slag. Experimental points [373, 375, 380] and calculated lines.....263

Figure 9.24. Slag–matte–SiO_2–$P(SO_2)$ = 1 atm equilibrium in the Cu–Fe–O–S–Si system at fixed temperature and total pressure of 1 atm. Sulfur content of slag. Experimental points [373, 375, 380] and calculated lines.....264

Figure 9.25. Slag–matte–SiO_2–$P(SO_2)$ = 1 atm equilibrium in the Cu–Fe–O–S–Si system at fixed temperature and total pressure of 1 atm. Oxygen content of matte. Experimental points [373-375, 380] and calculated lines. 264

Figure 9.26. Slag–matte–SiO_2–$P(SO_2)$ = 1 atm equilibrium in the Cu–Fe–O–S–Si system at fixed temperature and total pressure of 1 atm. Sulfur content of matte. Experimental points [373, 380] and calculated lines. 265

Figure 9.27. Slag–matte–SiO_2–$P(SO_2)$ = 1 atm equilibrium in the Cu–Fe–O–S–Si system at fixed temperature and total pressure of 1 atm. Iron content of matte. Experimental points [373, 380] and calculated lines. 265

Figure 9.28. Slag–matte–SiO_2–$P(SO_2)$ = 1 atm equilibrium in the Cu–Fe–O–S–Si system at fixed temperature and total pressure of 1 atm. Partial pressure of S_2. Experimental points [15, 380] and calculated lines. 266

Figure 9.29. Slag–matte–SiO_2–$P(SO_2)$ = 1 atm equilibrium in the Cu–Fe–O–S–Si system at fixed temperature and total pressure of 1 atm. Partial pressure of O_2. Experimental points [15, 380] and calculated lines. 266

Figure 10.1. Sulfide capacity of slag in the Ca–Fe–O–S system. Experimental points [366]. Calculated lines at 1600 °C correspond to $\log_{10}[P(O_2)$, atm] = -7 and $\log_{10}[P(S_2)$, atm] = -2. Calculated lines at 1400 and 1500 °C correspond to $\log_{10}[P(O_2)$, atm] = -8 and $\log_{10}[P(S_2)$, atm] = -3. Dotted lines – [354], solid lines – this study. 273

Figure 10.2. Sulfide capacity of slag in the Ca–O–S–Si system. Experimental points [368, 382-386]. Calculated lines correspond to $\log_{10}[P(O_2)$, atm] = -9 and $\log_{10}[P(S_2)$, atm] = -2. Dotted lines – [354], solid lines – this study. 273

Figure 10.3. Liquidus in the Ca–O–S–Si system. Experimental points [19, 387] and calculated lines. 274

Figure 10.4. Activity of ½(Cu_2O) in slag vs. copper content of silica saturated slag in the Ca–Cu–Fe–O–Si system. Experimental points [360, 362, 363, 388] and calculated lines. Experimental points for Ca-free slags are taken from Figure 9.1. 275

Figure 10.5. Black lines and green symbols [389, 390]: phase diagram of the Ca–Fe–O–Si system at 1300 °C and $P(O_2) = 10^{-6}$ atm. Red lines and symbols [1, 325]: liquid region of the phase diagram of the Ca–Cu–Fe–O–Si system at 1300 °C, $P(O_2) = 10^{-6}$ atm and in equilibrium with copper. 275

Figure 10.6. Copper content of slag for slag–matte equilibrium in the Ca–Cu–Fe–O–S system at 1250 °C, Cu saturation or fixed $P(SO_2)$, total iron content of slag as in Figure 10.8 and total pressure of 1 atm. Experimental points [391-393] and calculated lines. 276

Figure 10.7. Sulfur content of slag for slag–matte equilibrium in the Ca–Cu–Fe–O–S system at 1250 °C, Cu saturation or fixed $P(SO_2)$, total iron content of slag as in Figure 10.8 and total pressure of 1 atm. Experimental points [391-393] and calculated lines. Legend is the same as in Figure 10.6. 277

Figure 10.8. Fe^{2+} and Fe^{3+} content of slag for slag–matte equilibrium in the Ca–Cu–Fe–O–S system at 1250 °C, Cu saturation or fixed $P(SO_2)$, total iron content of slag as in Figure 10.8 and total pressure of 1 atm. Experimental points [393] and calculated lines. 277

Figure 10.9. Iron content of matte for slag–matte equilibrium in the Ca–Cu–Fe–O–S system at 1250 °C, Cu saturation or fixed $P(SO_2)$, total iron content of slag as in Figure 10.8 and total pressure of 1 atm. Experimental points [392] and calculated lines. 278

Figure 10.10. Calcium content of matte for slag–matte equilibrium in the Ca–Cu–Fe–O–S system at 1250 °C, Cu saturation or fixed $P(SO_2)$, total iron content of slag as in Figure 10.8 and total pressure of 1 atm. Experimental points [391-393]. The solubility of Ca in matte is neglected in the present study. 278

Figure 10.11. Partial pressure of oxygen for slag–matte equilibrium in the Ca–Cu–Fe–O–S system at 1250 °C, Cu saturation or fixed $P(SO_2)$, total iron content of slag as in Figure 10.8 and total pressure of 1 atm. Experimental points [391, 393] and calculated lines. 279

Figure 10.12. Partial pressure of SO_2 for slag–matte equilibrium in the Ca–Cu–Fe–O–S system at 1250 °C, Cu saturation or fixed $P(SO_2)$, total iron content of slag as in Figure 10.8 and total pressure of 1 atm. Experimental points [391] and calculated lines. 279

Figure 10.13. Partial pressure of S_2 for slag–matte equilibrium in the Ca–Cu–Fe–O–S system at 1250 °C, Cu saturation or fixed $P(SO_2)$, total iron content of slag as in Figure 10.8 and total pressure of 1 atm. Experimental points [393] and calculated lines. 280

Figure 10.14. Copper content of slag for slag–matte–SiO_2–metal equilibrium in the Ca–Cu–Fe–O–S–Si system at fixed temperature, total pressure of 1 atm and different CaO contents of slag. Experimental points [365, 372] and calculated lines. The experimental points for Ca-free system are taken from Figure 9.6. 281

Figure 10.15. Sulfur content of slag for slag–matte–SiO_2–metal equilibrium in the Ca–Cu–Fe–O–S–Si system at fixed temperature, total pressure of 1 atm and different CaO contents of slag. Experimental points [365, 372] and calculated lines. The experimental points for Ca-free system are taken from Figure 9.7. 281

Figure 10.16. Iron content of slag for slag–matte–SiO_2–metal equilibrium in the Ca–Cu–Fe–O–S–Si system at fixed temperature, total pressure of 1 atm and different CaO contents of slag. Experimental points [365, 378] and calculated lines. 282

Figure 10.17. Silica content of slag for slag–matte–SiO_2–metal equilibrium in the Ca–Cu–Fe–O–S–Si system at fixed temperature, total pressure of 1 atm and different CaO contents of slag. Experimental points [365, 378] and calculated lines. 282

Figure 10.18. Value of the excess parameter $\Delta g^{011}_{\mathbf{CaSi/OO(S)}}$ 284

Figure 11.1. Location of ISASMELT™ plants that have been licensed to date [395]. 288

Figure 11.2. Copper ISASMELT™ capacity [394]. 289

Figure 11.3. The ISASMELT™ concept. 291

Figure 11.4. ILO smelter – original process flow diagram (before modernization) [398]. 296

Figure 11.5. Flow diagram of modernized Ilo smelter [398] 296

Figure 11.6. The ISASMELT™ furnace installation at Ilo copper smelter [398]. 297

Figure 11.7. Rotary holding furnaces at Ilo copper smelter [398]. 297

Figure 11.8. ISASMELT™ furnace refractory wear in Ilo smelter [399]. 299

Figure 11.9. The Excel-FactSage-Matlab bundle 303

Figure 11.10. Microstructure of the Southern Peru Ilo Smelter slag from rotary holding furnace. 307

Figure 11.11. Presence of matte in the RHF slag dam site. 308

List of symbols and abbreviations

A^{I}, A^{II}	^{I} and ^{II} are valencies
A^{+}, A^{2+}	$^{+}$ and $^{2+}$ are charges
$\gamma(i)$	Activity coefficient of a component *i*
CEF	Compound Energy Formalism
CRCT	Center for Research in Computational Thermochemistry, École Polytechnique de Montréal.
C_P	Molar heat capacity, $J \cdot mol^{-1}K^{-1}$
δ_{ij}	Kröneker delta ($\delta_{ij} = 0$ if $i \neq j$ and $\delta_{ij} = 1$ if $i = j$)
F_{ij} , I_{ij} , Δ_{ij} , Δ_{ijk}	Model parameters in the spinel solution, linear combinations of G_{ij} , $J \cdot mol^{-1}$
ΔG	Gibbs energy of fomation of a compound, $J \cdot mol^{-1}$ (Equation 2.1)
Δg_{ij}	Gibbs energy of pair exchange reaction, $J \cdot mol^{-1}$
ΔG_{mix}	Gibbs energy of mixing, J
ΔS^{config}	Configurational entropy of mixing, $J \cdot K^{-1}$
g	Molar Gibbs energy of a solution, $J \cdot mol^{-1}$
G	Gibbs energy of a solution, J
g^{excess}	Excess molar Gibbs energy of a solution, $J \cdot mol^{-1}$
g_i°	Molar Gibbs energy of pure component, $J \cdot mol^{-1}$
G_{ij}	Molar Gibbs energy of a pseudocomponent $(i)^{tetr}[j]_2^{oct}O_4$ in spinel solution, $J \cdot mol^{-1}$
$g_{ij/kl}$	Molar Gibbs energy of the *ij*/*kl* quadruplet, $J \cdot mol^{-1}$
G_m	Gibbs energy per formula unit of solution in CEF, $J \cdot mol^{-1}$
G_m^E	Excess molar Gibbs energy of a spinel solution, $J \cdot mol^{-1}$

$\Delta H^{o}_{298.15}$ Standard enthalpy of formation at 298.15 K, J·mol^{-1}

MQM Modified Quasichemical Model

MQMPA Modified Quasichemical Model in pair approximation

MQMQA Modified Quasichemical Model in quadruplet approximation

n_i Number of moles of component *i*

$n_{ij/kl}$ Number of moles of *ij*/*kl* quadruplet

$P(i)$ Partial pressure of *i*, atm

S_c Molar configurational entropy in CEF, J·mol^{-1}K^{-1}

$S^{o}_{298.15}$ Standard entropy at 298.15 K, J·mol^{-1}K^{-1}

X_i Molar fraction of a component *i* of a solution

X^{i}_{mn} Molar fraction of pairs (*m*-*n*)

Y_m "Coordination-equivalent" component fraction in MQM

Y_i^{tetr}, Y_j^{oct} Site fractions of components *i* or *j* in tetrahedral or octahedral sublattice, respectively, in spinel solution

Z_m Coordination number of *m*

Z^{m}_{mn} Coordination number of *m* if all pairs are *mn*

$Z^{m}_{mn//kl}$ Coordination number of *m* if all quadruplets are *mn/kl*

ζ Parameter, which determines the ratio of SNN and FNN pairs

Model parameters:

ω^{ij}_{mn} excess Gibbs energy binary parameter in the MQM in pair approximation; expansion in terms of mole fractions of components (slang name QUAS)

$\omega^{ijk}_{mn(p)}$ the same, ternary parameter – effect of *p* on the *m*-*n* interaction

g_{mn}^{ij} excess Gibbs energy binary parameter in the MQM in pair approximation; expansion in terms of pair fractions (slang name GUTS)

$g_{mn(p)}^{ijk}$ the same, ternary parameter – effect of *p* on the *m*-*n* interaction

q_{mn}^{ij} excess Gibbs energy binary parameter in the Bragg-Williams model; polynomial expansion (slang name BRAG GP)

$q_{mn(p)}^{ijk}$ the same, ternary parameter

L_{mn}^{i} excess Gibbs energy binary parameter in the Bragg-Williams model; Redlich-Kister expansion (slang name BRAG GR)

$\omega_{mn/kk}^{ij}$ excess Gibbs energy binary parameter in the MQM in quadruplet approximation; expansion in terms of mole fractions of components (slang name QUAS)

$g_{mn/kk}^{ij}$ excess Gibbs energy binary parameter in the MQM in quadruplet approximation; expansion in terms of pair fractions (slang name GUTS)

$q_{mn/kk}^{ij}$ excess Gibbs energy binary parameter in the Bragg-Williams model; polynomial expansion (slang name BRAG GP)

Phases:

DB Digenite-bornite phase, Cu_2S-Cu_2FeS_4 based

DB1 Digenite, Cu_2S based

DB2 Bornite, Cu_2FeS_4 based

Mono Monoxide, solution based on wüstite ($Fe_{1-x}O$), lime (CaO), MgO, NiO or CoO

Pyrr Pyrrhotite, $Fe_{1-x}S$ based

Sp Spinel

Sp1 Magnetite, Fe_3O_4 based spinel

Sp2 $CuFe_2O_4$ based spinel

Tal Talnakhite, $Cu_9Fe_8S_{16}$

Id	Idaite, Cu_3FeS_4
Mh	Mooihoekite, $Cu_9Fe_9S_{16}$
Hc	Haycockite, $Cu_4Fe_5S_8$
Cb	Cubanite, $CuFe_2S_3$

INTRODUCTION

Background

Copper plays a huge role in the modern technology. However, the industry of copper production is affected by market volatility as any other sphere of economics. Once profitable, a plant might find itself being detrimental for the company after the drastic change in prices of raw materials and products or after new environmental regulations. In order to restore the profitability, a quick response from the marketing department is required to estimate costs, and alternative process parameters are expected to be swiftly implemented by the plant operators. Ideally, process parameters should change constantly as a function of market prices to give the best economic yield. There exist companies which conduct such monitoring trying to achieve the "constantly optimized" way of production. Unfortunately, their knowledge of physico-chemical processes during the production of copper lacks the same level of specification as marketing or logistic models. In the past, a bit simplistic physico-chemical models are used to reason a change in the process. An example of rather successful process modeling attempt is the work of Nagamori et al (1994) [2]. Sophisticated numerical methods were used to resolve mass and energy balance equations. However, slag and matte compositions and activities of components are calculated using empirical coefficients. Hence, the results may be in contradiction with the laws of thermodynamics. Alternatively, the empirical models based on years of experience of operating a plant are created, and the major change in the process relies on the extrapolation of these models. Extrapolations may not work if they are not based on fundamental studies.

Thus, a demand exists from the metallurgical companies for research in a field of chemical thermodynamics, which predicts the ultimate result of chemical reactions and phase transitions if a sufficient time is given to the system for establishing equilibrium. These studies are usually started with an experimental investigation. Until recent times the experiments were complemented only by empirical correlations. With the development of chemical thermodynamics, fundamental laws came into use to verify the consistency of experimental results and give correct interpolations and extrapolations. The rising computing capabilities allowed creation of the electronic thermodynamic databases. These databases store thermodynamic properties of all possible phases in the system as functions of composition,

temperature and pressure and, combined with Gibbs energy minimization software, are able to calculate physico-chemical equilibrium of the complex system.

This thesis reports the results of a project aimed at creation of a thermodynamic database for the purpose of modeling of pyrometallurgical production of copper. The project is realized in collaboration with Pyrosearch group of the University of Queensland, Australia. The important lacking experimental data are provided by them.

Statement of the problem

The most important phases during the pyrometallurgical production of copper are liquid slag, matte and blister copper. Slag is mostly oxide liquid, matte is based on liquid sulfides and blister copper is a metallic liquid. These three liquids are able to mix with each other to a certain extent. It is desirable to know the distribution of all elements between these phases and how it is governed by process parameters.

The thermodynamic properties of solid phases, sulfides, oxides and metals, are required to predict possible precipitation from liquid phases, calculate the energy needed to melt inputs of the furnace and estimate the corrosion of refractory materials of the furnace walls. Very important and most challenging to model solid phase is the spinel solid solution.

The databases for solid and liquid phases must be consistent with each other and with the database for the gaseous phase to calculate the composition of outlet gases.

Objectives

The principal objective of the present project is to model the thermodynamic properties of liquid solutions, solid solutions and compounds in consistency with the gaseous phase for the chemical system which represents the process of the pyrometallurgical production of copper. It consists of sulfides, oxides and metals in the Al–Ca–Cu–Fe–Mg–O–S–Si chemical system. Drawbacks of the previous database [3] are to be corrected. For instance, the solubility of oxygen in matte and of sulfur in blister copper should be taken into account. Copper and calcium should be introduced into the spinel database. The effect of sulfur on the solubility of copper in the slag should be modeled. Liquid phases should be consistent with solid sulfides as well as with solid oxides. The database itself contains model parameters, which are obtained through the thermodynamic optimization procedure described further.

The principal objective includes the secondary objectives, such as the ability to calculate the solubilities and activities of components in phases, the temperatures and compositions of solidification, the energy balance during melting and burning of furnace feed. These calculations are possible by the integration of model parameters from the thermodynamic database with the FactSage^{TM} thermodynamic software [4].

Methodology

In the thermodynamic modeling (or thermodynamic optimization) of the system, the Gibbs energy functions are assigned to each possible phase. Gibbs energies are functions of temperature, pressure and composition, and certain model approximations are used for each phase of the system. The principal hypothesis on which this project is based is the following: for the purposes of the pyrometallurgical production of copper, it is possible to model the slag phase by the Modified Quasichemical Model (MQM) in quadruplet approximation, the matte phase – by MQM in pair approximation, and the spinel phase – by the model based on the Compound Energy Formalism (CEF). Once the functions of Gibbs energies are obtained, all other properties may be derived in an analytical way. Secondary hypotheses are also necessary, such as the existence of $Cu^{I} \leftrightarrow Cu^{II}$ and $Fe^{II} \leftrightarrow Fe^{III}$ equilibria in the matte phase, selective occupation of only octahedral sites by Ca^{2+} in the spinel phase, etc.

A systematic approach was used in this study to obtain values of model parameters. In the thermodynamic optimization, or CALPHAD-style (“CALculation of PHAse Diagrams”) optimization, all available thermodynamic and phase diagram data are evaluated simultaneously in order to obtain one set of model equations for the Gibbs energies of all phases as functions of temperature and composition. From these equations, all of the thermodynamic properties and the phase diagrams can be back-calculated. In this way, all the data are rendered self-consistent and consistent with thermodynamic principles. Thermodynamic property data, such as activity data, can aid in the evaluation of the phase diagram, and phase diagram measurements can be used to deduce thermodynamic properties. Discrepancies in the available data can often be resolved, and interpolations and extrapolations can be made in a thermodynamically correct manner. A small set of model parameters is obtained. This is ideal for computer storage and calculation of properties and phase diagrams. The methodology might be represented in the following steps:

- Step 1. Literature review of all available experimental data necessary for thermodynamic optimization: phase diagrams, calorimetric and activity measurements, partial pressure, element distributions between phases, etc.
- Step 2. Construction of thermodynamic models by defining the cation occupancies or possible species valencies.
- Step 3. Estimation of model parameters, beginning with solid compounds, then solid solutions and finally, liquid solutions. Initial calculations and comparison with experimental data. Identification of areas with lacking or contradictory experimental information.
- Step 4. Request for specific experimental information from Pyrosearch collaborators. The conditions of experiments are chosen using the initial thermodynamic calculations. Go back to Step 1.
- Step 5. Final set of model parameters is obtained. Models are justified in case all the experimental data are reproduced within the experimental error limits.

The resulting database will be transmitted to the Pyrosearch group, which in turn is going to use it for consulting of its industrial sponsors and customers, BHP Billiton, Outotec and Xstrata Copper to name few. In this way, the results of the present study will have an impact on major international copper producing companies.

Organization of the thesis

The thesis begins with the short overview of the pyrometallurgical production of copper in Chapter 1. The mathematical description of the thermodynamic models used in this study is then given in Chapter 2.

The next part is mainly devoted to the development of the matte database, which includes the review of the previously optimized Cu–S, Fe–S and Cu–Fe–S systems followed by necessary corrections (Chapter 3), an addition of oxygen to the Cu–S and Fe–S systems (Chapter 4 and Chapter 5, respectively), and joining the resulting databases to describe the Cu–Fe–O (Chapter 6) and Cu–Fe–O–S (Chapter 7) systems. Simultaneously, the existing compounds and solid solutions are modeled and included into the joint thermodynamic database.

Chapter 6 starts the developing of the spinel solid solution with the addition of Cu to the Fe_3O_4 spinel. This is continued by the addition of Ca and evaluation of all related systems in Chapter 8.

In Chapter 9, the effect of sulfur on the solubility of copper in the slag phase of the Cu–Fe–O–S–Si system is evaluated. In the next section (9.3), the calcium is added to the system and its influence is modeled.

Finally, the predictive ability of the thermodynamic database is verified by the simulation of a real industrial process (Chapter 11). Model predictions are compared with the plant data.

CHAPTER 1 PYROMETALLURGICAL PRODUCTION OF COPPER

Equation Chapter (Next) Section 1

Most important sources of copper are copper-iron-sulfide minerals [5], e.g. chalcopyrite ($CuFeS_2$), bornite (Cu_5FeS_4) and chalcocite (Cu_2S). About 80 % of the world`s copper-from-ore originates from copper-iron sulfides. These sulfide minerals are diluted by gangue minerals, mostly alumosilicates. At present, the economically profitable ore grade is limited to about 0.5 weight % Cu. Other sources of copper are scrap copper and oxidized materials form the earth crust. The world map of countries-exporters of refined copper is shown in Figure 1.1.

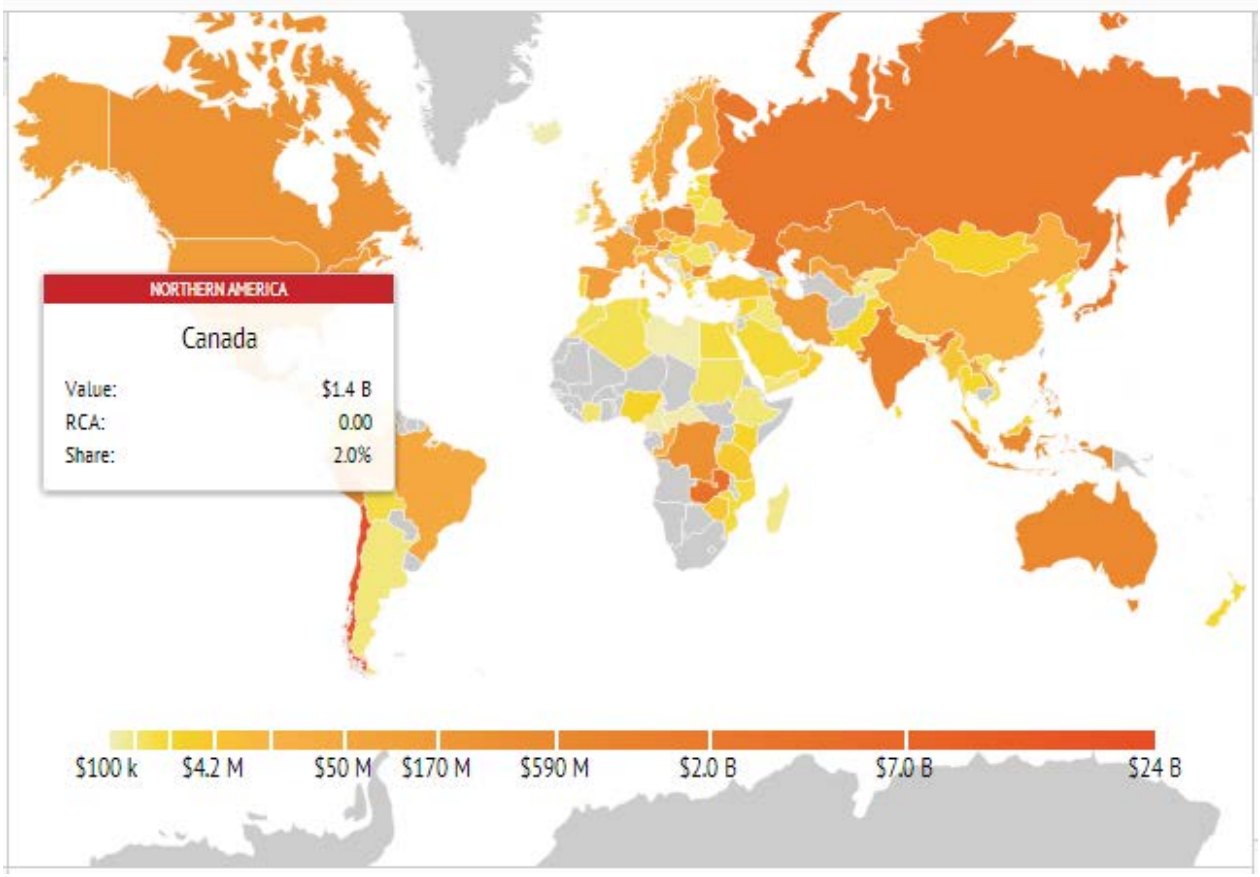

Figure 1.1. World export of refined copper and copper alloys in 2010.
http://atlas.media.mit.edu/explore/map/export/show/all/7403/2010/

Sulfide ores and copper scrap are mostly treated pyrometallurgically. Copper from oxidized minerals is usually produced by hydrometallurgical methods.

Principal stages for pyrometallurgical production of copper are presented in Figure 1.2 [5].

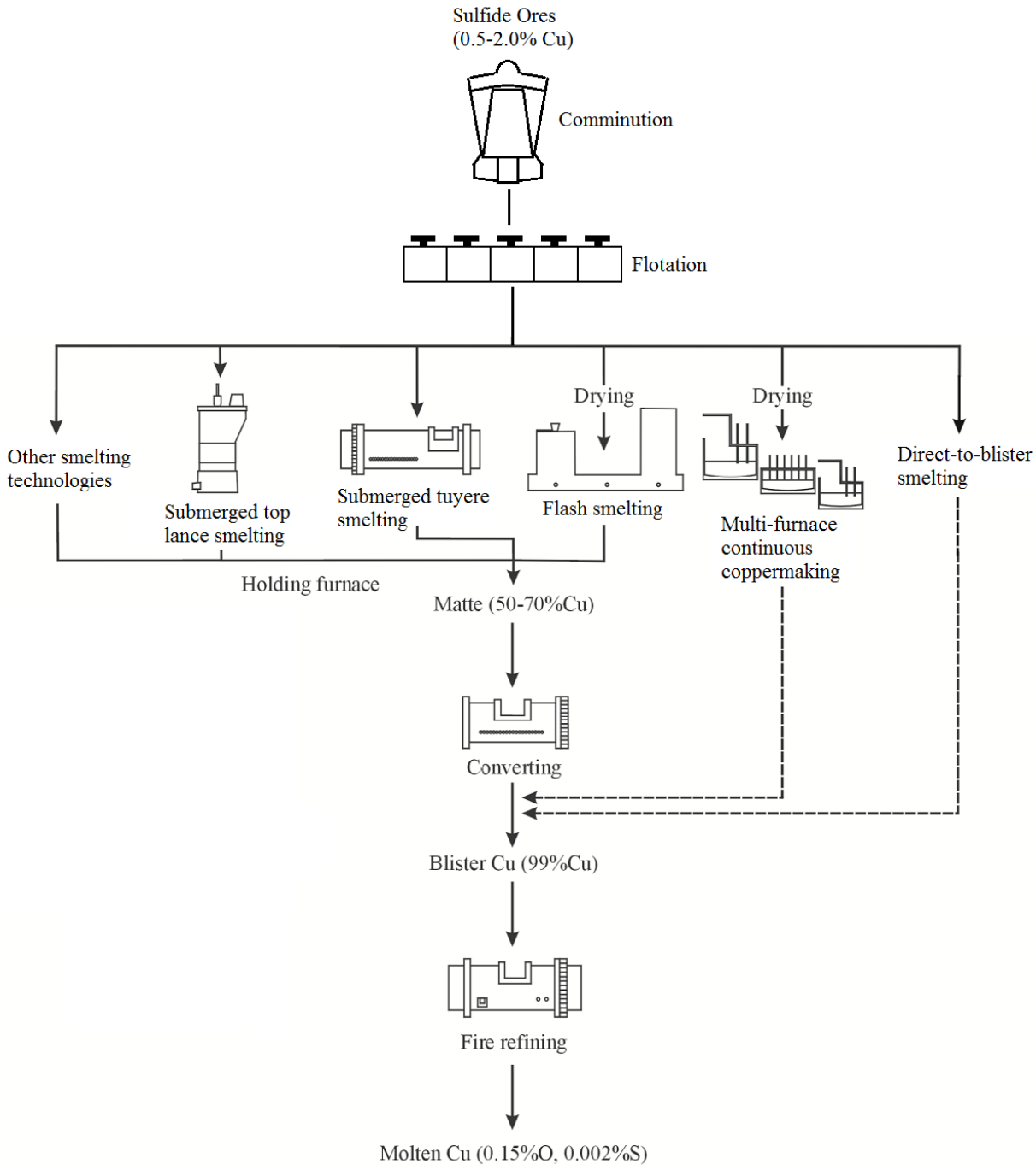

Figure 1.2. Principal processes for extracting copper from sulfide ores [5]. Parallel lines indicate alternative processes.

They are:

1. Crushing and froth flotation. At this stage ore is enriched in sulfides, giving copper concentrate

2. Smelting of the concentrate into high-Cu matte
3. Converting of the molten matte into impure molten copper (blister copper)
4. Fire- and electro-refining of blister copper to ultra-pure copper.

The first stage is required because the copper ores, currently being mined, are too lean in copper (0.5 – 2.0 wt.%) to be smelted directly. Melting of large quantity of waste rock would require prohibitive amount of energy. During the froth flotation, small particles of sulfides selectively attach to rising air bubbles, thus being carried away from «wetted » waste minerals. Special surface agents are used to archive the desired level of selectivity.

Concentrate feed for the smelting stage consists of small particles (less than 100 microns) and contains between 20 and 30 wt. % Cu (see Section 11.3 for example). The goal of smelting stage is to remove sulfur, iron and oxide impurities. Sulfur is partially oxidized and removed to the gas phase, mostly in the form of SO_2. Simultaneously, sulfide phases melt, forming liquid matte. Iron is oxidized as well, and reacts with SiO_2 flux forming the second liquid phase, named slag. This bunch of chemical reactions may be schematically represented as follows:

$$\underset{\text{(solid)}}{2CuFeS_2} + \underset{\text{(gas)}}{(1+1.5x)O_2} + \underset{\text{(solid)}}{xSiO_2} \xrightarrow{Fe^{2+} \leftrightarrow Fe^{3+} \text{ in slag}} \underset{\text{(liquid matte)}}{Cu_2S \cdot (FeS)_{2-x}} + \underset{\text{(liquid slag)}}{xFeO \cdot SiO_2} + \underset{\text{(gas)}}{(1+x)SO_2} \quad (1.1)$$

More details for reaction (1.1) are given in Section 11.1.3. In reality, matte and slag are mutually soluble to certain extent, so one should speak about preferable distribution of elements between matte, slag and gas rather than complete removal. The SiO_2 flux plays several roles: it decreases the melting temperature of slag, suppresses the mutual solubility between slag and matte and bonds iron oxide.

At the converting stage, the remaining sulfur and iron are removed to leave blister copper. The process is usually carried out in two stages:

1. Slag-forming stage (or “slag blow”) – iron sulfide from matte is oxidized by oxygen-enriched air and removed to the slag phase with the help of SiO_2 or CaO flux:

$$\underset{\text{(liquid matte)}}{Cu_2S \cdot (FeS)_x} + \underset{\text{(gas)}}{xO_2} + \underset{\text{(solid)}}{x\text{Flux}} \rightarrow \underset{\text{(matte)}}{Cu_2S} + \underset{\text{(slag)}}{xFeO \cdot \text{Flux}} + \underset{\text{(gas)}}{xSO_2} \quad (1.2)$$

2. Copper-making stage (or “copper blow”) – copper sulfide is converted to metallic copper by oxidation of remaining sulfur:

$$\underset{\text{(liquid matte)}}{Cu_2S} + \underset{\text{(gas)}}{O_2} \rightarrow \underset{\text{(liquid metal)}}{2Cu} + \underset{\text{(gas)}}{SO_2} \quad (1.3)$$

After removal of nearly all sulfur, oxygen partial pressure steeply rises and some copper inevitably oxidizes to Cu_2O, which is lost in the slag. That's why converting slag is often reprocessed in the smelting stage.

The blister copper product of converting is low in S and O (0.001-0.03% S, 0.1-0.8%O). Nevertheless, if this copper were cast, sulfur and oxygen would form SO_2 bubbles or blisters which give blister copper its name. Further cleaning is carried out through fire- or electro-refining.

The ultimate result of reactions (1.1-1.3) is governed by the thermodynamic properties participating phases. It is possible to calculate the heat effect, distribution of elements, partial pressures of components in the gas phase, etc., if appropriate thermodynamic models are chosen. The choice of the models is explained in the next chapter.

CHAPTER 2 THERMODYNAMIC APPROACH TO THE MODELING OF PYROMETALLURGICAL COPPER PRODUCTION

Equation Chapter (Next) Section 1

Chemical thermodynamics is able to predict the ultimate result of chemical reactions and phase transitions if a sufficient time is given to a system for establishing the equilibrium. The copper smelting and converting are conducted and high temperatures, > 1000 °C, and many reactions take place in liquid phases. The speed of these reactions is high enough to consider the chemical system to reach equilibrium. Within large reactors, mixing and heat transfer may play a significant role.

For instance, about 50% of the world's smelted copper is processed by the flash smelting. In this process the burning of fine sulfide particles in the oxygen-enriched air happens in a vertical reaction shaft. The reacting products settle in the hearth of the furnace to form slag and matte layers. It was shown [6] that oxygen partial pressure change through the reaction shaft and may have slightly different values at different depth of the settler. This indicates that gas, slag and matte phase are not in equilibrium during the process. However, some kind of dynamic local chemical equilibria (steady state equilibria) establish in every part of the furnace, as the partial pressure does not vary with time so much. It is possible to divide the Flash furnace into interacting reaction zones (volumes). A local thermodynamic equilibrium is assumed in each volume, mass outputs of the previous volume are the inputs of the next. The model will approach the continuous reacting flow of matter if the furnace is divided in more and more volumes. This is relatively new concept, which requires a great computational power and rather detailed knowledge of heat and mass transfer in the furnace. But the basic idea of local chemical equilibria in each volume still requires a thermodynamic database. An example of the consept is given in Ref. [7].

In modern chemical thermodynamics, a dedicated software is used to solve the Gibbs energy minimization problem under constrains of temperature, pressure and overall composition to give the set and compositions of phases in equilibrium. The software requires Gibbs energies of every phase as an explicit function of temperature, pressure and element composition. Although the solution of Gibbs energy minimization problem produces an exact answer, and thermodynamic

functions are inter-related analytically, Gibbs energy functions are model approximations of real phases. Certain assumptions are made in the course of this project. First of all, the pressure dependence of Gibbs energies of condensed phases is ignored, and gas is treated as ideal. This approximation is valid as soon as smelting and converting reactors operate at pressures, not far from 1 atm. Many solid phases are treated as stoichiometric compounds with one-point composition. Their Gibbs energies are independent of composition. The Gibbs energy of formation of a compound from elements in their standard state is at a temperature of T (K) and a pressure of 1 atm is given by:

$$\Delta G = \Delta H^{\circ}_{298.15} - T S^{\circ}_{298.15} + \int_{298.15}^{T} C_P(T) dT - T \int_{298.15}^{T} \frac{C_P(T)}{T} dT \qquad (2.1)$$

where $\Delta H^{\circ}_{298.15}$ is the standard enthalpy of formation at 298.15 K, $S^{\circ}_{298.15}$ is the standard entropy at 298.15 K and $C_P(T)$ is the molar heat capacity. In compounds, undergoing a magnetic transition, an additional contribution to Gibbs energy may be significant. The phenomenological approach proposed by Hillert and Jarl [8] was used to describe the magnetic contribution to thermodynamic functions.

2.1 Bragg-Williams formalism and geometric models

When a mutual solubility between stoichiometric phases is too large to be ignored, the solution models are introduced. The simplest one is the Bragg-Williams random mixing formalism. The Gibbs energy per mole of components is given by:

$$g = \sum_i X_i g_i^{\circ} + RT \sum_i X_i \ln X_i + g^{excess} \qquad (2.2)$$

where X_i are molar fractions of components and g_i° are standard Gibbs energies of pure components. Various models within the Bragg-Williams formalism differ from each other in a choice of components and in a way the excess Gibbs energy g^{excess} is approximated. Let us consider different models for g^{excess} on an example of a binary system first. The molar excess Gibbs energy of a binary system with components A and B is often expressed as

$$g^{excess}_{AB} = \alpha_{AB} X_A X_B \qquad (2.3)$$

where α_{AB} parameter may be expanded as a polynomial in the mole fractions, or written in a Redlich-Kister form:

$$\text{Polynomial form: } \alpha_{AB} = \sum_{i\geq 0}\sum_{j\geq 0} q_{AB}^{ij} X_A^i X_B^j \tag{2.4}$$

$$\text{Redlich-Kister form: } \alpha_{AB} = \sum_{i\geq 0} L_{AB}^i (X_A - X_B)^i \tag{2.5}$$

The set of coefficients q_{AB}^{ij} can be calculated from the set of L_{AB}^i and vice versa [9]. Equation (2.4) reduces to a simple regular solution model if $i = j = 0$. Excess parameters may be temperature dependent:

$$q_{AB}^{ij} = A + BT + CT\ln T + \ldots \tag{2.6}$$

For ternary systems, the interpolation of binary parameters may be done in several ways, i.e. several "geometric" models may be proposed. Two of them are used in this thesis and are illustrated in Figure 2.1. In each model, the g^{excess} of a ternary solution at a composition point P is estimated from the excess Gibbs energies of the tree binary subsystems at points 1, 2 and 3 by the equation [9]

$$g^{excess} = X_A X_B \alpha_{AB(1)} + X_B X_C \alpha_{BC(2)} + X_A X_C \alpha_{AC(3)} + (\textit{ternary terms}) \tag{2.7}$$

where $\alpha_{AB(1)}$, $\alpha_{BC(2)}$ and $\alpha_{AC(3)}$ are the binary α-functions evaluated at points 1, 2 and 3. The "ternary terms" are polynomial terms which are identically zero in the three binary subsystems.

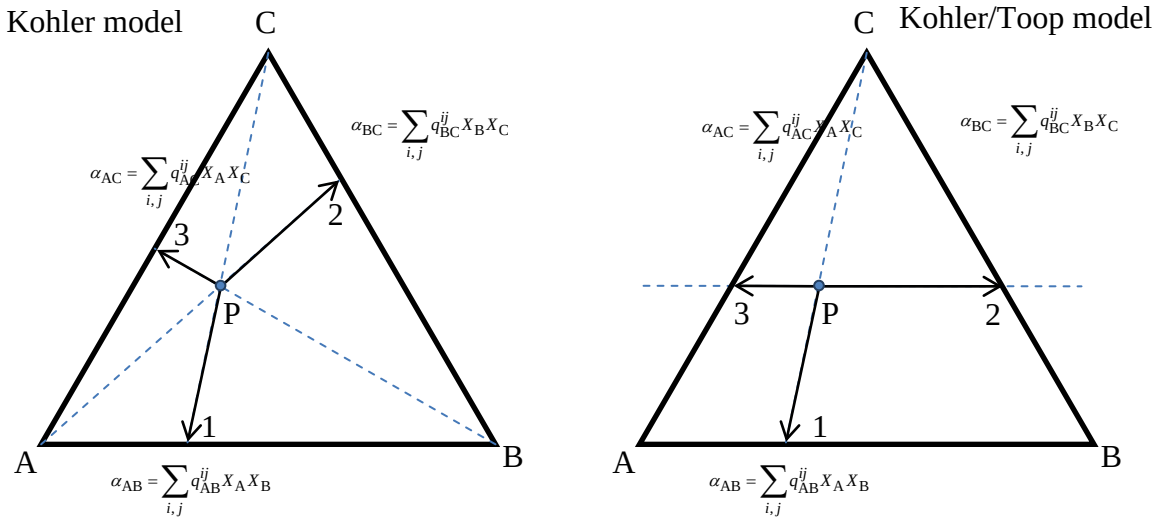

Figure 2.1. Geometric models for estimating ternary thermodynamic properties from optimizaed binary data.

The Kohler model in Figure 2.1 is symmetric, while in the Kohler/Toop model the component C is singled out. It was shown [9] that symmetric and asymmetric models may give very different results if g^{excess} is large and α-functions depend strongly on composition. An asymmetric Kohler/Toop model is more physically reasonable if one component is chemically different from the other two. In general, rather than speaking of a model for a ternary A-B-C system, the geometric approximation (Kohler- or Toop-type) for each of three α-functions may be defined. In this thesis, only 3 Kohler or 1 Kohler/ 2 Toop combinations are used, as shown in Figure 2.1. Mathematical formulas for the interpolation of α-functions in Kohler- or Toop-type approximation are given in [9]. The extension of geometric formalism into N-component system is also discussed in detail in [9].

In this study, the ternary terms in Equation (2.7) are designed to represent the effect of a third component upon the binary interaction. The contribution of a ternary parameter to the excess Gibbs energy also depends on the choice of the geometric model for a given ternary system. The mathematical formulas and detail discussion of ternary terms is given in [9].

In the present thesis, models based on the Bragg-Williams formalism, were developed to describe the thermodynamic properties of several solid solutions – fcc and bcc metals, several

oxide and sulfide solid solutions. Also, the Bragg-Williams contributions were used to describe the metal-metal interactions in the liquid metal/matte phase. In the slag phase, there were cases, when a large positive enthalpy of mixing between some components required the introduction of the Bragg-Williams terms. All these models are discussed in the corresponding sections of the thesis.

2.2 Matte (oxysulfide) and liquid metal

Liquid matte, produced during the pyrometallurgical production of copper, is often represented as a mixture of stoichiometric copper and iron sulfide: (Cu_2S, FeS). This is a simplistic approximation, because the sulfur content of mattes depends on the partial pressure of sulfur, so the better representation would be ($Cu_{2\pm x}S$, $Fe_{1\pm y}S$). Moreover, in the case of iron sulfide, the liquid phase extends all the way towards metallic liquid iron without a miscibility gap. The miscibility gap between liquid copper and copper sulfide is not very large as well. Thus, it is even better to consider mattes as (Cu, Fe, S) mixture with a high tendency for copper and iron to surround themselves by sulfur. In other words, there is a strong first nearest neighbor (FNN) short-range ordering (SRO) between iron and copper from one side and sulfur from the other side. Furthermore, oxygen is readily dissolved in mattes, as it is shown by many studies [10-15], and metals exibit FNN SRO with oxygen as well as with sulfur. The model for matte must include oxygen: (Cu, Fe, O, S). Later in the present thesis it is shown that, with the introduction of oxygen, copper and iron start to exhibit at least two different oxidation states, which has an impact on the thermodynamic properties. The final choice of components for the liquid metal/matte phase is:

$$\left(Cu^{I},\ Cu^{II},\ Fe^{II},\ Fe^{III},\ O,\ S\right) \tag{2.8}$$

Species in brackets occupy the same and only sublattice. Numbers I, II and III are not charges, but rather “valences”, they are used to calculate the metal/nonmetal ratio with the maximum short range ordering (SRO). The components O and S have “valence” of II, thus SRO is maximum at the compositions Cu^{I}:O = 2:1, Fe^{II}:S = 1:1, Fe^{III}:O = 2:3, etc. The model (2.8) represents liquid from metals to oxides, to sulfides, to nonmetals.

The Bragg-Williams formalism is not suitable to model the thermodynamic properties of such liquid. The strong first-nearest neighbor interaction between metals and nonmetals has a

dramatic effect on the entropy of mixing, so it no longer may be approximated by random mixing. The Modified Quasichemical formalism [16, 17] has been developed to address the problem of SRO.

For the liquid metal/matte phase, the Modified Quasichemical Model in pair approximation (MQMPA) was used. In MQMPA, the following pair exchange reaction is considered:

$$(\text{A-A}) + (\text{B-B}) = 2(\text{A-B});\ \ \Delta g_{\text{AB}} \tag{2.9}$$

where (i-j) represents a first-nearest-neighbor pair and Δg_{AB} is the non-configurational Gibbs energy change for the formation of two moles of (A-B) pairs.

When the solution is formed from pure components A and B, some (A-A) and (B-B) pairs break to form (A-B) pairs, so the Gibbs energy of mixing is given by [16]:

$$\Delta G_{mix} = G - (n_{\text{A}} g_{\text{A}}^{\circ} + n_{\text{B}} g_{\text{B}}^{\circ}) = -T\Delta \text{S}^{\text{config}} + \left(\frac{n_{\text{AB}}}{2} \right) \Delta g_{\text{AB}} \tag{2.10}$$

where g_{A}° and g_{B}° are the molar Gibbs energies of pure liquid components; n_{A}, n_{B} and n_{AB} are the numbers of moles of A, B and (A-B) pairs and $\Delta \text{S}^{\text{config}}$ is the configurational entropy of mixing given by randomly distributing the (A-A), (B-B) and (A-B) pairs. Since no exact expression is known for the entropy of this distribution in three dimensions, an approximate equation is used which was shown [16] to be an exact expression for a one dimensional lattice (Ising model) and to correctly reduce to the random mixing point approximation (Bragg Williams) expression when Δg_{AB} is equal to zero.

Δg_{AB} can be expanded as an empirical polynomial in terms of the mole fractions of pairs [16]:

$$\Delta g_{\text{AB}} = \Delta g_{\text{AB}}^{\circ} + \sum_{(i+j)\geq 1} g_{\text{AB}}^{ij} X_{\text{AA}}^{i} X_{\text{BB}}^{j} \tag{2.11}$$

or in terms of component fractions

$$\Delta g_{\text{AB}} = \Delta g_{\text{AB}}^{\circ} + \sum_{(i+j)\geq 1} \omega_{\text{AB}}^{ij} Y_{\text{A}}^{i} Y_{\text{B}}^{j} \tag{2.12}$$

where $\Delta g^{\circ}_{\mathrm{AB}}$ and g^{ij}_{AB} are the parameters of the model which can be functions of temperature. In practice, only the parameters g^{i0}_{AB} and g^{0j}_{AB} need to be included. The definition for "coordination-equivalent" component fraction Y_m is given in Ref. [17].

The composition of maximum short-range ordering is determined by the ratio of the coordination numbers. Let Z_{A} and Z_{B} be the coordination numbers of A and B. These coordination numbers can vary with composition as follows [16]:

$$\frac{1}{Z_{\mathrm{A}}} = \frac{1}{Z^{\mathrm{A}}_{\mathrm{AA}}}\left(\frac{2n_{\mathrm{AA}}}{2n_{\mathrm{AA}}+n_{\mathrm{AB}}}\right) + \frac{1}{Z^{\mathrm{A}}_{\mathrm{AB}}}\left(\frac{n_{\mathrm{AB}}}{2n_{\mathrm{AA}}+n_{\mathrm{AB}}}\right) \tag{2.13}$$

$$\frac{1}{Z_{\mathrm{B}}} = \frac{1}{Z^{\mathrm{B}}_{\mathrm{BB}}}\left(\frac{2n_{\mathrm{BB}}}{2n_{\mathrm{BB}}+n_{\mathrm{AB}}}\right) + \frac{1}{Z^{\mathrm{B}}_{\mathrm{BA}}}\left(\frac{n_{\mathrm{AB}}}{2n_{\mathrm{BB}}+n_{\mathrm{AB}}}\right) \tag{2.14}$$

where $Z^{\mathrm{A}}_{\mathrm{AA}}$ and $Z^{\mathrm{A}}_{\mathrm{AB}}$ are the values of Z_{A} when all nearest neighbors of an A are As, and when all nearest neighbors of an A are Bs, respectively, and where $Z^{\mathrm{B}}_{\mathrm{BB}}$ and $Z^{\mathrm{B}}_{\mathrm{BA}}$ are defined similarly. For example, in order to set the composition of maximum short-range ordering at the molar ratio $n_{\mathrm{A}}/n_{\mathrm{B}} = 2$, one can set the ratio $Z^{\mathrm{B}}_{\mathrm{BA}}/Z^{\mathrm{A}}_{\mathrm{AB}} = 2$. Values of $Z^{\mathrm{B}}_{\mathrm{BA}}$ and $Z^{\mathrm{A}}_{\mathrm{AB}}$ are unique to the A-B binary system, while the value of $Z^{\mathrm{A}}_{\mathrm{AA}}$ is common to all systems containing A as a component.

Even though the model is sensitive to the ratio of the coordination numbers, it is less sensitive to their absolute values. It was found by experience that selecting values of the coordination numbers which are smaller than actual values often yields better results. This is due to the inaccuracy introduced by an approximate equation for the configurational entropy of mixing which is only exact for a one dimensional lattice. The smaller coordination numbers partially compensate this inaccuracy in the model equations, being more consistent with a one dimensional lattice. Therefore, the "coordination numbers" in our model are essentially treated as model parameters which are used mainly to set a physically reasonable composition of maximum short-range ordering. In general, coordination numbers are not equal to valencies of species in (2.8).

The similar reasoning about the interpolation of binary parameters into a multicomponent system is true for quasichemical parameters as for Bragg-Williams parameters. The latter was given in Section 2.1. The application of geometric models for the Modified Quasichemical

formalism is discussed in details by Pelton and Chartrand [17]. The components of liquid solution (2.8) are divided into two groups: metals (Cu^{I}, Cu^{II}, Fe^{II} and Fe^{III}) and nonmetals (O, S). By this means, in every ternary subsystem, either three components belong to the same group or one belongs to a different group. The "Kohler-like" extrapolation is applied in the first case; the "Toop-like" extrapolation is used in the second case, with the different component considered as an asymmetric one.

2.3 Slag

With the introduction of silica into metal oxide melt, the structure of the liquid solution becomes more complicated. As before, metals surround themselves by oxygen, but at the same time there is a strong tendency to get Si^{4+} cations second next to basic cations (Ca^{2+}, Fe^{2+}, etc.):

$$(\text{Ca-O-Ca}) + (\text{Si-O-Si}) = 2(\text{Ca-O-Si}),\ \ \Delta g_{\text{CaSi/OO}} \tag{2.15}$$

In other words, slags exhibit a significant second nearest neighbor (SNN) short-range ordering (SRO) between basic cations and acidic Si^{4+} cations. The existing thermodynamic models are not able to model simultaneously FNN and SNN SRO for species in one sublattice. However, in case of slags it is not necessary, because the range of nonstoichiometry towards metal and toward nonmetal is usually very small. Sulfur is soluble in slags, but to a relatively small extend, so the nonstoichiometry of sulfides does not play a significant role. Thus, it is reasonable to place cation and anion species on separate sublattices:

$$\left(Al^{3+}, Ca^{2+}, Cu^{1+}, Fe^{2+}, Fe^{3+}, Mg^{2+}, Si^{4+}\right)\left(O^{2-}, S^{2-}\right) \tag{2.16}$$

In this way, the magnitude of FNN SRO would be represented by the Gibbs energies of the slag solution end-members: oxides CaO, FeO, SiO_2 and sulfides CaS, Cu_2S, FeS, etc. These Gibbs energies are the most important model parameters. To take into account the effect of SNN SRO on the thermodynamic properties of slag liquid, the Modified Quasichemical Model in quadruplet approximation (MQMQA) was used [18]. The Gibbs energy expression is:

$$G = \sum_{\substack{i,j \\ k,l}} n_{ij/kl} g_{ij/kl} - T\Delta S^{\text{config}} \tag{2.17}$$

where i,j = Al^{3+}, Ca^{2+}, Cu^{1+}, Fe^{2+}, Fe^{3+}, Mg^{2+}, Si^{4+} and k,l = O^{2-}, S^{2-}, $n_{ij/kl}$ and $g_{ij/kl}$ are the number of moles and the molar Gibbs enegy of the ij/kl quadruplet, ΔS^{config} is the configuration entropy of mixing.

Let us first consider the Gibbs energies of quadruplets.

1) For unary quadruplets, Gibbs energies are obtained from those of pure oxides or sulfides. For example [19]:

$$g_{\mathrm{CaCa/OO}} = \left(\frac{2}{Z^{\mathrm{Ca}}_{\mathrm{CaCa/OO}}} \right) g^{\circ}_{\mathrm{CaO}} \tag{2.18}$$

where $Z^{\mathrm{Ca}}_{\mathrm{CaCa/OO}}$ is the coordination number of Ca species when (hypothetically) all Ca species exist in CaCa/OO quadruplet, g°_{CaO} is the standard molar Gibbs energy of pure liquid CaO. For details, see Ref. [18].

2) For binary quadruplets, Gibbs energies are obtained as follows [19]. For example, Reaction (2.15) for the SNN pair exchange reaction in the $CaO–SiO_2$ system is equivalent to the following reaction among quadruplets:

$$(\mathrm{CaCa/OO})_{quad} + (\mathrm{SiSi/OO})_{quad} = 2(\mathrm{CaSi/OO})_{quad},\ \Delta g_{\mathrm{CaSi/OO}} \tag{2.19}$$

Hence,

$$2g_{\mathrm{CaSi/OO}} = g_{\mathrm{CaCa/OO}} + g_{\mathrm{SiSi/OO}} + \Delta g_{\mathrm{CaSi/OO}} \tag{2.20}$$

where $\Delta g_{\mathrm{CaSi/OO}}$ is a model parameter, which represents the degree of SNN SRO. Similar reasoning is true for the binary quadruplets of AA/XY type.

3) Finally, the Gibbs energy of the reciprocal quadruplet may be obtained by the reaction below [19]:

$$(\mathrm{CaSi/OO})_{quad} + (\mathrm{CaSi/SS})_{quad} + (\mathrm{CaCa/OS})_{quad} + (\mathrm{SiSi/OS})_{quad} = 4(\mathrm{CaSi/OS})_{quad},\ \Delta g_{\mathrm{CaSi/OS}} \tag{2.21}$$

$$4g_{\mathrm{CaSi/OS}} = g_{\mathrm{CaSi/OO}} + g_{\mathrm{CaSi/SS}} + g_{\mathrm{CaCa/OS}} + g_{\mathrm{SiSi/OS}} + \Delta g_{\mathrm{CaSi/OS}} \tag{2.22}$$

ΔS^{config} is given by randomly distributing the quadruplets over the sublattices, taking into the account the fact that anion-cation pairs are shared among quadruplets. Because the exact mathematic expression for such distribution is not known, the configurational entropy is

approximated by a cluster-variation equation. There now exist two variants of the MQMQA, with the difference in mathematical expression for ΔS^{config}. The first is [19]:

$$-\Delta S^{config}/R = \sum_{i=\text{cation}} n_i \ln X_i + \sum_{k=\text{anion}} n_k \ln X_k + \sum_{\substack{i=\text{cation}\\k=\text{anion}}} n_{i/k} \ln \frac{X_{i,k}}{Y_i Y_k} + \sum_{\substack{i,j=\text{cation}\\k,l=\text{anion}}} n_{i,j/k,l} \ln \frac{X_{i,j/k,l}(Y_i Y_j Y_k Y_l)}{(2-\delta_{ij})(2-\delta_{kl}) X_{i/k} X_{j/k} X_{i/l} X_{j/l}} \quad (2.23)$$

where n_i is the number of moles of *i*, X_i is the site fraction of *i*, $n_{i/k}$ is the number of moles of the (*i*-*j*) FNN pair, $X_{i,k}$ is the pair fraction of the (*i*-*j*) FNN pair, Y_i is the equivalent fraction of *i*, δ_{ij} is the Kröneker delta (δ_{ij} = 0 if $i \neq j$ and δ_{ij} = 1 if $i = j$). The definition of this variables can be found in Ref. [18]. The second variant is given in Appendix 1 of Ref. [20]:

$$-\Delta S^{config}/R = \sum_{i=\text{cation}} n_i \ln X_i + \sum_{k=\text{anion}} n_k \ln X_k + \sum_{\substack{i=\text{cation}\\k=\text{anion}}} n^*_{i/k} \ln \frac{X^*_{i,k}}{F_i F_k} + \sum_{\substack{i,j=\text{cation}\\k,l=\text{anion}}} n_{i,j/k,l} \ln \left[\frac{X_{i,j/k,l}(Y_i Y_j Y_k Y_l)}{(2-\delta_{ij})(2-\delta_{kl}) X_{i/k} X_{j/k} X_{i/l} X_{j/l}} \cdot \frac{(X_{i/k} X_{j/k} X_{i/l} X_{j/l})^{1/4}}{(Y_i Y_j Y_k Y_l)^{1/2}} \right] \quad (2.24)$$

The difference between $n_{i/k}$ and $n^*_{i/k}$, $X_{i,k}$ and $X^*_{i,k}$, Y_i and F_i, Y_k and F_k in the third term of Equations (2.23) and (2.24) arises from the difference in the definition of variable ζ (see Equation (17) in Ref. [18]). It determines the ratio of SNN and FNN pairs, emanating from different species. The first variant of MQMQA assumes that ζ is the same for all species, in the second variant ζ varies depending on composition. This allows more flexibility in calculation of FNN pairs. For details the reader is referred to Ref. [18] and Annex 1 of Ref. [20]. Two variants of MQMQA give different results only in reciprocal systems, i.e. when at least two cations and two anions are present. The newer second variant is used in the present study.

2.4 Spinel

The structure of spinel may be derived from the fcc close packing of oxygen anions. Cations occupy half of the octahedral interstices and one-eighth of the tetrahedral interstices [21] (Figure

2.2). Tetrahedral and octahedral sublattices of spinels are distinguishable, it is a common practice to represent spinels as $(A, B, \ldots)^{tetr}[A, B, \ldots]^{oct}{}_2O_4$[1], where A, B, etc. are cations with charges +2 and +3, rarely +4 or +1. Oxygen has charge -2. The condition of electroneutrality must be always obeyed. Cations have preference to occupy either tetrahedral or octahedral sublattice, but exclusive occupation of any particular sublattice is prevented by the entropy effect. Historically, the spinels with tetrahedral sublattice occupied only by divalent cations, and octahedral – only by trivalent cations are called "normal" spinels. If trivalent cations are situated on the tetrahedral sublattice, and all divalent cations are on the octahedral one, the spinel is called "inverse". The cation distribution of real spinels is intermediate between normal and inverse.

The Compound Energy Formalism (CEF) [22, 23] was specially designed for solid solutions with distinct sublattices. It was successfully applied to modeling olivine, pyroxene solutions and spinels [24, 25].

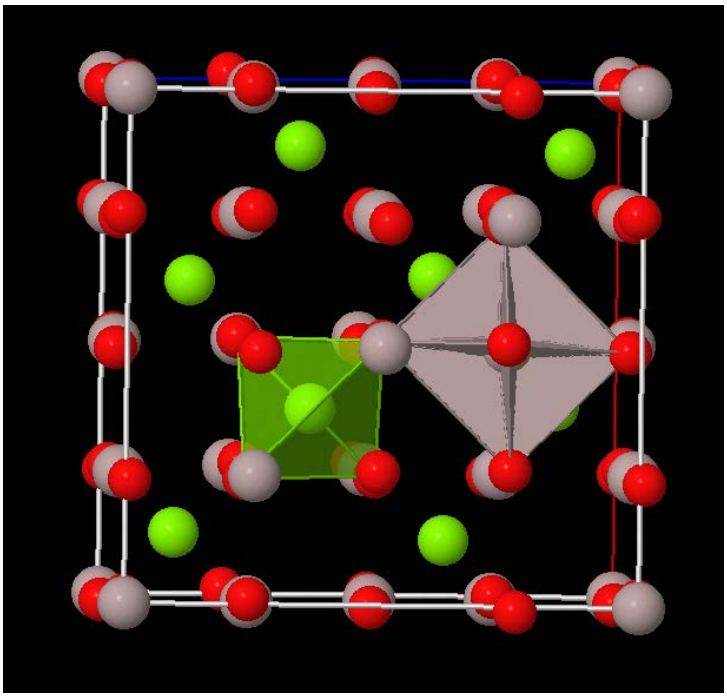

Figure 2.2. The 3D model of $MgAl_2O_4$ completely normal spinel. Mg (green) occupy 1/8 of the tetrahedral interstices, Al (grey) occupy half of the octahedral interstices. http://www.chemtube3d.com/solidstate/_spinel(final).htm.

[1] The formation of tio-spinels, $Ni^{2+}Ni^{3+}{}_2S_4$, $Fe^{2+}Fe^{3+}{}_2S_4$, etc., may be important in nickel pyrometallurgical processing, but no reports were found in the literature on the presence of tio-spinels during the copper production.

For the two sublattice spinel solution, the Gibbs-energy expression in the CEF per formula unit is [22, 23]:

$$G_m = \sum_i \sum_j Y_i^{\text{tetr}} Y_j^{\text{oct}} G_{ij} - T\Delta S_c + G_m^E \tag{2.25}$$

where $Y_i^{'}$ and $Y_j^{''}$ represent the site fractions of constituents *i* and *j* on the first and second sublattices, respectively, G_{ij} is the Gibbs energy of an end-member $(i)^{\text{tetr}}[j]_2^{\text{oct}}\text{O}_4$, S_c is the configurational entropy. Taking into the account, that the second sublattice has 2 mole sites of cations per mole of solution:

$$\Delta S_c = -R\left(\sum_i Y_i^{\text{tetr}} \ln Y_i^{\text{tetr}} + 2\sum_j Y_j^{\text{oct}} \ln Y_j^{\text{oct}} \right) \tag{2.26}$$

and G_m^E is the excess Gibbs energy,

$$G_m^E = \sum_i \sum_j \sum_k Y_i^{\text{tetr}} Y_j^{\text{tetr}} Y_k^{\text{oct}} L_{ij:k} + \sum_i \sum_j \sum_k Y_k^{\text{tetr}} Y_i^{\text{oct}} Y_j^{\text{oct}} L_{k:ij} \tag{2.27}$$

$L_{ij:k}$ and $L_{k:ij}$ are the interaction energies between cations *i* and *j* on one sublattice when the other sublattice is occupied only by *k*.

The spinel solution, developed during this study, is represented by the formula

$$(\text{Al}^{+3},\text{Cu}^{+2},\text{Fe}^{+2},\text{Fe}^{+3},\text{Mg}^{+2})^{\text{tetr}}[\text{Al}^{+3},\text{Ca}^{+2},\text{Cu}^{+2},\text{Fe}^{+2},\text{Fe}^{+3},\text{Mg}^{+2},\text{Va}]_2^{\text{oct}}\text{O}_4^{-2} \tag{2.28}$$

According to Equation (2.25), 35 Gibbs energy expressions are required for the preudocomponents of the spinel. For the simplicity of formulas, the following notations are used: *F* for Al^{+3}, *M* for Cu^{+2}, *A* for Fe^{+2}, *E* for Fe^{+3}, *B* for Mg^{+2}, *P* for Ca^{+2} and *V* for vacancy Va. Letters are rather arbitrary and their selection has historical reasons to comply with internal notations used at CRCT. For instance, G_{MF} is the Gibbs energy of $\left((\text{Cu}^{+2})^{\text{tetr}}[\text{Al}^{+3}]_2^{\text{oct}}\text{O}_4^{-2}\right)^0$, and G_{AP} is the Gibbs energy of $\left((\text{Fe}^{+2})^{\text{tetr}}[\text{Ca}^{+2}]_2^{\text{oct}}\text{O}_4^{-2}\right)^{2-}$.

The thermodynamic properties of pseudocomponents are related to those of real spinels, but they should not be confused. Even if *MF* pseudocomponent is electroneutral, the spinel with stoichiometric composition CuAl_2O_4 would be represented by the model as a mixture of *MF*,

MM, *FF* and *FM*. The amounts of the pseudocomponents are calculated through a Gibbs energy minimization procedure.

In addition to the CEF, a reasonable procedure to obtain G_{ij} from available experimental data is required. As it was shown by Decterov et al. [21] it is preferable to optimize linear combinations of G_{ij}, rather than fix them directly but arbitrarily. In other words, an appropriate model within the Compound Energy Formalism should be developed. The following linear combinations were applied as model parameters in this study:

Stoichiometric Fe_3O_4 [21]

$$F_{AE} = \frac{1}{7}G_{AE} = \frac{1}{7}G_{EA} \Rightarrow G_{AE}, G_{EA} \tag{2.29}$$

$$I_{AE} = G_{EE} + G_{EA} - 2G_{AE} \Rightarrow G_{EE} \tag{2.30}$$

$$\Delta_{AE} = G_{AA} + G_{EE} - G_{EA} - G_{AE} \Rightarrow G_{AA} \tag{2.31}$$

Non-stoichiometry towards Fe_2O_3 [21]

$$V_E = G_{EV} - \frac{5}{7}G_{EA} \Rightarrow G_{EV} \tag{2.32}$$

$$\Delta_{EAV} = G_{AA} + G_{EV} - G_{EA} - G_{AV} \Rightarrow G_{AV} \tag{2.33}$$

Stoichiometric $FeAl_2O_4$ [25]

$$F_{AF} = \frac{1}{7}G_{AF} \Rightarrow G_{AF} \tag{2.34}$$

$$\left.\begin{aligned} I_{AF} &= G_{FF} + G_{FA} - 2G_{AF} \\ \Delta_{AF} &= G_{AA} + G_{FF} - G_{FA} - G_{AF} \end{aligned}\right\} \Rightarrow G_{FF}, G_{FA} \tag{2.35}$$

Non-stoichiometry towards Al_2O_3 [25]

$$\left.\begin{aligned} 40F_{FV} &= 8G^{\circ}_{\gamma-Al_2O_3} - 2RT(5\ln 5 - 6\ln 6) \\ G_{FV} &= 40F_{FV} - 5G_{FF} - \frac{5}{6}L_{F:FV} \end{aligned}\right\} \Rightarrow G_{FV} \tag{2.36}$$

Solution Al–Fe–O [25]

$$\Delta_{AEF} = G_{EE} + G_{AF} - G_{AE} - G_{EF} \Rightarrow G_{EF} \tag{2.37}$$

$$\Delta_{EF} = G_{EE} + G_{FF} - G_{FE} - G_{EF} \Rightarrow G_{FE} \tag{2.38}$$

Stoichiometric $MgAl_2O_4$ [24]

$$F_{BF} = \frac{1}{7} G_{BF} \Rightarrow G_{BF} \tag{2.39}$$

$$I_{BF} = G_{FF} + G_{FB} - 2G_{BF} \Rightarrow G_{FB} \tag{2.40}$$

$$\Delta_{BF} = G_{BB} + G_{FF} - G_{FB} - G_{BF} \Rightarrow G_{BB} \tag{2.41}$$

Non-stoichiometry towards excess oxygen [24]

$$\Delta_{FBV} = G_{BB} + G_{FV} - G_{FB} - G_{BV} \Rightarrow G_{BV} \tag{2.42}$$

Stoichiometric $MgFe_2O_4$ [24]

$$F_{BE} = \frac{1}{7} G_{BE} \Rightarrow G_{BE} \tag{2.43}$$

$$I_{BE} = G_{EE} + G_{EB} - 2G_{BE} \Rightarrow G_{EB} \tag{2.44}$$

Solution Mg–Fe–O [24]

$$\Delta_{ABE} = G_{BB} + G_{AE} - G_{AB} - G_{BE} \Rightarrow G_{AB} \tag{2.45}$$

$$\Delta_{BAE} = G_{AA} + G_{BE} - G_{BA} - G_{AE} \Rightarrow G_{BA} \tag{2.46}$$

Stoichiometric $CuFe_2O_4$

$$F_{ME} = \frac{1}{7} G_{ME} \Rightarrow G_{ME} \tag{2.47}$$

$$I_{ME} = G_{EE} + G_{EM} - 2G_{ME} \Rightarrow G_{EM} \tag{2.48}$$

Solution Cu–Fe–O and non-stoichiometry towards excess oxygen

$$\Delta_{ME} = G_{MM} + G_{EE} - G_{EM} - G_{ME} \Rightarrow G_{MM} \tag{2.49}$$

$$\Delta_{EMA} = G_{MM} + G_{AE} - G_{EM} - G_{MA} \Rightarrow G_{MA} \tag{2.50}$$

$$\Delta_{EAM} = G_{AA} + G_{EM} - G_{EA} - G_{AM} \Rightarrow G_{AM} \tag{2.51}$$

$$\Delta_{EMV} = G_{MM} + G_{EV} - G_{EM} - G_{MV} \Rightarrow G_{MV} \tag{2.52}$$

Stoichiometric $CuAl_2O_4$

$$F_{MF} = \frac{1}{7} G_{MF} \Rightarrow G_{MF} \tag{2.53}$$

$$I_{MF} = G_{FF} + G_{FM} - 2G_{MF} \Rightarrow G_{FM} \tag{2.54}$$

Solubility of Ca in spinel:

$$G^{\circ}_{\text{orthorhombic-CaFe}_2\text{O}_4} + (\Delta_{\text{orthorhombic}\rightarrow\text{spinel}}\text{H} - T\Delta_{\text{orthorhombic}\rightarrow\text{spinel}}\text{S}) = G_{E(EP)} = 0.5G_{EE} + 0.5G_{EP} + 2RT\cdot[0.5\ln 0.5 + 0.5\ln 0.5] \Rightarrow G_{EP} \quad (2.55)$$

$$\Delta_{EAP} = G_{EP} + G_{AA} - G_{EA} - G_{AP} \Rightarrow G_{AP} \quad (2.56)$$

$$G^{\circ}_{\text{monoclinic-CaAl}_2\text{O}_4} + (\Delta_{\text{monoclinic}\rightarrow\text{spinel}}\text{H} - T\Delta_{\text{monoclinic}\rightarrow\text{spinel}}\text{S}) = G_{F(FP)} = 0.5G_{FF} + 0.5G_{FP} + 2RT\cdot[0.5\ln 0.5 + 0.5\ln 0.5] \Rightarrow G_{FP} \quad (2.57)$$

$$\Delta_{EMP} = G_{MM} + G_{EP} - G_{EM} - G_{MP} \Rightarrow G_{MP} \quad (2.58)$$

$$\Delta_{BME} = G_{BE} + G_{MM} - G_{BM} - G_{ME} \Rightarrow G_{BM} \quad (2.59)$$

$$\Delta_{BMB} = G_{BB} + G_{MM} - G_{BM} - G_{MB} \Rightarrow G_{MB} \quad (2.60)$$

The solution of equations (2.29)-(2.60), giving the expression G_{ij} through F, I, Δ and other parameters, is given in Section 8.6, Table 8–1 with the values of parameters. The sequence of parameters (2.29)-(2.60) corresponds to the order in which systems were optimized, and this order is not arbitrary. Spinels form two closed circles as is shown in (2.61). A link of the circle inherits the properties of the previous link, so fewer and fewer parameters are available in a sequence of optimizations. That is why optimizations start with those systems where more experimental data are available. When it comes to the last link, only a few parameters are available to fit the data. Sometimes, the simultaneous optimization of the whole circle is required if it is not possible to fit the data in the last link. This is what happened during the optimization of the Fe_3O_4–$FeAl_2O_4$–$NiAl_2O_4$–$NiFe_2O_4$ conducted by a colleague V. Prostakova [25]. The re-optimization of the Al–Fe–O system was required, which had an effect on the spinel of this study. Thus, the work was done in collaboration. The Fe_3O_4–$FeAl_2O_4$–$MgAl_2O_4$–$MgFe_2O_4$ part of the spinel database was created previously by In-Ho Jung [24].

$$\begin{array}{ccccc} & & \text{"CaAl}_2\text{O}_4\text{"} & & \\ & & \uparrow & & \\ \text{CuAl}_2\text{O}_4 & \rightarrow & \text{FeAl}_2\text{O}_4 & \rightarrow & \text{MgAl}_2\text{O}_4 \\ \uparrow & & \uparrow & & \downarrow \\ \text{CuFe}_2\text{O}_4 & \leftarrow & \text{Fe}_3\text{O}_4 & \leftarrow & \text{MgFe}_2\text{O}_4 \\ & & \downarrow & & \\ & & \text{"CaFe}_2\text{O}_4\text{"} & & \end{array} \quad (2.61)$$

Many of spinels exhibit magnetic properties with magnetic transitions at certain temperatures. These transitions have an effect on the thermodynamic properties of spinels. The

phenomenological approach proposed by Hillert and Jarl [8] was used to describe the magnetic contribution to thermodynamic functions. Due to the lack of experimental data, it was assumed that the Curie or Neel temperatures, T_C and T_N, and the average magnetic moment per atom, β, are independent of the degree of inversion in pure AB_2O_4 spinels. It was further assumed that these values change linearly with composition from AB_2O_4 to CB_2O_4. The formulae that are used in the CEF to describe the magnetic contribution to thermodynamic functions of a solution were discussed in more detail by Decterov *et al.* [21]. It was shown what values can be assigned to T_{ij} and β_{ij} of the charged pseudocomponents and to excess magnetic parameters in order to obtain simple linear dependences of T_C and β on composition of the spinel solution.

CHAPTER 3 EVALUATION OF PREVIOUSLY MODELED SYSTEMS

Equation Chapter (Next) Section 1

3.1 Fe–S system

The Fe–S system was previously optimized at the CRCT by Waldner and Pelton [26]. The phase diagram is given in Figure 3.1. No miscibility gap was found between liquid metal and sulfide phases. However, a miscibility gap should exist between iron sulfide and liquid sulfur. In the study of Waldner and Pelton [26], liquid phase was described using one solution in the whole range of compositions. The key experimental data on the partial pressure of sulfur above this liquid and on the enthalpy of mixing are compared with the calculated lines in Figure 3.2 and Figure 3.3. The solubility of sulfur in the metallic fcc and bcc iron is shown in Figure 3.4. Partial pressure of sulfur (S_2) over different 2-phase regions of the Fe–S system is given in Figure 3.5. As can be seen from Figure 3.1-Figure 3.5, the agreement between the experimental data and the optimization of Waldner and Pelton [26] is very good. But, in the metallic region at temperatures 1500–1600 °C, $P(S_2)$ calculated using the parameters of Waldner and Pelton [26] seems to be systematically higher (Figure 3.2 (b)). The calculated enthalpy of mixing between Fe(liq) and $1/2S_2$ at 1600 °C is slightly lower than the experimental points (Figure 3.3). The former fact is more evident if $P(S_2)$ is recalculated to the activity coefficient of sulfur:

$$\gamma(S) = \frac{[P(S_2), \text{atm}]^{1/2}}{X(S)} \tag{3.1}$$

The comparison between the experimental and calculated activity coefficient of sulfur is shown in Figure 3.6-Figure 3.8. The inconsistency was confirmed later during the study of the ternary Fe–O–S system. It was not possible to describe the experimental data of Hayashi et al. [27], which are presented in Figure 3.6-Figure 3.8, without lowering the activity coefficient of sulfur in the binary Fe–S system. With all this evidence, it was decided to slightly modify the description of the Fe–S system in this study. The task was complicated by the fact that all the experimental data above and below 1500–1600 °C temperature region were perfectly described, so any modifications of the existing parameters or addition of new ones would result in worse results outside the region of interest.

Finally, the following change was suggested to the main excess parameter

$$\Delta g^{\circ}_{Fe^{II}S}(Waldner) = -104888.10 + 0.3388T,\ \ J \cdot mol^{-1}$$
$$\Delta g^{\circ}_{Fe^{II}S}(This\ study) = -122334.14 + 112.4659T - 13.7582T \ln T\ ,\ J \cdot mol^{-1} \quad (3.2)$$

The values of the main parameter in this study and of Waldner and Pelton [26] are shown in Figure 3.9. They are essentially the same in the temperature interval of 700–1300 °C. As a result of the modification (3.2), the enthalpy of mixing at 1600 °C and $P(S_2)$ above metallic iron at 1500–1600 °C are described better. $P(S_2)$ above metallic iron at 1650–1730 °C is slightly compromised (Figure 3.2 (b)). It was decided to give preference to the experimental data at 1500–1600 °C as these data are closer to industrial conditions and should have higher precision than the data at 1650–1730 °C.

The second change in the liquid solution was introduced in this study when working on the Fe–O system. It was possible to describe the literature data for the Fe–O liquid only after implementation of two differently coordinated iron particles Fe^{II} and Fe^{III} in the solution. Later, the Fe–O solution was joined with the Fe–S solution, forming the (Fe^{II}, Fe^{III}, O, S) liquid phase. As a result, the Fe–S system also inherited the Fe^{III} particle:

$$Waldner:\ (Fe^{II},S)$$
$$This\ study:\ (Fe^{II},Fe^{III},S) \quad (3.3)$$

A large positive enthalpy was assigned to the Fe^{III} particle to prevent its formation in the metal and sulfide liquid. It was found that Fe^{III} had negligible effect in the (Fe^{II}, Fe^{III}, S) solution.

Finally, changes made for the liquid phase decreased sulfur solubility in the Fe(bcc) phase. The interaction parameter was slightly corrected:

$$L_{Fe,S}(Waldner) = -31041.0 - 10.65759T,\ \ J \cdot mol^{-1}$$
$$L_{Fe,S}(This\ study) = -29973.6 - 11.74268T,\ \ J \cdot mol^{-1} \quad (3.4)$$

The calculations made using the database of this study may be compared with the results of Waldner and Pelton [26] in Figure 3.1-Figure 3.8.

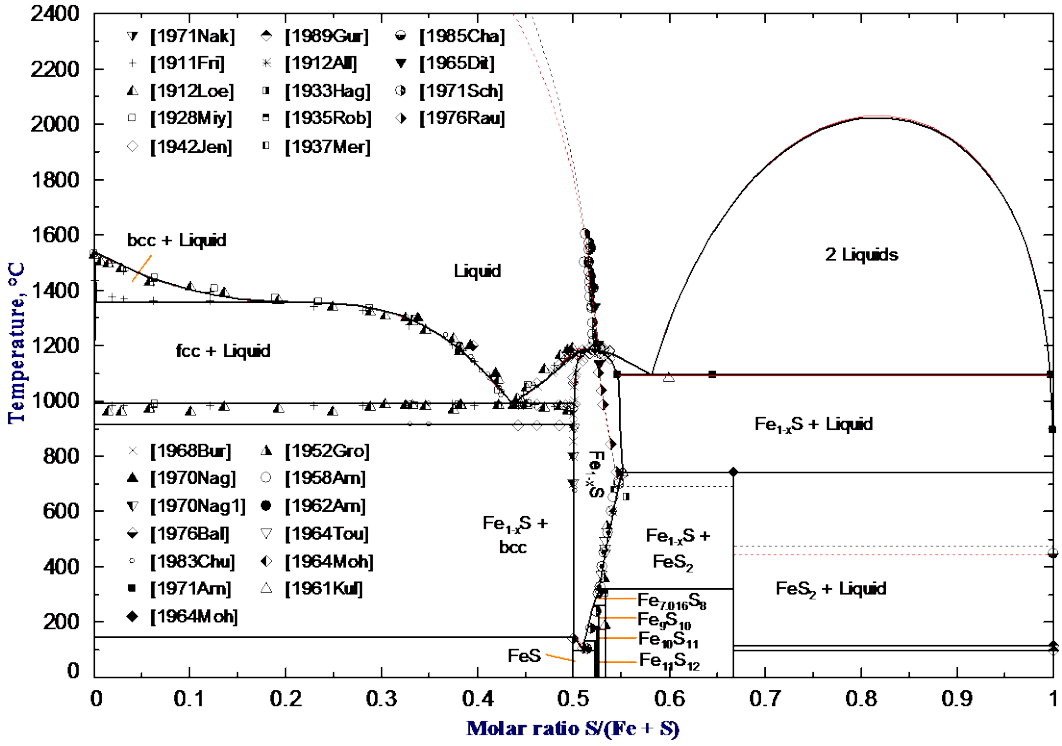

Figure 3.1. Phase diagram of the Fe–S system and S_2-isobar at 1 atm. Experimental points [28-54] and calculated lines: thin red lines – [26], black lines – this study.

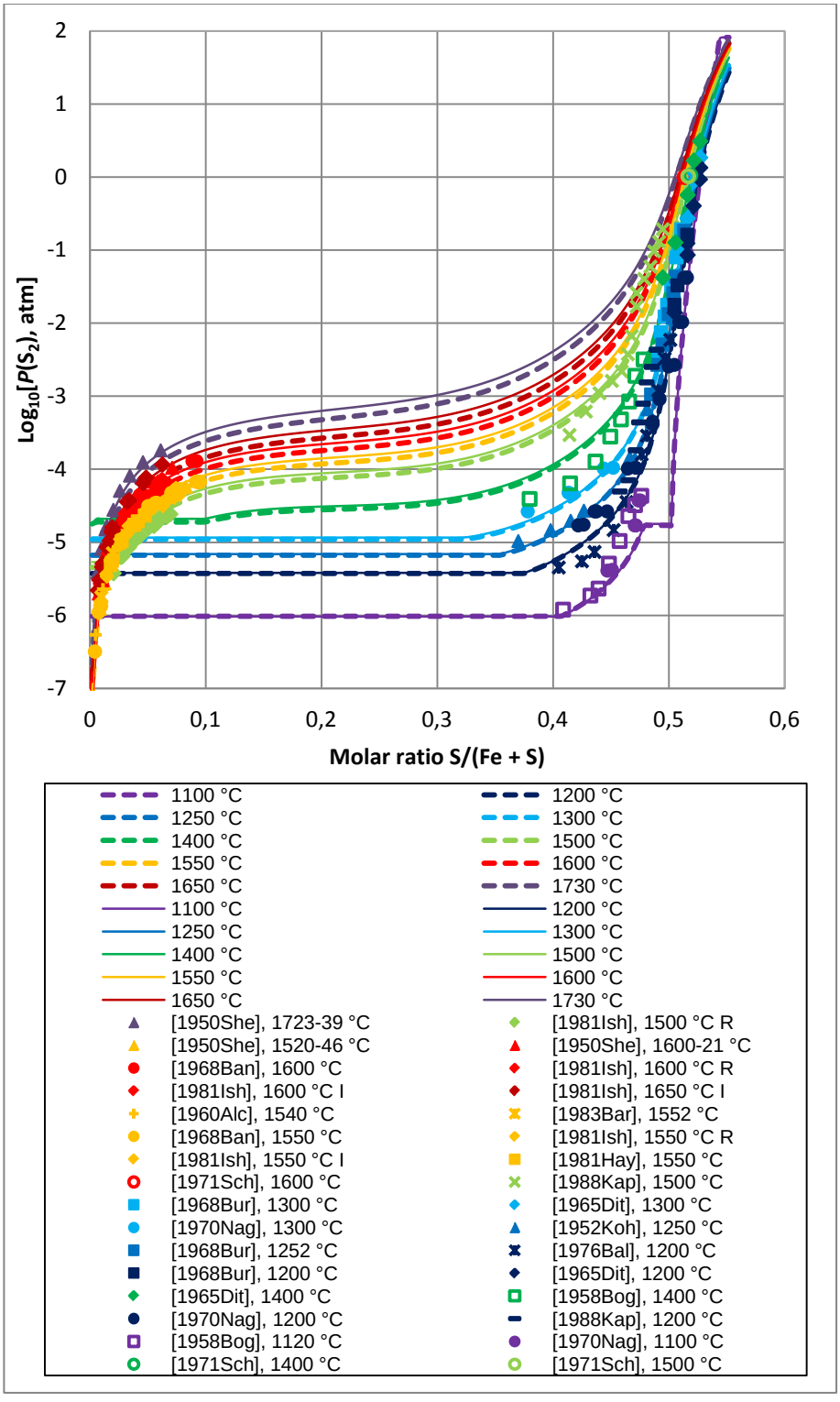
2
1
0
-1
-2
-3
-4
-5
-6
-7
Log10[P(S2), atm]
0
0,1
0,2
0,3
0,4
0,5
0,6
Molar ratio S/(Fe + S)
1100 °C
1200 °C
1250 °C
1300 °C
1400 °C
1500 °C
1550 °C
1600 °C
1650 °C
1730 °C
1100 °C
1200 °C
1250 °C
1300 °C
1400 °C
1500 °C
1550 °C
1600 °C
1650 °C
1730 °C
[1950She], 1723-39 °C
[1981Ish], 1500 °C R
[1950She], 1520-46 °C
[1950She], 1600-21 °C
[1968Ban], 1600 °C
[1981Ish], 1600 °C R
[1981Ish], 1600 °C I
[1981Ish], 1650 °C I
[1960Alc], 1540 °C
[1983Bar], 1552 °C
[1968Ban], 1550 °C
[1981Ish], 1550 °C R
[1981Ish], 1550 °C I
[1981Hay], 1550 °C
[1971Sch], 1600 °C
[1988Kap], 1500 °C
[1968Bur], 1300 °C
[1965Dit], 1300 °C
[1970Nag], 1300 °C
[1952Koh], 1250 °C
[1968Bur], 1252 °C
[1976Bal], 1200 °C
[1968Bur], 1200 °C
[1965Dit], 1200 °C
[1965Dit], 1400 °C
[1958Bog], 1400 °C
[1970Nag], 1200 °C
[1988Kap], 1200 °C
[1958Bog], 1120 °C
[1970Nag], 1100 °C
[1971Sch], 1400 °C
[1971Sch], 1500 °C

(a)

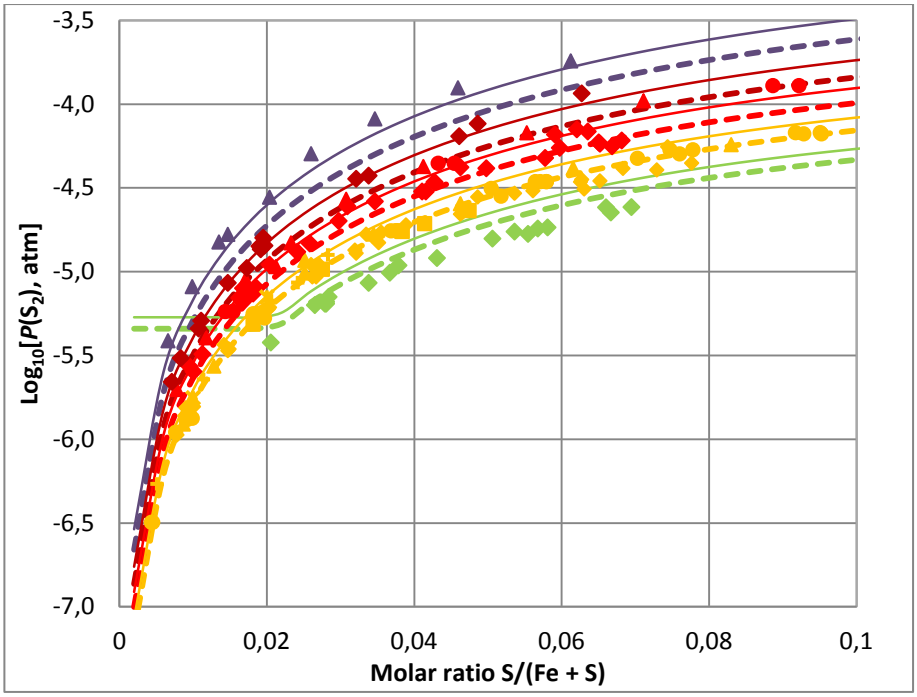

(b)

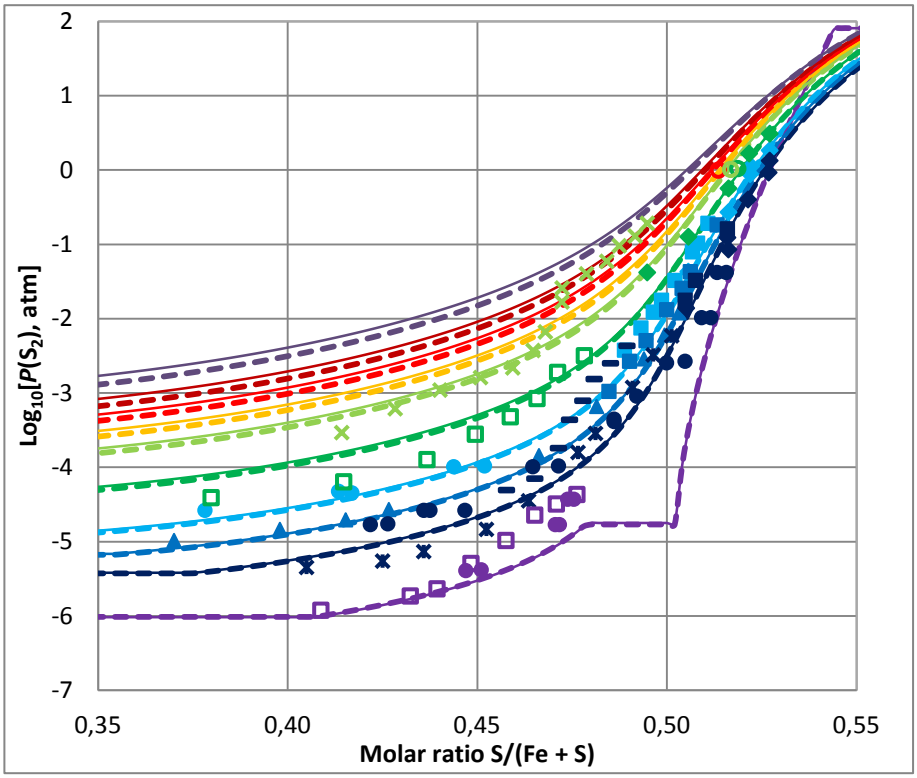

(c)

Figure 3.2. Activity of sulfur in the Fe–S system expressed as $P(S_2)$, (a) – the overview (b) – metal region (c) – sulfide region. Experimental points [33, 34, 36, 53-63] and calculated lines: thin solid – [26], thick dashed – this study.

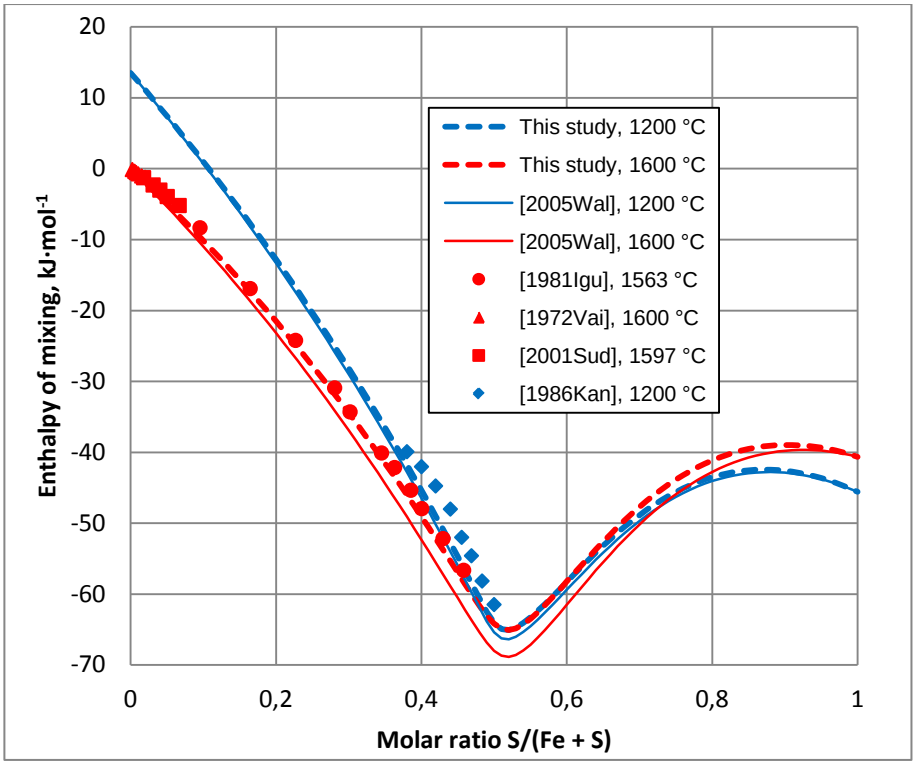

Figure 3.3. Enthalpy of mixing of ½ S_2(gas) and either Fe(fcc) at 1200 °C or liquid iron at other temperatures. Experimental points [64-67] and calculated lines: thick dashed – this study, thin solid lines – [26].

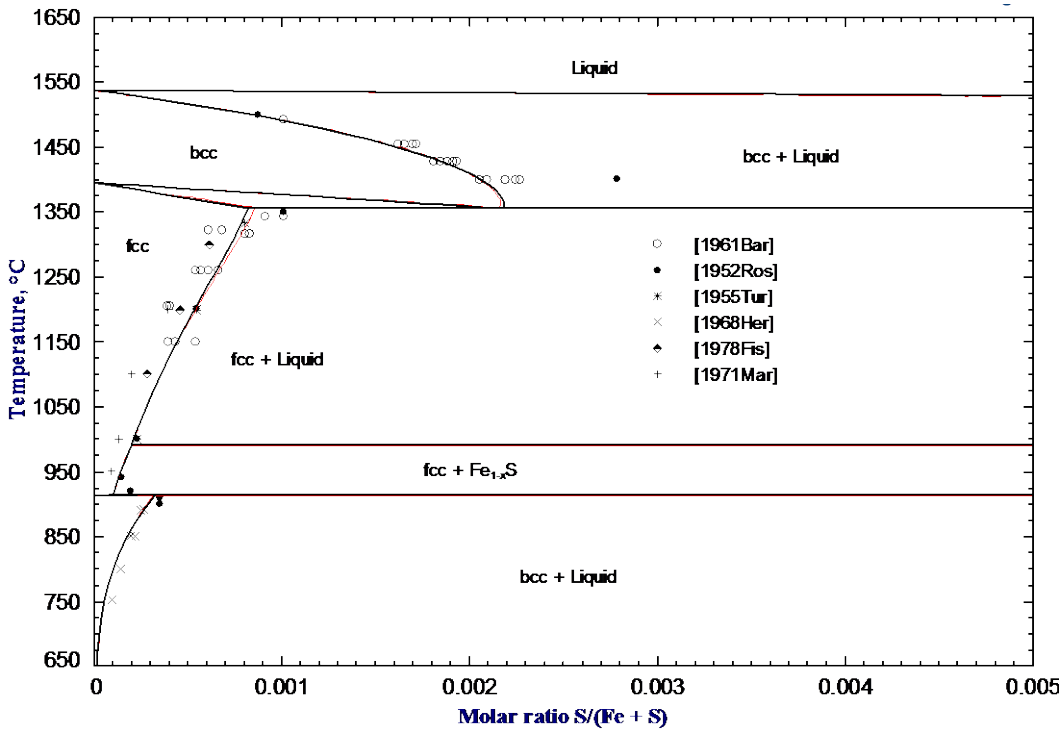

Figure 3.4. Phase diagram of the Fe–S system in the metal region. Experimental points [68-73] and calculated lines: thin red lines – [26], black lines – this study.

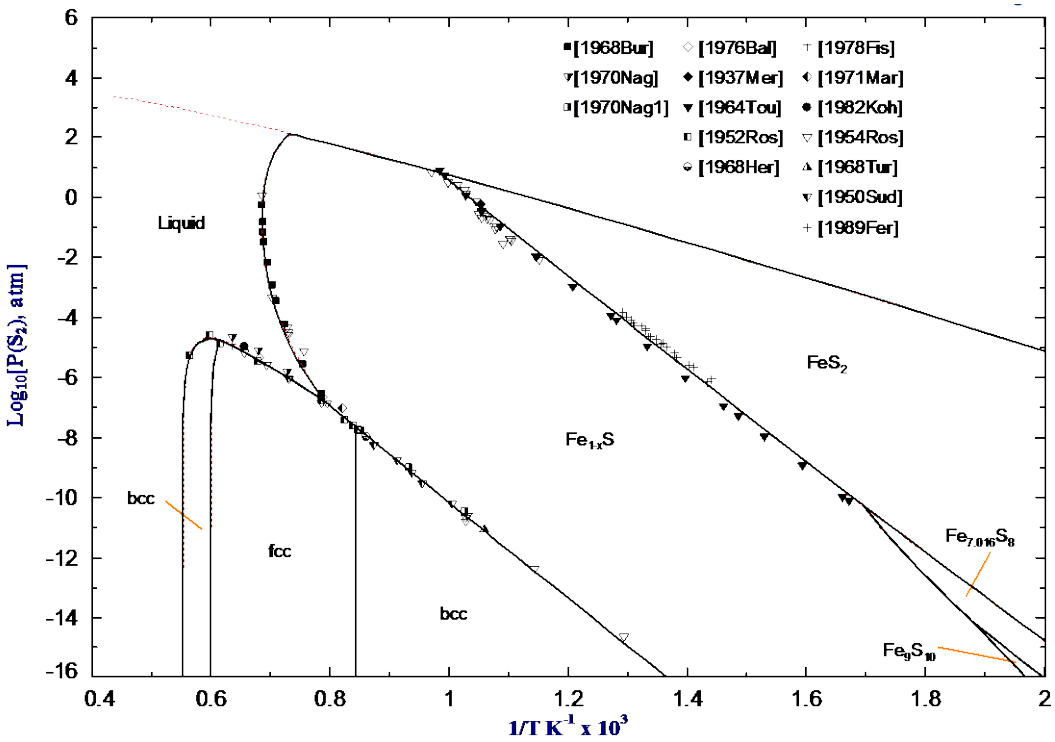

Figure 3.5. Potential phase diagram of the Fe–S system. Experimental points [33-36, 41, 47, 60, 69, 71-77] and calculated lines: solid – this study, dashed red line – [26].

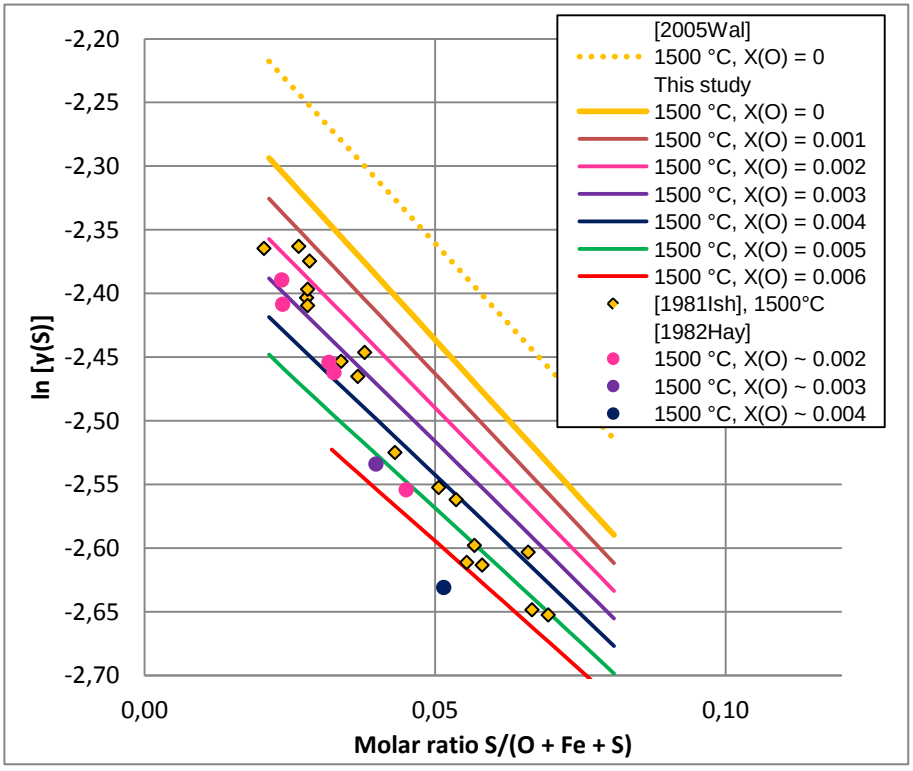

Figure 3.6. Activity coefficient of sulfur in Fe–O–S liquid in the metal region at 1500 °C. Experimental points [27, 57] and calculated lines: solid – this study, dotted line – [26].

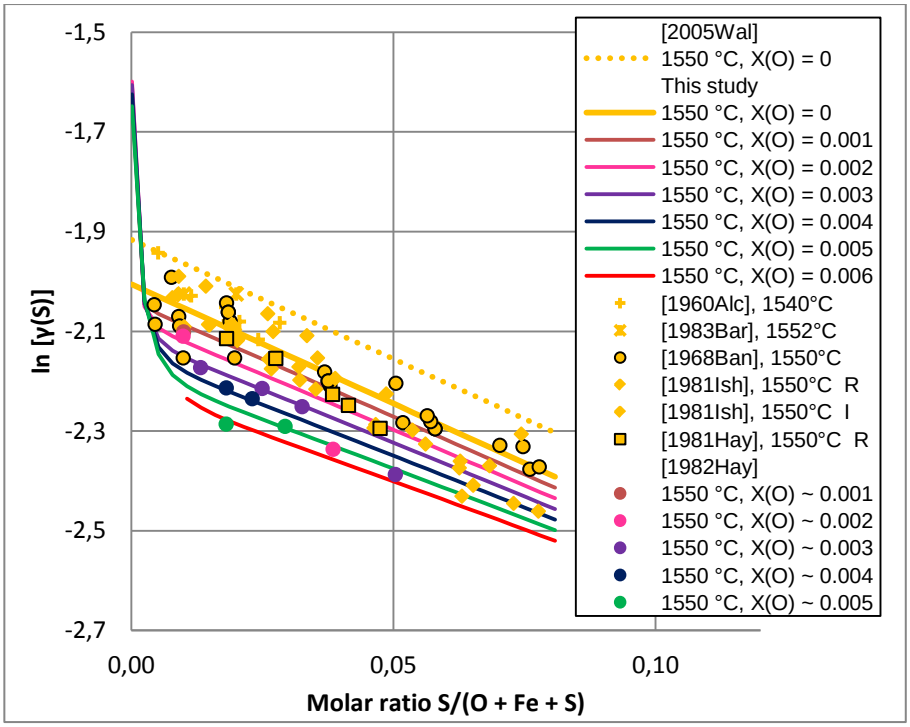

Figure 3.7. Activity coefficient of sulfur in Fe–O–S liquid in the metal region at 1550 °C. Experimental points [27, 56, 57, 61-63] and calculated lines: solid – this study, dotted line – [26].

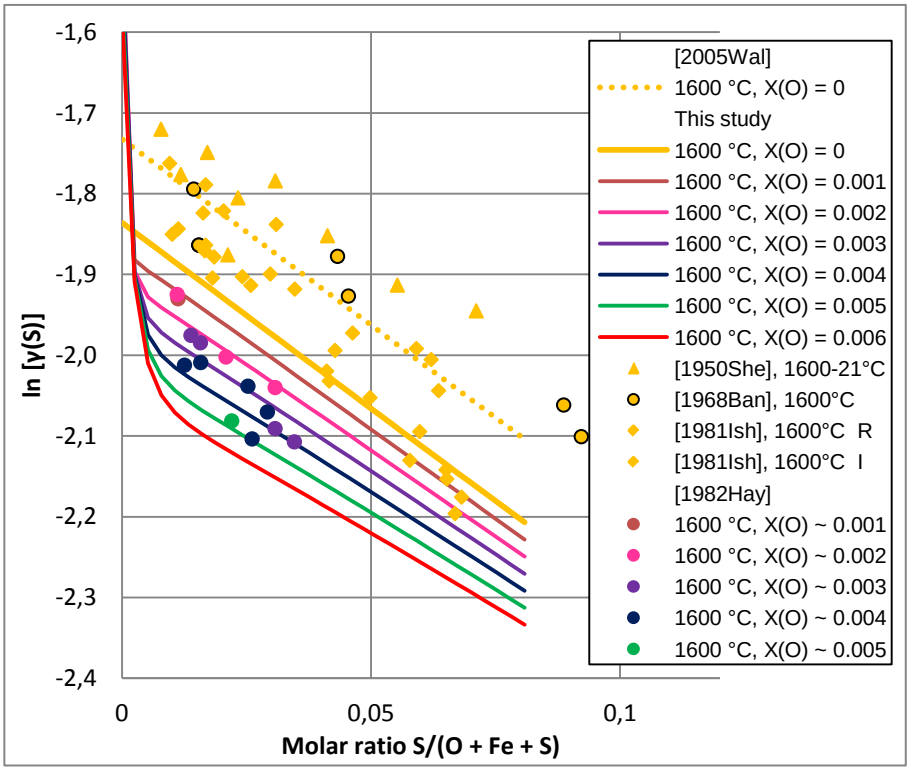

Figure 3.8. Activity coefficient of sulfur in Fe–O–S liquid in the metal region at 1600 °C. Experimental points [27, 55-57] and calculated lines: solid – this study, dotted line – [26].

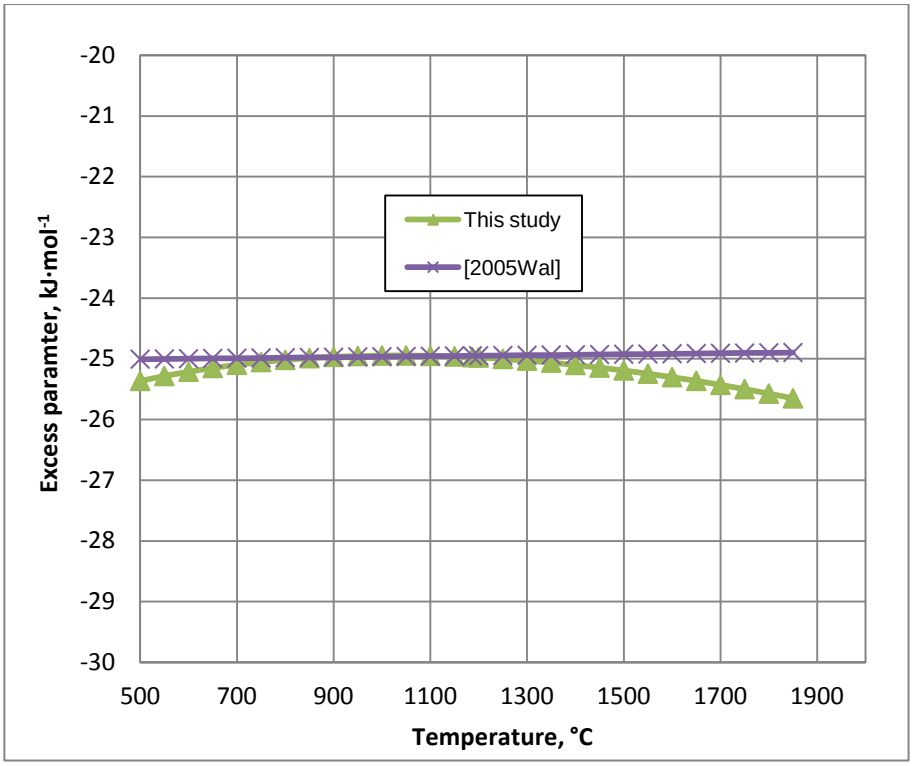

Figure 3.9. Value of the main excess parameter $\Delta g^{\circ}_{Fe^{I}S}$ in the present study and in the optimization of Waldner and Pelton [26].

3.2 Cu–S system

Similar to the Fe–S system, the liquid phase in the Cu–S system was described by Waldner [78] using only one solution in the whole range of compositions. Available experimental data were described rather well. However, in the liquid metal region, the activity coefficient of sulfur seemed to be lower than the experimental observations (Figure 3.11c). This was later confirmed by the experimental data available for the ternary Cu–O–S system (see Figure 4.17): the calculated solubility of sulfur was higher than the experimental data. It was decided to introduce a small correction parameter without complete re-optimization of the Cu–S system:

$$g^{90}_{Cu^{I}S}(This\ study) = -212683.2 + 1204.0134T - 145.1413T\ln T\ ,\ J\cdot mol^{-1} \qquad (3.5)$$

A high power on Cu in the excess parameter (3.5) prevents changes in areas of the Cu–S system other than metallic region and in higher-order systems, which was confirmed through re-calculation of all available phase diagrams and plots. This assured that all available experimental data were well described. The absolute value of the parameters (3.5) is plotted in Figure 3.12.

In addition, the model was slightly changed in order to optimize the Cu–O system. As in the case of the Fe–O system, it was necessary to introduce second differently coordinated copper particle. The merge of Cu–S and Cu–O databases resulted in the change of the model:

$$\begin{aligned} &\textit{Waldner}: \ (Cu^{I},S) \\ &\textit{This study}: \ (Cu^{I},Cu^{II},S) \end{aligned} \qquad (3.6)$$

A large positive enthalpy was assigned to the Cu^{II} particle to prevent its formation in the metal and sulfide liquid. It was found that Cu^{II} had negligible effect in the (Cu^{I}, Cu^{II}, S) solution. The calculations made employing the database of this study may be compared with the results of Waldner [78] in Figure 3.10-Figure 3.13.

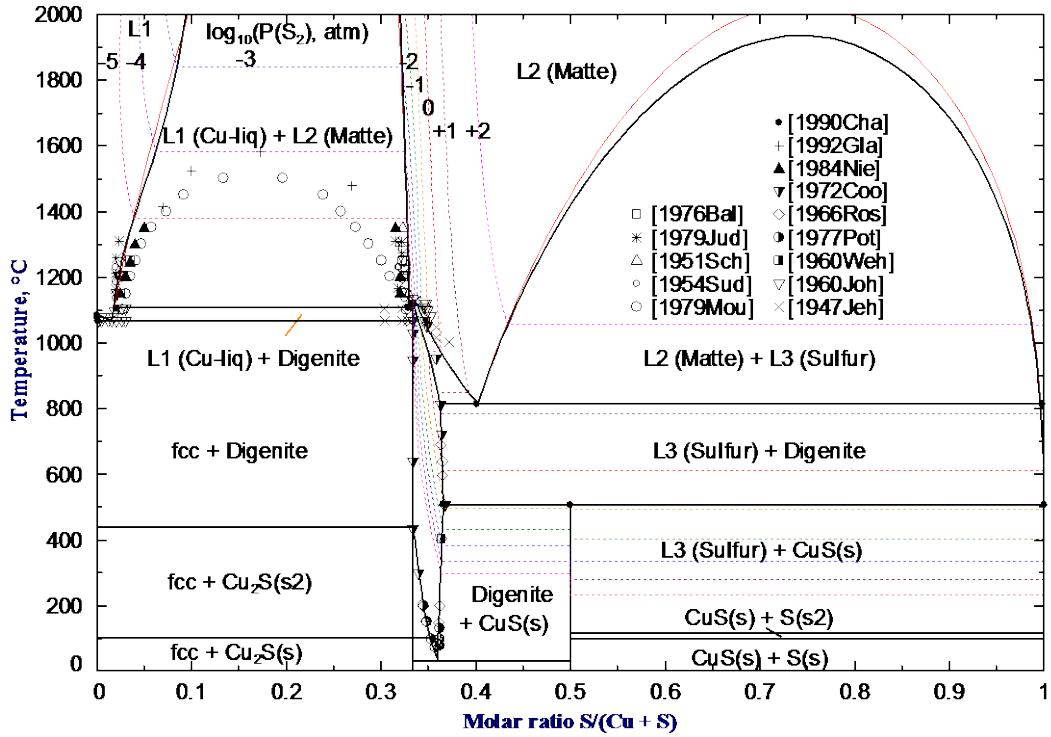

Figure 3.10. Phase diagram of the Cu–S system. Gas phase is suppressed. Experimental points [36, 79-91] and calculated lines: thin red lines – [92], black solid lines – phase boundaries in this study, dashed lines – sulfur isobars in this study.

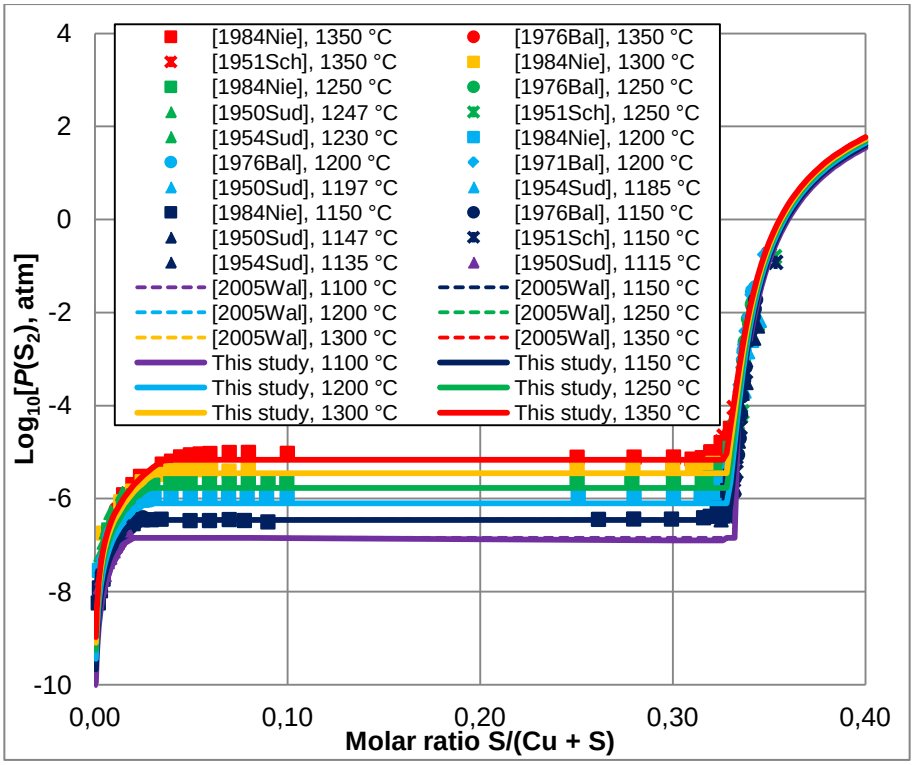
[1984Nie], 1350 °C
[1976Bal], 1350 °C
[1951Sch], 1350 °C
[1984Nie], 1300 °C
[1984Nie], 1250 °C
[1976Bal], 1250 °C
[1950Sud], 1247 °C
[1951Sch], 1250 °C
[1954Sud], 1230 °C
[1984Nie], 1200 °C
[1976Bal], 1200 °C
[1971Bal], 1200 °C
[1950Sud], 1197 °C
[1954Sud], 1185 °C
[1984Nie], 1150 °C
[1976Bal], 1150 °C
[1950Sud], 1147 °C
[1951Sch], 1150 °C
[1954Sud], 1135 °C
[1950Sud], 1115 °C
[2005Wal], 1100 °C
[2005Wal], 1150 °C
[2005Wal], 1200 °C
[2005Wal], 1250 °C
[2005Wal], 1300 °C
[2005Wal], 1350 °C
This study, 1100 °C
This study, 1150 °C
This study, 1200 °C
This study, 1250 °C
This study, 1300 °C
This study, 1350 °C
4
2
0
-2
-4
-6
-8
-10
0,00
0,10
0,20
0,30
0,40
Log10[P(S2), atm]
Molar ratio S/(Cu + S)

(a)

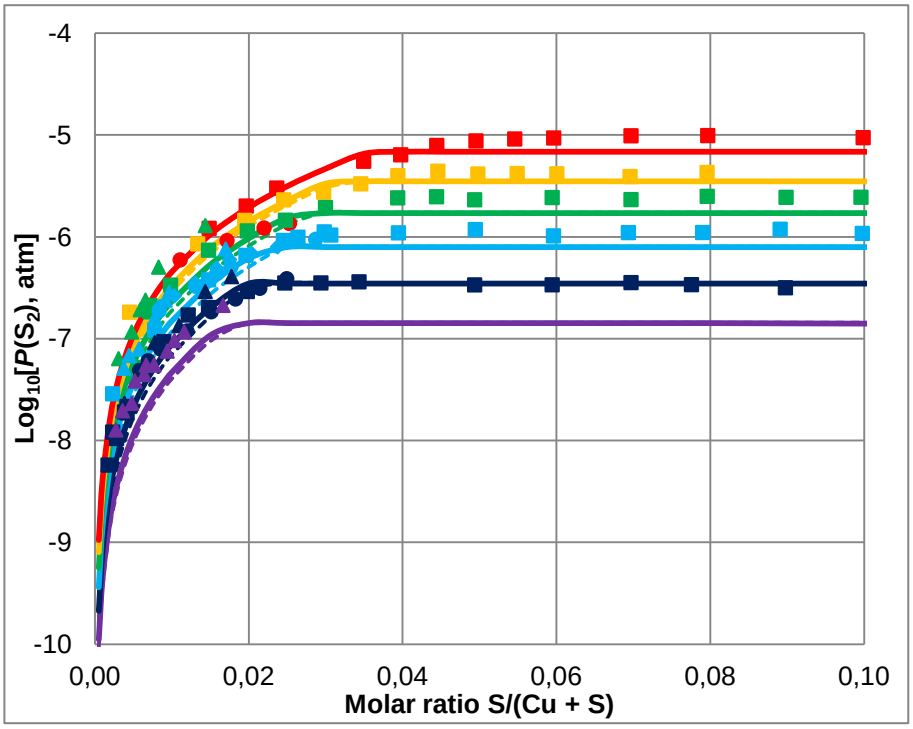
-4
-5
-6
-7
-8
-9
-10
0,00
0,02
0,04
0,06
0,08
0,10
Log10[P(S2), atm]
Molar ratio S/(Cu + S)

(b)

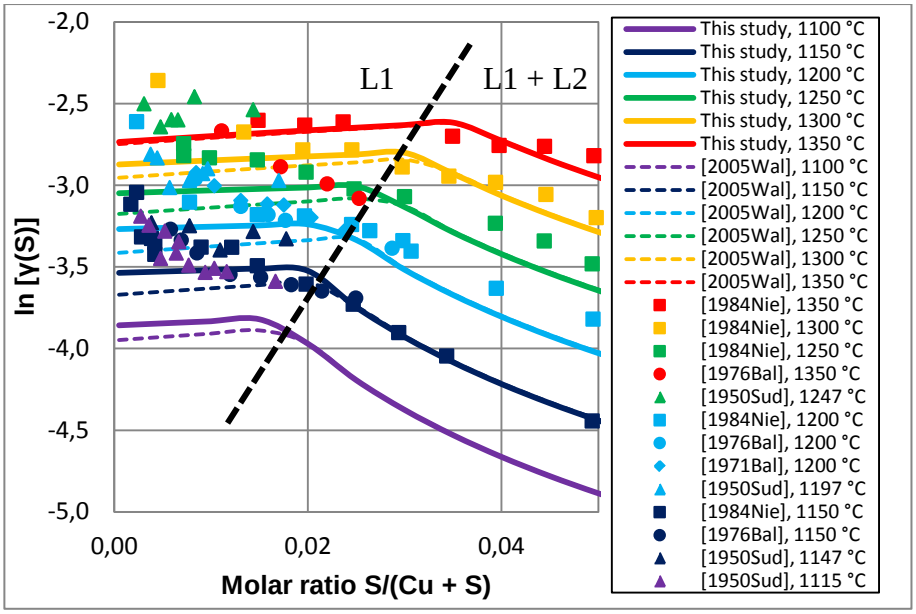

(c)

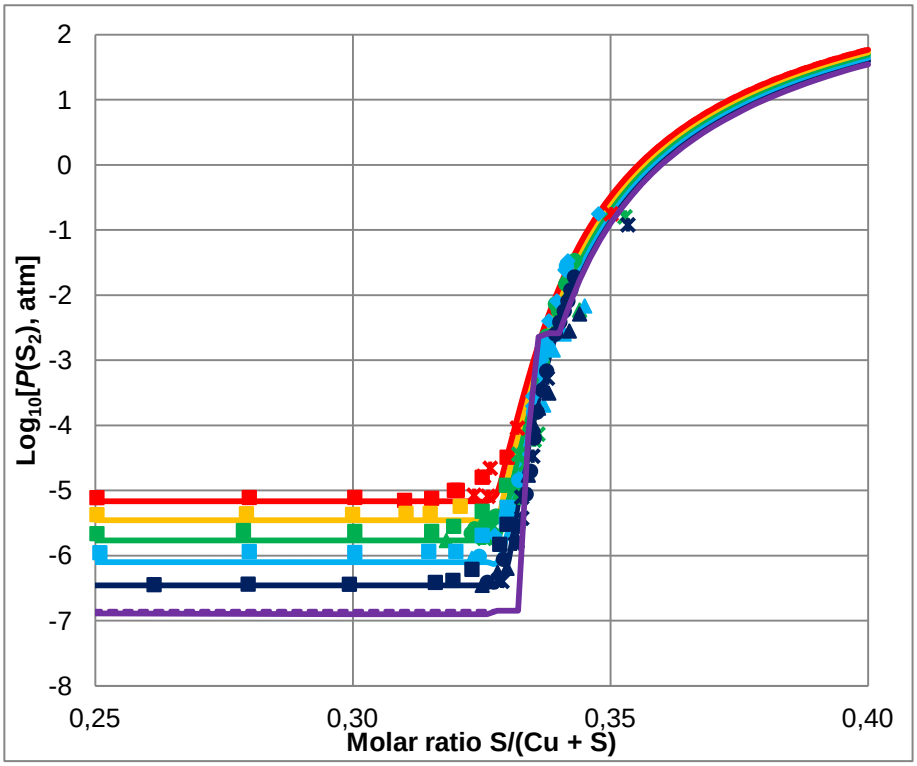

(d)

Figure 3.11. Activity of sulfur in the Cu–S system expressed as $P(S_2)$, (a) – the overview (b,c) – metal region (d) – sulfide region. Experimental points [36, 80, 81, 85, 93, 94] and calculated lines: dashed – [92], solid – this study.

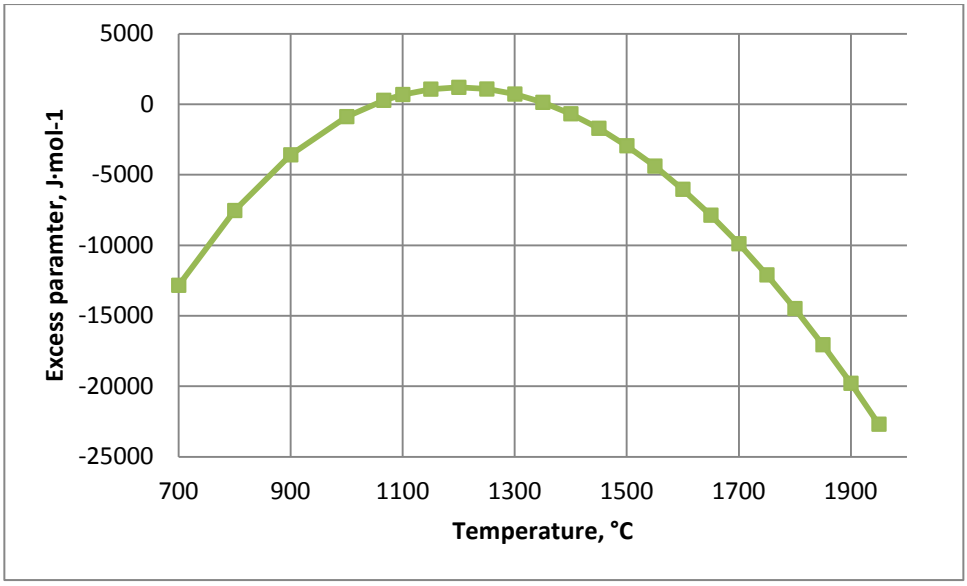

Figure 3.12. Excess parameter $g^{90}_{Cu^1S}$ in the Cu–S system.

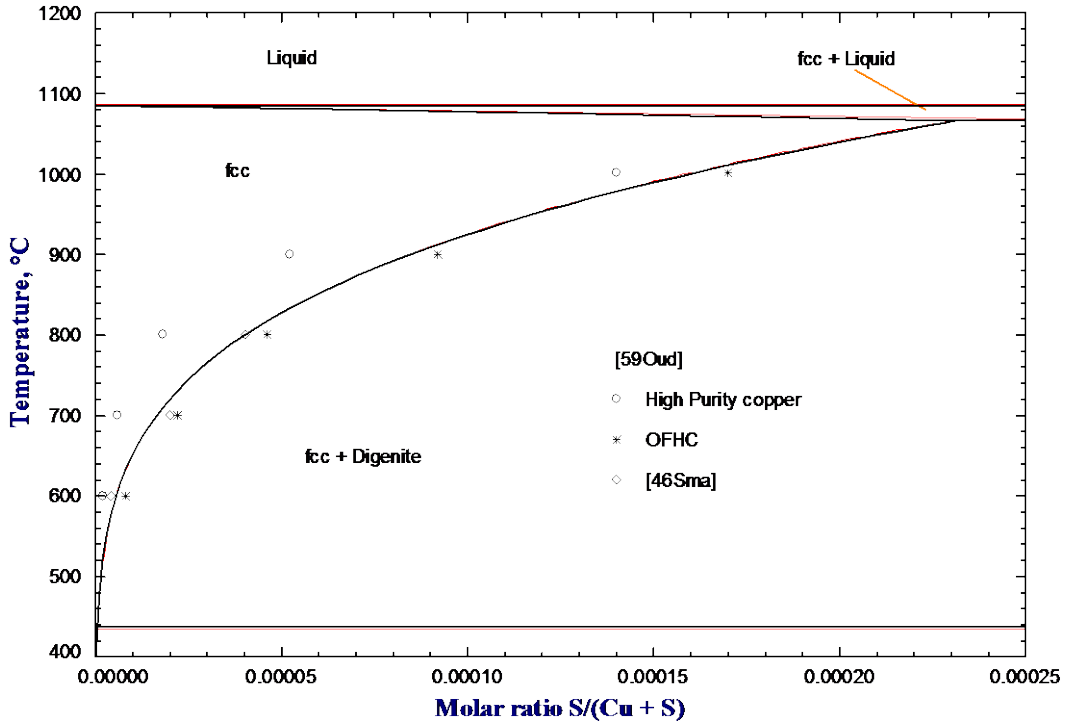

Figure 3.13. Metal region of the Cu–S phase diagram. Experimental points [95, 96] and calculated lines: thin red lines – [92], black lines – this study.

3.3 Cu–Fe–S system

The Cu–Fe–S system was earlier evaluated by Waldner and Pelton [92]. They suggested describing the liquid phase without introducing any ternary model parameters. However, there

were some inconsistencies between calculated phase diagrams and the experimental data from literature. The temperature of melting of ISS phase was higher, than the experimental data [97, 98] (Figure 3.14). The digenite-bornite (DB) liquidus in Figure 3.15 was higher than the experimental data [99] as well. The Pyrr + DB + bcc + L invariant in Figure 3.16 was much lower than the data of Schlegel and Schuller [97]. During the evaluation of the quaternary Cu–Fe–O–S system, it became evident that the predicted temperature of the eutectic point Pyrr + DB + wüstite (monoxide) + bcc + L was also very low: 800 °C against 840 °C, the latter experimentally measured by Yazawa and Kameda [100]. Obviously, these eutectics from ternary Cu–Fe–S and quaternary Cu–Fe–O–S systems are related. Later, during the optimization of the Cu–Fe–O–S–Si system, it became clear that the interaction between "Cu_2S" and "FeS" in matte phase was not strong enough. In the calculated distribution of sulfur between matte and slag, too much sulfur dissolved in slag. This was easily prevented by the introduction of the negative ternary parameter FeS(Cu) into the model for the matte phase.

Another modification in the Cu–Fe–S system was required for the ISS (intermediate solid solution) phase. Its composition is well shown in Figure 3.23. During the optimization of the Cu–Fe–O–S system it was found that, according to the experimental study of Rosenqvist and Hofseth [101], ISS should be stable up above 820 °C in the ISS + Pyrr + spinel (Fe_3O_4) and ISS + bornite + spinel (Fe_3O_4) phase assemblages. When the model parameters of Waldner and Pelton [92] were used, ISS decomposed much earlier. Hence, it should be more stable.

In order to improve the description of the Cu–Fe–S, Cu–Fe–O–S and Cu–Fe–O–S–Si systems, the re-optimization of some model parameters have been performed.

For the liquid metal/matte phase:

$$\begin{aligned} &\textit{Waldner}: \ \textit{no ternary parameters} \\ &\textit{This study}: g^{001}_{Fe^{II}S(Cu^{I})} = 29450.8 - 25.1040T \quad J \cdot mol^{-1}, \\ &g^{002}_{Cu^{I}S(Fe^{II})} = 1882.8 \quad J \cdot mol^{-1}, g^{011}_{Fe^{II}S(Cu^{I})} = \text{-}29288, J \cdot mol^{-2} \end{aligned} \tag{3.7}$$

For the ISS phase:

$$
\begin{aligned}
L^{0}_{\mathrm{Fe,Cu:S}}(Waldner) &= -209200.0 \\
L^{1}_{\mathrm{Fe,Cu:S}}(Waldner) &= 209200.0 \\
L^{0}_{\mathrm{Fe,Cu:S}}(This\ study) &= -198970.9 - 11.7152T \\
L^{1}_{\mathrm{Fe,Cu:S}}(This\ study) &= 198970.9 + 11.7152T
\end{aligned}
\tag{3.8}
$$

For the digenite-bornite (DB) phase:

$$
\begin{aligned}
L^{0}_{\mathrm{Fe,Cu:S}}(Waldner) &= -96232.0 \\
L^{0}_{\mathrm{Fe,Cu:S}}(This\ study) &= -88092.7 - 9.8968T
\end{aligned}
\tag{3.9}
$$

All other model parameters for the Cu–Fe–S system remained unchanged. They are listed in Table 7-2. Some additional differences between the optimization of Waldner and Pelton [92] and this study arose from the changes in the Fe–S and the Cu–S systems, as discussed in Sections 3.1 and 3.2

After all modifications, the agreement between calculated lines and experimental data in Figure 3.14, Figure 3.15 and Figure 3.16 is much better. The calculated composition of liquid Cu phase in the L1 + L2 + fcc equilibrium at 1350 °C (Figure 3.18) is in better agreement with experiment of Krivsky and Schuhmann [102]. The agreement between calculated and experimentally measured sulfur potential above liquid phase (Figure 3.26-Figure 3.29) is slightly better at some points and slightly worse at other points. In the calculated $Cu_{0.5}Fe_{0.5}$–S section the DB + Pyrr + ISS phase field extends to lower temperatures, which is in agreement with the experimental data of Barton [103] (empty triangles in Figure 3.31). At the same time, the stability field of the Tal ($Cu_9Fe_8S_{16}$) phase is wider which is not supported by experimental data. In general, the descriprion of experimental data in all other figures is not worse than that of Waldner and Pelton [92].

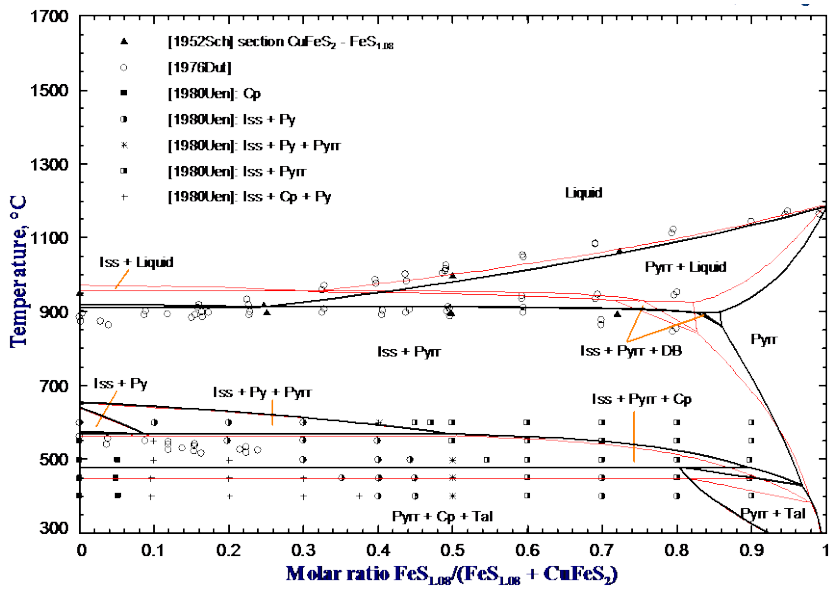

Figure 3.14. $CuFeS_2$–$FeS_{1.08}$ section of the phase diagram of the Cu–Fe–S system. Experimental points [97, 98, 104] and calculated lines: thin red lines – [92], black lines – this study. Formation of gas phase is suppressed.

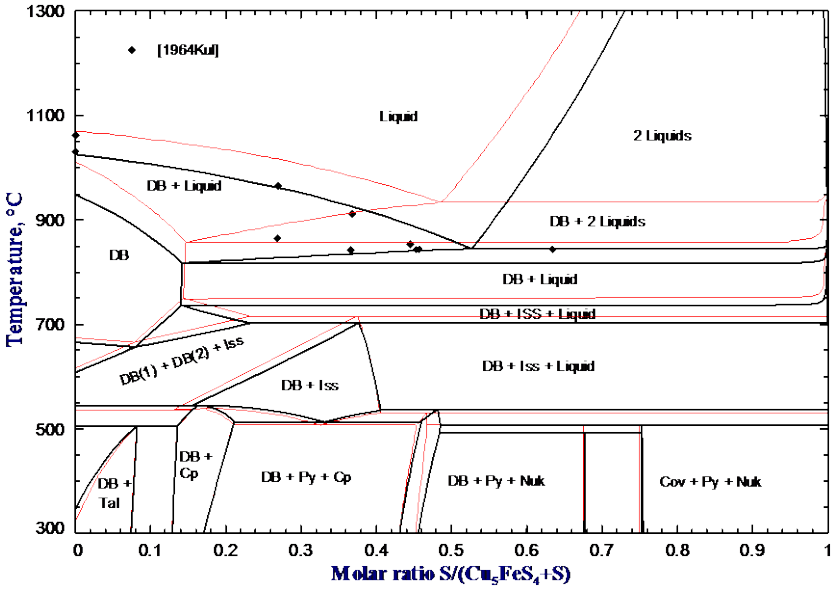

Figure 3.15. Cu_5FeS_4–S section of the phase diagram of the Cu–Fe–S system. Experimental points [99] and calculated lines: thin red lines – [92], black lines – this study. Formation of gas phase is suppressed.

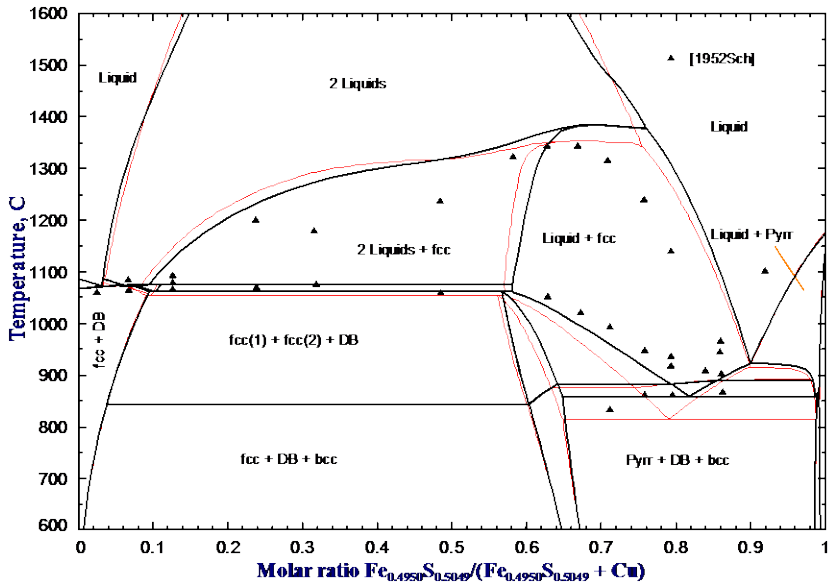

Figure 3.16. $Cu–Fe_{0.4950}S_{0.5049}$ (Fe/S = 1/1.02) section of the phase diagram of the Cu–Fe–S system. Experimental points [97] and calculated lines: thin red lines – [92], black lines – this study. Formation of gas phase is suppressed.

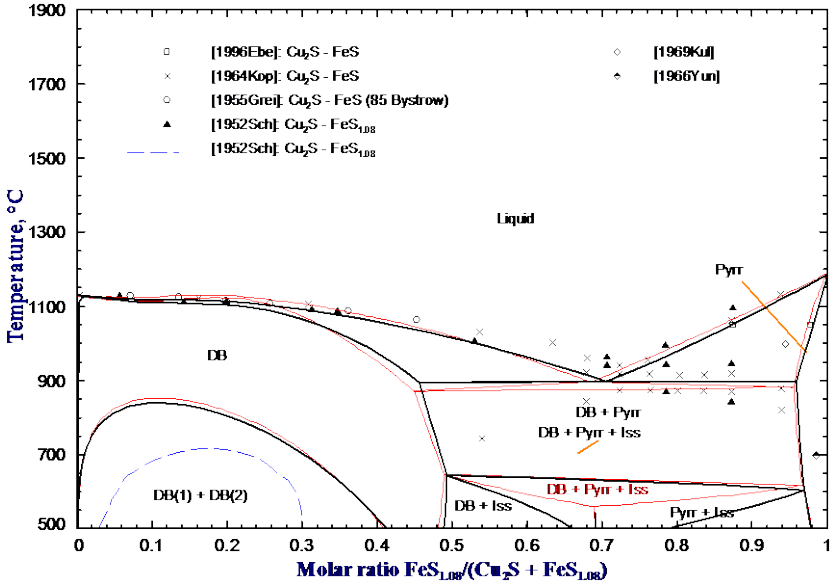

Figure 3.17. $Cu_2S–FeS_{1.08}$ section of the phase diagram of the Cu–Fe–S system. Experimental points [97, 105-109] and calculated lines: thin red lines – [92], black lines – this study. Formation of gas phase is suppressed.

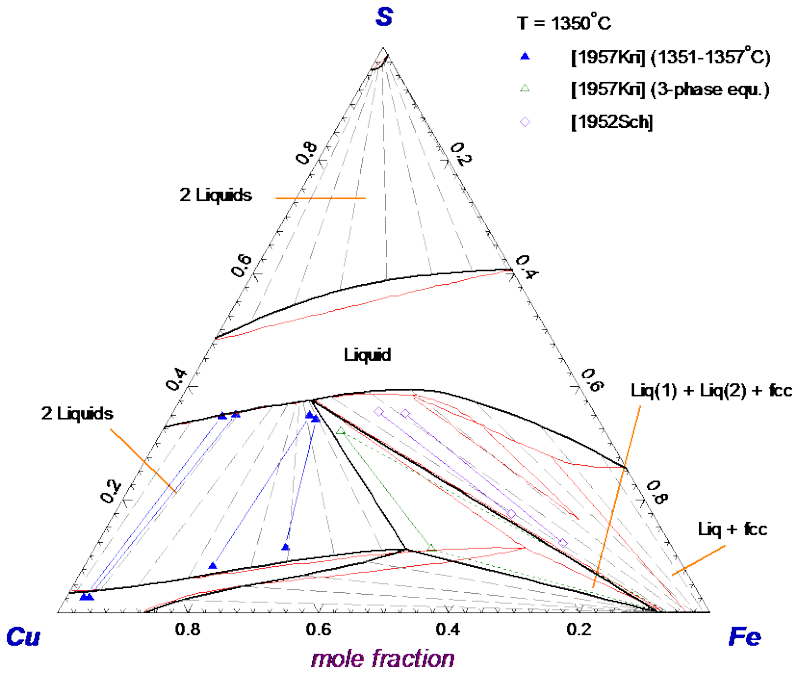

Figure 3.18. Isothermal section of the Cu–Fe–S phase diagram at 1350 °C. Experimental points [97, 102] and calculated lines: thin red lines – [92], black lines – this study. Formation of gas phase is suppressed.

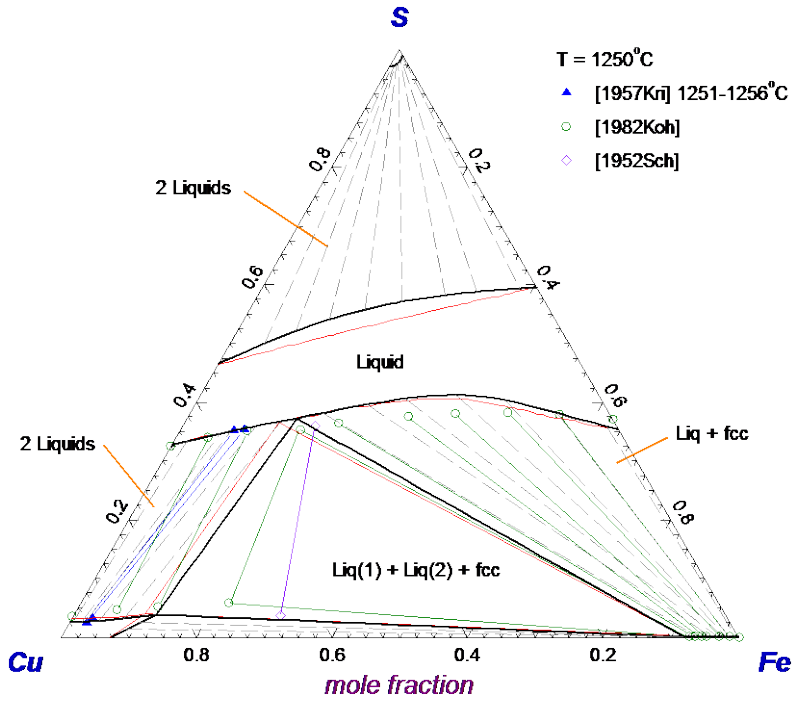

Figure 3.19. Isothermal section of the Cu–Fe–S phase diagram at 1250 °C. Experimental points [60, 97, 102] and calculated lines: thin red lines – [92], black lines – this study. Formation of gas phase is suppressed.

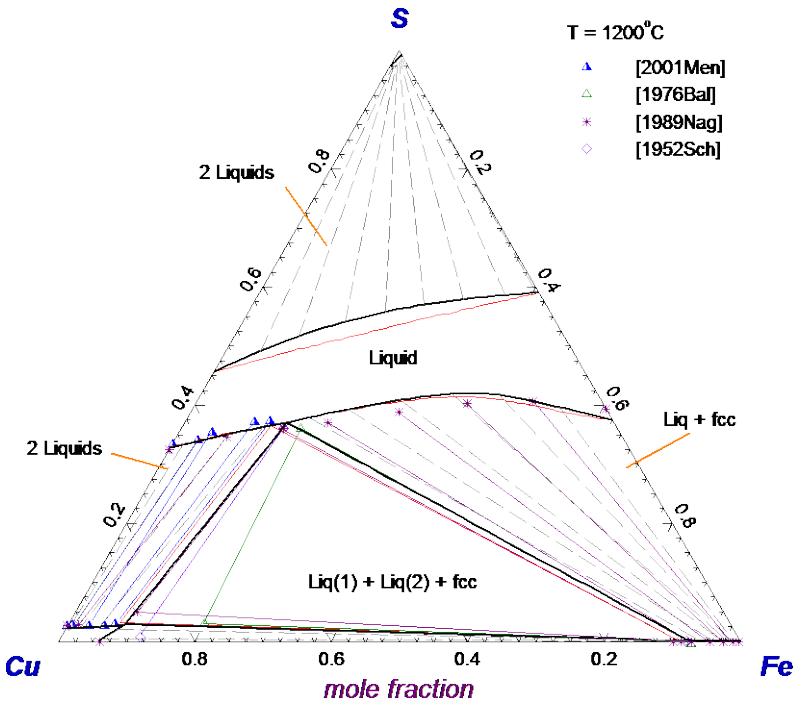

Figure 3.20. Isothermal section of the Cu–Fe–S phase diagram at 1200 °C. Experimental points [36, 97, 110, 111] and calculated lines: thin red lines – [92], black lines – this study. Formation of gas phase is suppressed.

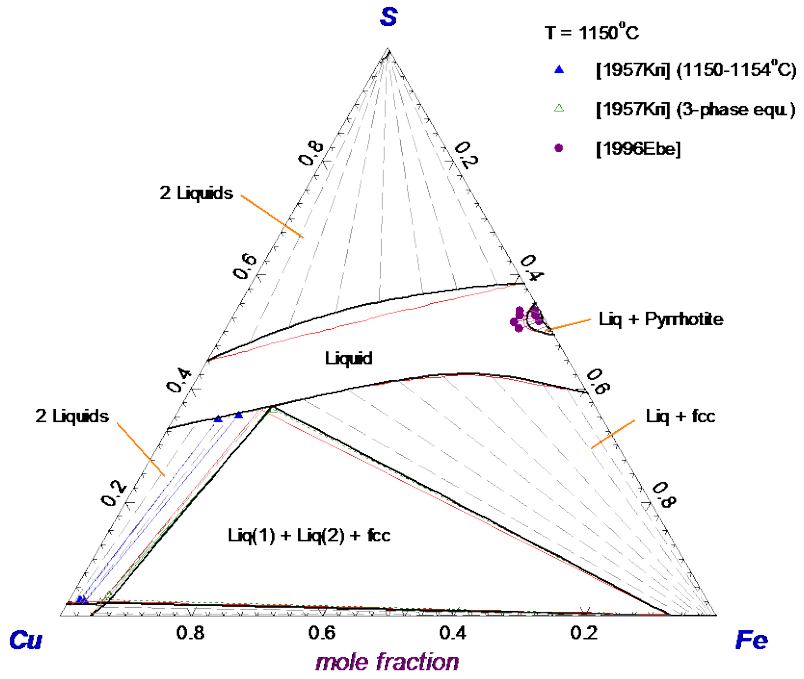

Figure 3.21. Isothermal section of the Cu–Fe–S phase diagram at 1150 °C. Experimental points [102, 105] and calculated lines: thin red lines – [92], black lines – this study. Formation of gas phase is suppressed.

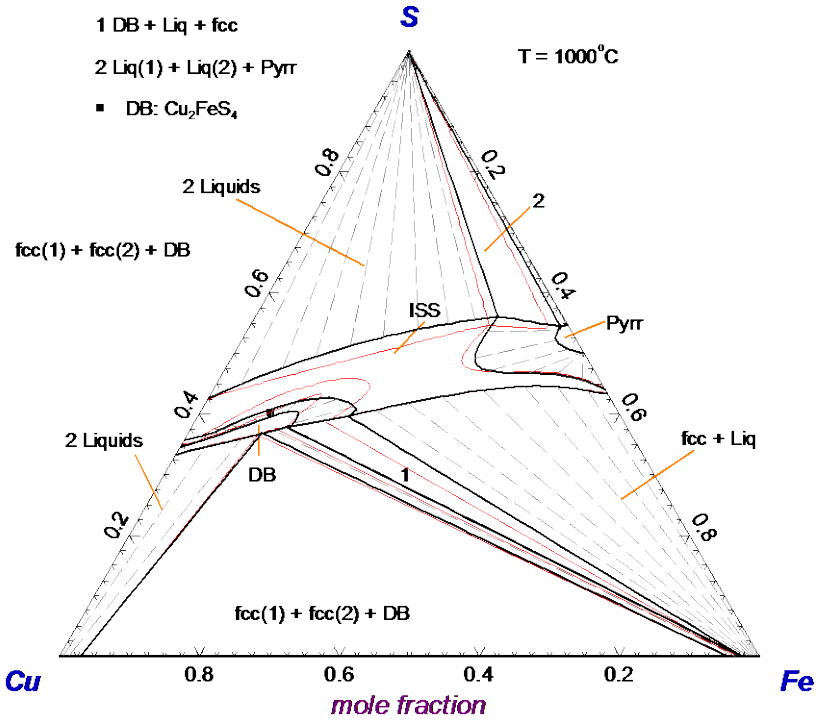

Figure 3.22. Isothermal section of the Cu–Fe–S phase diagram at 1000 °C. Calculated lines: thin red lines – [92], black lines – this study. Formation of gas phase is suppressed.

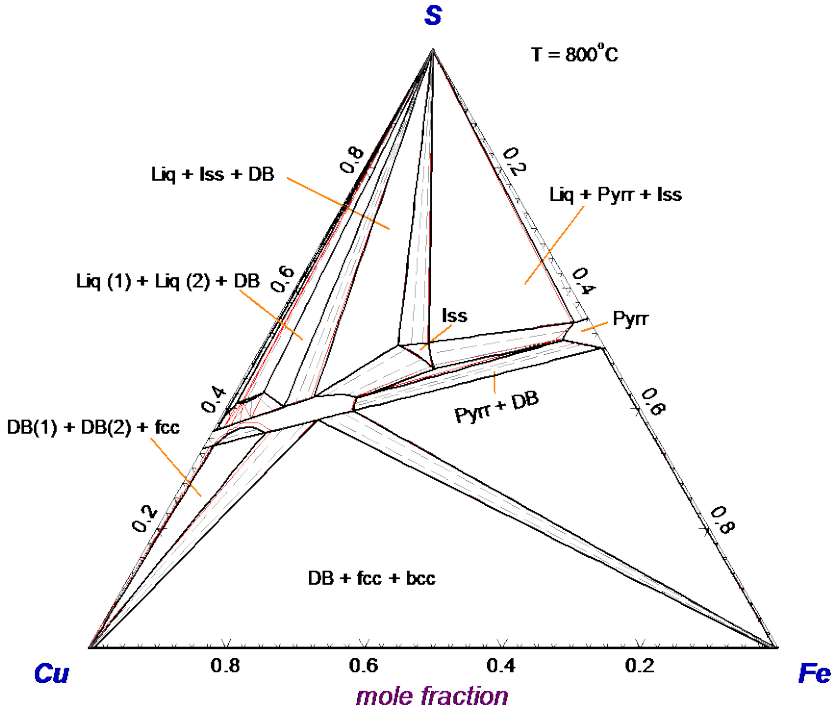

Figure 3.23. Isothermal section of the Cu–Fe–S phase diagram at 800 °C. Calculated lines: thin red lines – [92], black lines – this study. Formation of gas phase is suppressed.

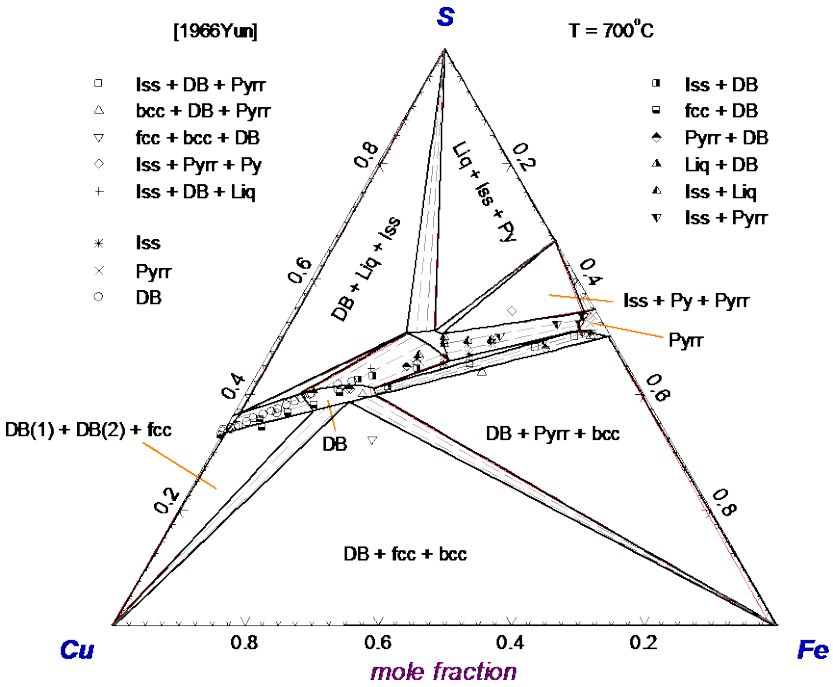

Figure 3.24. Isothermal section of the Cu–Fe–S phase diagram at 700 °C. Experimental points [109] and calculated lines: thin red lines – [92], black lines – this study. Formation of gas phase is suppressed.

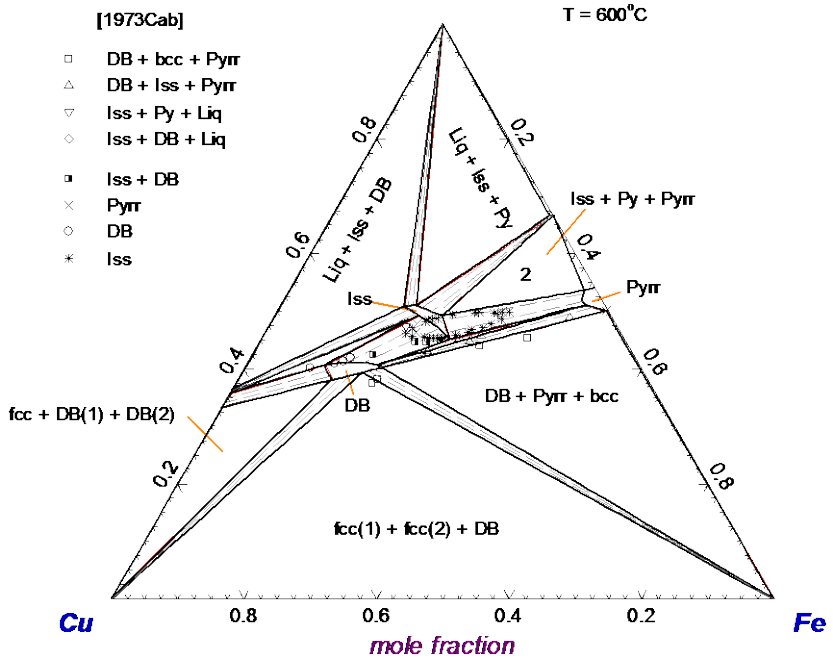

Figure 3.25. Isothermal section of the Cu–Fe–S phase diagram at 600 °C. Experimental points [112] and calculated lines: thin red lines – [92], black lines – this study. Formation of gas phase is suppressed.

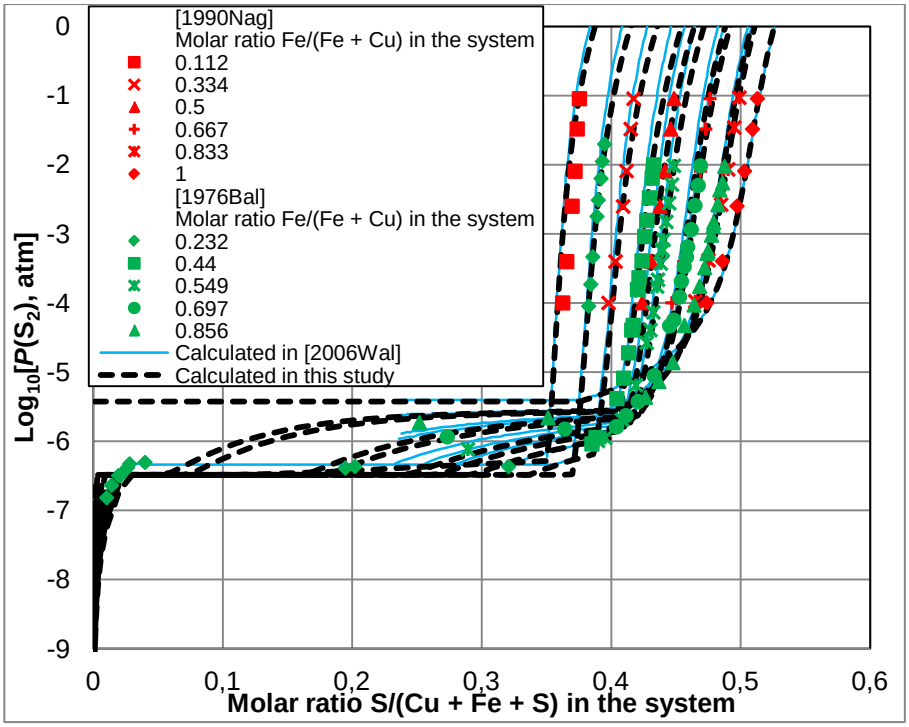

Figure 3.26. Sulfur potential (expressed as equilibrium partial pressure of S_2) in the Cu–Fe–S system at 1200 °C. Experimental points [36, 111] and calculated lines: thin solid line – [92], thick dashed line – this study. Calculated lines correspond to experimental conditions.

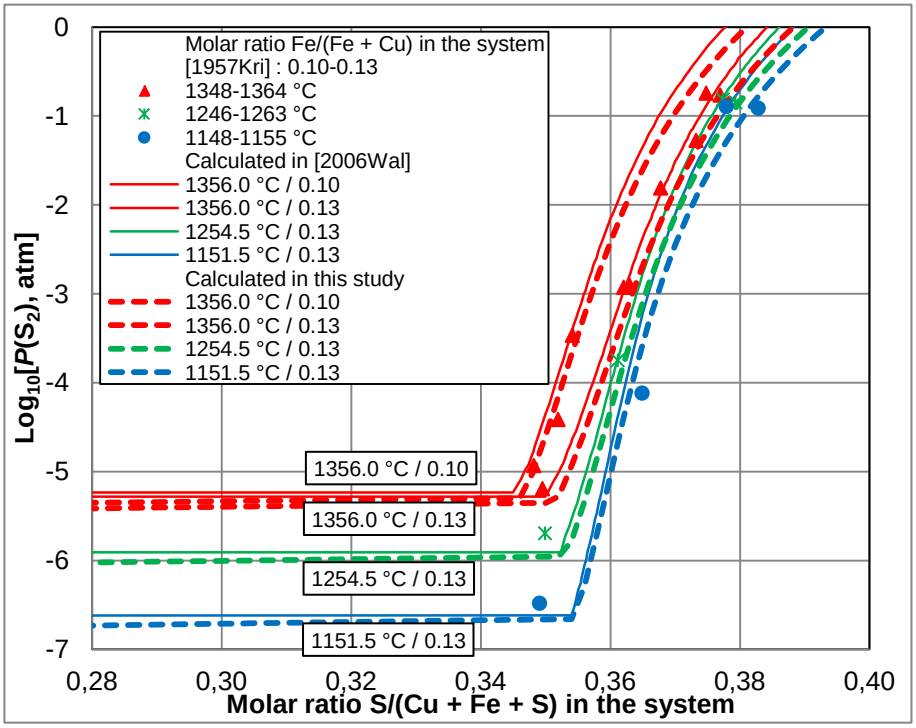

Figure 3.27. Sulfur potential (expressed as equilibrium partial pressure of S_2) in the Cu–Fe–S system. Experimental points [102] and calculated lines: thin solid line – [92], thick dashed line – this study. Calculated lines correspond to experimental conditions.

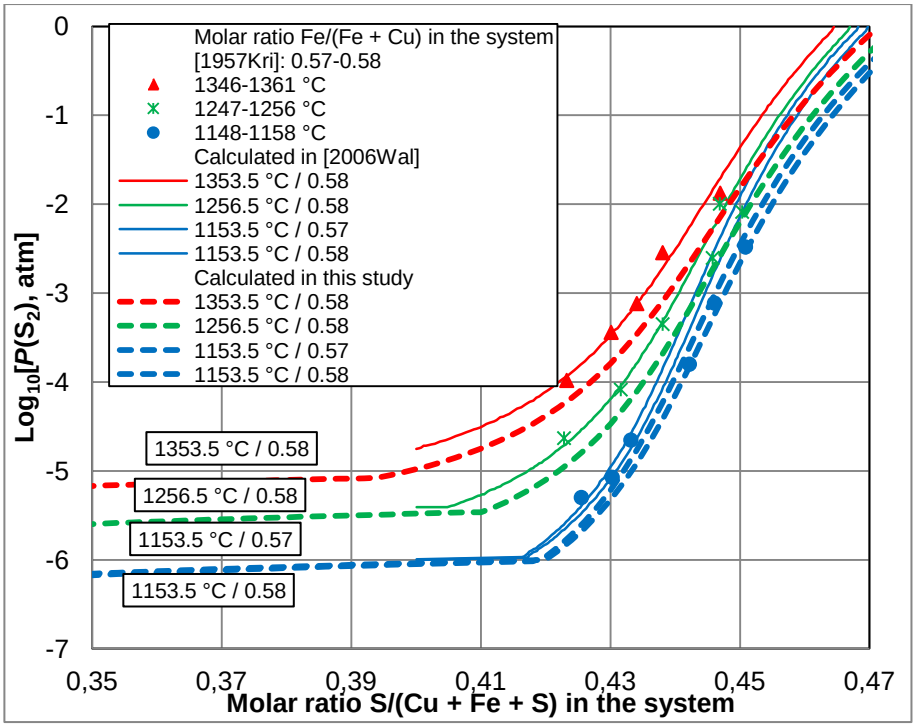

Figure 3.28. Sulfur potential (expressed as equilibrium partial pressure of S_2) in the Cu–Fe–S system. Experimental points [102] and calculated lines: thin solid line – [92], thick dashed line – this study. Calculated lines correspond to experimental conditions.

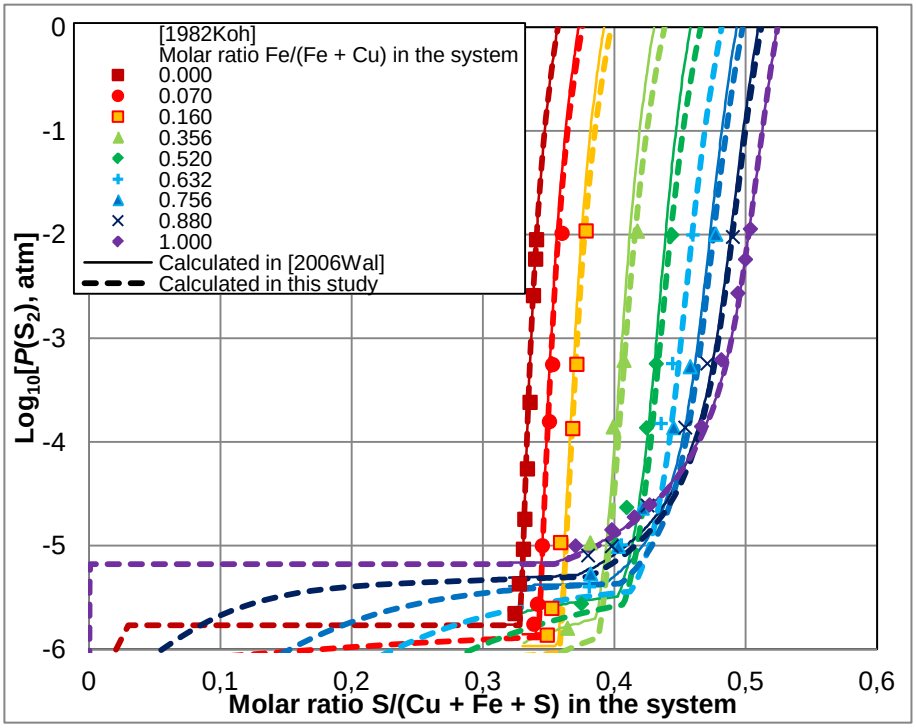

Figure 3.29. Sulfur potential (expressed as equilibrium partial pressure of S_2) in the Cu–Fe–S system at 1250 °C. Experimental points [60] and calculated lines: thin solid line – [92], thick dashed line – this study. Calculated lines correspond to experimental conditions.

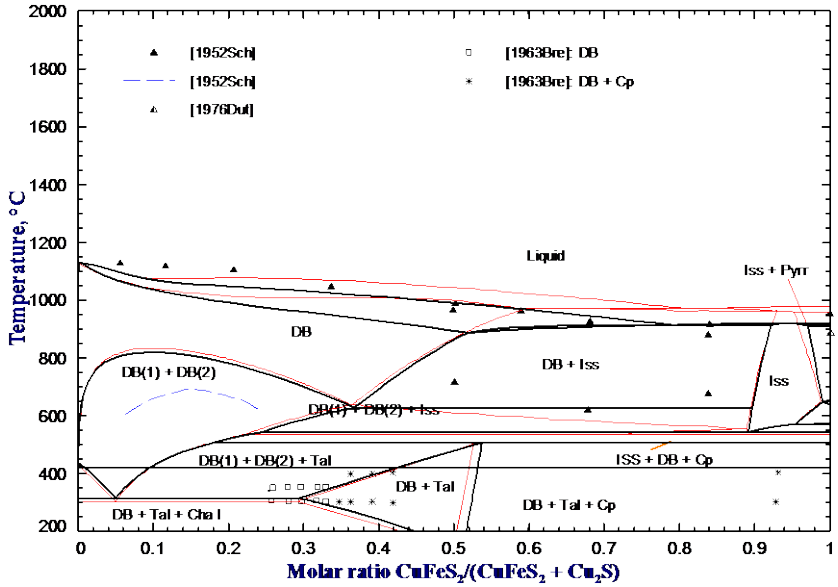

Figure 3.30. $CuFeS_2$–Cu_2S section of the phase diagram of the Cu–Fe–S system. Experimental points [97, 98, 113] and calculated lines: thin red lines – [92], black lines – this study. Formation of gas phase is suppressed.

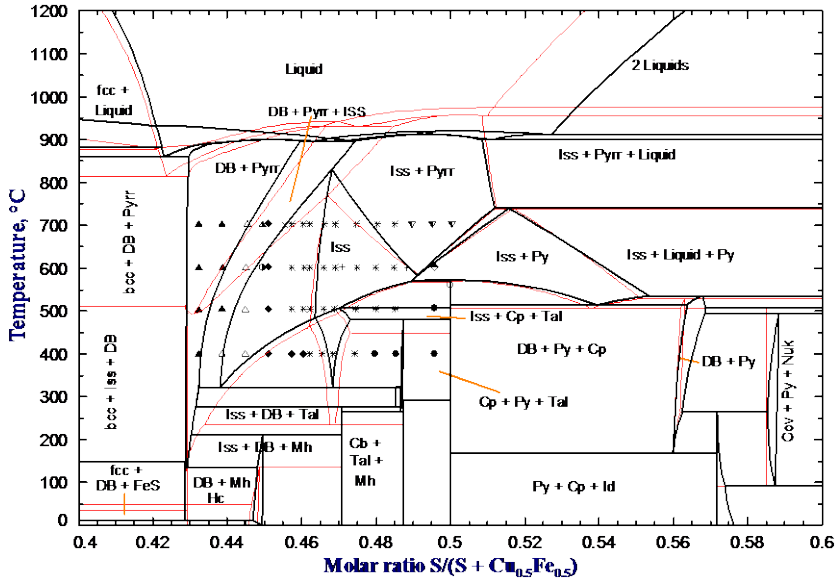

[76Dut]	[73Bar]	[66Yun]	[73Cab]
○ Cp ⇒ Iss+Cp	▲ DB+Pyrr	▼ Iss+liq	◑ DB+Iss
	△ DB+Pyrr+Iss	▲ DB+Pyrr+Iss	+ Iss
	◆ DB+Iss	× Iss	◓ Iss+Py
	✳ Iss		
	● Iss+Cp		

Figure 3.31. $Cu_{0.5}Fe_{0.5}$–S section of the phase diagram of the Cu–Fe–S system. Experimental points [98, 103, 109, 112] and calculated lines: thin red lines – [92], black lines – this study. Formation of gas phase is suppressed.

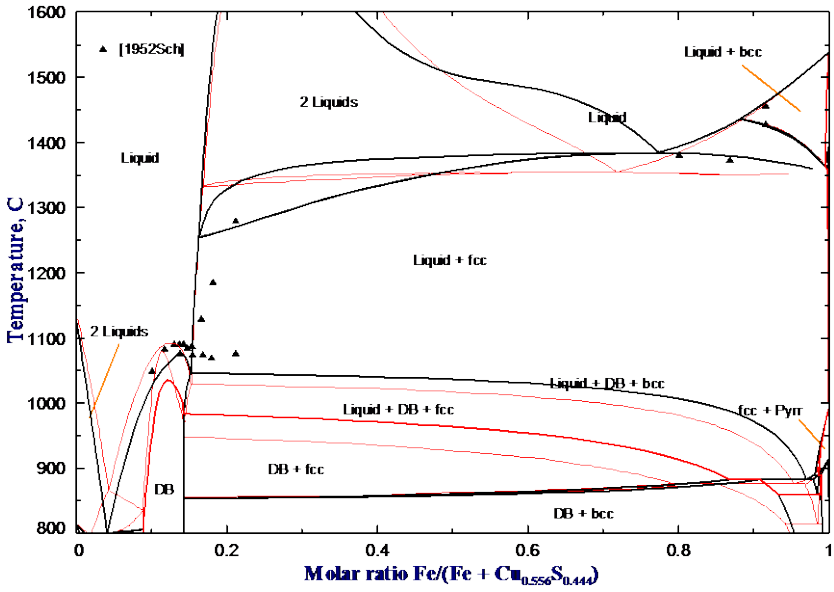

Figure 3.32. $Cu_{0.556}S_{0.444}$–Fe (Cu/S = 5/4) section of the phase diagram of the Cu–Fe–S system. Experimental points [97] and calculated lines: thin red lines – [92], black lines – this study. Formation of gas phase is suppressed.

CHAPTER 4 ARTICLE 1: CRITICAL ASSESSMENT AND THERMODYNAMIC MODELING OF THE Cu–O AND Cu–O–S SYSTEMS

Sourced from published article: D. Shishin and S.A. Decterov [114]

Equation Chapter (Next) Section 1 Critical evaluation, thermodynamic modeling and optimization of the Cu–O and Cu–O–S systems are presented. The liquid phase over the whole composition range from metallic liquid to sulfide melt to oxide melt is described by a single model developed within the framework of the quasichemical formalism. The model reflects the existence of strong short-range ordering in oxide, sulfide and oxysulfide liquids. Two ranges of maximum short-range ordering in the Cu–O system at approximately the Cu_2O and CuO compositions are taken into account. Parameters of thermodynamic models are optimized to reproduce all available thermodynamic and phase equilibrium data within experimental error limits. The optimization of the Cu–O and Cu–O–S systems performed in the present study is of particular importance for the description of the solubility of oxygen in matte and liquid copper. The obtained self-consistent set of model parameters can be used as a basis for development of a thermodynamic database for simulation of copper smelting and converting.

Comparing to the published work [114], minor modifications of parameters were made in the present thesis as it is described in Section 7.3. All experimental data presented in the Cu–O–S article [114] remained in agreement with the calculated lines. In the present thesis, all diagrams in the Cu–O–S system were calculated with updated parameters.

4.1 Introduction

The present study is part of an ongoing research project which is aimed at developing a thermodynamic database for simulation of copper extraction from sulfide concentrates. The major phases that form during copper smelting and converting are: blister copper (a liquid metal phase rich in Cu), matte (a molten sulfide phase containing mainly Cu, S and Fe), slag (a molten oxide phase) and gas. In principle, all three liquid phases represent just one liquid with miscibility gaps. Liquid metal, matte and slag can be completely miscible over certain ranges of temperature and composition, even though this normally does not happen under industrial

conditions. It is desirable to have one general thermodynamic model which can describe all three liquid phases simultaneously, but this is very difficult to achieve because the model must reflect quite different atomic interactions that are intrinsic to metallic, sulfide and oxide phases.

In early studies, matte was often modeled as a mixture of stoichiometric sulfides Cu_2S–FeS. Sometimes, stoichiometric oxide components were also added to account for the solubility of oxygen in the matte phase [2]. In reality, the composition of matte can substantially deviate from the stoichiometric sulfides, even though matte exhibits strong short-range ordering (SRO) which results from the fact that metal-sulfur nearest-neighbor pairs are energetically favored over metal-metal and sulfur-sulfur pairs. This was successfully described by the modified quasichemical model (MQM) [3, 115]. However, matte and blister copper were modeled as two different phases in the resulting thermodynamic database that was developed for simulation of copper smelting and converting [3].

Later, Waldner and Pelton [26, 92] applied the generalized version of the MQM [16, 17] to describe matte and liquid metal in the Cu–Fe–S system as one continuous solution. The present work was undertaken to add oxygen to this solution with a view to account for appreciable solubility of oxygen in industrial matte and liquid copper [11, 13] which is of practical importance. The second objective was to explore the possibility of describing all three phases, liquid metal, matte and slag, by one solution. To this end, all oxygen-containing subsystems of the Cu–Fe–O–S system must be optimized using the Calphad technique. The optimizations of the Cu–O and Cu–O–S systems are presented in this article, and the other subsystems will be reported elsewhere.

In a thermodynamic “optimization” of a system, all available thermodynamic and phase diagram data are evaluated simultaneously in order to obtain one set of model equations for the Gibbs energies of all phases as functions of temperature and composition. From these equations, all of the thermodynamic properties and the phase diagrams can be back-calculated. In this way, all the data are rendered self-consistent and consistent with thermodynamic principles. Thermodynamic property data, such as activity data, can aid in the evaluation of the phase diagram, and phase diagram measurements can be used to deduce thermodynamic properties. Discrepancies in the available data can often be resolved, and interpolations and extrapolations can be made in a thermodynamically correct manner. A small set of model parameters is

obtained. This is ideal for computer storage and calculation of properties and phase diagrams. In the present study, all calculations were carried out using the FactSage thermochemical software and databases [4].

4.2 Thermodynamic models

4.2.1 Liquid solution

Modeling of the liquid phase in the Cu–O–S system is a challenging task. No attempts were found in the literature to model this liquid over the entire composition range from liquid metal to oxysulfide melt. The thermodynamic model must describe drastic changes in the activity of sulfur and oxygen which are the result of strong short-range ordering at the Cu_2S and Cu_2O compositions, respectively. Furthermore, in the Cu–O system, there must be a maximum in short-range ordering at the CuO composition as well, even though no experimental data are available in this region because the oxygen pressure is too high.

Schmid [116] and later Clavaguera-Mora *et al.* [117] modeled the Cu–O liquid using an associated solution model. Schmid [116] optimized 7 temperature-dependent parameters, whereas Clavaguera-Mora *et al.* [117] described the liquid with one excess parameter, but only up to the composition of Cu_2O. In the Cu–O system, Hallstedt *et al.* [118, 119] successfully used the two-sublattice ionic liquid model with Cu^{+1} and Cu^{+2} on the first sublattice and O^{-2} and charged vacancy on the second one. Schramm *et al.* [120] added Cu^{+3} on the first sublattice to better describe the CuO liquidus at high oxygen pressures.

In the present work, a model for the liquid phase is developed within the framework of the quasichemical formalism [16, 17]. It has just one sublattice containing four species: Cu^{I}, Cu^{II}, S and O, where Cu^{I} and Cu^{II} correspond to two oxidation states of copper atoms. In the Cu–O system, the fraction of the Cu^{I}–O pairs goes through a maximum at about the Cu_2O composition, while the Cu^{II}–O pairs are most abundant at the CuO composition. All species are not charged, so the condition of electroneutrality is not imposed and the model represents the liquid phase from metal to nonmetals.

Figures 4.1 and 4.2 illustrate the concept of two oxidation states of Cu which bring about two compositions of maximum short-range ordering in Cu–O liquid. The calculated entropy of

mixing between pure liquid Cu and hypothetical pure liquid oxygen has two local minima which correspond to maximum short-range ordering at the Cu_2O and CuO compositions. There are no reliable experimental data on the oxidation states of copper in the liquid phase, but the drastic transition of Cu^I to Cu^{II} between the Cu_2O and CuO compositions seems physically reasonable. The curves in Figures 4.1-4.2 were calculated using the optimized model parameters for the liquid phase; for the sake of simplicity, the miscibility gap in the liquid and formation of all other phases were suppressed.

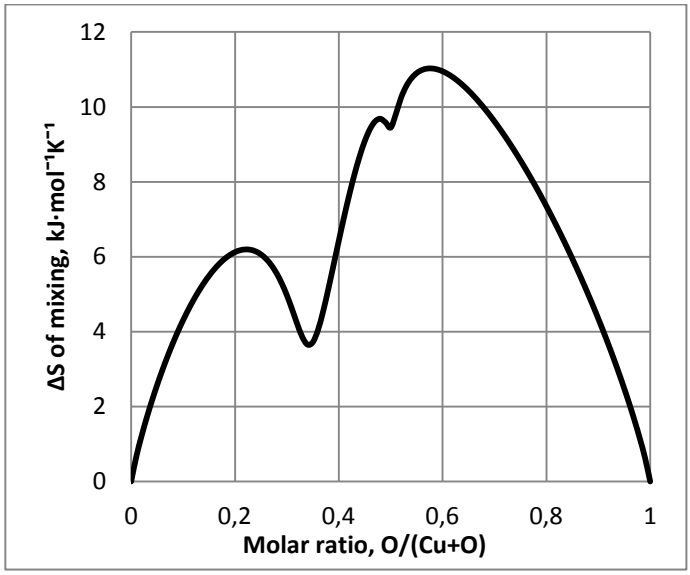

Figure 4.1. Calculated entropy of mixing in Cu–O liquid at 1200 °C.

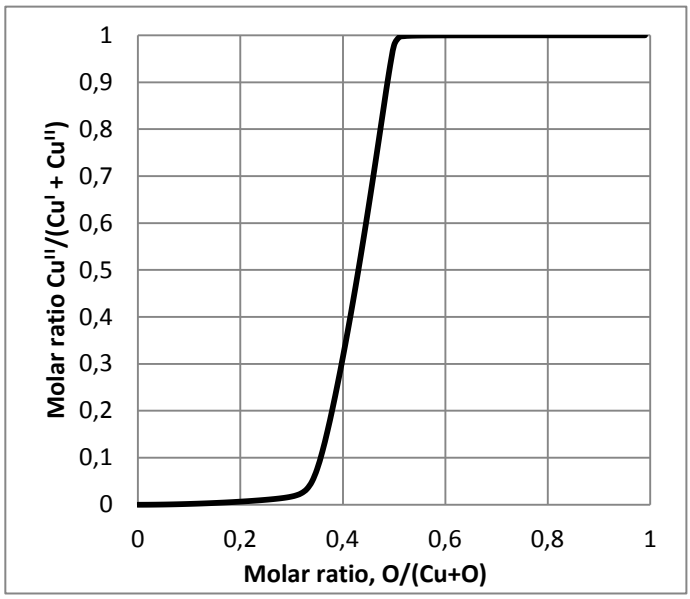

Figure 4.2. Calculated distribution of copper between Cu^I and Cu^{II} in Cu–O liquid at 1200 °C.

To explain the meaning of parameters of the quasichemical formalism, let us consider a binary solution formed by components A and B. The formulae and notations of the quasichemical formalism were described in detail elsewhere [16, 17] and Section 2.2.

There are ten possible pairs formed by the species Cu^{I}, Cu^{II}, O, and S in the Cu–O–S liquid phase. The fractions of all pairs are calculated by the Gibbs energy minimization procedure built into the FactSage software [4] using the optimized model parameters. Cu^{I}-Cu^{I}, O-O and S-S are the predominant pairs at compositions close to pure Cu, O and S, respectively. The Cu^{I}-O, Cu^{II}-O and Cu^{I}-S pairs are dominant in the oxide and sulfide liquids, whereas the fractions of the Cu^{I}-Cu^{II}, Cu^{II}-Cu^{II}, O-S and Cu^{II}-S pairs are small at all compositions of interest.

Extrapolation of binary terms into the Cu^{I}–Cu^{II}–O–S system is done by an asymmetric Kohler/Toop method [17]. The components are divided into two groups: metals (Cu^{I} and Cu^{II}) and nonmetals (S and O). By this means in every ternary subsystem, one component belongs to a different group than the other two. “Toop-like” extrapolation is applied, taking this “different” component as an asymmetric component. Except for the binary terms, the model can have ternary terms, $\Delta g_{AB(C)}$, which give the effect of the presence of component C upon the energy Δg_{AB} of pair exchange reaction (2.9). Ternary terms are also expanded as empirical polynomials having model parameters $g^{ijk}_{AB(C)}$. The formulae for ternary terms and for extrapolation of binary and ternary terms into a multicomponent system are discussed in detail elsewhere [17].

4.2.2 Solid FCC copper

Sulfur and oxygen are soluble to some extent in Cu metal, which has an FCC structure at the conditions of interest. Simple Bragg-Williams random mixing model was used with the following formula (per mole of atoms):

$$g = (X_{Cu} g^{o}_{Cu} + X_{O} g^{o}_{O} + X_{S} g^{o}_{S}) + RT(X_{Cu} \ln X_{Cu} + X_{O} \ln X_{O} + X_{S} \ln X_{S}) + X_{Cu} X_{S} L_{Cu,S} + X_{Cu} X_{O} L_{Cu,O} \quad (4.1)$$

where X_i and g°_i are the mole fraction and molar Gibbs energy of component i, $L_{i,j}$ represents an interaction energy between i and j, which can be a function of temperature and composition.

4.2.3 Digenite

Digenite is a copper sulfide mineral with the formula $Cu_{2-x}S$. In the present study, this name is reserved for the solid solution which is stable above about 73 °C and has a cubic structure, space group $Fm\bar{3}m$. Digenite containing a substantial amount of dissolved iron is called bornite. The nature of the nonstoichiometry in digenite and bornite is complex and can be explained by the formation of different defects, for example by the substitution of one Cu^{2+} cation and a vacancy for two Cu^{1+} cations or by the substitution of a charged vacancy for one Cu^{1+} cation. The digenite solid solution was described by Waldner and Pelton [92] using a simple Bragg-Williams random mixing model applied to the formula unit $(Cu_2,Va)S$:

$$g = (X_{Cu_2S} g^{o}_{Cu_2S} + X_{VaS} g^{o}_{VaS}) + RT(X_{Cu_2S} \ln X_{Cu_2S} + X_{VaS} \ln X_{VaS}) + X_{Cu_2S} X_{VaS} \sum_{k=0}^{n} L^{k}_{Cu_2S,VaS} (X_{VaS} - X_{Cu_2S})^{k} \quad (4.2)$$

where X_i and g_i° are the mole fraction and molar Gibbs energy of component i, and the last term represents an expansion of the interaction energy between i and j in a Redlich–Kister power series. A Bragg-Williams random mixing model applied to the formula unit $(Cu,Va)_2S$ has also been tested, but it required twice the number of parameters for a similar description of the data on sulfur potential. Furthermore, the first formula unit written as $(Cu_2,Fe,Va)S$ appeared to be more suitable for expansion to the bornite solid solution [92]. The solubility of oxygen in digenite was not modeled due to the lack of experimental data.

4.3 The Cu–S system

The Cu–S system was optimized by Waldner and Pelton [92]. The phase diagram is shown in Figure 3.10 along with the experimental data [36, 79-91] and the optimized model parameters are given in Table 2. Solid CuS, S and low-temperature Cu_2S were assumed to be stoichiometric phases, while FCC and digenite (high-temperature Cu_2S) were modeled as solid solutions. Contrary to Cu–O liquid, the Cu–S liquid phase was modeled in such a way that Cu exists almost exclusively as Cu^{I} over the whole composition range from metal to sulfur. This is because CuS is much less stable than solid CuO and there is no experimental evidence for strong short-range ordering in the liquid phase at the CuS composition which corresponds to very high S_2 partial pressures. Contradictory experimental data have been reported for the miscibility gap on the Cu-

rich side of the phase diagram. Waldner and Pelton [92] gave preference to the data suggesting a wider miscibility gap with high convolution temperature. This choice resulted in correct prediction of thermodynamic properties and phase equilibria in the Cu–Fe–S ternary system from the binaries without introducing ternary parameters. Details of the optimization will be reported elsewhere.

4.4 The Cu–O system

4.4.1 Phase diagrams

The phase diagram of the Cu–O system is shown in Figure 4.3. This system has been much studied experimentally for compositions between Cu and Cu_2O. There is more uncertainty in experimental measurements over the range of mole fractions of oxygen from 0.33 to 0.45 and no data are available beyond $X_O = 0.45$.

The Cu–O system was critically assessed by Hallstedt *et al.* [118, 119] who suggested the following invariant points [118]:

A. Eutectic: L (Cu liquid) $\rightleftharpoons$ Cu (FCC) + Cu_2O

B. Monotectic: L (oxide liquid) $\rightleftharpoons$ L (Cu liquid) + Cu_2O

C. Congruent melting point of Cu_2O: $Cu_2O \rightleftharpoons$ L (oxide liquid)

D. Eutectic: L (oxide liquid) $\rightleftharpoons$ Cu_2O + CuO

E. Melting of Cu_2O in air: $Cu_2O + O_2 \rightleftharpoons$ L (oxide liquid)

F. Melting of CuO in oxygen: CuO $\rightleftharpoons$ L (oxide liquid) + O_2

G. Convolution point: L (Cu liquid) + L (oxide liquid) $\rightleftharpoons$ L

H. Congruent melting point of CuO: CuO $\rightleftharpoons$ L (oxide liquid)

These points and experimental data [121-140] are shown in Figures 4 and 5. The scatter of the experimental data collected by Hallstedt *et al.* [118] for each invariant point is shown by bars. No data are available for point H because the oxygen pressure is too high to suppress the formation of the gas phase and measure the melting temperature.

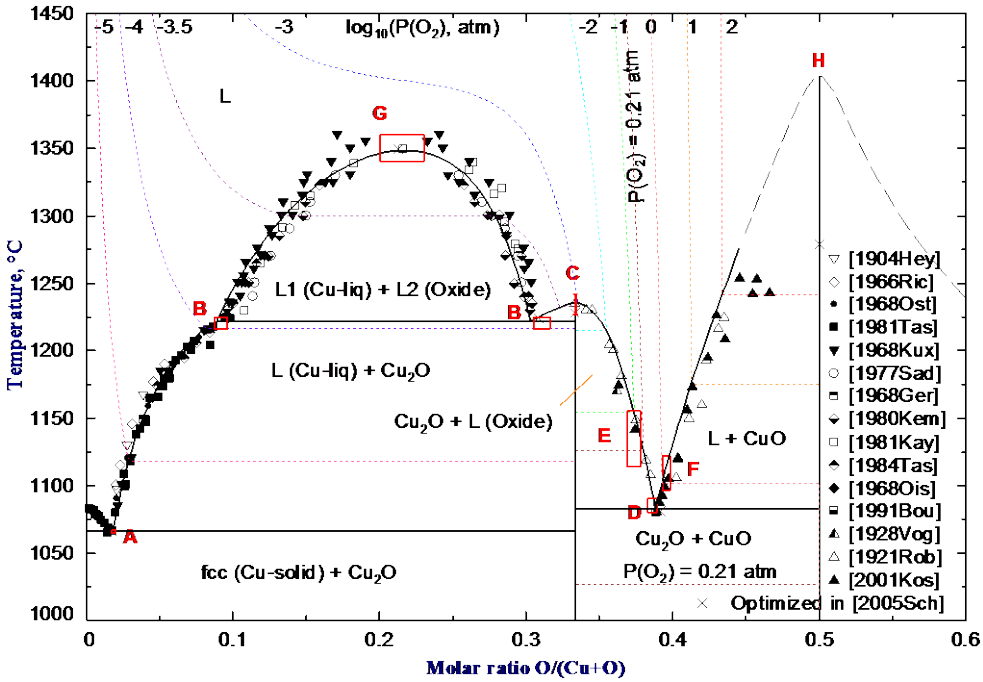

Figure 4.3. Calculated phase diagram of the Cu–O system along with experimental points [121-136] and special points from assessment [120]. Dashed lines are calculated oxygen isobars. The scatter of the experimental data collected by Hallstedt *et al.* [118] for each special point is shown by red rectangles. Gas phase is suppressed.

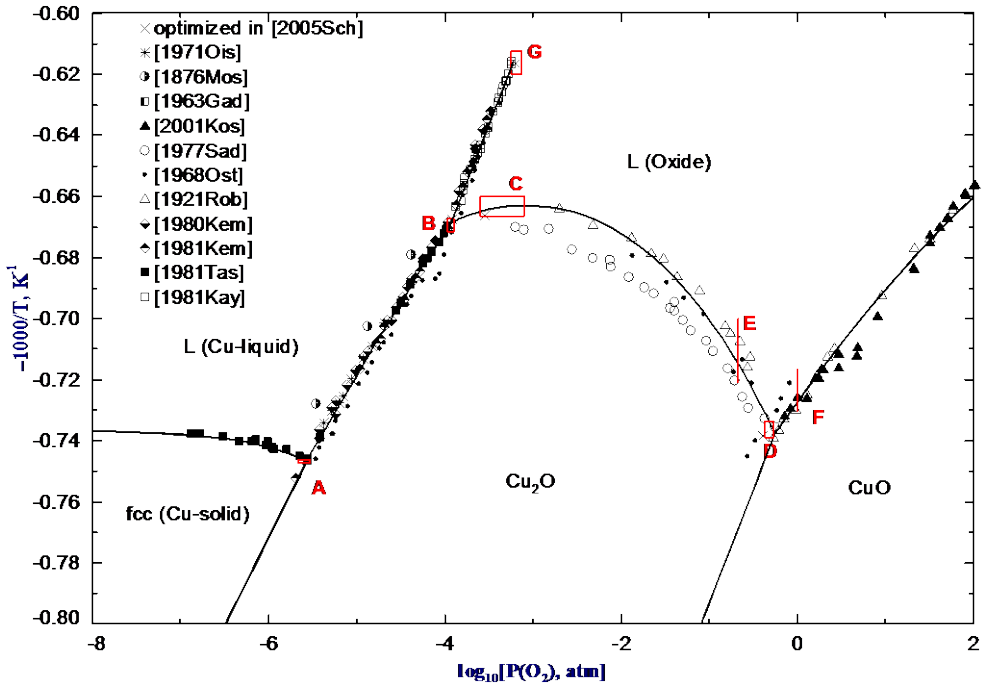

Figure 4.4. Calculated potential phase diagram of the Cu–O system along with experimental points [124, 125, 127, 129, 130, 135-140] and invariant points from assessment [120]. The scatter of the experimental data collected by Hallstedt *et al.* [118] for each invariant point is shown by bars. The gas phase is suppressed.

4.4.2 Solid Cu_2O and CuO

Thermodynamic properties of solid stoichiometric compounds Cu_2O and CuO have been well studied. A comprehensive review of the experimental data was reported by Hallstedt *et al.* [118] and their optimized thermodynamic functions of solid Cu_2O and CuO were accepted in the present study.

4.4.3 Liquid phase

A drastic increase of the oxygen potential is observed in the liquid phase near the Cu_2O composition, as can be seen from Figure 4.5. This is the result of short-range ordering. Hallstedt *et al.* [118] recalculated the EMF vs. T data of Taskinen [125, 132] into isotherms $\log_{10}P(O_2)$ vs. X_O which are plotted in Figure 4.5. The equilibrium oxygen contents of the liquid phase higher than 0.34 were measured at fixed $P(O_2)$ as a function of temperature [127, 137]. The nearly linear shape of these isobars (see Figure 4.3) makes it possible to interpolate the X_O values to a given temperature and plot the data as $\log_{10}P(O_2)$ vs. X_O isotherms, as shown in Figure 4.5.

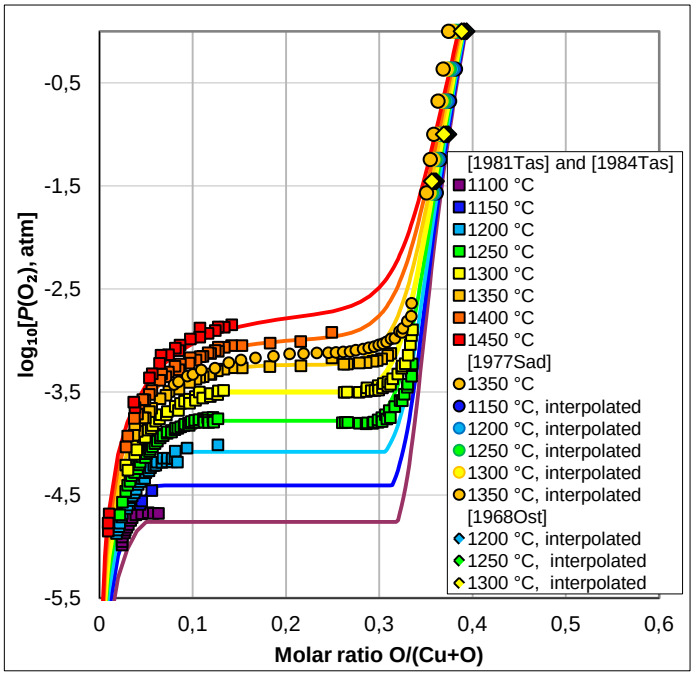

Figure 4.5. Calculated oxygen potential in Cu–O liquid expressed as isotherms along with experimental points [125, 127, 132, 137].

The solubility of oxygen in liquid copper at high dilution has been studied repeatedly. The most thorough are the latest measurements of Otsuka and Kozuka [141] and Taskinen [125, 132]. The equality of the chemical potentials of oxygen in the liquid and gas phase can be written as

$$\mu_{\mathrm{O}} = 0.5\mu^{+}_{\mathrm{O}_2}(T) + RT\ln(\gamma_{\mathrm{O}} X_{\mathrm{O}}) = 0.5[\mu^{+}_{\mathrm{O}_2}(T) + RT\ln P(\mathrm{O}_2)] \tag{4.3}$$

where $\mu^{+}_{\mathrm{O}_2}$ is the Gibbs energy of ideal O_2 gas at 1 atm, γ_{O} is the activity coefficient of oxygen in the liquid phase and $P(\mathrm{O}_2)$ is the equilibrium oxygen partial pressure in atm. Hence

$$\ln\gamma_{\mathrm{O}} = 0.5\ln P(\mathrm{O}_2) - \ln X_{\mathrm{O}} \tag{4.4}$$

In the Cu-rich region up to $X_{\mathrm{O}} \approx 0.1$, $\ln\gamma_{\mathrm{O}}$ changes nearly linearly with composition. Hallstedt *et al.* [118] suggested recalculating all available experimental data in this region into $\ln\gamma_{\mathrm{O}}$ and expressing it as a linear function:

$$\ln\gamma_{\mathrm{O}} = \ln\left(\gamma^{\circ}_{\mathrm{O}}(T)\right) + \varepsilon^{\mathrm{O}}_{\mathrm{O}}(T) X_{\mathrm{O}} \tag{4.5}$$

where $\gamma^{\circ}_{\mathrm{O}}(T)$ is the activity coefficient of oxygen at infinite dilution and $\varepsilon^{\mathrm{O}}_{\mathrm{O}}(T)$ is the first-order interaction coefficient.

It is common practice to recalculate $\gamma^{\circ}_{\mathrm{O}}(T)$ into the "Gibbs energy of dissolution of oxygen in liquid Cu at infinite dilution with 1 mole % O liquid and 1 atm O_2 gas as reference states" defined as:

$$\Delta G^{\circ}_{1\%\mathrm{O}(liq)}(T) \equiv RT\ln\left(\frac{\gamma^{\circ}_{\mathrm{O}}(T)}{100}\right) \tag{4.6}$$

Substitution of Eqs. (4.4) and (4.5) into Eq. (4.6) gives

$$\Delta G^{\circ}_{1\%\mathrm{O}(liq)}(T) = \lim_{X_{\mathrm{O}}\to 0}\left[-RT\ln\left(\frac{100 X_{\mathrm{O}}}{\sqrt{P(\mathrm{O}_2), atm}}\right)\right] \tag{4.7}$$

$\Delta G^{\circ}_{1\%\mathrm{O}(liq)}(T)$ is convenient because it is a nearly linear function of temperature. The first-order interaction coefficient, $\varepsilon^{\mathrm{O}}_{\mathrm{O}}(T)$, is close to be a linear function of inverse temperature (in K). These functions are presented in Figures 7 and 8. The lines calculated from the model parameters optimized in the present study are shown along with the assessment of Hallstedt *et al.* [118] and selected experimental data [125, 127, 132, 141] recalculated by Hallstedt *et al.* [118].

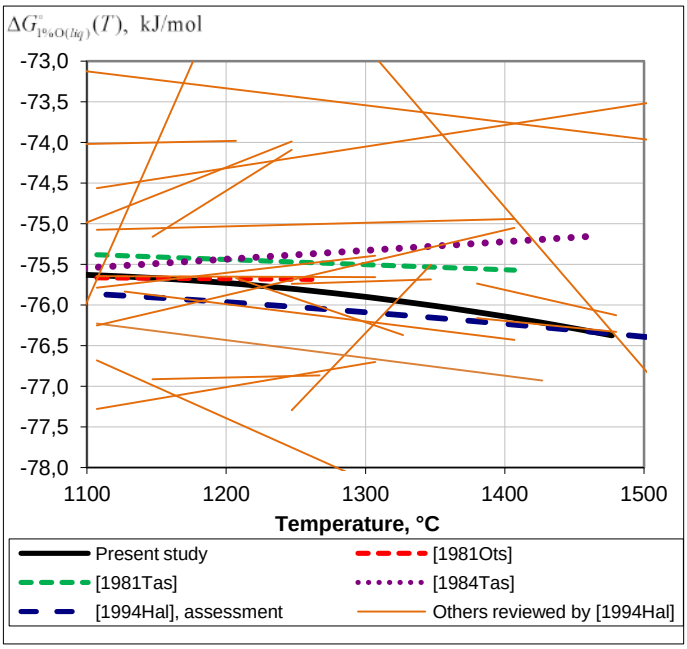

Figure 4.6. Gibbs energy of dissolution of oxygen in liquid Cu at infinite dilution with 1 mole % O liquid and 1 atm O_2 gas as reference states. Dotted and dashed lines represent the experimental data [125, 132, 141] and the assessment of Hallstedt *et al.* [118]. Thin solid lines show other series of experimental data reviewed by Hallstedt *et al.* [118]. Thick black line is calculated using the model parameters of the present study.

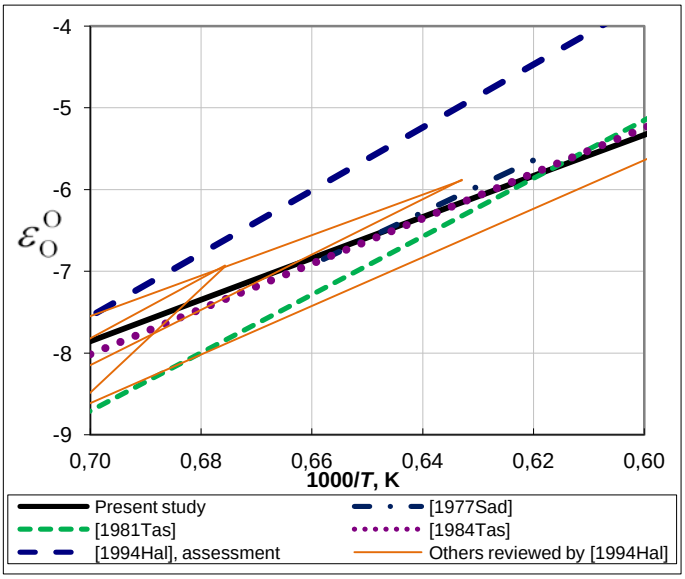

Figure 4.7. First-order interaction coefficient for O in liquid Cu. Dotted and dashed lines represent the experimental data [125, 127, 132] and the assessment of Hallstedt *et al.* [118]. Thin solid lines show other series of experimental data reviewed by Hallstedt *et al.* [118]. Thick black line is calculated using the model parameters of the present study.

The Gibbs energy of formation of liquid Cu_2O from liquid copper and O_2 gas at 1 atm was estimated by Taskinen [132] from EMF studies. His data along with the results of other authors

are shown in Figure 4.8. He also measured the Gibbs energy of formation of solid Cu_2O by an EMF technique. From the temperature dependencies of these Gibbs energies, the enthalpy of melting of Cu_2O was evaluated to be 73 kJ/mol [132]. A more direct measurement of the enthalpy of melting was reported by Mah *et al.* [142] who studied the heat content of Cu_2O. The heat content data [142, 143] are shown in Figure 4.9. The enthalpy of congruent melting of Cu_2O derived from the measurements of Mah *et al.* [142] is 64.7 kJ/mol, which is in good agreement with the value of 64.4 kJ/mol optimized in the present study.

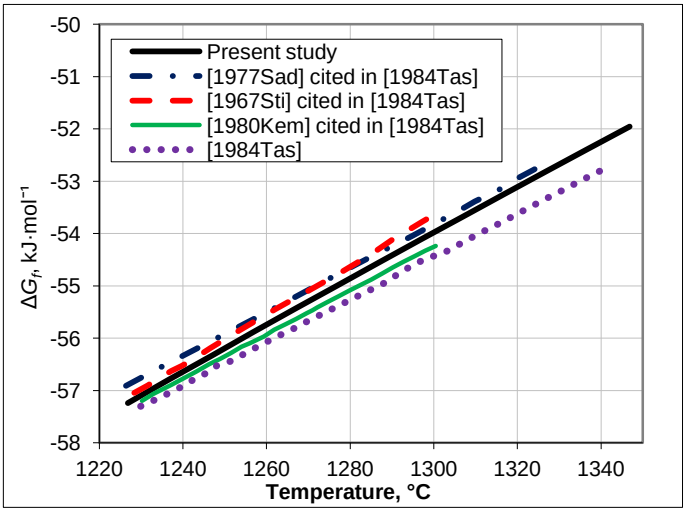

Figure 4.8. Gibbs energy of formation of liquid Cu_2O from liquid copper and O_2 gas at 1 atm. The solid line is calculated from the model parameters for the liquid phase optimized in the present study. The other lines were derived by Taskinen [132] from EMF measurements [127, 129, 132, 144].

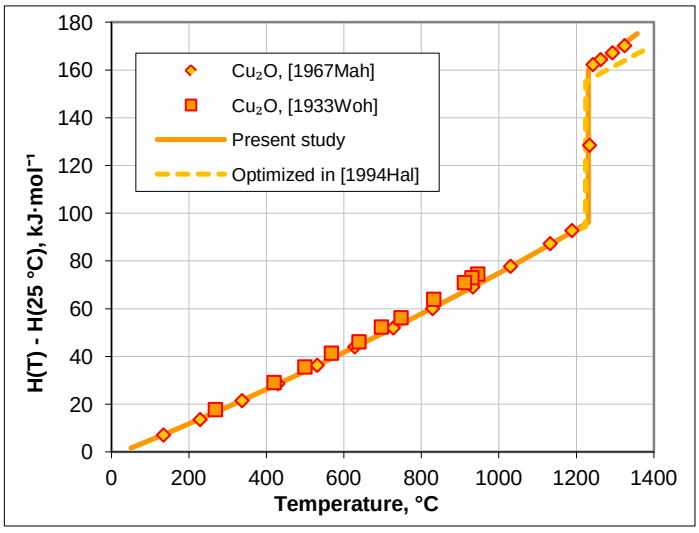

Figure 4.9. Heat content of Cu_2O: experimental points [142, 143] and calculated lines indicating optimizations of the present study and of Hallstedt *et al.* [118].

The optimized model parameters are given in Table 2. The end members of the liquid phase are pure liquid Cu^{I}, Cu^{II} and O, hypothetical monoatomic pure liquid oxygen which should not be confused with real liquid oxygen. The Gibbs energy of pure liquid copper, $g^{\circ}_{Cu^{I}}$, was taken from the SGTE database [145]. $g^{\circ}_{Cu^{II}}$ is essentially the same, but a positive value is added to suppress its formation in pure Cu (see Figure 4.2). A positive excess parameter $\Delta g^{\circ}_{Cu^{I}Cu^{II}}$ is added for the same purpose.

The Gibbs energy of hypothetical pure liquid oxygen, g°_{O}, is not known and was estimated in the present study from the thermodynamic properties of liquid oxides in the FactSage database [4]. For example, the standard entropy of liquid oxygen at 298.15 K, $S^{\circ}_{298}(O)$, can be obtained as a first approximation from the entropies of liquid Mn_2O_3 and MnO, assuming the additivity of entropies: $S^{\circ}_{298}(O) = S^{\circ}_{298}(Mn_2O_3) - 2S^{\circ}_{298}(MnO)$. Other pairs of liquid oxides were also considered: TiO_2 and Ti_2O_3, CuO and Cu_2O, and FeO and Fe_2O_3. The heat capacity of pure liquid oxygen can be estimated similarly. The properties of supercritical fluid oxygen reported by Stewart *et al.* [146] provide the upper limit for $S^{\circ}_{298}(O)$ and the lower limit for $C_P(O)$. Finally, the slope of the heat content data above the melting temperature of Cu_2O shown in Figure 4.9 is well reproduced by the model, which indicates that the estimated heat capacity of pure liquid oxygen gives the right heat capacity of the liquid phase at the Cu_2O composition.

Several optimization attempts were made with different values of g°_{O}. The resulting excess parameters were rather different, but the thermodynamic properties of the liquid phase at $X_O \le 0.5$ were almost the same. This means that the Gibbs energy of the liquid phase is well constrained by the experimental data which are adequately fitted by the model. Large negative parameters $\Delta g^{\circ}_{Cu^{I}O}$ and $\Delta g^{\circ}_{Cu^{II}O}$ were required to reproduce the liquidus in the Cu_2O–CuO region. It is the balance between $\Delta g^{\circ}_{Cu^{I}O}$ and $\Delta g^{\circ}_{Cu^{II}O}$ that defines the shape of the liquidus and $P(O_2)$ in this region. The miscibility gap between metallic and oxide liquid is created by a positive parameter $g^{10}_{Cu^{I}O}$. During the optimization, all available experimental points were considered simultaneously and two more excess parameters were required to adequately reproduce all of them. The optimized parameters are strongly correlated and, therefore, are given in Table 2 with relatively large numbers of significant digits.

As can be seen from Figures 4.4 to 4.10, the experimental data are well reproduced by the model. The composition of maximum short-range ordering between Cu^I and O was moved from X_O = 0.333 to 0.348 in order to prevent the $P(O_2)$ vs X_O isotherms in Figure 4.5 from rising too early. This is done by changing the ratio Z^B_{BA} / Z^A_{AB}, as it is explained in Section 2.2. The isotherms still look a little too steep at X_O from 0.30 to 0.33, but the error does not exceed 0.4 in $\log_{10}P(O_2)$ which is less than the estimated accuracy of the measurements.

4.4.4 FCC solid solution

The solubility of oxygen in solid Cu which has an FCC structure is shown in Figure 4.10. The experimental data were assessed by Hallstedt *et al.* [118] and Clavaguera-Mora [117] who concluded that studies [147-151] reporting lower solubility of oxygen were more reliable than the earlier measurements [152-154]. One temperature-dependent model parameter, $L_{Cu,O}$, was optimized to fit these data. It is given in Table 2. The Gibbs energy of hypothetical oxygen with an FCC structure, g^o_O, was fixed assuming that the transition O(FCC) → O(liq) occurs at 50 °C with the enthalpy of melting equal to 1 kJ/mol. This is in line with the trend of decreasing melting temperatures and enthalpies of melting in a series Te, Se, S, O. The heat capacities of hypothetical FCC and liquid oxygen were assumed to be the same. Of course, the stable form of oxygen at all temperatures and pressures of interest is gaseous O_2.

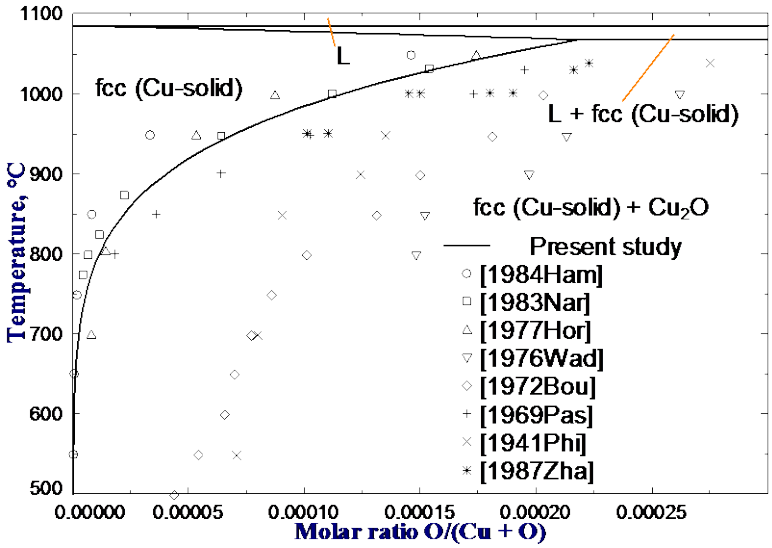

Figure 4.10. Solubility of oxygen in fcc (solid Cu) phase: experimental points [147-154] and calculated lines.

4.5 The Cu–O–S system

4.5.1 Phase diagrams

There are three ternary compounds in the Cu–O–S system, $CuSO_4$, $(CuO)CuSO_4$ and Cu_2SO_4, which decompose with formation of the gas phase before melting at ambient pressure. Three liquids may appear in the system: liquid copper with some solubility of oxygen and sulfur, liquid matte expanding from molten Cu_2S towards Cu_2O and oxide liquid based on molten Cu_2O. Liquid metal may coexist with oxysulfide melt, but at ambient pressure formation of the gas phase containing mainly SO_2 separates matte and oxide liquid. The evaluated phase diagram of the Cu–O–S system at 1250 °C and a total pressure of 1 atm is shown in Figure 4.11.

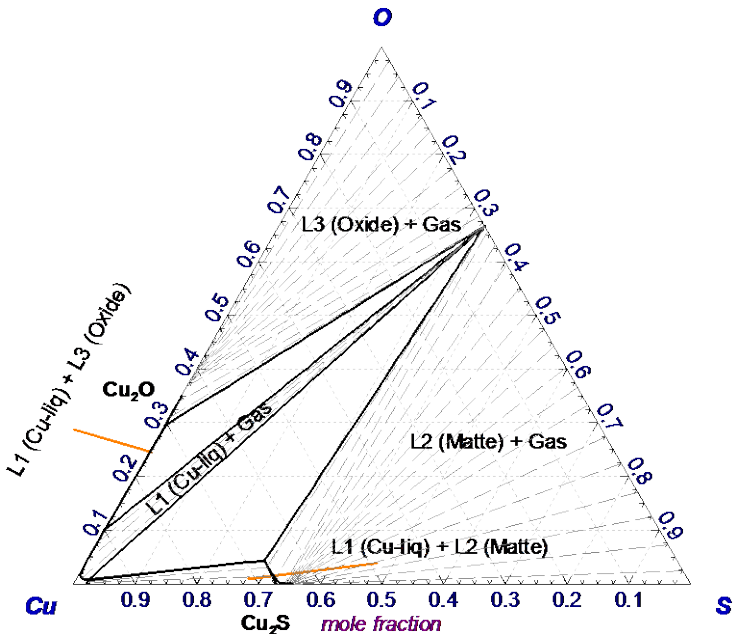

Figure 4.11. Calculated isothermal section of the Cu–O–S phase diagram at 1250 °C and *P* = 1 atm.

The Cu–O–S system is rather well studied in the region of liquid metal and matte at pressures up to 1 atm. No experimental data has been found on the solubility of sulfur in liquid Cu_2O and on equilibrium between liquid metal and liquid oxide in the Cu–O–S system. The lack of experimental data is due to high $P(SO_2)$ in this region.

Schmiedl et al [155] equilibrated liquid copper with matte at controlled $P(SO_2)$ and temperatures ranging from 1100 to 1250 °C. In both phases, they measured the oxygen content

by the hydrogen reduction method and the sulfur content by the combustion method. The experimental compositions at 1100 and 1250 °C are shown in Figure 4.12 (a) and (b).

Kuxmann and Benecke [156] measured the oxygen content of Cu–O–S matte equilibrated with liquid copper at fixed $P(SO_2)$. The sulfur content was not measured, so it is not possible to determine the matte phase boundary from their data.

Equilibrium $P(SO_2)$ over liquid metal + matte tie-lines rises with increasing oxygen content and finally becomes more than 1 atm, as shown in Figure 4.13. Weight percent of oxygen is chosen as the X-axis in Figure 4.13 (a) to compare the results of Schmiedl [155] and Kuxmann and Benecke [156]. Points of Kuxmann and Benecke [156] at 1200 and 1250 °C were obtained by linear interpolation of their $P(SO_2)$ isobars. The latter are shown in Figure 4.13 (b) along with the interpolated points of Schmiedl [155].

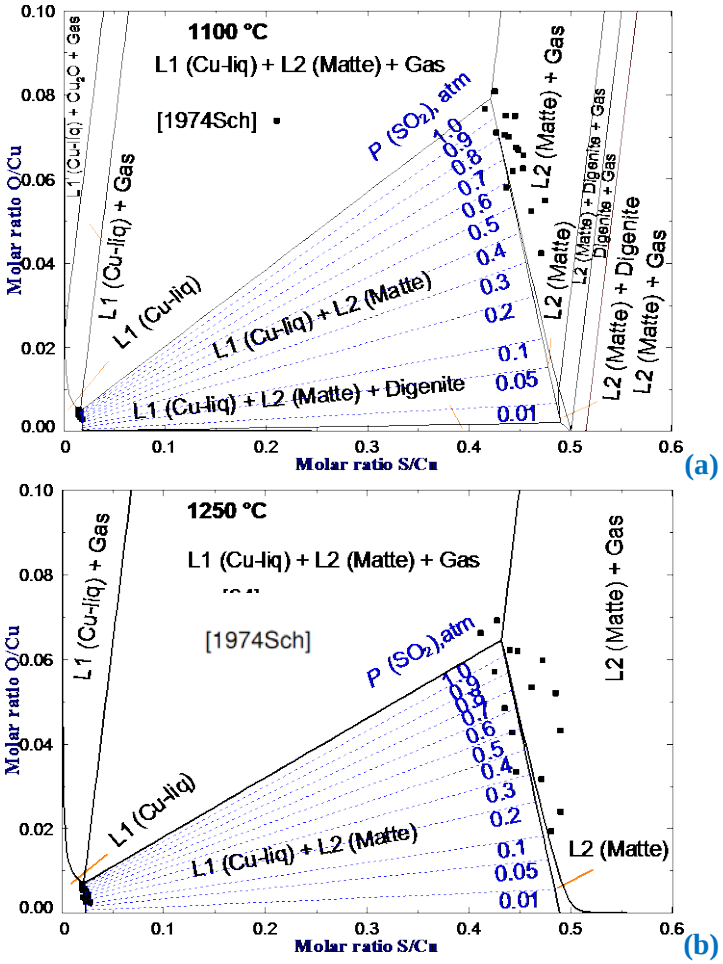

Figure 4.12. Liquid metal + matte region on the Cu–O–S isothermal sections at *P* = 1 atm: experimental points [155] and calculated lines. The corresponding $P(SO_2)$ is indicated for each metal – matte tie-line. (a) 1100 °C, (b) 1250 °C.

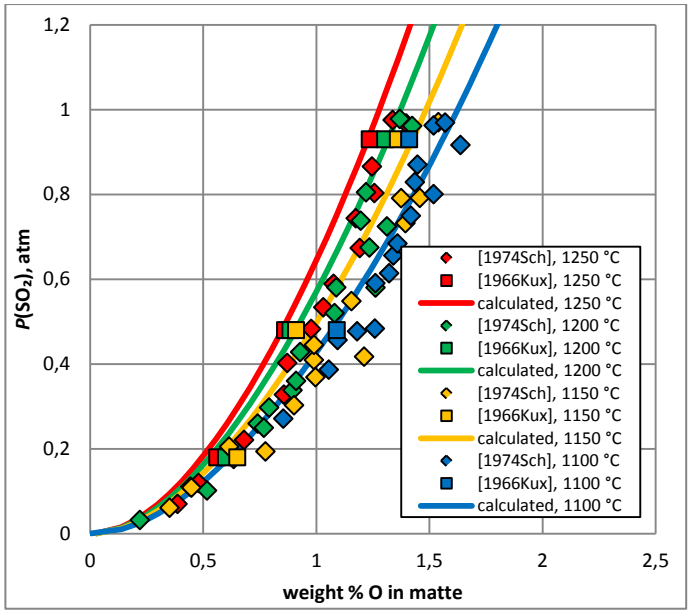

(a)

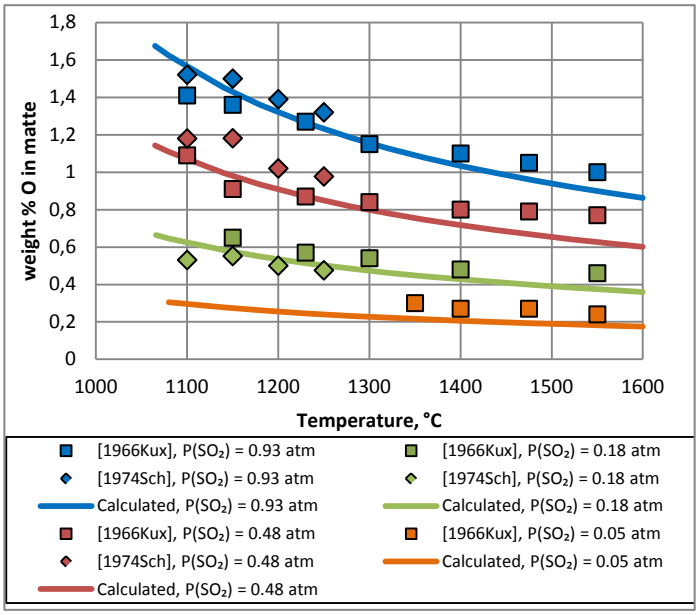

(b)

Figure 4.13. (a) Equilibrium $P(SO_2)$ over liquid metal + matte tie-lines in the Cu–S–O system. (b) Solubility of oxygen in Cu–S–O matte in equilibrium with liquid copper and SO_2/N_2 gas mixtures. Experimental points [155, 156] and calculated lines.

Equilibrium $P(O_2)$ and $P(S_2)$ over liquid metal + matte tie-lines was studied by Jalkanen and Tikkanen [157, 158]. The compositions of metal and matte were not measured. The gas

equilibrated with two liquids was analyzed by gas chromatography for CO, CO_2 and SO_2, which allowed $P(O_2)$ and $P(S_2)$ to be calculated. The results are shown in Figure 4.14.

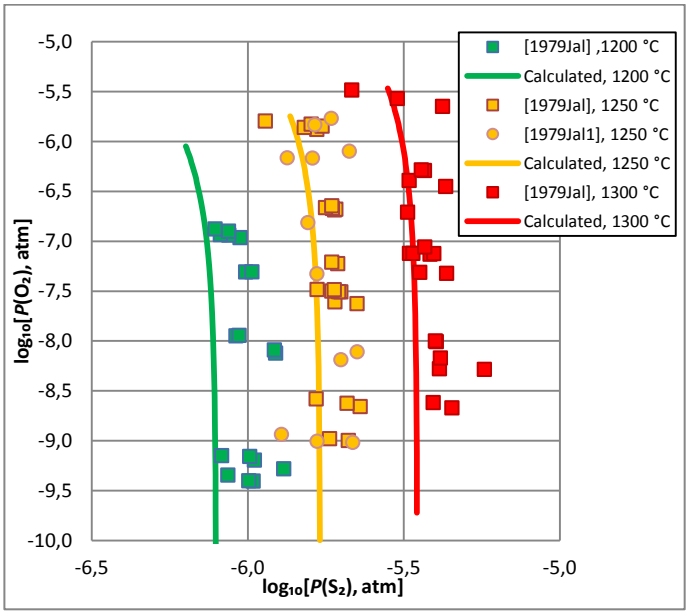

Figure 4.14. $P(S_2)$ vs $P(O_2)$ dependence in the liquid metal + matte region of the Cu–O–S system: experimental points [157, 158] and calculated lines.

If formation of the gas phase is suppressed by applying high total pressure, continuous oxysulfide liquid will exist from Cu_2O to Cu_2S. Oelsen [159] reported a schematic representation of the "Cu_2O–Cu_2S" phase diagram and estimated the equilibrium pressure of SO_2 along this join at different temperatures. The maximum $P(SO_2)$ at 1200 °C was suggested to be 7.0 atm. These results are shown in Figures 4.16 and 4.17. Oelsen [159] provided no details on how his estimations were made. He only cited the work of Lange [160] who, in turn, quoted Reinders and Goudriaan [161]. The latter two publications deal with temperatures up to 730 °C and do not have any information about the liquid phase. Nevertheless, the diagram of Oelsen [159] was accepted and later cited by several authors [156, 162] as the "Cu_2O–Cu_2S phase diagram in equilibrium with copper". The partial pressures of SO_2 shown in Figure 4.16 were not calculated exactly for compositions located on the Cu_2O–Cu_2S section, but rather for compositions $(1–X)Cu_2O + XCu_2S + 0.5$ Cu, so that these $P(SO_2)$ correspond to tie-lines between solid or liquid metallic copper and oxysulfide phases which are slightly shifted off the Cu_2O–Cu_2S join.

Recently Trofimov and Mikhailov [163] estimated $P(SO_2)$ over Cu_2O–Cu_2S melts. Without providing sufficient information on the estimation method, they concluded that the SO_2 partial pressure over oxysulfide liquid at 1200 °C can reach several thousand atmospheres which is much higher than estimated by Oelsen [159].

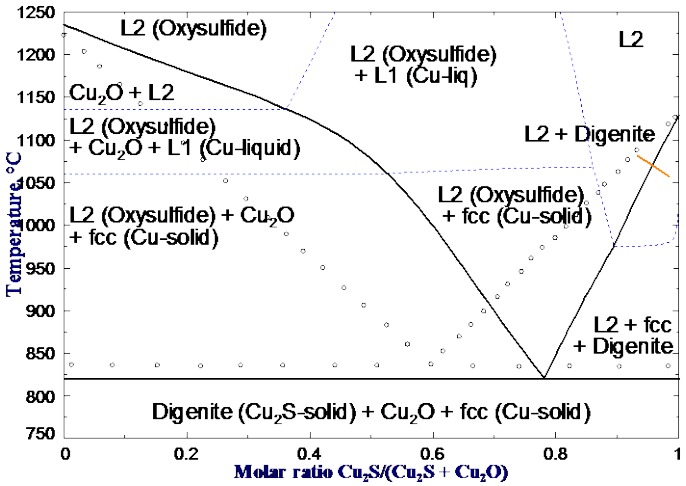

Figure 4.15. Cu_2O–Cu_2S isopleth. Formation of the gas phase is suppressed. Circles represent the phase diagram estimated by Oelsen [159], lines are calculated from the model parameters optimized in the present study.

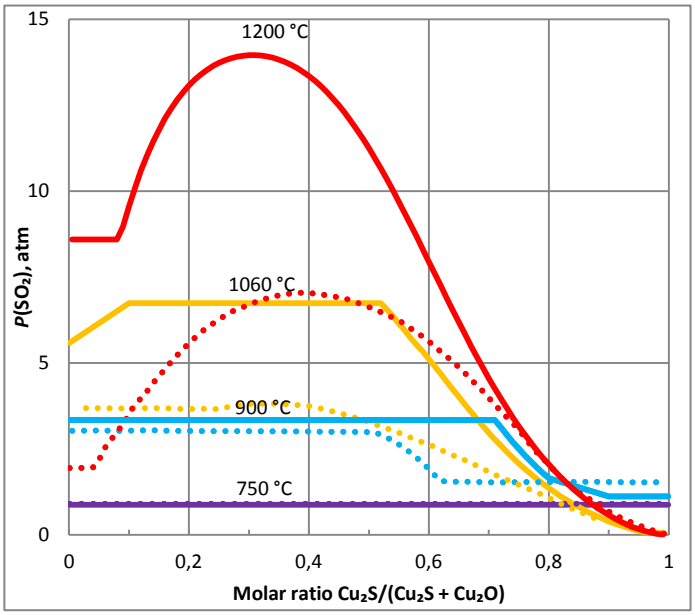

Figure 4.16. $P(SO_2)$ over tie-lines between metallic Cu phases and oxysulfide phases located approximately along the Cu_2O–Cu_2S join. Formation of the gas phase is suppressed. Full lines are calculated from the model parameters optimized in the present study, the other lines represent $P(SO_2)$ estimated by Oelsen [159].

4.5.2 Solubility of oxygen in liquid copper and matte

The solubility of oxygen and sulfur in liquid copper was measured in several studies [155, 164, 165] at fixed $P(SO_2)$. These data are presented in Figure 4.17 which shows the enlarged stability region of liquid Cu from Figure 4.11. The phase boundary between the liquid Cu and (Cu + matte) field measured by Schmiedl [155] at fixed $P(SO_2)$ is also shown in Figure 4.17. The SO_2 isobars of Johannsen and Kuxmann [164] extrapolated up to this phase boundary are in agreement with $P(SO_2)$ reported by Schmiedl [155].

Sano and Sakao [166] equilibrated liquid copper with flowing gas at a given $P(SO_2)$ and a certain CO/CO_2 ratio at 1206 °C. After quenching, copper was analyzed for O and S. Since no special attempts were made to move along SO_2 isobars, the resulting points are scattered over the stability field of liquid copper.

A more systematic approach was taken by Johannsen and Kuxmann [164] and Oishi *et al.* [165]. They equilibrated liquid copper containing various amounts of sulfur and oxygen with SO_2–N_2 or SO_2–Ar gas mixtures, respectively. The O and S content of every sample changed, so that the final composition lies on a certain SO_2 isobar. These isobars are shown in Figure 4.17.

In addition, Oishi *et al.* [165] measured $P(O_2)$ at every point by an oxygen sensor with a CaO-stabilized ZrO_2 electrolyte. The $P(O_2)$ values measured by Oishi *et al.* [165] can be compared with the ones calculated from CO/CO_2 ratios reported by Sano and Sakao [166]. As can be seen from Figure 4.18, the results of these two studies are in good agreement. It is worth noting that the lines in Figure 4.18, cannot be extrapolated to zero oxygen content because they correspond to a $P(SO_2)$ isobar: as the mole fraction of oxygen in liquid copper decreases, the sulfur content increases, which finally results in the phase transition L1 → L1 + L2 as shown in Figure 4.17.

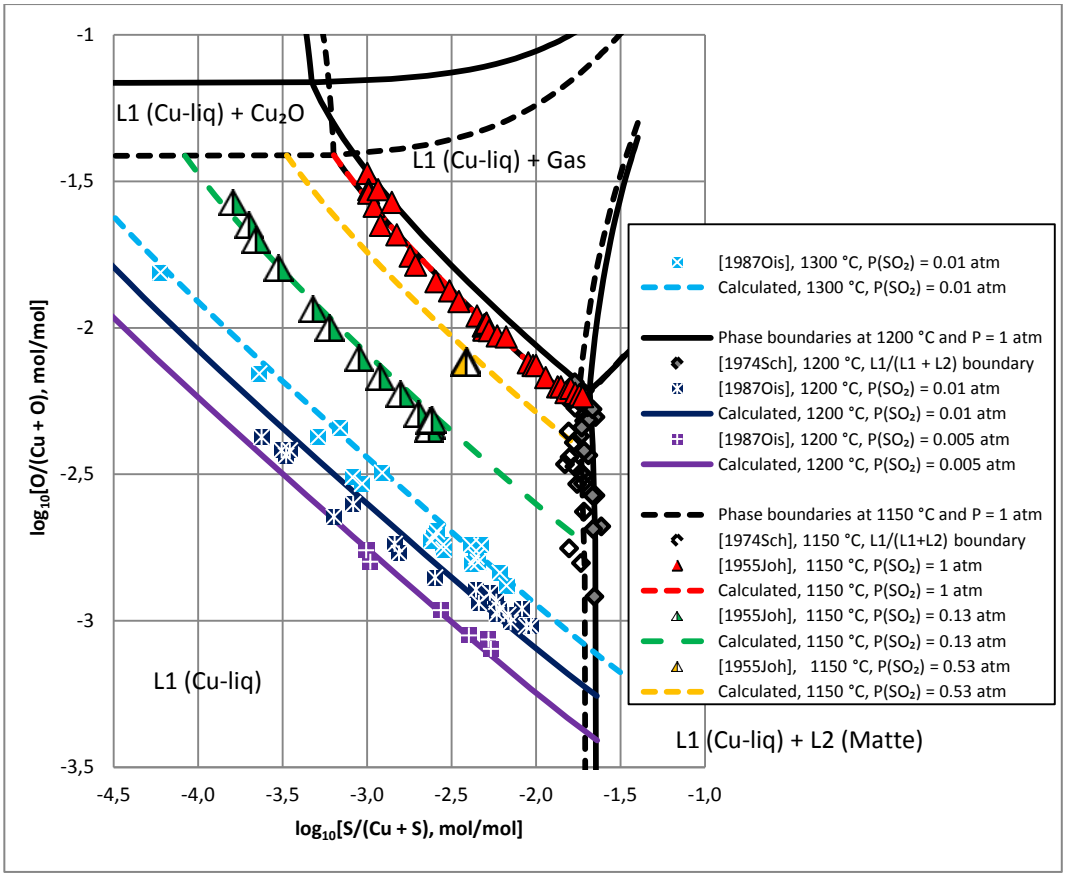

Figure 4.17. Liquid copper region of the Cu–O–S phase diagram: experimental points [155, 164, 165] and calculated phase boundaries and $P(SO_2)$ isobars.

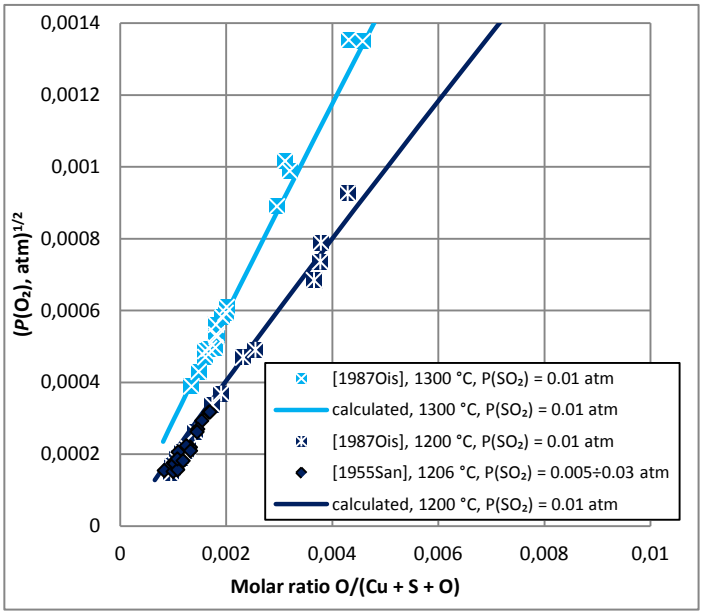

Figure 4.18. Relationship between $P(O_2)$ and oxygen content of liquid copper in the Cu–O–S system at fixed $P(SO_2)$. Experimental points [165, 166] and calculated lines.

Otsuka and Chang [167] studied the equilibrium oxygen partial pressure over liquid copper and matte using EMF determinations on the galvanic cell

$$\text{O (in Cu-S melts)} \;|ZrO_2(+CaO)|\; \text{air, Pt} \qquad (4.8)$$

The oxygen content was measured by coulometric titration and it was always less than 0.2 mole %. The sulfur content was determined before the experiment from the starting materials and after the equilibration by combustion and analysis. These data recalculated to $\ln\gamma_O$ as defined by Equation (4.4) are shown in Figure 4.19 along with the results of Sano and Sakao [166].

Janke and Fisher [168] used an EMF cell similar to (4.8), but they did not report the method of analysis for oxygen and sulfur. They proposed the following linear approximation for $\ln\gamma_O$:

$$\ln\gamma_O = \ln\left(\gamma_O^\circ(T)\right) + \varepsilon_O^O(T)X_O + \varepsilon_O^S(T)X_S \qquad (4.9)$$

where X_O and X_S are the mole fractions of oxygen and sulfur in Cu–O–S melt. Janke and Fisher [168] did not report the measured oxygen partial pressures and compositions, but rather plotted the third term from Equation (4.9) as a function of X_S at 1150 °C. To compare these data with the results of Otsuka and Chang [167] and Sano and Sakao [166], one has to evaluate the value of $\ln\left(\gamma_O^\circ(T)\right)$. It should be noted that since the oxygen contents were very low in all three studies, the second term in Equation (4.9) has almost no effect on $\ln\gamma_O$. From a separate experiment in the Cu–O system performed by Janke and Fisher [168], the value $\ln\left(\gamma_O^\circ(1150^\circ C)\right) = -1.61$ can be obtained, which corresponds to $\Delta G^\circ_{1\%O(liq)}(1150\ ^oC) = -73.6$ kJ/mol according to Equation (4.6). As can be seen from Figure 4.6, the latter value is substantially higher than the optimized value $\Delta G^\circ_{1\%O(liq)}(1150\ ^oC) = -75.7$ kJ/mol. Therefore, we used the corresponding optimized value $\ln\left(\gamma_O^\circ(1150\ ^oC)\right) = -1.79$ to recalculate the plot of Janke and Fisher [168] into $\ln\gamma_O$. As can be seen from Figure 4.19, the results of studies [166-168] for the activity coefficient of oxygen in liquid copper are in fairly good agreement.

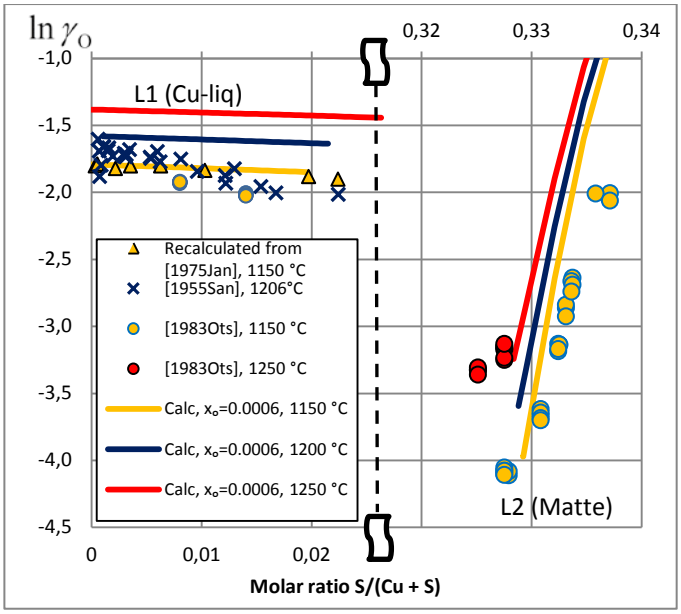

Figure 4.19. Activity coefficient of oxygen in Cu–O–S liquid: experimental points [166-168] and calculated lines. The break in the X-axis is introduced to enlarge the liquid metal and matte regions.

4.5.3 Results of optimization

The thermodynamic description of the Cu–S system [92] was combined with the model parameters for the Cu–O system optimized in the present study to predict the thermodynamic properties and phase equilibria in the Cu–O–S system. All available experimental data in the liquid metal region were in agreement with the calculations, but in the metal + matte region the calculated $P(SO_2)$ increased faster with rising oxygen content than suggested by the measurements shown in Figure 4.13 (a). The maximum $P(SO_2)$ over tie-lines between metallic Cu phases and oxysulfide phases at 1200 °C (Figure 4.16) calculated without ternary parameters was around 15 atm.

One ternary parameter $g^{011}_{Cu^{I}S(O)}$ was introduced to fit the data of Schmiedl *et al.* [155] by affecting the properties of the liquid phase in the matte region. This parameter has virtually no effect on the liquid metal region. The measurements of Kuxmann and Benecke [156] shown in Figure 4.13 (b) are also described better with this parameter. Furthermore, the calculated Cu_2O–Cu_2S isopleth (Figure 4.15) and the calculated $P(SO_2)$ curves in Figure 4.16 became similar to the estimations of Oelsen [159]. Even though the $P(SO_2)$ isotherms calculated for the compositions located exactly on the Cu_2O–Cu_2S section have higher maxima than shown in

Figure 4.16 (for example, the maximum $P(SO_2)$ equals to 82 atm at $X_{Cu_2S} = 0.13$ and 1200 °C), these values are still much lower than several thousand atmospheres estimated by Trofimov and Mikhailov [163].

The final description of the available experimental data is shown by the calculated lines in Figures 12 to 20. The agreement is within experimental error limits. The $P(SO_2)$ vs composition data of Sano and Sakao [166] for the metallic liquid region are also well reproduced by the model.

The thermodynamic properties of stoichiometric $CuSO_4$ and $(CuO)(CuSO_4)$ were taken from JANAF [169]. The thermodynamic functions of Cu_2SO_4 estimated by Barin et al. [170] were accepted in the present study, but the enthalpy of formation was made more negative to be consistent with the experimental observations of Jacinto et al. [171], who found traces of Cu_2SO_4 at ambient pressure and temperatures up to 500 °C during non-equilibrium reduction of $CuSO_4$. Cu_2SO_4 is stable up to 450 °C on the calculated potential diagram at $P(SO_2)$ = 1 atm shown in Figure 21. The thermodynamic properties of all stoichiometric compounds and model parameters are given in Table 2.

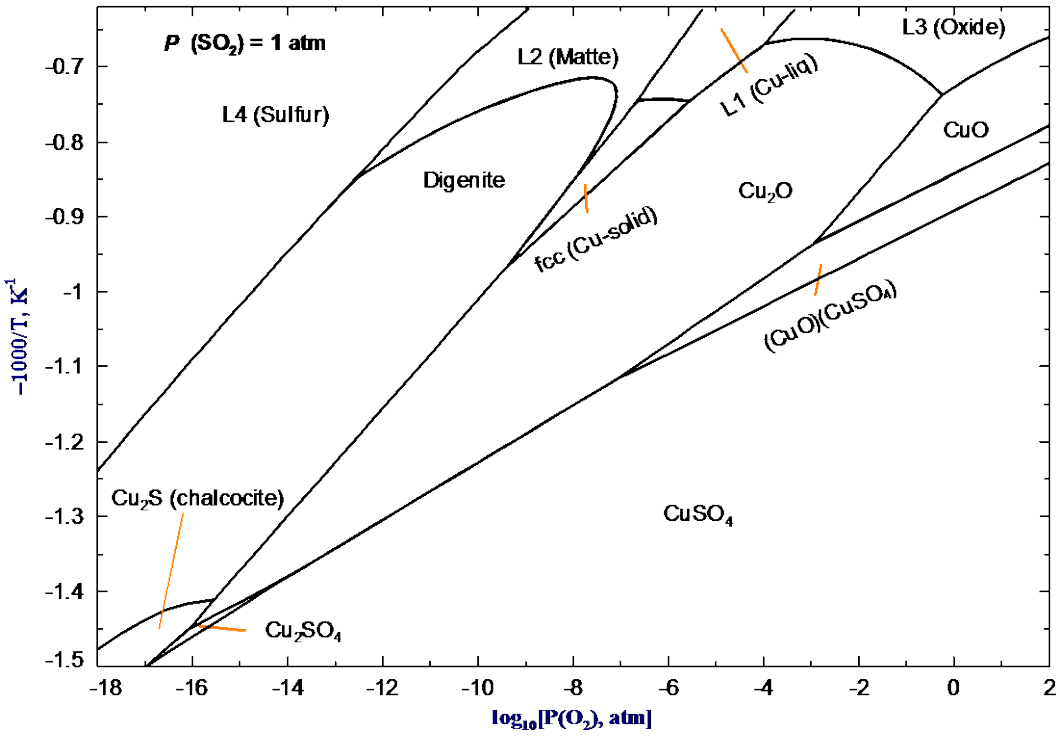

Figure 4.20. Calculated potential phase diagram of the Cu–O–S system at $P(SO_2)$ = 1 atm.

The calculated liquidus projection in the oxysulfide liquid region is shown in Figure 4.21 and the calculated invariant points are given in Table 1. As can be seen from the liquidus projection, the Cu_2O–Cu_2S section crosses the primary phase regions of FCC and liquid Cu. The corresponding phase boundaries separating the fields L2(Oxysulfide), L2(Oxysulfide) + FCC(Cu-solid) and L2(Oxysulfide) + L1(Cu-liquid) appear on the Cu_2O–Cu_2S isopleth shown in Figure 4.15. On the other hand, the compositions of the oxysulfide liquid phase in equilibrium with L1(Cu-liquid) or fcc(Cu-solid) are shifted off the Cu_2O–Cu_2S section, so $P(SO_2)$ shown in Figure 4.16 corresponds to the compositions of oxysulfide liquid on the corresponding isotherms in Figure 4.21.

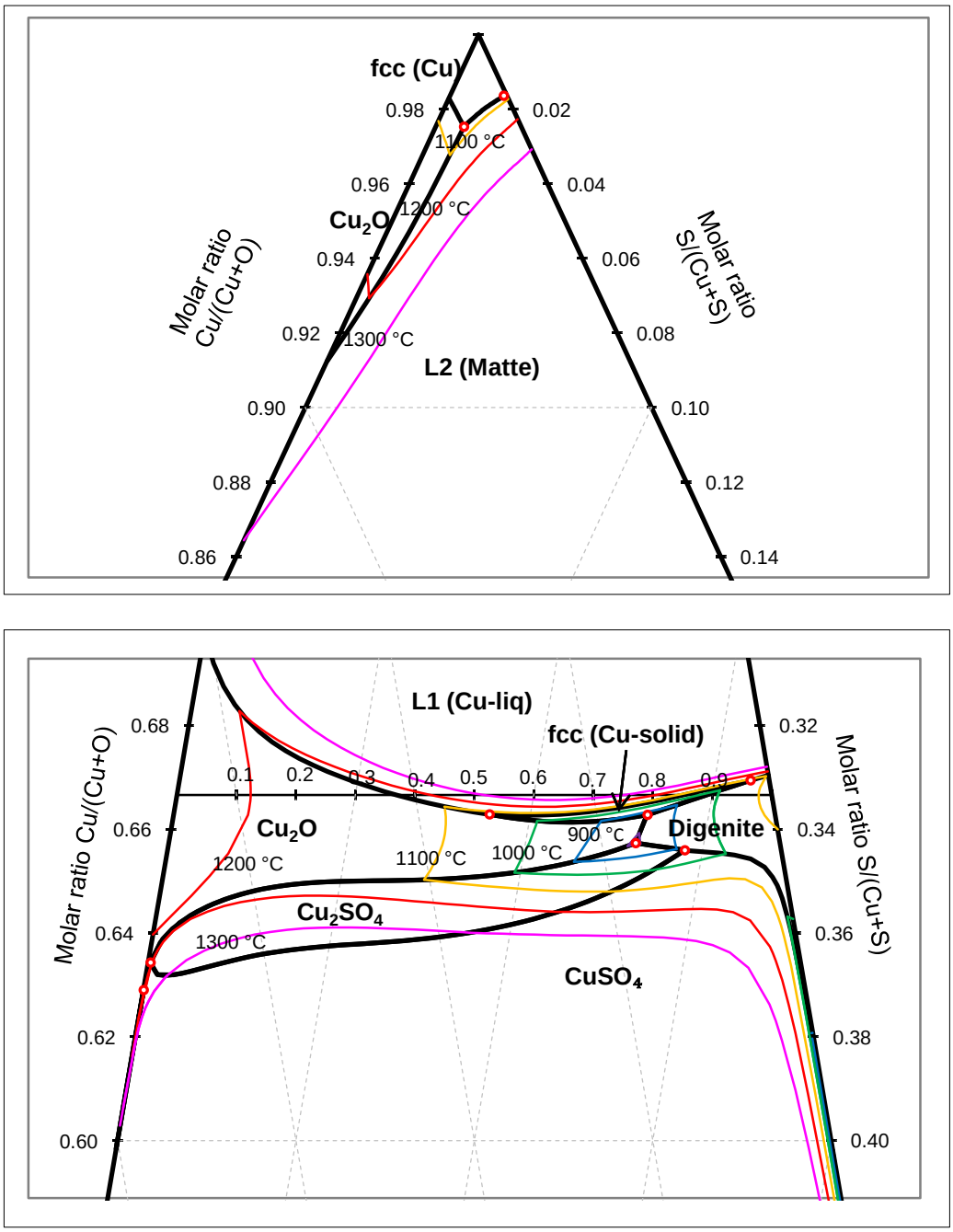

Figure 4.21. Calculated liquidus projection for the Cu–O–S system in the oxysulfide liquid region. Gas phase is suppressed.

Table 4-1. Calculated invariant points in the Cu–O–S system.

		T, °C	Cu	O	S	$\log_{10}[P(O_2)$, atm]	$\log_{10}[P(S_2)$, atm]	$\log_{10}[P(SO_2)$, atm]
1	Digenite + L1 + L2 +fcc	1065.9	0.6694	0.0105	0.3201	-8.05	-7.15	-1.33
			0.9836	0.0009	0.0155			
2	Cu_2O + L1 + L2 + fcc	1058.8	0.6629	0.1601	0.1771	-5.64	-7.81	0.83
			0.9753	0.0165	0.0082			
3	Cu_2O + digenite + Cu_2SO_4 +L2	785.0	0.6573	0.0809	0.2618	-7.09	-7.92	2.99
4	Cu_2O + digenite + fcc +L2	821.3	0.6628	0.0716	0.2657	-8.45	-9.40	0.30
5	(CuO)($CuSO_4$) + Cu_2O + $CuSO_4$ + L2	1163.3	0.6290	0.3708	0.0002	-1.12	-9.39	3.53
6	Cu_2O + Cu_2SO_4 + $CuSO_4$ + L2	1181.3	0.6343	0.3643	0.0014	-1.39	-7.77	3.90
7	$CuSO_4$ + Cu_2SO_4 +digenite + L2	919.7	0.6559	0.0541	0.2900	-5.20	-5.24	4.21

4.6 Conclusions

A complete critical evaluation and optimization of the Cu–O and Cu–O–S systems has been performed. A model for the liquid phase has been developed within the framework of the quasichemical formalism. This model describes simultaneously metallic liquid, sulfide liquid (matte) and oxide liquid (slag). For the Cu–O system, the model reflects the existence of two ranges of maximum short-range ordering at approximately the Cu_2O and CuO compositions. All available thermodynamic and phase equilibrium data have been critically evaluated to obtain one set of optimized model parameters for the Gibbs energies of all phases that can reproduce the experimental data within experimental error limits.

The present study forms a basis for development of a thermodynamic database for the simulation of copper smelting and converting. In particular, the model developed for the liquid

phase and the optimized model parameters can be used to provide a description of the solubility of oxygen in matte and liquid copper. Additional major components such as Fe, Si and Ca are being added to the database as well as Al, Mg and other minor components.

4.7 Acknowledgements

Valuable discussions with Professor E. Jak from the Pyrometallurgy Research Centre at The University of Queensland, Australia, are gratefully acknowledged.

Table 4-2. Optimized properties of stoichiometric compounds and model parameters for the liquid, fcc and digenite solid solutions in the Cu–O–S system (J·mol^{-1} and J mol^{-1}·K^{-1})

Compounds	**Temperature range (K)**	$\Delta H^{o}_{298.15}$	$S^{o}_{298.15}$	$C_P(T)$
CuO (Tenorite)	298 − 3000	-155192.1	43.0626	$49.0300 + 0.006940T - 780000T^{-2}$
Cu_2O	298 − 3000	-170258.2	92.6796	$66.2600 + 0.015920T - 748000T^{-2}$
CuS (Covellite)	298 − 1000	-48575.8	75.8612	$43.6710 + 0.020136T - 4.7200\times10^{-9}T^{2} - 210120T^{-2}$
	>1000			63.5925
Cu_2S (Chalcocite)	298 − 376	-83515.5	116.7648	$53.0000 + 0.078743T$
	>376			82.6073
Cu_2S (High T chalcocite)	298 − 923	-81278.2	122.1507	$111.0000 - 0.0307524T$
	>923			82.6155
S (Orthorhombic)	298 − 368.3	0.0000	32.05400	$11.0070 + 0.053058T - 4.6526\times10^{-5}T^{2}$
	368.3 − 1300			$17.9418 + 0.021790T - 8.4153\times10^{-6}T^{2} - 79820T^{-2}$
	>1300			32.0000
S (Monoclinic)	298 − 388.36	361.6	33.02366	$17.3180 + 0.020243T$
	388.36 − 1300			$21.1094 + 0.017208T - 6.7085\times10^{-6}T^{2} - 241480T^{-2}$
	>1300			32.0000
$CuSO_4$	298 − 2000	-769982.0	109.25395	$-38.4487 + 0.030146T + 13239629T^{-2} - 192652.41T^{-1} + 10802.62175T^{-0.5}$
Cu_2SO_4	298 − 1000	-752850.0	182.42240	$99.5792 + 0.069454T$
	>1000			169.0336
$(CuO)(CuSO_4)$	298 − 1500	-927593.0	157.31802	$-43.4719 + 0.065865T + 10404443.8T^{-2} - 184939.21T^{-1} + 11535.83175T^{-0.5}$

Table 4-2.(Continued) Optimized properties of stoichiometric compounds and model parameters for the liquid phase, fcc and digenite solid solutions in the Cu–O–S system (J mol^{-1} and J mol^{-1}·K^{-1})

Solutions	Temperature range (K)	Molar Gibbs energy g (T)
Liquid (Metal, Oxide, Sulfide)	Modified Quasichemical Model (Cu^{I}, Cu^{II}, O, S), Grouping: Cu^{I}, Cu^{II} in group 1; O, S in Group 2	
$Z^{Cu^{I}}_{Cu^{I}Cu^{I}} = Z^{Cu^{II}}_{Cu^{II}Cu^{II}} = Z^{S}_{SS} = Z^{O}_{OO} = Z^{Cu^{I}}_{Cu^{I}Cu^{II}} = Z^{Cu^{II}}_{Cu^{II}Cu^{I}} = Z^{O}_{OS} = Z^{S}_{SO} = 6$, $Z^{Cu^{I}}_{Cu^{I}S} = 1.5$, $Z^{S}_{SCu^{I}} = 3$, $Z^{Cu^{I}}_{Cu^{I}O} = 1.6$, $Z^{O}_{OCu^{I}} = 3$, $Z^{S}_{SCu^{II}} = Z^{Cu^{II}}_{Cu^{II}S} = 3$, $Z^{O}_{OCu^{II}} = Z^{Cu^{II}}_{Cu^{II}O} = 2$		
g°_{O}	298 − 2990	$121184.8 + 136.0406T - 24.50000T\ln T - 9.8420\times10^{-4}T^{2} - 0.12938\times10^{-6}T^{3} + 322517T^{-1}$
	299 − 3500	$102133.3 + 231.9844T - 36.20000T\ln T$
$g^{\circ}_{Cu^{I}}$	298 − 1358	$5194.4 + 120.9752T - 24.11239T\ln T - 0.00265684T^{2} + 0.12922\times10^{-6}T^{3} + 52478T^{-1} - 5.83932\times10^{-21}T^{7}$
	1358 − 3500	$-46.9 + 173.8837T - 31.38000T\ln T$
$g^{\circ}_{Cu^{II}}$	298 − 3500	$g^{\circ}_{Cu^{I}} + 4781.5$
g°_{S}	298 − 388.36	$-4001.5 + 77.9057T - 15.50400T\ln T - 0.0186290T^{2} - 0.24942\times10^{-6}T^{3} - 113945T^{-1}$
	388.36 − 428.15	$-5285183.2 + 118449.6004T - 19762.4000T\ln T + 32.79275100T^{2} - 10221.417\times10^{-6}T^{3} + 264673500T^{-1}$
	428.15 − 432.25	$-8174994.8 + 319914.0872T - 57607.2990T\ln T + 135.3045000T^{2} - 52997.333\times10^{-6}T^{3}$
	432.25 − 453.15	$-219408.8 + 7758.8558T - 1371.8500T\ln T + 2.8450351T^{2} - 1013.8033\times10^{-6}T^{3}$
	453.15 − 717	$92539.8 - 1336.3502T + 202.9580T\ln T - 0.2531915T^{2} + 51.8835\times10^{-6}T^{3} - 8202200T^{-1}$
	717 − 3500	$-6890.0 + 176.3709T - 32.0000T\ln T$
$\Delta g^{\circ}_{Cu^{I}S}$		$-67166.116 - 8.695398T$
$g^{10}_{Cu^{I}S}$		$55282.59 - 5.6751299T$
$g^{20}_{Cu^{I}S}$		7511.4858
$g^{30}_{Cu^{I}S}$		-24638.853
$g^{90}_{Cu^{I}S}$		$-212683.22 + 1204.0135T - 145.14135T\ln T$

Table 4-2.(Continued) Optimized properties of stoichiometric compounds and model parameters for the liquid phase, fcc and digenite solid solutions in the Cu–O–S system (J mol^{-1} and J mol^{-1}·K^{-1})

Solutions	Temperature range (K)	Molar Gibbs energy g (T)
$g^{01}_{Cu^{I}S}$		11621.957
$g^{02}_{Cu^{I}S}$		36336.6 − 15.02049T
$g^{04}_{Cu^{I}S}$		33205
$\Delta g^{\circ}_{Cu^{I}O}$		-189802.98 + 2.21752T
$g^{10}_{Cu^{I}O}$		43618.2 − 13.598T
$g^{20}_{Cu^{I}O}$		-4142.16
$g^{50}_{Cu^{I}O}$		7252.2667 − 2.3709333T
$\Delta g^{\circ}_{Cu^{II}O}$		-228446.4 − 16.736T
$\Delta g^{\circ}_{Cu^{I}Cu^{II}}$		83680
$g^{011}_{Cu^{I}S(O)}$		-221752
fcc (Solid Cu)	Bragg-Williams (Cu, O, S)	
g°_{Cu}	298 − 1358	-7770.5 + 130.4854T – 24.1124Tln$T$ − 0.002657T^{2} + 0.12922×10$^{-6}T^{3}$ + 52478T^{-1}
	1358 − 2000	-13542.3 + 183.8042T – 31.3800Tln$T$ + 3.64643×10$^{29}T^{-9}$
g°_{S}	298 – 368.3	60442.6 + 67.0953T – 11.0070Tln$T$ − 0.026529T^{2} + 2.3×10$^{-5}T^{-1}$
	368.3 – 2000	59932.6 + 103.2150T – 17.9418Tln$T$ − 0.010895T^{2} + 1.40256×10$^{-6}T^{3}$ + 39910T^{-1}
g°_{O}	298 − 2000	120184.8 + 139.1406 T – 24.5000Tln$T$ – 9.8420×10$^{-4}T^{2}$ – 0.12938×10$^{-6}T^{3}$ + 322517T^{-1}
$L_{Cu,S}$		-62550.39 − 38.424305T

Table 4-2.(Continued) Optimized properties of stoichiometric compounds and model parameters for the liquid phase, fcc and digenite solid solutions in the Cu–O–S system (J mol^{-1} and J mol^{-1}·K^{-1})

Solutions	**Temperature range (K)**	**Molar Gibbs energy g (T)**
$L_{Cu,O}$		-170498 − 21.00368T
Digenite	Bragg-Williams (Cu_2, Vacancy)S	
$g^{\circ}_{Cu_2S}$	298 − 1450	-99688.1 + 420.44593T – 83.0000Tln$T$
g°_{VaS}	298 − 363.3	60853.7 + 65.02737T – 11.0070Tln$T$ – 0.026529T^2 + 7.754333×10$^{-6}T^3$
	363.3 − 1300	59568.9 + 104.30253T – 17.9418Tln$T$ – 0.010895T^2 + 1.402558×10$^{-6}T^3$ + 39910 T^{-1}
$L^1_{Cu,Va:S}$		-70031.8 + 15.712907T
$L^2_{Cu,Va:S}$		59052.83

The Gibbs energy of formation of a compound from elements in their standard state at a temperature of T (K) and a pressure of 1 atm is given by $\Delta G = \Delta H^{o}_{298.15} - T S^{o}_{298.15} + \int_{298.15}^{T} C_P(T)dT - T\int_{298.15}^{T} \frac{C_P(T)}{T}dT$, where $\Delta H^{o}_{298.15}$ is the enthalpy of formation of the compound at 1 atm and 298.15 K, $S^{o}_{298.15}$ is the entropy of the compound at 1 atm and 298.15 K, and $C_P(T)$ is the heat capacity at constant pressure.

CHAPTER 5 CRITICAL ASSESSMENT AND THERMODYNAMIC MODELING OF THE Fe–O AND Fe–O–S SYSTEMS

Equation Chapter (Next) Section 1

Critical evaluation, thermodynamic modeling and optimization of the Fe–O and Fe–O–S systems at ambient pressures are presented. The liquid phase over the whole composition range from metallic liquid to sulfide melt to oxide melt is described by a single model developed within the framework of the quasichemical formalism. The model reflects the existence of strong short-range ordering in oxide, sulfide and oxysulfide liquid. Two ranges of maximum short-range ordering in the Fe–O system at approximately FeO and Fe_2O_3 compositions are taken into account. Parameters of thermodynamic models are optimized to reproduce all available thermodynamic and phase equilibrium data within experimental error limits. The optimization of the Fe–O and Fe–O–S systems performed in the present study is of particular importance for the description of the solubility of oxygen in matte and liquid iron. The obtained self-consistent set of model parameters can be used as a basis for development of a thermodynamic database for simulation of copper smelting and converting.

The present study is a part of an ongoing research project which is aimed at developing a thermodynamic database for simulation of copper extraction from sulfide concentrates. The previous one dealt with the Cu–O–S system [114]. The major phases that form during copper smelting and converting are: blister copper (a liquid metal phase rich in Cu), matte (a molten sulfide phase containing mainly Cu, S and Fe), slag (a molten oxide phase) and gas. In principle, all three liquid phases represent just one liquid with miscibility gaps. Liquid metal, matte and slag can be completely miscible over certain ranges of temperature and composition, even though this normally does not happen under industrial conditions. It is desirable to have one general thermodynamic model which can describe all three liquid phases simultaneously, but this is very difficult to achieve because the model must reflect quite different atomic interactions that are intrinsic to metallic, sulfide and oxide phases.

As in the case of slags, mattes exhibit strong First Nearest Neighbor (FNN) short-range ordering (SRO). Metal-sulfur pairs are energetically favored over metal-metal and sulfur-sulfur oxygen pairs. But unlike in the slag systems, such as $CaO–SiO_2$, where the ratio O/(Ca + 2Si) is

always very close to 1, the composition of matte can substantially deviate from stoichiometric sulfides both towards metals and nonmetals. In the Fe–S system there is even no miscibility gap between liquid metal and liquid sulfide.

The modeling of the Fe–O and Fe–O–S systems is presented in this study. Thus, all subsystems of the Cu–Fe–O–S system are optimized using the Calphad technique: Cu–Fe–S system by Waldner and Pelton [26, 78, 92], Cu–O–S and Cu–Fe–O systems by Shishin and Decterov [114, 172]. Combined together, they form the Cu–Fe–O–S database, which is able to predict thermodynamic properties and phase equilibria in the quaternary system. The evaluation of experimental data and the comparison with database predictions in the Cu–Fe–O–S system will be reported elsewhere.

In a thermodynamic “optimization” of a system, all available thermodynamic and phase diagram data are evaluated simultaneously in order to obtain one set of model equations for the Gibbs energies of all phases as functions of temperature and composition. From these equations, all of the thermodynamic properties and the phase diagrams can be back-calculated. In this way, all the data are rendered self-consistent and consistent with thermodynamic principles. Thermodynamic property data, such as activity data, can aid in the evaluation of the phase diagram, and phase diagram measurements can be used to deduce thermodynamic properties. Discrepancies in the available data can often be resolved, and interpolations and extrapolations can be made in a thermodynamically correct manner. A small set of model parameters is obtained. This is ideal for computer storage and calculation of properties and phase diagrams. In the present study, all calculations were carried out using the FactSage thermochemical software and databases [4].

5.1 Thermodynamic models

The following section contains descriptions of models for liquid phase, monoxide, bcc and fcc solid solutions. The model for spinel (magnetite) may be found in [21], the model for the pyrrhotite ($Fe_{1-x}S$) is described in [26].

5.1.1 Liquid solution

Modeling of the liquid phase in the Fe–O–S system over entire composition range from liquid metal to oxysulfide melt is a challenging task. No attempts were found in the literature. The thermodynamic model must describe drastic changes in the activity of sulfur and oxygen which are the result of strong short-range ordering at the FeS and FeO compositions, respectively. Furthermore, in the Fe–O system, there must be a maximum in short-range ordering at the Fe_2O_3 composition as well, even though no experimental data are available in this region because the oxygen pressure is too high.

The literature review on the Fe–S liquid modeling and experimental studies was done by Waldner and Pelton [26].

The Fe–O liquid was modeled Sundman [173] using the ionic two-sublattice model $(Fe^{+2}, Fe^{+3})_P(O^{-2}, Va^{-Q})_Q$ with charged vacancies. Later Fe^{+3} was replaced by neutral $FeO_{1.5}$ species [174] resulting in the $(Fe^{+2},)_P(O^{-2}, FeO_{1.5}, Va^{-Q})_Q$ scheme. In this form the model was accepted by several authors and has been used recently to optimize higher-order systems [175-177]. In the latest publication [177] the model for Fe–O contains 3 Gibbs-energy functions and 5 excess parameters (2 temperature-depended).

Kowalski and Spencer [178] suggested a simpler associated solution model (Fe, FeO, $FeO_{1.5}$) with one sublattice. Luoma [179] extended their Fe–O solution and presented the thermodynamic database for the Fe–Cr–Ni–C–O system. The Fe–O liquid was modeled with 3 Gibbs-energy functions and 5 excess parameters (2 temperature-depended).

Degterov *et al.* [21] modeled oxide liquid in the Fe–O system with a modified quasi-chemical model [16, 17] as (FeO, $FeO_{1.5}$). The metallic melt was modeled as a separate solution [180]. As the liquid phase in [21] did not extend to metal, Degterov *et al.* [21] managed only with 2 Gibbs-energy functions and 2 temperature-depended model parameters. This oxide database was further used in many higher-order systems [181-185] as a part of the large *Slag* database.

In the present study, a model for the liquid phase is developed within the framework of the quasichemical formalism [16, 17]. It has one sublattice containing four species: Fe^{II}, Fe^{III}, S and O, where Fe^{II} and Fe^{III} correspond to two oxidation states of Fe. In the Fe–O system, the fraction of the Fe^{II}–O pairs goes through a maximum close to the FeO composition, while the Fe^{III}–O

pairs are most abundant at the Fe_2O_3 composition. All species are not charged, so the condition of electroneutrality is not imposed and the model is capable of representing [26] the liquid phase from metal to nonmetals.

Figure 5.1 and Figure 5.2 illustrate the concept of two oxidation states of Fe which bring about two compositions of maximum short-range ordering in the Fe–O liquid. The calculated enthalpy of mixing between pure liquid Fe and hypothetical pure liquid oxygen has two inflections which correspond to maximum short-range ordering at the FeO and Fe_2O_3 compositions. The special point at $X_O = 0.5$ is better seen on the derivative of enthalpy of mixing with respect to X_O. There are no reliable experimental data on the oxidation states of iron in the liquid phase, but the drastic transition of Fe^{II} to Fe^{III} between the compositions of FeO and Fe_2O_3 seems physically reasonable. The curves in Figure 5.1 and Figure 5.2 were calculated using the optimized model parameters for the liquid phase; for the sake of simplicity, the miscibility gap in the liquid and formation of all other phases were suppressed.

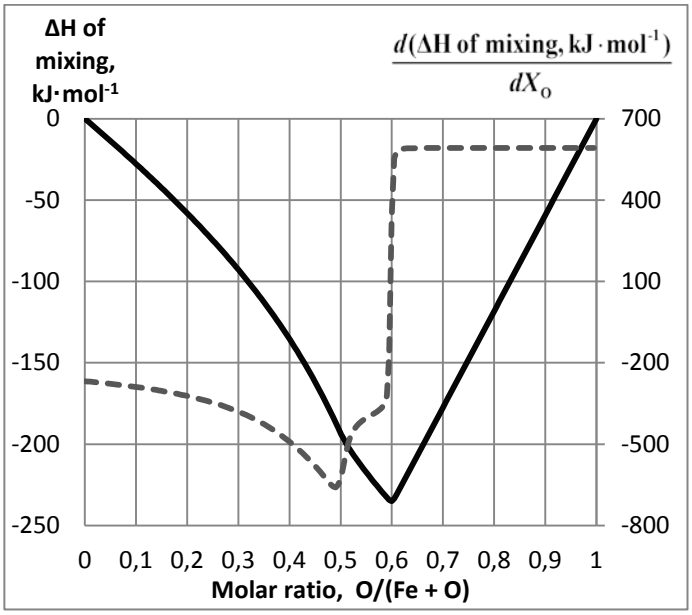

Figure 5.1. Calculated enthalpy of mixing (solid line) and its derivative (dashed line) in Fe–O liquid at 1600 ° C.

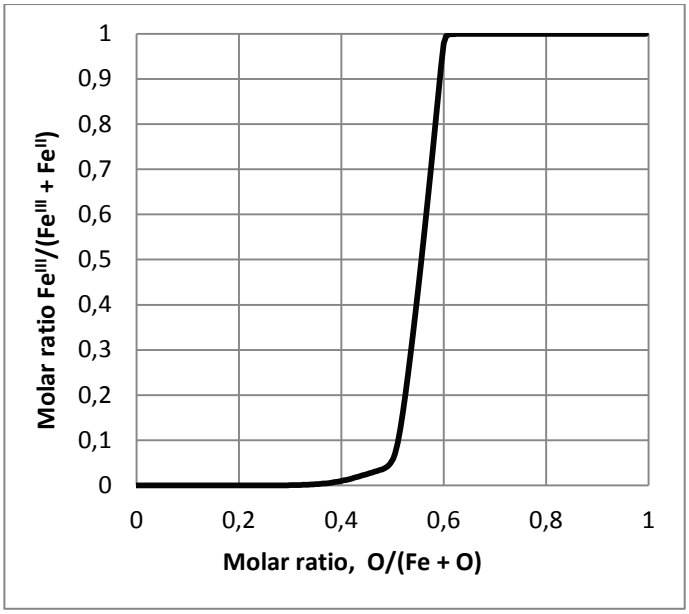

Figure 5.2. Calculated distribution of iron between Fe^{II} and Fe^{III} in Fe–O liquid at 1600 °C.

The formulae and notations of the quasichemical formalism have been described in detail elsewhere [16, 17] and only a brief summary is given here. To explain the meaning of parameters of the quasichemical formalism, let us consider a binary solution formed by components A and B. In the pair approximation of the modified quasichemical model, the following pair exchange reaction is considered:

$$(\text{A-A}) + (\text{B-B}) = 2(\text{A-B});\ \ \Delta g_{\text{AB}} \tag{5.1}$$

where (*i*-*j*) represents a first-nearest-neighbor pair and Δg_{AB} is the non-configurational Gibbs energy change for the formation of two moles of (A-B) pairs.

When the solution is formed from pure components A and B, some (A-A) and (B-B) pairs break to form (A-B) pairs, so the Gibbs energy of mixing is given by [16]:

$$\Delta g_{mix} = g - (n_{\text{A}} g_{\text{A}}^{\circ} + n_{\text{B}} g_{\text{B}}^{\circ}) = -T\Delta S^{\text{config}} + \left(\frac{n_{\text{AB}}}{2}\right)\Delta g_{\text{AB}} \tag{5.2}$$

where g_{A}° and g_{B}° are the molar Gibbs energies of pure liquid components; n_{A}, n_{B} and n_{AB} are the numbers of moles of A, B and (A-B) pairs and ΔS^{config} is the configurational entropy of mixing given by randomly distributing the (A-A), (B-B) and (A-B) pairs. Since no exact expression is known for the entropy of this distribution in three dimensions, an approximate equation is used which was shown [16] to be an exact expression for a one dimensional lattice

(Ising model) and to correctly reduce to the random mixing point approximation (Bragg Williams) expression when Δg_{AB} is equal to zero.

Δg_{AB} can be expanded as an empirical polynomial in terms of the mole fractions of pairs [16]:

$$\Delta g_{\mathrm{AB}} = \Delta g^{\circ}_{\mathrm{AB}} + \sum_{(i+j)\geq 1} g^{ij}_{\mathrm{AB}} X^{i}_{\mathrm{AA}} X^{j}_{\mathrm{BB}} \tag{5.3}$$

where $\Delta g^{\circ}_{\mathrm{AB}}$ and g^{ij}_{AB} are the parameters of the model which can be functions of temperature. In practice, only the parameters g^{i0}_{AB} and g^{0j}_{AB} need to be included.

The composition of maximum short-range ordering is determined by the ratio of the coordination numbers. Let Z_{A} and Z_{B} be the coordination numbers of A and B. These coordination numbers can vary with composition as follows [16]:

$$\frac{1}{Z_{\mathrm{A}}} = \frac{1}{Z^{\mathrm{A}}_{\mathrm{AA}}}\left(\frac{2n_{\mathrm{AA}}}{2n_{\mathrm{AA}}+n_{\mathrm{AB}}}\right) + \frac{1}{Z^{\mathrm{A}}_{\mathrm{AB}}}\left(\frac{n_{\mathrm{AB}}}{2n_{\mathrm{AA}}+n_{\mathrm{AB}}}\right) \tag{5.4}$$

$$\frac{1}{Z_{\mathrm{B}}} = \frac{1}{Z^{\mathrm{B}}_{\mathrm{BB}}}\left(\frac{2n_{\mathrm{BB}}}{2n_{\mathrm{BB}}+n_{\mathrm{AB}}}\right) + \frac{1}{Z^{\mathrm{B}}_{\mathrm{BA}}}\left(\frac{n_{\mathrm{AB}}}{2n_{\mathrm{BB}}+n_{\mathrm{AB}}}\right) \tag{5.5}$$

where $Z^{\mathrm{A}}_{\mathrm{AA}}$ and $Z^{\mathrm{A}}_{\mathrm{AB}}$ are the values of Z_{A} when all nearest neighbors of an A are As, and when all nearest neighbors of an A are Bs, respectively, and where $Z^{\mathrm{B}}_{\mathrm{BB}}$ and $Z^{\mathrm{B}}_{\mathrm{BA}}$ are defined similarly. For example, in order to set the composition of maximum short-range ordering at the molar ratio $n_{\mathrm{A}}/n_{\mathrm{B}} = 2$, one can set the ratio $Z^{\mathrm{B}}_{\mathrm{BA}}/Z^{\mathrm{A}}_{\mathrm{AB}} = 2$. Values of $Z^{\mathrm{B}}_{\mathrm{BA}}$ and $Z^{\mathrm{A}}_{\mathrm{AB}}$ are unique to the A-B binary system, while the value of $Z^{\mathrm{A}}_{\mathrm{AA}}$ is common to all systems containing A as a component.

Even though the model is sensitive to the ratio of the coordination numbers, it is less sensitive to their absolute values. We have found by experience that selecting values of the coordination numbers which are smaller than actual values often yields better results. This is due to the inaccuracy introduced by an approximate equation for the configurational entropy of mixing which is only exact for a one dimensional lattice. The smaller coordination numbers partially compensate this inaccuracy in the model equations, being more consistent with a one dimensional lattice. Therefore, the “coordination numbers” in our model are essentially treated as

model parameters which are used mainly to set a physically reasonable composition of maximum short-range ordering.

There are ten possible pairs formed by the species Fe^{II}, Fe^{III}, O, and S in the Fe–O–S liquid phase. The fractions of all pairs are calculated by the Gibbs energy minimization procedure built into the FactSage software [4] using the optimized model parameters. Fe^{II}–Fe^{II}, O–O and S–S are the predominant pairs at compositions close to pure Fe, O and S, respectively. The Fe^{II}–O, Fe^{III}–O and Fe^{II}–S pairs are dominant in the oxide and sulfide liquids, whereas the fractions of the Fe^{II}–Fe^{III}, Fe^{III}–Fe^{III}, O–S and Fe^{III}–S pairs are small at all compositions of interest.

Extrapolation of binary terms into the Fe^{II}–Fe^{III}–O–S system is done by an asymmetric "Toop-like" method [17]. The components are divided into two groups: metals (Fe^{II} and Fe^{III}) and nonmetals (S and O). By this means in every ternary subsystem, one component belongs to a different group than the other two. "Toop-like" extrapolation is applied, taking this "different" component as an asymmetric component. Except for the binary terms, the model can have ternary terms, $\Delta g_{AB(C)}$, which give the effect of the presence of component C upon the energy Δg_{AB} of pair exchange reaction (5.1). Ternary terms are also expanded as empirical polynomials having model parameters $g^{ijk}_{AB(C)}$. The formulae for ternary terms and for extrapolation of binary and ternary terms into a multicomponent system are discussed in detail elsewhere [17].

The flexibility of the Quasichemical Formalism makes it possible to combine the quasichemical description of the Fe–S and Fe–O systems, which exhibit strong short-range ordering, with the simple Bragg-Williams approximation based on the assumption of random mixing.

5.1.2 Solid FCC and BCC iron

Sulfur and oxygen are soluble to some extent in Fe metal, which has an fcc or bcc structure at the conditions of interest. Simple Bragg-Williams random mixing model was used for both phases with the following formula (per mole of atoms):

$$g = (X_{Fe} g^{o}_{Fe} + X_{O} g^{o}_{O} + X_{S} g^{o}_{S}) + RT(X_{Fe} \ln X_{Fe} + X_{O} \ln X_{O} + X_{S} \ln X_{S}) + X_{Fe} X_{S} L_{Fe,S} + X_{Fe} X_{O} L_{Fe,O} \quad (5.6)$$

where X_i and g_i° are the mole fraction and molar Gibbs energy of component i, $L_{i,j}$ represents an interaction energy between i and j, which can be a function of temperature and composition.

5.1.3 Monoxide

In the present study the non-stoichiometry of the wüstite phase towards oxygen is modeled using the Bragg-Williams approach, assuming random mixing of Fe^{2+} and Fe^{3+} ions on cation sites. Vogel and Fulling [186] suggested the immiscibility between FeO and FeS based on equilibration-quenching-analysis experiments. No sulfur was introduced in monoxide in the current study. Gibbs energy per mole of components FeO and $FeO_{1.5}$ is given by [21]

$$g = (X_{\mathrm{FeO}} g^{\circ}_{\mathrm{FeO}} + X_{\mathrm{FeO_{1.5}}} g^{\circ}_{\mathrm{FeO_{1.5}}}) + RT(X_{\mathrm{FeO}} \ln X_{\mathrm{FeO}} + X_{\mathrm{FeO_{1.5}}} \ln X_{\mathrm{FeO_{1.5}}}) + X_{\mathrm{FeO}} X_{\mathrm{FeO_{1.5}}} L_{\mathrm{FeO,FeO_{1.5}}} \quad (5.7)$$

where g_M° is the Gibbs energy of pure component *M* and X_M is the mole fraction. The interaction energy $L_{M,N}$ between components *M* and *N* is expanded as a polynomial in the mole fractions of the components:

$$L_{M,N} = \sum_{i,j\geq 0} q^{ij}_{M,N} X^i_M X^j_N \quad (5.8)$$

where $q^{ij}_{M,N}$ are the binary model parameters.

5.2 The Fe–S system

The Fe–S system was optimized by Waldner and Pelton [26]. The phase diagram is shown in Figure 6.1. Comparisons with experimental data, descriptions of thermodynamic models and optimized model parameters for all phases are given in [26]. Contrary to the Fe–O liquid, the Fe–S liquid phase was modeled in such a way that Fe exists almost exclusively as Fe^{II} over the whole composition range from metal to sulfur. This is because solid Fe_2S_3 is not stable and there is no experimental evidence for strong short-range ordering in the liquid phase at the Fe_2S_3 composition which corresponds to very high S_2 partial pressures.

Small modification of the $\Delta g^{\circ}_{\mathrm{Fe^{II}S}}$ parameter was made in this study to improve the description in the liquid iron region at 1500-1600 °C, which will be discussed in Section 5.4.3. The changes in the description of the system below 1500 °C are minimal compared to the study of Waldner

and Pelton [26]. Only in the range of 1600-1730 °C some of experimental data were slightly compromised. The 1500-1600 °C region is more important for industrial applications and experimental measurements are more accurate there.

5.3 The Fe–O system

5.3.1 Phase diagram

The phase diagram of the Fe–O system is shown in Figure 6.22. This system has been extensively studied experimentally in the subsolidus region. These data are evaluated elsewhere [21]. There is more uncertainty in experimental measurements in the liquid region. As can be seen from Figure 6.22, there is a wide miscibility gap in the Fe–O system between metal and oxide with the convolution point at very high temperature. Ohtani and Ringwood [187] suggested that metallic and oxide liquid become fully miscible at temperatures > 2800 °C. The calculation with the evaluated parameters of this study gives 2875 °C.

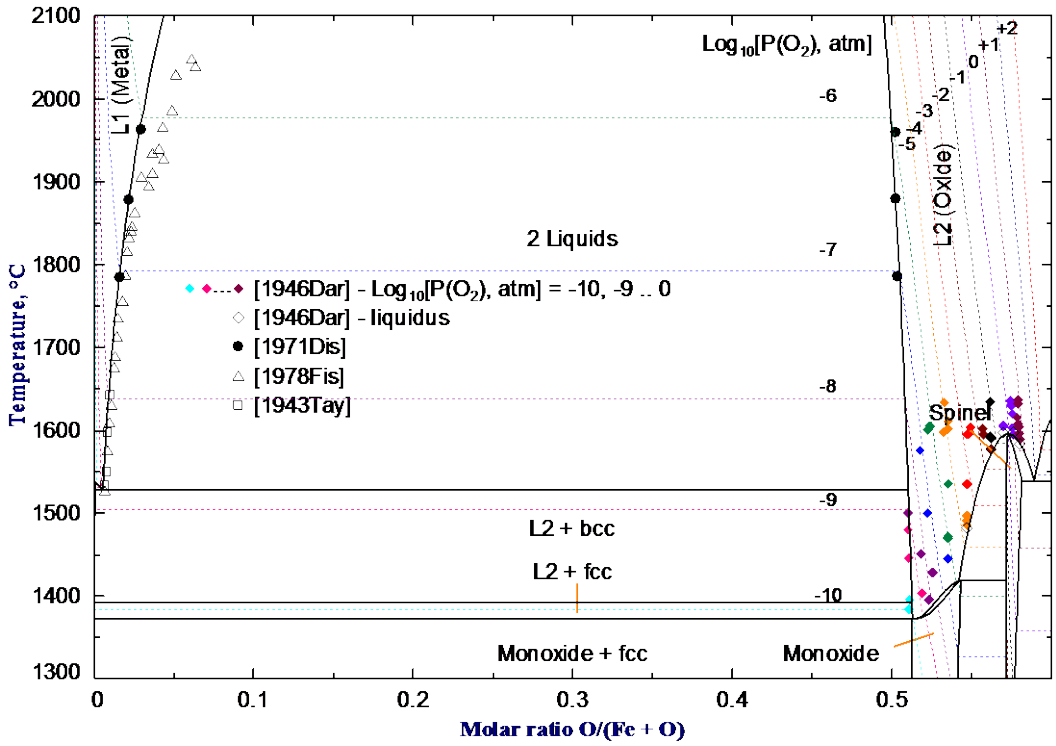

(a)

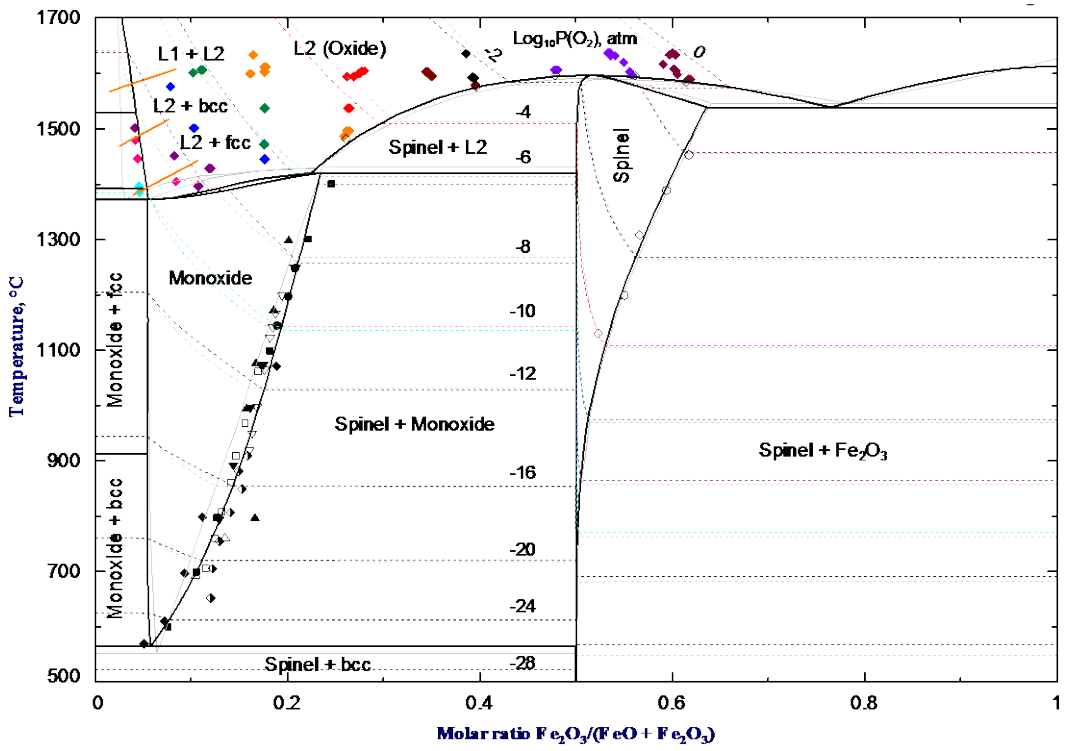

(b)

Figure 5.3. (a) Calculated phase diagram of the Fe–O system along with experimental points [188-191]. Dashed lines are calculated oxygen isobars. Gas phase is suppressed. (b) Enlarged FeO–Fe_2O_3 part of the same diagram. Grey thin lines are from previous optimization [21]. References for subsolidus experimental points are given in [21].

5.3.2 Monoxide and spinel

Thermodynamic properties of solid nonstoichiometric phases – wüstite and magnetite – were assessed by Decterov *et al.* [21]. The phases were modeled under the names of monoxide and spinel accordingly. In the current study, the model parameters for spinel were used without changes, while parameters in monoxide database were slightly changed in order to describe the Monoxide – (Spinel + Monoxide) border in Figure 5.3. The agreement with other experimental data in the subsolidus region of the Fe–O system remains excellent. The final set of parameters is listed in Table 6-1. Currently monoxide and spinel solutions form a basis for large oxide databases. Monoxide solution contains oxides of Fe, Ca, Mg, Zn, Al, Ni, Co, Mn, Cu, Cr, Ti, Zr. The spinel database contains oxides of Fe, Al, Mg, Cr, Co, Ni, Zn, Mn, Cu and Ca.

5.3.3 Liquid phase

A drastic increase of the oxygen potential is observed in the liquid phase between the FeO and Fe_2O_3 composition, as can be seen from Figure 5.4. This is the result of short-range ordering. Sundman [173] assessed the data of [192-195] on the activity of oxygen in liquid iron up to $X_O = 0.015$. More experimental data of Floridis and Chipman [196] and of Goksen [197] were added in this study. Experimental results are expressed as isotherms $\log_{10}P(O_2)$ vs. X_O and shown in Figure 5.4. The equilibrium measurements of Darken and Gurry [188] were performed at $P(O_2)$ fixed with a coupled gas flow (CO/CO_2, CO_2/H_2, H_2/H_2O, O_2/N_2). Their initial data-points lie close to oxygen isobars as shown in Figure 5.3. In this study they also were interpolated to $\log_{10}P(O_2)$ vs. X_O isotherms and plotted in Figure 5.4. It is difficult to see the scatter of the experimental data in the metallic region in Figure 5.4, but it may be revealed as described further.

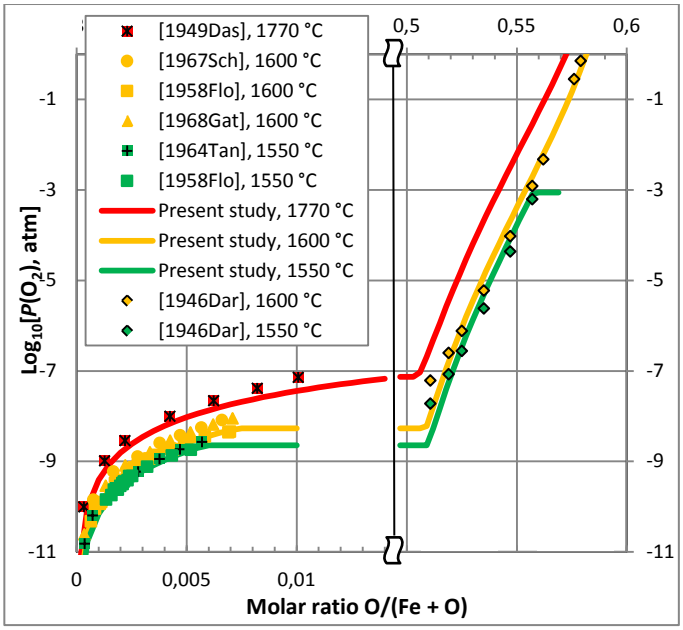

Figure 5.4. Calculated oxygen potential in Fe–O liquid expressed as isotherms along with experimental points [188, 192-197].

In the above mentioned experiments the equilibrium was reached when the chemical potential of gaseous oxygen equaled that in the liquid iron:

$$\mu_O = 0.5\mu^+_{O_2}(T) + RT\ln(\gamma_O X_O) = 0.5[\mu^+_{O_2}(T) + RT\ln P(O_2)] \qquad (5.9)$$

where $\mu^{+}_{O_2}$ is the Gibbs energy of ideal O_2 gas at 1 atm, γ_O is the activity coefficient of oxygen in the liquid phase and $P(O_2)$ is the equilibrium oxygen partial pressure in atm. Hence

$$\ln \gamma_O = 0.5 \ln P(O_2) - \ln X_O \tag{5.10}$$

In the Fe-rich region up to $X_O \approx 0.05 - 0.1$, $\ln \gamma_O$ changes nearly linearly with composition. It is a common practice to recalculate the experimental data in this region into $\ln \gamma_O$ and express it as a linear function:

$$\ln \gamma_O = \ln\left(\gamma^{\circ}_O(T)\right) + \varepsilon^{O}_{O}(T) X_O \tag{5.11}$$

or

$$\gamma^{\circ}_O(T) = \lim_{X_O \to 0}\left[\frac{P(O_2)^{1/2}}{X_O}\right] \text{ and } \varepsilon^{O}_{O}(T) = \lim_{X_O \to 0}\left[\frac{\partial \ln \gamma_O}{\partial X_O}\right] \tag{5.12}$$

where $\gamma^{\circ}_O(T)$ is the activity coefficient of oxygen at infinite dilution and $\varepsilon^{O}_{O}(T)$ is the first-order interaction coefficient.

The $\gamma^{\circ}_O(T)$ is often recalculated into the "Gibbs energy of dissolution of oxygen in liquid Fe at infinite dilution with 1 mole % O liquid and 1 atm O_2 gas as reference states" defined as:

$$\Delta G^{\circ}_{1\%O(liq)}(T) \equiv RT \ln\left(\frac{\gamma^{\circ}_O(T)}{100}\right) \tag{5.13}$$

Substitution of Eqs. (5.10) and (5.11) into Eq. (5.13) gives

$$\Delta G^{\circ}_{1\%O(liq)}(T) = \lim_{X_O \to 0}\left[-RT \ln\left(\frac{100 X_O}{\sqrt{P(O_2), atm}}\right)\right] \tag{5.14}$$

$\Delta G^{\circ}_{1\%O(liq)}(T)$ is a convenient form of representing experimental results because it is a nearly linear function of temperature. The first-order interaction coefficient, $\varepsilon^{O}_{O}(T)$, is usually close to a linear function of inverse temperature (in K). These functions are presented in Figure 5.5 and Figure 5.6. The lines calculated from the model parameters optimized in the present study are shown along with the selected experimental data [192-198]. The scatter of experimental points is well seen in Figure 5.5 and Figure 5.6. It is worth comparing our results with the assessment given in Steelmaking data sourcebook [199]. In technical literature a slightly different notation is

often used. It is based on the weight percent of elements rather than molar fractions. In general case of the solubility of i and j in liquid Fe [199]:

$$\Delta G^{\circ}_{1\%wt.\mathrm{O}(liq)}(T) \equiv RT\ln\left(\frac{A_r(\mathrm{Fe})}{A_r(\mathrm{O})}\cdot\frac{\gamma^{\circ}_{\mathrm{O}}(T)}{100}\right) = \Delta G^{\circ}_{1\%\mathrm{O}(liq)}(T) + RT\ln\frac{A_r(\mathrm{Fe})}{A_r(\mathrm{O})} \tag{5.15}$$

$$f_{\mathrm{O}} = \frac{a_{\mathrm{O}}(\%)}{wt.\%\mathrm{O}} \tag{5.16}$$

$$e^{\mathrm{O}}_{\mathrm{O}} = \lim_{wt.\%Fe\to 100}\left[\frac{\partial\log_{10} f_{\mathrm{O}}}{\partial wt.\%\mathrm{O}}\right] = \frac{\log_{10} e}{100}\left[(\varepsilon^{\mathrm{O}}_{\mathrm{O}} - 1)\frac{A_r(\mathrm{Fe})}{A_r(\mathrm{O})} + 1\right] \tag{5.17}$$

where $\Delta G^{\circ}_{1\%wt.\mathrm{O}(liq)}$, $a_{\mathrm{O}}(\%)$ and f_{O} are the Gibbs energy of dissolution, activity and activity coefficient of oxygen with Henrian 1 weight % as the standard state, respectively. A_r is the atomic mass, $e^{\mathrm{O}}_{\mathrm{O}}$ is the the first-order interaction coefficient in mass percent notation. The table values given in Steelmaking data sourcebook [199] were recalculated from weight percent to mole fraction notation and plotted in Figure 5.5 and Figure 5.6.

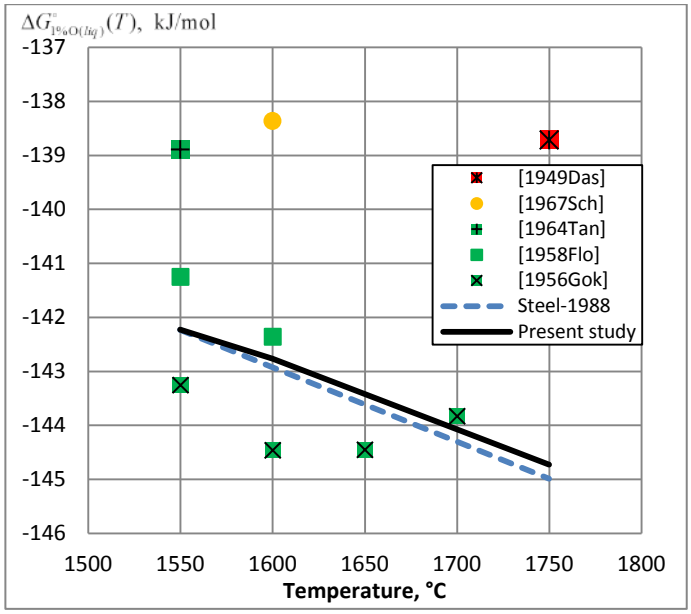

Figure 5.5. Gibbs energy of dissolution of oxygen in liquid Fe at infinite dilution with 1 mole % O liquid and 1 atm O_2 gas as reference states. Experimental data [192-198]. Dotted line is the assessment from [199].

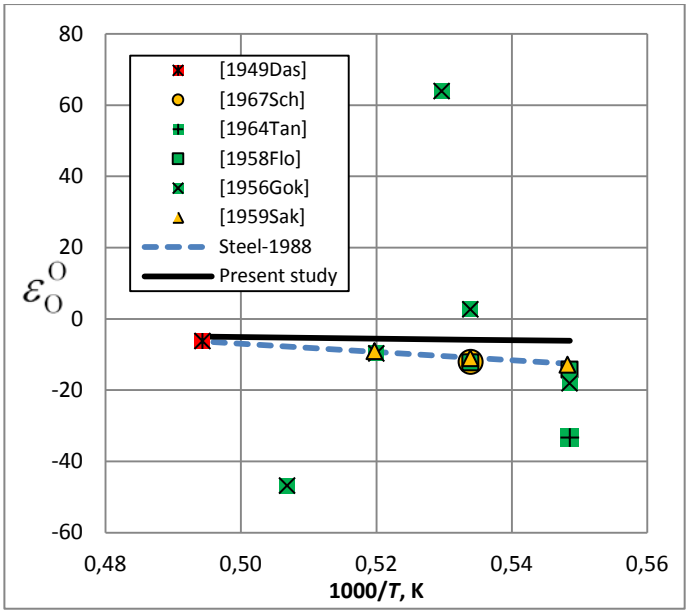

Figure 5.6. First-order interaction coefficient for O in liquid Cu. Experimental data [192-198]. Dotted line is the assessment from [199].

The optimized model parameters for liquid phase are given in Table 5-2. The end members of the liquid phase are pure liquid Fe^{II}, Fe^{III} and hypothetical pure liquid oxygen which should not be confused with real molecular liquid oxygen. The Gibbs energy of pure liquid iron, $g^{\circ}_{Fe^{II}}$, was taken from the SGTE database [145]. $g^{\circ}_{Fe^{III}}$ is essentially the same, but a positive value was added to suppress its formation in pure Fe (see Figure 5.2) and oxygen-free sulfides. A positive excess parameter $\Delta g^{\circ}_{Fe^{II}Fe^{III}}$ is added for the same purpose.

The Gibbs energy of pure liquid oxygen, g°_{O}, has been estimated in the previous study [114].

Large negative parameters $\Delta g^{\circ}_{Fe^{II}O}$ and $\Delta g^{\circ}_{Fe^{III}O}$ were required to reproduce the liquidus in the FeO–Fe_2O_3 region. It is mostly the balance between $\Delta g^{\circ}_{Fe^{II}O}$ and $\Delta g^{\circ}_{Fe^{III}O}$ that defines the shape of the liquidus and $P(O_2)$ in this region. Small Bragg-Williams parameter $q^{001}_{Fe^{II},Fe^{III}(O)}$ was also required to correct the liquidus. The miscibility gap between metallic and oxide liquid is created by a positive parameter $g^{10}_{Fe^{II}O}$. Two positive parameters $g^{20}_{Fe^{III}O}$, $\Delta g^{\circ}_{Fe^{II}Fe^{III}}$ were set rather arbitrarily in order to suppress the formation of Fe^{III} in the Fe–FeO region. During the optimization, all available experimental points were considered simultaneously and two more excess parameters were required to adequately reproduce all of them. The optimized parameters are strongly

correlated and, therefore, are given in Table 6-1 with relatively large numbers of significant digits.

As can be seen from Figure 5.3 and Figure 5.6, the experimental data are well reproduced by the model. The description was attained with 4 variable parameters (2 temperature-dependent) and 2 fixed parameters.

5.3.4 FCC and BCC solid solutions

The solubility of oxygen in solid Fe, which has an fcc or bcc structure, is shown in Figure 5.7. The experimental data were assessed by Kowalski and Spencer [178]. One temperature-dependent model parameter, $L_{\mathrm{Fe,O}}$, was optimized in each phase to fit these data. They are given in Table 6-1. The choice of the Gibbs energy of hypothetical oxygen with an fcc structure, g_{O}°, was explained in the previous paper [114]. Although in theory oxygen in BCC structure should have a different Gibbs energy expression, it is of no practical importance to speculate about the difference between these two forms of oxygen. Each of them is purely hypothetical, and the description of the experimental data depends almost entirely on the $L_{\mathrm{Fe,O}}$ parameter, not on g_{O}°. Thus the same g_{O}° was assigned to bcc oxygen.

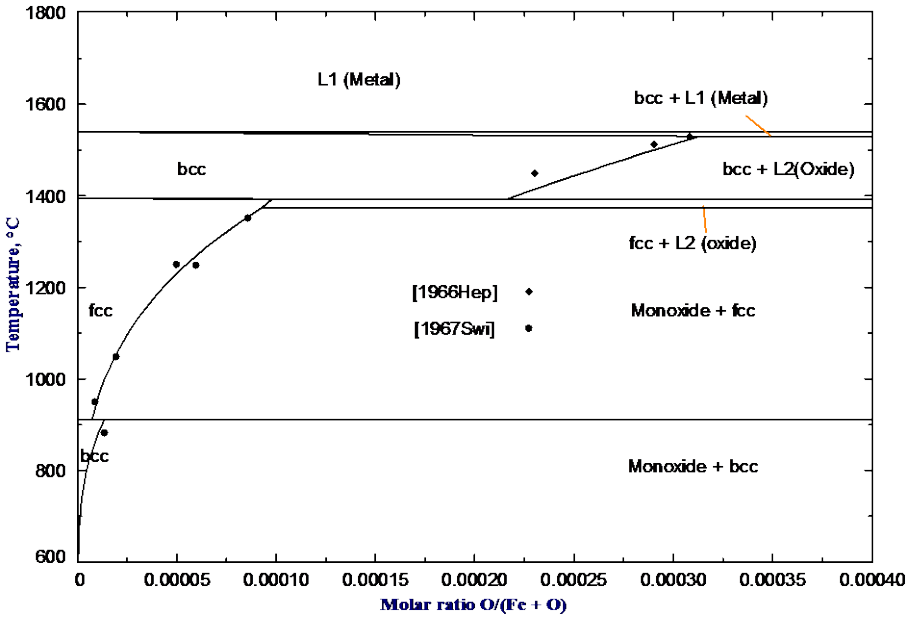

Figure 5.7. Solubility of oxygen in FCC and BCC (solid Fe) phase: experimental points [200, 201] and calculated lines.

5.4 The Fe–O–S system

5.4.1 Phase diagrams

There are two ternary compounds in the Fe–O–S system, $FeSO_4$ and $Fe_2(SO_4)_3$, which decompose with the formation of the gas phase before melting at ambient pressure. Subsolidus reactions were studied by Skeaf and Espelund [202], Hsieh and Chang [203], Rosenqvist and Hofseth [101], Musbah and Chang [204], Schaefer [205] and Espelund and Jynge [206] using the EMF technique. Their data are summarized in Figure 5.8. Rosenqvist and Hynne [207] concluded that FeS does not enter Fe_3O_4 spinel based on equilibration-quenching-analysis experiments.

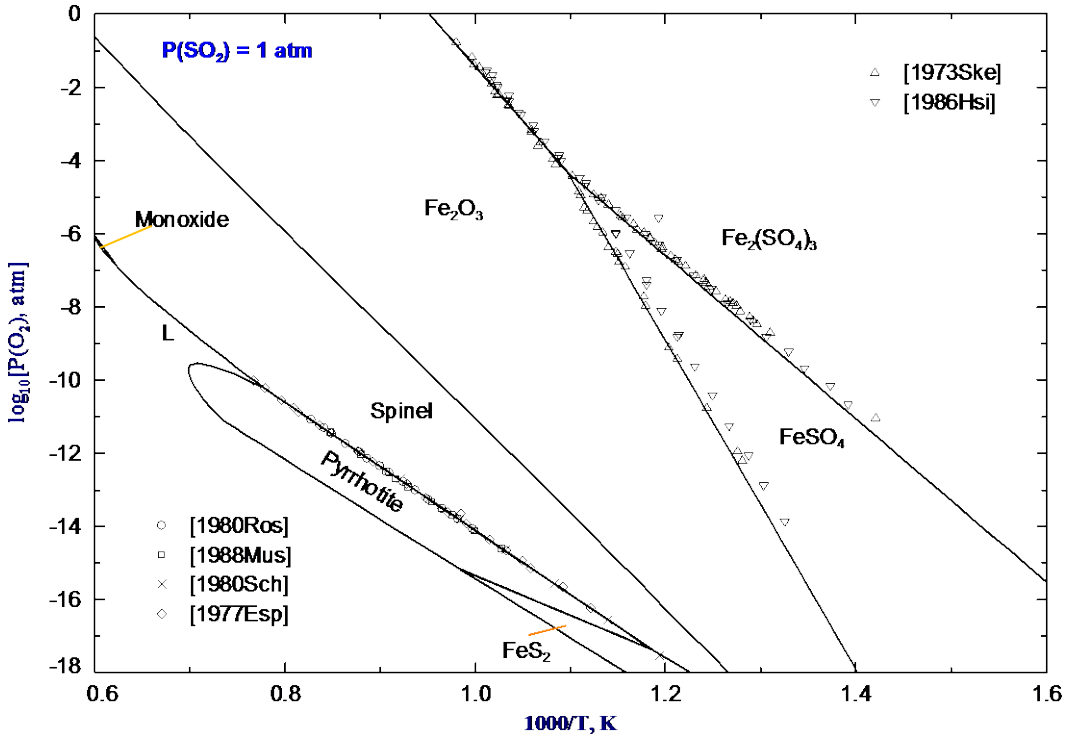

Figure 5.8. Potential phase diagram of the Fe–O–S system at $P(SO_2)$ = 1 atm.

Liquid that appears in the system expands from molten nonstoichiometric FeS towards FeO. At high temperature it spreads to liquid metal as well. The evaluated phase diagram of the Fe–O–S system at 1200 °C and at the total pressure of 1 atm is shown in Figure 5.9.

Phase equilibria in the Fe–S–O system were studied by Hilty and Crafts in 1952 [208], Darken and Gurry (cited in [209]), Rosenqvist and Hartvig in 1958 [210], Bog and Rosenqvist in

1959 [211], Naldrett in 1969 [212], Vogel and Fulling in 1948 [186], Takeda in 1997 [15], Ueda *et al.* in 2008 [213] and Johto and Henao in 2013 [214].

Naldrett [212] determined the iron-wüstite-troilite-liquid (Fe–"FeO"–"FeS"–L) ternary eutectic temperature by melting pyrrhotite, wüstite and iron in silica, iron or silver crucibles. Experiments in silica and iron crucibles gave 915±2 °C, in silver crucible – 905±2 °C. The position of this eutectic was determined by melting in silver crucible and shown in Figure 5.10. Although the temperature obtained with silver crucible is lower, authors claim that the presence of Ag has only small effect on the Fe:S:O ratio at eutectic temperature. Naldrett [212] reported the temperature and the composition of the magnetite-wüstite-troilite-liquid ("Fe_3O_4"–"FeO"–"FeS"–L) ternary peritectic. Experiments were conducted in evacuated, sealed, silica tubes. Thus it was possible to study melts with high vapor pressure without change in composition. However, in the presence of silica tubes, the system becomes quaternary and should be considered as Fe–O–S–Si at SiO_2 saturation. Authors suggested that as the presence of SiO_2 did not affect the temperature of Fe–"FeO"–"FeS"–L eutectic it would not have a strong effect on the "Fe_3O_4"–"FeO"–"FeS"–L invariant temperature and composition. Temperature was found to be 934±2 °C. The position is shown in Figure 5.10.

The experiment of Hilty and Crafts [208] involved melting mixtures of FeS and Fe_2O_3 in iron crucibles. The melting was carried out in Ar, assuming that due to the low $P(SO_2)$ and $P(S_2)$ in the iron-saturated system, the composition would not shift significantly. Taking into the account the fluctuations of cool Ar flow, the accuracy in temperature determination suggested by authors was ±10 °C. Preliminary studies were conducted to prove that the reaction time of 2 hours was sufficient for equilibration. After equilibration samples were quenched in water and studied by chemical analysis and microscopic examination. The results are plotted in Figure 5.10, Figure 5.11 (a-f) and Figure 5.12.

Darken and Gurry (cited in [209]) melted the charge of pyrrhotite and wüstite. The composition of pyrrhotite corresponded to $FeS_{0.942}$ and of wüstite – to $FeO_{1.054}$. Samples were placed in an iron crucible in the atmosphere of purified N_2 and kept under controlled temperature. No special precautions were made in order to keep samples on the $FeS_{0.942}$–$FeO_{1.054}$ section, so changes in Fe/(O + S) ratio probably took place. The melting temperature was defined by microscopic examination of samples quenched in mercury. The structural details of the polished

sample made it possible to determine whether it was quenched from the temperature above or below the liquidus. The resulted points are plotted in Figure 5.12. The liquidus line was interpolated to the desired temperatures and the points corresponding to liquid saturated in iron and wüstite were plotted in Figure 5.11 (a-d).

Rosenqvist and Hartvig [210] equilibrated the mixtures of iron sulfide and oxide with a flow of SO_2 and S_2 at 1 atm and 1135 °C or 1185 °C. Crucibles were made from alumina lined with magnetite. Samples were analyzed for Fe, S by conventional methods – precipitation as Fe_2O_3 and electro-deposition as $BaSO_4$. Oxygen was determined by heating the sample in hydrogen followed by absorption of water with P_2O_5. This technique is usually referred to as the hydrogen-reduction method. The average composition of samples is plotted in Figure 5.11 (b,c) as liquid saturated with magnetite at $P(SO_2)$ = 1 atm.

Bog and Rosenqvist [211] prepared the H_2S–H_2O–H_2 gas mixtures of certain composition and equilibrated them with iron sulfide at 1120 °C. The composition of resulting melt was determined by unspecified chemical methods. Some experiments were conducted at iron saturation. The compositions of the samples in equilibrium with iron along with oxygen and sulfur isobars are plotted in Figure 5.11 (b).

Vogel and Fulling [186] melted mixtures of Fe, Fe_2O_3 and S in Ar atmosphere. Quenched samples were examined microscopically. They suggested the Fe–"FeS"–"FeO"–L eutectic temperature of 920 °C. The composition of the eutectic is shown in Figure 5.10. The FeO liquidus is shown in Figure 5.12.

Ueda and Yamaguchi [213] melted mixtures of Fe, Fe_2O_3 and FeS in iron crucibles at 1000-1400 °C. The oxygen partial pressure was measured with the following oxygen concentration cell:

$$\text{Pt} \mid \text{Ni,NiO} \mid \text{ZrO}_2(\text{CaO}) \mid \text{specimen} \mid \text{Re} \mid \text{Pt} \qquad (5.18)$$

After reaction the crucible was quenched in water bath. Compositions of the specimens were determined by chemical analysis. Oxygen and sulfur contents were determined by reduction with hydrogen. Iron was determined by titration methods and mass balance. The phase equilibrium results are given in Figure 5.11 (a,b,c,d,e). Oxygen potential measurements are given in the next Section in Figure 5.13 and Figure 5.14.

Takeda [15] melted the Fe–S–O matte in an iron crucible at 1200 and 1300 °C and measured the oxygen potential with a sensor similar to (5.18). The analytical method was not specified. The results are shown in Figure 5.11 (c,d) and in the next Section in Figure 5.13.

Johto and Henao [214] heated mixtures of Fe, FeS and Fe_2O_3 in crucibles lined with iron foil. First series of experiments was conducted under Ar atmosphere. After heat treatment, the samples were quenched. Microscopic observations showed that Fe–"FeS"–"FeO"–L eutectic should be between 915 and 920 °C. The compositions of liquid in equilibrium with solid phases were determined by EMPA analysis. The iron and sulfur content was measured directly, oxygen was found by difference. The position of the eutectic point suggested by Johto and Henao [214] is shown in Figure 5.10 and Figure 5.12. The second series of experiments was done at $P(O_2)$ controlled with CO/CO_2 flow and the rest of procedures were the same. Compositions of liquid in equilibrium with solid phases from both series are plotted in Figure 5.11 (a),(c). The dependence between the liquid composition and $P(O_2)$ is discussed in the next Chapter and in Figure 5.13.

Yazawa and Kameda [100] presented the Cu_2S–FeO–FeS phase diagram at iron saturation. The extrapolation of their liquidus to the FeO–FeS section is given in Figure 5.12.

Thus, phase relations in the Fe–S–O system are rather complex and, in some sense, unusual. The liquid phase, which is nonstoichiometric towards metals and nonmetals, splits into two liquids at high temperature. The miscibility gap, contrast to most cases, becomes wider with an increase of temperature. The FeO–FeS diagram is not binary, but rather a section through the ternary system. To experimentally measure the liquidus along this section, it is necessary to fix the total pressure and two more degrees of freedom: the O/S ratio and either Fe/O or Fe/S ratio. No experimental works were done in this way. Instead of fixing the Fe/O or Fe/S ratio, the measurements were done at iron saturation, which inevitably shifts the composition of liquid from the FeO–FeS section to higher Fe content. The calculated phase diagram at iron saturation is shown in Figure 5.12.

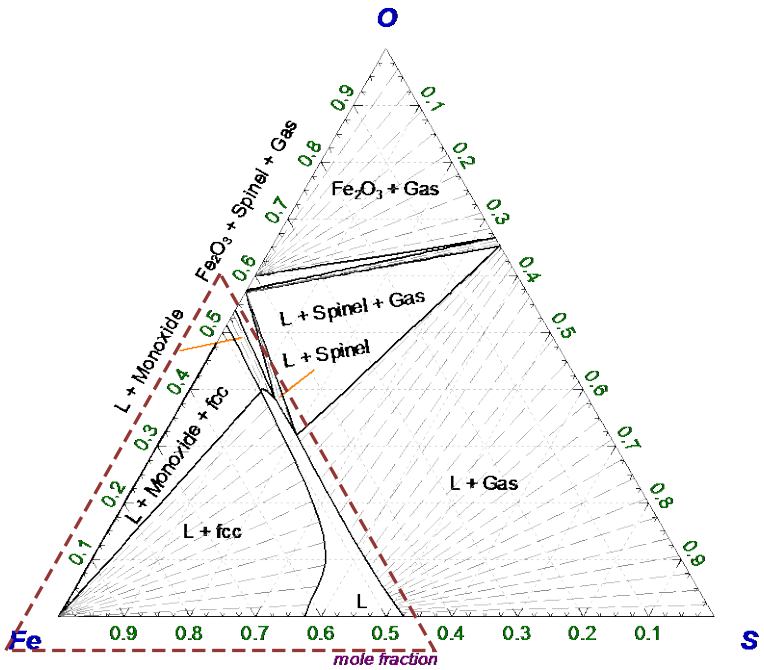

Figure 5.9. Calculated isothermal section of the Fe–O–S phase diagram at 1200 °C and *P* = 1 atm.

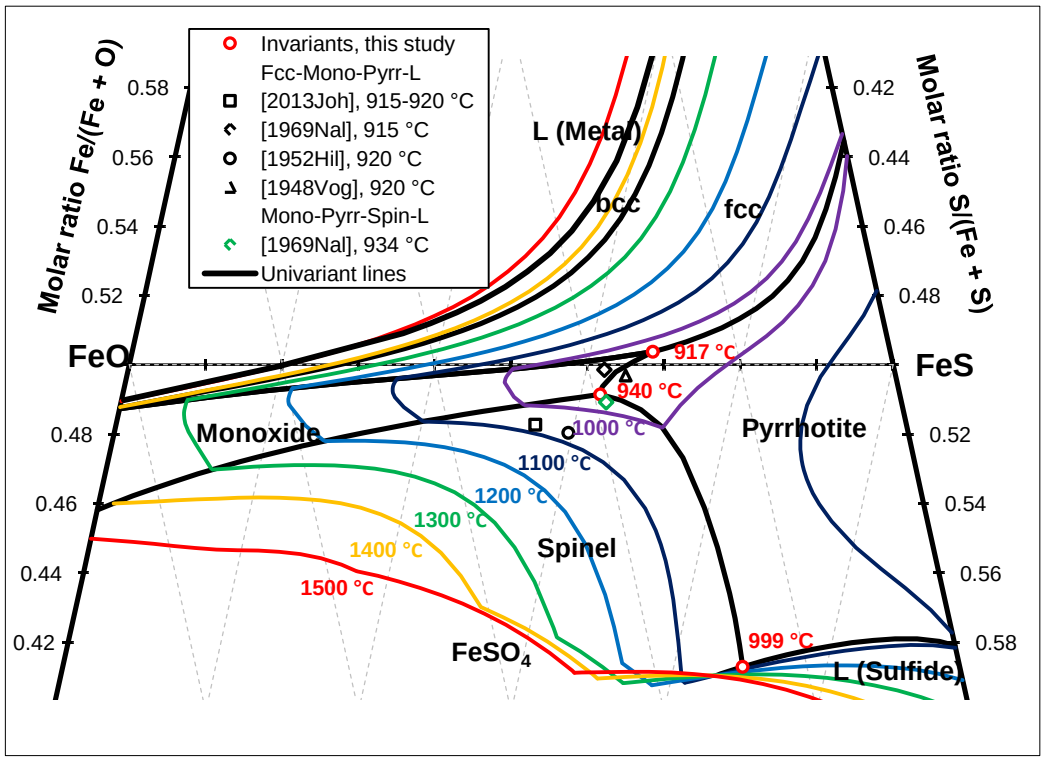

Figure 5.10. Liquidus projection of the Fe–O–S system (FeO–FeS region). The formation of the gas phase is suppressed. Experimental invariant points from [186, 208, 212, 214].

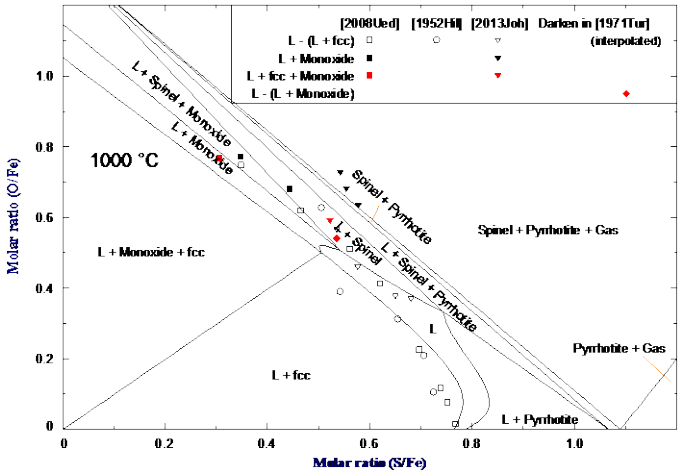
[2008Ued] [1952Hil] [2013Joh] Darken in [1971Tur]
L - (L + fcc)
L + Monoxide
L + fcc + Monoxide
L - (L + Monoxide)
(interpolated)
1000 °C
L + Spinel + Monoxide
L + Monoxide
Spinel + Pyrrhotite
L + Spinel
L + Spinel + Pyrrhotite
Spinel + Pyrrhotite + Gas
L + Monoxide + fcc
L
Pyrrhotite + Gas
L + fcc
L + Pyrrhotite
Molar ratio (O/Fe)
Molar ratio (S/Fe)

(a)

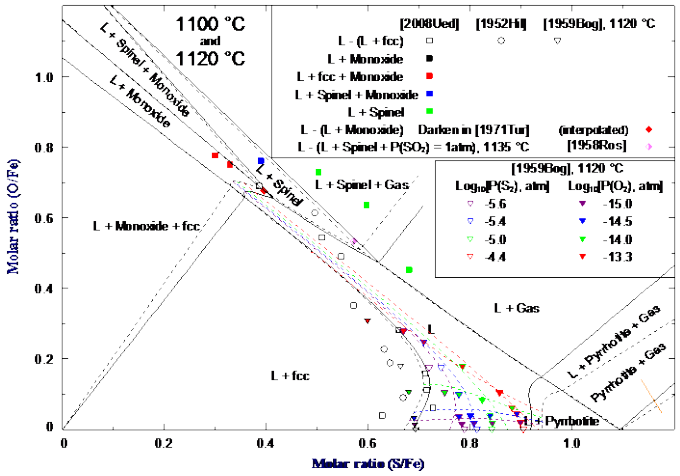
1100 °C
and
1120 °C
[2008Ued] [1952Hil] [1959Bog], 1120 °C
L - (L + fcc)
L + Monoxide
L + fcc + Monoxide
L + Spinel + Monoxide
L + Spinel
L - (L + Monoxide) Darken in [1971Tur] (interpolated)
L - (L + Spinel + P(SO2) = 1atm), 1135 °C [1958Ros]
[1959Bog], 1120 °C
Log10P(S2), atm Log10P(O2), atm
-5.6 -15.0
-5.4 -14.5
-5.0 -14.0
-4.4 -13.3
L + Monoxide + fcc
L + Spinel + Gas
L + Gas
L + fcc
L + Pyrrhotite + Gas
Pyrrhotite + Gas
L + Pyrrhotite
Molar ratio (O/Fe)
Molar ratio (S/Fe)

(b)

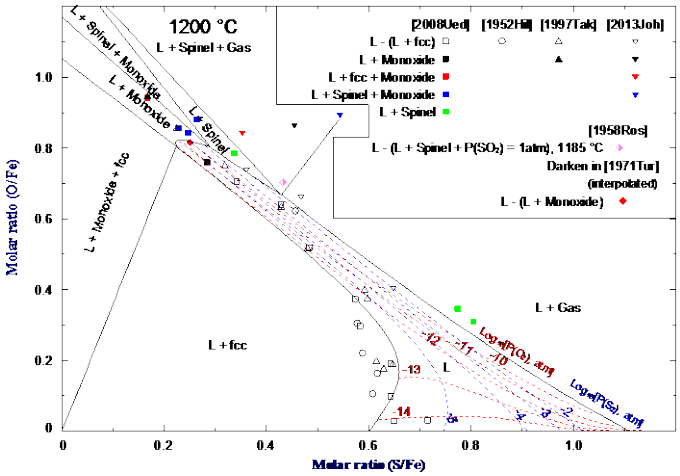
1200 °C
L + Spinel + Gas
[2008Ued] [1952Hil] [1997Tak] [2013Joh]
L - (L + fcc)
L + Monoxide
L + fcc + Monoxide
L + Spinel + Monoxide
L + Spinel
[1958Ros]
L - (L + Spinel + P(SO2) = 1atm), 1185 °C
Darken in [1971Tur]
(interpolated)
L - (L + Monoxide)
L + Monoxide + fcc
L + Gas
L + fcc
L
Log10P(O2), atm
Log10P(S2), atm
Molar ratio (O/Fe)
Molar ratio (S/Fe)

(c)

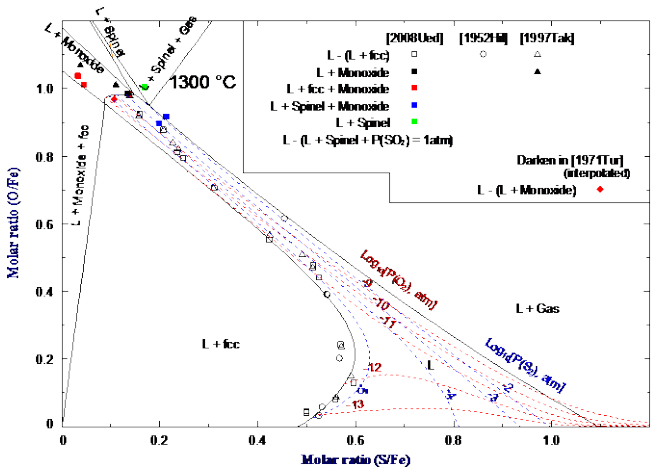

(d)

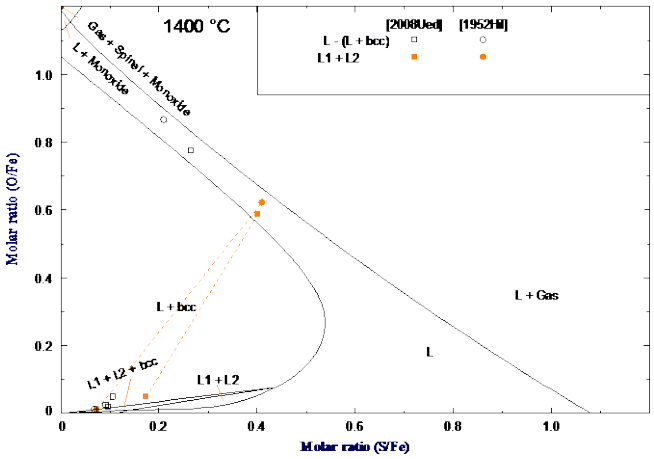

(e)

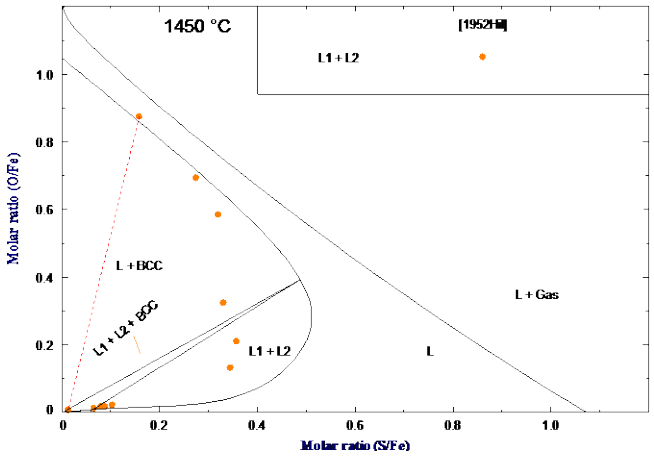

(f)

Figure 5.11. Isothermal sections of the Fe–S–O phase diagram with superimposed O_2 and S_2 isobars at a) 1000 °C b) 1100 °C and 1120 c) 1200 °C d) 1300 °C e) 1400 °C f) 1450 °C and P = 1 atm. Experimental points from [15, 208-211, 213]. Solid lines – calculated.

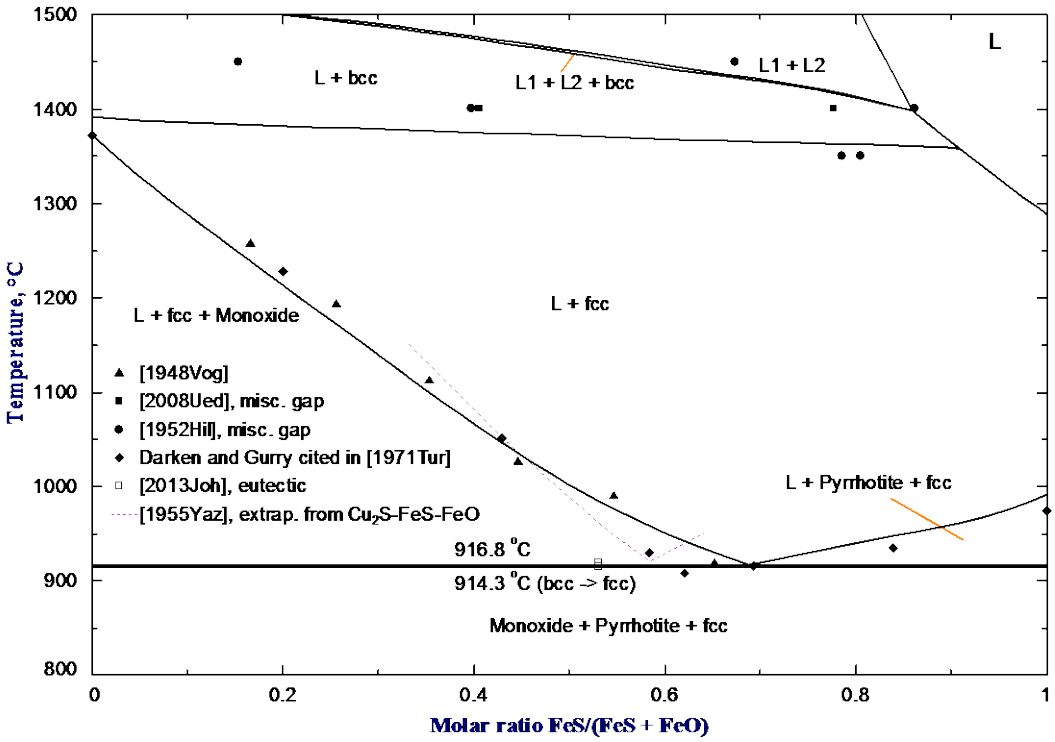

Figure 5.12. Projection of the Fe–S–O phase diagram in equilibrium with iron on the FeS–FeO section through the Fe corner. Experimental points from [100, 208, 209, 213, 214].

5.4.2 Solubility of oxygen and sulfur in matte

The solubility of oxygen and sulfur in the matte region was measured by Bog and Rosenqvist [211], Dewing and Richardson [215], Nagamori and Kameda [216], Kameda and Yazawa [217], Stofko and Schmiedl [218], Mintsis and Ryabko [219], Blatov and Burylev [220], Nagamori and Yazawa [221], Rose and Brenan [222], Fonseca and Campbell [223], Ueda and Yamaguchi [213] and Johto and Henao [214].

Bog and Rosenqvist [211] equilibrated the Fe–O–S melt with H_2 + H_2S + H_2O mixtures at 1120 °C. The crucible material and the analytical method were not reported. In their article authors presented the $P(H_2)/P(H_2S)$, $P(H_2)/P(H_2O)$ and the interpolated composition of melts. These data were used to plot iso-$P(S_2)$ and iso-$P(O_2)$ points in Figure 5.11 (b).

Dewing and Richardson [215] heated small samples of the condensed phase in a stream of N_2–S_2–SO_2. The melts were held in platinum spiral. After attaining the equilibrium, samples were quenched and analyzed by treatment in hydrogen. The resulting H_2S was absorbed by zinc acetate

solution. Residual metal was dissolved in acid giving the iron content. Insoluble platinum was weighted. It was found final samples contained up to 2 mole % of platinum sulfide at high $P(S_2)$. Thus, iron, sulfur and platinum were determined directly and oxygen by difference. Most data points were obtained at 1206 °C. Partial pressures of S_2 and SO_2 were given by the authors. Equilibrium $P(O_2)$ is calculated in this study. The data are plotted in Figure 5.14.

Nagamori and Kameda [216] equilibrated Fe–O–S melts with CO–CO_2–SO_2 mixtures at 1200 °C. Alumina crucibles were used for the fusion. The quenched samples were analyzed for iron content – by titration with $KMnO_4$, sulfur – by precipitation as $BaSO_4$, oxygen – by the hydrogen reduction method. No initial gas compositions were reported by the authors, only calculated $P(S_2)$ and $P(O_2)$. The results are presented in Figure 5.14.

Kameda and Yazawa [217] equilibrated Cu–Fe–O–S mattes with CO–CO_2–SO_2 mixtures at 1150-1225 °C. Alumina crucibles were used. The copper, iron and sulfur contents were determined analytically, oxygen content – by the hydrogen reduction method. Although 10 different CO/CO_2/SO_2 ratios were used, only the results for one gas composition were reported. Equilibrium $P(O_2)$ and $P(S_2)$ are calculated in this study. The copper-free point is plotted in Figure 5.14.

Stofko and Schmiedl [218] studied the equilibrium of Fe–S–O melts and N_2–S_2–SO_2 gas flow at 1200 °C. Alumina crucibles were used. The quenched samples were analyzed for iron content – by titration with $KMnO_4$, for sulfur – by precipitation as $BaSO_4$, and for oxygen – by the hydrogen reduction method. No initial gas compositions were reported by the authors, instead, the calculated $P(S_2)$ and $P(O_2)$ were given. The data are plotted in Figure 5.14.

Mintsis and Ryabko [219] equilibrated Fe–O–S melts and CO–CO_2–SO_2 gas mixtures at 1200 and 1300 °C. The quenched samples were analyzed for iron and sulfur content chemically. Oxygen was determined by difference in some samples and by an unspecified analytical method in controlled samples. The CO/CO_2/SO_2 ratios were reported and used in the present study to calculate $P(O_2)$ and $P(S_2)$. The results for 1200 °C are presented in Figure 5.14.

Nagamori and Yazawa [221] equilibrated Fe–O–S melt with CO–CO_2–SO_2 gas mixtures at 1200 °C in alumina crucibles. The melted samples were quenched and analyzed for oxygen, sulfur and iron. Sulfur and iron were determined gravimetrically; sulfur as $BaSO_4$ and iron as

Fe_2O_3. Oxygen was analyzed by the hydrogen reduction. The analytical results and compositions of ingoing $CO–CO_2–SO_2$ gas were reported. The data are given in Figure 5.14.

Fonseca and Campbell [223] equilibrated Fe–O–S melt with $CO–CO_2–SO_2$ gas mixtures at 1200-1400 °C in silica crucibles. Electron microprobe analysis (EMPA) was used to measure the compositions of the samples, even for oxygen. The $CO/CO_2/SO_2$ ratios were reported. Results for 1200 °C are presented in Figure 5.14.

Blatov and Burylev [220] and Rose and Brenan [222] equilibrated Fe–O–S melts with $CO–CO_2–SO_2$ gas mixtures at 1300 °C. The crucible material and the analytical method were not reported in the first paper. In the second work San Carlos olivine mega crystal was used as a crucible. EMPA was used for analysis of quenched samples. $CO/CO_2/SO_2$ ratios were reported in both studies.

From Figure 5.14 it is clear that there are some discrepancies between the results of different authors at 1200 °C. Nagamori and Kameda [216] suggest lower sulfur contents and higher oxygen contents at ambient $P(S_2)$ than Dewing and Richardson [215], Kameda and Yazawa [217] and even Stofko and Schmiedl [218]. On the sonstrast, Fonseca and Campbell [223] give higher sulfur contents and lower oxygen contents compared to the same authors. Stofko and Schmiedl [218] give the overlapping data at high $P(S_2)$, as well as Mintsis and Ryabko [219]. Data of Blatov and Burylev [220], Rose and Brenan [222], Mintsis and Ryabko [219] and Fonseca and Campbell [223] at 1300 °C (not shown) are very scattered.

The experimental results for the oxygen partial pressure over liquid saturated with solid iron [15, 211, 213, 214] are summarized in Figure 5.13. These data are much more reliable and consistent. It may be concluded that the techniques involving fixing $P(S_2)$ in the gaseous phase are not well established and reproducible, especially at high $P(S_2)$.

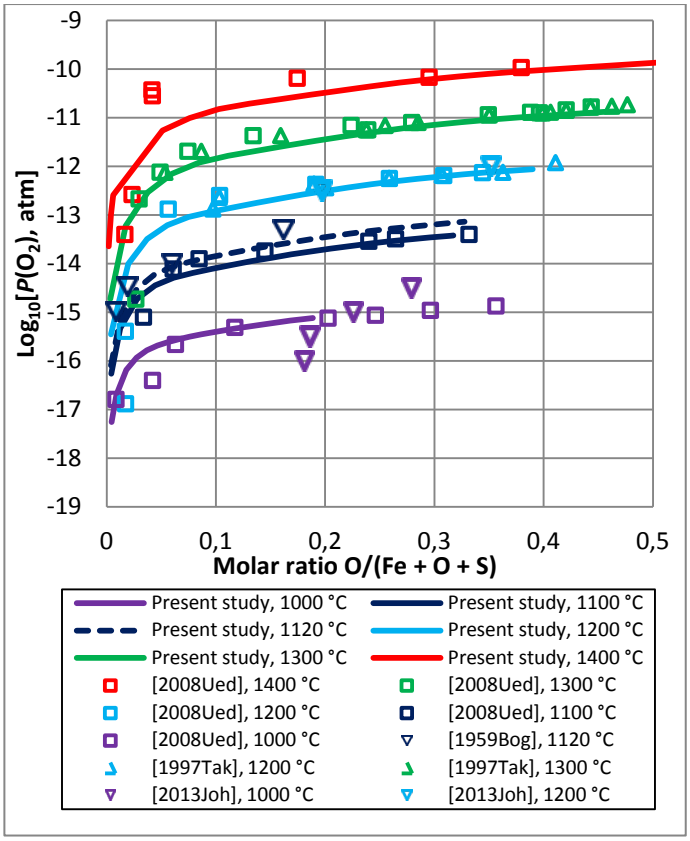

Figure 5.13. Partial pressure of oxygen along the matte-iron border in the Fe–O–S system. Experimental points: [15, 211, 213, 214].

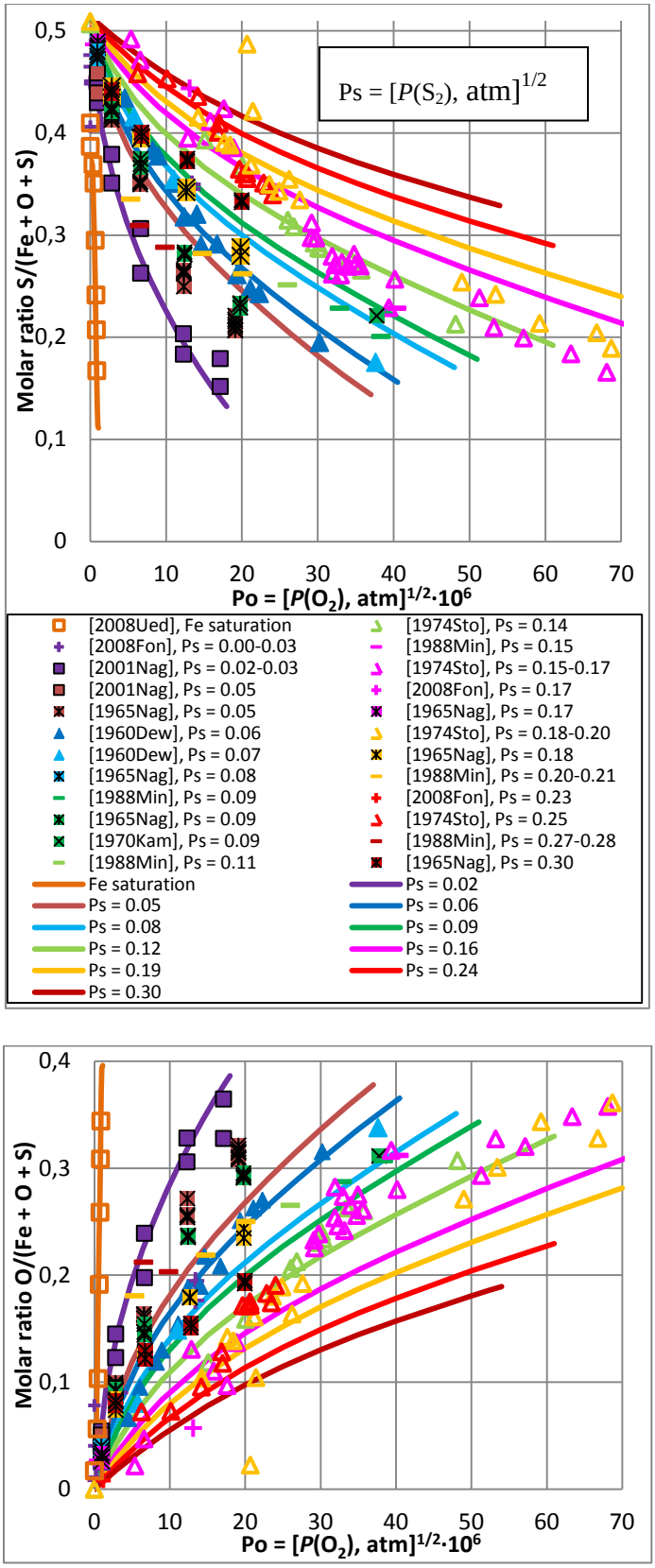

Figure 5.14. Solubility of oxygen and sulfur in Fe–O–S oxysulfide melt at 1200 °C.

5.4.3 Solubility of oxygen and sulfur in liquid iron

The solubility of oxygen and sulfur in the region of liquid iron was measured by Hilty and Crafts [208], Hayashi and Uno [27], Schenck and Hinze [224].

Hilty and Crafts [208] studied the equilibrium between Fe-rich liquid (liquid iron) and FeO-rich liquid (slag) in the Fe–S–O system using the rotating furnace at 1450-1650 °C. Samples were melted in magnesia crucibles under an Ar atmosphere. Slag was contaminated with MgO (up to 2.5 wt. %) and by SiO_2 (up to 4 wt. %), though this is much less than the equilibrium solubility of MgO and SiO_2 in slag under the conditions of the experiment. As a first approximation, the experiment of Hilty and Crafts [208] might be considered as the L1 + L2 equilibrium in the Fe–O–S system. Samples of liquid iron (L1) were analyzed. A variant of the vacuum-fusion method was used to determine O. Sulfur was measured gravimetrically. The experimental results are plotted in Figure 5.15.

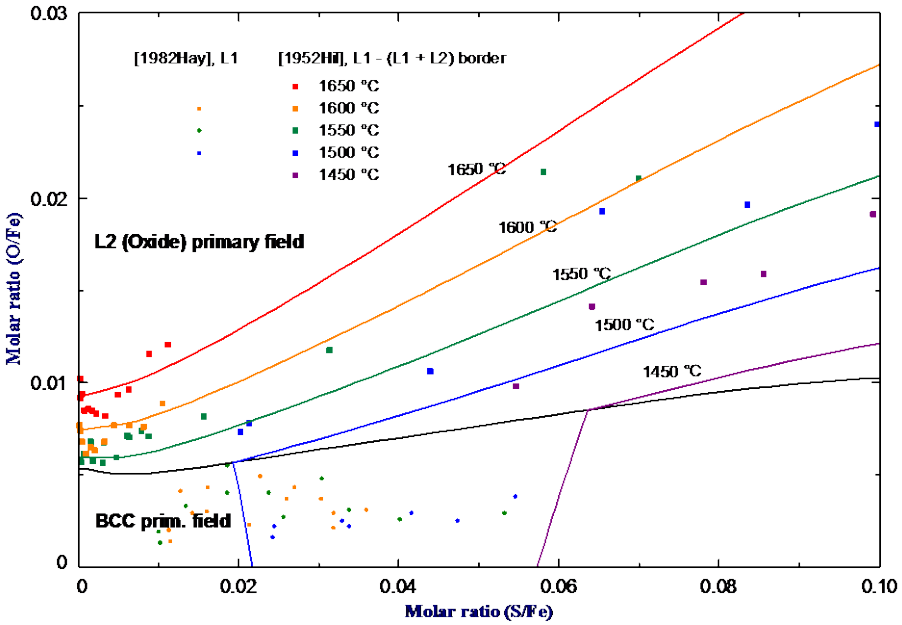

Figure 5.15. Liquidus projection of the Fe–S–O system near the Fe corner. Experimental points [208] and calculated lines.

Hayashi and Uno [27] equilibrated liquid iron with H_2S–H_2O–H_2–Ar mixtures at 1500-1600 °C in alumina crucibles. The equilibrium $P(O_2)$ and $P(S_2)$ were calculated from the gas compositions. The activity coefficient of oxygen according to (5.10) is plotted in Figure 5.16. The activity coefficient of sulfur was calculated in a similar way:

$$\ln \gamma_S = 0.5 \ln P(S_2) - \ln X_S \tag{5.19}$$

It is shown in Figure 5.17. The compositions, for which γ_O and γ_S were calculated, are shown in Figure 5.15.

Schenck and Hinze [224] equilibrated liquid iron with CO/CO_2 gas of known compositions in alumina crucibles at 1600 and 1650 °C. The quenched samples were analyzed for oxygen content by gas chromatography. The experiments were done using the sulfur-free samples, and then the effect of sulfur on the oxygen content was measured by addition of known amounts of FeS. As a result, the first-order interaction coefficient e_O^S was obtained:

$$\begin{aligned} e_O^S(T) &= \lim_{wt.\%Fe \to 100} \left[\frac{\partial \log_{10} f_O}{\partial wt.\%S} \right]; \; e_S^O(T) = \lim_{wt.\%Fe \to 100} \left[\frac{\partial \log_{10} f_S}{\partial wt.\%O} \right] \\ \varepsilon_O^S(T) &= \lim_{X_O \to 0} \left[\frac{\partial \ln \gamma_O}{\partial X_S} \right]; \; \varepsilon_S^O(T) = \lim_{X_O \to 0} \left[\frac{\partial \ln \gamma_S}{\partial X_O} \right] \end{aligned} \tag{5.20}$$

No direct experiments were conducted to study the effect of oxygen on the sulfur activity coefficient; however, the first-order interaction coefficient, e_S^O, was calculated from e_O^S using the following equations:

$$e_i^j = \frac{\log_{10} e}{100} \left[(\varepsilon_i^j - 1) \frac{A_r(\text{Fe})}{A_r(j)} + 1 \right]; \; \varepsilon_i^j = \varepsilon_j^i \tag{5.21}$$

where A_r is the atomic mass.

The values of e_S^O and e_O^S obtained by Schenck and Hinze [224] were adopted by the Steelmaking data sourcebook [199]. Dashed lines in Figure 5.16 and Figure 5.17 were calculated using e_S^O and e_O^S of Schenck and Hinze [224] assuming they were independent of temperature.

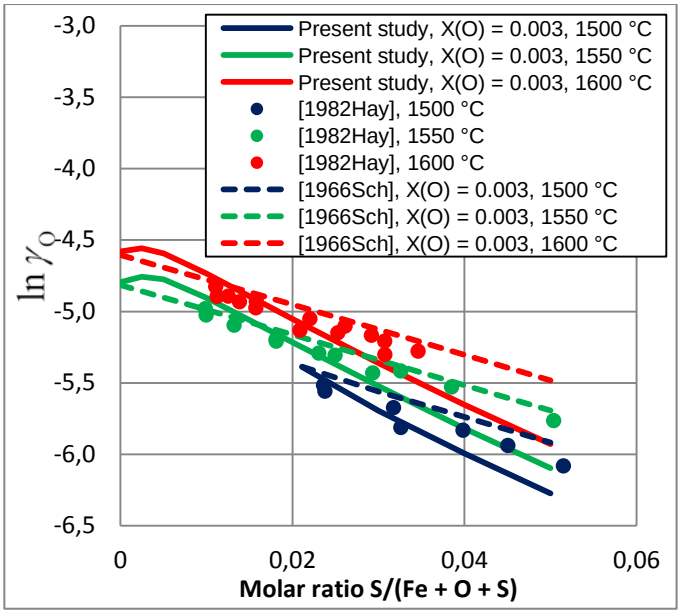

Figure 5.16. Effect of sulfur on the activity coefficient of oxygen in Fe–O–S metallic liquid: experimental points [27], dashed lines – calculated using parameters from [224], solid lines – calculated in this study.

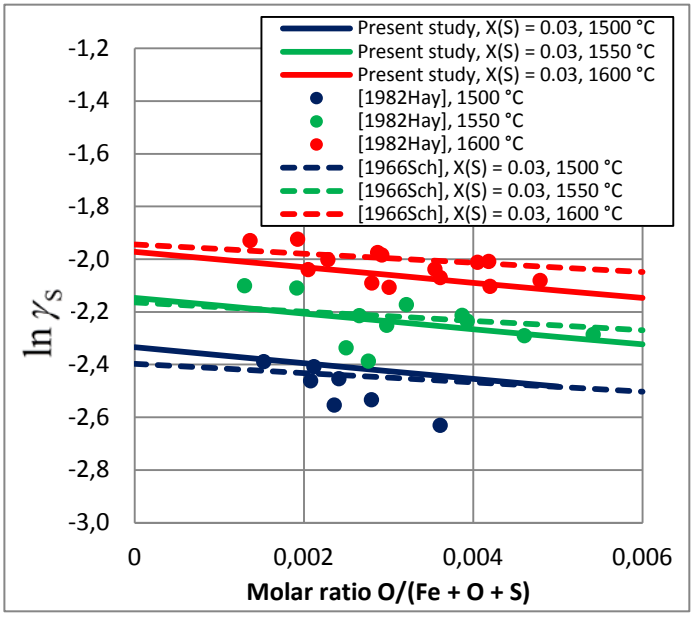

Figure 5.17. Effect of oxygen on the activity coefficient of sulfur in Fe–O–S metallic liquid: experimental points [27], dashed lines – calculated using parameters from [224], solid lines – calculated in this study.

5.4.4 Optimization

The database for the Fe–S system [26] was combined with the model parameters for the Fe–O system optimized in the present study to predict the thermodynamic properties and phase

equilibria in the Fe–O–S system. The thermodynamic properties of stoichiometric $FeSO_4$ and $Fe_2(SO_4)_3$ were taken from JANAF [169].

The phase relations in the Fe–O–S system predicted using only binary parameters for the liquid were qualitatively correct, but the agreement with the experimental data was not satisfactory quantitatively. Ternary parameters $g^{001}_{Fe^{II}S(O)}$ and $g^{002}_{Fe^{II}S(O)}$ were introduced to rise the monoxide liquidus and the eutectic temperature (Figure 5.12). One more ternary parameter $g^{101}_{Fe^{II}O(S)}$ and a polynomial Bragg-Williams parameter $q^{102}_{Fe^{II},S(O)}$ were required to suppress the early (low temperature) immiscibility between liquid FeS_{1-x} and FeO and increase the iron content in iron-saturated liquid (Figure 5.11). Another ternary parameter, $g^{002}_{Fe^{III}O(S)}$, was added to shift the $P(SO_2)$ = 1 atm phase border to higher S and O contents (Figure 5.11). The $\Delta g^{\circ}_{Fe^{II}S}$ parameter in the Fe–S system was adjusted to describe the data of Hayashi and Uno [27] in Figure 5.17. This did not impair the overall description of the experimental data in the Fe–S system. An additional parameter, $g^{15\ 01}_{Fe^{II}O(S)}$, was used to raise γ_O and γ_S in liquid iron (Figure 5.16, Figure 5.17). However, with increasing γ_O, the solubility of oxygen in liquid iron equilibrated with slag falls (Figure 5.15). When the data of Hayashi and Uno [27] and of Schenck and Hinze [224] are described there is a large disagreement with the solubility data of Hilty and Crafts [208], and also with the miscibility gap in Figure 5.11(e,f) as reported by Hilty and Crafts [208], Ueda *et al.* [213]. And vice versa, if the miscibility gap betwee liquid iron and liquid oxysulfide is described, the activity coefficient of oxygen in Figure 5.16 would fall dramatically. In order to completely reject of confirm any of these sets of data, more experimental studies are required in the liquid iron region of the Fe–O–S system. In this study, the final values of parameters were selected to attain a reasonable compromise between the data of Hayashi and Uno [27], Schenck and Hinze [224] on the one hand and Hilty and Crafts [208] on the other hand.

The thermodynamic properties of all stoichiometric compounds and the final values of model parameters are given in Table 5-2.

The resulting description of the available experimental data is shown by the calculated lines in Figure 5.10-Figure 5.17. In most cases the agreement is within the experimental error limits. However, the shape of the miscibility gap L1 + L2 beyond 1350 °C (Figure 5.11 e, f and Figure

5.15) is somewhat different from the data of Hilty and Crafts [208] and Ueda *et al.* [213]. The propagation of the calculated miscibility gap with increasing temperature falls behind the experimental one. The calculated L1 + L2 + bcc triangle at 1470 °C is closer to the experimental triangle at 1400 °C, and at 1505 °C – to the experimental triangle at 1450 °C.

From the optimized data on the solubility of oxygen and sulfur at fixed $P(O_2)$ and $P(S_2)$ (Figure 5.14), oxygen and sulfur isobars over matte may be back-calculated. These isobars are of great importance for the copper industry. Results at 1200 and 1300 °C are presented in Figure 5.11 c, d.

Table 5-1. Calculated invariant points in the Fe–O–S system.

	T, °C	Fe	O	S	$\log_{10}[P(O_2)$, atm]	$\log_{10}[P(S_2)$, atm]	$\log_{10}[P(SO_2)$, atm]
Pyrrhotite + Monoxide + fcc + L	916.8	0.50376	0.34087	0.15537	-16.49	-7.62	-8.24
Pyrrhotite + Monoxide + Spinel + L	939.8	0.49145	0.31262	0.19593	-13.90	-5.02	-4.64
$FeSO_4$ + Pyrrhotite + Spinel	999.2	0.41288	0.14206	0.44507	-7.66	1.84	4.31

5.5 Summary of results

A complete critical evaluation and optimization of the Fe–O and Fe–O–S systems have been performed. A model for the liquid phase has been developed within the framework of the quasichemical formalism. This model describes simultaneously metallic liquid, sulfide liquid (matte) and oxide liquid (slag). For the Fe–O system, the model reflects the existence of two ranges of maximum short-range ordering at approximately the FeO and Fe_2O_3 compositions. All available thermodynamic and phase equilibrium data have been critically evaluated to obtain one set of optimized model parameters for the Gibbs energies of all phases that can reproduce most experimental data within experimental error limits. The Fe–S–O miscibility gap between metallic and oxysulfide phases at high temperatures is described semi-quantitatively.

The present study continues the development of a thermodynamic database for the simulation of copper smelting and converting. In particular, the model developed for the liquid phase and the optimized model parameters can be used to provide a description of the solubility of oxygen in matte and liquid copper. Additional major components such as Cu, Si and Ca are being added to the database as well as Al, Mg and other minor components.

Table 5-2. Optimized properties of stoichiometric compounds and model parameters for liquid and solid solutions in the Fe–O–S system (J·mol^{-1} and J mol^{-1}·K^{-1})

Compounds	**Temperature range (K) or reference**	$\Delta H^{o}_{298.15}$	$S^{o}_{298.15}$	$C_P(T)$
Fe_2O_3 (hematite)	298 – 2500 [21]	-825787.0	87.7285	$137.0089 - 2907640T^{-2}$
	>2500			136.5437
Magnetic properties	T_{Neel} = 955.67 K			Magnetic moment = 8.37 Structure-dependent parameter P = 0.28
S	[114]			
FeS (troilite), FeS_2(pyrite), 'Fe_7S_8' (monoclinic pyrrhotite), Fe_9S_{10}, $Fe_{10}S_{11}$, $Fe_{11}S_{12}$	[26]			
$FeSO_4$	298 − 800	-928848.0	120.9570	$192.5487 + 0.023205T - 2.1757\times10^{-5}T^2 + 4436931T^{-2} - 43771.41T^{-1}$
	800 – 2000			$150.7843 + 0.011427T - 6732240T^{-2}$
	>2000			171.9552
$Fe_2(SO_4)_3$	298 − 800	-2582992.0	307.5240	$502.1294 + 0.067233T - 6.0172\times10^{-5}T^2 + 11507266T^{-2} - 113714.98T^{-1}$
	800 – 2000			$346.0460 + 0.034563T - 9573125T^{-2} - 61977.26T^{-1} + 3167.13425T^{-0.5}$
	>2000			452.6104

Table 5-2. (Continued) Optimized properties of stoichiometric compounds and model parameters for liquid and solid solutions in the Fe–O–S system (J·mol^{-1} and J mol^{-1}·K^{-1})

Solutions	Temperature range (K) or reference	Molar Gibbs energy g (T)
Liquid (Metal, Oxide, Sulfide)	Modified Quasichemical Model (Fe^{II}, Fe^{III}, O, S), Grouping: Fe^{II}, Fe^{III} in group 1; O, S in group 2	
$Z^{Fe^{II}}_{Fe^{II}Fe^{II}} = Z^{Fe^{III}}_{Fe^{III}Fe^{III}} = Z^{S}_{SS} = Z^{O}_{OO} = Z^{Fe^{II}}_{Fe^{II}Fe^{III}} = Z^{Fe^{III}}_{Fe^{III}Fe^{II}} = Z^{O}_{OS} = Z^{S}_{SO} = 6$, $Z^{Fe^{II}}_{Fe^{II}S} = Z^{S}_{SFe^{II}} = 2$, $Z^{Fe^{II}}_{Fe^{II}O} = 2.05$, $Z^{O}_{OFe^{II}} = 2$, $Z^{S}_{SFe^{III}} = 3$, $Z^{Fe^{III}}_{Fe^{III}S} = 2$, $Z^{O}_{OFe^{III}} = 3$, $Z^{Fe^{III}}_{Fe^{III}O} = 2$		
g°_{O}	[114]	
$g^{\circ}_{Fe^{II}}$	298 − 1811 [145]	$13265.9 + 117.5756T - 23.5143T\ln T - 0.00439752T^{2} - 5.89269\times10^{-8}T^{3} + 77358.5T^{-1} - 3.6751551\times10^{-21}T^{7}$
	1811 – 6000 [145]	$-10838.8 + 291.3020T - 46.0000T\ln T$
$g^{\circ}_{Fe^{III}}$	298 − 3500	$g^{\circ}_{Fe^{II}} + 6276.0$
g°_{S}	[114]	
$\Delta g^{\circ}_{Fe^{II}S}$		$-104888.10 + 0.3388T$ [26] $-122334.14 + 112.4659T - 13.7582T\ln T$ (This study)
$g^{01}_{Fe^{II}S}$, $g^{02}_{Fe^{II}S}$, $g^{03}_{Fe^{II}S}$, $g^{10}_{Fe^{II}S}$, $g^{20}_{Fe^{II}S}$, $g^{40}_{Fe^{II}S}$	[26]	
$\Delta g^{\circ}_{Fe^{II}O}$		-394258.32
$g^{10}_{Fe^{II}O}$		$126746.40 - 27.5966T$
$\Delta g^{\circ}_{Fe^{III}O}$		$-398819.24 - 14.4744T$
$g^{20}_{Fe^{III}O}$		125520.00
$q^{001}_{Fe^{II},Fe^{III}(O)}$	(Bragg-Williams)	-25104.00
$\Delta g^{\circ}_{Fe^{II}Fe^{III}}$		83680.00

Table 5-2. (Continued) Optimized properties of stoichiometric compounds and model parameters for liquid and solid solutions in the Fe–O–S system (J·mol^{-1} and J mol^{-1}·K^{-1})

Solutions	Temperature range (K) or reference	Molar Gibbs energy g (T)
$q^{102}_{S,\,O,(Fe^{II})}$	(Bragg-Williams)	$433951.27 - 322.9754T$
$g^{001}_{Fe^{II}S(O)}$		$32617.03 - 25.69122T$
$g^{002}_{Fe^{II}S(O)}$		5020.80
$g^{101}_{Fe^{II}O(S)}$		-25104.00
$g^{15\ 01}_{Fe^{II}O(S)}$		42676.80
$g^{002}_{Fe^{III}O(S)}$		-21756.80
fcc (Solid Fe)	Bragg-Williams (Fe, O, S)	
g°_{Fe}	298 – 1811 [145]	$-236.5 + 132.4156T - 24.6643T\ln T - 0.003758T^{2} + 77359.0T^{-1} - 5.8927\times10^{-8}T^{3}$
	1811 – 6000 [145]	$-27097.2 + 300.2521T - 46.0000T\ln T - 2.78854\times10^{31}T^{-9}$
g°_{S}	[114]	
g°_{O}	[114]	
$L_{Fe,S}$		$-59070.74 - 34.61218T$
$L_{Fe,O}$		$-312818.28 - 24.94644T$
Magnetic properties of Fe	[225]	T_{Neel} = 67 K Magnetic moment β =0.70 Structure-dependent parameter P = 0.28
bcc (Solid Fe)	Bragg-Williams (Fe, O, S)	

Table 5-2. (Continued) Optimized properties of stoichiometric compounds and model parameters for liquid and solid solutions in the Fe–O–S system (J·mol^{-1} and J mol^{-1}·K^{-1})

Solutions	Temperature range (K) or reference	Molar Gibbs energy g (T)
g°_{Fe}	298 − 1811	$10375.2 + 114.5502T - 23.5143T\ln T - 0.004398T^2 + 77359.0T^{-1} - 5.8927\times10^{-8}T^3$
g°_{S}	298 – 368.3	$19725.8 + 41.0945T - 11.0070T\ln T - 0.026529T^2 + 7.754333\times10^{-6}T^3$
	368.3 – 1300	$18441.0 + 80.3697T - 17.9418T\ln T - 0.010895T^2 + 1.402558\times10^{-6}T^3 + 39910T^{-1}$
g°_{O}	Same as in fcc	
$L_{Fe,S}$		$-29973.6 - 11.74268T$
$L_{Fe,O}$		$-312048.67 - 17.59327T$
Magnetic properties of Fe	[225]	T_{Curie} = 1043 K, Magnetic moment β =2.22, Structure-dependent parameter P = 0.40
Pyrrhotite ("$Fe_{1-x}S$")	[26]	
Monoxide (wüstite, "$Fe_{1-x}O$")		
g^{o}_{FeO}	298 − 2500	$-321553.4 - 330.6874T + 18.02447T\ln T - 0.015304T^2 + 1266650.0T^{-1} + 6003.6T^{0.5}$
	2500− 9000	$-340131.9 + 589.1465T - 88.108328T\ln T$
$g^{o}_{FeO_{1.5}}$	298 − 2500	$-414328.5 + 455.5081T - 73.4292T\ln T + 1394195.5T^{-1} - 43802324T^{-2}$
	2500− 9000	$-412160.9 + 451.5024T - 73.0000T\ln T$
$q^{00}_{FeO,\ FeO_{1.5}}$		$-8276.0 - 11.57294T$
$q^{01}_{FeO,\ FeO_{1.5}}$		-49145.3
Spinel (magnetite, Fe_3O_4)	[21]	

The Gibbs energy of formation of a compound from elements in their standard state at a temperature of T (K) and a pressure of 1 atm is given by $\Delta G = \Delta H^{o}_{298.15} - T S^{o}_{298.15} + \int_{298.15}^{T} C_P(T)dT - T\int_{298.15}^{T} \frac{C_P(T)}{T}dT$, where $\Delta H^{o}_{298.15}$ is the enthalpy of formation of the compound at 1 atm and 298.15 K, $S^{o}_{298.15}$ is the entropy of the compound at 1 atm and 298.15 K, and $C_P(T)$ is the heat capacity at constant pressure.

CHAPTER 6 ARTICLE 2: CRITICAL ASSESSMENT AND THERMODYNAMIC MODELING OF THE Cu–Fe–O SYSTEM

Sourced from published article: D. Shishin et al [172]

Equation Chapter (Next) Section 1Critical evaluation, thermodynamic modeling and optimization of the Cu–Fe–O system are presented. The model for the liquid phase is developed within the framework of the Quasichemical Formalism. It describes liquid over the whole composition range from metal alloy to oxide melt. The model for spinel is developed within the framework of the Compound Energy Formalism. The spinel solution expands from magnetite, Fe_3O_4, to cupric ferrite, $CuFe_2O_4$. A small solubility of copper in wüstite is described by a simple Bragg-Williams model. Parameters of thermodynamic models have been optimized to reproduce all available thermodynamic and phase equilibrium data within experimental error limits. The thermodynamic optimization of the Cu–Fe–O system performed in the present study lays the groundwork for modeling the solubility of oxygen in sulfide liquid (matte) and in liquid metal alloys, which is of particular importance for simulation of copper smelting and converting.

6.1 Introduction

The present study is part of an ongoing research project which is aimed at developing a thermodynamic database for simulation of copper extraction from sulfide concentrates. The major phases that form during copper smelting and converting are: blister copper (a liquid metal phase rich in Cu), matte (a molten sulfide phase containing mainly Cu, S and Fe), slag (a molten oxide phase) and gas. In principle, all three liquid phases represent just one liquid with miscibility gaps. Liquid metal, matte and slag can be completely miscible over certain ranges of temperature and composition, even though this normally does not happen under industrial conditions. It is desirable to have one general thermodynamic model which can describe all three liquid phases simultaneously, but this is very difficult to achieve because the model must reflect quite different atomic interactions that are intrinsic to metallic, sulfide and oxide phases. Thermodynamic properties of the liquid phase containing at least four major components, Cu, Fe, S and O, are needed to calculate the solubility of oxygen in matte and liquid metal.

The spinel phase is also important for copper industry. It was shown [226] that under certain conditions spinel could precipitate from liquid slag, causing not only copper losses, but even an

occlusion of the reactor. On the other hand, spinel-based materials are used as refractories in reactors. Hence, it is necessary for metallurgists to be able to predict the stability range and the composition of the spinel phase. The Cu–Fe–O system contains the Fe_3O_4–$CuFe_2O_4$ spinel solution which is essential for the addition of copper to the multicomponent FactSage spinel database [4].

A thermodynamic "optimization" of the Cu–Fe–O system is reported in the present study. In a thermodynamic "optimization" of a system using the CALPHAD approach, all available thermodynamic and phase diagram data are evaluated simultaneously in order to obtain one set of model equations for the Gibbs energies of all phases as functions of temperature and composition. From these equations, all of the thermodynamic properties and the phase diagrams can be back-calculated. In this way, all the data are rendered self-consistent and consistent with thermodynamic principles. Thermodynamic property data, such as activity data, can aid in the evaluation of the phase diagram, and phase diagram measurements can be used to deduce thermodynamic properties. Discrepancies in the available data can often be resolved, and interpolations and extrapolations can be made in a thermodynamically correct manner. A small set of model parameters is obtained. This is ideal for computer storage and calculation of properties and phase diagrams. In the present study, all calculations were carried out using the FactSage thermochemical software and databases [4]. The Cu–O–S and Fe–O–S systems were optimized earlier [114, 227].

An optimization of the Cu–Fe–O system was recently reported by Khvan et *al.* [177]. Their calculated phase diagrams are compared with the results of the present study in Sections 6.4.2 and 6.4.4.

6.2 Binary systems

The optimization of the Cu–Fe system by Ansara and Jansson [225] was accepted in the present study. The calculated phase diagram is shown in Figure 6.1 and compared with another assessment by Swartzendruber [228].

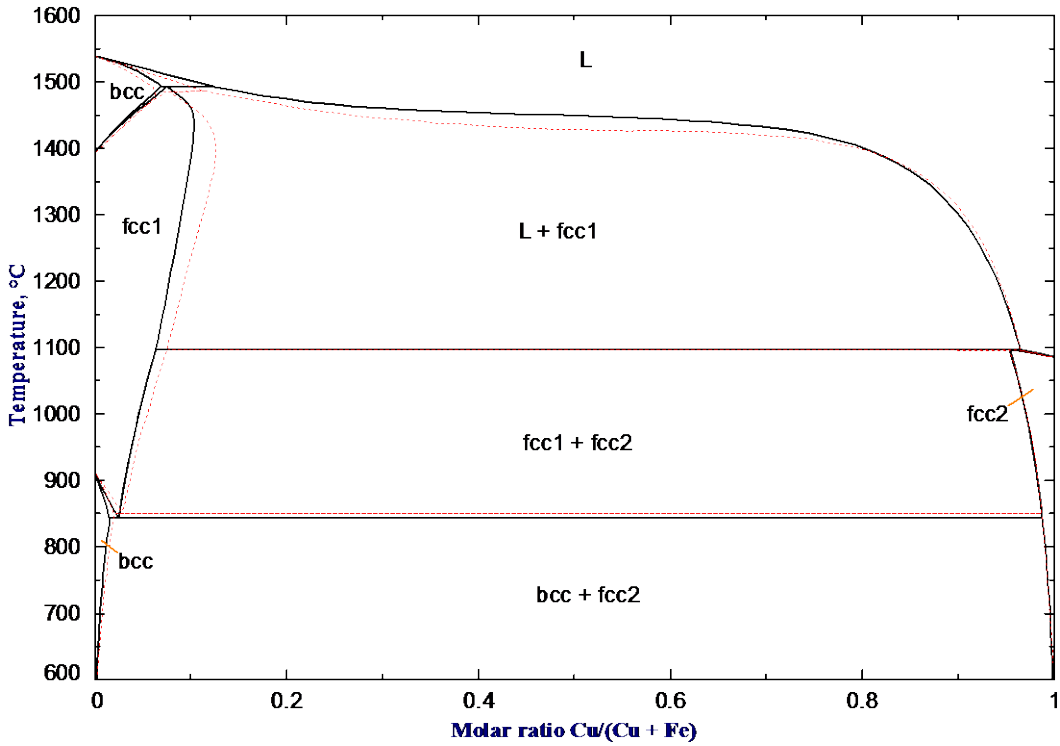

Figure 6.1. Phase diagram of the Cu–Fe system. Solid and dashed lines are calculated based on the optimizations of Ansara and Jansson [225] and of Swartzendruber [228], respectively.

The Cu–O and Fe–O systems have been optimized earlier [114, 227]. The liquid phase was modeled as a single solution expanding from pure metals to oxide melts. The evaluated phase diagrams are shown in Figure 6.2 and Figure 6.3.

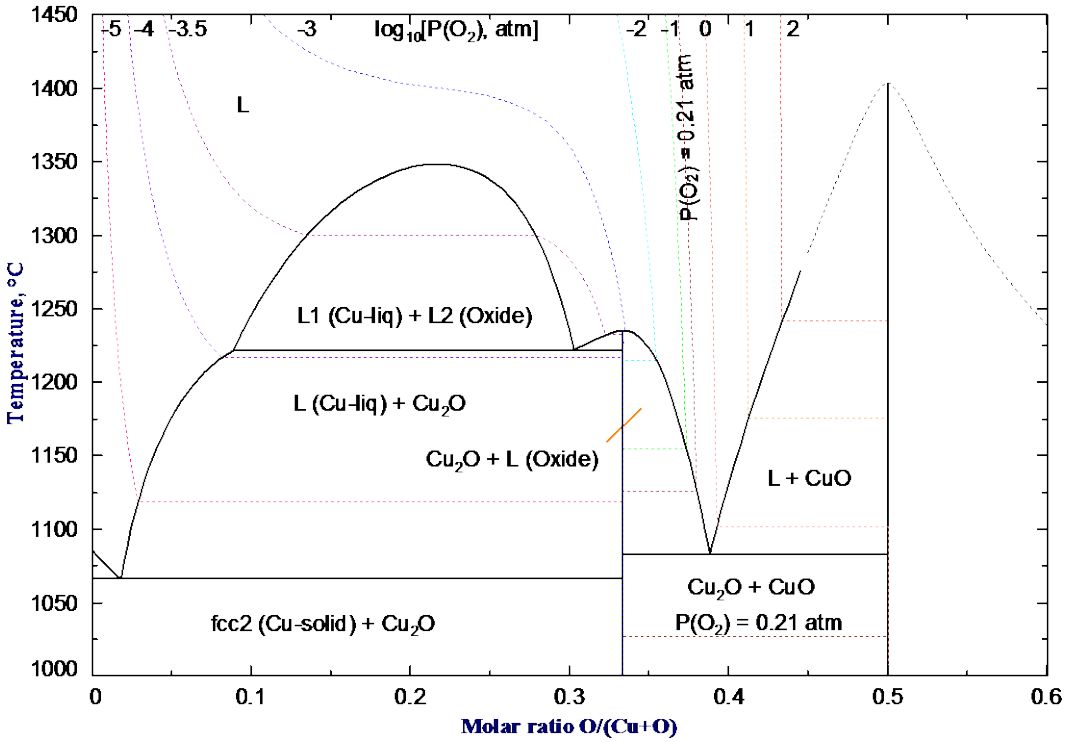

Figure 6.2. Calculated phase diagram of the Cu–O system [114]. Oxygen isobars are shown by the short-dashed lines.

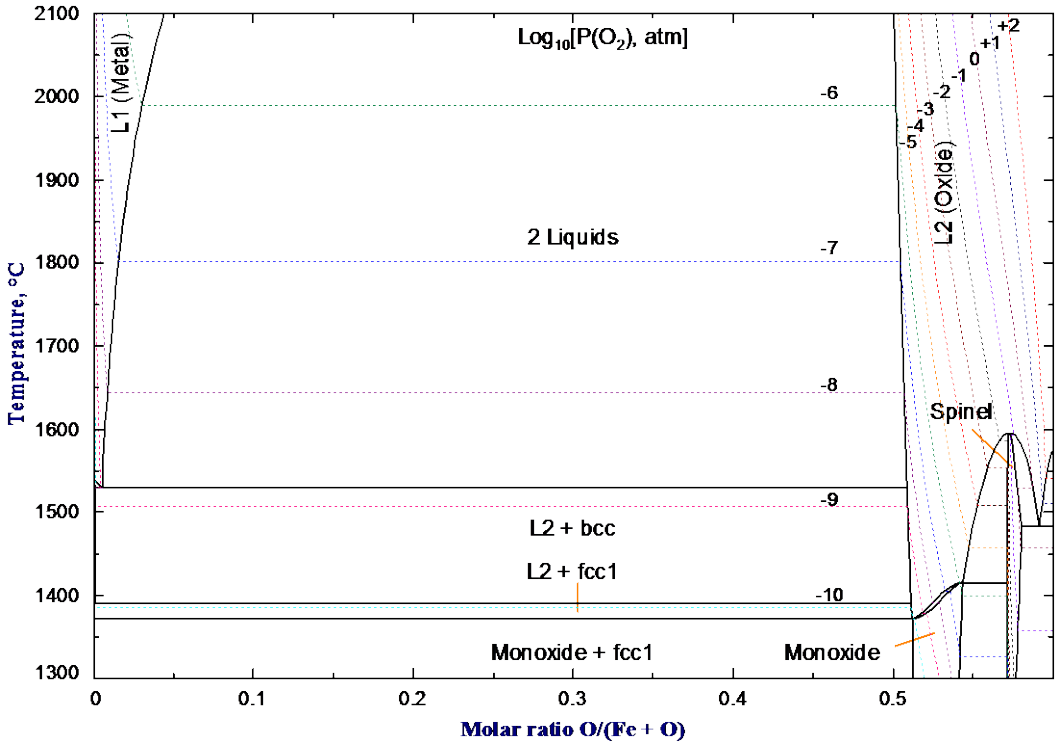

Figure 6.3. Calculated phase diagram of the Fe–O system [227]. Oxygen isobars are shown by the short-dashed lines.

6.3 Thermodynamic models

There are five stable solution phases in the Cu–Fe–O system: liquid, cubic spinel, monoxide (wüstite), fcc and bcc alloys. The homogeneity ranges of CuO, Cu_2O, Fe_2O_3 and $CuFeO_2$ (cuprous ferrite, delafossite) are negligible, so these phases were considered to be stoichiometric compounds. The $CuFe_2O_4$-rich cubic spinel phase is metastable with respect to decomposition to $CuO+Fe_2O_3+CuFeO_2$ below about 544 °C. However, it can be quenched to lower temperatures due to slow cation diffusion in the solid state. Even though the cubic phase can remain metastable at very low temperatures, it can also transform to the tetragonal structure below about 410 °C [229, 230]. Since the tetragonal spinel is most likely metastable at all temperatures, it was not modeled in the present study.

6.3.1 fcc and bcc

As can be seen from Figure 6.1, both iron and copper can exist as an fcc phase. Even though the structure is the same, Fe and Cu are only partially miscible in each other. Oxygen is also soluble in the fcc phase. The Bragg-Williams model that assumes random mixing of atoms was used for this solid solution. The Gibbs energy per mole of atoms is given by

$$g = (X_{\mathrm{Cu}} g^{\circ}_{\mathrm{Cu}} + X_{\mathrm{Fe}} g^{\circ}_{\mathrm{Fe}} + X_{\mathrm{O}} g^{\circ}_{\mathrm{O}}) + RT(X_{\mathrm{Cu}} \ln X_{\mathrm{Cu}} + X_{\mathrm{Fe}} \ln X_{\mathrm{Fe}} + X_{\mathrm{O}} \ln X_{\mathrm{O}}) + X_{\mathrm{Cu}} X_{\mathrm{Fe}} L_{\mathrm{Cu,Fe}} + X_{\mathrm{Cu}} X_{\mathrm{O}} L_{\mathrm{Cu,O}} + X_{\mathrm{Fe}} X_{\mathrm{O}} L_{\mathrm{Fe,O}} \quad (6.1)$$

where g°_{M} is the Gibbs energy of pure component *M* and X_M is the mole fraction. The interaction energy $L_{M,N}$ between components *M* and *N* is expanded as a Redlich-Kister polynomial:

$$L_{M,N} = \sum_{i \geq 0} L^{i}_{M,N} (X_N - X_M)^i \quad (6.2)$$

where $L^{i}_{M,N}$ are the binary model parameters that can be temperature-dependent. The binary terms are extrapolated into the ternary system using the Toop method [9] with O as an asymmetric component. The model for the bcc phase is the same. No ternary terms were used for the fcc and bcc phases in the present study.

6.3.2 Liquid solution

In the recent assessment of Khvan et *al.* [177], the two-sublattice model for ionic liquids was used:

$$(Fe^{+2},Cu^{+1},Cu^{+2})_P(O^{-2},Va^{-Q}, FeO_{1.5})_Q \quad (6.3)$$

In addition to the model parameters for the binary Cu–O and Fe–O systems, six more adjustable parameters were introduced.

In the present study, the model for the liquid phase was developed within the framework of the Quasichemical Formalism [16, 17, 114, 227]. The Cu–O, Fe–O and Cu–Fe liquid solutions were joined together in the present study, resulting in the model (Cu^{I}, Cu^{II}, Fe^{II}, Fe^{III}, O), where Fe^{II}, Fe^{III}, Cu^{I} and Cu^{II} correspond to different oxidation states of iron and copper. All species are placed on one sublattice and are not charged, so the condition of electroneutrality is not imposed. Hence, the model describes the liquid phase from metals to nonmetals. The metal-oxygen nearest-neighbor pairs are energetically more favorable than the metal-metal and oxygen-oxygen pairs. This results in strong first-nearest-neighbor short-range ordering, which is explicitly taken into account by the model.

In the Fe–O system, the fraction of the Fe^{II}–O pairs goes through a maximum close to the FeO composition, while the Fe^{III}–O pairs are most abundant at the Fe_2O_3 composition. In the Cu–O system, the Cu^{I}–O pairs prevail at the Cu_2O composition, and Cu^{II}–O pairs dominate at the composition of CuO. In the metallic liquid, the concentration of Fe^{III} and Cu^{II} is negligible.

In the ternary Cu–Fe–O liquid phase, the amounts of Cu and Fe species in different oxidation states depend on the partial pressure of oxygen. There are 15 possible pairs formed by the species Cu^{I}, Cu^{II}, Fe^{II}, Fe^{III} and O. The fractions of all pairs are calculated by the Gibbs energy minimization procedure built into the FactSage software [4], using the optimized model parameters. Cu^{I}–Cu^{I}, Fe^{II}–Fe^{II} and O–O are predominant pairs at compositions close to pure Cu, Fe and O, respectively. The Cu^{I}–Fe^{II} pairs form in the metallic liquid. The Cu^{I}–O, Cu^{II}–O, Fe^{II}–O and Fe^{III}–O pairs are dominant in the oxide liquid, whereas the fractions of the Cu^{I}–Cu^{II}, Cu^{II}–Cu^{II}, Fe^{II}–Fe^{III}, Fe^{III}–Fe^{III}, Cu^{I}–Fe^{III}, Cu^{II}–Fe^{II}, and Cu^{II}–Fe^{III} pairs are small at all compositions of interest.

The formulae and notations of the Quasichemical Formalism were described in detail elsewhere [16, 17, 114, 227]. The flexibility of the Quasichemical Formalism makes it possible to combine the

quasichemical description of the Cu–O and Fe–O systems, which exhibit strong short-range ordering, with the simple Bragg-Williams approximation based on the assumption of random mixing that was used to optimize the Cu–Fe system. The Gibbs energy expression for the Cu–Fe liquid is the same as for the Cu–Fe fcc phase discussed in Section 6.3.1.

Extrapolation of binary terms into the Cu^{I}–Cu^{II}–Fe^{II}–Fe^{III}–O system is done by a grouping method [9, 17]. The components are divided into two groups: metals (Cu^{I}, Cu^{II}, Fe^{II} and Fe^{III}) and nonmetal (O). In every ternary subsystem, either all three components belong to the first group or one of the components is oxygen and belongs to the second group. The "Kohler-like" symmetric extrapolation is applied in the first case, while the "Toop-like" asymmetric extrapolation is used in the second case, where oxygen is an asymmetric component. Except for the binary terms, the model can have ternary terms, $\Delta g_{\mathrm{AB(C)}}$, which give the effect of the presence of component C upon the energy Δg_{AB} of the pair exchange reaction (A–A) + (B–B) = 2(A–B). The ternary terms are also expanded as empirical polynomials containing model parameters $g^{ijk}_{\mathrm{AB(C)}}$. The formulae for the ternary terms and the extrapolation of binary and ternary terms into a multicomponent system are discussed elsewhere [17].

6.3.3 Monoxide

A small solubility of CuO in wüstite was reported by Katkov and Lykasov [231]. This solid solution was modeled as a simple random mixture of Fe^{2+}, Fe^{3+} and Cu^{2+} ions on cation sites with simple polynomial excess Gibbs energy terms. It is assumed that cation vacancies remain associated with Fe^{3+} ions to comply with the local charge balance condition and so do not contribute to the configurational entropy. The Gibbs energy per mole of components FeO, $FeO_{1.5}$ and CuO is given by

$$\begin{aligned} g = {} & (X_{\mathrm{FeO}} g^{\mathrm{o}}_{\mathrm{FeO}} + X_{\mathrm{FeO_{1.5}}} g^{\mathrm{o}}_{\mathrm{FeO_{1.5}}} + X_{\mathrm{CuO}} g^{\mathrm{o}}_{\mathrm{CuO}}) \\ & + RT(X_{\mathrm{FeO}} \ln X_{\mathrm{FeO}} + X_{\mathrm{FeO_{1.5}}} \ln X_{\mathrm{FeO_{1.5}}} + X_{\mathrm{CuO}} \ln X_{\mathrm{CuO}}) \\ & + X_{\mathrm{FeO}} X_{\mathrm{FeO_{1.5}}} L_{\mathrm{FeO,FeO_{1.5}}} + X_{\mathrm{CuO}} X_{\mathrm{FeO_{1.5}}} L_{\mathrm{CuO,FeO_{1.5}}} + X_{\mathrm{CuO}} X_{\mathrm{FeO}} L_{\mathrm{CuO,FeO}} \end{aligned} \qquad (6.4)$$

where g^{o}_{M} is the Gibbs energy of pure component *M* and X_M is the mole fraction. The interaction energy $L_{M,N}$ between components *M* and *N* is expanded as a polynomial in the mole fractions of the components:

$$L_{M,N} = \sum_{i,j\geq 0} q^{ij}_{M,N} X^{i}_{M} X^{j}_{N} \quad (6.5)$$

where $q^{ij}_{M,N}$ are the binary model parameters. No ternary terms were used for monoxide in the present study. The binary terms are extrapolated into the ternary system using the Toop method [9] with $FeO_{1.5}$ as an asymmetric component.

The solubility of copper in monoxide was not modeled in the study of Khvan et *al.* [177]. In the Fe–O subsystem, Fe^{3+} cations in combination with vacancies were used to describe the excess of oxygen in wüstite, FeO_{1+x}, compared to the FeO stoichiometry. The formula unit of the solution can be represented as

$$(Fe^{+2},Fe^{+3}, Va)_1(O^{-2})_1 \quad (6.6)$$

and it was assumed that cations and vacancies mix randomly on cation sites.

6.3.4 Spinel

The solid solution between magnetite, Fe_3O_4, and cupric ferrite, $CuFe_2O_4$, has a cubic spinel structure, Pearson symbol *cF56*, space group $Fd\bar{3}m$, prototype $MgAl_2O_4$ [232]. The structure of spinel may be derived from the fcc close packing of oxygen anions. Cations occupy half of the octahedral interstices and one-eighth of the tetrahedral interstices [21]. It is a common practice to distinguish tetrahedral and octahedral sublattices and represent spinels as $(A, B, \ldots)^{tetr}[A, B, \ldots]^{oct}{}_2O_4$, where A, B, etc. are cations with charges +2 and +3, rarely +4 or +1. Oxygen has charge -2. The condition of electroneutrality must be always obeyed.

The model for spinel was developed within the framework of the Compound Energy Formalism (CEF). The Gibbs-energy expression in the CEF per formula unit is [22, 23]:

$$G_m = \sum_i \sum_j Y_i' Y_j'' G_{ij} - TS_c + G_m^E \quad (6.7)$$

where Y_i' and Y_j'' represent the site fractions of constituents *i* and *j* on the first and second sublattices, respectively, G_{ij} is the Gibbs energy of a pseudocomponent $(i)[\ j\ ]_2O_4$, S_c is the configurational entropy,

$$S_c = -R\left(\sum_i Y_i' \ln Y_i' + 2\sum_j Y_j'' \ln Y_j'' \right) \quad (6.8)$$

and G_m^E is the excess Gibbs energy,

$$G_m^E = \sum_i \sum_j \sum_k Y_i' Y_j' Y_k'' L_{ij:k} + \sum_i \sum_j \sum_k Y_k' Y_i'' Y_j'' L_{k:ij} \quad (6.9)$$

$L_{ij:k}$ and $L_{k:ij}$ are the interaction energies between cations *i* and *j* on one sublattice when the other sublattice is occupied only by *k*.

In $CuFe_2O_4$, copper and iron are present on both tetrahedral and octahedral sublattices. The actual cation occupancies are intermediate between the so called "normal" and "inverse" spinels. If copper resides only on the tetrahedral sites, the spinel is called normal: $(Cu^{+2})^{tetr}[Fe^{+3}]_2^{oct}O_4^{-2}$. If all Cu^{+2} cations occupy the octahedral sites, the spinel is called inverse: $(Fe^{+3})^{tetr}[Cu_{0.5}^{+2}, Fe_{0.5}^{+3}]_2^{oct}O_4^{-2}$. For intermediate cases, the cation distribution can be expressed as $(Cu_{1-s}^{+2},Fe_s^{+3})^{tetr}[Cu_{s/2}^{+2},Fe_{1-s/2}^{+3}]_2^{oct}O_4^{-2}$, where *s* is the degree of inversion, $0 \le s \le 1$. $CuFe_2O_4$ tends to be predominantly inverse at low temperatures, that is $s \to 1$. It experiences randomization with increasing temperature due to the entropic effect. The configurational entropy is maximized at random distribution, which corresponds to *s* = 2/3.

The cation distribution in $CuFe_2O_4$ was experimentally obtained by Kiran *et al.* [233], Sawant and Patil [234, 235], and Petrakovskii *et al.* [236] from saturation magnetization measurements; by Rana *et al.* [237], Kolekar *et al.* [238], Patil *et al.*[239], Roy and Ghose [240], and Kulkarni *et al.* [241] from XRD data; by Liberman *et al.* [242], Kulkarni *et al.* [243], and Lee *et al.* [244] from Mössbauer spectra; by Sawant and Patil [245-247] from the Curie temperature measurements. As can be seen from Figure 6.4, the experimental data are in fair agreement except for the results of Roy and Ghose [240]. The results of Sawant and Patil are widely scattered and the sample of Patil *et al.* [239] was slowly cooled from 950 °C, so the studied cation distribution corresponds to a lower temperature.

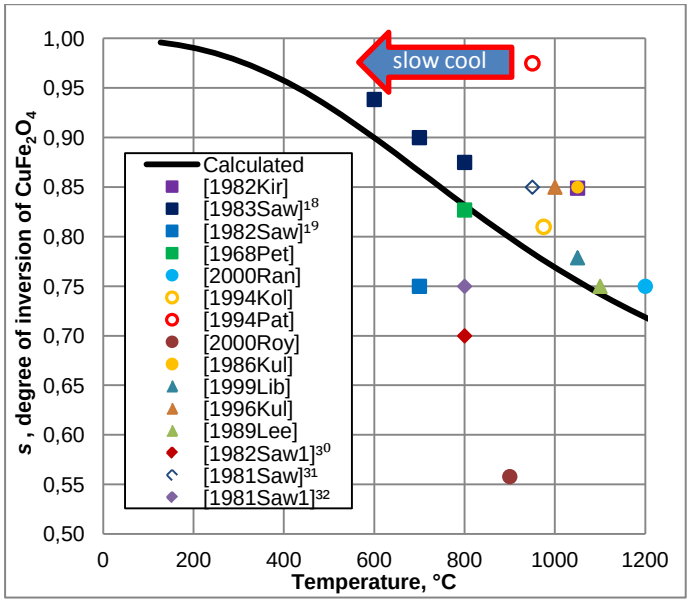

Figure 6.4. Degree of inversion of $CuFe_2O_4$ spinel: s is the number of moles of copper on the octahedral sublattice.

The lattice parameter of the Fe_3O_4–$CuFe_2O_4$ solid solution exhibits a maximum at the composition of $Cu_{0.5}Fe_{2.5}O_4$ [248, 249]. This anomaly is often explained by the appearance of Cu^{+1} cations according to the reaction:

$$Cu^{+2} + Fe^{+2} \rightleftharpoons Cu^{+1} + Fe^{+3} \qquad (6.10)$$

Even though different authors agree that the amount of Cu^{+1} is negligible in $CuFe_2O_4$ and should have a maximum at the $Cu_{0.5}Fe_{2.5}O_4$ composition, they report contradictory data on the amounts and sublattice occupancies of Cu^{+1} ions at compositions between Fe_3O_4 and $CuFe_2O_4$. Kitzinger and Simsa [250] suggested that copper stays almost exclusively as Cu^{2+} in $Cu_{0.5}Fe_{2.5}O_4$. Their measurements of the electrical properties of the sample quenched from 1250 °C indicated the presence of a large amount of Fe^{2+}, and therefore the equilibrium of reaction (6.10) should be shifted to the left. Simsa [251] quenched $Cu_{0.5}Fe_{2.5}O_4$ from 1250 °C and reported that about half of copper ions existed as Cu^{+1} on the tetrahedral sublattice and the other half were the Cu^{2+} cations on the octahedral sublattice. This conclusion was based on the saturation magnetization data. Tsitsenovskaya [252] studied $Cu_{0.5}Fe_{2.5}O_4$ quenched from 1250 °C by neutron diffraction and suggested, based on her data and the results of chemical analysis of Simsa [251], that about 40% of copper ions were Cu^{+1} which occupied mostly the tetrahedral sites. D'Huysser *et al.* [253] measured the X-ray induced photoelectron spectra (XPS) of $Cu_{0.5}Fe_{2.5}O_4$. In this method, the positions of peaks depend on the valence state of a metal and on the sublattice that it occupies. Intensities are

proportional to the amounts of different ions, although there are difficulties with the peak separation. It was not possible to distinguish between Cu^{+1} and Cu^{+2} on the octahedral sublattice, but about two thirds of total copper was found on this sublattice. Both Cu^{+1} and Cu^{+2} were found on the tetrahedral sites, but, interestingly, their proportion depended on the temperature of the measurement. Spectra were obtained at –50 and +50 °C for the same sample, quenched from 1300 °C. At –50 °C the ratio $(Cu^{+1})^{tetr}/(Cu^{+2})^{tetr}$ was 0.01/0.15, while at +50 °C it was 0.14/0.03. Hence, these data indicate that electron hopping according to reaction (6.10) takes place even at low temperatures and that the reaction shifts to the left with decreasing temperature. In another XPS study, which was made by Kester and Gillot [254] on the $Cu_{0.4}Fe_{2.6}O_4$ and $Cu_{0.32}Fe_{2.68}O_4$ samples quenched from 1250 °C in air, only Cu^{+1} was found on the tetrahedral sublattice. Nagarajan and Agajanian [255] reported the low temperature (4.2 K) magneto-Mössbauer study of $Cu_{0.5}Fe_{2.5}O_4$ quenched from 1300 °C and found no evidence of Fe^{2+} ions in the spectra. According to reaction (6.10), all copper must then be present as Cu^{+1}, which is in disagreement with the temperature dependence of the Cu^{+1} content reported by D'Huysser *et al.* [253]. Nagarajan and Agajanian suggested nearly equal distribution of Cu^{+1} between the tetrahedral and octahedral sublattices to describe their saturation magnetization measurements. Kuehn *et al.* [256] used the same method and reported that all copper was present as Cu^{1+}, while the ratio $(Cu^{+1})^{tetr}/(Cu^{+1})^{oct}$ was 0.24/0.26. This confirms the results of Nagarajan and Agajanian [255], but is in disagreement with the saturation magnetization data of Simsa [251].

To properly take into account the presence of different copper species in spinel, reliable experimental data are needed on the equilibrium amounts of Cu^{+2} and Cu^{+1} cations and their distribution between the octahedral and tetrahedral sublattices. Such data can only be obtained *in-situ* at high temperatures, because reaction (6.10) requires only electron hopping and cannot be quenched. On the other hand, the distribution of Cu and Fe atoms between the octahedral and tetrahedral sites becomes frozen at about 600–1000 °C due to slow diffusion in the solid state. Hence, any experimental data on the amounts of Cu^{+2} and Cu^{+1} obtained at room temperature, even if these data were not contradictory, cannot correspond to a true equilibrium state of spinel because the equilibrium distribution of Cu and Fe between the sublattices cannot be achieved. The goal of the present study is to obtain thermodynamic properties of spinel for calculations of phase equilibria at high temperatures, i.e. when cation occupancies of the sublattices are close to their equilibrium values. Even though reaction (6.10) can affect thermodynamic properties of spinel at high

temperatures, this can be taken into account without explicitly introducing Cu^{+1} cations. In particular, an additional "excess" parameter

$$M_{Fe^{+2}Cu^{+2}} = \frac{1}{2}L_{Fe^{+2}:Fe^{+2}Cu^{+2}} = \frac{1}{2}L_{Cu^{+2}:Fe^{+2}Cu^{+2}} = \frac{1}{2}L_{Fe^{+3}:Fe^{+2}Cu^{+2}} \quad (6.11)$$

provides a very similar contribution to the Gibbs energy of spinel as reaction (6.10): there is no contribution for the Fe_3O_4 and $CuFe_2O_4$ compositions, the contribution is proportional to the amounts of Cu^{+2} and Fe^{+2} cations, and the effect reaches its maximum at the $Cu_{0.5}Fe_{2.5}O_4$ composition. This excess parameter of the spinel model can be temperature dependent and will indirectly describe the contribution of reaction (6.10) to the Gibbs energy after being optimized based on experimental thermodynamic properties and phase equilibria.

The distribution of copper and iron between the tetrahedral and octahedral sublattices in the $(1–x)Fe_3O_4–xCuFe_2O_4$ solution is shown in Figure 6.5. The experimental data have been recalculated to the formula unit $(Cu_{x-s},Fe_{1-x+s})^{tetr}[Cu_{s/2},Fe_{1-s/2}]_2^{oct}O_4$ of the solution and the degree of inversion, *s*, is plotted in Figure 6.5. In addition to the above mentioned literature data [250-256], the XRD-based cation distributions of Mexmain [257] and of Tang *et al.* [258] are also shown in Figure 6.5. Lisnyak *et al.* [249] made certain model assumptions about interatomic distances and deduced the amounts of Fe^{+3}, Fe^{+2}, Cu^{+2} and Cu^{+1} cations by fitting the lattice parameters and magnetization data for spinel samples quenched from unspecified temperatures, presumably, within the stability field of spinel at various compositions. The degree of inversion recalculated from the cation occupancies suggested by Lisnyak *et al.* [249] are plotted in Figure 6.5, even though it is not possible to assign particular temperatures to these points.

It should be noted that the distribution of Cu and Fe between the sublattices was studied mostly on spinel samples prepared at fixed $P(O_2)$, usually in air. As will be discussed in more detail in Section 6.4.4, the region of stability of single-phase spinel in air is limited at a given temperature and progressively shifts from $CuFe_2O_4$-rich to Fe_3O_4-rich compositions with rising temperature (see Figure 6.18). This trend is reflected in the experimental measurements that could not be made at a constant temperature over the whole composition range of spinel from Fe_3O_4 to $CuFe_2O_4$, although some of the studied compositions still fall outside the spinel stability field, indicating that either a metastable sample or a two-phase mixture was actually studied. The lines in Figure 6.5 were calculated by suppressing formation of other phases outside the stability region of spinel. It should also be noted that it is very difficult to quench the cation distribution in spinel from high

temperatures. Some redistribution of cations during quenching occurs unless special efforts are made to ensure a very high rate of cooling throughout the sample. For ordinary quenching methods from temperatures above 1000 °C, the cation distribution usually freezes somewhere in the interval from 600 to 1000 °C, depending on the cooling rate. Hence, most of the points in Figure 6.5 for samples annealed at 1250 °C actually correspond to cation distributions at lower temperatures, which should result in higher degrees of inversion than the equilibrium values at 1250 °C.

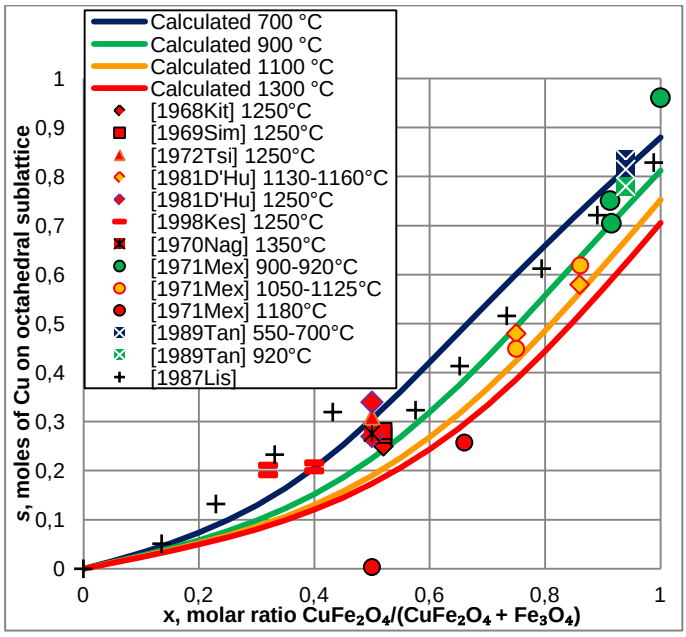

Figure 6.5. Degree of inversion in Fe_3O_4–$CuFe_2O_4$ spinel: experimental points [249-258] and calculated lines. *s* is the number of moles of Cu on the octahedral sublattice per formula unit of spinel $(Cu_{x-s},Fe_{1-x+s})^{tetr}[Cu_{s/2},Fe_{1-s/2}]_2^{oct}O_4$.

The non-stoichiometry of spinel towards oxygen was reported in several studies [251, 259, 260]. It was modeled by introducing neutral vacancies (Va) on the octahedral sublattice as suggested earlier [21, 173].

Hence, the model for spinel in the Cu–Fe–O system is based on the following formula unit:

$$(Cu^{+2},Fe^{+2},Fe^{+3})^{tetr}[Cu^{+2},Fe^{+2},Fe^{+3},Va]_2^{oct}O_4^{-2} \qquad (6.12)$$

The same set of model parameters as proposed earlier [21] for the Zn–Fe–O spinel are used in the present study:

$$F_{Fe^{+2}Fe^{+3}} = \frac{1}{7}G_{Fe^{+2}Fe_2^{+3}O_4} = \frac{1}{7}G_{[Fe^{+3}Fe_2^{+2}O_4]^{-1}} \qquad (6.13)$$

$$I_{Fe^{+2}Fe^{+3}} = G_{[Fe^{+3}Fe_2^{+3}O_4]^{+1}} + G_{[Fe^{+3}Fe_2^{+2}O_4]^{-1}} - 2G_{Fe^{+2}Fe_2^{+3}O_4} \quad (6.14)$$

$$\Delta_{Fe^{+2}Fe^{+3}} = G_{[Fe^{+2}Fe_2^{+2}O_4]^{-2}} + G_{[Fe^{+3}Fe_2^{+3}O_4]^{+1}} - G_{[Fe^{+3}Fe_2^{+2}O_4]^{-1}} - G_{Fe^{+2}Fe_2^{+3}O_4} \quad (6.15)$$

$$V_{Fe^{+3}} = G_{[Fe^{+3}Va_2O_4]^{-5}} - \frac{5}{7}G_{[Fe^{+3}Fe_2^{+2}O_4]^{-1}} \quad (6.16)$$

$$\Delta_{Fe^{+3}Fe^{+2}Va} = G_{[Fe^{+2}Fe_2^{+2}O_4]^{-2}} + G_{[Fe^{+3}Va_2O_4]^{-5}} - G_{[Fe^{+3}Fe_2^{+2}O_4]^{-1}} - G_{[Fe^{+2}Va_2O_4]^{-6}} \quad (6.17)$$

$$F_{Cu^{+2}Fe^{+3}} = \frac{1}{7}G_{Cu^{+2}Fe_2^{+3}O_4} \quad (6.18)$$

$$I_{Cu^{+2}Fe^{+3}} = G_{[Fe^{+3}Fe_2^{+3}O_4]^{+1}} + G_{[Fe^{+3}Cu_2^{+2}O_4]^{-1}} - 2G_{Cu^{+2}Fe_2^{+3}O_4} \quad (6.19)$$

$$\Delta_{Cu^{+2}Fe^{+3}} = G_{[Cu^{+2}Cu_2^{+2}O_4]^{-2}} + G_{[Fe^{+3}Fe_2^{+3}O_4]^{+1}} - G_{[Fe^{+3}Cu_2^{+2}O_4]^{-1}} - G_{Cu^{+2}Fe_2^{+3}O_4} \quad (6.20)$$

$$\Delta_{Fe^{+3}Cu^{+2}Va} = G_{[Cu^{+2}Cu_2^{+2}O_4]^{-2}} + G_{[Fe^{+3}Va_2O_4]^{-5}} - G_{[Fe^{+3}Cu_2^{+2}O_4]^{-1}} - G_{[Cu^{+2}Va_2O_4]^{-6}} \quad (6.21)$$

$$\Delta_{Fe^{+3}Fe^{+2}Cu^{2+}} = G_{[Fe^{+2}Fe_2^{+2}O_4]^{-2}} + G_{[Fe^{+3}Cu_2^{+2}O_4]^{-1}} - G_{[Fe^{+3}Fe_2^{+2}O_4]^{-1}} - G_{[Fe^{+2}Cu_2^{2+}O_4]^{-2}} \quad (6.22)$$

$$\Delta_{Fe^{+3}Cu^{+2}Fe^{2+}} = G_{[Cu^{+2}Cu_2^{+2}O_4]^{-2}} + G_{[Fe^{+3}Fe_2^{+2}O_4]^{-1}} - G_{[Fe^{+3}Cu_2^{+2}O_4]^{-1}} - G_{[Cu^{+2}Fe_2^{2+}O_4]^{-2}} \quad (6.23)$$

All 12 Gibbs energies of pseudocomponents can be expressed as linear combinations of parameters (6.13)-(6.23) as shown in Reference [21]. Parameters (6.13) to (6.17) for spinel in the Fe–O system were discussed and optimized earlier [21]. *F* parameter (6.18) is the Gibbs energy (per atom) of the completely normal, hypothetical simple spinel $CuFe_2O_4$. Parameters (6.19) and (6.20) are used to describe the degree of inversion and thermodynamic properties of the real spinel $CuFe_2O_4$. Parameter (6.21) affects the amount of vacancies and oxygen nonstoichiometry in $CuFe_2O_4$ and in the Fe_3O_4–$CuFe_2O_4$ solid solution. Finally, parameters (6.11), (6.22) and (6.23) are used for reproducing the thermodynamic properties of the solution between Fe_3O_4 and $CuFe_2O_4$.

Magnetite is ferromagnetic below its Curie temperature of 575 °C and $CuFe_2O_4$ is ferrimagnetic below the Curie temperature of 478 °C. The phenomenological approach proposed by Hillert and Jarl [8] was used to describe the magnetic contribution to thermodynamic functions. Due to the lack of experimental data, it was assumed that the Curie temperature, T_C, and the average magnetic moment per atom, β, are independent of the degree of inversion in pure Fe_3O_4 and $CuFe_2O_4$. It was further assumed that these values change linearly with composition from Fe_3O_4 to $CuFe_2O_4$. The formulae that are used in the CEF to describe the magnetic contribution to thermodynamic functions of a solution were discussed in more detail by Decterov *et al.* [21]. It was shown what values can be

assigned to T_C and β of the charged pseudocomponents and to excess magnetic parameters in order to obtain simple linear dependences of T_C and β on composition of the spinel solution.

Contrary to the present study, Khvan et *al.* [177] explicitly introduced Cu^{+1} ions into their spinel model, which is also based on the Compound Energy Formalism. No attempt was made to evaluate the distribution of Cu^{+1} between the tetrahedral and octahedral sublattices and Cu^{+1} cations were assumed to be present only on the tetrahedral sites. Furthermore, the oxygen nonstoichiometry and magnetism of spinel were neglected. Thus, the model for spinel is based on the following formula unit:

$$(Cu^{+2},Cu^{+1},Fe^{+2},Fe^{+3})^{tetr}[Cu^{+2},Fe^{+2},Fe^{+3}]_2^{oct}O_4^{-2} \quad (6.24)$$

which can be compared with formula unit (6.12) that is used in the present study. Evidently, the two models are different, even though both are based on the Compound Energy Formalism and have the same number of end-members.

6.4 Assessment of experimental data

6.4.1 Subsolidus phase equilibria

Subsolidus phase relations studied by Yund and Kullerud [261-263], Fredriksson and Rosen [264], Schmahl and Muller [265], Schaefer *et al.* [266], Jacob *et al.* [267] and others were critically evaluated by Perrot *et al.* [232]. Based on these experimental results, the isothermal sections of the Cu–Fe–O phase diagram at 650–1500 °C were suggested, but no attempts of thermodynamic modeling were made. In the present study, these phase diagrams were calculated using the developed thermodynamic database. The calculated diagrams are in agreement with the experimental data reviewed by Perrot *et al.* [232] and with their assessment. The isothermal sections of the Cu–Fe–O phase diagram at 600, 800 and 1000 °C are shown in Figures 6 to 8. Phase transitions below 650 °C were not assessed by Perrot *et al.* [232].

It is known that wüstite is not stable against Fe and Fe_3O_4 below 570 °C [268]. Copper ferrite (spinel), which is stable at 650 °C, was reported to be unstable at room temperature [269]. Hence, it must decompose somewhere between 25 and 650 °C. This reaction is kinetically hindered and was not studied experimentally. As can be seen in Figure 6.9, our calculations based on the optimized thermodynamic database suggest the decomposition of $CuFe_2O_4$-rich spinel at 544 °C.

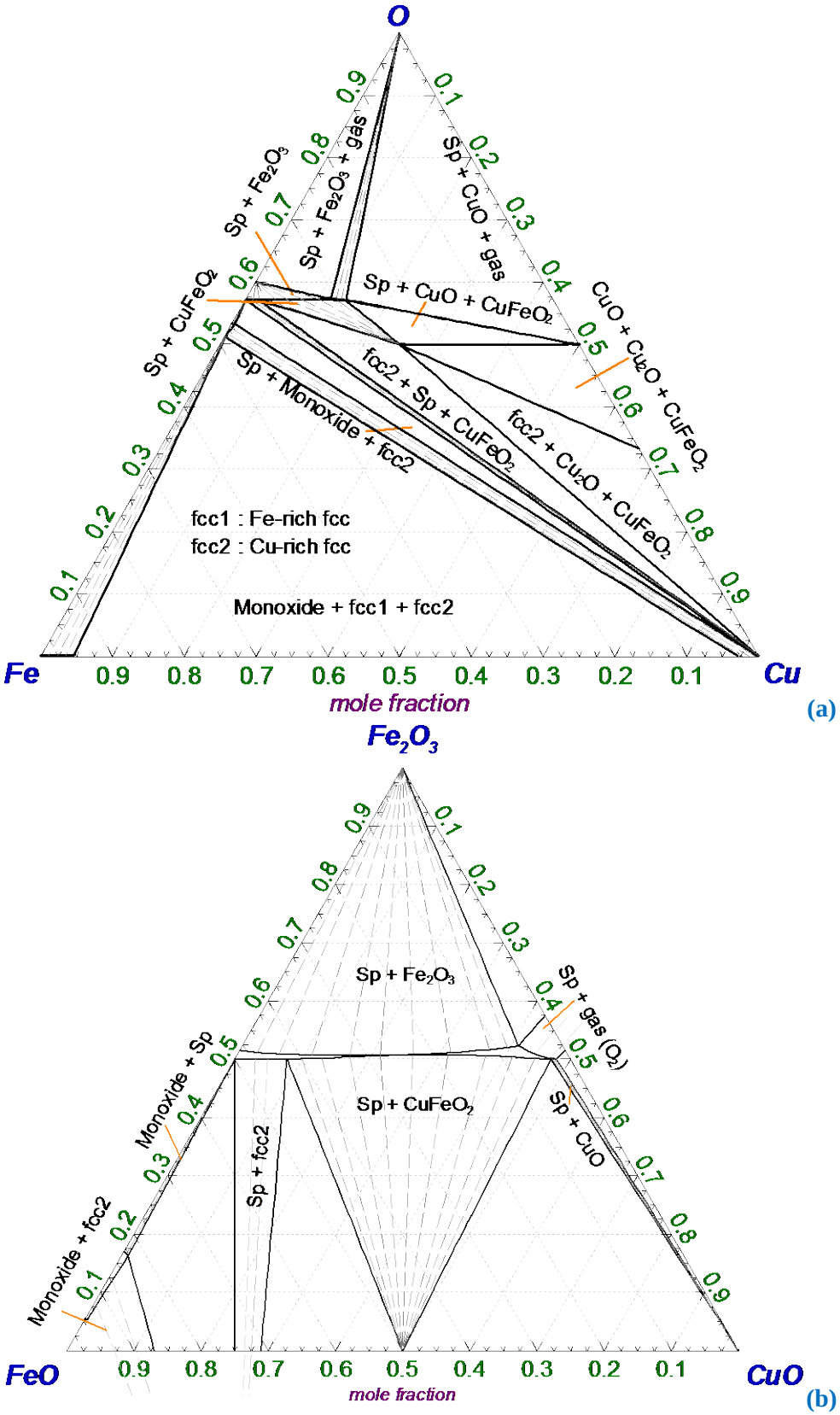

Figure 6.6. (a) Calculated isothermal section of the Cu–Fe–O phase diagram at 1000 °C and *P* = 1 atm. (b) Magnification of the oxide part of the Cu–Fe–O diagram.

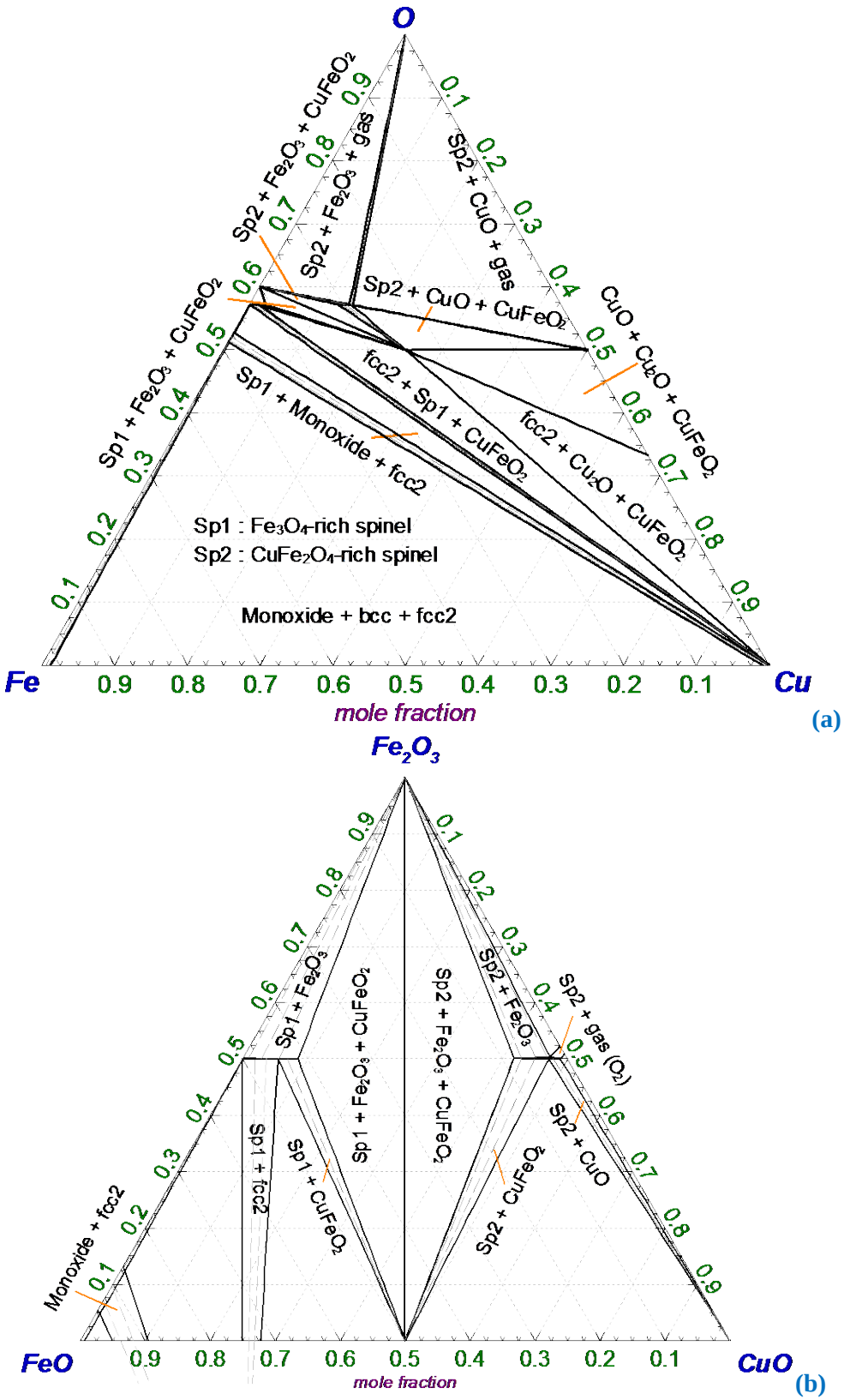

Figure 6.7. (a) Calculated isothermal section of the Cu–Fe–O phase diagram at 800 °C and *P* = 1 atm. (b) Magnification of the oxide part of the Cu–Fe–O diagram.

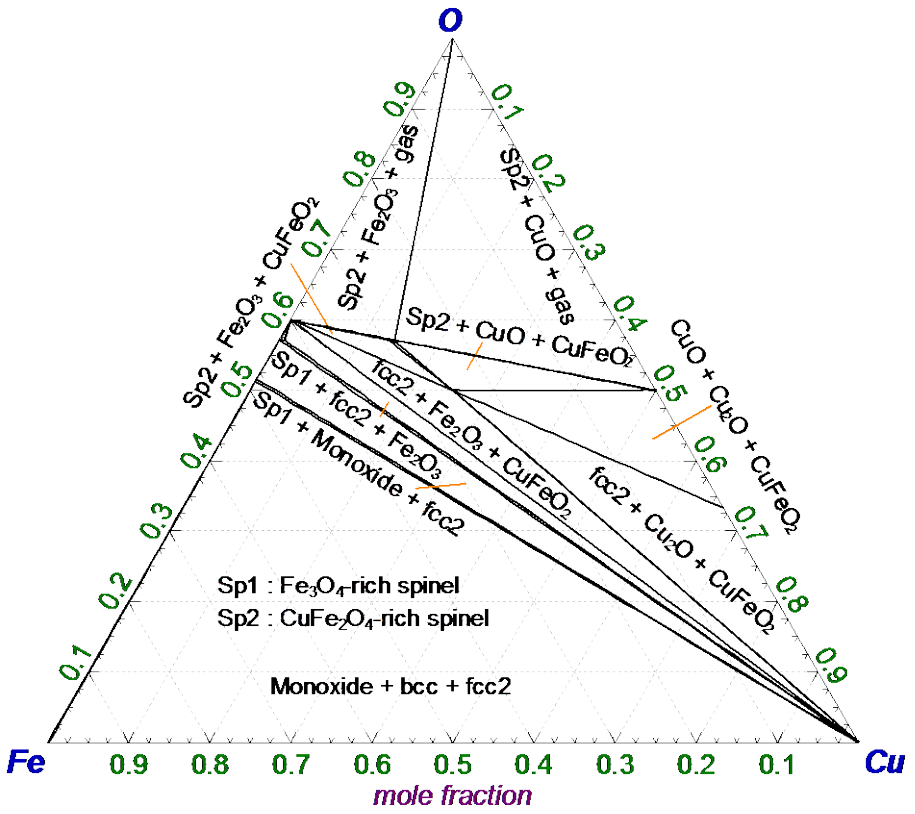

Figure 6.8. Calculated isothermal section of the Cu–Fe–O phase diagram at 600 °C and *P* = 1 atm.

The mutual solubility between Fe_3O_4 and $CuFe_2O_4$ increases with temperature, and at certain temperature they form a continuous solid solution. This point is usually referred to as the eutectoid decomposition. It is easy to understand what happens during the eutectoid decomposition from a comparison of Figures 6(b) and 7(b). The spinel stability field and other phase relations in the Fe_3O_4–$CuFe_2O_4$ section of the phase diagram are shown in Figure 6.9 along with the experimental data [177, 226, 262, 264, 267, 270-272]. The composition of spinel is very close to this section, but it is shifted slightly off towards oxygen due to the presence of a small amount of vacancies as will be discussed in more detail in Section 6.4.5. Yamaguchi and Shiraishi [270] studied the eutectoid decomposition of spinel solid solution by the quenching method. Samples were prepared by annealing under controlled, but unreported oxygen pressures. After annealing at each temperature, the specimens were quenched into water and subjected to microscopic and X-ray diffraction analysis. According to their results, the temperature of eutectoid decomposition was around 1030 °C. Simsa and Holba [259] found by DTA that $Cu_{0.52}Fe_{2.48}O_{4+\gamma}$ decomposed at 1000 °C. They showed that the temperature of decomposition was independent of γ. Jacob *et al.* [267] argued that the decomposition temperature should be near 980 °C based on the oxygen potential measurements

in the spinel region. This temperature was later supported by Katkov and Lykasov [271], who made EMF measurements involving $Cu_xFe_{1-x}O_4$ spinels of different compositions. Extrapolation of the data obtained by Fredriksson and Rosen [264] also points out to the temperature between 980 and 1000 °C. As shown in Figure 6.9, the data of different authors for the phase boundary Spinel Fe_2O_3 + $CuFeO_2$ are in good agreement except for the results of Yamaguchi and Shiraishi [270], who reported much higher phase boundary at Fe_3O_4-rich compositions (their phase boundary is located between the solid and empty triangles).

Jacob *et al.* [267] gave the compositions of spinel in equilibrium with Cu and $CuFeO_2$, which correspond to the line between (Spinel + Cu) and (Spinel + $CuFeO_2$) fields in Figure 6.9. He separated magnetically the spinel phase which was heated with equimolar amounts of Cu and $CuFeO_2$ in silica crucible. The Cu/Fe ratio in the spinel was measured using the wet chemical analysis. Fredriksson and Rosen [264] obtained points on the same line by interpretation of their EMF results based on the fact that at constant temperature, $P(O_2)$ varies in the two-phase area (Spinel + Cu) but remains constant in the three-phase region (Spinel + Cu + $CuFeO_2$). Liu *et al.* [272] used the electron-probe microanalysis (EPMA) to measure the Cu/Fe ratio in spinel equilibrated with Cu and $CuFeO_2$. The achievement of equilibrium state in the samples was ensured by doubling or tripling the equilibration time. As can be seen in Figure 6.9, the Cu/Fe ratios of Fredriksson and Rosen [264] and Liu *et al.* [272] are in agreement and somewhat higher than those of Jacob *et al.* [267].

The equilibrium between spinel, liquid copper and molten Cu–Fe–O oxide (slag) was studied by Nikolic *et al.* [226]. They obtained the Cu/Fe ratios in spinel using quenching followed by EPMA. The compositions of spinel are close to the Fe_3O_4–$CuFe_2O_4$ section and are plotted in Figure 6.9. The liquid phase is discussed in Section 6.4.4

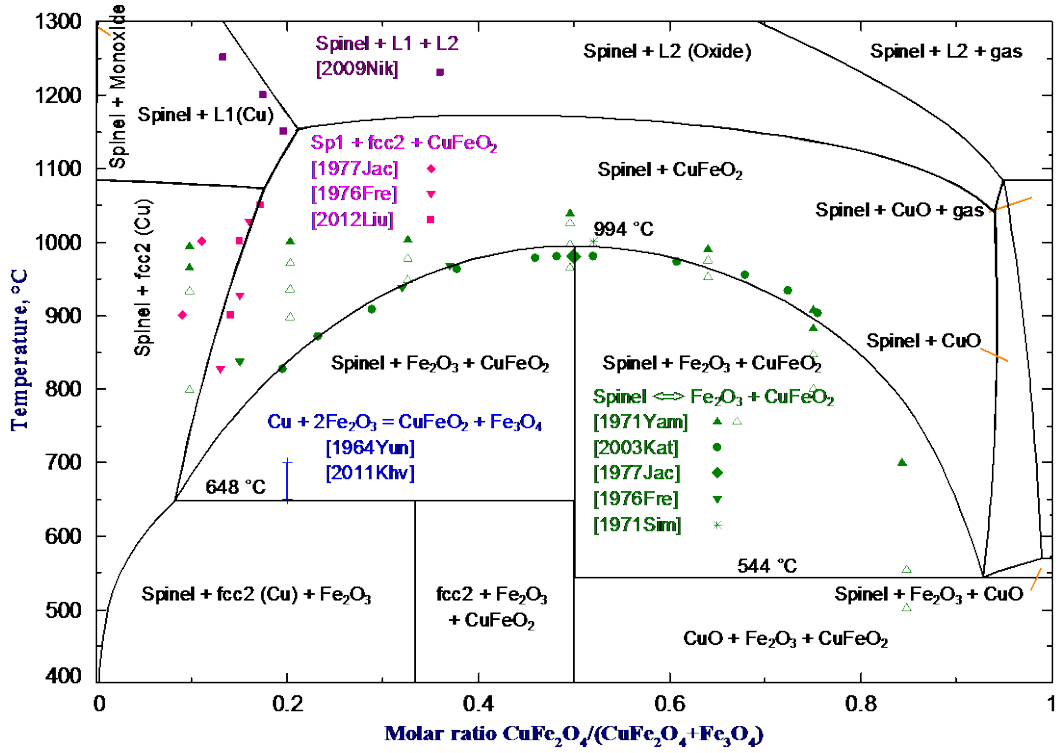

Figure 6.9. Fe_3O_4–$CuFe_2O_4$ section of the Cu–Fe–O system at P = 1 atm: experimental data [177, 226, 259, 262, 264, 267, 270-272] and calculated lines.

6.4.2 Equilibrium oxygen partial pressure

The equilibrium partial pressure of oxygen over various three-phase regions at temperatures from 600 to 1100 °C is summarized in Figure 6.10. It should be noted that thermodynamic properties of phases in the Cu–Fe–O system are severely constrained by this type of data.

The low oxygen pressure phase fields (Monoxide + bcc (or fcc1) + fcc2) and (Sp1 + Monoxide + fcc2) were investigated by Katkov and Lykasov [231] using EMF measurements.

The equilibrium (fcc2 + Sp1 + $CuFeO_2$) was studied by Jacob *et al.* [267], Paulsson et al. [273] and Fredriksson and Rosen [264] by an EMF technique. Jacob *et al.* [267] used the Ni–NiO pair as the reference electrode, while Paulsson *et al.* [273] and Fredriksson and Rosen [264] used air. The former measurements are probably more reliable since the oxygen potential of the Ni–NiO electrode is closer to the $P(O_2)$ over the studied mixture. Zalazinskii *et al.* [274] derived the $P(O_2)$ over the (fcc2 + Sp1 + $CuFeO_2$) three-phase field from the measurements of water vapor pressure during hydrogen reduction of $CuFeO_2$. His results are closer to those of Jacob *et al.* [267].

No data were found in the literature on the oxygen partial pressure over the (fcc2 (Cu) + Cu_2O + $CuFeO_2$) field.

For the (Sp1 + Fe_2O_3 + $CuFeO_2$) and (Sp2 + Fe_2O_3 + $CuFeO_2$) three-phase mixtures, the data of Katkov and Lykasov [271], Rosenqvist and Hofseth [101] are available and may be compared with the only point of Fredriksson and Rosen [264]. The results of the former two studies are in disagreement for the (Sp2 + Fe_2O_3 + $CuFeO_2$) region. The line calculated in the present study is more consistent with the measurements of Rosenqvist and Hofseth [101] and is supported by the agreement of the calculated lines with the experimental data of several authors for the other three-phase regions containing Sp2. Furthermore, the sharp angle between the lines (Sp1 + Fe_2O_3 + $CuFeO_2$) and (Sp2 + Fe_2O_3 + $CuFeO_2$) reported by Katkov and Lykasov [271] is qualitatively incorrect and would indicate a discontinuity in the thermodynamic properties of spinel.

The $P(O_2)$ over the (CuO + Cu_2O + $CuFeO_2$) field is rather high, which makes direct pressure measurements possible. Floyd and Willis [275] and Schmahl and Muller [265] used this method and reported consistent results. The data points of Rosenqvist and Hofseth [101] obtained by an EMF technique are in agreement with the direct pressure measurements.

For the (Sp2 + CuO + $CuFeO_2$) region, different types of data are available: the EMF data of Eriksson and Tegman [276], direct $P(O_2)$ measurements of Floyd and Willis [275] and of Schmahl and Muller [265], H_2/H_2O reduction data of Zinovik [277], results of Schaefer *et al.* [266] for equilibration with N_2–O_2 mixtures and dissociation curves in O_2–He reported by Ono *et al.* [278]. The results of all studies are in good agreement, except for the data of Zinovik [277] that are somewhat higher and the point of Ono *et al.* [278] that is lower.

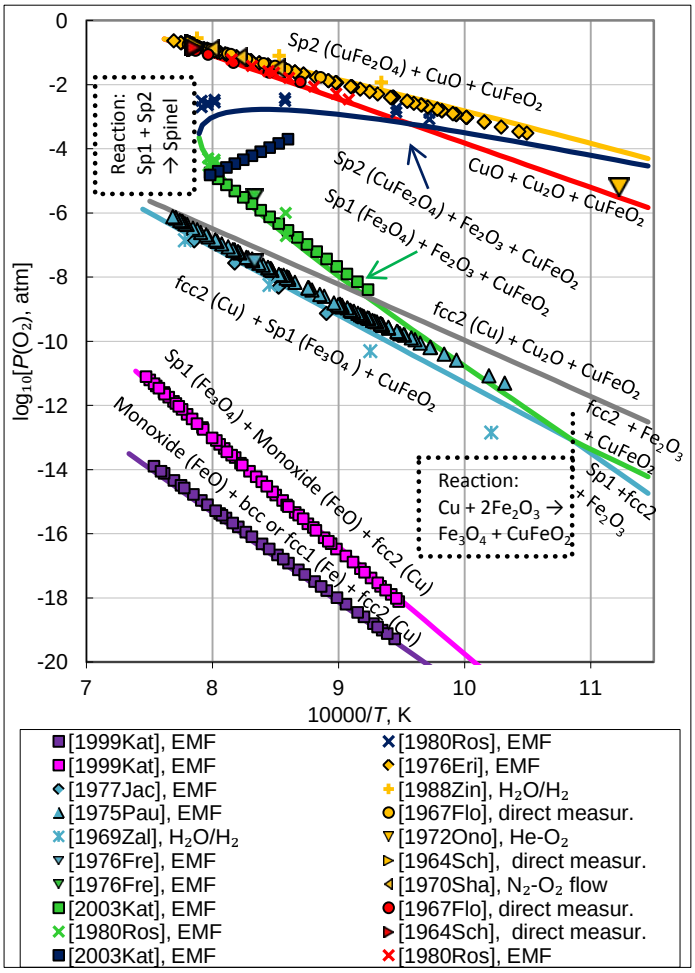

Figure 6.10. Equilibrium oxygen partial pressures over three-phase regions in the Cu–Fe–O system: calculated lines and experimental points [231, 264-267, 273-277].

The $P(O_2)$ versus composition phase diagram at constant temperature just above the eutectoid decomposition of spinel is shown in Figure 6.11. Jacob *et al.* [267] measured the $P(O_2)$ over $Cu_xFe_{1-x}O_4$ spinel in equilibrium with Fe_2O_3. The measurements were made manometrically for $x > 0.4$ and using an EMF cell with the Fe_2O_3–Fe_3O_4 reference electrode for $x < 0.4$. They also calculated the $P(O_2)$ over spinel in equilibrium with $CuFeO_2$, using their spinel model. These points are shown in Figure 6.11, even though they are not experimental. The results of Jacob *et al.* [267] can be compared with the $P(O_2)$ data of Katkov and Lykasov [271], who carried out EMF measurements using the $ZrO_2(Y_2O_3)$ solid electrolyte and a mixture of $CuO+Cu_2O$ as the reference electrode. Zalazinskii *et al.* [279] obtained the oxygen potentials using hydrogen reduction accompanied by measurements of the water vapor pressure. Liu *et al.* [272] and Hidayat [280] equilibrated spinel with another phase at controlled oxygen pressures, then quenched the samples and measured the

composition of spinel by EPMA. The narrowing of the spinel field at $P(O_2)$ from 10^{-3} to 10^{-4} atm results in the eutectoid decomposition of spinel at 994 °C as shown in Figure 6.9.

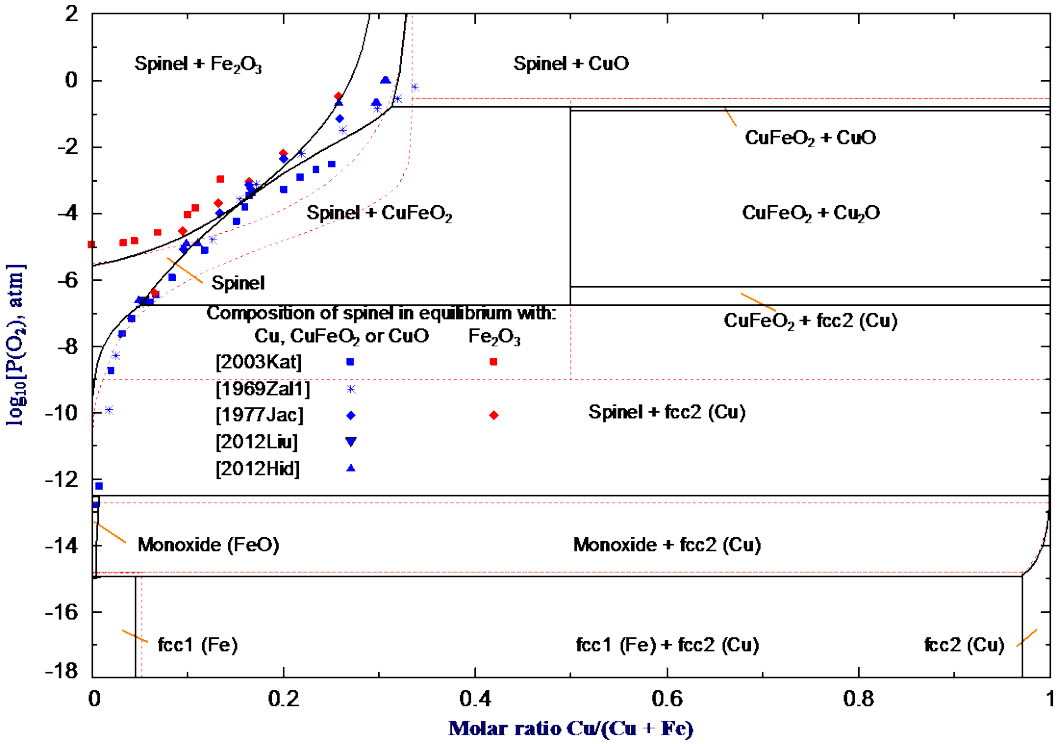

Figure 6.11. Phase diagram of the Cu–Fe–O system at 1000 °C. Equilibrium oxygen partial pressure versus molar metal ratio: points indicate experimental data [267, 271, 272, 279, 280], solid lines are calculated from model parameters optimized in this study and dashed lines represent the optimization of Khvan et *al.* [177].

6.4.3 Solubility of copper in monoxide

Katkov and Lykasov [231] reported EMF measurements on the galvanic cell

$$\text{Pt, Fe} - \text{"FeO"} \mid \text{ZrO}_2\left(+\text{Y}_2\text{O}_3\right) \mid \text{Fe}_{1-c}\text{Cu}_c\text{O}_y\text{, Pt} \qquad (6.25)$$

Experiments were made in the wüstite region, c was <0.01 and y was close to 1. The composition $\text{Fe}_{1-c}\text{Cu}_c\text{O}_y$ was varied by mixing analytical grade Fe, Fe_2O_3 and CuO. To prevent the change of composition during sintering, the mixtures were pressed into pellets and sealed in zirconia tubes. The solubility limits of CuO in wüstite were determined from the slope changes in the dependence of the EMF on composition. The phase boundaries of monoxide and the equilibrium oxygen pressure are shown in Figures 12 and 13. The oxygen partial pressures over the three-phase regions (Monoxide + fcc1 + fcc2) and (Sp1 + Monoxide + fcc2) were also reported by Katkov and Lykasov [231] and are shown in Figure 6.10.

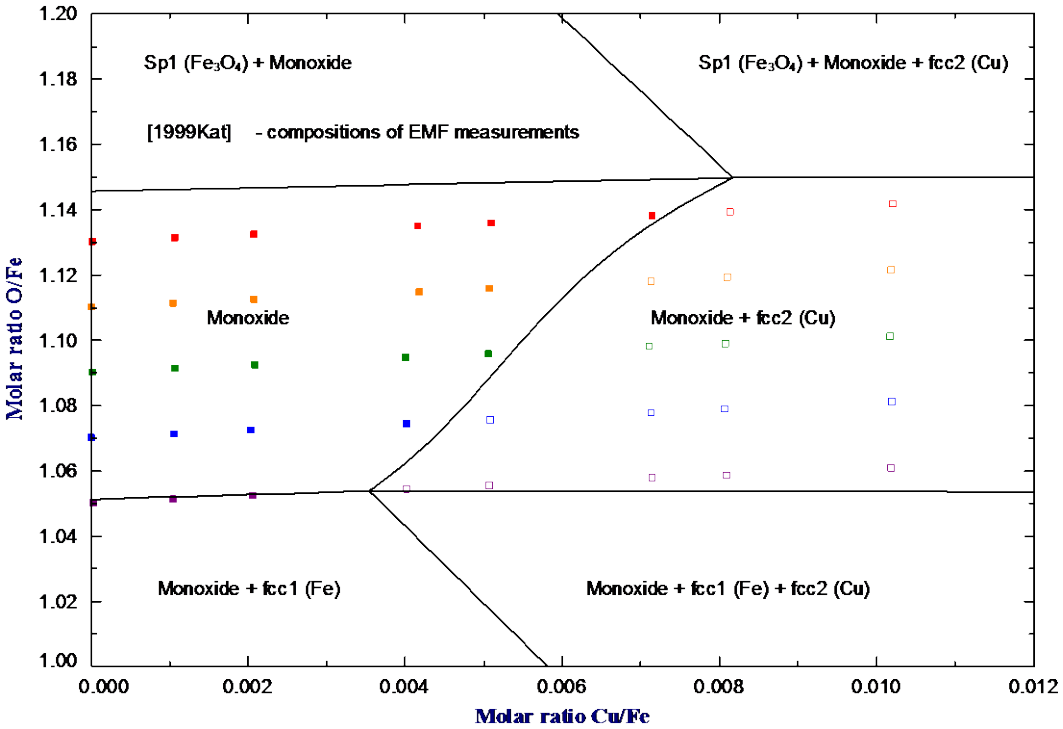

Figure 6.12. Solubility of CuO in wüstite at 1000 °C in the Cu–Fe–O system: experimental points [231] and calculated lines. Solid and open squares indicate single-phase and two-phase regions, respectively.

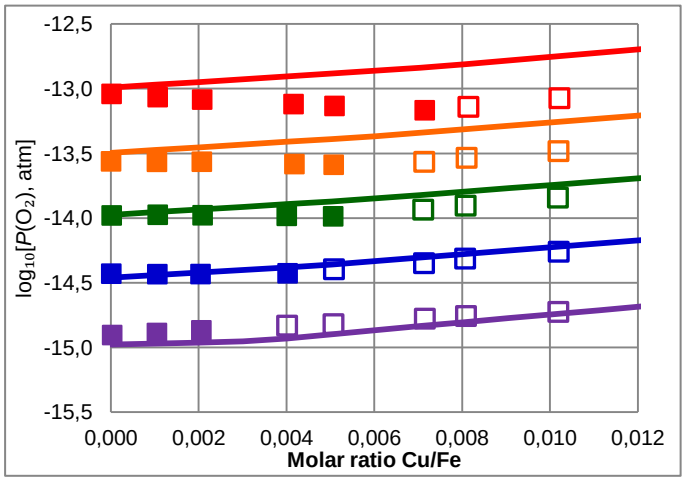

Figure 6.13. Oxygen partial pressure in the monoxide region of the Cu–Fe–O system at 1000 °C: experimental points [231] and calculated lines. Solid and open squares indicate single-phase and two-phase regions, respectively. The compositions of points are shown in the previous figure.

The deviation of the calculated lines from the experimental points in Figure 6.3 originates not only from the experimental uncertainties in the EMF measurements, but also from the uncertainties in the compositions of the samples. In particular, the oxygen content of the samples was calculated from the initial mixtures of Fe, Fe_2O_3 and CuO. If the actual O/Fe ratio decreased by only 0.01

during sealing of pellets in zirconia tubes or during experiments, this would account for the maximum difference between the experimental points and the calculated lines at high O/Fe ratios. It should be noted that the oxygen pressures reported by Katkov and Lykasov [231] for the equilibrium mixtures Sp1 (Fe_3O_4) + monoxide + fcc2 (Cu) are in excellent agreement with the calculated line as can be seen from Figure 6.10, even though the O/Fe ratios for monoxide in this three-phase region are higher than for the points shown in Figure 6.3. Hence, the model parameters optimized in the present study reproduce the data of Katkov and Lykasov [231] within experimental error limits.

6.4.4 Liquid phase

The liquid phase in the Cu–Fe–O system exhibits a large miscibility gap between the metal and oxide phases. In the Cu–O system, the immiscibility between metallic and oxide liquids disappears at about 1350 °C [114] (see Figure 6.2). As can be seen in Figure 6.3, the miscibility gap in the Fe–O system is much more pronounced and the consolute point is 2875 °C according to our estimation [227].

The properties of the Cu–Fe–O oxide liquid were studied by Acuna *et al.* [281]. Mixtures of Cu_2O, CuO, Cu and Fe_2O_3 were melted at 1200 °C in alumina crucibles under an atmosphere of pure oxygen, air or argon-air. The quenched samples were analyzed for Cu, Fe, O and Al_2O_3, although the analytical method is not specified. The reported compositions were adjusted to 100% Cu+Fe+O. The results are plotted in Figure 6.14 as oxygen isobars.

Oishi *et al.* [282] equilibrated oxide and metallic liquid at 1500 °C in high purity magnesia crucibles. The oxygen potential was measured using ZrO_2(MgO) as the solid electrolyte and a mixture of Mo+MoO_2 as the reference electrode. After quenching, the oxide phase was analyzed for Cu, Fe, Mg and Zr. The analysis showed up to 4 wt% Mg and 0.5% Zr. Mg and Zr were assumed to dissolve as MgO and ZrO_2, respectively. The remaining oxygen was calculated by difference. The metallic phase was analyzed for Cu, Fe and O. The oxygen content was determined by an inert gas fusion infrared absorption method. The results are recalculated to 100% Cu+Fe+O and plotted in Figure 6.15.

Figures 15 (c) and 16 show the calculated oxidation states of Cu and Fe in oxide liquid. Clearly, copper remains mostly Cu^{I} even at high oxygen pressures, whereas iron is mainly Fe^{III} in air and at $P(O_2)$ = 0.01 atm. As can be seen from Figure 6.15 (c), Fe^{III} can be the predominant species even at

metal saturation. The steep rise of Fe^{III} concentrations seen in this figure is correlated with the rapid increase of the experimentally measured oxygen pressure shown in Figure 6.15 (b).

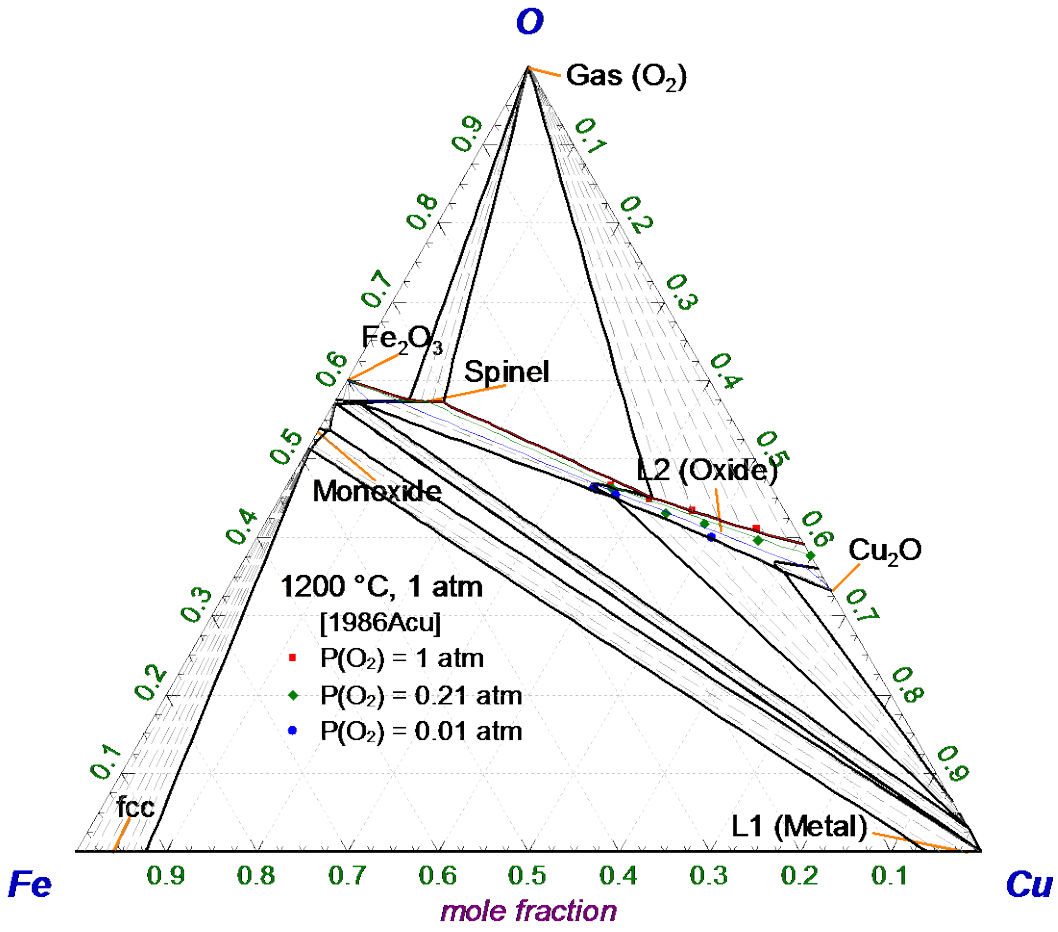

Figure 6.14. Calculated isothermal section of the Cu–Fe–O phase diagram at 1200 °C and *P* = 1 atm. Calculated and experimental [281] oxygen isoactivity lines are superimposed over the oxide liquid region.

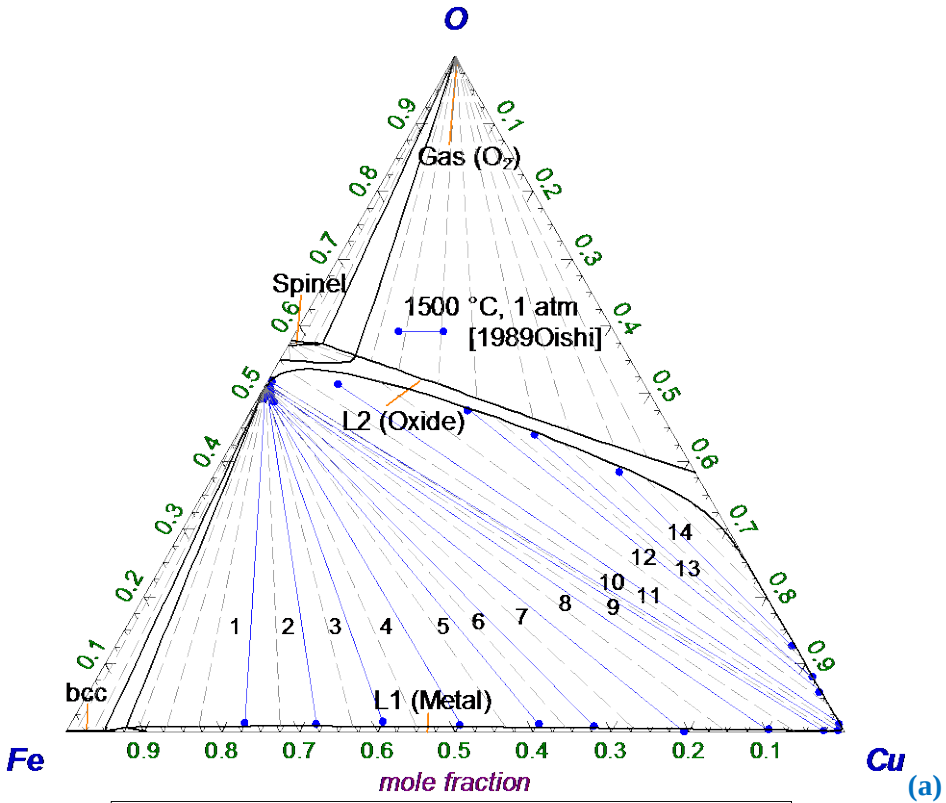

(a)

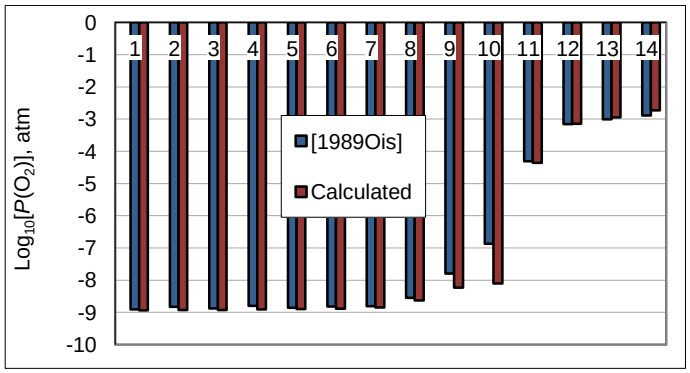

(b)

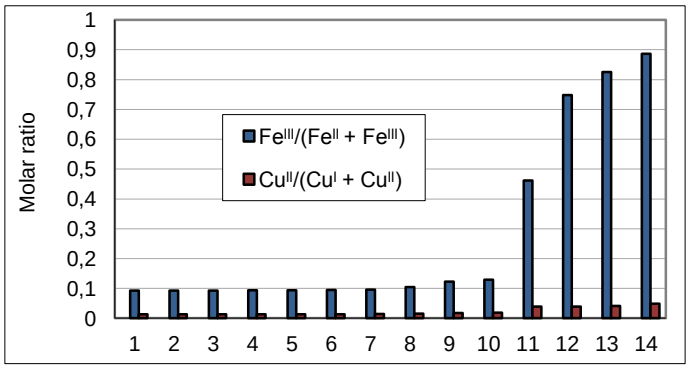

(c)

Figure 6.15. (a) Calculated isothermal section of the Cu–Fe–O phase diagram at 1500 °C and *P* = 1 atm. Calculated and experimental [282] tie-lines between liquid oxide and liquid metal. (b) Equilibrium $P(O_2)$ corresponding to these tie-lines. (c) Calculated distribution of iron between the Fe^{II} and Fe^{III} species and of copper between the Cu^{I} and Cu^{II} species in the oxide liquid end of these tie-lines.

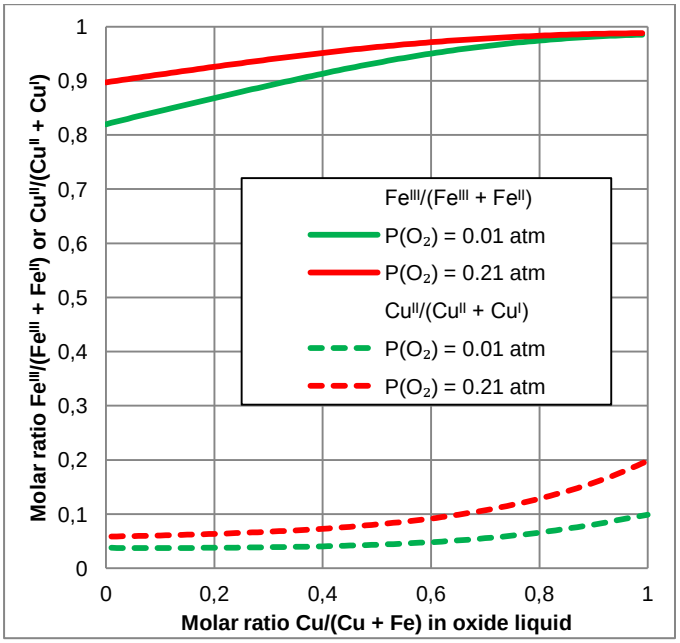

Figure 6.16. Calculated distribution of iron between the Fe^{II} and Fe^{III} species and of copper between the Cu^{I} and Cu^{II} species in Cu–Fe–O oxide liquid at 1500 °C and fixed oxygen pressure. The formation of solid oxide phases is suppressed.

The Fe_3O_4–Cu_2O quasi-binary section of the Cu–Fe–O system is shown in Figure 6.17. Solid or liquid metallic copper is present in equilibrium with oxide phases almost everywhere on this section. One notable exception is the region of Cu_2O-rich oxide liquid, which expands beyond the Cu_2O composition towards Cu in the Cu–O system.

Liquidus at copper saturation was studied by Takeda [283], Ilyushechkin *et al.* [284] and Nikolic *et al.* [226]. Takeda [283] melted the mixtures of Cu, Cu_2O and Fe_3O_4 in magnesia crucibles. After quenching, samples were cut vertically and quenched slag was separated from solid phases. Metal ratios in both slag and solid phases were obtained by chemical analysis. The temperatures of invariant equilibria were determined by thermal analysis. The solubility of MgO in the liquid and solid phases increased with temperature. The slag phase contained less than 1 wt% of MgO even at 1400 °C, but spinel dissolved up to 16 wt% of MgO, and a reaction layer formed on the crucible walls, which most likely was magnesiowustite containing up to 60 wt% FeO. It should be noted that MgO is completely miscible with wustite at these temperatures. Spinel also forms a complete range of solid solutions from Fe_3O_4 to $MgFe_2O_4$ [285], whereas 16 wt% of MgO in spinel corresponds to more than 80 mol% of $MgFe_2O_4$. Hence, the experiments of Takeda [283] were made for the Cu–Fe–Mg–O system and the solid phases contained substantial amounts of MgO that

rapidly increased with temperature. Nevertheless, the compositions of slag were recalculated to the Cu–Fe–O basis and plotted in Figure 6.17, as well as the invariant temperatures.

Ilyushechkin *et al.* [284] and Nikolic *et al.* [226] also reported the phase diagram at copper saturation. They applied the primary-phase substrate technique, where the crucible was laid either with Fe_3O_4 or with Cu_2O, eliminating contamination of the Cu–Fe–O system by reactions with crucibles. The samples were annealed, quenched and analyzed by EPMA.

Yazawa and Eguchi [286] reported the Cu_2O–Fe_2O_3 phase diagram that was studied in a stream of nitrogen gas by DTA and by EPMA analysis of quenched samples. No mention was made of crucible materials or the presence of metallic copper in the samples. The phase diagram obtained in nitrogen corresponds to unspecified, but low, oxygen pressure. Nonetheless, the diagram of Yazawa and Eguchi [286] was recalculated to the Cu_2O–Fe_3O_4 section and plotted in Figure 6.17 for comparison. It should be noted that only metal ratios were measured for the liquid phase in studies [226, 283, 284]. Strictly speaking, these points do not exactly correspond to any particular phase diagram. These compositions were projected through the oxygen corner to the Fe_3O_4–Cu_2O quasi-binary section in order to obtain experimental points shown in Figure 6.17 and to allow comparison with the calculated phase boundaries. Since the actual compositions of the oxide liquid phase are not far from the Fe_3O_4–Cu_2O section, the error introduced by projecting the measured metal ratios is small compared to the experimental uncertainties.

The results of all studies [226, 283, 284] indicate that the $CuFeO_2$–Cu_2O–L1(Cu)–L2(Oxide) ternary eutectic should be around 1135 °C. However, the Sp–$CuFeO_2$–L1(Cu)–L2(Oxide) invariant temperature of 1184 °C reported by Yazawa and Eguchi [286] is higher than 1140 to 1150 °C suggested by Takeda [283], Nikolic *et al.* [226] and Ilyushechkin *et al.* [284]. The latter value was selected in the present study.

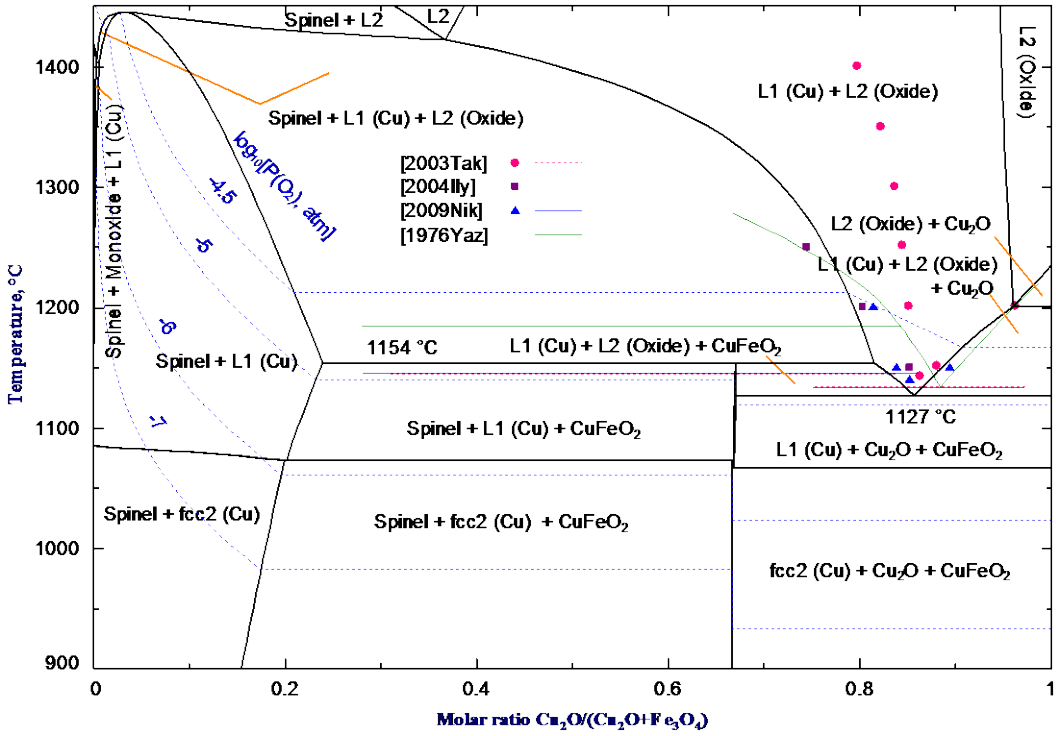

Figure 6.17. Phase diagram of the Fe_3O_4–Cu_2O quasi-binary section. Oxide phases are in equilibrium with solid or liquid metal copper for the majority of compositions and temperatures. Points and thin lines indicate experimental liquidus and invariant temperatures [226, 283, 284, 286]. Thick solid lines and dotted lines are calculated phase boundaries and oxygen isobars, respectively.

Yamaguchi [287] studied the Cu–Fe–O system in air. Samples of known Cu/Fe ratios were equilibrated in platinum crucibles and quenched into water. Phase boundaries were determined by visual and microscopic examination accompanied with X-ray diffraction. Buist *et al.* [288] annealed mixtures of CuO and Fe_2O_3 in an alumina crucible lined with a platinum foil. Samples were placed on a thermobalance to determine the atomic ratio O/(Cu + Fe) from the change of weight during equilibration. From these dissociation curves, the temperatures of phase transitions in air were obtained. Zinovik *et al.* [289-291] studied the stability range of delafossite and spinel in air by thermographic investigation of the CuO–Fe_2O_3 mixtures and by quenching experiments. The experimental data [287-291] are shown in Figure 6.18. The additional experimental results of Ristic *et al.* [292], Yamaguchi and Shiraishi [270], Mexmain [257], Kenfanck and Langbein [293], Nanba and Kobayashi [294], Katayama *et al.* [295] and Shaefer *et al.* [266] generally confirm the results of Yamaguchi [287] and Buist *et al.* [288]. There is, however, some uncertainty in the temperature and composition of the eutectic L = $CuFeO_2$+Cu_2O in air. While Yamaguchi [287] suggested the eutectic temperature of 1080 °C, Buist *et al.* [288] plotted his liquidus down to as low as 1036 °C. The

limiting slope of the Cu_2O liquidus is more consistent with the results of Buist *et al.* [288]. The phase diagram calculated from the optimization of Khvan *et al.* [177] is also shown in Figure 6.18.

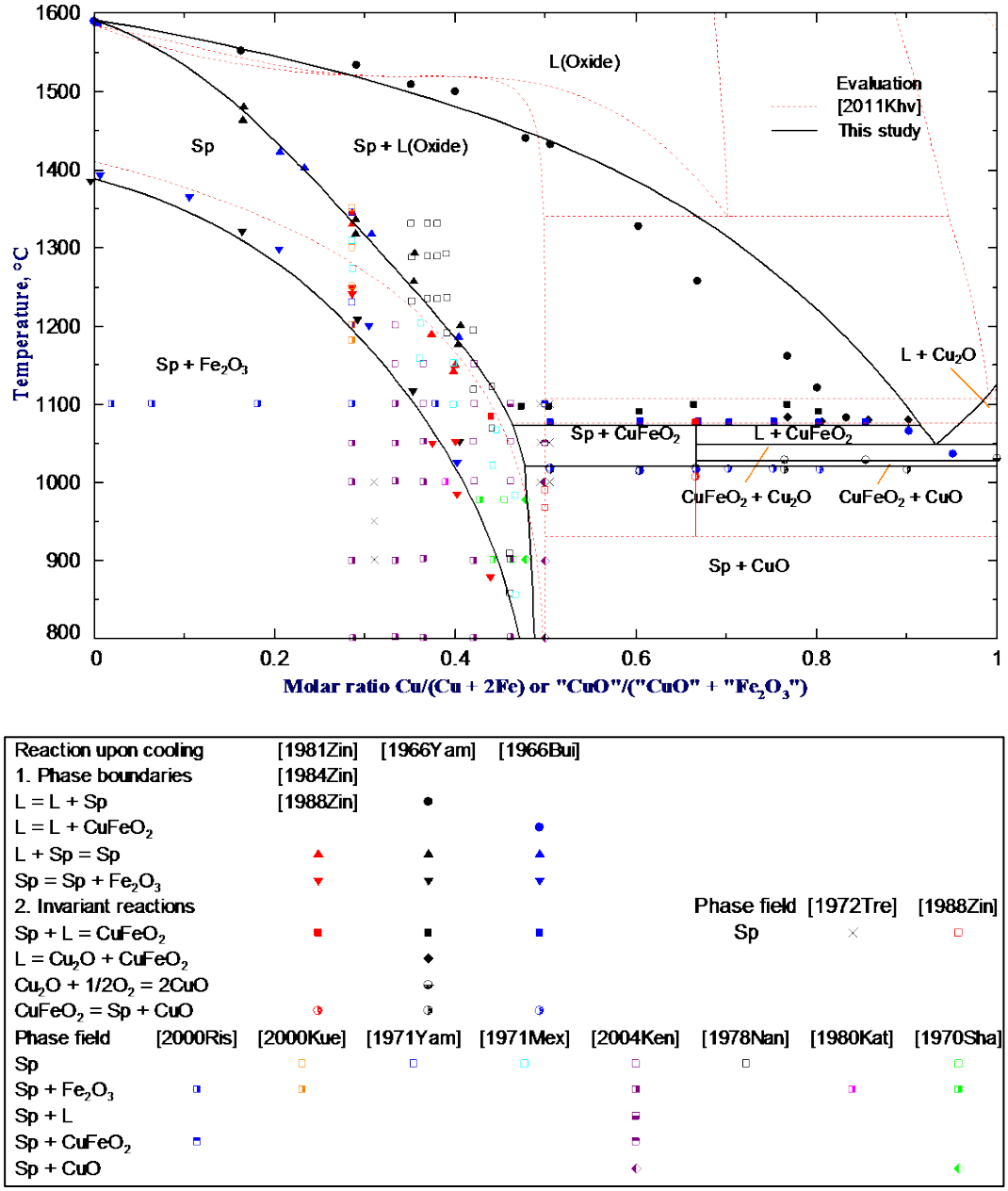

Figure 6.18. Phase diagram of the Cu–Fe–O system in air. Experimental points are from References [257, 266, 270, 287-295], solid lines are calculated from the model parameters optimized in the present study and dashed lines are calculated from the optimization of Khvan *et al.* [177].

The phase diagram of the Cu–Fe–O system in oxygen is shown in Figure 6.19. It was studied by Gadalla and White [296], who used the same technique as Buist *et al.* [288]. Small deviations of the

calculated phase boundaries from the experimental points of Buist *et al.* [288] and Gadalla and White [296] in Figures 18 and 19 may be attributed to the uncertainties inherent in the dissociation curves method, where the location of a phase boundary is obtained from a discontinuity in the weight curves that are measured with a fairly large step (e.g. see Figure 6 in Reference [288]).

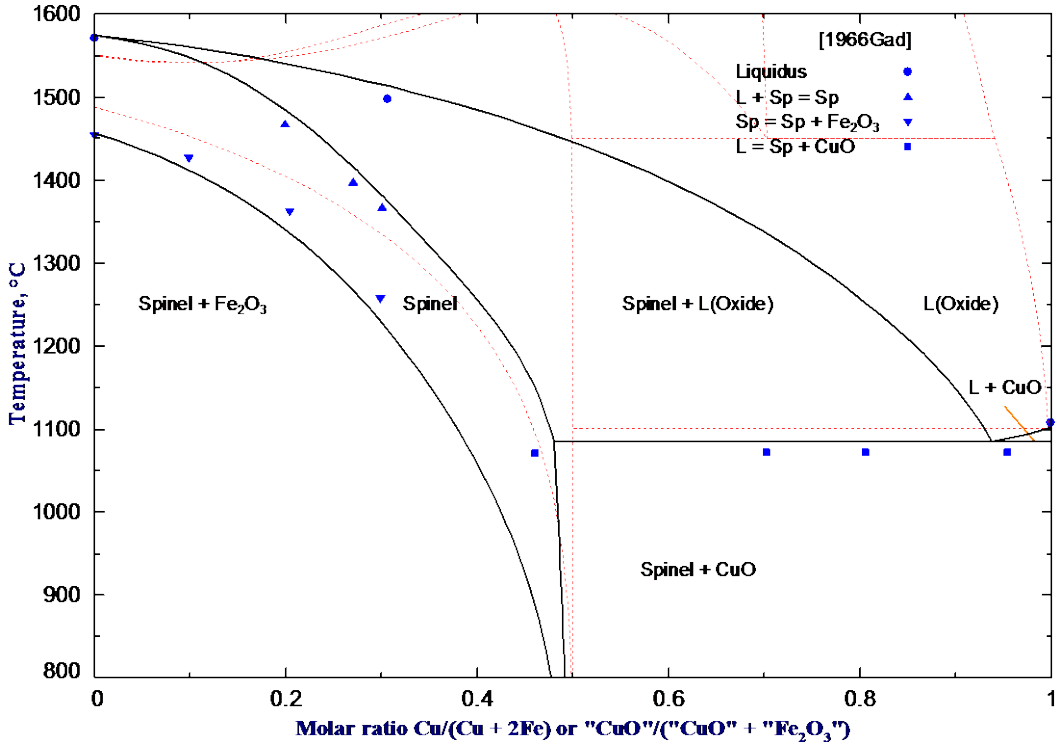

Figure 6.19. Phase diagram of the Cu–Fe–O system at $P(O_2)$ = 1 atm. Experimental points are from Gadalla and White [296], solid lines are calculated from the model parameters optimized in the present study and dotted lines are calculated from the optimization of Khvan *et al.* [177].

6.4.5 Oxygen non-stoichiometry of spinel

The oxygen non-stoichiometry of spinel was studied by Simsa *et al.* [251, 259] and Tret'yakov *et al.* [260]. In the study of Simsa *et al.* [251, 259], a polycrystalline spinel sample with the $Cu_{0.52}Fe_{2.48}O_{4+\gamma}$ composition was annealed at 1245-1255 °C in atmosphere with controlled $P(O_2)$ that varied from 0.01 to 1 atm. The oxygen content of quenched samples was obtained by wet chemical analysis, which was the potentiometric titration of Fe^{2+} using Mohr's salt. The measured values of γ varied between –0.068 and +0.055, depending on the oxygen pressure. As can be seen from Figure 6.20, the results are in excellent agreement with the calculated isobars. Clearly, the measurements at lower oxygen pressures correspond not to single-phase spinel, but to the spinel +

liquid oxide phase region. It should be noted that the phase composition was verified by X-ray diffraction only for the samples prepared in air.

Tret'yakov *et al.* [260] varied the oxygen content in spinel samples by coulometric titration. Samples were prepared by annealing in air at 1000 °C. According to chemical analysis, the following ferrites were obtained: $Cu_{0.984}Fe_{2.016}O_{4+\gamma}$, $Cu_{1.011}Fe_{1.989}O_{4+\gamma}$ and $Cu_{0.551}Fe_{2.449}O_{4+\gamma}$. Even though the samples were reported [260] to be single-phase spinels based on X-ray diffraction conducted before the coulometric titration, these compositions fall outside the spinel stability field in air measured by other authors (see crosses in Figure 6.18). The coulometric measurements for the last sample were made at 900, 950 and 1000 °C. Even if $P(O_2)$ is not fixed by equilibrium with air, the spinel phase of this composition is stable only above ⌴ 980 °C as is evident from Figure 6.9. Finally, the oxygen pressures reported by Tret'yakov *et al.* [260] cannot be reconciled with the results of Simsa *et al.* [251, 259]. Most likely, the measurements of Tret'yakov *et al.* [260] correspond to non-equilibrium heterogeneous mixtures.

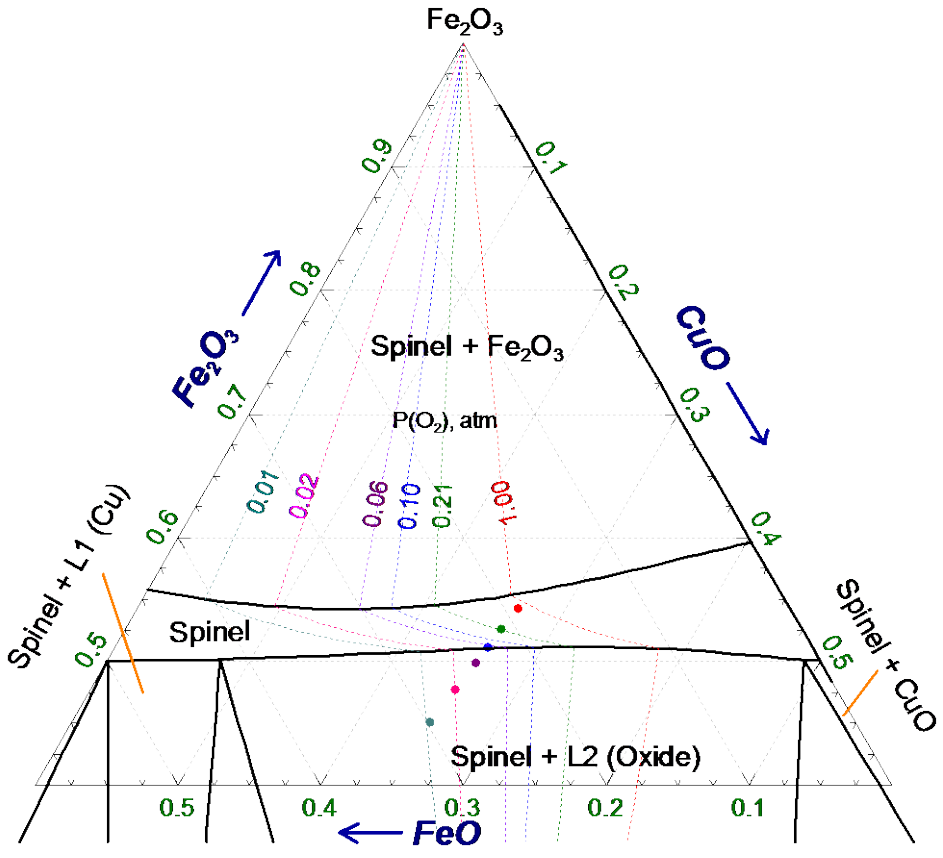

Figure 6.20. Calculated Fe_3O_4–$CuFe_2O_4$–Fe_2O_3 region of the Cu–Fe–O phase diagram at 1250 °C and *P* = 1 atm. Calculated oxygen isobars are shown by dotted lines and correspond to experimental points [251, 259].

6.4.6 Solubility of oxygen in liquid Cu–Fe alloys

The activities of oxygen in liquid Cu–Fe alloys were studied by Floridis and Chipman [196], Fischer *et al.* [297], Tankins [298-300], Biswas and Seow [301] and Oishi *et al.* [282]. To the best of our knowledge, the solubility and activity of oxygen in fcc and bcc Cu–Fe alloys have not been reported.

Fischer *et al.* [297] measured the EMF of the following galvanic cell:

$$\mathrm{Air}\left|\ \mathrm{ZrO_2}\ (+\mathrm{CaO},\ \mathrm{MgO})\right|\ \mathrm{O(in\ liquid\ metal)},\ \mathrm{Pt} \tag{6.26}$$

The measurements started with pure liquid iron in a corundum crucible, then copper was added at constant temperature. Upon reaching constant EMF readings, the liquid metal phase of certain Cu/(Cu + Fe) ratio was sampled and analyzed for iron, copper and oxygen. The mole fraction of oxygen was found to be between 0.001 and 0.004 by the inert gas carrier method. No primary experimental data were reported by the authors. Instead, the results were presented as the difference between the EMF measured for Cu–Fe melts and for liquid iron at the same oxygen content [297]. The optimized thermodynamic properties of Fe–O liquid [227] were used in the present study to compare the data of Fischer *et al.* [297] with the results of other authors. In this work we used our optimized values of $\Delta G^{\circ}_{1\%\mathrm{O}(liq)}$ for the Cu–O [114] and Fe–O systems to recalculate results of Fischer *et al.* [297] into $\Delta G^{\circ}_{1\%\mathrm{O}(liq)}$ in ternary Cu–Fe–O system at 1600 °C.

Floridis and Chipman [196] equilibrated liquid metal in MgO or Al_2O_3 crucibles with a controlled mixture of water vapor, hydrogen and argon. The samples were quenched in a stream of cold helium and analyzed for oxygen by the vacuum fusion method. The mole fraction of oxygen varied from 0.002 to 0.004. The experimental results were recalculated to the "equilibrium constant"

$$K_{eq} = \frac{P(\mathrm{H_2O})}{P(\mathrm{H_2}) \cdot \mathrm{wt\ \%\ O}} \tag{6.27}$$

which was presented as a function of wt % O and wt % Cu.

Biswas and Seow [301] also equilibrated Cu–Fe liquid alloys in alumina crucibles with H_2–H_2O–Ar mixtures. The amount of oxygen dissolved in the liquid was obtained by measuring the increase of weight during equilibration. The results were presented as K_{eq} versus wt % O curves at constant temperature and wt % Fe.

Tankins [298-300] bubbled H_2–H_2O–Ar mixtures through Cu–Fe melts in alumina crucibles. After equilibration, the samples were quenched and analyzed for oxygen by the vacuum fusion method. The primary data were reported only for some samples. The mole fraction of O was around 0.001–0.002. K_{eq} was given as a function of 1/*T* for several Cu–Fe alloys. The results were also summarized as the composition dependence of the "Gibbs energy of dissolution of oxygen in liquid metal at infinite dilution with 1 mole % O liquid and 1 atm O_2 gas as reference states" defined as:

$$\Delta G^{\circ}_{1\%\mathrm{O}(liq)}(T) \equiv RT \ln\left(\frac{\gamma^{\circ}_{\mathrm{O}}(T)}{100}\right) = \lim_{X_{\mathrm{O}}\to 0}\left[-RT\ln\left(\frac{100X_{\mathrm{O}}}{\sqrt{P(\mathrm{O}_2), atm}}\right)\right] \qquad (6.28)$$

where *R* is the universal gas constant, $\gamma^{\circ}_{\mathrm{O}}(T)$ is the activity coefficient of oxygen at infinite dilution, X_{O} is the mole fraction of oxygen and $P(\mathrm{O}_2)$ is the equilibrium partial pressure of oxygen. As was discussed in more detail earlier [114], it is common practice to use this Gibbs energy to present the measurements of the activity of oxygen in liquid metals, because $\Delta G^{\circ}_{1\%\mathrm{O}(liq)}(T)$ is a nearly linear function of temperature.

The experimental results of different authors obtained at various temperatures, Cu/Fe ratios and oxygen concentrations can be compared if recalculated to $\Delta G^{\circ}_{1\%\mathrm{O}(liq)}(T)$. The condition of infinite dilution, $X_{\mathrm{O}} \to 0$, is obeyed for oxygen dissolved in Cu–Fe alloys because the solubility of oxygen is very small. Indeed, Floridis and Chipman [196] reported that K_{eq} was nearly independent of the wt % O up to the oxygen saturation for every studied Cu–Fe alloy. This means that the expression in the square brackets of Equation (6.28) is also nearly independent of the oxygen content.

The $\frac{P(\mathrm{H_2O})}{P(\mathrm{H_2})}$ ratios of Floridis and Chipman [196], Tankins [298-300] and Biswas and Seow [301] were recalculated to $P(O_2)$, using the FactSage thermodynamic database [4] for gaseous species. Then the values of $\Delta G^{\circ}_{1\%\mathrm{O}(liq)}(T)$ were calculated from Equation (6.28). The $P(O_2)$ data of Oishi *et al.* [282] obtained at oxygen saturation and discussed in Section 6.4.4 were also recalculated into $\Delta G^{\circ}_{1\%\mathrm{O}(liq)}(T)$. As can be seen from Figure 6.21, the results of Fischer *et al.* [297] and Floridis and Chipman [196] are somewhat higher than those of Tankins [298-300], while the measurements of Oishi *et al.* [282] are scattered between the two sets. Overall, the experimental data are in fairly

good agreement and the present optimization appears to be more consistent with the former two studies.

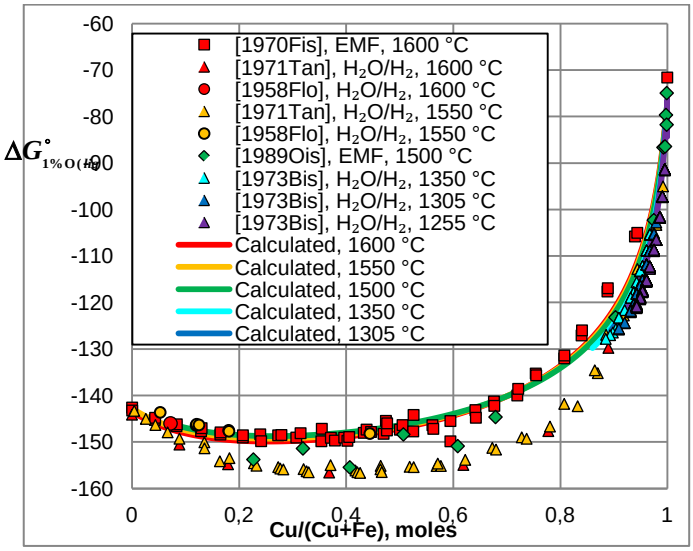

Figure 6.21. Gibbs energy of dissolution of oxygen in liquid Cu–Fe alloys at infinite dilution with 1 mole % O liquid and 1 atm O_2 gas as reference states: experimental points [196, 282, 297-301] and calculated lines.

6.4.7 $CuFeO_2$ (Delafossite)

6.4.7.1 Literature data

Delafossite ($CuFeO_2$) is a stoichiometric compound, Pearson symbol *hR**, space group $R\bar{3}m$, prototype $CuFeO_2$ [232]. The low-temperature heat capacity of $CuFeO_2$ was measured by Barany *et al.* [269] from 52 to 296 K (-221 to 23 °C). By integrating these data, they obtained the entropy of $CuFeO_2$ at 25 °C, $S^{o}_{298.15K}(CuFeO_2)$ = 88.7 J·mol^{-1}·K^{-1}. In fact, delafossite undergoes a magnetic transition with a Neel temperature of 13±3 K [302, 303]. The magnetic transition gives a contribution to the heat capacity and entropy, which was not taken into account by Barany *et al.* [269], therefore, their entropy value must be lower than the real standard entropy at 25 °C. The heat capacity of $CuFeO_2$ is shown in Figure 6.22.

Barany *et al.* [269] has also measured the heat content of $CuFeO_2$ between 125 and 1230 °C by drop calorimetry. These data are plotted in Figure 6.23. The samples were sealed in Pt–Rh capsules, which means that $P(O_2)$ was not fixed externally. The heat content data define the high–temperature

heat capacity, as well as the temperature and the heat of fusion of $CuFeO_2$. Delafossite melts incongruently, decomposing into liquid and spinel.

The enthalpy of formation was measured by Barany *et al.* [269] by dissolution of delafossite in the $K_2Cr_2O_7$–H_2SO_4 aqueous solution at 73.7 °C. The determination of the enthalpy of formation of $CuFeO_2$ from oxides by Hess law required the enthalpies of 10 other reactions. Finally, the enthalpy $\Delta_f^{ox}H(25\ ^\circ\mathrm{C}) = -34.9\ \mathrm{kJ\cdot mol^{-1}}$ was obtained for the reaction

$$0.5Cu_2O + 0.5Fe_2O_3 = CuFeO_2 \qquad (6.29)$$

The enthalpy of formation and entropy of delafossite are also constrained by the oxygen potential data for the three-phase equilibria involving $CuFeO_2$ shown in Figure 6.10.

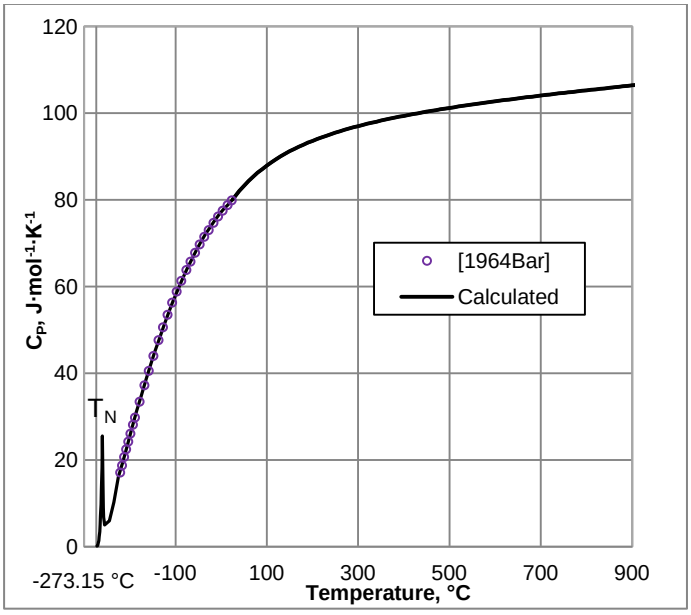

Figure 6.22. Heat capacity of $CuFeO_2$. Experimental points [269] and calculated line.

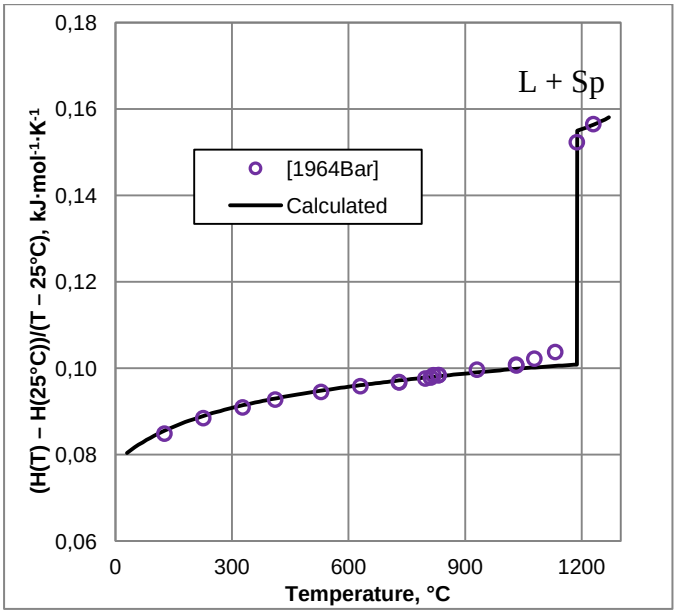

Figure 6.23. Heat content of $CuFeO_2$. Experimental points [269] and calculated line. The break in the heat content corresponds to the incongruent melting of $CuFeO_2$.

6.4.7.2 Thermodynamic assessment

The calculated heat capacity and heat content of $CuFeO_2$ shown in Figures 22 and 23 are in good agreement with the experimental data of Barany *et al.* [269].

The entropy and enthalpy of formation of $CuFeO_2$ were optimized to reproduce the experimental data on phase equilibria, in particular: the temperature of the transformation Cu + $2Fe_2O_3$ = $CuFeO_2$ + Fe_3O_4-based spinel (see Figure 6.9), the equilibrium $P(O_2)$ over the three-phase regions involving $CuFeO_2$ that are shown in Figure 6.10 and the stability region of $CuFeO_2$ in air shown in Figure 6.18. For example, the enthalpy of formation of $CuFeO_2$ defines the position of the fcc2 (Cu) + Sp1 + $CuFeO_2$ line in Figure 6.10 and the entropy constrains the slope. The calculated line is in excellent agreement with the EMF data of Jacob *et al.* [267].

The optimized entropy at 25 °C is 100.3 $J \cdot mol^{-1} \cdot K^{-1}$, which is higher than the value suggested by Barany *et al.* [269]. The difference may be attributed to the magnetic transition of $CuFeO_2$ to the antiferromagnetic state at 13±3 K [302, 303]. The peak on the heat capacity shown in Figure 6.22 was calculated using the equations proposed by Hillert and Jarl [8]. The magnetic moment corresponding to the transition was optimized to obtain $S^{o}_{298.15K}(CuFeO_2)$ = 100.3 $J \cdot mol^{-1} \cdot K^{-1}$ by integration of the heat capacity from 0 K. The resulting height of the peak appears to be reasonable.

The optimized enthalpy of formation of $CuFeO_2$ from oxides at 25 °C is –49.7 kJ·mol^{-1}, which is lower than the value of –34.9 kJ·mol^{-1} obtained by solution calorimetry [269]. It is believed that the difference is within the error limits of the calorimetric data. The experimental uncertainty must be relatively large, because the final enthalpy of formation from oxides was obtained by subtracting large heat effects of several reactions, which normally results in accumulation of experimental errors. The equilibrium oxygen partial pressures for the three-phase equilibria shown in Figure 6.10 are more accurate and constrain the enthalpy of formation with a smaller margin of error.

As can be seen from Figure 6.23, the temperature and the heat of fusion of $CuFeO_2$ are in excellent agreement within the heat content data of Barany *et al.* [269].

6.4.8 $CuFe_2O_4$ (Spinel)

6.4.8.1 Literature data

Barany *et al.* [269] reported that cupric ferrite $CuFe_2O_4$ is unstable with respect to its constituent oxides at 25 °C. At high temperatures and ambient pressure, pure stoichiometric $CuFe_2O_4$ does not exist either [257, 287], since the exact composition of $CuFe_2O_4$ is located in the $(1–x)CuFe_2O_4–xFe_3O_4$(solid solution) + CuO + O_2 phase field as can be seen in Figures 6 (b) and 9. However, x is small at medium temperatures and spinel approaches the composition of stoichiometric $CuFe_2O_4$ (see Figure 6.7 (b)).

Decomposition of $CuFe_2O_4$ into stable phases requires cation diffusion and is rather slow. The second order phase transition between the low-temperature tetragonal and high-temperature cubic modifications of $CuFe_2O_4$ was reported at about 400 °C [229, 230, 304, 305]. This transition does not require diffusion and can occur faster than the decomposition into equilibrium phases. However, Reznitskii and Filippova [230] reported that rapidly cooled cubic modification of $CuFe_2O_4$ remains cubic at room temperature and only slow cooling resulted in the violet tint, which is characteristic of the tetragonal modification.

The thermodynamic properties of $CuFe_2O_4$ have been reported in the literature. The heat capacity is shown in Figure 6.24. The C_P was measured by King and Kelley [306] over the temperature range from 54 to 296 K (–219 to 23 °C). The sample was quenched from 900 °C and X-ray analysis revealed the cubic spinel structure, even though the tetragonal modification is thermodynamically more stable at low temperatures. The residual configurational entropy at 0 K

was tentatively assumed to be 5.8 $J \cdot mol^{-1}K^{-1}$, which is one-half of the configurational entropy of completely inverse spinel under the assumption of random mixing: $-2R(0.5\ln 0.5 + 0.5\ln 0.5)$. Based on this assumption and the C_P measurements, King and Kelley [306] calculated the entropy at 25 °C: S(25 °C, $CuFe_2O_4$) = 135.2 (from the integration of C_P) + 5.8 (S at 0 K) = 141.0 $J \cdot mol^{-1}K^{-1}$.

The second order phase transition between the low-temperature tetragonal and high-temperature cubic modifications of $CuFe_2O_4$ was reported at about 400 °C [229, 230, 304, 305]. The tetragonal-cubic transition is the left λ-peak in Figure 6.24. The C_P measurements by adiabatic calorimetry of Inoue and Iida [229] and Reznitskii and Filippova [230] show similar transition temperatures, but somewhat different widths of the λ-peak. Presumably, this may be attributed to incomplete cubic to tetragonal transition of the sample of Reznitskii and Filippova [230] on cooling. The right λ-peak in Figure 6.24 is the magnetic transition of cubic $CuFe_2O_4$, which is ferrimagnetic [232] at room temperature and has a Curie temperature of 500±10 °C [307, 308].

Barany *et al.* [269] measured the heat content of $CuFe_2O_4$ by drop calorimetry (Figure 6.25). The sample was annealed at 800 to 850 °C, but no information on the quenching procedure and the crystal structure of the sample was reported. The heat of solution of $CuFe_2O_4$ in $H_2SO_4/K_2Cr_2O_7$ at 73.7 °C was also measured. Assuming that the samples for the heat content and heat of solution measurements were the same, it is possible to calculate the enthalpy of formation of $CuFe_2O_4$ from CuO and Fe_2O_3 in the temperature interval of 25 to 830 °C. Navrotsky and Kleppa [309] obtained the enthalpy of formation of $CuFe_2O_4$ from oxides at 697 °C by high-temperature drop solution calorimetry, measuring the heats of dissolution of $CuFe_2O_4$, CuO and Fe_2O_3 in molten $9PbO{:}3CdO{:}4B_2O_3$. The $CuFe_2O_4$ sample was sintered from pure oxides at 900 °C and quenched. The obtained enthalpy of formation of $CuFe_2O_4$ from oxides at 697 °C is 21.1 $kJ \cdot mol^{-1}$ [309], which is in good agreement with the value of 19.2 $kJ \cdot mol^{-1}$ calculated from the heat content and heat of solution data of Barany *et al.* [269].

6.4.8.2 Thermodynamic assessment

The heat capacity of cubic spinel is the sum of three contributions: lattice (mainly vibrational), magnetic and “configurational”. The configurational part originates from the heat effect that is caused by the change in the distribution of cations between the sublattices with temperature. This part is not present in the C_P measurements at relatively low temperatures because the cation distribution is frozen and does not change on the time scale of the experiment. The configurational

contribution would be maximized for very slow measurements where the cation distribution always attains equilibrium values. As a first approximation and due to the lack of any experimental evidence to the contrary, it was assumed that the degree of inversion in $CuFe_2O_4$ does not have a large effect on both the lattice and magnetic contributions to the C_P. The calculated lines in Figure 6.24 show the optimized heat capacity of *cubic* $CuFe_2O_4$. The lattice and magnetic contributions were optimized to fit the low-temperature heat capacity measured by King and Kelley [306], the data of Inoue and Iida [8] above 415 °C and the heat content data of Barany *et al.* [269] shown in Figure 6.25. The heat effect of changes in the cation distribution and thus the configurational part of the C_P comes from the optimization of all phase equilibria at high temperatures involving the spinel phase. As can be seen from Figure 6.25, the heat contents measured by Barany *et al.* [269] above about 500 °C fall between the dotted and solid lines, which were calculated assuming no variation in the cation distribution during the experiments or the equilibrium cation distribution, respectively. At these temperatures, some partial ordering of cations between the sublattices could have occurred.

The entropy of cubic $CuFe_2O_4$ is well constrained by the oxygen partial pressure data shown in Figure 6.10 and the experimental high-temperature phase equilibria. The entropy of $CuFe_2O_4$ at 900 °C obtained by the optimization of these high-temperature data is 413.7 $J \cdot mol^{-1}K^{-1}$, which is in excellent agreement with the value of 414.5 $J \cdot mol^{-1}K^{-1}$ calculated by the integration of the C_P shown by the solid line in Figure 6.24 from -273.15 to 900 °C, assuming that the residual entropy at -273.15 °C is the configurational entropy of the completely inverse spinel.

The measured enthalpy of formation of spinel should depend upon the cation distribution between the sublattices in the studied samples. It is not known what was the degree of inversion for the samples used in the calorimetric measurements of Barany *et al.* [269] and of Navrotsky and Kleppa [309], but the cation distribution probably corresponds to a temperature between 900 and 697 °C. The calculated enthalpies of formation of $CuFe_2O_4$ from CuO and Fe_2O_3 at 697 °C for the samples with the equilibrium degree of inversion and with the one frozen from 900 °C is 19.6 $kJ \cdot mol^{-1}$ and 20.9 $kJ \cdot mol^{-1}$, respectively. This is in excellent agreement with the experimental values of 19.2 $kJ \cdot mol^{-1}$ and 21.1 $kJ \cdot mol^{-1}$ mentioned in the previous section. Hence, the uncertainty in the calorimetric measurements due to unknown cation distribution in $CuFe_2O_4$ should be less than 1.3 $kJ \cdot mol^{-1}$.

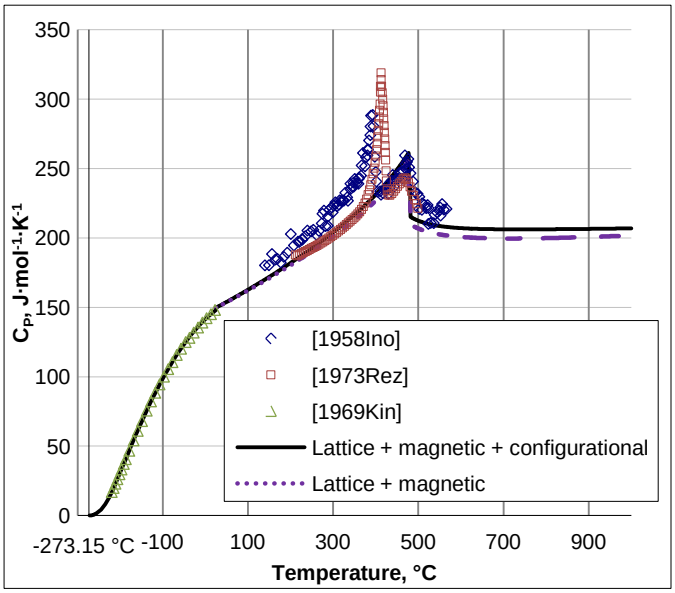

Figure 6.24. Heat capacity of $CuFe_2O_4$. Points indicate experimental data [229, 230, 306]. Calculated solid and dotted lines correspond to cubic spinel with equilibrium and with frozen cation distributions, respectively.

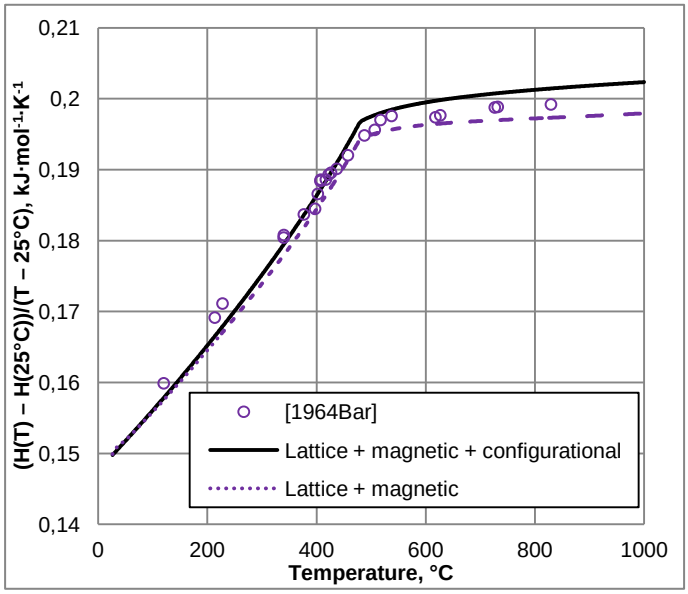

Figure 6.25. Heat content of $CuFe_2O_4$. Points are experimental data of Barany *et al.* [269]. Calculated solid and dotted lines correspond to *cubic* spinel with equilibrium and with frozen cation distributions, respectively.

6.5 Results of optimization

The parameters of the models described in Section 6.3 were obtained by an iterative procedure. At first, the thermodynamic properties of delafossite, $CuFeO_2$, and of the $CuFe_2O_4$ end-member of the spinel solution were optimized as discussed in Sections 6.4.7.2 and 6.4.8.2. Phase diagrams and

equilibrium oxygen partial pressures were calculated and compared with the experimental data. Then, the necessary excess parameters were introduced for the spinel and monoxide solid solutions. After the subsolidus phase equilibria were adequately reproduced, the properties of the liquid phase were optimized. Finally, all parameters were optimized simultaneously in order to obtain one set which describes best the thermodynamic properties, oxygen pressures and phase diagram data, distribution of cations between the spinel sublattices, etc. The calculated lines in all figures were obtained with the final set of optimized model parameters which are given in Table 6-1 and 2.

For the monoxide solid solution, a sufficiently large positive enthalpy *H*(CuO, monoxide)–*H*(CuO, tenorite) was introduced to suppress formation of the monoxide solution in the CuO-rich part of the system. Then, negative interaction parameters $q^{00}_{CuO,FeO}$ and $q^{00}_{CuO,FeO_{1.5}}$ were added to describe the data of Katkov and Lykasov [231]. The calculated solubility of CuO in wüstite and the oxygen partial pressure in the monoxide region of the Cu–Fe–O system are shown in Figures 12 and 13. For the $q^{00}_{CuO,FeO}$ parameter, the positive temperature dependence was required to suppress the solubility of CuO at high temperatures in order to describe the liquidus data in the Ca–Cu–Fe–O–Si system at 1300 °C [1].

The heat capacity, entropy and enthalpy of formation of $CuFe_2O_4$ are reflected in the parameter $F_{Cu^{+2}Fe^{+3}}$ of the spinel model, which is the Gibbs energy (per atom) of the completely normal, hypothetical simple spinel $CuFe_2O_4$. Parameters $I_{Cu^{+2}Fe^{+3}}$ and $\Delta_{Cu^{+2}Fe^{+3}}$ were used to describe the degree of inversion and the thermodynamic properties of the real spinel $CuFe_2O_4$. All experimental data on $CuFe_2O_4$ mentioned above, including the temperature dependence of the cation distribution between the tetrahedral and octahedral sites shown in Figure 6.4, are well reproduced by the model. The cation distribution has a strong effect on phase equilibria.

The vacancy parameter $\Delta_{Fe^{+3}Cu^{+2}Va}$ affects the amount of vacancies and oxygen nonstoichiometry in spinel. It was optimized to reproduce the oxygen isobars shown in Figure 6.20.

Parameters $\Delta_{Fe^{+3}Fe^{+2}Cu^{2+}}$, $\Delta_{Fe^{+3}Cu^{+2}Fe^{2+}}$ and $M_{Fe^{+2}Cu^{+2}}$ can be used for reproducing the thermodynamic properties of the spinel solution between Fe_3O_4 and $CuFe_2O_4$. The first parameter was set equal to zero and the last two parameters were optimized to fit all available subsolidus phase equilibria shown in Figures 6 to 11. These parameters also have a strong effect on the cation distribution shown in Figure 6.5. The isothermal sections of the Cu–Fe–O phase diagram in Figures

6 to 8 are in agreement with the evaluation of Perrot *et al.* [232]. The Fe_3O_4–$CuFe_2O_4$ section presented in Figure 6.9 was particularly important for constraining the parameters of the spinel model. The temperature of eutectoid decomposition of spinel and the calculated phase boundaries are in excellent agreement with the experimental data summarized in Figure 6.9. The parameter $M_{Fe^{+2}Cu^{+2}}$ indirectly takes into account the formation of Cu^{+1} in spinel according to reaction (6.10).

Phase equilibria involving the liquid phase are shown in Figures 9, 14, 15, 17-19. The calculated enthalpy of fusion of $CuFeO_2$ can be compared with the experimental data in Figure 6.23. Three model parameters for the liquid phase, $g^{001}_{Fe^{III}O(Cu^{I})}$, $g^{001}_{Fe^{III}O(Cu^{II})}$ and $g^{001}_{Fe^{II}O(Cu^{I})}$, were optimized to fit all these data, including phase boundaries and equilibrium oxygen partial pressures. The experimental data on the activities of oxygen dissolved in metallic liquid are summarized in Figure 6.21 and reproduced by two additional model parameters, $g^{101}_{Fe^{II}O(Cu^{I})}$ and $g^{102}_{Cu^{I}O(Fe^{II})}$.

In general, the self-consistent set of model parameters optimized in the present study reproduces all reliable thermodynamic and phase equilibrium data within experimental error limits. As can be seen from Figures 11, 18, 19, this optimization describes the phase diagrams substantially better than the optimization reported by Khvan et *al.* [177].

6.6 Conclusions

A complete critical evaluation of all available phase diagram and thermodynamic data for the Cu–Fe–O system at a total pressure of 1 atm has been made, and parameters of thermodynamic models have been optimized to reproduce all experimental data within experimental error limits.

The evaluation/optimization of the Cu–Fe–O system reported in this study is part of a wider research program aimed at complete characterization of phase equilibria and thermodynamic properties of the entire eight-component system Cu–Al–Ca–Fe–Mg–Si–O–S for computer simulation of copper smelting and converting. In particular, a model for the liquid phase has been developed within the framework of the Quasichemical Formalism. It is applicable over the whole composition range from metallic to oxide liquid. The optimized model parameters can be used in combination with the earlier optimizations of the Cu–O–S and Fe–O–S systems [114, 227] to predict the solubility of oxygen in matte (sulfide liquid) and in liquid copper.

The model for spinel has been developed within the framework of the Compound Energy Formalism. The formation of Cu^{+1} by electron hopping due to the reaction $Cu^{+2} + Fe^{+2} \rightarrow Cu^{+1} + Fe^{+3}$ was taken into account indirectly by introducing an excess model parameter. The description of the Fe_3O_4–$CuFe_2O_4$ spinel solid solution obtained in this study forms the basis for adding copper to the multicomponent FactSage spinel database [4].

6.7 Acknowledgements

Financial assistance from the Natural Sciences and Engineering Research Council of Canada is gratefully acknowledged.

Table 6-1. Optimized properties of stoichiometric compounds in the Cu–Fe–O system

Compounds	**Temperature range or reference**	$\Delta H^{o}_{298.15}$ **J·mol^{-1}**	$S^{o}_{298.15}$ **J·mol^{-1}·K^{-1}**	$C_P(T)$ **J·mol^{-1}·K^{-1}**
Fe_2O_3, CuO, Cu_2O	[114, 227]			
$CuFeO_2$ (delafossite)	0–50 K	–498652.1	100.2620	$0.000963T + 6738.1770\times10^{-6}T^{2} + 0.05405T^{-0.5}$
	50–298 K			$-6.5371 + 0.487128T - 661.8136\times10^{-6}T^{2}$
	298–1273 K			$97.3800 + 0.008790T - 0.0004\times10^{-6}T^{2} - 1773515T^{-2}$
	>1273 K			107.3700
Magnetic properties	T_{Neel} = 14 K			Magnetic moment β = 2.54 Structure-dependent parameter P = 0.28

The Gibbs energy of formation of a compound from elements in their standard state at a temperature of T (K) and a pressure of 1 atm is given by $\Delta G = \Delta H^{o}_{298.15} - T S^{o}_{298.15} + \int_{298.15}^{T} C_P(T)dT - T\int_{298.15}^{T} \frac{C_P(T)}{T}dT$, where $\Delta H^{o}_{298.15}$ is the enthalpy of formation of the compound at 1 atm and 298.15 K, $S^{o}_{298.15}$ is the entropy of the compound at 1 atm and 298.15 K, and $C_P(T)$ is the heat capacity at constant pressure.

Table 6-2. Optimized model parameters for liquid and solid solutions in the Cu–Fe–O system

Solutions	**Temperature range or reference**	**Molar Gibbs energy J·mol^{-1}**
Liquid (Metal, Oxide)	Quasichemical Formalism (Cu^{I}, Cu^{II}, Fe^{II}, Fe^{III}, O); Grouping: Cu^{I}, Cu^{II},Fe^{II}, Fe^{III} in group 1; O in group 2	
Coordination numbers Z [114, 227]		
g°_{O}, $g^{\circ}_{Cu^{I}}$, $g^{\circ}_{Cu^{II}}$	[114]	
$g^{\circ}_{Fe^{II}}$, $g^{\circ}_{Fe^{III}}$	[227]	
Excess parameters Cu–O	[114]	
Excess parameters Fe–O	[227]	
$L^{0}_{Fe^{II},Cu^{I}}$	[225]	$15589.30 - 1.98846T$

Table 6-2. (Continued) Optimized model parameters for liquid and solid solutions in the Cu–Fe–O system

Solutions	**Temperature range or reference**	**Molar Gibbs energy J·mol^{-1}**
$L^{1}_{Fe^{II},Cu^{I}}$	[225]	–14023.54 + 4.82577T
$L^{2}_{Fe^{II},Cu^{I}}$	[225]	13807.18 − 4.80397T
$L^{0}_{Fe^{II},Fe^{III}} = L^{0}_{Cu^{I},Fe^{III}} = L^{0}_{Fe^{II},Cu^{II}} = L^{0}_{Cu^{I},Cu^{II}}$		83680
$g^{001}_{Fe^{III}O(Cu^{I})}$		3138.00
$g^{001}_{Fe^{III}O(Cu^{II})}$		23012.00
$g^{001}_{Fe^{II}O(Cu^{I})}$		33472.00
$g^{101}_{Fe^{II}O(Cu^{I})}$		–54392.00
$g^{102}_{Cu^{I}O(Fe^{II})}$		–37656.00
fcc (Fe-rich and Cu-rich metals)	Bragg-Williams (Cu, Fe, O); Grouping: Cu, Fe in group 1; O in group 2	
g°_{Fe} , g°_{Cu}	[114, 225, 227]	
g°_{O}	[114]	
$L^{0}_{Fe,O}$	[227]	
$L^{0}_{Cu,O}$	[114]	
$L^{0}_{Cu,\,Fe}$	[225]	48232.57 − 8.60954T
$L^{1}_{Cu,\,Fe}$	[225]	8861.88 − 5.28975T
Magnetic properties of Fe	[225]	T_{Neel} = 67 K, Magnetic moment β =0.70, Structure-dependent parameter P = 0.28

Table 6-2. (Continued) Optimized model parameters for liquid and solid solutions in the Cu–Fe–O system

Solutions	**Temperature range or reference**	**Molar Gibbs energy J·mol^{-1}**
bcc (Fe-rich)	Bragg-Williams (Cu, Fe, O)	
g°_{Fe} , g°_{O}	[225, 227]	
g°_{Cu}	298–1358 K	$-3753.5 + 129.2304T - 24.1124T\ln T - 0.002657T^2 + 52478.0T^{-1}$
	1358–3200 K	$-9525.3 + 182.5492T - 31.3800T\ln T + 3.64643\times10^{29}T^{-9}$
$L^0_{Fe,O}$	[227]	
$L^0_{Cu,Fe}$	[225]	$39257.98 - 4.14983T$
Magnetic properties of Fe	[225]	T_{Curie} = 1043 K, Magnetic moment β =2.22, Structure-dependent parameter P = 0.40
Monoxide (wüstite)	Bragg-Williams (FeO, $FeO_{1.5}$, CuO); Grouping: CuO, FeO in group 1; $FeO_{1.5}$ in group 2	
g^{o}_{FeO} , $g^{o}_{FeO_{1.5}}$, $q^{00}_{FeO,FeO_{1.5}}$, $q^{01}_{FeO,FeO_{1.5}}$	[227]	
g^{o}_{CuO}		G(CuO) + 17572.8
$q^{00}_{CuO,FeO}$		$-178545.23 + 55.7867T$
$q^{00}_{CuO,FeO_{1.5}}$		–36400.8
Spinel (Fe_3O_4–$CuFe_2O_4$)	Compound Energy Formalism: $(Cu^{+2},Fe^{+2},Fe^{+3})^{tetr}[Cu^{+2},Fe^{+2},Fe^{+3},Va]^{oct}_2O^{-2}_4$	
$7F_{Fe^{+2}Fe^{+3}}$, $I_{Fe^{+2}Fe^{+3}}$, $\Delta_{Fe^{+2}Fe^{+3}}$, $V_{Fe^{+3}}$, $\Delta_{Fe^{+3}Fe^{+2}Va}$	[21]	
$7F_{Cu^{+2}Fe^{+3}}$	0–52 K	$-968964.6 - 22.3197T + 0.022950T^2 - 1.069436\times10^{-3}T^3 - 0.1180138T^{1.5}$
	53–297 K	$-967475.1 - 189.1154T + 42.0000T\ln T - 0.522712T^2 + 0.228535\times10^{-3}T^3 - 10239T^{-1}$
	298–755 K	$-983332.3 + 585.0649T - 104.5582T\ln T - 0.072488T^2$
	755–1600 K	$-1004508.9 + 1059.4320T - 181.5856T\ln T - 0.007615T^2$

Table 6-2. (Continued) Optimized model parameters for liquid and solid solutions in the Cu–Fe–O system

Solutions	**Temperature range or reference**	**Molar Gibbs energy J·mol^{-1}**
$I_{Cu^{+2}Fe^{+3}}$		–22447.16 + 20.92000T
$\Delta_{Cu^{+2}Fe^{+3}}$		21448.86 + 13.38880T
$\Delta_{Fe^{+3}Cu^{+2}Va}$		94140.00
$\Delta_{Fe^{+3}Fe^{+2}Cu^{2+}}$		0
$\Delta_{Fe^{+3}Cu^{+2}Fe^{2+}}$		66944.00
$M_{Fe^{+2}Cu^{+2}}$		–188464.10 + 117.15200T
Magnetic properties		Structure-dependent parameter P =0.28
$\beta_{Fe^{+2}Fe^{+3}} = \beta^{i}_{Fe^{+2}Fe^{+3}}$	[21]	44.54
$T_{Fe^{+2}Fe^{+3}} = T^{i}_{Fe^{+2}Fe^{+3}}$	[21]	848 K
$\beta_{Cu^{+2}Fe^{+3}} = \beta^{i}_{Cu^{+2}Fe^{+3}}$		4.00
$T_{Cu^{+2}Fe^{+3}} = T^{i}_{Cu^{+2}Fe^{+3}}$		751 K

CHAPTER 7 EQUILIBRIA IN THE Cu–Fe–O–S SYSTEM

Equation Chapter (Next) Section 1

Previously obtained thermodynamic databases for the Cu–Fe–S, Cu–Fe–O, Fe–O–S and Cu–O–S ternary systems have been combined and used to predict thermodynamic equilibria in the quaternary Cu–Fe–O–S system. The available experimental data were compared with model predictions. Minor modifications of model parameters were required to better describe the experimental points in the quaternary system; the effect of these changes on the ternary subsystems was verified. The liquid phase over the whole composition range from metallic liquid to sulfide melt to oxide melt has been described by a single model developed within the framework of the quasichemical formalism. The obtained self-consistent set of model parameters can be used as a basis for development of a thermodynamic database for simulation of copper smelting and converting.

This is the fourth article in the series devoted to the ongoing research project which is aimed at developing a thermodynamic database for the simulation of copper extraction from sulfide concentrates. The first arlicle dealt with the Cu–O–S system [114], the second was devoted to the Fe–O–S system [227] and the third described the Cu–Fe–O system [172]. The Cu–Fe–S system was optimized earlier by P. Waldner [92], but has not been published yet.

The list of phases used in the Cu–Fe–O–S system is presented in Table 7-2. According to the evaluation of Rosenqvist [310], there is no quaternary phases in this system. Solid solubility between $CuSO_4$ and $FeSO_4$ is possible due to similarities in their structure, but it was not studied experimentally. No attempts of systematic thermodynamic modeling of the Cu–Fe–O–S system were found in the literature. In this study, the liquid phase, fcc and bcc metals are modeled as quaternary phases, that is all four components are included in the model. The solubility of O and S in solid metals is very small.

A region of the liquid phase originating from the Fe_2S–Cu_2S sulfides dissolves a significant amount of oxygen and is usually referred to as oxysulfide or matte in the literature. The copper industry is interested in having a good description of matte in order to optimize the copper yield during smelting and converting. Most of the experimental studies devoted to matte delivered empirical expressions relating the composition of matte and the activities of sulfur and oxygen.

As a matter of fact, empirical expressions have low predicting abilities outside the range, where the experimental points were directly obtained. On the other hand, in the present study, relations, between the molar fractions of Cu, Fe, O and S and $P(S_2)$ and $P(O_2)$ in the quaternary system have been obtained in a thermodynamically consistent manner. The available experimental data have been critically evaluated and compared with model predictions.

The ability to predict the formation and dissolution of spinel is also essential for the optimization of industrial processes. The spinel phase may cause difficulties in the smelting process either by forming a refractory crust, or, more seriously, by being present as finely dispersed skeletons in the slag which hinder the settling of matte droplets [210]. Activities of components in the system are the most important factors influencing the spinel precipitation. Relations between the matte composition, $P(S_2)$ and $P(O_2)$ and the formation of spinel will be discussed in detail in this article.

7.1 Thermodynamic models

The following section contains descriptions of thermodynamic models for the liquid solution, fcc and bcc metals and sulfide solid solutions used in this work. The models for the monoxide and spinel phases were discussed earlier [172]. The model parameters for all phases are listed in Table 7-2.

7.1.1 Liquid solution

A literature survey and a detailed description of models for the liquid phase in the Cu–O, Cu–S, Fe–O, Fe–S, Cu–Fe, Cu–O–S, Fe–O–S and Cu–Fe–O subsystems of the Cu–Fe–O–S system were given earlier [26, 114, 172, 227]. The liquid phase in the Cu–Fe–S system is discussed in the corresponding article [92]. The Modified Quasichemical Model (MQM) in pair approximation [16, 17] was used for all the systems, except Cu–Fe. A simple Bragg-Williams random mixing model was used for the Cu–Fe system.

In the present study, all solutions were joined together resulting in the (Cu^{I}, Cu^{II}, Fe^{II}, Fe^{III}, O, S) model. All species occupy the same sublattice. Numbers I, II and III are not charges, but rather “valences”, they are used to calculate the metal/nonmetal ratio corresponding to maximum short-range ordering (SRO). The components O and S have “valence” of II, thus maximum SRO

occurs at the compositions Cu^{I}:O = 2:1, Fe^{II}:S = 1:1, Fe^{III}:O = 2:3, etc. Fe^{III} and Cu^{II} appear only at relatively high oxygen partial pressures, of about 10^{-7} atm and 0.21 atm at 1200 °C, respectively. In the Cu–Fe and Cu–Fe–S subsystems, Cu and Fe exist almost exclusively as Cu^{I} and Fe^{II}, over the whole range of compositions. As all species are placed on one sublattice and are not charged, no condition of electroneutrality is imposed. Hence, the model represents the liquid phase from metals to oxides, to sulfides, to nonmetals.

Model parameters of MQM are the coordination numbers of constituents, binary parameters Δg_{AB} – the Gibbs energies of pair formation, and ternary parameters $\Delta g_{AB(C)}$, which give the effect of the presence of component C upon the energy of pair exchange reaction. Coordination numbers are composition-dependent; binary and ternary terms are expanded as empirical polynomials. The formulae and notations of the quasichemical formalism were described in detail elsewhere [16, 17] and [114, 227].

Extrapolation of binary terms into the Cu^{I}–Cu^{II}–Fe^{II}–Fe^{III}–O–S system is made by applying a grouping method [17]. The components are divided into two groups: metals (Cu^{I}, Cu^{II}, Fe^{II} and Fe^{III}) and nonmetals (O, S). By this means, in every ternary subsystem, either three components belong to the same group or one belongs to a different group. The “Kohler-like” extrapolation is applied in the first case; the “Toop-like” extrapolation is used in the second case, with different component considered as an asymmetric one.

7.1.2 Solid FCC and BCC metal

Sulfur and oxygen are soluble to a certain extent in solid the Cu–Fe metal phases, which have an fcc or a bcc structure at the conditions of interest. A simple Bragg-Williams random mixing model was used for both phases, with the following formula for the Gibbs energy (per mole of atoms):

$$g = (X_{Fe}g^{o}_{Fe} + X_{Cu}g^{o}_{Cu} + X_{O}g^{o}_{O} + X_{S}g^{o}_{S}) + RT(X_{Fe}\ln X_{Fe} + X_{Cu}\ln X_{Cu} + X_{O}\ln X_{O} + X_{S}\ln X_{S}) + X_{Fe}X_{S}L_{Fe,S} + X_{Fe}X_{O}L_{Fe,O} + X_{Cu}X_{O}L_{Cu,O} + X_{Cu}X_{S}L_{Cu,S} + X_{Cu}X_{Fe}L_{Cu,Fe} \quad (1)$$

where X_i and g_i° are the mole fraction and molar Gibbs energy of component i, $L_{i,j}$ represents an interaction energy between i and j, which can be a function of temperature and composition. No ternary terms were introduced.

7.1.3 Pyrrhotite, pyrite, ISS, covellite, digenite-bornite

Solid solutions in the Cu–Fe–S system were optimized [92] using a random mixing Bragg-Williams model:

$$g = \sum_i X_i g_i^o + RT \sum_i X_i \ln X_i + \sum_{i,j} X_i X_j L_{i,j} \quad (2)$$

High-temperature pyrrhotite $Fe_{1-x}S$ described by Waldner and Pelton [26] dissolves a certain amount of CuS. The (Fe, Cu, Vacancy):S model was chosen, which includes the following Gibbs energies of end-members: g^o_{FeS}, g^o_{CuS} and g^o_{VaS}.

A small solubility of CuS_2 in pyrite FeS_2 was described using the (Fe, Cu):S_2 model. The Gibbs energies of end-members in this case are $g^o_{FeS_2}$ and $g^o_{CuS_2}$.

The ternary solution phase, which does not emanate from any of the binary sub-systems, is usually denoted as ISS (intermediate solid solution) in the literature. A cubic sphalerite-type structure is reported for this phase. After extensive calculations carried out in the study by Waldner and Pelton [92], the (Cu_2,Fe,Vacancy):S model was selected. It should be noted that several authors who observed this phase experimentally denoted it as chalcopyrite $CuFeS_2$. In fact, chalcopyrite $CuFeS_2$ transforms to ISS around 560 °C [103]. Contrary to chalcopyrite, which can be treated as stoichiometric, ISS shows an extended homogeneity range. The Gibbs energies of the end-members in the model for ISS are $g^o_{Cu_2S}$, g^o_{FeS} and g^o_{VaS}.

A small solubility of FeS in covellite CuS was described by the model (Cu, Fe):S. In this case, the Gibbs energies of end-members are g^o_{CuS} and g^o_{FeS}.

Digenite, which is the name, used in the literature for the binary solution phase $Cu_{2+x}S$, and the bornite phase (Cu_5FeS_4) are described as one solution. The model with its optimized parameters predicts a miscibility gap between these phases at low temperatures, which is in agreement with the experimental observations [311]. This phase is represented as (Cu_2, Fe, Vacancy):S, with the following end-member Gibbs energies: $g^o_{Cu_2S}$, g^o_{FeS} and g^o_{VaS}.

7.2 Phase equilibria

The FactSage software [4] used in this study is capable to calculate the equilibrium for any number components in the system. For 4-component systems, when the overall composition, temperature and pressure are fixed, the software determines phases in equilibrium, their compositions, activities or partial pressures of species in the system. Some algorithms require the calculation of the Gibbs energy for the mesh of compositions, in order to construct the convex hull around the Gibbs energy surface in *n*-dimension space. They use the convex hull to determine the phases in equilibrium. Unlike these "geometric" algorithms, the one used in FactSage software performs "in point" equilibrium calculation, meaning that the Gibbs energy minimization procedure runs for every composition independently. The software respects the Gibbs phase rule automatically. It can use a series of "in point" equilibrium calculations for the construction of phase diagrams in Cartesian coordinates or in Gibbs triangle.

Topology of phase diagrams is defined by the Gibbs phase rule. For instance, isothermal sections of phase diagrams of ternary systems at constant pressure are commonly plotted in the so called Gibbs triangle (see Figure 7.1-Figure 7.4 as an example). The composition of a phase in a single-phase region is represented by an area. In a two-phase region, the composition of a phase lies on a line. In a three-phase region, the composition of each phase is invariant and is shown as a point[2]. These three points form vertices of the triangle. Inside each triangle, activities, partial pressures of species are fixed. The list of all the triangles for a given temperature and pressure, showing phases stable in equilibrium, is sometimes referred to as triangulation of a ternary system.

Similarly, it is possible to construct a "Gibbs tetrahedron" for the isothermal section of the phase diagram of the quaternary system. In this case, Gibbs triangles of ternary phase diagrams form four faces of the Gibbs tetrahedron. Inside, the composition of a phase in a single-phase region is represented by a volume. In a two-phase region, the composition of a phase lies on a surface. In a three-phase region, the composition of a phase is given by a line, the intersection of two surfaces. In a four-phase region, the composition of each phase is invariant and shown as a

[2] The composition of stoichiometric phases will always appear as a point on calculated diagrams, but this is a model approximation.

point. These four points form vertices of the four-phase tetrahedron. Inside each tetrahedron, activities, partial pressures of components and species are fixed. By analogy, we may call the list of all the tetrahedrons for a given temperature and pressure, showing phases stable in equilibrium, the “tetrangulation” of the quaternary system.

The isothermal sections of the phase diagrams of the ternary sub-systems Cu–O–S, Cu–Fe–S, Cu–Fe–O, Fe–O–S at 700 °C and 900 °C and P = 1 atm that represent the sides of the Cu–Fe–O–S tetrahedron are shown in Figure 7.1-Figure 7.4. The tetrahedrons themselves are shown in Figure 7.5. The calculation procedure was as follows. First, a grid was created inside the tetrahedron, with a total number of 9896 points. Then, “in point” equilibria were calculated using the Equilib module of the FactSage software [4]. Results were sorted by the fact whether the points of the grid belong to 1-, 2-, 3- or 4-phase equilibrium regions. The invariant four-phase equilibria in the Cu–Fe–O–S tetrahedron represented by 4-phase tetrahedrons are listed in Table 7-1. The relative sizes of 4-phase tetrahedrons may be compared by the number of points in the grid that they enclose (see last column in Table 7-1).

Table 7-1. Calculated four-phase invariant equilibria in the Cu–Fe–O–S system at 700, 900 and 1200 °C and P = 1 atm

Phases	$\log_{10}[P(O_2)$, atm]	$\log_{10}[P(S_2)$, atm]	$\log_{10}[P(SO_2)$, atm]	Size, %
T = 700 °C				
Monoxide + Bcc(Fe) + Pyrr + DB2	-21.6	-10.6	-11.4	9.7
Monoxide + Bcc(Fe) + Fcc(Cu) + DB2	-21.6	-11.5	-11.8	9.4
Monoxide + Fcc(Fe) + Fcc(Cu) + DB2	-21.7	-11.5	-11.8	8.5
Cu_2O + $CuFeO_2$ + Gas + DB1	-10.2	-10.8	0	5.8
Gas + Sp1 + Pyrr + ISS	-14.6	-2	0	4.0
Fe_2O_3 + $CuFeO_2$ + Gas + DB1	-10.7	-9.7	0	2.8
Cu_2O + $CuFeO_2$ + Fcc(Cu) + DB1	-10.5	-11	-0.3	2.7
Gas + Sp1 + ISS + DB2	-14.5	-2.2	0	2.7

Table 7-1. (Continued) Calculated four-phase invariant equilibria in the Cu–Fe–O–S system at 700, 900 and 1200 °C and P = 1 atm

Phases	$Log_{10}[P(O_2)]$, atm]	$Log_{10}[P(S_2)]$, atm]	$Log_{10}[P(SO_2)]$, atm]	Size, %
$CuFeO_2$ + Sp1 + Fcc(Cu) + DB1	-11.9	-11	-1.8	2.2
CuO + $CuO{\cdot}CuSO_4$ + Gas + Sp2	0	-37.1	-2.9	2.0
Sp1 + Monoxide + Fcc(Cu) + DB2	-20.7	-11.1	-10.6	1.8
Cu_2O + $CuFeO_2$ + $CuO{\cdot}CuSO_4$ + Gas	-5	-21.1	0	1.3
Gas + Sp1 + DB1 + DB2	-14.2	-2.9	0	1.3
Gas + Sp1 + Pyrr + DB2	-14.6	-2	0	1.0
Fe_2O_3 + $Fe_2(SO_4)_3$ + $CuSO_4$ + Gas	-2.1	-27.2	-0.1	1.0
Sp1 + Monoxide + Pyrr + DB2	-20.7	-9.6	-9.9	0.9
Sp1 + Fcc(Cu) + DB1 + DB2	-20.5	-11	-10.4	0.9
Fe_2O_3 + $CuFeO_2$ + $CuSO_4$ + Gas	-4.3	-22.6	0	0.7
Fe_2O_3 + $CuSO_4$ + $CuO{\cdot}CuSO_4$ + Gas	0	-35.7	-2.2	0.7
CuO + Cu_2O + $CuFeO_2$ + $CuO{\cdot}CuSO_4$	-4.2	-24.5	-0.8	0.6
Fe_2O_3 + $CuO{\cdot}CuSO_4$ + Gas + Sp2	0	-36.3	-2.6	0.6
Fe_2O_3 + Gas + Sp1 + DB1	-11.7	-7.8	0	0.4
CuO + $CuFeO_2$ + $CuO{\cdot}CuSO_4$ + Sp2	-3.1	-27.8	-1.4	0.3
Fe_2O_3 + $CuFeO_2$ + Sp1 + DB1	-11.5	-10.5	-1.2	0.2
Sp1 + Pyrr + ISS + DB2	-16.3	-4	-2.7	0.2
$CuFeO_2$ + $CuSO_4$ + $CuO{\cdot}CuSO_4$ + Gas	-4.5	-22.3	0	0.1
Fe_2O_3 + $CuFeO_2$ + $CuSO_4$ + $CuO{\cdot}CuSO_4$	-4.1	-23.5	-0.2	0.1
Fe_2O_3 + $CuFeO_2$ + $CuO{\cdot}CuSO_4$ + Sp2	-3.7	-25	-0.6	0.1
T = 900 °C				
Monoxide + Fcc(Fe) + Fcc(Cu) + DB2	-16.8	-8.9	-9	9.5
$CuFeO_2$ + Gas + Fcc(Cu) + DB1	-8	-8.6	0	5.5
Monoxide + L(Oxysulfide) + Fcc(Fe) + DB2	-16.8	-8.1	-8.6	4.0
Gas + Sp1 + L(Oxysulfide) + Pyrr	-11.5	-1.6	0	3.8
Gas + Sp1 + L(Oxysulfide) + DB2	-11.5	-1.6	0	3.0
Cu_2O + $CuFeO_2$ + Gas + Fcc(Cu)	-7.4	-9.8	0	3.0
$CuFeO_2$ + Gas + Sp1 + DB1	-8.1	-8.4	0	2.8
$CuFeO_2$ + Sp1 + Fcc(Cu) + DB1	-8.2	-8.6	-0.2	2.1
CuO + Cu_2O + $CuFeO_2$ + Gas	-1.8	-21	0	1.5
Sp1 + Monoxide + Fcc(Cu) + DB1	-14.8	-8.6	-6.8	1.3
Monoxide + L(Oxysulfide) + Bcc(Fe) + Pyrr	-16.8	-7.8	-8.4	0.6

Table 7-1. (Continued) Calculated four-phase invariant equilibria in the Cu–Fe–O–S system at 700, 900 and 1200 °C and P = 1 atm

Phases	$Log_{10}[P(O_2)$, atm]	$Log_{10}[P(S_2)$, atm]	$Log_{10}[P(SO_2)$, atm]	Size, %
$CuO + CuFeO_2$ + Gas + Sp2	-1.4	-21.9	0	0.6
Sp1 + Monoxide + L(Oxysulfide) + DB2	-14.8	-5.8	-5.5	0.3
Sp1 + Monoxide + L(Oxysulfide) + Pyrr	-14.8	-5.7	-5.4	0.2
$Fe_2O_3 + CuFeO_2$ + Gas + Sp1	-6.5	-11.6	0	0.1
$Fe_2O_3 + CuFeO_2$ + Gas + Sp2	-2.8	-19	0	0.1
Gas + L(Oxysulfide) + Pyrr + ISS	-12.2	-0.5	-0.2	0.1
Monoxide + L(Oxysulfide) + Bcc(Fe) + Fcc(Fe)	-16.8	-7.8	-8.4	0.0
Gas + L(Oxysulfide) + ISS + DB2	-12.2	-0.6	-0.2	0.0
T = 1200 °C				
Gas + Sp1 + L(Metal) + L(Oxysulfide)	-5.9	-6.2	0	8.2
Monoxide + L(Metal) + L(Oxysulfide) + Fcc(Fe)	-12	-6.6	-6.3	5.2
L(Metal) + L(Oxysulfide1) + L(Oxysulfide2) + Fcc(Fe)	-12	-6.6	-6.3	5.2
Sp1 + Monoxide + L(Metal) + L(Oxysulfide)	-8.8	-6.1	-2.9	0.7
Monoxide + L(Metal) + L(Oxysulfide1) + L(Oxysulfide2)	-12	-6.6	-6.3	0.6
Cu_2O + Gas + L(Metal) + L(Oxysulfide)	-4.2	-9.7	0	0.6
Monoxide + L(Oxysulfide) + Fcc(Fe) + Fcc(Cu)	-12	-6.7	-6.3	0.2

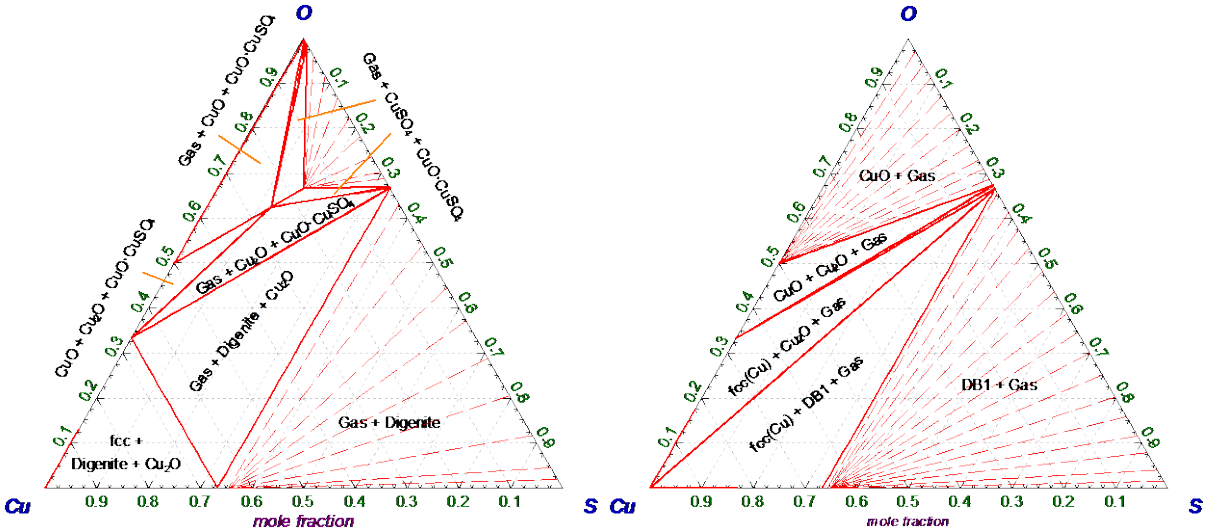

Figure 7.1. Isothermal section of the Cu–O–S phase diagram at 700 °C and 900 °C and P = 1 atm.

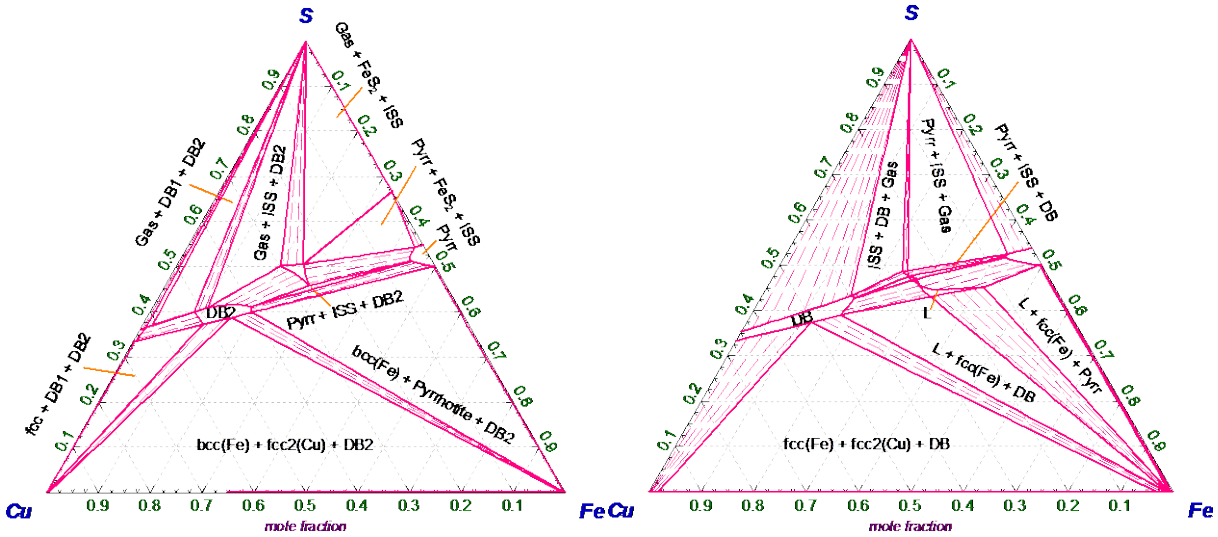

Figure 7.2. Isothermal section of the Cu–Fe–S phase diagram at 700 °C and 900 °C and P = 1 atm.

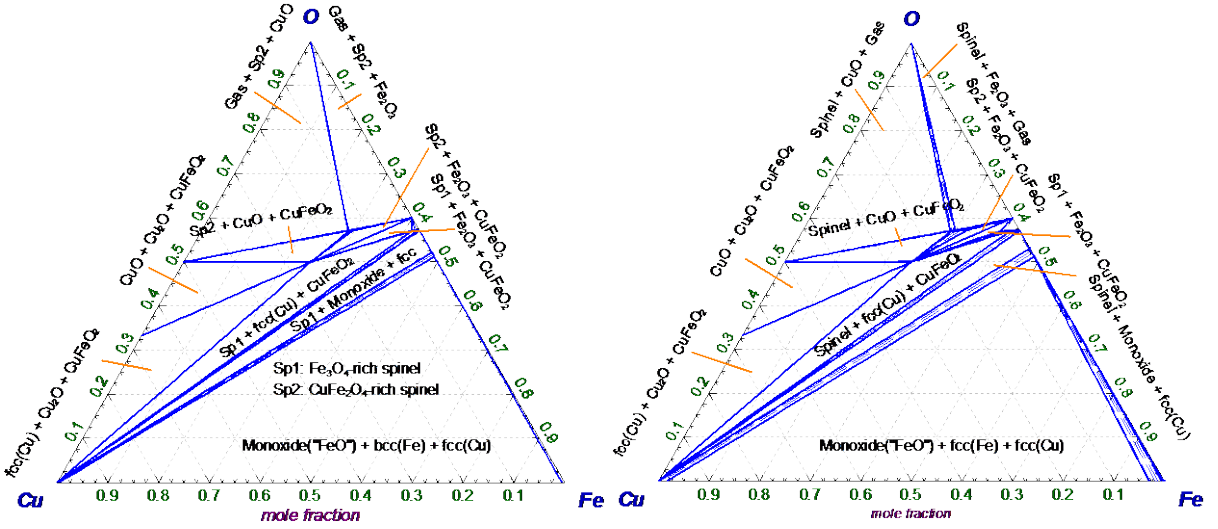

Figure 7.3. Isothermal section of the Cu–Fe–O phase diagram at 700 °C and 900 °C and P = 1 atm.

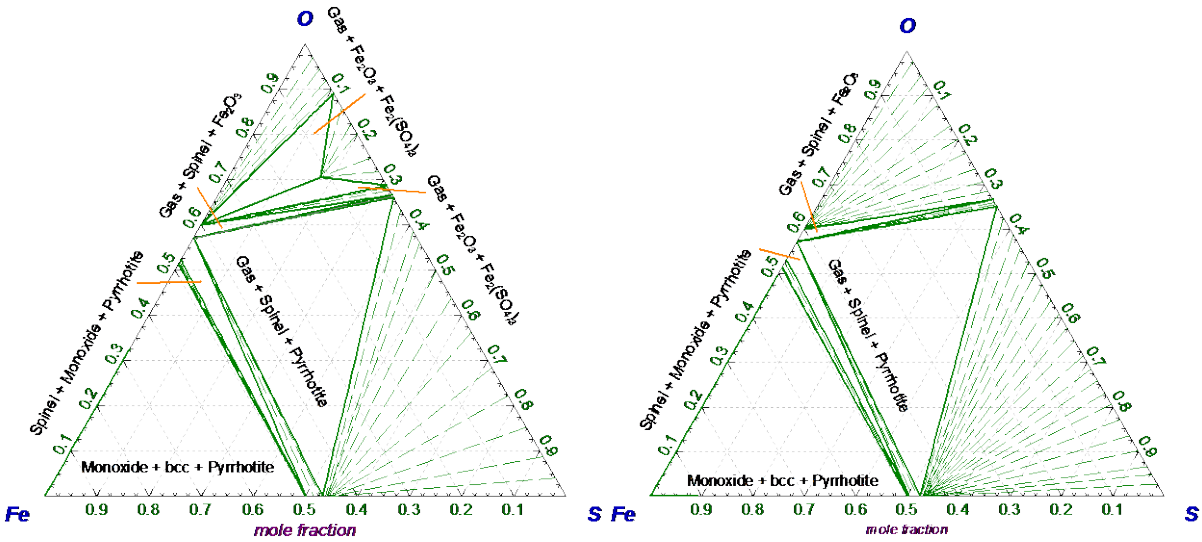

Figure 7.4. Isothermal section of the Fe–O–S phase diagram at 700 °C and 900 °C and P = 1 atm.

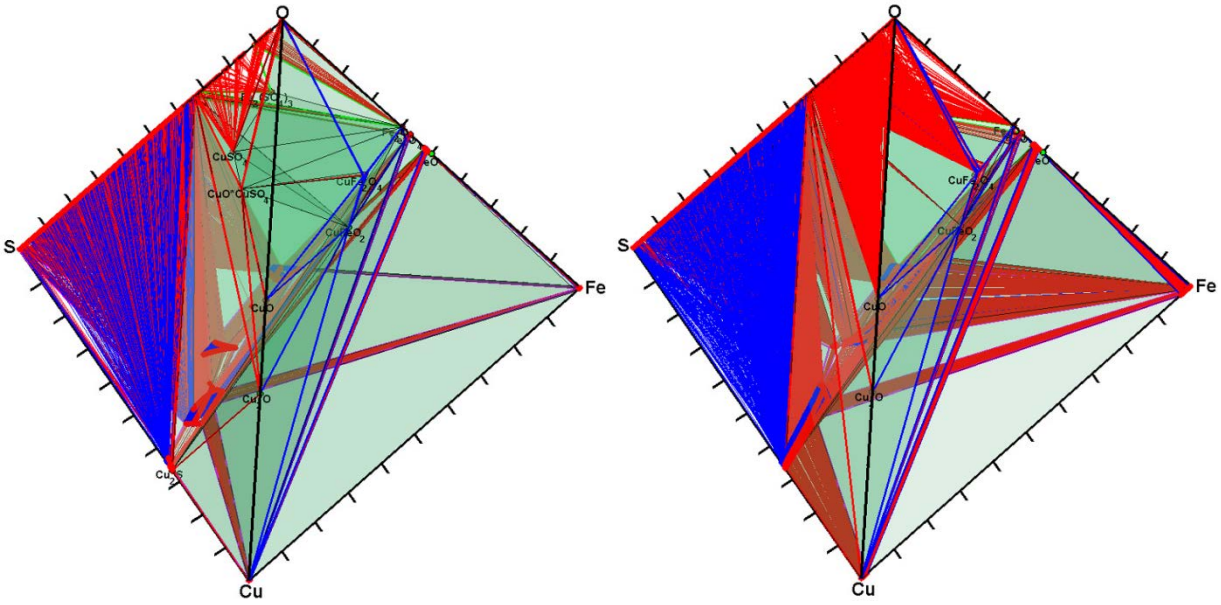

Figure 7.5. Isothermal section of the Cu–Fe–O–S phase diagram at 700 °C and 900 °C and P = 1 atm. 2-phase equilibria are shown using blue lines, 3-phase – using red lines, 4-phase equilibria – using black lines and facets. The 3-D figure files are available in the supplementary data. They may be opened by the MATLAB® software.

At 900 °C, liquid phase appears inside the Monoxide + Bcc(Fe) + Pyrr + DB2 tetrahedron. Yazawa and Kameda [100] conducted the thermal analysis and microscopic examination of the "Cu_2S"–"FeS"–"FeO" mixtures in an iron crucible. They observed a break in the cooling curves at 840 °C, which was related to the temperature of the quaternary eutectic Monoxide + Bcc(Fe) +

Pyrr + DB2 + L. In this study, the temperature of this eutectic is calculated as 840 °C. The calculated temperature of the Monoxide + Fcc(Fe) + Fcc(Cu) + DB2 + L eutectic is 1043 °C.

The liquid phase extends further with rising temperature and occupies a larger part of the Cu–Fe–O–S tetrahedron at 1200 °C. Phase equilibria at this temperature are shown in Figure 7.6-Figure 7.10. Calculations show that oxysulfide liquid is bounded by surfaces of saturation with Fe(fcc), spinel, liquid copper, monoxide and a sulfur-oxygen gas phase at 1 atm, which is in agreement with the evaluation of Rosenqvist [310]. It may be seen from Figure 7.10 that the appearance of metallic copper, oxysulfide and oxide liquids is predicted (3 blue areas). The latter is situated close to the Cu_2O–Fe_3O_4 section. All these liquids are modeled with one solution. In the oxysulfide liquid, there is an additional miscibility gap, between the Cu–Fe–S and Fe–S–O rich sides. It is shown with thin blue lines in Figure 7.10b. The existence of this miscibility gap will be discussed further in Section 7.3.

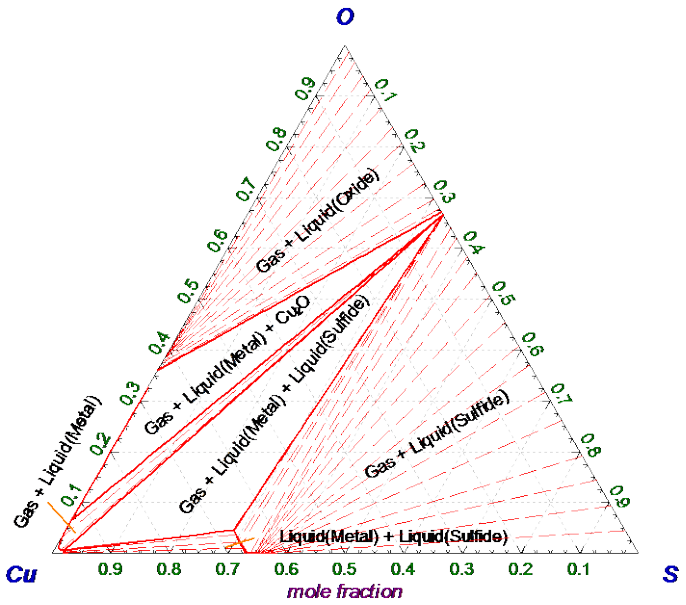

Figure 7.6. Isothermal section of the Cu–O–S phase diagram at 1200 °C and P = 1 atm.

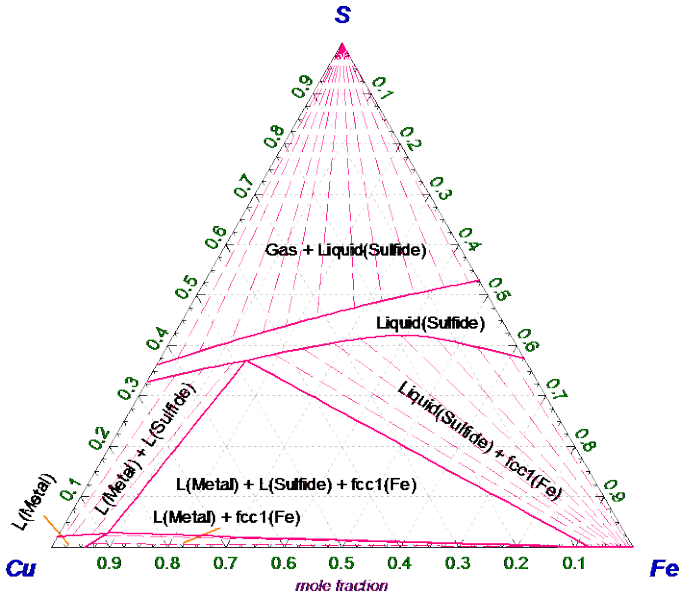

Figure 7.7. Isothermal section of the Cu–Fe–S phase diagram at 1200 °C and P = 1 atm.

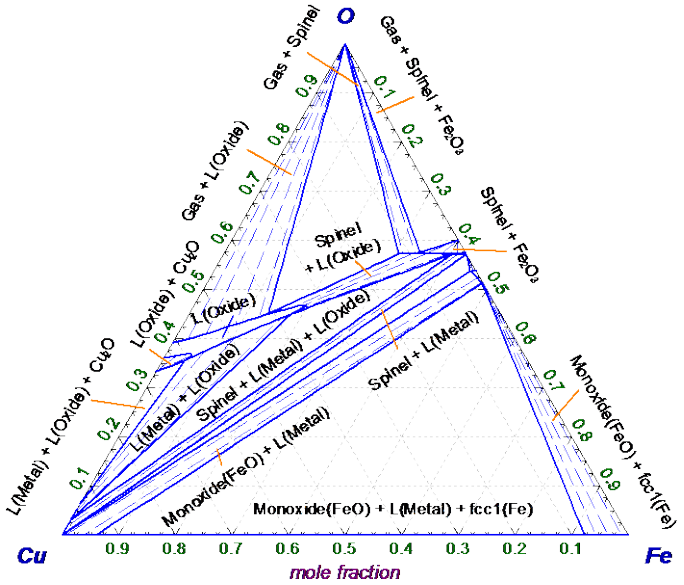

Figure 7.8. Isothermal section of the Cu–Fe–O phase diagram at 1200 °C and P = 1 atm.

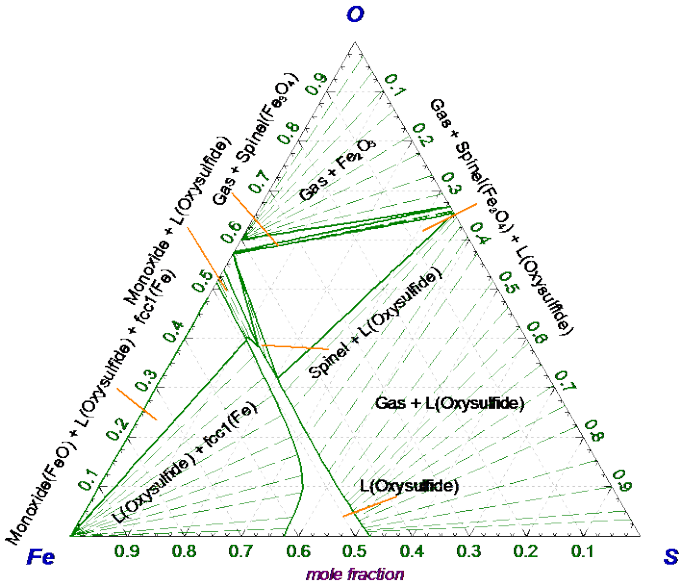

Figure 7.9. Isothermal section of the Fe–O–S phase diagram at 1200 °C and P = 1 atm.

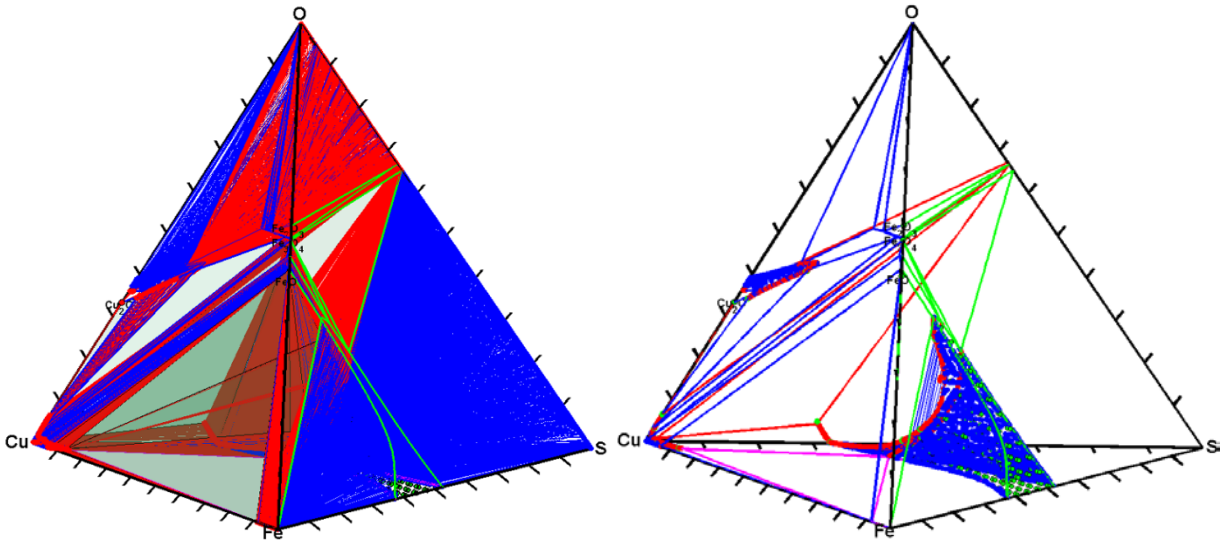

(a) **(b)**

Figure 7.10. (a) Isothermal section of the Cu–Fe–O–S phase diagram at 1200 °C and P = 1 atm. Single phase regions are shown using green points, 2-phase equilibria are shown using blue lines and points, 3-phase – using red lines and points, 4-phase equilibria – using black lines and facets. (b) The same, but only the liquid phases are shown. The 3-D figure file is available in the supplementary data. It may be opened with the MATLAB® software.

7.2.1 Subsolidus equilibria at $P(SO_2)$ = 1 atm

Rosenqvist and Hofseth [101] investigated the oxygen potential for different 4-phase combinations (3 solids + gas) in the Cu–Fe–O–S system at 700-1000 °C and at a total gas

pressure (SO_2 + S_2 + O_2 + etc.) of 1 atm. The experimental apparatus was an EMF cell, with oxygen at 1 atm as the reference electrode. The sample consisting of a certain phase combination was placed in CaO-stabilized ZrO_2, which served as a crucible and a solid electrolyte. In the majority of experiments, the temperature dependence of EMF was measured. From the observed EMF values, the oxygen potential was calculated using Nernst equation. As the actual pressure of SO_2 was slightly less than 1 atm due to formation of other gaseous species, mostly S_2 at low $P(O_2)$ and SO_3 at high $P(O_2)$, the corrections of oxygen potentials were made by the authors to correspond exactly to 1 atm of SO_2. The results of the temperature-dependent measurements are shown in Figure 7.11-Figure 7.13. In the legend, the numeration of assemblages studied experimentally corresponds to that of Rosenqvist and Hofseth [101]. Lines were calculated for the same assemblages, using the thermodynamic database of the present study. The calculated lines are in excellent agreement with the experimental data of Rosenqvist and Hofseth [101].

For measurements of the equilibrium between sulfides and spinel, the isothermal mode was used, in such a way that EMF was obtianed as a function of the molar ratio Fe/(Cu + Fe) in the sulfide phase.

Using the results of isothermal and temperature-dependent EMF measurements, Rosenqvist and Hofseth [101] suggested the isothermal $P(O_2)$ – Fe/(Cu + Fe) diagrams for the Cu–Fe–O–S system at $P(SO_2)$ = 1 atm (Figure 7.14-Figure 7.16). The same diagrams were calculated in this study. In general, the calculated and experimental $P(O_2)$ of phase transitions are in agreement. The main difference is that the diagrams calculated in this study take into account the formation of liquid and the miscibility gap between DB1 and DB2 phases. There is also a disagreement in the $P(O_2)$ of Spinel + DB1 → DB1 + Fe_2O_3 transition at 727 °C (Figure 7.14), but it seems like the line drawn by Rosenqvist and Hofseth [101] was not supported by any experimental measurements.

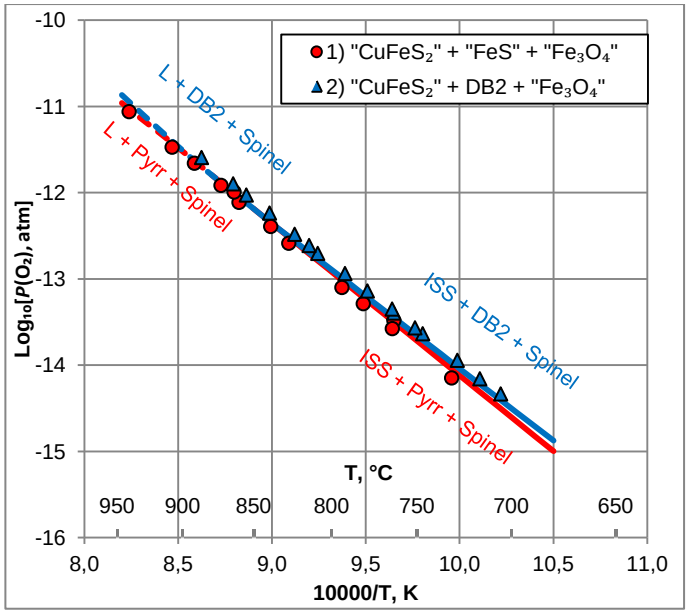

Figure 7.11. Oxygen potential for 1 atm of SO_2 as a function of temperature for assemblages in the Cu–Fe–O–S system: calculated lines and experimental points [101].

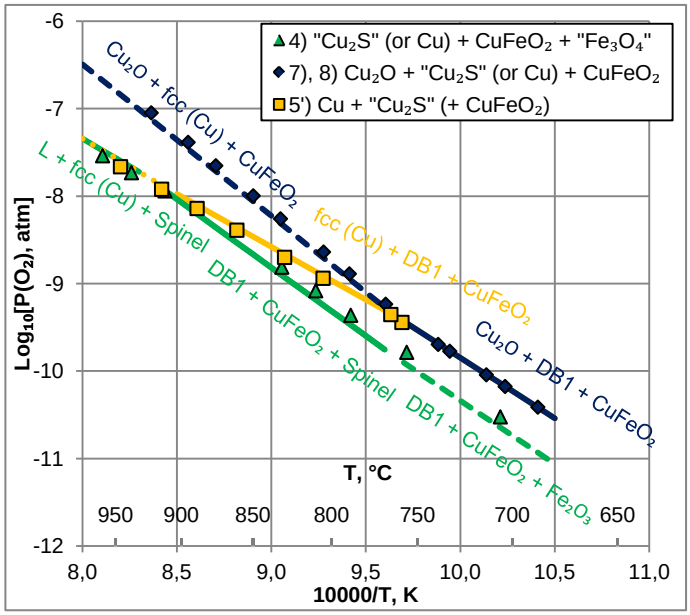

Figure 7.12. Oxygen potential for 1 atm of SO_2 as a function of temperature for assemblages in the Cu–Fe–O–S system: calculated lines and experimental points [101].

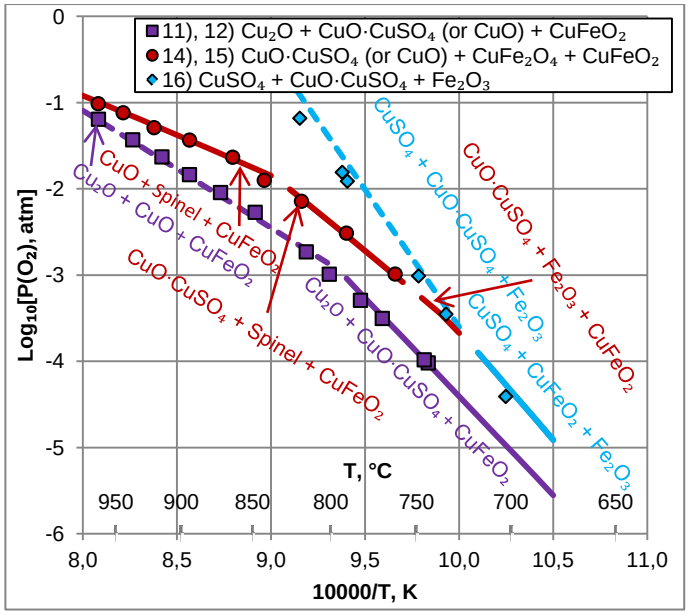

Figure 7.13. Oxygen potential for 1 atm of SO_2 as a function of temperature for assemblages in the Cu–Fe–O–S system: calculated lines and experimental points [101].

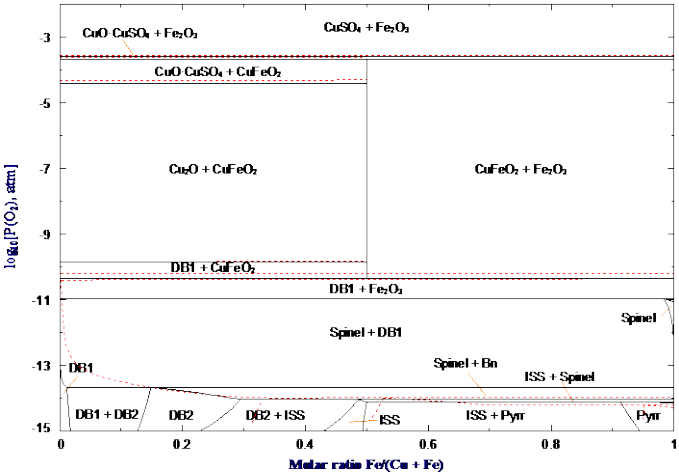

Figure 7.14. Oxygen potential in the Cu–Fe–O–S system at 727 °C and $P(SO_2)$ = 1 atm. Solid lines are model calculations, dashed lines are the assessment of Rosenqvist and Hofseth [101].

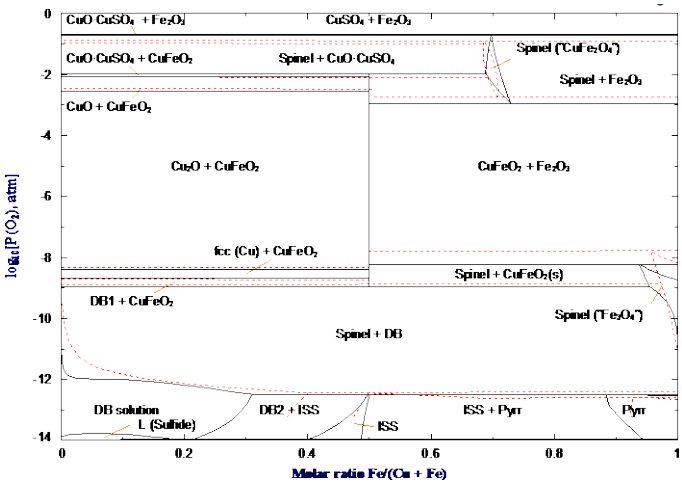

Figure 7.15. Oxygen potential in the Cu–Fe–O–S system at 827 °C and $P(SO_2)$ = 1 atm. Solid lines are model calculations, dashed lines are the assessment of Rosenqvist and Hofseth [101].

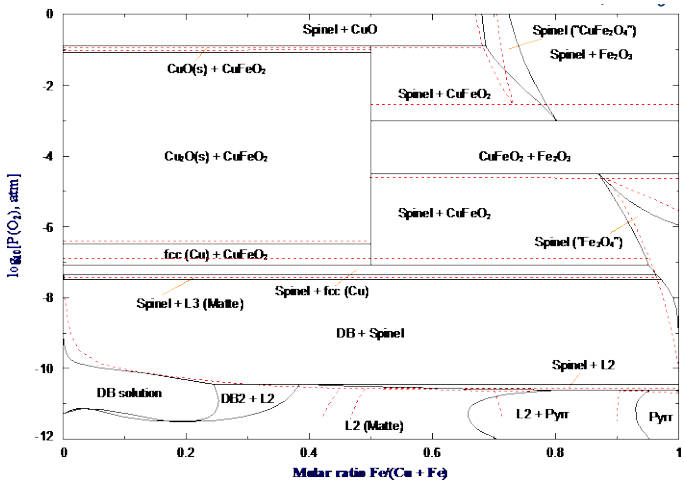

Figure 7.16. Oxygen potential in the Cu–Fe–O–S system at 977 °C and $P(SO_2)$ = 1 atm. Solid lines are model calculations, dashed lines are the assessment of Rosenqvist and Hofseth [101].

7.2.2 Oxygen and sulfur content of single-phase matte

The activities of components in the single-phase oxysulfide (matte) region, shown in Figure 7.10, were experimentally studied.

In order to fix the quaternary system in the one-phase region at constant temperature and total pressure, three more degrees of freedom should be set. They may be, for instance, Cu/Fe ratio, $P(O_2)$ and $P(S_2)$. In most of the experimental studies presented further, the equilibration of melted matte with the flow of gaseous CO–CO_2–SO_2 of known composition is used. Since iron and copper do not form volatile components, their ratio in matte remains fixed. The oxygen and sulfur partial pressures are fixed by the continuous flow of CO–CO_2–SO_2. In this case, the

number of components is increased from 4 to 5, resulting in the C–Cu–Fe–O–S chemical system. The number of phases in equilibrium increases as well, they are matte + gas. Therefore, the system remains fixed according to the Gibbs phase rule. The experimentalists believe that carbon is not soluble in condensed phases under the conditions of interest. The same approximation was made in the model presented in the present study. For the sake of simplicity, the following discussion will be held in terms of the Cu–Fe–O–S system, keeping in mind that all calculations in gas were done with carbon included.

Often, the results of studies on O and S content of matte are presented as functions of Po, Ps and y, where Po = $10^6 \cdot (P(O_2), \text{atm})^{1/2}$, Ps = $(P(S_2), \text{atm})^{1/2}$ and y is the molar ratio Fe/(Fe + Cu) in matte. These functions were calculated using the model parameters listed in Table 7-2 and are presented in Figure 7.18-Figure 7.27. To understand the behavior of the calculated curves, let us consider Figure 7.19 as an example. At constant partial pressure of sulfur (Ps) and low partial pressure of oxygen (Po), the sulfur content changes from about 0.33 in the Cu–O–S system (on the left) to nearly 0.5 in the Fe–O–S system (on the right). These values are close to the compositions of Cu_2S and FeS, respectively. In this case, the oxygen content is always small. With the increase of Po, oxygen starts to compete with sulfur on the Fe–O–S side. In terms of chemical affinity, the Fe-O bonds are more favorable than Fe-S, while the Cu-S bonds are preferable to Cu-O. That's why the sulfur content goes through a maximum at y = 0.4-0.6. The oxygen content always rises with rising Fe/(Fe + Cu). If we consider two lines calculated at different Ps but constant Po (see solid and dashed lines of the same color in Figure 7.20), the one with higher Ps will always have higher sulfur content and lower oxygen content. At low Ps and high Po, solid monoxide (mostly "FeO") or spinel (mostly Fe_3O_4) precipitate from the liquid.

Kameda and Yazawa [217] melted mattes of known iron-to-copper ratio in alumina crucibles under the flow of CO–CO_2–SO_2 mixture of a certain composition at 1150 and 1200 °C. The inlet gas composition is given in their article. The rapidly cooled samples of matte were analyzed for oxygen using the hydrogen reduction followed by H_2O-absorption in P_2O_5. The contents of copper, iron and sulfur were determined by chemical analysis. Unfortunately, only results for one gas composition were given in the article. These results are plotted in Figure 7.21.

The same experimental technique and analytical methods were used by Luraschi and Elliott [312], although they made experiments only at 1200 °C. The results for several CO-CO_2-SO_2 mixtures were reported. They are plotted in Figure 7.18-Figure 7.21.

Kaiser and Elliott [313] used the same methods, but at 1195 °C. In runs with less than 1 weight % of O in matte, SiO_2 crucibles were used instead of Al_2O_3. All samples were analyzed for the oxygen content; some of them were analyzed for copper and iron after the equilibration. The sulfur concentration was computed using the measured O content and weight change of the sample. No initial data on the compositions of the CO–CO_2–SO_2 mixtures were given by the authors. Only derived values of $P(O_2)$ and $P(S_2)$ were given. The results on one-phase equilibration are shown in Figure 7.19-Figure 7.21. The results on matte-spinel equilibria will be discussed further (Figure 7.28-Figure 7.32).

Somsiri and Gaskell [314] conducted the experiments in a similar way at 1300 °C, although in addition to matte and CO–CO_2–SO_2 gas, the metallic platinum phase was introduced into the system. As long as the platinum foil was small and did not dissolve much Cu and Fe, it was believed that the Cu/Fe ratio in matte remained the same and fixed. At the same time, it was assumed by the authors that the Fe and Cu contents in platinum reached the equilibrium values, resulting in equal activities of Cu and Fe both in Pt-metal and in matte. Using the experimental data on compositional dependence of Cu and Fe activities in the Cu–Fe–Pt system, authors calculated those activities. More assumptions were made, such as that the presence of S and O did not affect the Cu–Fe–Pt system. No initial compositions of the CO–CO_2–SO_2 mixtures were given by the authors, only derived values of $P(O_2)$ and $P(S_2)$. The measured oxygen and sulfur contents are shown in Figure 7.24-Figure 7.26.

Rose and Brenan [222] used the similar equilibration technique as Kameda and Yazawa [217] at 1300 °C, but with crystal olivine as a crucible. The analysis was conducted not by chemical methods, but using the Electron Probe Microanalysis (EPMA), even for oxygen. Light elements such as oxygen are very difficult to analyze with EMPA quantitatively, due to the problems in preparing the diffracting crystal, shifting of peak position of the element in different electronic environments and absorption of its characteristic X-rays by other elements. Nevertheless, the analytical results of Rose and Brenan [222] are plotted in Figure 7.25 and Figure 7.27.

Nagamori and Yazawa [315] repeated the experiments of Kameda and Yazawa [217] at 1200 °C. Their study covers a wide range of partial pressures of oxygen and of sulfur. The results are plotted in Figure 7.18-Figure 7.23.

Fonseca et al. [223] conducted similar experiments at 1200-1400 °C. The SiO_2 crucible and EPMA analysis were used. The experimental points are plotted in Figure 7.18 and Figure 7.19.

In addition, the experimental results of Bog and Rosenqvist [211], Nagamori and Kameda [216], Dewing and Richardson [215], Stofko and Schmiedl [218], Mintsis and Ryabko [219], Blatov et al. [220] for the Fe–O–S system are plotted in Figure 7.18-Figure 7.27. They were discussed in detail in the previous article [227].

Figure 7.17 explains the symbols used for different experimental articles.

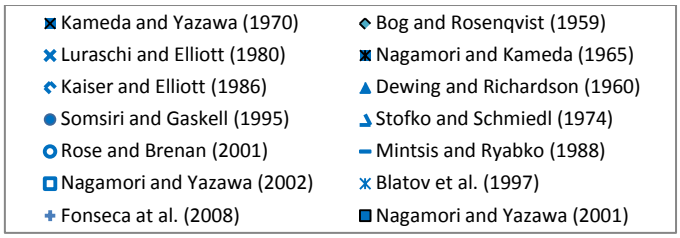

Figure 7.17. Symbol shapes used in the following figures.

The calculations were made at approximately the same Ps and Po as the experimental studies and, therefore, may be directly compared. There is a good agreement between the calculated lines and the experimental data of Kameda and Yazawa [217], Luraschi and Elliott [312], Kaiser and Elliott [313] at 1200 °C. There is a small inconsistency in the predicted Po of saturation with monoxide or spinel (Figure 7.18 and Figure 7.19) and the data of Luraschi and Elliott [312], but it is easy to miss this point in the experiment if no special precautions are made. Sulfur and oxygen content were measured in bulk quenched samples, hence, if any solid phase precipitates during the equilibration it contributes to overall composition. The formation of metastable supersaturated liquid is also possible. The results of Kameda and Yazawa [217] at 1150 °C agree with the model predictions as well, although they are not shown here. The predicted sulfur content of mattes at low Ps (Figure 7.18 and Figure 7.19) agrees with the measurements of Fonseca et al. [223], but the modeled oxygen content is different. Nevertheless, there is no systematic deviation: some calculated lines are higher, some – lower than the points of Fonseca et

al. [223]. Thus, these discrepancies are attributed to the difficulties in the measurement of oxygen content with the EPMA.

There is, however, a systematic deviation of the calculated lines from the data points of Nagamori and Yazawa [315] at Ps > 0.04 (Figure 7.20-Figure 7.23). The calculated sulfur contents are always higher and the oxygen contents are lower than those suggested by Nagamori and Yazawa [315]. The calculated lines at 0.05 < Ps < 0.17 are supproted by other authors, who made measurements in this region. For the Cu–Fe–O–S mattes at Ps > 0.17, the data of Nagamori and Yazawa [315] are the only available. They are supported by the measurements in the Fe–O–S system by Nagamori and Kameda [216], but are in disagreement with the Fe–S–O data suggested by Stofko and Schmiedl [218]. The results of Nagamori and Kameda [216] in the Fe–S–O sytem deviate systematically from the data of other authors (see Figure 5.14). The same trend is observed for the data of Nagamori and Yazawa [315] in the Cu–Fe–O–S mattes, that is why less weight were given to their results during the optimization.

The experimental data of Somsiri and Gaskell [314] and of Rose and Brenan [222] at 1300 °C, as well as the data of other authors for the Fe–O–S system [219, 220, 223], are rather scattered, but it seems that there is no systematic deviation from the calculated lines.

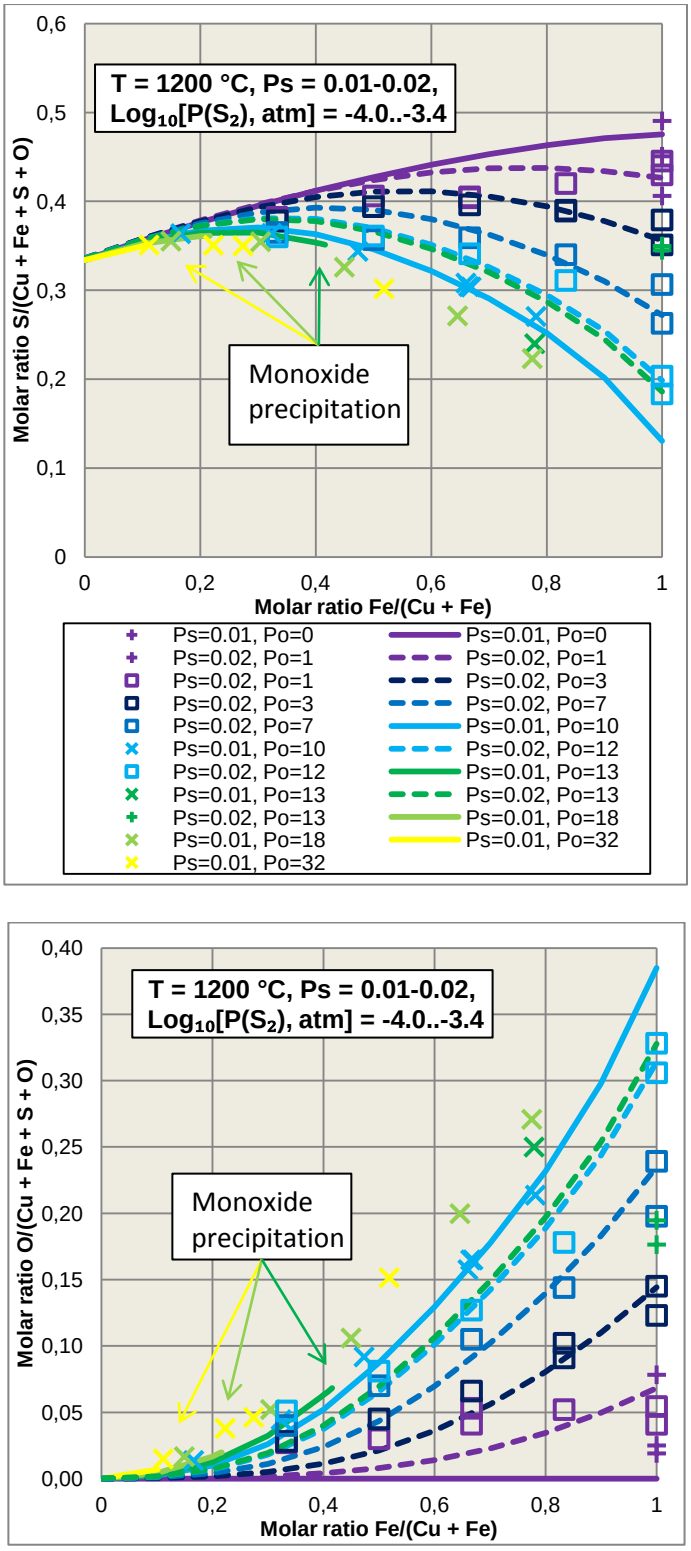

Figure 7.18. Calculated sulfur and oxygen content of the Cu–Fe–O–S matte as functions of Po, Ps and Fe/(Cu + Fe) ratio. Experimental points (see Figure 7.17) and calculated lines.

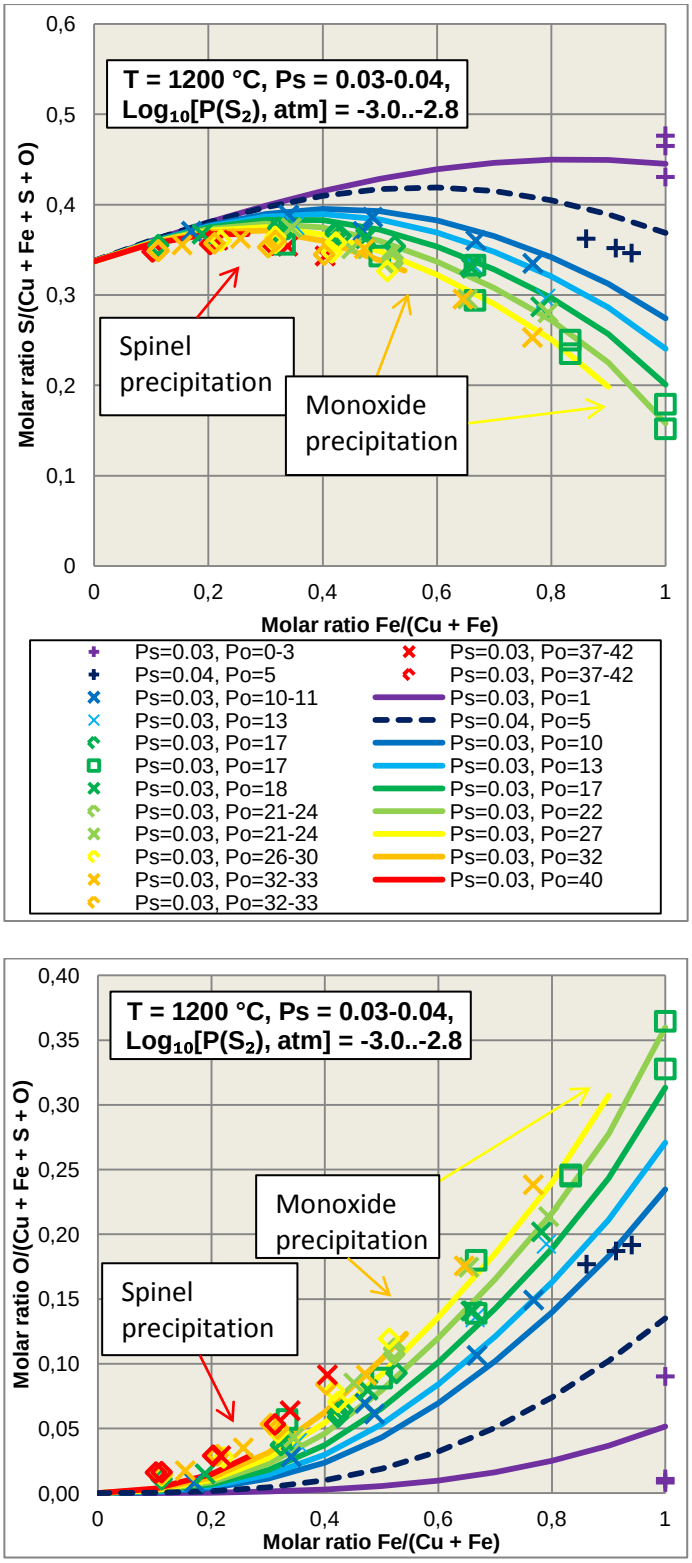

Figure 7.19. Calculated sulfur and oxygen content of the Cu–Fe–O–S matte as functions of Po, Ps and Fe/(Cu + Fe) ratio. Experimental points (see Figure 7.17) and calculated lines.

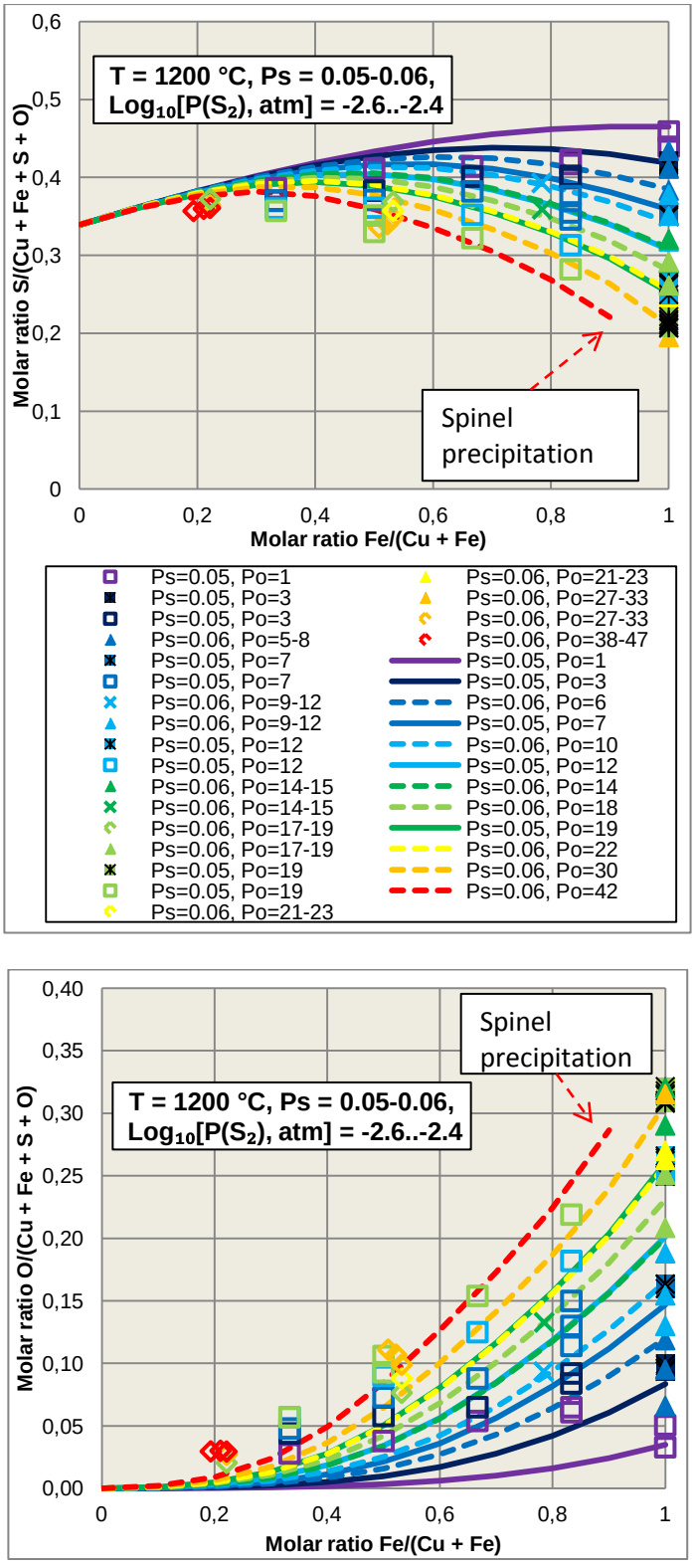

Figure 7.20. Calculated sulfur and oxygen content of the Cu–Fe–O–S matte as functions of Po, Ps and Fe/(Cu + Fe) ratio. Experimental points (see Figure 7.17) and calculated lines.

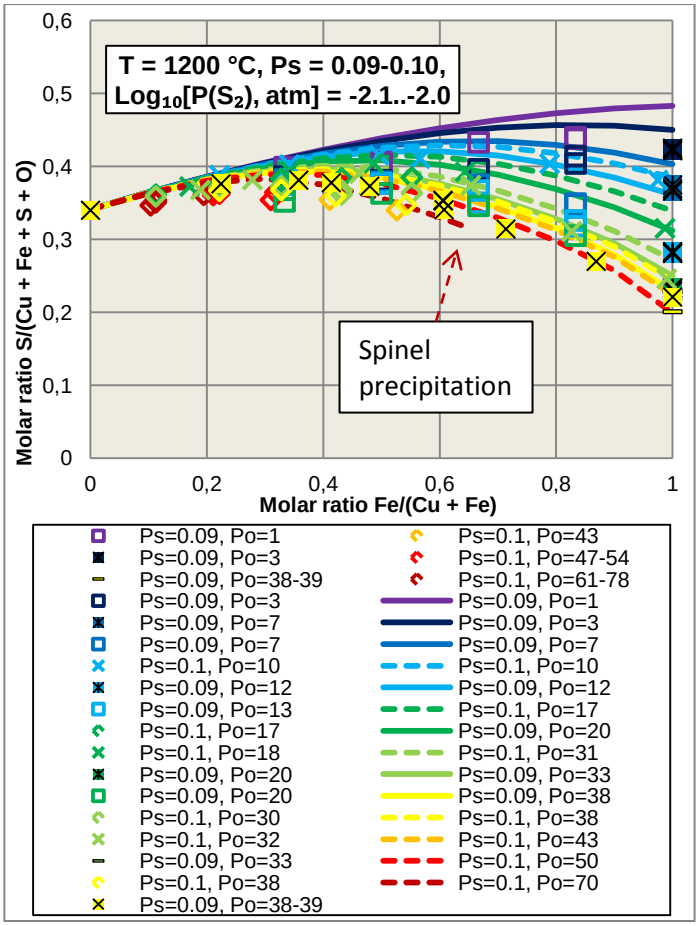

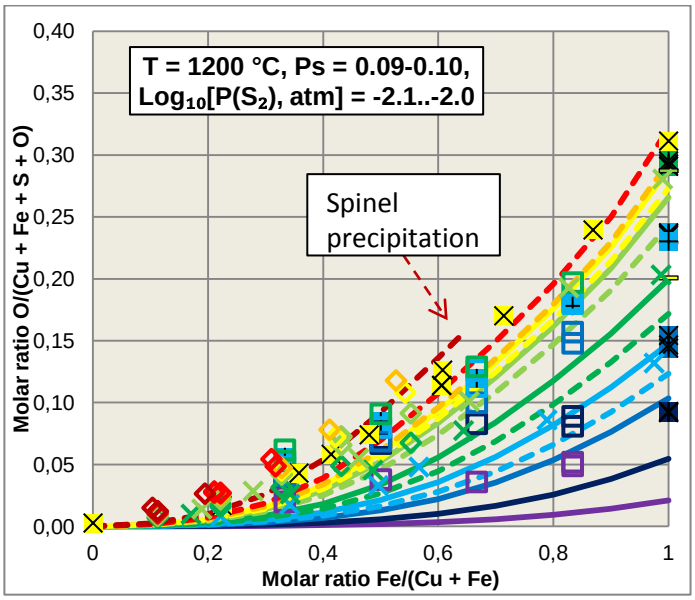

Figure 7.21. Calculated sulfur and oxygen content of the Cu–Fe–O–S matte as functions of Po, Ps and Fe/(Cu + Fe) ratio. Experimental points (see Figure 7.17) and calculated lines.

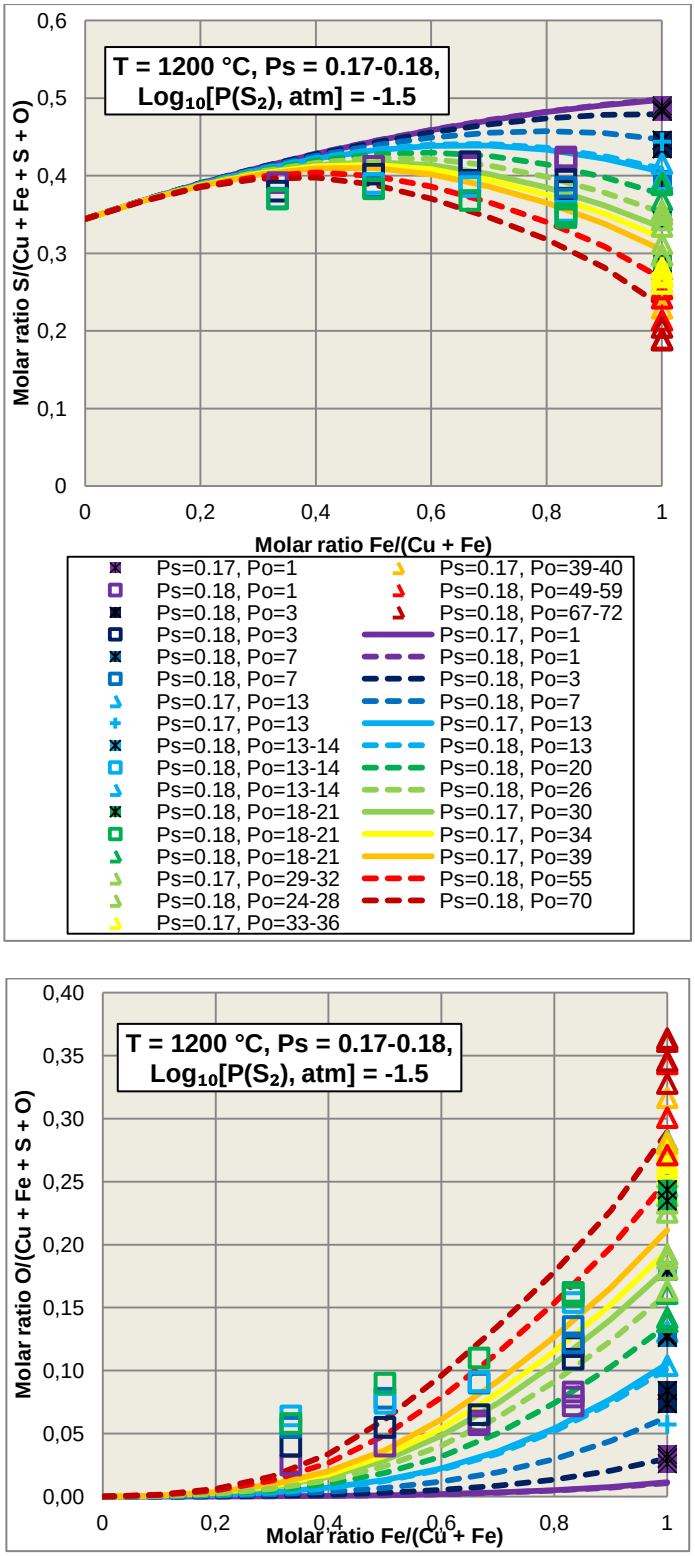

Figure 7.22. Calculated sulfur and oxygen content of the Cu–Fe–O–S matte as functions of Po, Ps and Fe/(Cu + Fe) ratio. Experimental points (see Figure 7.17) and calculated lines.

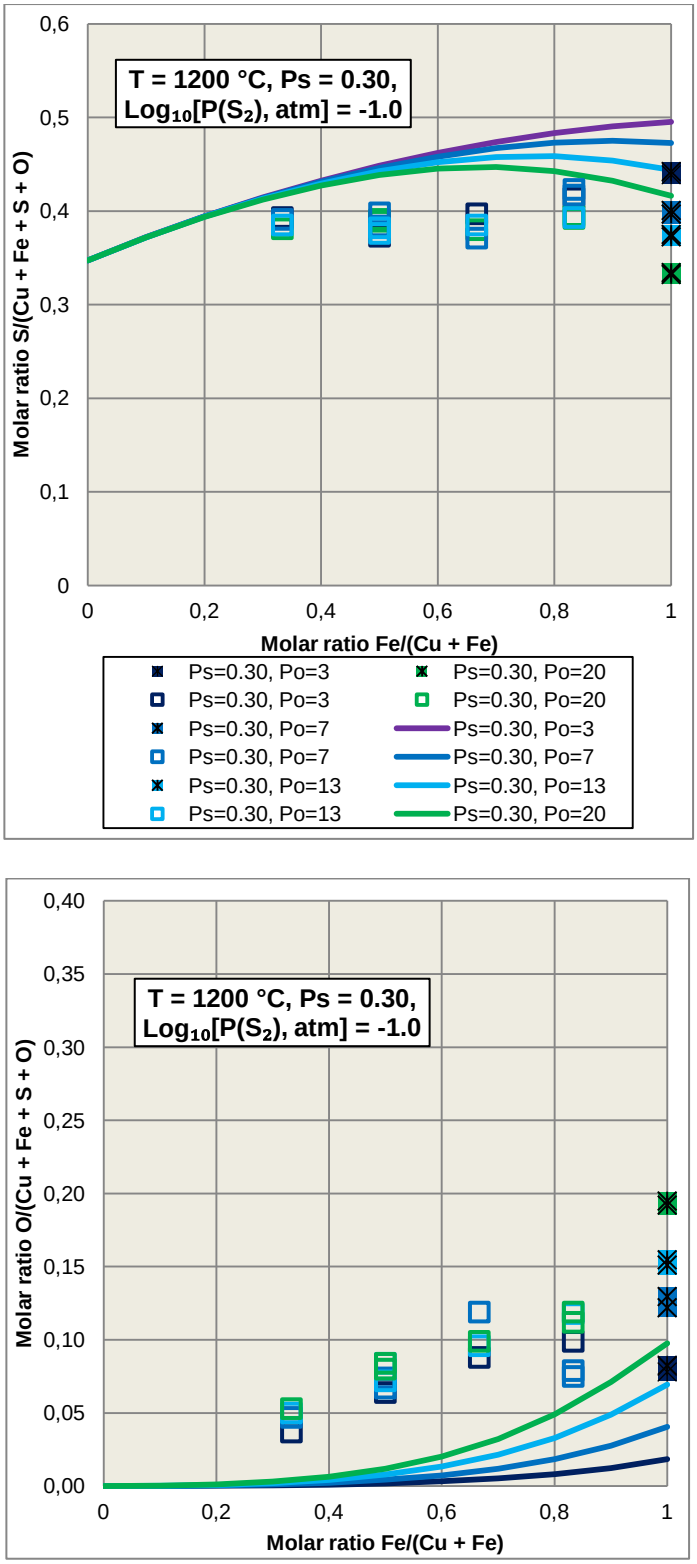

Figure 7.23. Calculated sulfur and oxygen content of the Cu–Fe–O–S matte as functions of Po, Ps and Fe/(Cu + Fe) ratio. Experimental points (see Figure 7.17) and calculated lines.

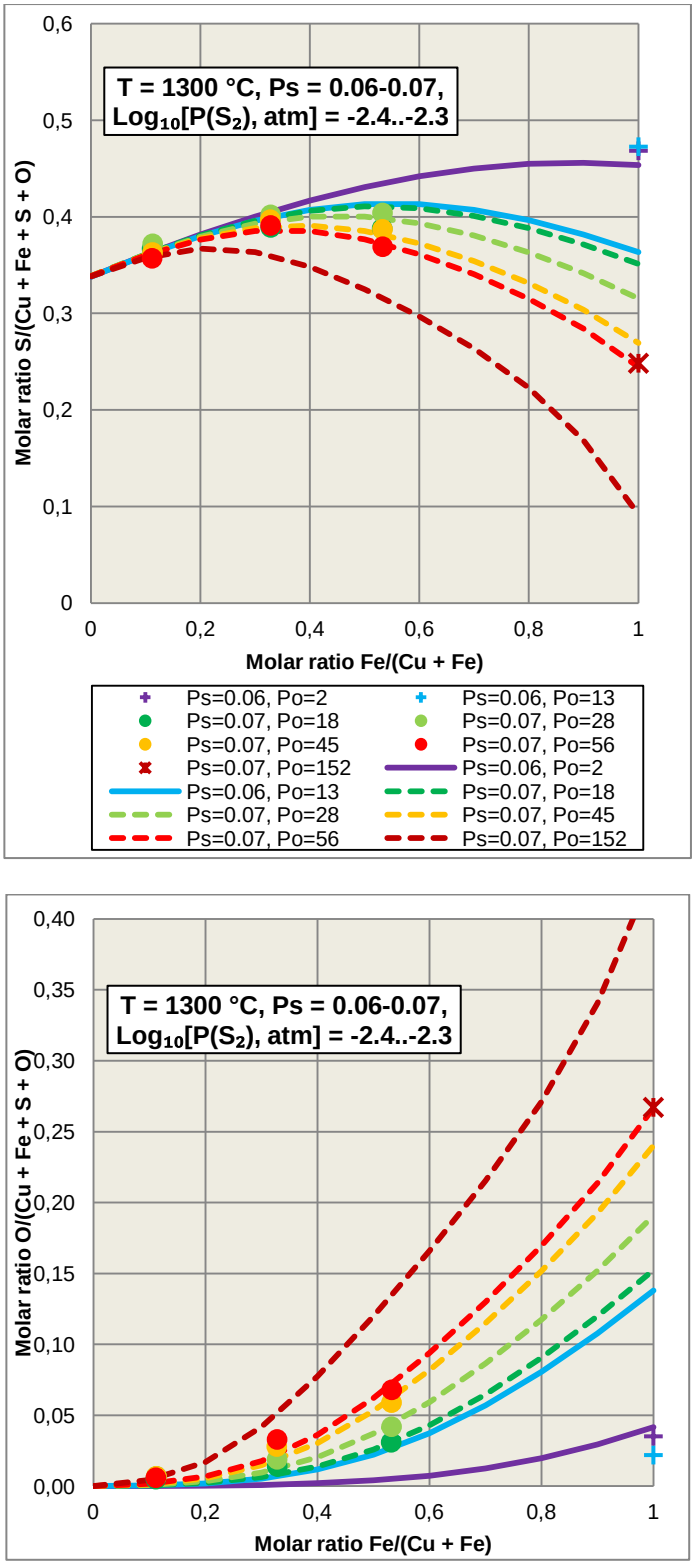

Figure 7.24. Calculated sulfur and oxygen content of the Cu–Fe–O–S matte as functions of Po, Ps and Fe/(Cu + Fe) ratio. Experimental points (see Figure 7.17) and calculated lines.

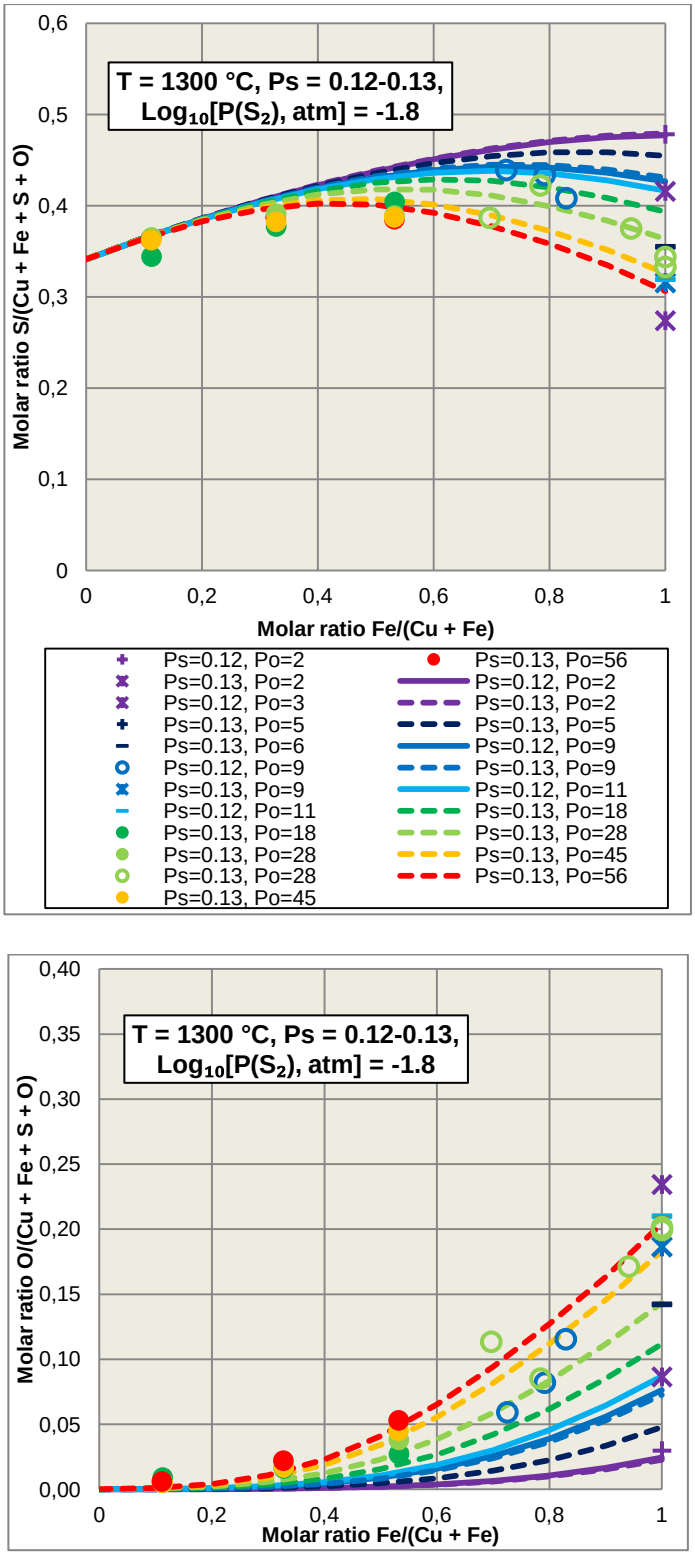

Figure 7.25. Calculated sulfur and oxygen content of the Cu–Fe–O–S matte as functions of Po, Ps and Fe/(Cu + Fe) ratio. Experimental points (see Figure 7.17) and calculated lines.

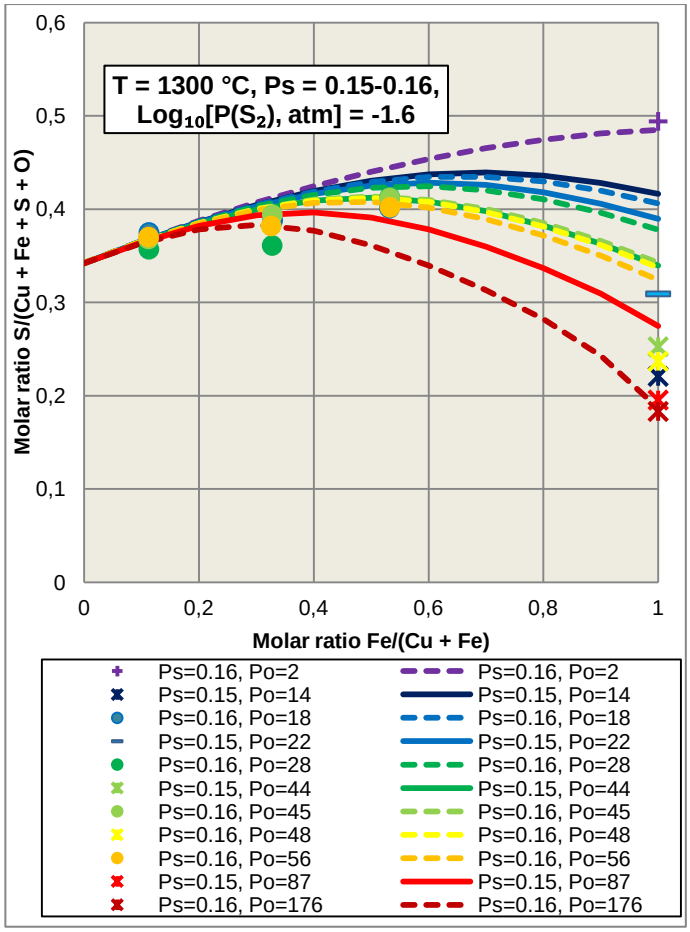

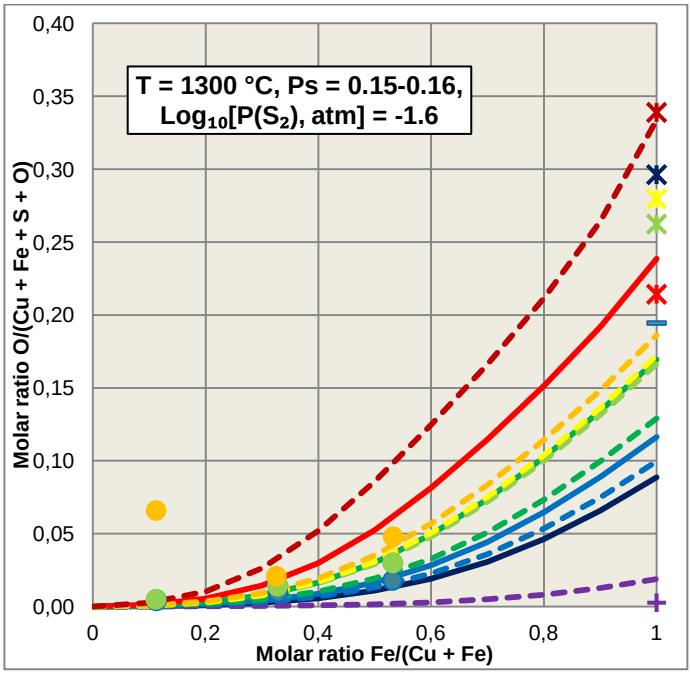

Figure 7.26. Calculated sulfur and oxygen content of the Cu–Fe–O–S matte as functions of Po, Ps and Fe/(Cu + Fe) ratio. Experimental points (see Figure 7.17) and calculated lines.

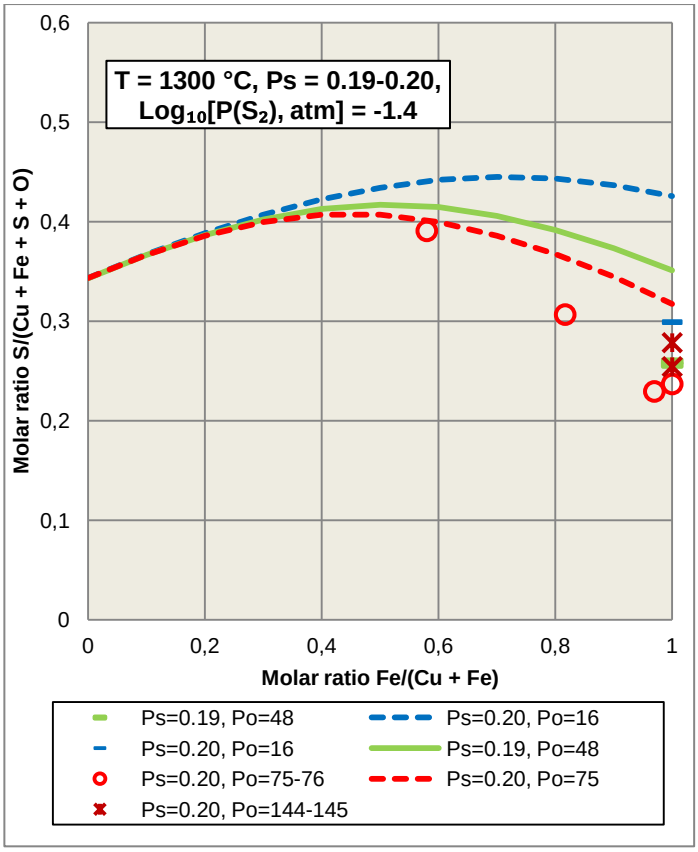

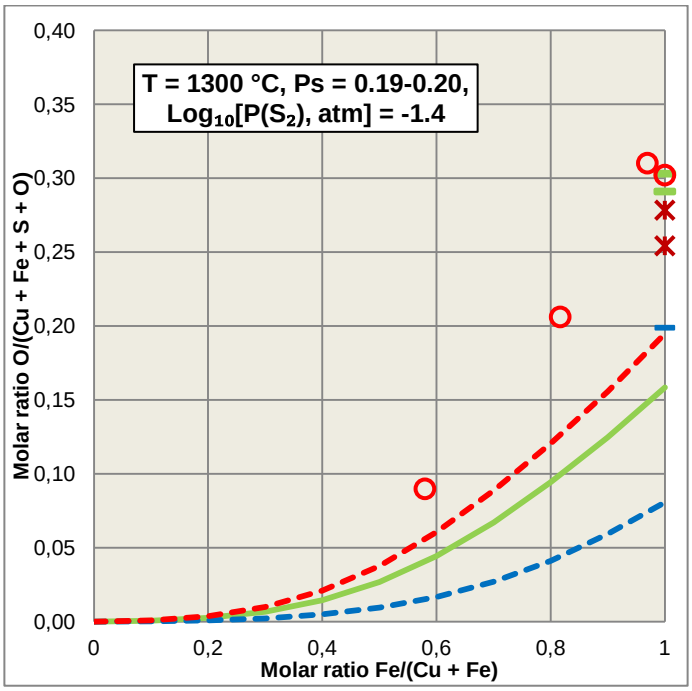

Figure 7.27. Calculated sulfur and oxygen content of the Cu–Fe–O–S matte as functions of Po, Ps and Fe/(Cu + Fe) ratio. Experimental points (see Figure 7.17) and calculated lines.

7.2.3 Matte–spinel equilibrium

The two-phase equilibrium matte-spinel at a constant temperature and total pressure in the Cu–Fe–O–S system is bivariant. This means that it is necessary to set two degrees of freedom in order to fix the thermodynamic system. Usually, $P(SO_2)$ and $P(S_2)$ or $P(S_2)$ and $P(O_2)$ are set in experimental studies. It is not possible to fix the equilibrium Cu/Fe ratio in matte, in the same way as it was done for the single-phase-liquid experiments, by mixing the appropriate amount of iron and copper compounds. The precipitation of spinel causes changes in the Cu/Fe ratio. In the calculations, it is easier to set $P(SO_2)$ and wt. % Cu in matte to fix the system. In this case, the oxygen, iron and sulfur content in matte, $P(O_2)$, and $P(S_2)$ will be their functions, as shown in Figure 7.28-Figure 7.32. However, it is not the advisable way for an experimental setup, because, even if the final copper content of matte is measured, it is necessary to verify $P(SO_2)$ in the outlet gas. Whatever degrees of freedom are fixed, the calculations and experiments should give the same plots, similar to those in Figure 7.28-Figure 7.32.

Rosenqvist and Hartvig [210] passed 1 atm gas mixture SO_2–S_2 of known $P(S_2)$ through the Cu_2S–FeS–FeO reaction mixture at 1135 and 1185 °C in Al_2O_3 crucibles lined with magnetite (spinel). Thus, the pair $P(SO_2)$ and $P(S_2)$ was set. The composition of the gas leaving the reaction furnace was determined as well. The system was believed to reach equilibrium when the compositions of inlet and outlet gases were equal. Samples of the matte phase were taken by a syringe protected with a sieve to prevent contamination by spinel. They were analyzed for the copper, iron, sulfur and oxygen contents by conventional methods, as described earlier. The presence of the spinel phase was confirmed by X-ray investigation of samples from the solid crucible lining. However, the activity of spinel was somewhat affected by the formation and dissolution of iron aluminate. Oxygen partial pressure was not measured. Since $P(S_2)$ in the study was never higher than 0.05, the data approximately correspond to $P(SO_2)$ = 1 atm. The experimental results are compared with the model predictions in Figure 7.28-Figure 7.31.

Kaiser and Elliott [316] used the same method as Kaiser and Elliott [313], described in previous section, to study the matte-spinel equilibrium. In their work, $P(O_2)$ and $P(S_2)$ were fixed by the flow of CO–CO_2–SO_2. The oxygen partial pressure was varied in order to cause the precipitation of spinel (mostly Fe_3O_4). The precipitation was confirmed by microscopic examination. The Cu/Fe ratio in matte varied due to the elimination of iron from the liquid phase

in the form of spinel. Using the derived values of $P(O_2)$ and $P(S_2)$ provided by the authors, $P(SO_2)$ was calculated in this work. The results are plotted in Figure 7.28-Figure 7.32.

Similar experiments were conducted by Johannsen and Knahl [317]. They passed pure SO_2 at 1 atm through the reaction mixture in the spinel lined crucibles at 1185 °C. The final wt. % Cu in matte was set as the second degree of freedom, but the composition of the outlet gas was not verified. Thus, the system was not properly fixed. This might be a reason for significant deviations of oxygen and sulfur contents in matte reported by Johannsen and Knahl [317] from those of Rosenqvist and Hartvig [210] and from the calculated lines (Figure 7.28 and Figure 7.29). Johannsen and Knahl [317] cited the work of Lander [318], who passed the mixture of SO_2–CO_2 over spinel saturated matte. Not much details were provided, but Lander's points are in agreement with the other authors and calculations (Figure 7.28).

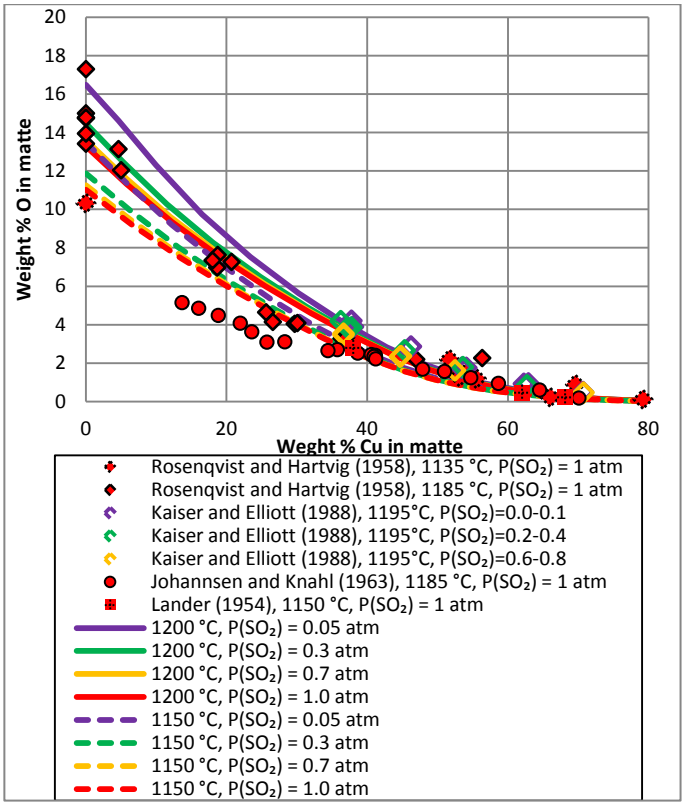

Figure 7.28. Matte–spinel equilibrium. Weight percent of oxygen in matte. Experimental points [210, 316-318] and calculated lines.

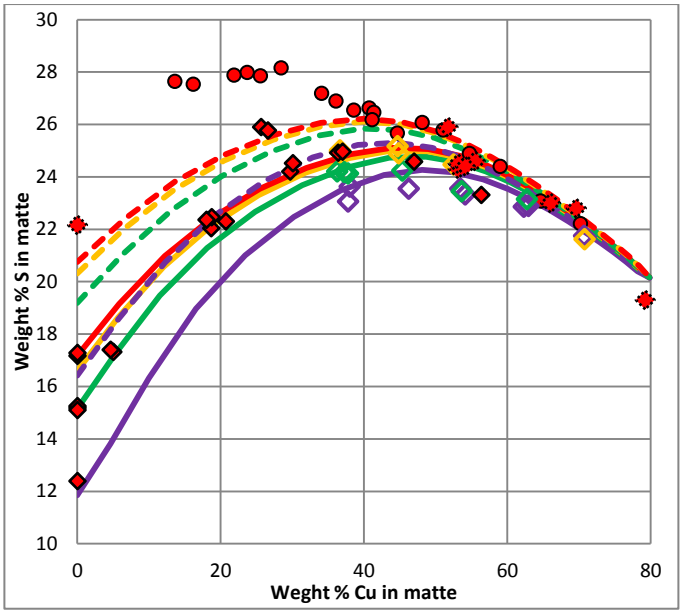

Figure 7.29. Matte–spinel equilibrium. Weight percent of sulfur in matte. Experimental points [210, 316, 317] and calculated lines.

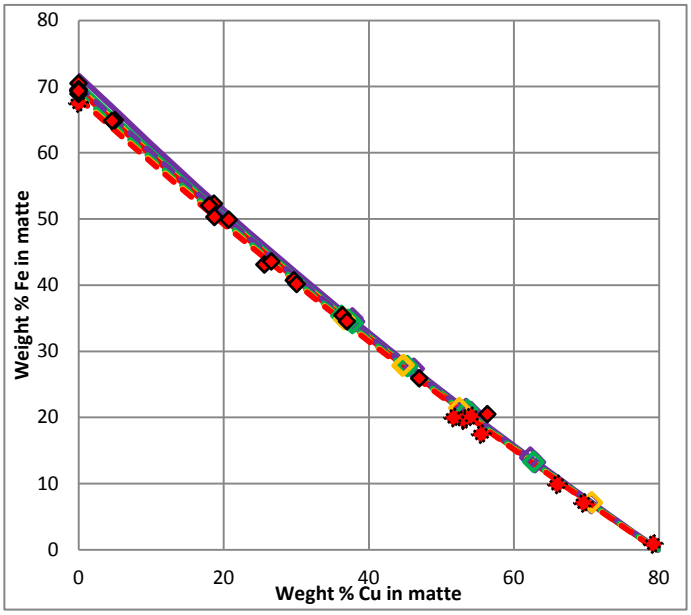

Figure 7.30. Matte–spinel equilibrium. Weight percent of iron in matte. Experimental points [210, 316] and calculated lines.

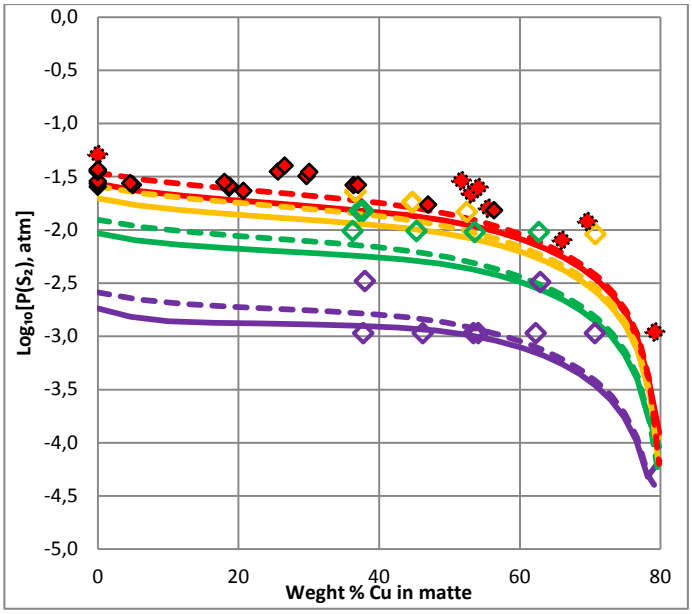

Figure 7.31. Matte–spinel equilibrium. Partial pressure of sulfur. Experimental points [210, 316] and calculated lines.

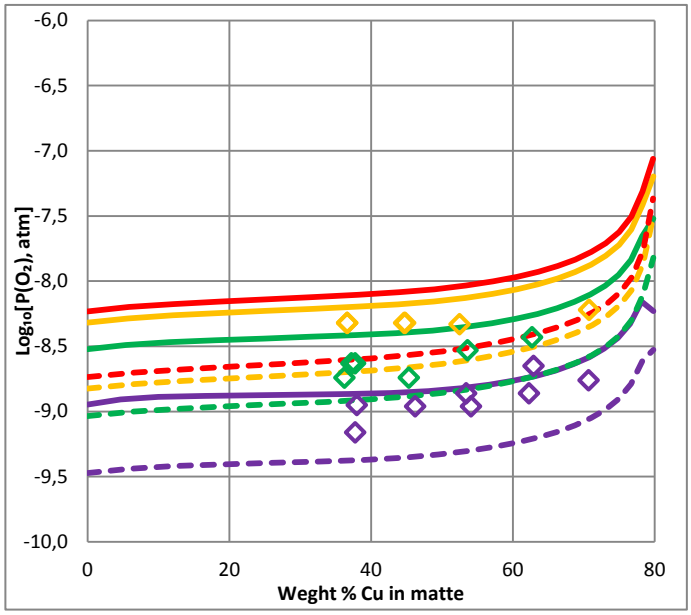

Figure 7.32. Matte–spinel equilibrium. Partial pressure of oxygen. Experimental points [316] and calculated lines.

7.3 Optimization of parameters

To describe the experimental data for the Cu–Fe–O–S system, minor modifications of model parameters have been made. First, the undesirable appearance of the liquid phase in the Cu_2S–S–SO_2 region of the Cu–O–S system at low temperatures (< 400 °C) has been corrected. The

parameter $g^{011}_{Cu^{I}O(S)}$ = -217568 J from originally published article [114] was substituted by the parameter $g^{011}_{Cu^{I}S(O)}$ = -221752 J. Secondly, the enthalpy of formation of $CuSO_4$ has been changed, as it is shown in Table 7-2, in order to describe the data of Rosenqvist and Hofseth [101] for the $CuSO_4$–$CuO{\cdot}CuSO_4$–Fe_2O_3–$P(SO_2)$= 1 atm equilibrium (Figure 7.13). This changed insignificantly the model predictions in the Cu–O–S system. All experimental data presented in the Cu–O–S article [114] remain in agreement with the calculated lines. In the present thesis, all diagrams in the Cu–O–S system (Chapter 4) were calculated with updated parameters $g^{011}_{Cu^{I}S(O)}$ and $\Delta H^{\circ}_{f}(CuSO_4)$.

The new parameter $q^{001}_{Fe^{III}Cu^{I}(S)}$ = 167360 J (Bragg-Williams) in liquid has been introduced. This parameter does not affect model predictions in the Cu–Fe–S system, because Fe^{III} does not appear there. Moreover, the parameter makes the formation of Fe^{III} even more unfavorable. In the Cu–Fe–O–S system, it makes the oxygen content vs. copper content curves (Figure 7.28) more concave and the sulfur content vs. copper content plots (Figure 7.29) more convex.

Large positive parameter $q^{001}_{Fe^{III}Cu^{I}(S)}$ in combination with positive parameter $g^{001}_{Fe^{II}O(Cu)}$ arisen from the Cu–Fe–O system, were required to increase the curvature of the oxygen and sulfur contents (Figure 7.19-Figure 7.29), but they cause the appearance of an additional miscibility gap between Cu–Fe–S-rich and Fe–S–O-rich oxysulfide liquids in the quaternary Cu–Fe–O–S system (Figure 7.10b). Experimental data indicate a tendency to a miscibility gap, but no measurements were done under conditions where it should apprear. The calculated equilibrium $P(S_2)$ for the L(Metal) + L(Oxysulfide1) + L(Oxysulfide2) + Fcc(Fe) and Monoxide + L(Metal) + L(Oxysulfide1) + L(Oxysulfide2) equilibria et 1200 °C is $10^{-6.6}$ atm (Table 7-1). The experimental techniques used in the evaluated studies do not allow the control of such low $P(S_2)$. The possible experimental technique to confirm or deny the existence of this miscibility gap should include the equilibration of the Cu–Fe–O–S sample of certain bulk composition in a sealed inert capsule, followed by rapid quenching and EMPA analysis. The bulk composition of the sample should lie inside the L(Metal) + L(Oxysulfide1) + L(Oxysulfide2) + Fcc(Fe) or Monoxide + L(Metal) + L(Oxysulfide1) + L(Oxysulfide2) tetrahedrons and may be calculated using the thermodynamic database of the present study.

7.4 Summary of results

The thermodynamic database, combined from the earlier obtained Cu–O–S, Fe–O–S, Cu–Fe–O and Cu–Fe–S databases, proved to be capable of predicting chemical and phase equilibria in the Cu–Fe–O–S system. The ternary parameter $q^{001}_{Fe^{III}Cu^{I}(S)}$ was optimized to describe better the experimental data in the Cu–Fe–O–S system. This parameter could not be obtained from the data in ternary Cu–Fe–S system and have no influence on it. The predicting power of the present database will be further tested in the Cu–Fe–O–S–Si system by calculations of the distribution of components between matte and slag.

Table 7-2. Optimized properties of stoichiometric compounds and model parameters for liquid and solid solutions in the Cu–Fe–O–S system (J·mol^{-1} and J·mol^{-1}·K^{-1})

Compounds	**Temperature range (K) or reference**	$\Delta H^{o}_{298.15}$	$S^{o}_{298.15}$	$C_P(T)$
CuO, Cu_2O, Cu_2S, S	[114]			
$CuSO_4$, Cu_2SO_4, $CuO{\cdot}CuSO_4$	[114], $\Delta H^{o}_{298.15}(CuSO_4)$ changed to -770982.0 from -769982.0			
FeS, 'Fe_7S_8', Fe_9S_{10}, $Fe_{10}S_{11}$, $Fe_{11}S_{12}$	[26]			
Fe_2O_3, $FeSO_4$, $Fe_2(SO_4)_3$	[227]			
$CuFeO_2$	[172]			
$CuFeS_2$, chalcopyrite	298-830	-187024.8	125.1016	$93.1275 + 0.043045T - 681992T^{-2}$
	>830			127.8648
$CuFe_2S_3$, cubanite	298-1000	-289867.5	187.6526	$139.6912 + 0.064568T - 1022988T^{-2}$
	>1000			203.2362
Cu_3FeS_4, idaite	298-1000	-319186.0	227.2400	$174.6840 + 0.080545T - 0.0189\times10^{-6}T^{2} - 840480T^{-2}$
	>1000			254.3698
Cu_3FeS_8, fukuchilite	298-1000	-318151.4	375.3045	$279.3824 + 0.129134T - 2045976T^{-2}$
	>1000			406.4704
$Cu_4Fe_5S_8$, haycockite	298-1000	-788474.8	531.6821	$395.7918 + 0.182942T - 2898466T^{-2}$
	>1000			575.8353
$Cu_9Fe_8S_{16}$, talnakhite	298-1000	-1515076.5	1059.4099	$768.3016 + 0.355122T - 5626434T^{-2}$
	>1000			1117.7972
$Cu_9Fe_9S_{16}$, mooihoekite	298-1000	-1566698.8	1063.3635	$791.5835 + 0.365882T - 5796932T^{-2}$
	>1000			1151.6686
$Cu_{11}Fe_2S_{13}$, nukundamit	298-1000	-866406.7	874.5100	$567.7230 + 0.261772T - 0.0614\times10^{-6}T^{2} - 2731560T^{-2}$
	>1000			826.7021

Table 7-2. (Continued) Optimized properties of stoichiometric compounds and model parameters for liquid and solid solutions in the Cu–Fe–O–S system (J·mol^{-1} and J·mol^{-1}·K^{-1})

Solutions	**Temperature range (K) or reference**	**Molar Gibbs energy $g(T)$**
Liquid (Metal, Oxide, Sulfide)	Modified Quasichemical Model (Cu^{I}, Cu^{II}, Fe^{II}, Fe^{III}, O, S), Grouping: Cu^{I}, Cu^{II},Fe^{II}, Fe^{III} in group 1; O, S in Group 2	
Coordination numbers Z [114, 227]		
g°_{O}, g°_{S}, $g^{\circ}_{Cu^{I}}$, $g^{\circ}_{Cu^{II}}$	[114]	
$g^{\circ}_{Fe^{II}}$, $g^{\circ}_{Fe^{III}}$	[227]	
Excess parameters Cu-O	[114]	
Excess parameters Fe-O	[227]	
Excess parameters Cu-Fe	[172]	
Excess parameters Cu-O-S	[114]	Parameter $g^{011}_{Cu^{I}O(S)}$ = -217568.00 was replaced by $g^{011}_{Cu^{I}S(O)}$ = -221752.00
Excess parameters Fe-O-S	[227]	
Excess parameters Cu-Fe-O	[172]	
Excess parameters Cu-Fe-S	$q^{001}_{Fe^{III}Cu^{I}(S)}$	167360 (Bragg-Williams)
	$g^{001}_{Fe^{II}S(Cu^{I})}$	29450.8 – 25.1040T
	$g^{002}_{Cu^{I}S(Fe^{II})}$	1882.8
	$g^{011}_{Fe^{II}S(Cu^{I})}$	-29288
Fcc , Fe and Cu metals	Bragg-Williams (Cu, Fe, O, S)	
g°_{Cu} , g°_{O} , g°_{S}	[114]	
g°_{Fe}	[227]	
Excess parameters Cu-O, Cu-S	[114]	

Table 7-2. (Continued) Optimized properties of stoichiometric compounds and model parameters for liquid and solid solutions in the Cu–Fe–O–S system (J·mol^{-1} and J·mol^{-1}·K^{-1})

Solutions	**Temperature range (K) or reference**	**Molar Gibbs energy $g(T)$**
Excess parameters Fe-O, Fe-S	[227]	
Excess parameters Cu-Fe	[172]	
Bcc, solid Fe metal	Bragg-Williams (Cu, Fe, O, S)	
g°_{Fe} , g°_{O} , g°_{S}	[227]	
g°_{Cu}	[172]	
Excess parameters Fe-O, Fe-S	[227]	
Excess parameters Cu-Fe	[172]	
Monoxide, "$Fe_{1-x}O$"-(CuO)	Bragg-Williams (FeO, $FeO_{1.5}$, CuO)	
g^{o}_{FeO} , $g^{o}_{FeO_{1.5}}$	[21]	
g^{o}_{CuO}	[172]	
Excess parameters Fe-O	[21]	
Excess parameters Cu-Fe-O	[172]	
Spinel, Fe_3O_4-$CuFe_2O_4$	Compound energy formalism: $(Cu^{+2},Fe^{+2},Fe^{+3})^{tetr}[Cu^{+2},Fe^{+2},Fe^{+3},Va]_2^{oct}O_4^{-2}$. Model is the same as for the Fe-Zn-O spinel [21].	
Parameters Fe-O	[21]	
Parameters Cu-Fe-O	[172]	
Pyrrhotite, $Fe_{1-x}S$-(CuS), Pyrr	Bragg-Williams (Fe, Cu, Vacancy)S	
g^{o}_{FeS} , g^{o}_{VaS}	[26]	

Table 7-2. (Continued) Optimized properties of stoichiometric compounds and model parameters for liquid and solid solutions in the Cu–Fe–O–S system (J·mol^{-1} and J·mol^{-1}·K^{-1})

Solutions	**Temperature range (K) or reference**	**Molar Gibbs energy $g(T)$**
Parameters Fe-S	[26]	
g^{o}_{CuS}	298-1000	-54828.0 + 223.8149T – 43.6710Tln$T$ − 0.010068T^{2} + 105060.0T^{-1}+ 0.000787×10^{-6}T^{3}
$L^{0}_{Cu,Fe:S}$		-29288.00
MeS_2, FeS_2-(CuS_2), pyrite	Bragg-Williams (FeS_2, CuS_2)	
$g^{o}_{FeS_2}$	[26]	The same as stoichiometric FeS_2
$g^{o}_{CuS_2}$	298-1350	-72810.8 + 355.9551T – 64.4350Tln$T$ − 0.010379T^{2} − 100.0T^{-1}+ 0.000373×10^{-6}T^{3}
Intermediate solid solution, CuS-FeS, ISS	Bragg-Williams (Cu_2, Fe, Vacancy)S	
$g^{o}_{Cu_2S}$	298-1450	-20192.1 + 420.4459T – 83.0000Tln$T$
g^{o}_{FeS}	298-1450	-67802.0 + 341.5458T – 60.0000Tln$T$
g^{o}_{VaS}	298-368.3	60853.7 + 65.0274T – 11.0070Tln$T$ − 0.026529T^{2} + 7.754333×10^{-6}T^{3}
	368.3-1300	59568.9 + 104.3025T – 17.9418Tln$T$ − 0.010895T^{2} + 39910T^{-1}+ 1.402558×10^{-6}T^{3}
$L^{0}_{Fe,Va:S}$		-177820.0
$L^{0}_{Cu,Va:S}$		-271960.0
$L^{0}_{Fe,Cu:S}$		-198970.9 – 11.7152T
$L^{1}_{Fe,Cu:S}$ (Redlich-Kister)		-198970.9 – 11.7152T

Table 7-2. (Continued) Optimized properties of stoichiometric compounds and model parameters for liquid and solid solutions in the Cu–Fe–O–S system (J·mol^{-1} and J·mol^{-1}·K^{-1})

Solutions	**Temperature range (K) or reference**	**Molar Gibbs energy $g(T)$**
Covellite, CuS-(FeS), Cov	Bragg-Williams (CuS, FeS)	
g^{o}_{CuS}	[114]	The same as stoichiometric CuS
g^{o}_{FeS}	298-1000	$1000000.0+ 232.4060T - 43.6710T\ln T - 0.010068T^{2} + 105060T^{-1} + 0.000787\times10^{-6}T^{3}$
Digenite-Bornite, Cu_2S-Cu_2FeS_4, DB1 and DB2	Bragg-Williams (Cu_2, Fe, Vacancy)S	
$g^{o}_{Cu_2S}$, g^{o}_{VaS}	[114]	
$L^{0}_{Cu,Va:S}$ $L^{1}_{Cu,Va:S}$ (Redlich-Kister)	[114]	There was a misprint in [114]. Should be $L^{0}_{Cu,Va:S}$ and $L^{1}_{Cu,Va:S}$ instead of $L^{1}_{Cu,Va:S}$, $L^{2}_{Cu,Va:S}$
g^{o}_{FeS}	>298	$-76170.0 + 341.5458T - 60.0000T\ln T$
$L^{0}_{Fe,Va:S}$		$-78954.34 - 124.5158T$
$L^{0}_{Fe,Cu:S}$		$-88092.7 - 9.8968T$
$L^{1}_{Fe,Cu:S}$ (Redlich-Kister)		$-144183.4 + 73.1363T$

The Gibbs energy of formation of a compound from elements in their standard state at a temperature of T (K) and a pressure of 1 atm is given by $\Delta G = \Delta H^{o}_{298.15} - T S^{o}_{298.15} + \int_{298.15}^{T} C_P(T)dT - T\int_{298.15}^{T} \frac{C_P(T)}{T}dT$, where $\Delta H^{o}_{298.15}$ is the enthalpy of formation of the compound at 1 atm and 298.15 K, $S^{o}_{298.15}$ is the entropy of the compound at 1 atm and 298.15 K, and $C_P(T)$ is the heat capacity at constant pressure.

CHAPTER 8 DEVELOPMENT OF THE SPINEL DATABASE IN THE Al–Ca–Cu–Fe–Mg–O SYSTEM

Equation Chapter (Next) Section 1 Spinel materials, such as $MgFe_2O_4$ are widely used as refractories in several metallurgical processes. The formation of Fe_3O_4 spinel during the copper production may cause the occlusion problems. The equilibration-quenching-EPMA experiments conducted at the Pyrosearch Center of Queensland University showed that copper and calcium dissolve in the spinel phase under conditions close to those of pyrometallurgical production of copper. These elements were added to the existing Al–Fe–Mg–O spinel database [24, 25] in the course of the current project. A systematic approach was used: all experimental data for the subsystems of the Al–Ca–Cu–Fe–Mg–O system were critically evaluated and model parameters of the spinel database were optimized simultaneously with the properties of stoichiometric compounds, slag, monoxide and other solutions. Copper was first added to the spinel database during the optimization of the Cu–Fe–O system [172]. The project was complicated by the fact that inconsistencies and deviations from the experimental data were found in the previously optimized Ca–Fe–O, Fe–O–Si and Ca–Fe–O–Si systems. Futhermore, new experimental data appeared for these systems and for the higher-order systems containing copper. The slag solution and some solid phases required re-optimization. Suddenly, the scope of the project dramatically increased. This re-optimization was done in collaboration with one more graduate student, Taufiq Hidayat, from the Pyrosearch Center. The following section outlines the results of this work.

8.1 Ca–Fe–O system

The comprehensive study of the Ca–Fe–O system is reported elsewhere by T. Hidayat [1]. The optimization of model parameters for slag, monoxide and the final adjustment of stoichiometric compound phases were performed by T. Hidayat, while the initial optimization of compounds, modeling of the spinel phase and the supervision of the overall consistency of all optimizations was the responsibility of the present author.

8.1.1 Thermodynamic model for spinel

The spinel solution is described using the sublattice model based on the Compound Energy Formalism (CEF) [319]. The spinel is described by considering Fe^{2+} and Fe^{3+} cations distributed

over tetrahedral (tetr) and octahedral (oct) sites. The Ca^{2+} ions in spinel are introduced only into the octahedral sites. Electrically-neutral vacancies were added previously [21] on the octahedral sites to describe excess of oxygen in spinel above the stoichiometric composition Fe_3O_4:

$$(Fe^{+2},Fe^{+3})^{tetr}[Ca^{+2},Fe^{+2},Fe^{+3},Va]_2^{oct}O_4^{-2} \quad (8.1)$$

The introduction of Ca^{2+} cations only into the octahedral sites was justified by a number of reasons: (i) it is well known that compounds such as $CaFe_2O_4$, $CaAl_2O_4$, $CaCr_2O_4$ do not have allotropes with the spinel crystal structure, because the entrance of the relatively large Ca^{2+} cation into small tetrahedral sites destabilizes the spinel lattice; and (ii) the solubility of Ca^{2+} is found to be much higher in Fe_3O_4 than in $FeAl_2O_4$, which may be explained by the fact that Fe_3O_4 is an inverse spinel, so that the divalent cation (Fe^{2+}) can be readily replaced by Ca^{2+} on the octahedral sites, while hercynite ($FeAl_2O_4$) is a normal spinel and Ca^{2+} cations entering the octahedral sites would have to displace Al^{3+} cations to the tetrahedral sites, increasing the enthalpy of the solution. If it were possible for Ca^{2+} to replace Fe^{2+} on the tetrahedral site, the solubility of calcium in $FeAl_2O_4$ and Fe_3O_4 would be of the same order as that in Fe_3O_4. The spinel from the optimization by Decterov *et al* [21] in the FeO–Fe_2O_3 system was used as a basis for the current solution. With the introduction of Ca^{2+} only on the octahedral sites, the model becomes rather simple, and the solubility of Ca^{2+} in spinel could be optimized with only one model function, *i.e.* the Gibbs energy of the hypothetical inverse spinel $(Fe^{+3})^{tetr}[Ca_{0.5}^{+2},Fe_{0.5}^{+3}]_2^{oct}O_4^{-2}$. The Gibbs energies of two new charged end-members containing calcium may be found using two model approximations:

$$G_{E(EP)} = 0.5G_{EE} + 0.5G_{EP} + 2RT\cdot[0.5\ln 0.5 + 0.5\ln 0.5] \quad (8.2)$$

$$\Delta_{EAP} = G_{EP} + G_{AA} - G_{EA} - G_{AP} \quad (8.3)$$

where $E(EP)$ is $\left((Fe^{+3})^{tetr}[Ca_{0.5}^{+2},Fe_{0.5}^{+3}]_2^{oct}O_4^{-2}\right)^0$, EE is $\left((Fe^{+3})^{tetr}[Fe^{+3}]_2^{oct}O_4^{-2}\right)^{1+}$, EP is $\left((Fe^{+3})^{tetr}[Ca^{+2}]_2^{oct}O_4^{-2}\right)^{1-}$, AA is $\left((Fe^{+2})^{tetr}[Fe^{+2}]_2^{oct}O_4^{-2}\right)^{2-}$, EA is $\left((Fe^{+3})^{tetr}[Fe^{+2}]_2^{oct}O_4^{-2}\right)^{1-}$ and AP is $\left((Fe^{+2})^{tetr}[Ca^{+2}]_2^{oct}O_4^{-2}\right)^{2-}$. Using G_{EE}, G_{AA} and G_{EA} from the previous optimization and $G_{E(EP)}$ and Δ_{EAP} as model parameters it is possible to find G_{EP} from (8.2) and G_{AP} from (8.3). The model function $G_{E(EP)}$ was estimated using the heat capacity of $CaFe_2O_4$ compound and two variable parameters: entropy and enthalpy of formation of $(Fe^{+3})^{tetr}[Ca_{0.5}^{+2},Fe_{0.5}^{+3}]_2^{oct}O_4^{-2}$.

8.1.2 Results of optimization

Selected results of modeling of the spinel phase together with slag, monoxide and solid compounds in the Ca–Fe–O system are shown in Figure 8.1-Figure 8.5. The properties of spinel are fixed by the slag – slag + spinel border in Figure 8.1 and Figure 8.2, and by the temperature of hematite – spinel transition in Figure 8.3 and Figure 8.4. The crucial experimental data on the solubility of calcium in spinel was obtained by Liu [272] using the equilibration/quenching/EMPA technique (Figure 8.5). The present optimization is compared with the experimental data and with the previous modeling of Decterov et al. [182] and of Selleby and Sundman [174]. The overall agreement with the experimental data in the present study is better than in previous optimizations. The optimized model function $G_{E(EP)}$ and other parameters are listed in Table 8–1.

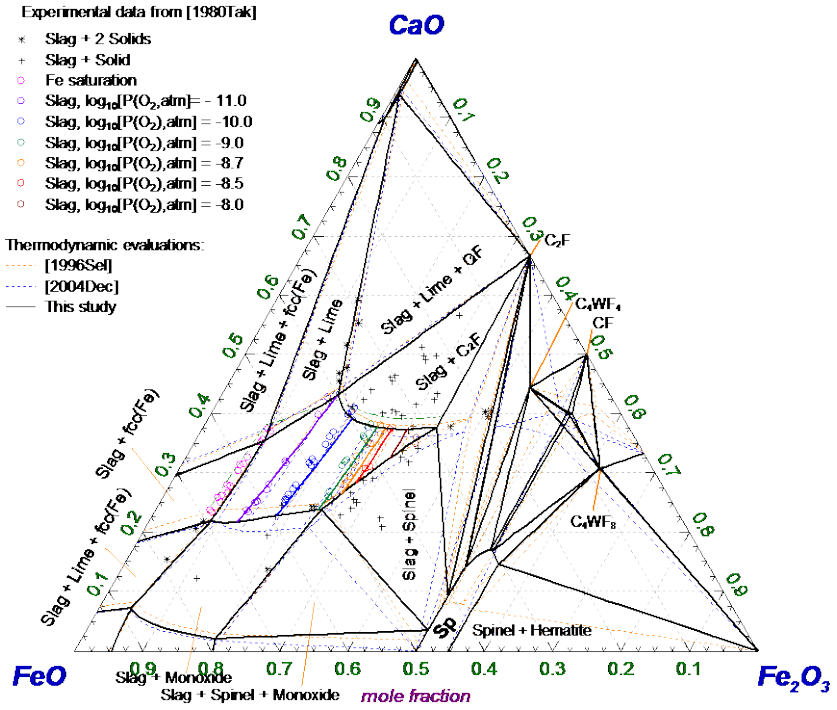

Figure 8.1. Isothermal section of the CaO–FeO–Fe_2O_3 system at 1200 °C. Experimental points [320] and calculated lines : dashed orange [174], dashed blue [182] and solid lines – this study.

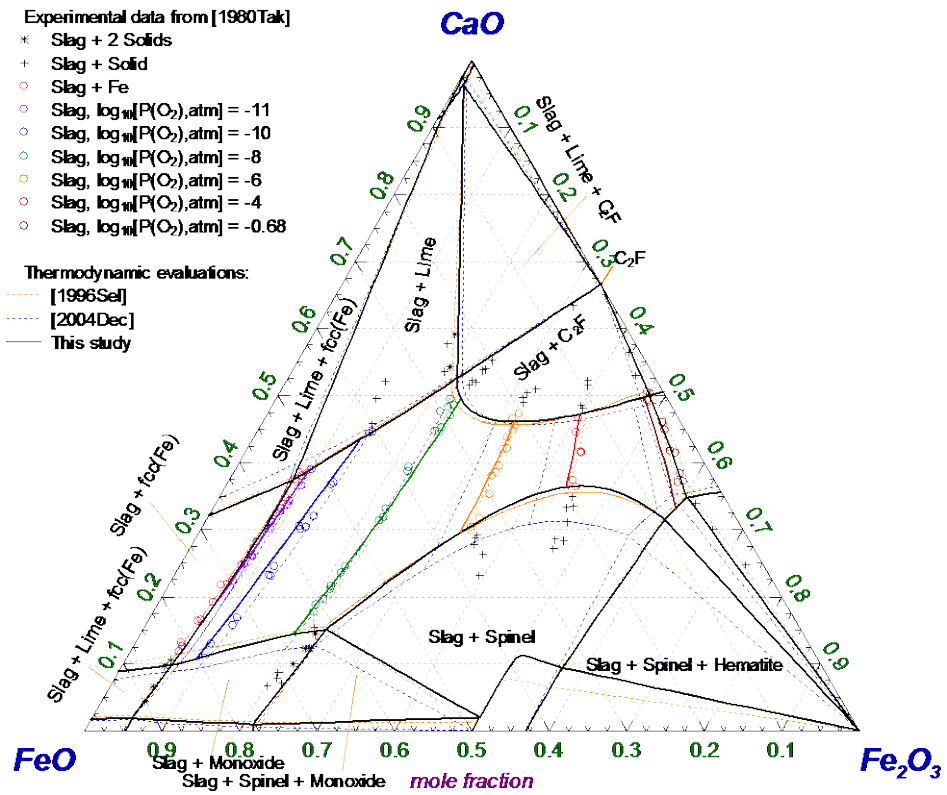

Figure 8.2. Isothermal section of the CaO–FeO–Fe_2O_3 system at 1300 °C. Experimental points [320] and calculated lines : dashed orange [174], dashed blue [182] and solid lines – this study.

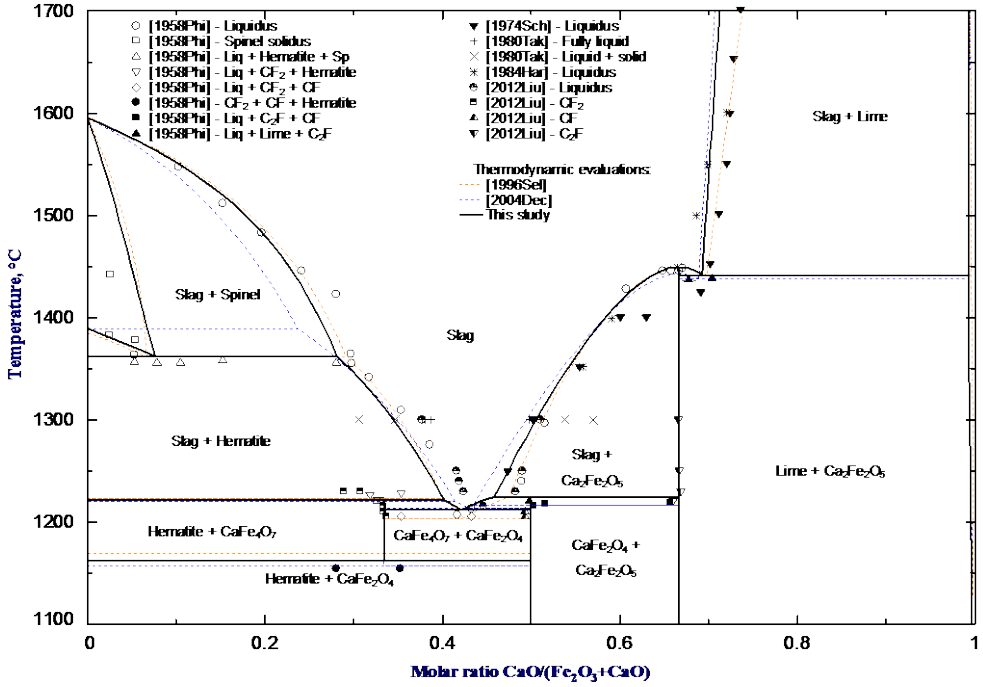

Figure 8.3. Phase diagram of the Ca–Fe–O system in air ($P(O_2)$ = 0.21 atm). Experimental points [272, 320-323] and calculated lines: dashed orange [174], dashed blue [182] and solid – this study.

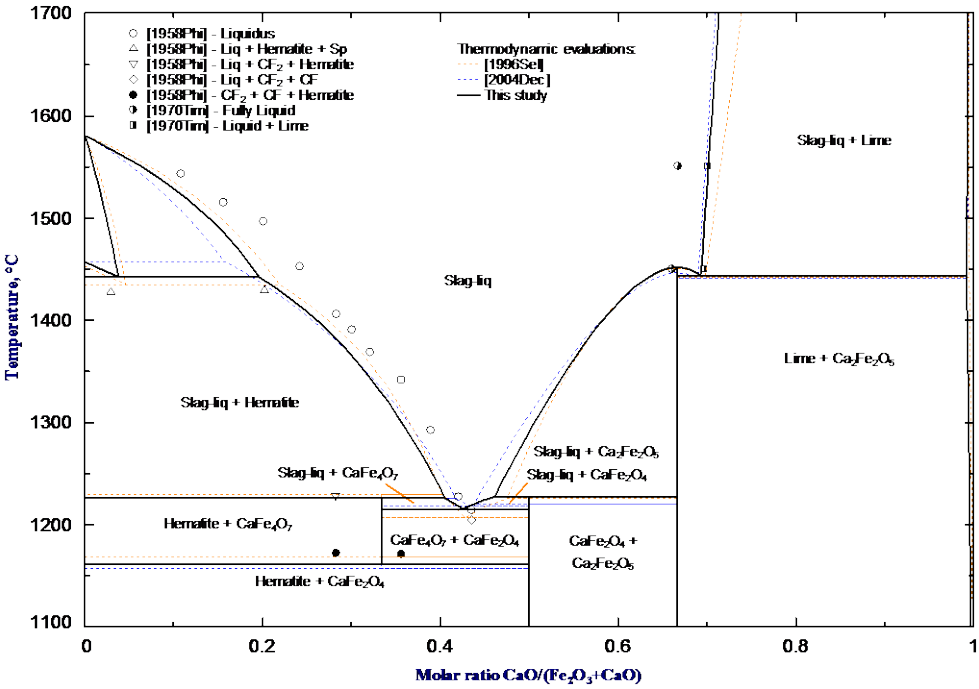

Figure 8.4. Phase diagram of the Ca–Fe–O system in oxygen ($P(O_2)$ = 1 atm). Experimental points [321, 324] and calculated lines: dashed orange [174], dashed blue [182] and solid – this study.

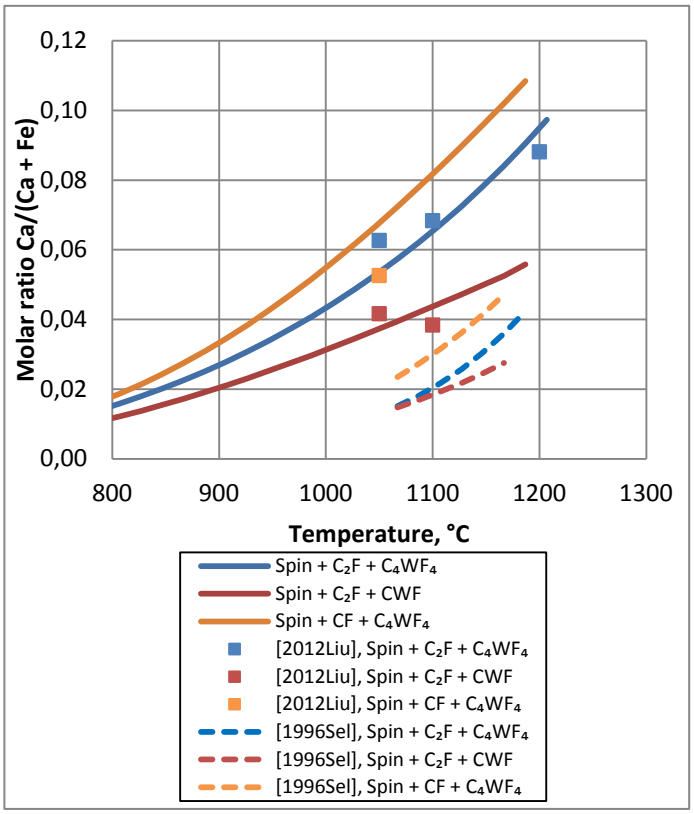

Figure 8.5. Calcium content of spinel in the Ca–Fe–O system at equilibria with two other solid phases. Experimental points [272] and calculated lines : dashed [174], solid – this study.

8.2 Ca–Cu–Fe–O system

The Ca and Cu content of the spinel phase in equilibrium with slag and liquid copper in the Ca–Cu–Fe–O system was measured by our colleagues at the Pyrosearch center [284, 325]. The equilibration/rapid-quenching/EPMA technique was applied. In this method, only metal ratios in the phases could be measured, while determination of oxygen is not possible. The measured phase compositions were projected through the oxygen corner to the $CaO–Cu_2O–Fe_3O_4$ plane. Under the conditions of the experiments, copper in slag exists almost exclusively as Cu^{+}, while the concentrations of Fe^{2+} and Fe^{3+} are of the same order of magnitude, and the ratio Fe^{2+}/Fe^{3+} varies depending on the slag composition, which explains why the projection to the $CaO–Cu_2O–Fe_3O_4$ plane was selected. The slag phase was modeled by T. Hidayat and the spinel phase was modeled by the present author.

8.2.1 Thermodynamic model for spinel

The spinel phase in the Ca–Cu–Fe–O system is the combination of previously modeled Ca–Fe–O [1] and Cu–Fe–O [172] spinels:

$$(Cu^{+2},Fe^{+2},Fe^{+3})^{tetr}[Ca^{+2}, Cu^{+2},Fe^{+2},Fe^{+3},Va]_2^{oct}O_4^{-2} \qquad (8.4)$$

Only one new end-member appears in the model, which is $\left((Cu^{+2})^{tetr}[Ca^{+2}]_2^{oct}O_4^{-2}\right)^{2-}$. Its Gibbs energy is calculated from the model parameter

$$\Delta_{EMP} = G_{MM} + G_{EP} - G_{EM} - G_{MP} \qquad (8.5)$$

where *MM* is $\left((Cu^{+2})^{tetr}[Cu^{+2}]_2^{oct}O_4^{-2}\right)^{2-}$, *EP* is $\left((Fe^{+3})^{tetr}[Ca^{+2}]_2^{oct}O_4^{-2}\right)^{1-}$, *EM* is $\left((Fe^{+3})^{tetr}[Cu^{+2}]_2^{oct}O_4^{-2}\right)^{1-}$, *MP* is $\left((Cu^{+2})^{tetr}[Ca^{+2}]_2^{oct}O_4^{-2}\right)^{2-}$. Using the previously obtained G_{MM}, G_{EM}, G_{MM} and varying Δ_{EMP}, it is possible to describe the experimental data on the Ca and Cu solubility in Fe_3O_4 spinel.

8.2.2 Results of optimization

The optimized value of the Δ_{EMP} parameter is given in Table 8–1. The results are presented on the phase diagrams shown in Figure 8.6-Figure 8.10. On these diagrams, black lines represent the borders of phase fields. They show, which phases co-exist in equilibrium at a given bulk

composition. The experimental points and the corresponding calculated red lines represent the projection of the equilibrium phase compositions onto the Cu_2O–CaO–Fe_3O_4 plane. Experimental points should be compared with red lines, not black lines.

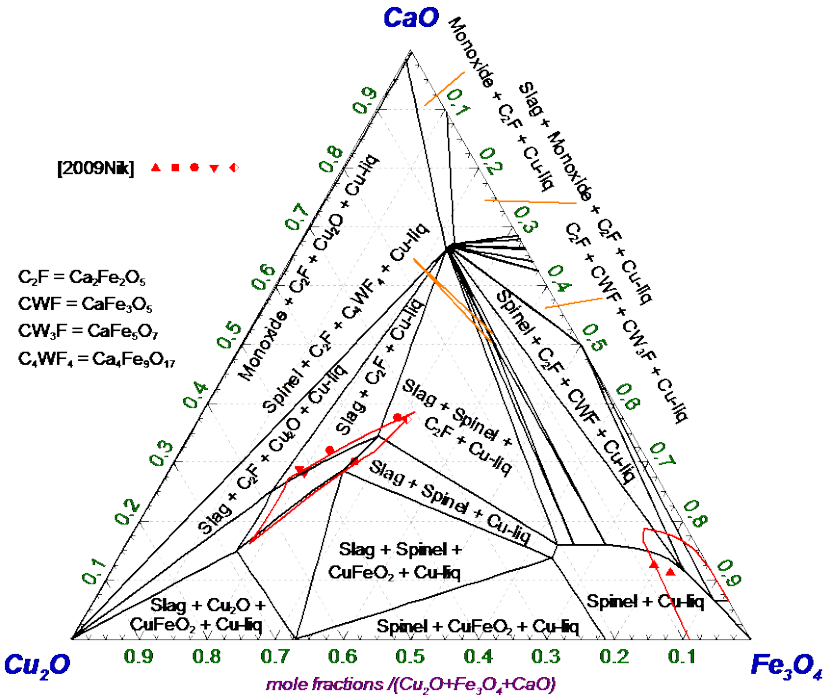

Figure 8.6. Black lines: Isothermal section of the phase diagram of the Ca–Cu–Fe–O system at 1100 °C and molar ratio Cu/(Cu_2O + Fe_3O_4 + CaO) = 0.1. Experimental points [325] and calculated red lines: composition of phases, projected from the oxygen corner of the Ca–Cu–Fe–O tetrahedron onto the CaO–Cu_2O–Fe_3O_4 plane. Triangles – compositions of spinel in equilibrium with slag and liquid Cu, squares compositions of slag in equilibrium with spinel and liquid Cu, circles – compositions of slag in equilibrium with $Ca_2Fe_2O_5$ and liquid Cu, inversed triangles compositions of slag in equilibrium with Cu_2O and liquid Cu, half-filled diamond compositions of slag in equilibrium with C_4WF_4 and liquid Cu.

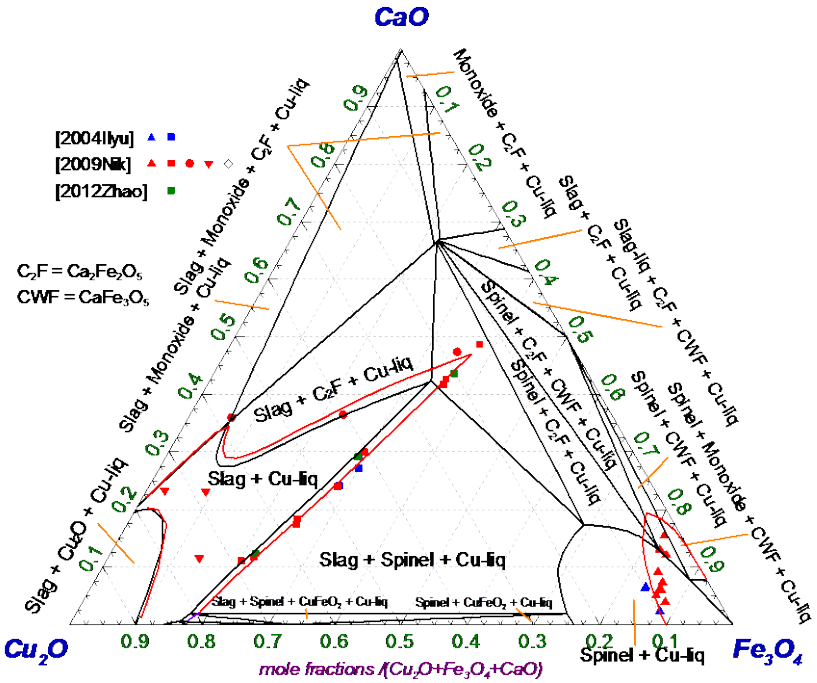

Figure 8.7. Black lines: Isothermal section of the phase diagram of the Ca–Cu–Fe–O system at 1150 °C and molar ratio Cu/(Cu_2O + Fe_3O_4 + CaO) = 0.1. Experimental points [284, 325, 326] and calculated red lines: composition of phases, projected from the oxygen corner of the Ca–Cu–Fe–O tetrahedron onto the CaO–Cu_2O– Fe_3O_4 plane. Symbols as in Figure 8.7.

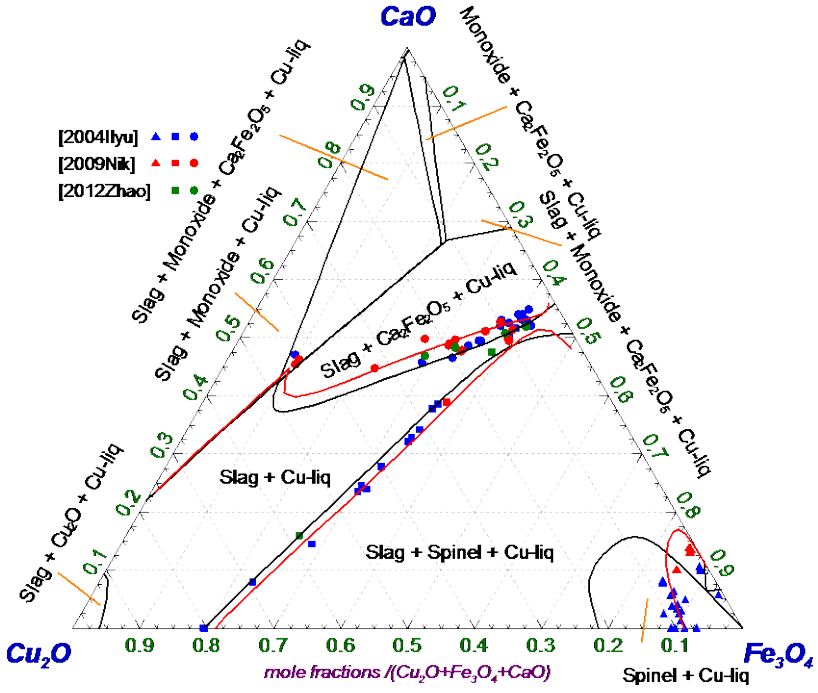

Figure 8.8. Black lines: Isothermal section of the phase diagram of the Ca–Cu–Fe–O system at 1200 °C and molar ratio Cu/(Cu_2O + Fe_3O_4 + CaO) = 0.1. Experimental points [284, 325, 326] and calculated red lines: composition of phases, projected from the oxygen corner of the Ca–Cu–Fe–O tetrahedron onto the CaO–Cu_2O– Fe_3O_4 plane. Symbols as in Figure 8.7.

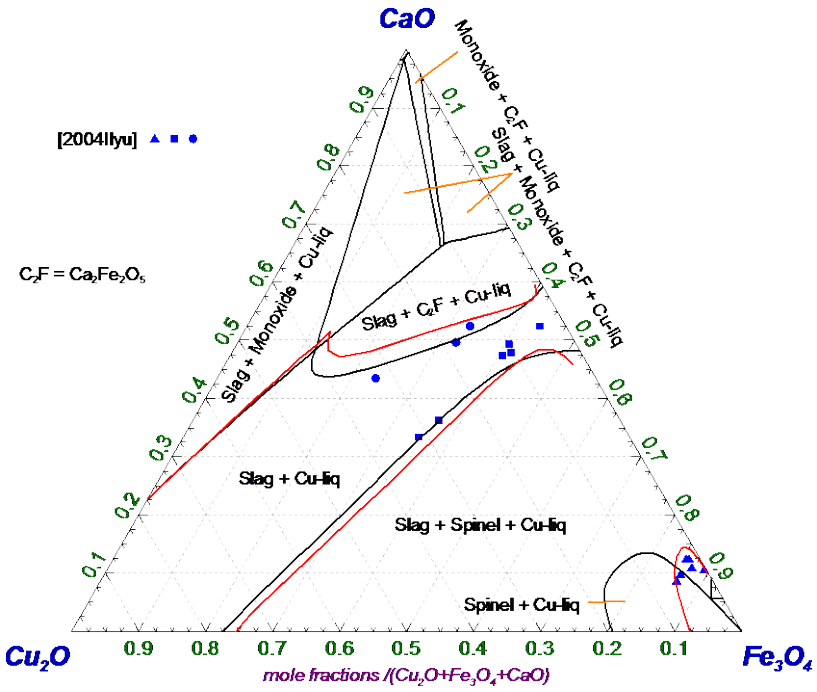

Figure 8.9. Black lines: Isothermal section of the phase diagram of the Ca–Cu–Fe–O system at 1235 °C and molar ratio Cu/(Cu_2O + Fe_3O_4 + CaO) = 0.1. Experimental points [284] and calculated red lines: composition of phases, projected from the oxygen corner of the Ca–Cu–Fe–O tetrahedron onto the CaO–Cu_2O– Fe_3O_4 plane. Symbols as in Figure 8.7.

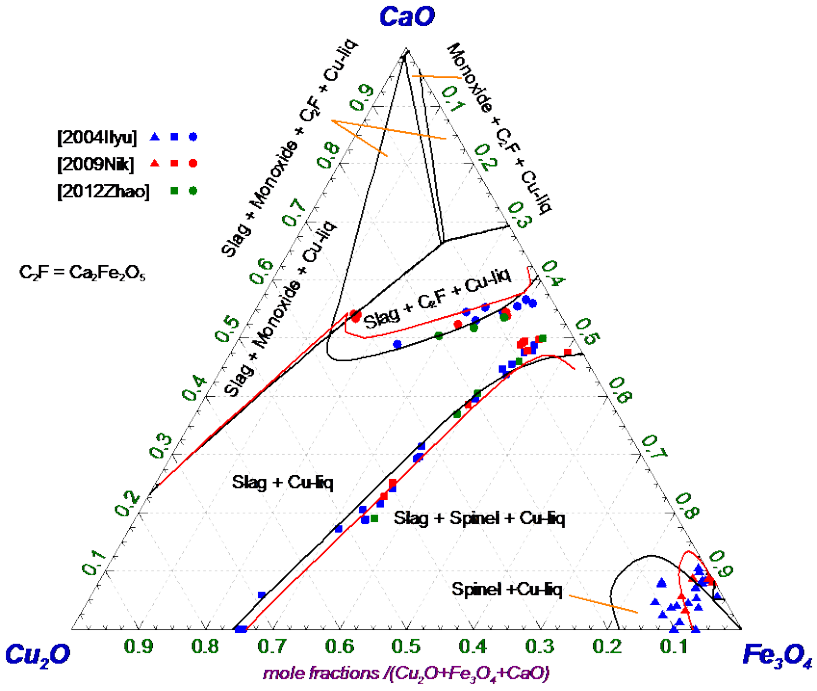

Figure 8.10. Black lines: Isothermal section of the phase diagram of the Ca–Cu–Fe–O system at 1250 °C and molar ratio Cu/(Cu_2O + Fe_3O_4 + CaO) = 0.1. Experimental points [284, 325, 326] and calculated red lines: composition of phases, projected from the oxygen corner of the Ca–Cu–Fe–O tetrahedron onto the CaO–Cu_2O– Fe_3O_4 plane. Symbols as in Figure 8.7.

8.3 Al–Cu–O and Al–Cu–Fe–O systems

The spinel phase extends to the Al–Cu–O system, with the composition close to $CuAl_2O_4$ (Figure 8.11). There is one more ternary compound with the composition of $CuAlO_2$. A systematic approach was used to model the spinel – all phases were modeled simultaneously and all available experimental data were taken into account.

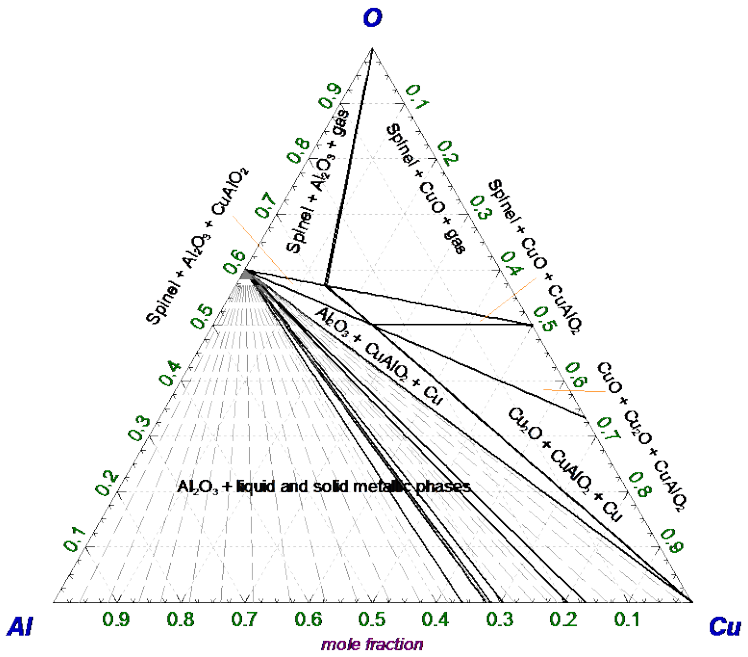

Figure 8.11. Phase diagram of the Al–Cu–O system at 1000 °C and P = 1 atm.

8.3.1 Thermodynamic model for spinel

Spinel solution in the Al–Cu–O system may be represented as follows:

$$(Cu^{+2}, Al^{+3})^{tetr}[Cu^{+2}, Al^{+3}, Va]_2^{oct}O_4^{-2} \qquad (8.6)$$

The Gibbs energies of the following six end-member are required: G_{MM} for $\left((Cu^{+2})^{tetr}[Cu^{+2}]_2^{oct}O_4^{-2}\right)^{2-}$, G_{MF} for $\left((Cu^{+2})^{tetr}[Al^{+3}]_2^{oct}O_4^{-2}\right)^{0}$, G_{MV} for $\left((Cu^{+2})^{tetr}[Va]_2^{oct}O_4^{-2}\right)^{6-}$, G_{FM} for $\left((Al^{+3})^{tetr}[Cu^{2+}]_2^{oct}O_4^{-2}\right)^{1-}$, G_{FF} for $\left((Al^{+3})^{tetr}[Al^{3+}]_2^{oct}O_4^{-2}\right)^{1+}$ and G_{FV} for $\left((Al^{+3})^{tetr}[Va]_2^{oct}O_4^{-2}\right)^{5-}$.

G_{MM}, G_{MV} are available from the optimization of the Cu–Fe–O system [172], and G_{FF}, G_{FV} – from the optimization of the Al–Fe–O system [25]. Thus, the spinel solution in the Al–Cu–O

system is dependent on the Cu–Fe–O and Al–Fe–O systems. In some sense it is the final link in the circle following chain

$$\begin{array}{ccc} CuAl_2O_4 & \rightarrow & CuFe_2O_4 \\ \uparrow & & \uparrow \\ FeAl_2O_4 & \leftarrow & Fe_3O_4 \end{array} \qquad (8.7)$$

The sequence of optimizations of the systems is shown by arrows. It is the Fe–O system, which was optimized first, then the Al–Fe–O and Cu–Fe–O systems and, finally, the Al–Cu–O system. This order is deliberate – there are a lot of available experimental data in the Fe–O, Al–Fe–O and Cu–Fe–O systems, much less – in the Al–Cu–O and almost none in the Al–Cu–Fe–O system, which is represented by $FeAl_2O_4 \rightarrow CuAl_2O_4$ and $CuFe_2O_4 \rightarrow CuAl_2O_4$ sides. More adjustable model parameters were reserved for the Fe–O, Al–Fe–O and Cu–Fe–O systems, only few – for the Al–Cu–O system and none – for the Al–Cu–Fe–O system. So, only G_{MF} and G_{FM} must be defined. G_{MF}, which is the Gibbs energy of the hypothetical completely normal $CuAl_2O_4$ spinel, was the model function, and G_{FM} was defined using the so called inversion parameter:

$$I_{MF} = G_{FF} + G_{FM} - 2G_{MF} \qquad (8.8)$$

It was not possible to describe all experimental data with only G_{MF} and G_{FM}. In addition, the small excess parameter $L_{k:Al^{3+},Cu^{2+}}$ was introduced.

8.3.2 Results of optimization

Thermodynamic properties, crystallographic, activity and phase diagram data were used to define the model function G_{MF}, the inversion parameter I_{MF} and the thermodynamic properties of $CuAlO_2$ (see Table 8–1). The heat capacities of $CuAlO_2$ and the hypothetical completely normal $CuAl_2O_4$ and were estimated as the sum of C_P of pure oxides. For real spinel $CuAl_2O_4$, the change in the degree of inversion with temperature results in the additional contribution to the heat capacity as shown in Figure 8.12. The enthalpy of formation of $CuAl_2O_4$ from CuO and Al_2O_3 at 697 °C was measured by Navrotsky and Kleppa [309] using oxide melt solution calorimetry. They obrained the value of +21.6 kJ·mol^{-1}. The enthalpy and entropy of G_{MF} were fixed in such a way that the calculated enthalpy of formation of $CuAl_2O_4$ was the same as the experimental value. The I_{MF} parameter has a major effect on the cation distribution of spinel

(Figure 8.13). The meaning of the degree of inversion, *s*, is clear from the formula $(Cu^{+2}_{1-s},Al^{+3}_{s})^{tetr}[Cu^{+2}_{s/2},Al^{+3}_{1-s/2}]^{oct}_{2}O^{-2}_{4}$. The calculated degree of inversion is in agreement with the experimental data in the temperature interval of 1000-1500 °C. It falls dramatically below 1000 °C, so that $CuAl_2O_4$ becomes completely normal spinel at low temperatures. This is an expected behavior: every spinel should become completely normal or completely inverse at low temperature if its cation distribution is not frozen or, in other words, if the mobility of cations remains sufficient for the re-distribution between the sublattices to occur. In reality the equilibrium distribution is not attained, and when spinel is cooled down, the cations distribution freezes at a certain temperature, which depends on the cooling rate.

Measurements of the oxygen partial pressure over three-phase regions in a ternary system are often used to determine the thermodynamic properties of oxide phases. In case of the Al–Cu–O system, large discrepancies between the $P(O_2)$ measurements of different authors were found (Figure 8.14). Experimental studies involving Al_2O_3 are difficult because reactions are rather slow. Some of the discrepancies can be attributed to the different allotropic modifcations of alumina used in the experiments. Making the calculations with either α- or γ-Al_2O_3, it was possible to reach a good agreement with the experimental data on $P(O_2)$ and the phase diagram.

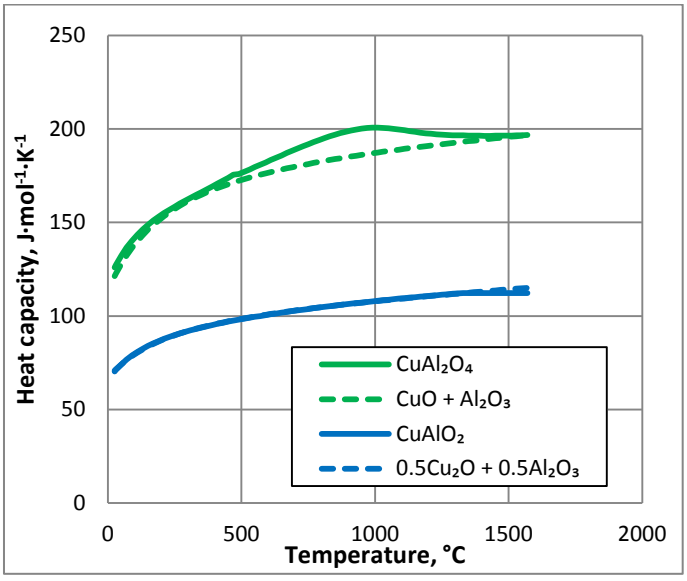

Figure 8.12. Heat capacities of $CuAl_2O_4$ and $CuAlO_2$ in comparison with the corresponding sum of oxides.

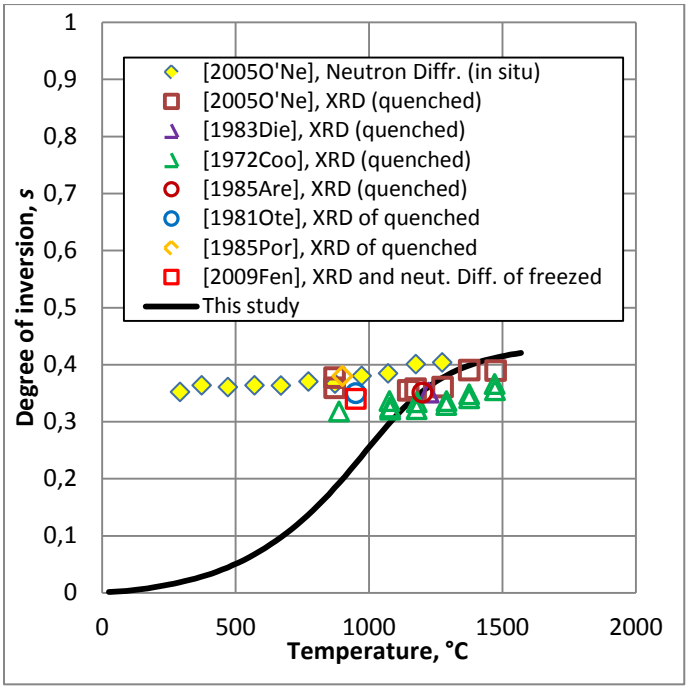

Figure 8.13. Degree of inversion of $CuAl_2O_4$ spinel : s is the number of moles of copper on the octahedral sublattice. Experimental points [327-333] and calculated line.

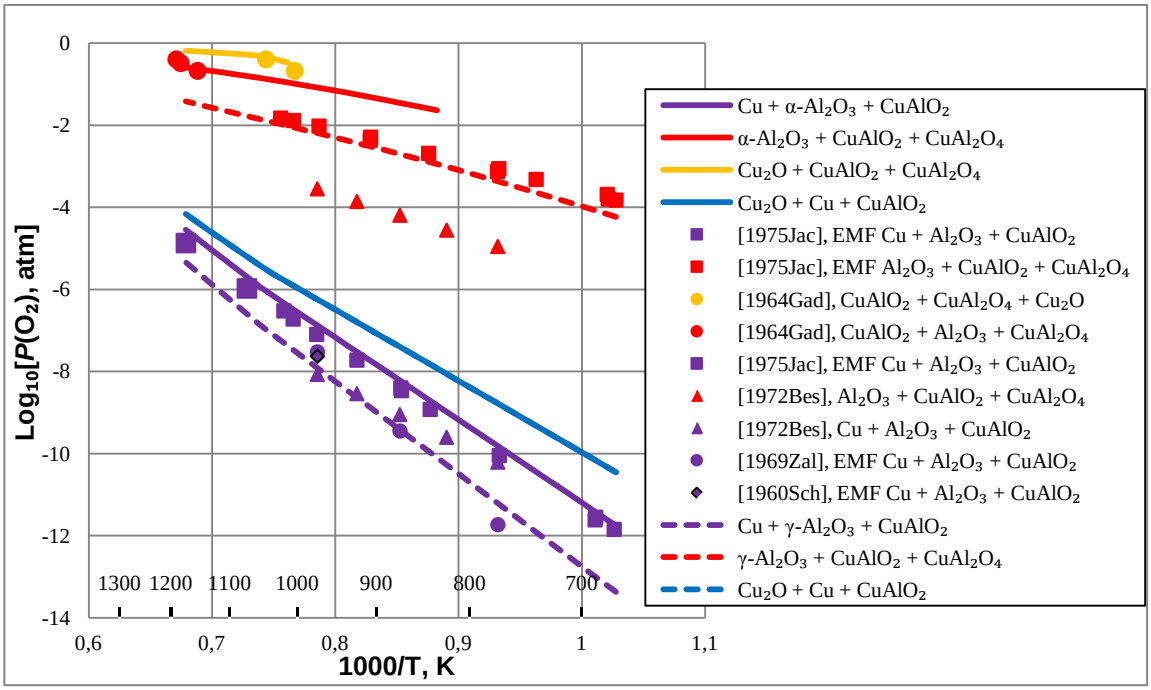

Figure 8.14. Equilibrium oxygen partial pressures over three-phase regions in the Al–Cu–O system : experimental points [334-337] and calculated lines.

Phase equilibria in the Al–Cu–O system were studied by Misra and Chaklader [338] using quenching and equilibration + cone-fusion methods in air; by Gadalla and White [335] using

dissociation curves in air, oxygen and N_2/O_2 mixtures; by Tsuchida et al. [339] – using DSC/TG + in-situ XRD in air, by Guedes et al. [340] – using DSC/TG in air or N_2, and by Hidayat [1] – using the equilibration/quenching/EMPA technique. The results in air are summarized in Figure 8.15.

The range of stability of spinel in air was reported to be from 805~850 °C [338] to 1150~1180 °C ([1] and [335]). The calculated range is 830-1155 °C. Liquidus in air cannot be described without introducing one more slag component, CuO, in addition to Cu_2O. However, these conditions are too far away from the pyrometallurgical production of copper, so it was decided not to introduce CuO into slag.

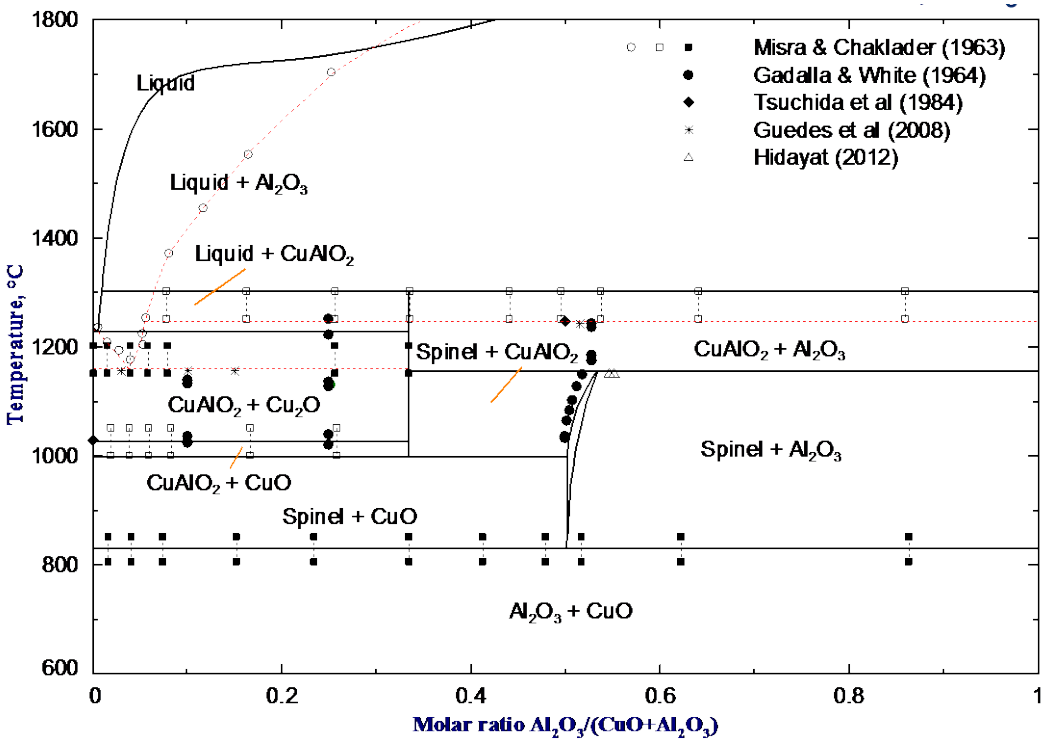

Figure 8.15. Phase diagram of Al–Cu–O system in air ($P(O_2)$ = 0.21 atm): experimental points [1, 335, 338-340], solid lines are calculated in the present study, dashed lines show the schematic phase diagram, which cannot be described without adding CuO to the slag components.

Cu_2O–Al_2O_3 slag in equilibrium with Cu was studied by Kuxman and Kurre [126], by Gerlach et al. [341] and by Hidayat [1]. Very small concentrations of Al_2O_3 were reported in slag by Kuxman and Kurre [126], which is in contradiction with the results of Wartenberg [342]. The small solubility of Al_2O_3 at 1300 °C was confirmed during the optimization of the Al–Cu–O–Si system by the data of Oishi et al. [343]. Large positive parameters were introduced in slag to increase the steepness of Al_2O_3 liquidus.

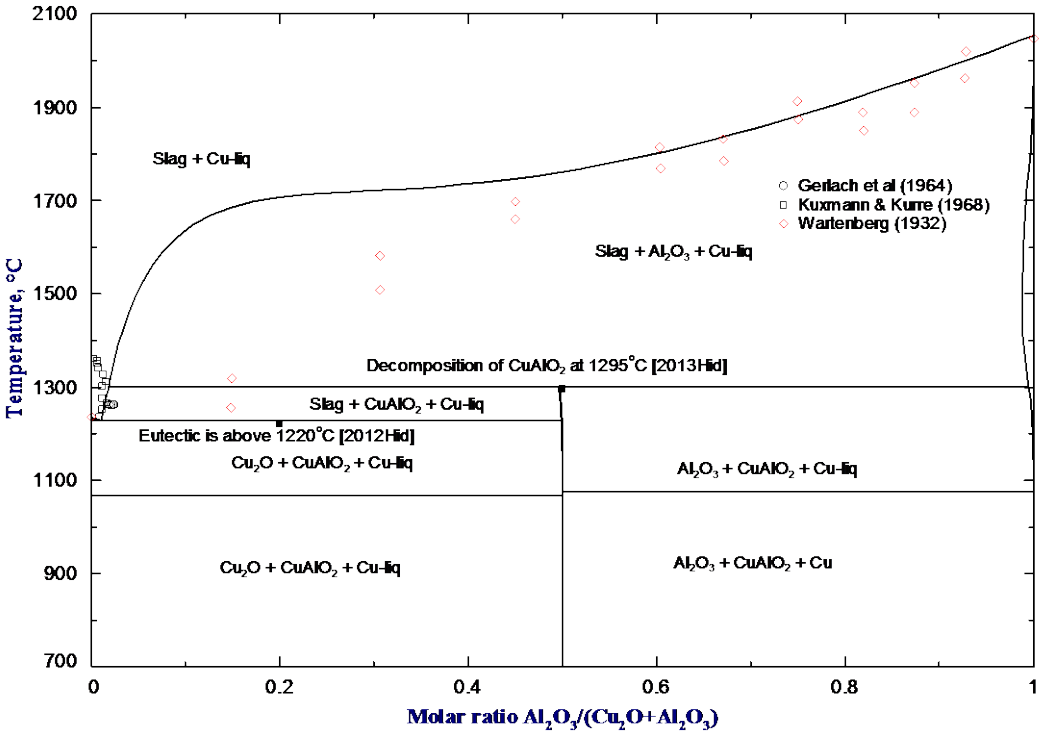

Figure 8.16. Phase diagram of Al–Cu–O system at copper saturation $Cu/(Cu_2O + Al_2O_3) = 0.03$: experimental points [1, 126, 341, 342] and calculated lines.

The only available data on spinel in the quaternary Al–Cu–Fe–O system was the $P(O_2)$ measurements of Zalazinskii et al. [344]for the reduction of the $CuFe_{1.75}Al_{0.25}O_4$ spinel at 1000 °C (Figure 8.17). The calculated sequence of phases in equilibrium for these reduction experiments is:

Spinel + CuO → Spinel + Cu_2O + CuO → Spinel + Cu_2O + $CuFeO_2$ → Spinel + $CuFeO_2$ → Spinel + Cu +$CuFeO_2$ → Spinel + Cu → Spinel + Cu + Monoxide → Spinel + Cu + Fe + Monoxide → Spinel + Cu + Fe

No additional parameters were introduced to model the spinel solution in the Al–Cu–Fe–O system.

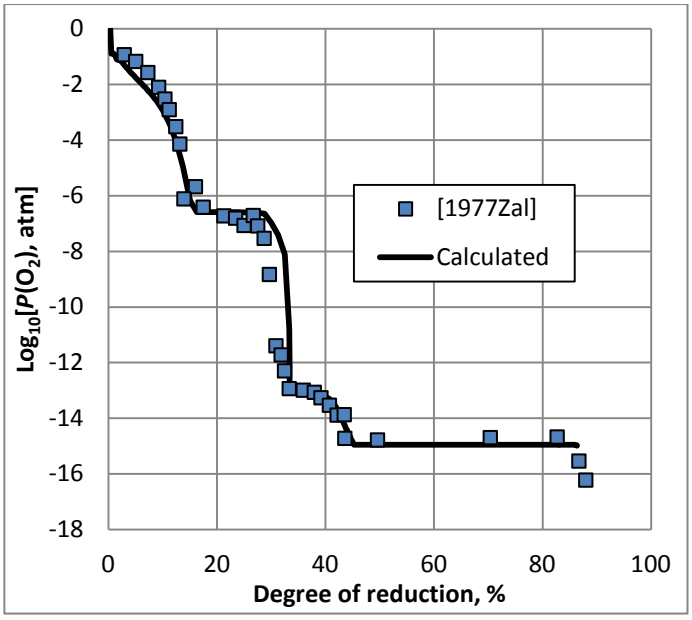

Figure 8.17. Reduction of $CuFe_{1.75}Al_{0.25}O_4$ spinel with H_2 at 1000 °C. Experimental points [344] and calculated line.

8.4 Al–Ca–Fe–O system

8.4.1 Thermodynamic model for spinel

The spinel solution in the Al–Ca–Fe–O system was modeled as follows:

$$(Fe^{+2}, Fe^{+3}, Al^{+3})^{tetr}[Ca^{2+}, Fe^{+2}, Fe^{+3}, Al^{+3}, Va]_2^{oct}O_4^{-2} \qquad (8.9)$$

In addition to already optimized model functions for the Gibbs energies of end-members, one more is required, G_{FP}, for the $\left((Al^{+3})^{tetr}[Ca^{2+}]_2^{oct}O_4^{-2}\right)^{1-}$ end member. It was found from the estimated Gibbs energy of the hypothetical completely inverse spinel $F(FP) = (Al^{+3})^{tetr}[Ca_{0.5}^{+2}, Al_{0.5}^{+3}]_2^{oct}O_4^{-2}$

$$G_{F(FP)} = 0.5G_{FF} + 0.5G_{FP} + 2RT \cdot [0.5\ln 0.5 + 0.5\ln 0.5] \qquad (8.10)$$

The heat capacity and entropy of *F(FP)* were assumed to be equal to those of $CaAl_2O_4$ compound and the enthalpy of formation of $(Al^{+3})^{tetr}[Ca_{0.5}^{+2}, Al_{0.5}^{+3}]_2^{oct}O_4^{-2}$ was a variable model parameter.

8.4.2 Results of optimization

Liu [272] studied the limits of solubility of Ca in $FeAl_2O_4$ spinel using the equilibration/quenching/EPMA technique. She observed the following phases in equilibrium: spinel + wüstite + $Ca(Fe,Al)_2O_4$ + Fe at 1200 °C, spinel + $Ca(Fe,Al)_4O_7$ + $Ca(Fe,Al)_2O_4$ + Fe at 1300 °C, spinel + $Ca(Fe,Al)_4O_7$ + slag + Fe at 1400 °C. The metal ratios in spinel, $Ca(Fe,Al)_2O_4$, and ib the $Ca(Fe,Al)_4O_7$ phase were measured. The measured Ca content in spinel was very small.

Phase diagrams of the Al–Ca–Fe–O system at iron saturation at 1200 and 1400 °C are shown in Figure 8.18 and Figure 8.19. The calculated equilibrium phase assemblages are in agreement with the observations of Liu [272]. The molar ratio Ca/(Al + Ca + Fe) in spinel for different 4-phase equilibria is shown in Figure 8.20. The molar ratio Fe/(Al + Ca + Fe) in $Ca(Fe,Al)_2O_4$ and $Ca(Fe,Al)_4O_7$ for the same 4-phase equilibria are shown in Figure 8.21 and Figure 8.22. An agreement with the experimental data is good.

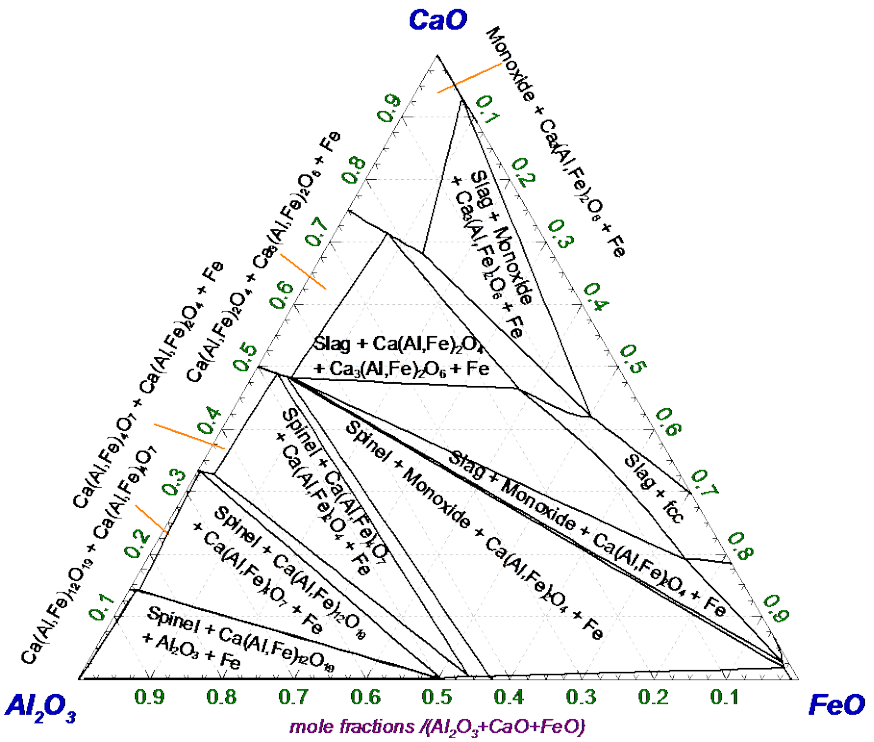

Figure 8.18. Isothermal section of the phase diagram of the Al–Ca–Fe–O system at 1200 °C and molar ratio Fe/(Al_2O_3 + FeO + CaO) = 0.5.

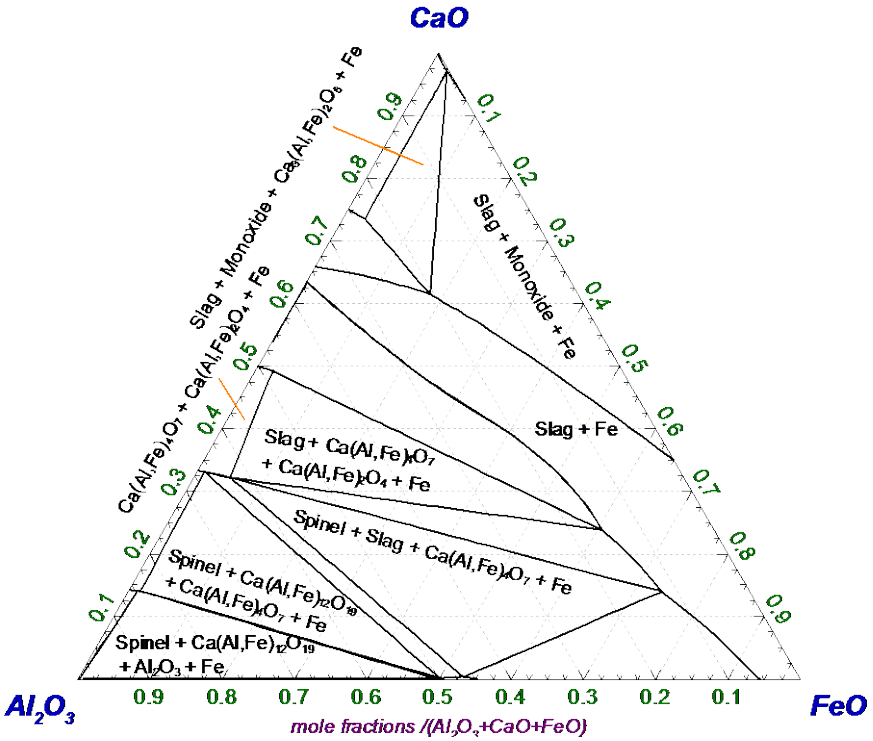

Figure 8.19. Isothermal section of the phase diagram of the Al–Ca–Fe–O system at 1400 °C and molar ratio Fe/(Al_2O_3 + FeO + CaO) = 0.5.

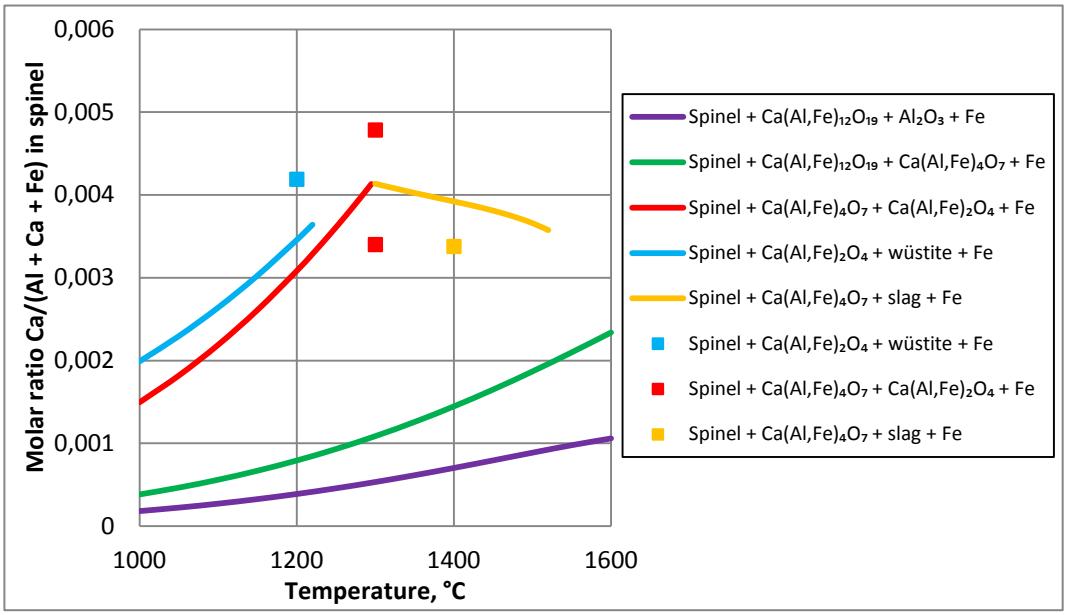

Figure 8.20. Molar ratio Ca/(Al + Ca + Fe) in spinel for different 4-phase equilibria in the Al–Ca–Fe–O system: experimental points [272] and calculated lines.

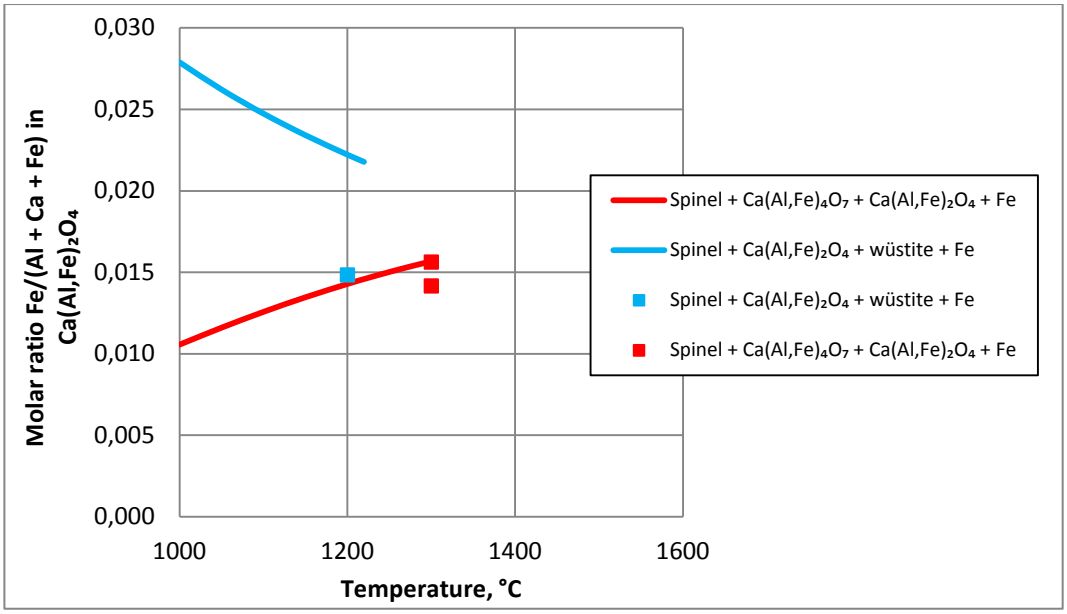

Figure 8.21. Molar ratio Fe/(Al + Ca + Fe) in the $Ca(Al, Fe)_2O_4$ phase for different 4-phase equilibria in the Al–Ca–Fe–O system: experimental points [272] and calculated lines.

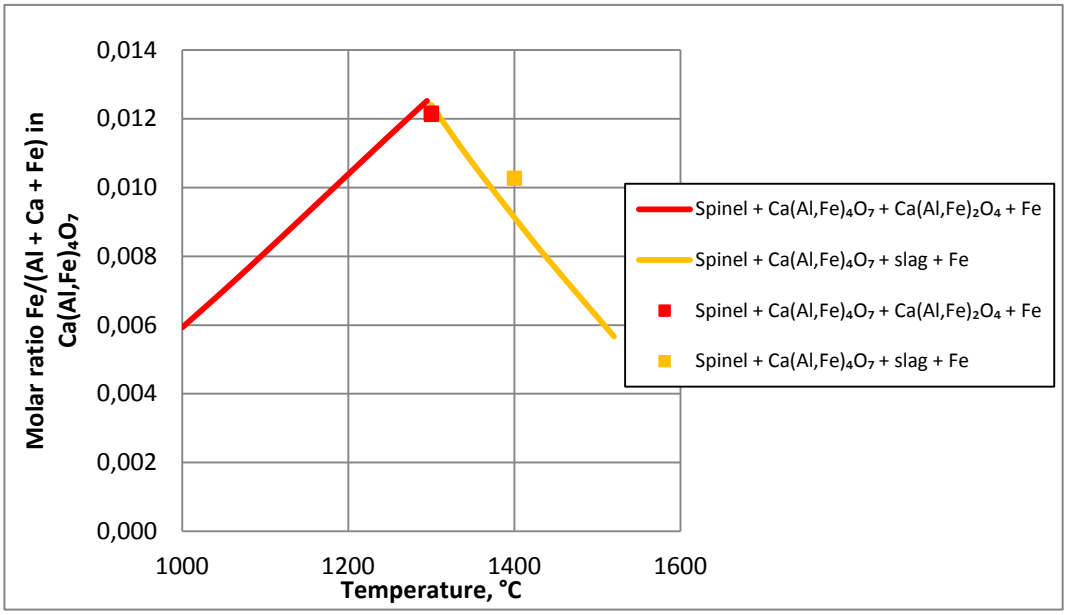

Figure 8.22. Molar ratio Fe/(Al + Ca + Fe) in the $Ca(Al, Fe)_4O_7$ phase for different 4-phase equilibria in the Al–Ca–Fe–O system: experimental points [272] and calculated lines.

8.5 Ca–Fe–Mg–O system

8.5.1 Thermodynamic model for spinel

Only one additional Gibbs energy function, G_{BP}, for the spinel end-member $\left((Mg^{+2})^{tetr}[Ca^{+2}]_2^{oct}O_4^{-2}\right)^{2-}$ has to be defined for spinel containing both Ca and Mg. The following model parameter was used:

$$\Delta_{EBP} = G_{BB} + G_{EP} - G_{EB} - G_{BP} \qquad (8.11)$$

where *BB* is $\left((Mg^{+2})^{tetr}[Mg^{+2}]_2^{oct}O_4^{-2}\right)^{2-}$, *EP* is $\left((Fe^{+3})^{tetr}[Ca^{+2}]_2^{oct}O_4^{-2}\right)^{1-}$ and *EB* is $\left((Fe^{+3})^{tetr}[Mg^{+2}]_2^{oct}O_4^{-2}\right)^{1-}$. It was optimized in order to describe the solubility of Ca in Fe_3O_4–$MgFe_2O_4$ spinel.

8.5.2 Results of optimization

The solubility of Ca in Fe_3O_4–$MgFe_2O_4$ spinel in air was studied by Johnson and Muan [345] using an equilibration/quenching/X-ray and microscopic investigation techniques. Their results are presented in Figure 8.23. The model parameter Δ_{EBP} was set in such a way that the calculated phase boundaries between Spinel and Slag + Spinel, and between Spinel + Monoxide (MgO) and Monoxide (MgO) + Slag + Spinel phase regions lie between the experimental points. The melting relations close to the $Ca_2Fe_2O_5$–$MgFe_2O_4$ section of the Ca–Fe–Mg–O system in air were studied by Fusenig et al. [346] using the same method. As can be seen from Figure 8.24, the the calculated diagram is in agreement with the experimental data.

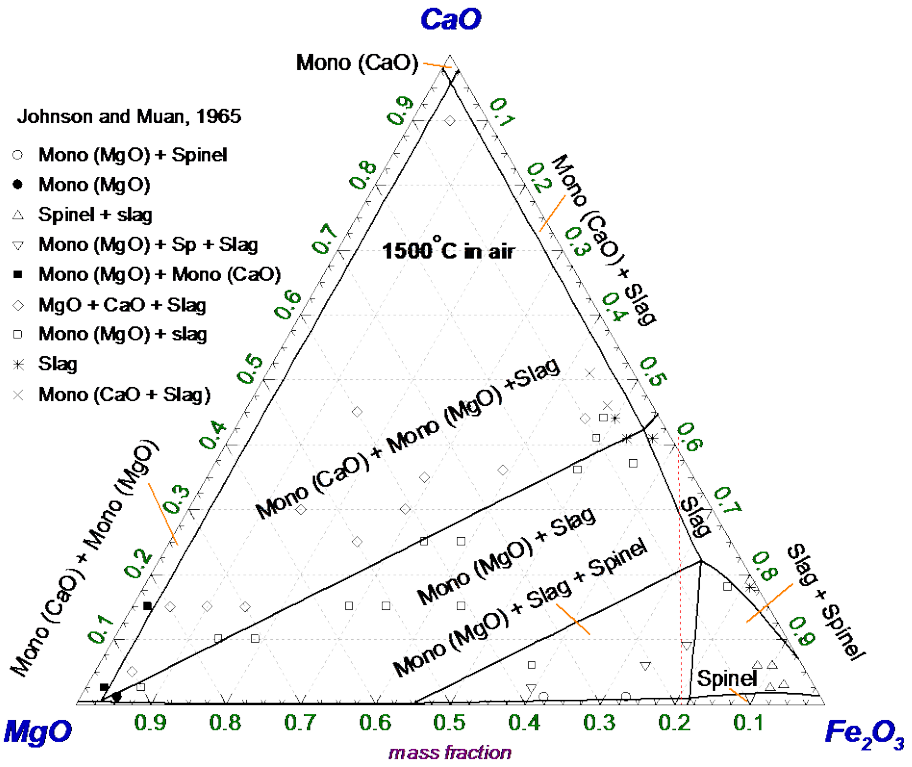

Figure 8.23. Isothermal section of the phase diagram of the Ca–Mg–Fe–O system at 1500 °C in air: experimental points [345] and calculated lines. Red dotted line corresponds to the section shown in the next figure.

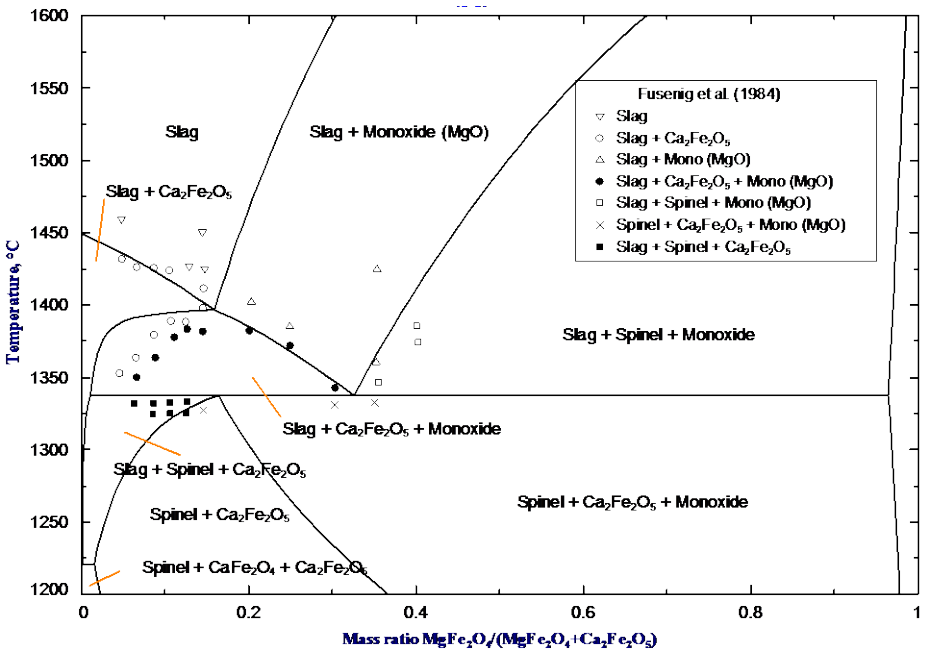

Figure 8.24. Phase diagram of the $Ca_2Fe_2O_5$-$MgFe_2O_4$ section with excess Fe_2O_3: mass ratio $Fe_2O_3/(Ca_2Fe_2O_5 + MgFe_2O_4) = 0.01$ in air. This section is shown by the red dashed line in the previous figure. Experimental points [346] and calculated lines.

8.6 Summary of results

Ca and Cu were added to the spinel solution. The thermodynamic functions of all solid phases and slag in the Al–Ca–Cu–Fe–Mg–O system were optimized previously [24, 25] and in the current study. The experimental data in the Cu–Fe–O, Ca–Fe–O, Al–Cu–O, Ca–Cu–Fe–O, Al–Cu–Fe–O, Al–Ca–Fe–O and Ca–Fe–Mg–O systems were evaluated and compared with the calculations. In order to complete the spinel database, the Gibbs energies for the last two end-members have been defined: G_{BM} for $\left((\mathrm{Mg}^{+2})^{\mathrm{tetr}}[\mathrm{Cu}^{+2}]_2^{\mathrm{oct}}\mathrm{O}_4^{-2}\right)^{2-}$ and G_{MB} for $\left((\mathrm{Cu}^{+2})^{\mathrm{tetr}}[\mathrm{Mg}^{+2}]_2^{\mathrm{oct}}\mathrm{O}_4^{-2}\right)^{2-}$. The following model parameters are used:

$$\Delta_{BME} = G_{BE} + G_{MM} - G_{BM} - G_{ME} \tag{8.12}$$

$$\Delta_{BMB} = G_{BB} + G_{MM} - G_{BM} - G_{MB} \tag{8.13}$$

where *BE* is $\left((\mathrm{Mg}^{+2})^{\mathrm{tetr}}[\mathrm{Fe}^{+3}]_2^{\mathrm{oct}}\mathrm{O}_4^{-2}\right)^{0}$, *MM* is $\left((\mathrm{Cu}^{+2})^{\mathrm{tetr}}[\mathrm{Cu}^{+2}]_2^{\mathrm{oct}}\mathrm{O}_4^{-2}\right)^{2-}$, *ME* is $\left((\mathrm{Cu}^{+2})^{\mathrm{tetr}}[\mathrm{Fe}^{+3}]_2^{\mathrm{oct}}\mathrm{O}_4^{-2}\right)^{0}$, and *BB* is $\left((\mathrm{Mg}^{+2})^{\mathrm{tetr}}[\mathrm{Mg}^{+2}]_2^{\mathrm{oct}}\mathrm{O}_4^{-2}\right)^{2-}$. No reliable experimental data were found on spinel in the Cu–Fe–Mg–O system, so the parameters Δ_{BME} and Δ_{BMB} were set equal to 0 as a first approximation.

Table 8–1. Optimized thermodynamic properties of stoichiometric compounds and model parameters for liquid and solid solutions in the Al–Ca–Cu–Fe–Mg–O system (J·mol^{-1} and J·mol^{-1}·K^{-1})

Compounds	**Temperature range (K) or reference**	$\Delta H^{o}_{298.15}$ **J·mol^{-1}**	$S^{o}_{298.15}$ **J·mol^{-1}·K^{-1}**	$C_P(T)$ **J·mol^{-1}·K^{-1}**
MgO, CaO	[347], [348]			
Al_2O_3, $CaAl_2O_4$, $CaAl_{12}O_{19}$, $CaAl_4O_7$, $Ca_3Al_2O_6$	[349]			
$FeAlO_3$	[25]			
$CuAlO_2$	298 – 1600	-936141.4	64.4099	$85.8445 + 0.023530T - 1974660T^{-2} - 4.09025\cdot10^{-6}T^2$
CuO, Cu_2O	[114]			
Fe_2O_3	[227]			
$CuFeO_2$	[172]			
$Ca_3MgAl_4O_{10}$, $CaMg_2Al_{16}O_{27}$, $Ca_2Mg_2Al_{28}O_{46}$	[350]			
$CaFe_2O_4$ (CF)	298 – 2000 [1]	-1480324.0	145.0943	$170.9880 + 0.016000T - 1818972T^{-2}$
$Ca_2Fe_2O_5$ (C_2F)	298 – 2000 [1]	-2125550.0	192.0000	$245.0855 + 0.004877T - 4799515T^{-2}$
$CaFe_3O_5$ (CWF)	298 – 2000 [1]	-1740463.5	222.3350	$177.7756 + 0.030608T - 6588086T^{-2} + 1366.9960T^{-0.5} + 102978788T^{-3}$
$CaFe_4O_7$ (CF_2)	298 – 2000 [1]	-2258859.0	272.8000	$325.8761 + 0.00244T - 6751852T^{-2} + 1.44\cdot10^{-10}T^2$
$CaFe_5O_7$ (CW_3F)	298 – 1644 [1]	-2263947.5	351.6455	$141.7267 + 0.091824T - 11654686T^{-2} + 4368.7960T^{-0.5} + 102978788T^{-3}$
	1644 – 2000			$400.3977 - 4054786T^{-2} - 133.9040T^{-0.5} + 102978788T^{-3}$
$Ca_4Fe_9O_{17}$ (C_4WF_4)	298 – 1644 [1]	-6167863.2	675.8603	$765.1759 + 0.030608T - 18752444T^{-2} + 965.2840T^{-0.5} + 411915151T^{-3}$
	1644 – 2000			$851.3996 - 16219144T^{-2} - 535.6160T^{-0.5} + 411915151T^{-3}$
$Ca_4Fe_{17}O_{29}$ (C_4WF_8)	298 – 1644 [1]	-9298298.1	1182.1637	$1313.2120 + 0.030608T - 30383004T^{-2} + 965.2840T^{-0.5} + 411915151T^{-3}$
	1644 – 2000			$1399.4353 - 27849704T^{-2} - 535.6160T^{-0.5} + 411915151T^{-3}$
$Cu_2Fe_4CaO_8$, $Cu_2Fe_6Ca_2O_{12}$	[1]			

Table 8-1. (Continued) Optimized thermodynamic properties of stoichiometric compounds and model parameters for liquid and solid solutions in the Al–Ca–Cu–Fe–Mg–O system (J·mol^{-1} and J·mol^{-1}·K^{-1})

Solutions	**Temperature range (K) or reference**	**Molar Gibbs energy $g(T)$**
Slag	Modified Quasichemical Formalism (Al^{3+}, Ca^{2+}, Cu^{1+}, Fe^{2+}, Fe^{3+}, Mg^{2+})(O^{2-})	
$Z^{Fe^{2+}}_{Fe^{2+}Fe^{2+}//OO} = Z^{Fe^{2+}}_{Cu^{1+}Fe^{2+}//OO} = Z^{Ca^{2+}}_{Ca^{2+}Ca^{2+}//OO} = Z^{Mg^{2+}}_{Mg^{2+}Mg^{2+}//OO} = 1.37744375$; $Z^{Fe^{3+}}_{Fe^{3+}Fe^{3+}//OO} = Z^{Al^{3+}}_{Al^{3+}Al^{3+}//OO} = 2.06616563$; $Z^{Cu^{1+}}_{Cu^{1+}Cu^{1+}//OO} = 0.68872188$; $Z^{Cu^{1+}}_{Cu^{1+}Fe^{2+}//OO} = 1.37744375$ Interpolation of binary parameters into ternary system (grouping): Al_2O_3–CaO–Fe_2O_3, Al_2O_3–CaO–MgO, Al_2O_3–FeO–MgO, Al_2O_3–Fe_2O_3–MgO, Cu_2O–FeO–Al_2O_3, Cu_2O–CaO–Al_2O_3 – Kohler/Toop method with Al_2O_3 as an assymetric component Fe_2O_3–CaO–MgO, FeO–Fe_2O_3–Cu_2O, CaO–Cu_2O–Fe_2O_3, Cu_2O–Fe_2O_3–MgO, CaO–FeO–Fe_2O_3 – Kohler/Toop method with Fe_2O_3 as an assymetric component CaO–Cu_2O–FeO, Cu_2O–FeO–MgO – Kohler/Toop method with FeO as an assymetric component Cu_2O–CaO–MgO – Toop method with Cu_2O as an assymetric component All other combinations – Kohler method		
g°_{FeO}	298–1644.15 [21]	$-290452.2 - 349.6572T + 18.0245T\ln T - 0.0153040T^2 + 1266650T^{-1} + 6003.600T^{0.5}$
$g^{\circ}_{Fe_2O_3}$	298 – 3000 [21]	$-805257.1 + 873.7736T - 146.8576T\ln T + 2788449T^{-1} - 87604525T^{-2}$
$g^{\circ}_{Cu_2O}$	298 –900 [1]	$-145246.5 + 363.4980T - 71.0551T\ln T - 0.007281T^2 + 374793T^{-1}$
	900 – 1350	$-115388.7 - 63.9919T - 8.5762T\ln T - 0.040869T^2$
	1350 – 3000	$-191327.1 + 740.2130T - 120.0000T\ln T$
$g^{\circ}_{Al_2O_3}$	298 – 2327 [349]	$-1615242.8 + 1240.3272T - 179.3655T\ln T + 0.004596124T^2 - 487670.4923T^{-1} - 3313.548T^{0.5} - 68180608T^{-2}$
	2327 – 9000	$-1750990.0 + 1342.1161T - 192.4640T\ln T$
g°_{CaO}	298 – 2845 [349]	$-571766.6 + 348.7358T - 58.7912T\ln T + 573572.9912T^{-1} - 535.616T^{0.5} - 17163131T^{-2}$
	2845 – 9000	$-596946.7 + 379.1801T - 62.7600T\ln T$

Table 8-1. (Continued) Optimized thermodynamic properties of stoichiometric compounds and model parameters for liquid and solid solutions in the Al–Ca–Cu–Fe–Mg–O system (J·mol^{-1} and J·mol^{-1}·K^{-1})

Solutions	Temperature range (K) or reference	Molar Gibbs energy $g(T)$
g°_{MgO}	298 – 3098 [347]	$-554894.2+490.9088T-72.7956T\ln T+0.001571092T^{2}-261376T^{-1}-1184.796T^{0.5}-974102T^{-2}$
	3098 – 9000	$-584985.6+437.1375T-66.9440T\ln T$
$\Delta g^{\circ}_{Al^{3+}Ca^{2+}//OO}$	[349]	$-121163.9+27.1959T$
$\omega^{40}_{Al^{3+}Ca^{2+}//OO}$	[349]	$-353674.3+115.0594T$
$\Delta g^{\circ}_{Al^{3+}Fe^{2+}//OO}$	[25]	6920.3
$\omega^{10}_{Al^{3+}Fe^{3+}//OO}$	[25]	9347.1
$\omega^{10}_{Al^{3+}Fe^{3+}//OO}$	[25]	28308.9
$\Delta g^{\circ}_{Al^{3+}Mg^{2+}//OO}$	[350]	-31518.0
$\omega^{30}_{Al^{3+}Mg^{2+}//OO}$	[350]	$-225764.5+66.7181T$
$\omega^{60}_{Al^{3+}Mg^{2+}//OO}$	[350]	80688.0
$\omega^{70}_{Al^{3+}Mg^{2+}//OO}$	[350]	-48435.8
$\Delta g^{\circ}_{Fe^{2+}Ca^{2+}//OO}$	[1]	-37868.0
$\omega^{101}_{Ca^{2+}Fe^{3+}(Fe^{2+})//OO}$	[1]	-53262.6
$\omega^{001}_{Fe^{2+}Fe^{3+}(Ca^{2+})//OO}$	[1]	$-67402.6+41.4957T$
$\Delta g^{\circ}_{Fe^{3+}Ca^{2+}//OO}$	[1]	$-137549.0+6.6057T$
$\omega^{10}_{Ca^{2+}Fe^{3+}//OO}$	[1]	111984.8

Table 8-1. (Continued) Optimized thermodynamic properties of stoichiometric compounds and model parameters for liquid and solid solutions in the Al–Ca–Cu–Fe–Mg–O system (J·mol^{-1} and J·mol^{-1}·K^{-1})

Solutions	Temperature range (K) or reference	Molar Gibbs energy $g(T)$
$\omega^{30}_{Ca^{2+}Fe^{3+}//OO}$	[1]	-45559.6
$\Delta g^{\circ}_{Mg^{2+}Ca^{2+}//OO}$	[347]	45331.0
$\omega^{10}_{Ca^{2+}Mg^{2+}//OO}$	[347]	-30582.8
$q^{01}_{Cu^{+}Fe^{2+}//OO}$	[1]	46651.6
$q^{30}_{Cu^{+}Fe^{3+}//OO}$	[1]	6904.5
$q^{01}_{Cu^{+}Fe^{3+}//OO}$	[1]	16306.3
$q^{001}_{Fe^{2+}Cu^{+}Fe^{3+}//OO}$	[1]	39242.5
$\Delta q^{\circ}_{Cu^{+}Al^{3+}//OO}$	[1]	33691.2
$q^{01}_{Cu^{+}Al^{3+}//OO}$	[1]	21904.4
$\Delta g^{\circ}_{Cu^{+}Ca^{2+}//OO}$	[1]	-31342.0
$\omega^{01}_{Cu^{+}Ca^{2+}//OO}$	[1]	-75728.4 + 63.0879T
$\Delta q^{\circ}_{Cu^{+}Mg^{2+}//OO}$	[1]	35103.8
$\omega^{003}_{Ca^{2+}Cu^{+}(Fe^{2+})//OO}$	[1]	-148540
$\omega^{003}_{Ca^{2+}Fe^{3+}(Cu^{+})//OO}$	[1]	16819.1
$\omega^{101}_{Ca^{2+}Fe^{3+}(Cu^{+})//OO}$	[1]	-25409.9
$\omega^{011}_{Cu^{+}Fe^{3+}(Ca^{2+})//OO}$	[1]	-52344.9 + 60.6680T

Table 8-1. (Continued) Optimized thermodynamic properties of stoichiometric compounds and model parameters for liquid and solid solutions in the Al–Ca–Cu–Fe–Mg–O system (J·mol^{-1} and J·mol^{-1}·K^{-1})

Solutions	**Temperature range (K) or reference**	**Molar Gibbs energy $g(T)$**
$\omega^{01}_{Fe^{2+}Fe^{3+}//OO}$		-18823.8
$\omega^{20}_{Fe^{2+}Fe^{3+}//OO}$		-9878.4
$\Delta g^{\circ}_{Fe^{2+}Mg^{2+}//OO}$	[285]	6276.0
$\Delta g^{\circ}_{Fe^{3+}Mg^{2+}//OO}$	[285]	-20920.0
$\omega^{001}_{Al^{3+}Ca^{2+}(Fe^{2+})//OO}$		-18828.0
$\omega^{001}_{Al^{3+}Fe^{3+}(Ca^{2+})//OO}$		20920.0
$q^{001}_{Al^{3+}Cu^{+}Fe^{2+}//OO}$	[1]	72847.8
$q^{001}_{Al^{3+}Ca^{2+}Cu^{+}//OO}$	[1]	41876.4
$q^{001}_{Ca^{2+}Cu^{+}Mg^{2+}//OO}$	[1]	83060.8
$\omega^{001}_{Mg^{2+}Cu^{1+}(Fe^{3+})//OO}$	[1]	-64223.6
$\omega^{002}_{Mg^{2+}Cu^{1+}(Fe^{2+})//OO}$	[1]	-86189.1
$\omega^{001}_{Fe^{2+}Cu^{1+}(Mg^{2+})//OO}$	[1]	-86231.7
$\omega^{001}_{Ca^{2+}Fe^{3+}(Mg^{2+})//OO}$		-9623.2
Spinel		Compound Energy Formalism $(Al^{+3},Cu^{+2},Fe^{+2},Fe^{+3},Mg^{+2})^{tetr}[Al^{+3},Ca^{+2},Cu^{+2},Fe^{+2},Fe^{+3},Mg^{+2},Va]^{oct}_{2}O^{-2}_{4}$; $Al^{3+} = F$, $Cu^{+2} = M$, $Fe^{+2} = A$, $Fe^{+3} = E$, $Mg^{+2} = B$, $Ca^{+2} = P$
$G_{AE} = G_{EA}$		$= 7F_{AE}$
F_{AE}	298-2500 [21]	$-163100.1 + 144.9340T - 24.9761T\ln T - 0.0011641708T^{2} - 206468T^{-1}$

Table 8-1. (Continued) Optimized thermodynamic properties of stoichiometric compounds and model parameters for liquid and solid solutions in the Al–Ca–Cu–Fe–Mg–O system (J·mol^{-1} and J·mol^{-1}·K^{-1})

Solutions	Temperature range (K) or reference	Molar Gibbs energy $g(T)$
G_{EE}		$= 7F_{AE} + I_{AE}$
I_{AE}	[21]	-31229.1 + 22.0630T
G_{AA}		$= 7F_{AE} - I_{AE} + \Delta_{AE}$
Δ_{AE}	[21]	15781.4
G_{EV}		$= 5F_{AE} + V_E$
V_E	[21]	29931.8 + 28.5474T
G_{AV}		$= 5F_{AE} - I_{AE} + \Delta_{AE} + V_E - \Delta_{EAV}$
Δ_{EAV}	[21]	0
G_{AF}		$= 7F_{AF}$
F_{AF}	298-360 [25]	-285499.2 – 33.9137T + 7.6608Tln$T$ – 0.063377T^2 + 2.416653·10$^{-5}T^3$ + 154.89731ln$T$
	360-2503 [25]	-285724.9 + 245.4743T – 34.2891Tln$T$ + 185486T^{-1} – 954.24739$T^{0.5}$ – 5983204T^{-2}
G_{FF}		$= -3.5F_{AE} + 10.5F_{AF} + 0.5I_{AE} + 0.5I_{AF} - 0.5\Delta_{AE} + 0.5\Delta_{AF}$
G_{FA}		$= 3.5F_{AE} + 3.5F_{AF} - 0.5I_{AE} + 0.5I_{AF} + 0.5\Delta_{AE} - 0.5\Delta_{AF}$
I_{AF}	[25]	56132.0 + 20.0000T
Δ_{AF}	[25]	89267.3 – 133.0617T
G_{FV}		$= -17.5F_{AE} - 52.5F_{AF} - 2.5I_{AE} - 2.5I_{AF} + 2.5\Delta_{AE} - 2.5\Delta_{AF} + 40F_{FV} - \frac{5}{6}L_{F:FV}$
F_{FV}	[25]	-336603.1 – 220.8396T – 31.0038Tln$T$ – 0.000586T^2 + 386136T^{-1} – 662.70962$T^{0.5}$ – 13636120T^{-2}
$L_{F:FV}$	[25]	0

Table 8-1. (Continued) Optimized thermodynamic properties of stoichiometric compounds and model parameters for liquid and solid solutions in the Al–Ca–Cu–Fe–Mg–O system (J·mol^{-1} and J·mol^{-1}·K^{-1})

Solutions	Temperature range (K) or reference	Molar Gibbs energy $g(T)$
G_{EF}		$=7F_{AF}+I_{AE}-\Delta_{AEF}$
Δ_{AEF}	[25]	-25443.0
G_{FE}		$=3.5F_{AE}+3.5F_{AF}+0.5I_{AE}+0.5I_{AF}-0.5\Delta_{AE}+0.5\Delta_{AF}+\Delta_{AEF}-\Delta_{EF}$
Δ_{EF}	[25]	$-11762.1-10.5073T$
$L_{i:EF}$	[25]	38492.8
G_{BF}		$=7F_{BF}$
F_{BF}	298-2500 [350]	$-342935.9+940.2311T-113.6382T\ln T+0.024089T^{2}+54425T^{-1}-8354.0894T^{0.5}+11398.541\ln T-2.3637357\cdot10^{-6}T^{3}$
G_{FB}		$=3.5F_{AE}-10.5F_{AF}+14F_{BF}-0.5I_{AE}-0.5I_{AF}+I_{BF}+0.5\Delta_{AE}-0.5\Delta_{AF}$
I_{BF}	[350]	$21756.8+19.6648T$
G_{BB}		$=7F_{AE}-21F_{AF}+21F_{BF}-I_{AE}-I_{AF}+I_{BF}+\Delta_{AE}-\Delta_{AF}+\Delta_{BF}$
Δ_{BF}	[350]	40000.0
G_{BV}		$=21F_{AE}-63F_{AF}+7F_{BF}-3I_{AE}-3I_{AF}+40F_{FV}+3\Delta_{AE}-3\Delta_{AF}+\Delta_{BF}-\frac{5}{6}L_{F:FV}-\Delta_{FBV}$
Δ_{FBV}	[25]	$-306825.3+135.2813T$
G_{BE}		$=7F_{BE}$
F_{BE}	298-2500 [285]	$-200446.3+566.7371T-72.6736T\ln T+0.010687T^{2}-4112.061T^{0.5}+3790.428\ln T-8.041454\cdot10^{-7}T^{3}$
G_{EB}		$=-7F_{AE}+14F_{BE}-I_{AE}+I_{BE}$
I_{BE}	[285]	$-112131.2+56.5798T$
G_{AB}		$=14F_{AE}-7F_{BE}-21F_{AF}+21F_{BF}-I_{AE}-I_{AF}+I_{BF}+\Delta_{AE}+\Delta_{BF}-\Delta_{AF}-\Delta_{ABE}$

Table 8-1. (Continued) Optimized thermodynamic properties of stoichiometric compounds and model parameters for liquid and solid solutions in the Al–Ca–Cu–Fe–Mg–O system (J·mol^{-1} and J·mol^{-1}·K^{-1})

Solutions	Temperature range (K) or reference	Molar Gibbs energy $g(T)$
Δ_{ABE}	[285]	-41840.0
G_{BA}		$= 7F_{BE} - I_{AE} + \Delta_{AE} - \Delta_{BAE}$
Δ_{BAE}	[285]	0
G_{ME}		$= 7F_{ME}$
F_{ME}	298-755 [172]	-140476.0 + 83.5807T – 14.9369Tln$T$ – 0.010355T^2
	755-1601 [172]	-143501.3 + 153.5105T – 25.9408Tln$T$ – 0.001088T^2
	1601-2500 [172]	-146289.6 + 179.2113T – 29.4241Tln$T$
G_{EM}		$= -7F_{AE} + 14F_{ME} - I_{AE} + I_{ME}$
I_{ME}	[172]	-22447.2 + 20.9200T
G_{MM}		$= -14F_{AE} + 21F_{ME} - 2I_{AE} + I_{ME} + \Delta_{ME}$
Δ_{ME}	[172]	21448.9 + 13.3888T
G_{MA}		$= 7F_{ME} - I_{AE} + \Delta_{ME} - \Delta_{EMA}$
Δ_{EMA}	[172]	94140
G_{AM}		$= -7F_{AE} + 14F_{ME} - 2I_{AE} + I_{ME} - \Delta_{EAM}$
Δ_{EAM}	[172]	0
G_{MV}		$= -2F_{AE} + 7F_{ME} - I_{AE} + V_E + \Delta_{ME} - \Delta_{EMV}$
Δ_{EMV}	[172]	66944
$L_{i:MA}$	[172]	-188464.1 + 117.1520T
G_{MF}		$= 7F_{MF}$

Table 8-1. (Continued) Optimized thermodynamic properties of stoichiometric compounds and model parameters for liquid and solid solutions in the Al–Ca–Cu–Fe–Mg–O system (J·mol^{-1} and J·mol^{-1}·K^{-1})

Solutions	Temperature range (K) or reference	Molar Gibbs energy $g(T)$
F_{MF}	298-1300	$-267309.0 + 137.0941T - 22.2599T\ln T - 0.001674T^2 + 238017T^{-1}$
	1300-2500	$-269405.0 + 165.8517T - 26.3296T\ln T$
G_{FM}		$= 3.5F_{AE} - 10.5F_{AF} + 14F_{MF} - 0.5I_{AE} - 0.5I_{AF} + I_{MF} + 0.5\Delta_{AE} - 0.5\Delta_{AF}$
I_{MF}		$4526.1 + 20.5530T$
$L_{i:FM}$		-4184.0
$L_{k:Al^{3+},Cu^{2+}}$		
G_{EP}		$= -7F_{AE} + 14F_{E(EP)} - I_{AE}$
$F_{E(EP)}$	298-2000	$-211668.2 + 142.4444T - 24.4269T\ln T - 0.001143T^2 + 129927T^{-1}$
G_{AP}		$= -7F_{AE} + 14F_{E(EP)} - 2I_{AE} + \Delta_{AE} - \Delta_{EAP}$
Δ_{EAP}		0
G_{FP}		$= 3.5F_{AE} - 10.5F_{AF} + 14F_{F(FP)} - 0.5I_{AE} - 0.5I_{AF} + 0.5\Delta_{AE} - 0.5\Delta_{AF}$
$F_{F(FP)}$	298-1877	$-319151.9 + 230.6638T - 32.4343T\ln T + 40057T^{-1} - 953.7714T^{0.5} + 2036667T^{-2}$
	1877-2000	$-329391.7 + 172.4472T - 26.9060T\ln T$
G_{MP}		$= -14F_{AE} + 7F_{ME} + 14F_{E(EP)} - 2I_{AE} + \Delta_{ME} - \Delta_{EMP}$
Δ_{EMP}		62760
G_{BM}		$= -14F_{AE} + 7F_{BE} + 14F_{ME} - 2I_{AE} + I_{ME} + \Delta_{ME} - \Delta_{BME}$
Δ_{BME}		0
G_{MB}		$= 7F_{AE} - 7F_{BE} - 21F_{AF} + 21F_{BF} + 7F_{ME} - I_{AE} - I_{AF} + I_{BF} + \Delta_{AE} + \Delta_{BF} - \Delta_{AF} + \Delta_{BME} - \Delta_{BMB}$
Δ_{BMB}		0

Table 8-1. (Continued) Optimized thermodynamic properties of stoichiometric compounds and model parameters for liquid and solid solutions in the Al–Ca–Cu–Fe–Mg–O system (J·mol^{-1} and J·mol^{-1}·K^{-1})

Solutions	**Temperature range (K) or reference**	**Molar Gibbs energy $g(T)$**
G_{BP}		$= 7F_{AE} - 14F_{BE} - 21F_{AF} + 21F_{BF} + 14F_{E(EP)} - I_{AE} - I_{BE} - I_{AF} + I_{BF} + \Delta_{AE} + \Delta_{BF} - \Delta_{AF} + \Delta_{EBP}$
Δ_{EBP}		-167360
Magnetic parameters:	[285]	$T_{BE} = T^{i}_{EB}$ = 689.5 K (Curie temperature) $\beta_{BE} = \beta^{i}_{EB}$ = 2.186 (magnetic moment), P = 0.28 (P factor)
	[21]	$T_{AE} = T^{i}_{EA}$ = 848.0 K (Curie temperature) $\beta_{AE} = \beta^{i}_{EA}$ = 44.54 (magnetic moment), P = 0.28 (P factor)
	[25]	$T_{AF} = T^{i}_{FA}$ = –24 K (Neel temperature 8 K) $\beta_{AF} = \beta^{i}_{FA}$ = –3.699 (magnetic moment), P = 0.28 (P factor)
	[172]	$T_{ME} = T^{i}_{EM}$ = 751 K (Curie temperature) $\beta_{ME} = \beta^{i}_{EM}$ = 4.00 (magnetic moment), P = 0.28 (P factor)
Monoxide		Bragg-Williams ($AlO_{1.5}$, CaO, CuO, FeO, $FeO_{1.5}$, MgO)
Interpolation of binary parameters into ternary system (grouping): FeO–MgO–Fe_2O_3, CaO–MgO–Fe_2O_3, FeO–CuO–Fe_2O_3, CaO–CuO–Fe_2O_3, MgO–CuO–Fe_2O_3 – Kohler/Toop method with Fe_2O_3 as an assymetric component FeO–CaO–Al_2O_3, FeO–MgO–Al_2O_3, FeO–CuO–Al_2O_3, CaO–MgO–Al_2O_3, CaO–CuO–Al_2O_3, MgO–CuO–Al_2O_3 – Kohler/Toop method with Al_2O_3 as an assymetric component FeO–CaO–MgO, FeO–CaO–Fe_2O_3, – Kohler/Toop method with CaO as an assymetric component FeO–Fe_2O_3–Al_2O_3, CaO–Fe_2O_3–Al_2O_3, MgO–Fe_2O_3–Al_2O_3, CuO–Fe_2O_3–Al_2O_3 – Kohler/Toop method with FeO, CaO, MgO and CuO as an assymetric component, respectively All other combinations – Kohler method		

Table 8-1. (Continued) Optimized thermodynamic properties of stoichiometric compounds and model parameters for liquid and solid solutions in the Al–Ca–Cu–Fe–Mg–O system (J·mol^{-1} and J·mol^{-1}·K^{-1})

Solutions	**Temperature range (K) or reference**	**Molar Gibbs energy $g(T)$**
g^{o}_{FeO}, $g^{o}_{FeO_{1.5}}$, $q^{00}_{FeO,\ FeO_{1.5}}$, $q^{01}_{FeO,\ FeO_{1.5}}$	[227]	
g^{o}_{CuO}, $q^{00}_{CuO,FeO}$, $q^{00}_{CuO,FeO_{1.5}}$	[172]	
g^{o}_{CaO}	[348]	
$q^{00}_{FeO,CaO}$, $q^{02}_{FeO,CaO}$	[1]	
g^{o}_{MgO}, $q^{00}_{MgO,CaO}$, $q^{01}_{MgO,CaO}$	[347]	
$q^{00}_{FeO,MgO}$, $q^{10}_{FeO_{1.5},MgO}$, $q^{02}_{FeO_{1.5},MgO}$	[285]	
$g^{o}_{AlO_{1.5}}$, $q^{00}_{MgO,AlO_{1.5}}$	[350]	
$Ca(Al,Fe)_{12}O_{19}$		Bragg-Williams $\left(\frac{1}{12}CaAl_{12}O_{19}, \frac{1}{12}CaFe_{12}O_{19}\right)$
$g^{\circ}_{\frac{1}{12}CaAl_{12}O_{19}}$		$= \frac{1}{12}G(CaAl_{12}O_{19})$
$g^{\circ}_{\frac{1}{12}CaFe_{12}O_{19}}$		$-484825.2 + 251.7672T - 48.4066T\ln T - 0.006728T^{2} + 270735T^{-1} + 827.811T^{0.5}$
$Ca(Al,Fe)_4O_7$		Bragg-Williams $\left(\frac{1}{4}CaAl_4O_7, \frac{1}{4}CaFe_4O_7\right)$
$g^{\circ}_{\frac{1}{4}CaAl_4O_7}$		$= \frac{1}{4}G(CaAl_4O_7)$

Table 8-1. (Continued) Optimized thermodynamic properties of stoichiometric compounds and model parameters for liquid and solid solutions in the Al–Ca–Cu–Fe–Mg–O system (J·mol^{-1} and J·mol^{-1}·K^{-1})

Solutions	Temperature range (K) or reference	Molar Gibbs energy $g(T)$
$g^{\circ}_{\frac{1}{4}CaFe_4O_7}$		$=\frac{1}{4}G(CaFe_4O_7)+76010.7-2.2594T$
$Ca(Al,Fe)_2O_4$		Bragg-Williams $\left(\frac{1}{2}CaAl_2O_4,\frac{1}{2}CaFe_2O_4\right)$
$g^{\circ}_{\frac{1}{2}CaAl_2O_4}$		$=\frac{1}{2}G(CaAl_2O_4)$
$g^{\circ}_{\frac{1}{2}CaFe_2O_4}$		$=\frac{1}{2}G(CaFe_2O_4)$
$Ca_3(Al,Fe)_2O_6$		Bragg-Williams $\left(\frac{1}{2}Ca_3Al_2O_6,\frac{1}{2}Ca_3Fe_2O_6\right)$
$g^{\circ}_{\frac{1}{2}Ca_3Al_2O_6}$		$=\frac{1}{2}G(Ca_3Al_2O_6)$
$g^{\circ}_{\frac{1}{2}Ca_3Fe_2O_6}$		$-1426480.2+928.8516T-151.938T\ln T-0.001219T^2+1486665T^{-1}-267.808T^{0.5}-8581566T^{-2}$
M_2O_3 (Corrundum)		Bragg-Williams ($AlO_{1.5}$, $FeO_{1.5}$)
$g^{o}_{FeO_{1.5}}$		$=\frac{1}{2}G(Fe_2O_3)$
$g^{o}_{AlO_{1.5}}$		$=\frac{1}{2}G(Al_2O_3)$
$q^{00}_{AlO_{1.5},\,FeO_{1.5}}$	[25]	$9464.2+13.3762T$
$q^{01}_{AlO_{1.5},\,FeO_{1.5}}$	[25]	-1464.4
$q^{10}_{AlO_{1.5},\,FeO_{1.5}}$	[25]	$12133.6-5.0848T$

CHAPTER 9 DEVELOPMENT OF THE THERMODYNAMIC DATABASE FOR COPPER SMELTING AND CONVERTING. THE Cu–Fe–O–S–Si SYSTEM

Equation Chapter (Next) Section 1Further development of the thermodynamic database for slag, matte, liquid metal and solid phases in the Cu–Fe–O–S–Si system is reported. Calculations of phase equilibria and distributions of elements among liquid phases in this system are of particular importance for the pyrometallurgical production of copper. In the latest version of the database, matte and metallic phases are described as one solution phase using the Modified Quasichemical Model (MQM) and (Cu^{I}, Cu^{II}, Fe^{II}, Fe^{III}, O, S) on one sublattice. Slag phase is modeled using MQM as well, but using two sublattices: (Cu^{1+}, Fe^{2+}, Fe^{3+}, Si^{4+})(O^{2-}, S^{2-}). This approach results in more realistic description of distribution of all elements, particularly sulfur and oxygen, among liquid metal, slag and matte.

The 1999 study of Decterov and Pelton [3] contains one of the most comprehensive assessments of the Cu–Fe–O–S–Si system for the purpose of copper smelting and converting. The thermodynamic models suggested in [3] are able to predict phase equilibria between solid and liquid phases, solubilities and activities of components in these phases. They are based on the extensive collected and evaluated experimental data. However, since that time, the Modified Quasichemical Model (MQM) used for the description of the liquid phases underwent further development. Particularly important modifications include i) expansion of the energy of pair formation in terms of the pair fractions rather than the component fraction and permission for coordination numbers to vary with composition [16]; ii) possibility to join Bragg-Williams and MQM excess terms in one solution database [17]; iii) introduction of the quadruplet formalism in systems with several cations and anions [18, 351].

The first improvement has helped to create the joint solution database for matte and liquid metal (further referred to as the *Matte/Metal* database) [26, 78, 114, 172, 227, 352]. They were described as one phase with a miscibility gap, which disappears at certain conditions. The solubility of oxygen and sulfur in matte and liquid metal were properly described in a wide range of conditions.

The second change in MQM allowed a correct description of the Cu_2O–FeO–Fe_2O_3–SiO_2 subsystem [1] of the slag database (further referred to as *Slag*). It appears that the use of positive Bragg-Williams parameters is preferable when the positive enthalpy of mixing is observed, as in the case of the Cu_2O–SiO_2 system.

The last modification prompted the change in the approach for modeling of the sulfur solubility in *Slag*. Earlier the sulfide capacity model [353] was used in combination with MQM, but in the new model, the solubility of sulfur in slag is described by placing S^{2-} anions on the second sublattice of the slag solution. In this way, the sulfide capacity of many slags in the Al–Ca–Fe–Mg–Mn–Ti–O system was reproduced [354]. In this study, the new approach resulted in a good description of "sulfidic dissolution of copper" in slag [355], which was ignored in the old database [3].

Even though only matte and liquid metal were joined into one solution phase in the current study, in reality all three liquids, i.e. matte, slag and liquid metal dissolve in each other and under certain conditions become fully miscible. However, describing all three liquids as one solution phase would be very difficult due to practical and theoretical reasons. The practical obstacle is the fact that the *Slag* database used in the current study already covers a wide range of chemical systems (Al–Ca–Cu–Fe–Mg–Mn–Ni–Ti–Si–…–O–S), and joining the *Slag* and *Matte/Metal* solutions would require re-optimization of all the subsystems in the framework of a new model.

The theoretical problem arises from the necessity to account for both the First Nearest Neighbor (FNN) and Second Nearest Neighbor (SNN) Short Range Ordering (SRO) when describing metallic, oxidic and sulfidic liquids simultaneously. Slag is ionic liquid, that is cations are always surrounded by anions. The complete FNN SRO is practically imposed. In liquids with sulfur as a major component, deviations from stoichiometric sulfides both towards metal and towards sulfur are significant, which requires the existence of metal-metal and nonmetal-nonmetal FNN pairs. For instance, in the Fe–S system the liquid phase extends from liquid iron to FeS and further without immiscibility [26].

Slags containing SiO_2 exhibit an additional type of ordering – a strong interaction between acidic and basic oxides. For instance, a strongly negative, sharp enthalpy of mixing between FeO and SiO_2 suggests the existence of ordering in this system (SNN SRO). *Slag* database is able to take into account complete FNN SRO and flexible SNN SRO, however the generalized model,

which takes into account both flexible FNN and flexible SNN SRO would be too complicated. Fortunately, under the conditions of interest to pyrometallurgy of copper, matte and metal do not dissolve much silica, and the composition of slag does not deviate much from the mixture of stoichiometric oxides towards excess metal or nonmetal. Thus, it is possible to use the advantages of the well-established *Slag* database from the FACTSage package [4] in combination with the new *(Matte/Metal)* database. Liquid rich in silica and poor in sulfur is modeled as the *Slag* solution. Metallic and sulfide liquids are modeled as the *(Matte/Metal)* solution. *Slag* database describes well interactions between basic and acidic oxides; *(Matte/Metal)* is able to predict the nonstoichiometry of oxysulfide melts towards metals and nonmetals.

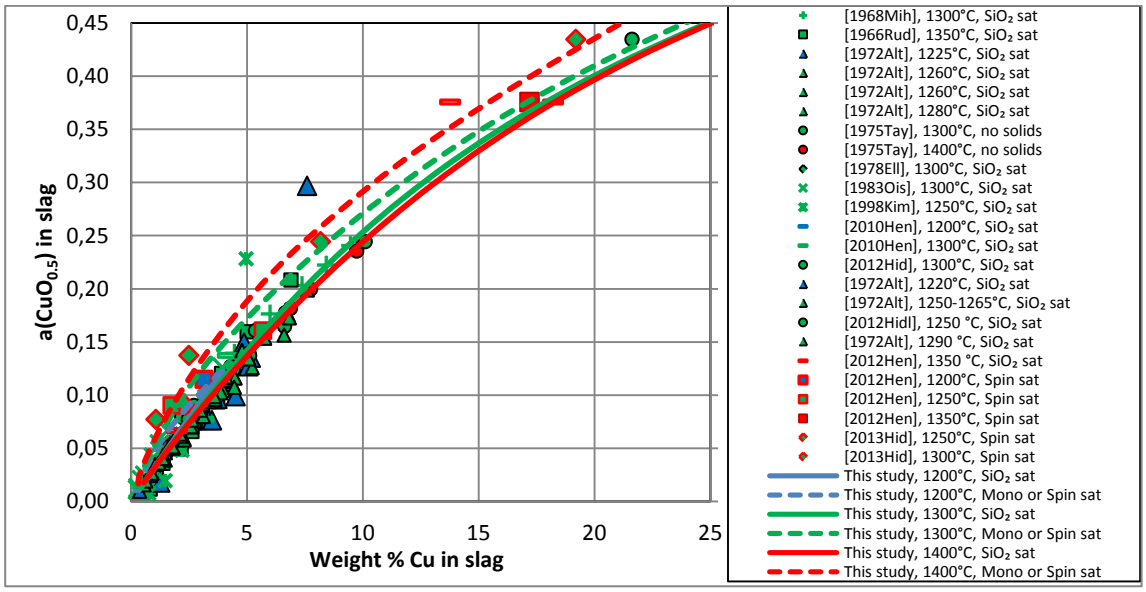

Figure 9.1 Activity of ½(Cu_2O) in slag vs. copper content of slag in the Cu–Fe–O–Si system: experimental points [1, 356-363] and calculated lines.

According to the Quasichemical formalism in the quadruplet approximation [18], molten slag containing sulfur is modeled using two sublattices [354]:

$$\left(Cu^{1+},\ Fe^{2+},\ Fe^{3+},\ Si^{4+}\right)\left(O^{2-},\ S^{2-}\right) \tag{9.1}$$

The Gibbs energies of unary quadruplets are defined by the Gibbs energies of pure oxides and sulfides, the Gibbs energies of binary and reciprocal quadruplets are obtained from the Gibbs energies of unary quadruplets and model excess parameters as described in Section 2.3. The optimization of the thermodynamic properties of the *Slag* database for the Cu–Fe–O–Si system is reported in details elsewhere [1]. As an example, the activity of copper oxide against the Cu content in slag is plotted in Figure 9.1.

9.1 Fe–O–S–Si system

It was shown in Section 5.4.1 that FeO and FeS are completely soluble in each other in the liquid phase. It is the addition of SiO_2 that creates the miscibility gap between oxide and sulfide liquids, which makes possible the pyrometallurgical extraction of metals using slag-matte equilibria. MacLean (1969) [364], Yazawa and Kameda (1953) [14], Shimpo et al. (1986) [365] and Takeda (1997) [15] studied the formation of the miscibility gap in the Fe–O–S–Si system.

MacLean [364] conducted equilibration/quenching experiments with mixtures of wüstite, magnetite, pyrrhotite and silica in alumina or iron crucibles. Quenched samples were studied by optical microscopy. Formation of a miscibility gap between matte and slag was observed. The phase diagram at iron saturation proposed by MacLean [364] is shown in Figure 9.2. It is clear that the miscibility gap is widening with increasing silica content until the saturation with SiO_2. At low SiO_2 content, the miscibility gap disappears, e.g. matte and slag become fully miscible. On the calculated diagram, however, the miscibility gap never disappears. It is not possible for matte and slag to join because they are modeled using two different solutions. This model approximation is acceptable as long as the system is close to silica saturation, or contains copper. As it will be shown later (Section 9.2), in the copper containing systems, slags dissolve less sulfur and mattes dissolve less oxygen and silica, so that these two liquids remain separate. It is not the case for the Ca–Cu–Fe–O–S system (SiO_2 free), where matte and slag are fully miscible at copper content less than about 50 wt% (see Section 10.3).

Yazawa and Kameda [14] equilibrated mixtures of wüstite, pyrrhotite and silica in iron crucibles, quenched and conducted the chemical analysis of the slag and matte layers.

Takeda [15] melted the FeO–SiO_2 slag and Fe–S matte in iron crucibles. Oxygen potential in the melt was measured with an oxygen sensor. The slag and matte compositions in the quenched samples were determined by chemical analysis. Shimpo et al. (1986) [365] used a similar experimental technique, but instead of iron crucibles, silica crucibles were utilized to achieve SiO_2 saturation. Metallic iron powder was introduced.

The calculated and experimental compositions of slag and matte in equilibrium with iron and silica are plotted in Figure 9.3. Even though in Figure 9.2 the composition of matte seems to deviate from that suggested by MacLean [364], more rigorous experiments of Yazawa and

Kameda [14] and of Takeda [15] are in excellent agreement with the calculations. As for the slag composition, there is a disagreement between the last two authors in Fe and O (Fe-bonded) content, but the results of Takeda [15] are supported by Shimpo et al. [365]. Fe-bonded oxygen is the conception to represent the analytical results of quenched slag samples and distinguish from oxygen, bounded in SiO_2. It has nothing to do with the pair formation in real liquid slag and matte. The calculated slag compositions are in reasonable agreement with the experiment, considering the fact that copper-free system is far enough from the conditions of pyrometallurgical production of copper.

The "sulfide capacity" of Fe–O–Si slag at high temperature was evaluated in the work of Kang and Pelton (2009) [354]. Sulfide capacity of slag, C_S, is defined as

$$C_S = (\text{wt.\%S}) \cdot \left(\frac{P(O_2)}{P(S_2)} \right)^{1/2} \tag{9.2}$$

If the sulfur content is small (Henry's Law behavior), C_S will be independent of wt.%S, $P(O_2)$ and $P(S_2)$ for the slag of given oxide composition. The comparison between the sulfide capacity calculated in this study, the evaluation of Kang and Pelton [354] and the experimental data [366-368] is given in Figure 9.5.

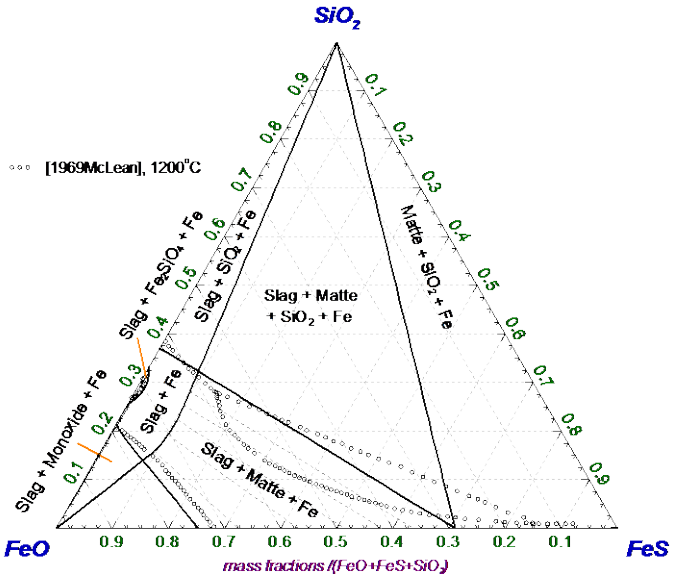

Figure 9.2. Phase diagram of the FeO–FeS–SiO_2 system in equilibrium with Fe at 1200 °C: experimental evaluation [364] and calculated lines.

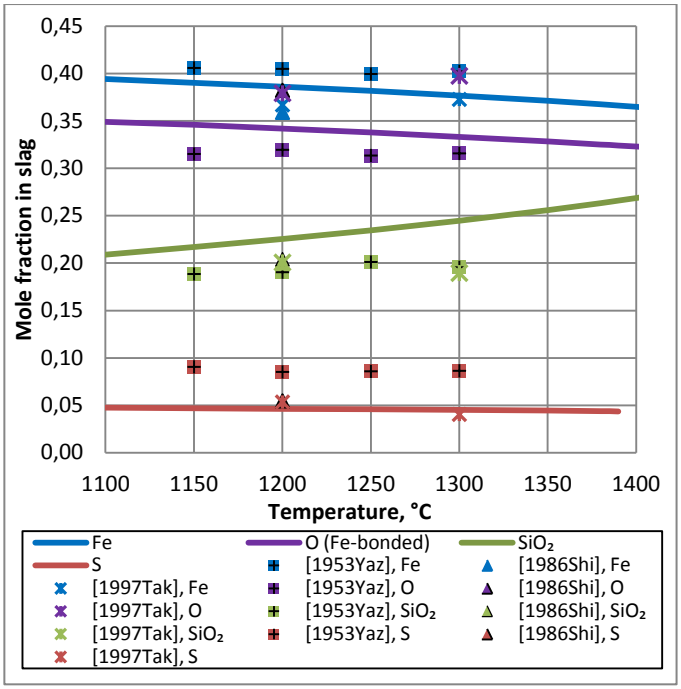

(a)

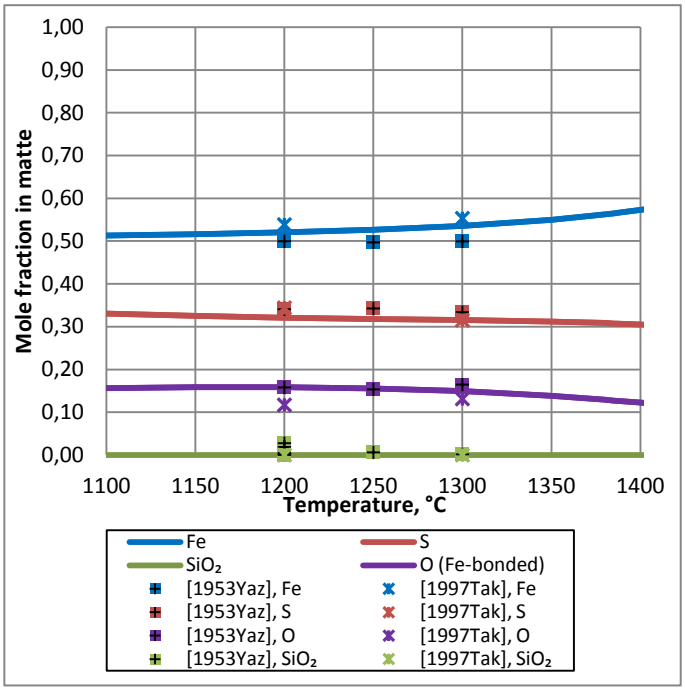

(b)

Figure 9.3. Slag–matte–SiO_2–Fe equilibrium in the Fe–O–S–Si system with varying temperature and total pressure of 1 atm. (a) Composition of slag; (b) composition of matte. Experimental points [14, 15] and calculated lines.

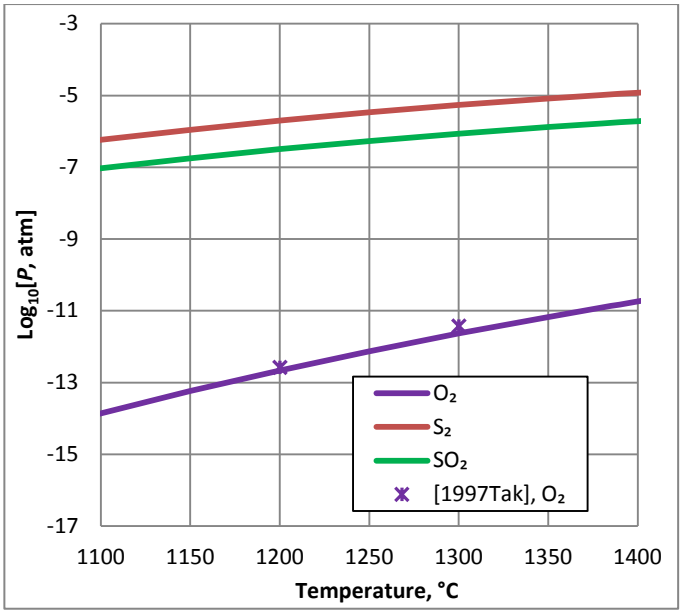

Figure 9.4. Slag–matte–SiO_2–Fe equilibrium in the Fe–O–S–Si system with varying temperature and total pressure of 1 atm. Partial pressures of O_2, S_2 and SO_2: experimental points [15] and calculated lines.

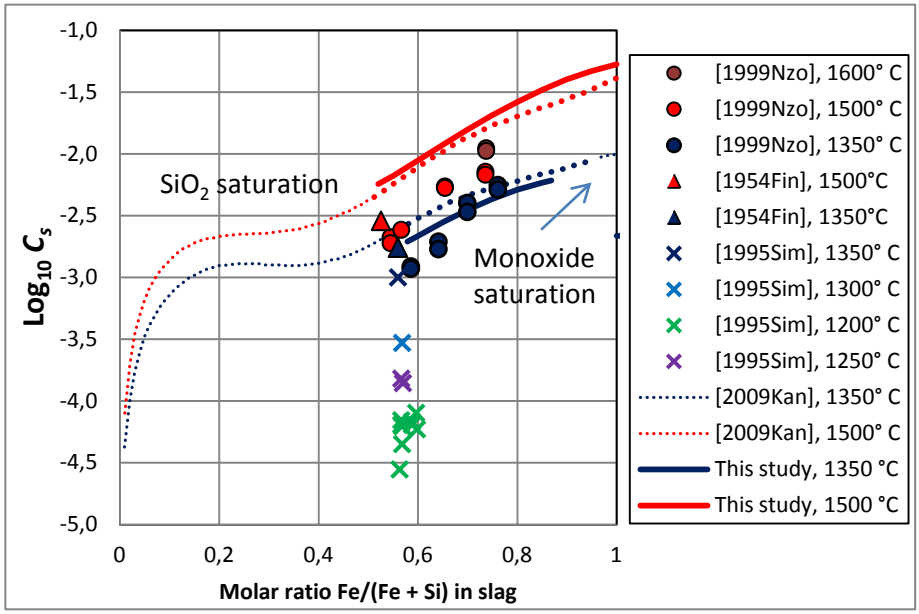

Figure 9.5. Sulfide capacity of slag in the Fe–O–S–Si system. Experimental points [366-368]. Calculated lines correspond to $\log_{10}[P(O_2)$, atm] = -7 and $\log_{10}[P(S_2)$, atm] = -3. Dotted lines – [354], solid lines – this study.

9.2 Experimental studies of slag–matte equilibrium

The thermodynamic equilibria between slag and matte in the Cu–Fe–O–S–Si system were studied by the following authors: Kameda and Yazawa (1961) [11], Geveci and Rosenqvist

(1973) [13], Nagamori (1974) [369], Kaiura et al (1980) [370], Jalkanen (1981) [371], Yazawa et al. (1983) [372], Shimpo et al. (1986) [365], Tavera and Bedolla (1990) [10], Korakas (1964) [373], Kuxmann and Bor (1965) [374], Tavera and Davenport (1979) [375], Li and Rankin (1994) [376] and Henao and Jak (2013) [377].

In order to study the Cu–Fe–O–S–Si system experimentally, 7 degrees of freedom must be fixed. All experiments were conducted at total pressure of 1 atm and at fixed temperature. The presence of slag and matte phases fixes the third and fourth degrees of freedom. Slags were saturated with SiO_2, which eliminates the fifth degree of freedom. The sixth one was either fixed by presence of metal phase [10, 13, 365, 369-372] or by controlled partial pressure of SO_2 [370, 373-377]. The last degree of freedom usually is an easy to measure value – copper content of matte. The variation of copper content in matte is often achieved by changing the initial ratio of sulfides in the sample. Then, it is used as an X-axis in plots representing the distribution of elements between liquid phases and properties of the system.

9.2.1 Slag–matte–SiO_2–metal equilibrium

The experimental results at metal saturation are summarized in Figure 9.6-Figure 9.15. At low copper content in matte (wt. % Cu^{Matte}), the system coexists with a solid metallic phase, which is almost iron. At wt. % Cu^{Matte} higher than 40-60%, the drastic increase of the equilibrium oxygen partial pressure is observed (Figure 9.13), which is accompanied by formation of the liquid metallic solution, mainly consisting of copper, instead of solid iron. In the pyrometallurgy of copper, this solution is usually referred to as blister copper. According to the experimental results [10, 13, 365, 369, 371, 372], the solubility of copper in slag (Figure 9.6) rises up to around 30 wt. % Cu^{Matte}. It remains constant, or even decreases, as reported by some authors [365, 372], till 70 wt. % Cu^{Matte}. At higher copper contents in matte, the solubility of copper rises dramatically. For comparison, the results of Yazawa and Kameda (1954) [378] are also plotted. In the latter study, slag contained around 11 wt. % of CaO. It is clear that the presence of CaO in slag reduces the Cu solubility. The related effect may be found in Figure 9.7, where the solubility of sulfur is plotted. Even though the experimental results for CaO-free slags [10, 13, 365, 369-372] are somewhat scattered, they show higher sulfur content, than those of Yazawa and Kameda (1954) [378].

The available experimental data [10, 11, 13] for the oxygen content of matte are shown in Figure 9.8. The Cu-free data of Yazawa and Kameda [14] and of Takeda [15] are plotted as well to show the limiting case. In the experiments of Bor and Tarassoff (1971) [12], matte was equilibrated with slag containing CaO and Al_2O_3. Nevertheless, their data agree well with the other studies, which may indicate that matte doesn't dissolve much CaO and Al_2O_3. The sulfur content of matte is shown in Figure 9.9. In addition to the above mentioned works, the results of Yazawa and Kameda (1955) [379] are also plotted. In their study, the experiments were carried out in silica crucible under the flow of N_2. Thus, metal saturation was not reached and experimental results correspond to a small, but undefined $P(SO_2)$ (Figure 9.10).

The partial pressures of SO_2, S_2 and O_2 corresponding to the univariant slag–matte–SiO_2–metal equilibrium are presented in Figure 9.11-Figure 9.13. In the study of Tavera and Bedolla [10], variation of wt. % Cu^{Matte} was achieved by changing the composition of the SO_2–S_2–O_2 flow. This gas flow was equilibrated with the sample. It seems like the system was "overfixed" in their experiments. When the composition of the SO_2–S_2–O_2 flow is set, two degrees of freedom are fixed: $P(O_2)$ and $P(S_2)$. However, only one is needed in this case. This is why the partial pressures of gases suggested by Tavera and Bedolla [10] apparently do not correspond to the slag–matte–SiO_2–metal equilibrium in the Cu–Fe–O–S–Si system. In the study of Geveci and Rosenqvist [13], the partial pressure of SO_2 was measured in the effluent (equilibrated) gas, and Jalkanen (1981) [371] fixed only $P(O_2)$ by CO/CO_2 mixture.

This explains the disagreement between the results of Tavera and Bedolla [10] and Geveci and Rosenqvist [13] in the measured oxygen and sulfur contents of liquid copper (Figure 9.14 and Figure 9.15). Since the gas flow in the experiments of Tavera and Bedolla [10] did not allow the system to reach equilibrium, liquid copper dissolved more oxygen and less sulfur.

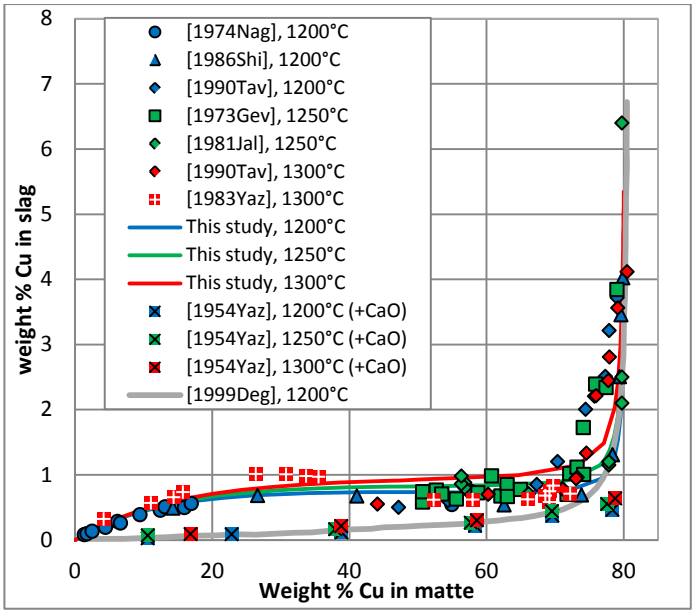

(a)

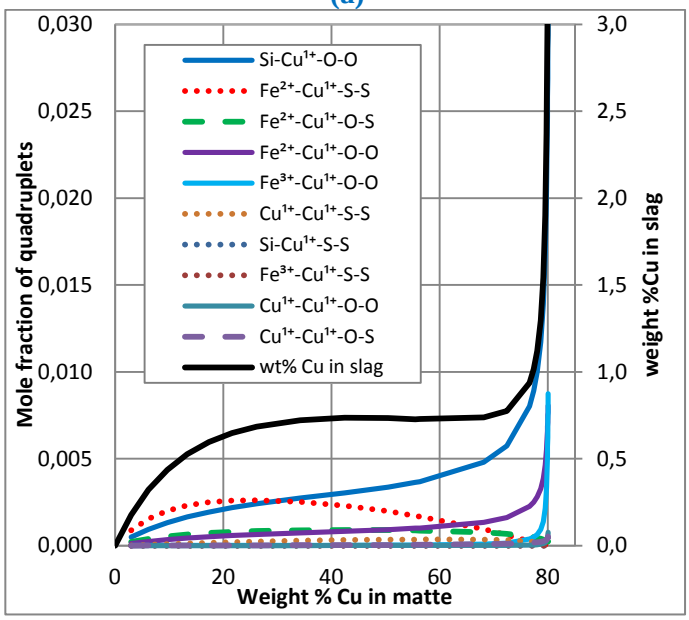

(b)

Figure 9.6. Slag–matte–SiO_2–metal equilibrium in the Cu–Fe–O–S–Si system at fixed temperature and total pressure of 1 atm. a) Copper content of slag. Experimental points [10, 13, 365, 369, 371, 372] and calculated lines: grey – [3], colored – this study. b) Calculated mole fractions of copper-containing quadruplets in the slag phase at 1200 °C.

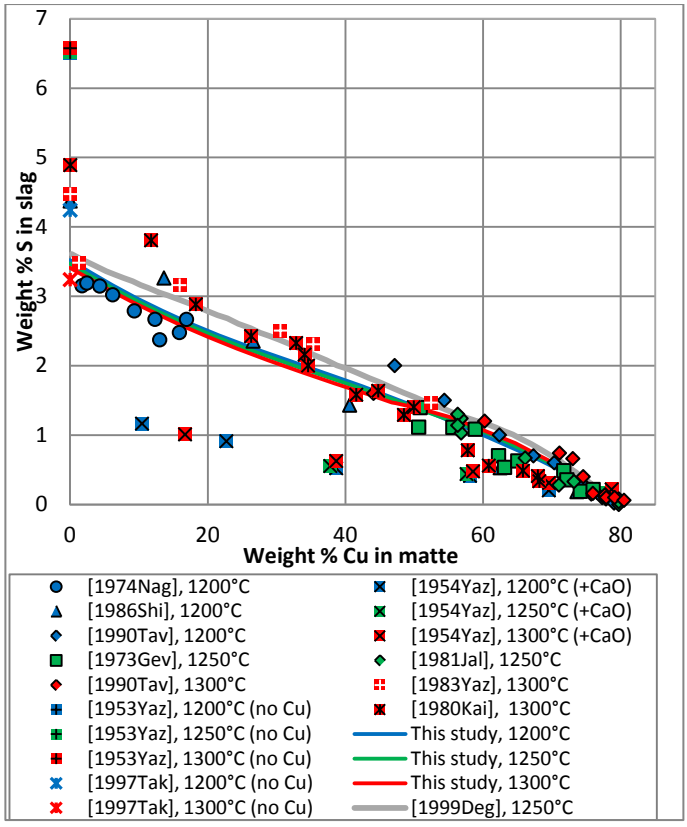

Figure 9.7. Slag–matte–SiO_2–metal equilibrium in the Cu–Fe–O–S–Si system at fixed temperature and total pressure of 1 atm. Sulfur content of slag. Experimental points [10, 13-15, 365, 369-372] and calculated lines: grey – [3], colored – this study.

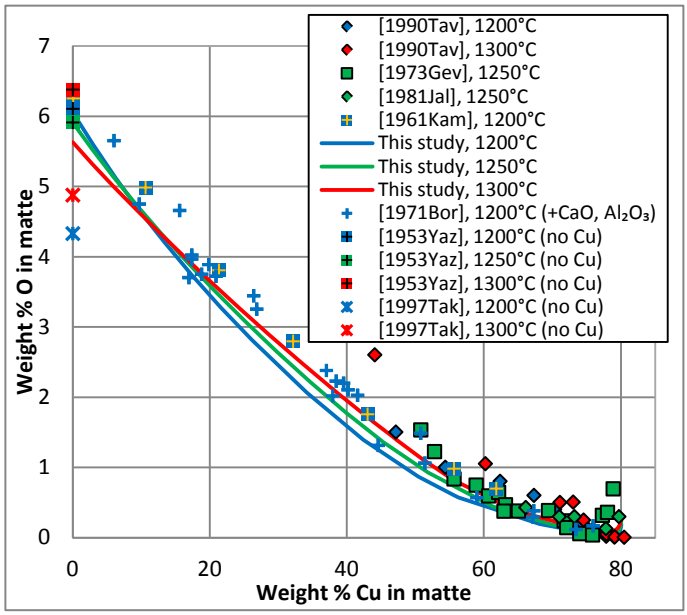

Figure 9.8. Slag–matte–SiO_2–metal equilibrium in the Cu–Fe–O–S–Si system at fixed temperature and total pressure of 1 atm. Oxygen content of matte. Experimental points [10-15] and calculated lines.

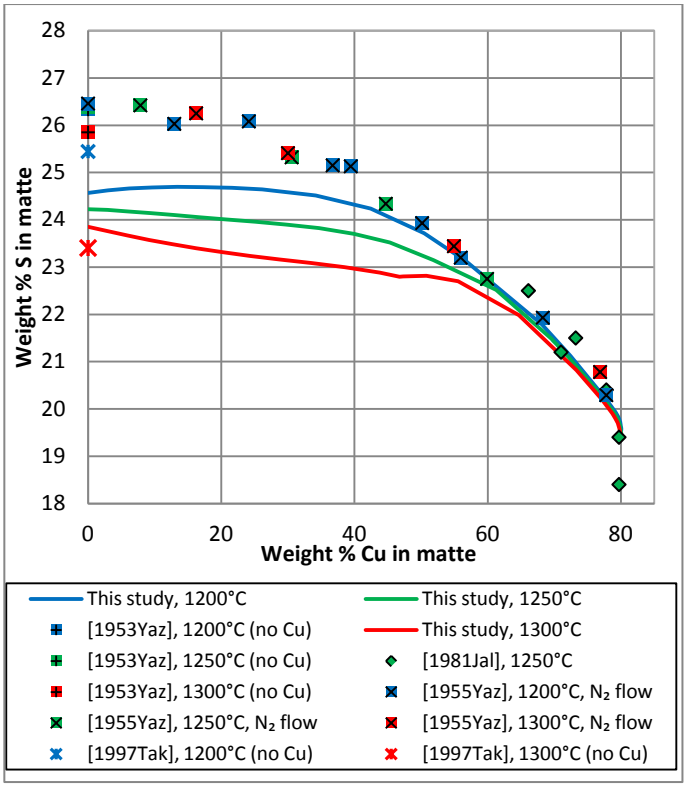

Figure 9.9. Slag–matte–SiO_2–metal equilibrium in the Cu–Fe–O–S–Si system at fixed temperature and total pressure of 1 atm. Sulfur content of matte. Experimental points [14, 15, 371, 379] and calculated lines.

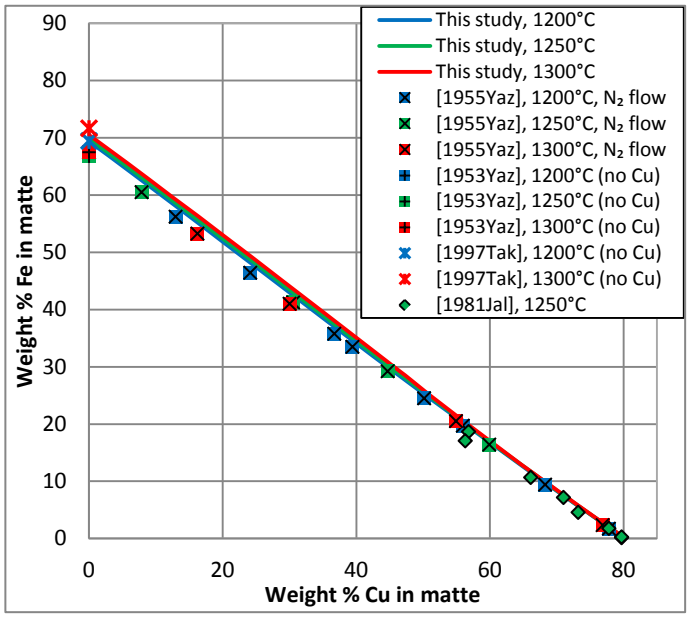

Figure 9.10. Slag–matte–SiO_2–metal equilibrium in the Cu–Fe–O–S–Si system at fixed temperature and total pressure of 1 atm. Iron content of matte. Experimental points [14, 15, 371, 379] and calculated lines.

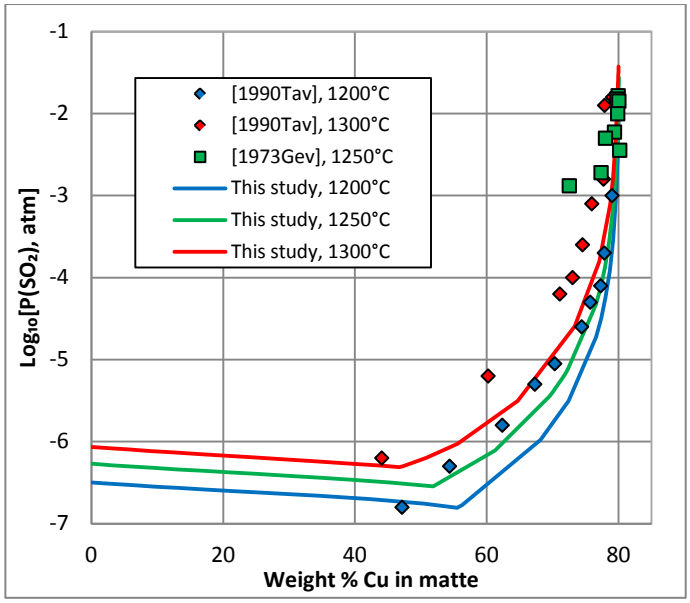

Figure 9.11. Slag–matte–SiO_2–metal equilibrium in the Cu–Fe–O–S–Si system at fixed temperature and total pressure of 1 atm. Partial pressure of SO_2. Experimental points [10, 13] and calculated lines.

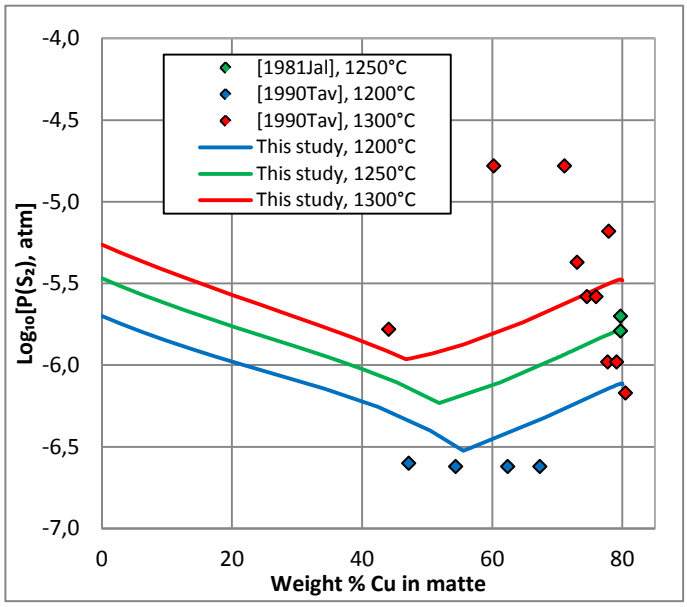

Figure 9.12. Slag–matte–SiO_2–metal equilibrium in the Cu–Fe–O–S–Si system at fixed temperature and total pressure of 1 atm. Partial pressure of S_2. Experimental points [10, 371] and calculated lines.

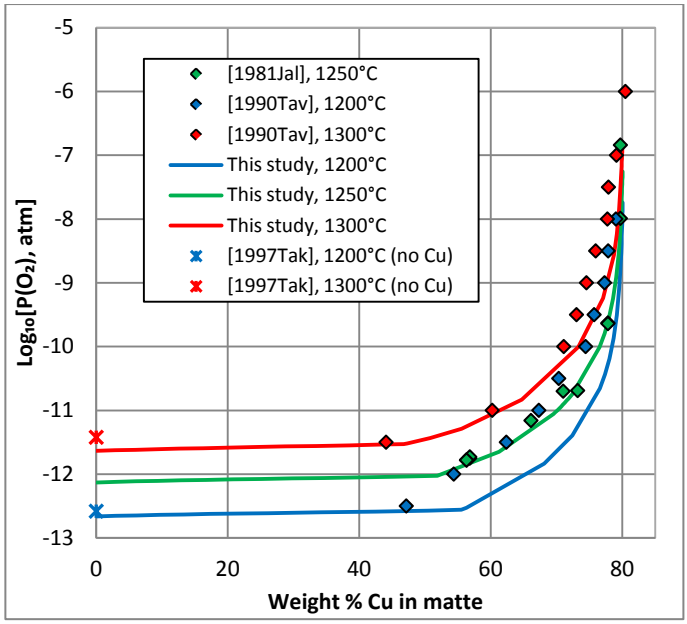

Figure 9.13. Slag–matte–SiO_2–metal equilibrium in the Cu–Fe–O–S–Si system at fixed temperature and total pressure of 1 atm. Partial pressure of O_2. Experimental points [10, 15, 371] and calculated lines.

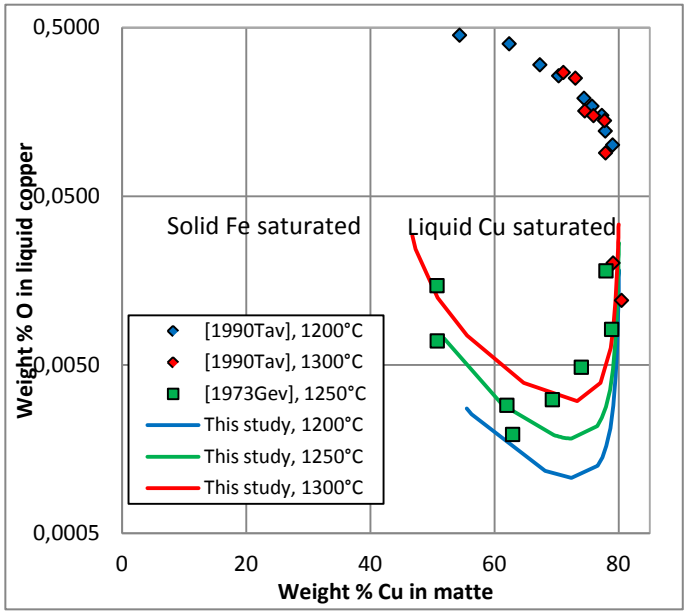

Figure 9.14. Slag–matte–SiO_2–metal equilibrium in the Cu–Fe–O–S–Si system at fixed temperature and total pressure of 1 atm. Oxygen content of liquid copper. Experimental points [10, 13] and calculated lines.

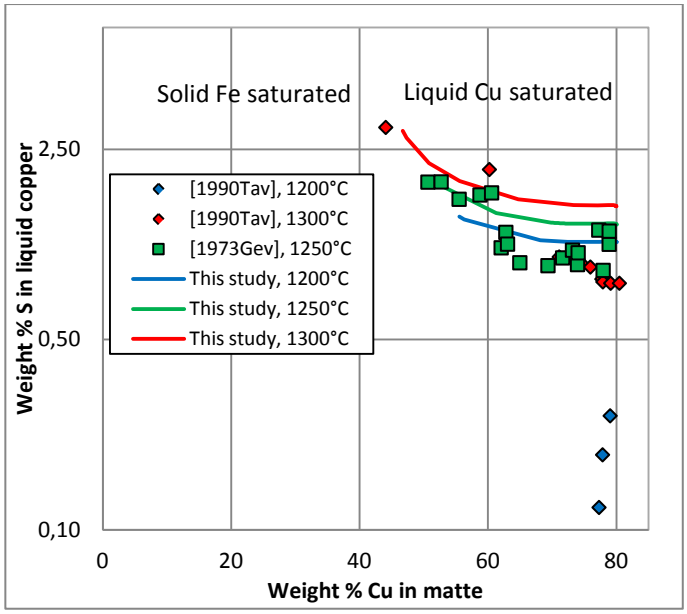

Figure 9.15. Slag–matte–SiO_2–metal equilibrium in the Cu–Fe–O–S–Si system at fixed temperature and total pressure of 1 atm. Sulfur content of liquid copper. Experimental points [10, 13] and calculated lines.

9.2.2 Slag–matte–SiO_2–SO_2 equilibrium

The experimental results at $P(SO_2)$ = 0.1 atm are collected in Figure 9.16-Figure 9.22, at $P(SO_2)$ = 1 atm – in Figure 9.23-Figure 9.29.

It is apparent from Figure 9.16, Figure 9.17, Figure 9.23 and Figure 9.24 that the slag phase in the experiments of Korakas (1964) [373] was contaminated with matte, since he reported copper and sulfur contents of slag, which are substantially higher that the results of other authors. Nevertheless, the analyzed composition of the matte phase should be correct, which is confirmed by Takeda [15], Kuxmann and Bor [374] and by calculations (Figure 9.18, Figure 9.19, Figure 9.25, Figure 9.26).

Slags in the experiments of Takeda [15] and of Font et al. [380] contained MgO, 5-9 wt. % and up to 6 wt. %, respectively. This can explain somewhat smaller copper content of slag, compared to that of Henao and Jak [377]. The latter study is the most recent one. It was conducted at the Pyrosearch Center using the equilibration/quenching/EMPA technique.

The copper content of slag was smaller in the experiments of Tavera and Davenport [375]. Their slag did not contain CaO, MgO or Al_2O_3, yet the measured copper solubility was even lower than that measured by Font et al [380] in the MgO-containing slag. At the same time the

moasures sulfur content of slag and oxygen content of matte were too high, which puts into question the quality of analysis used by Tavera and Devenport [375].

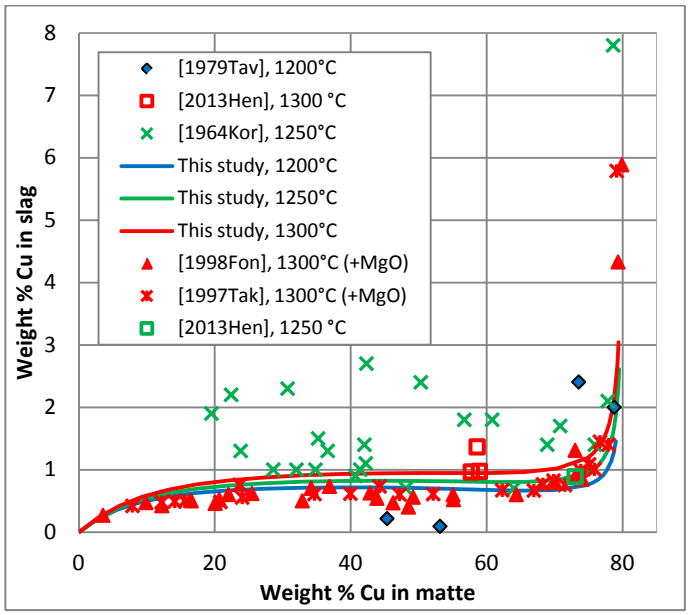

Figure 9.16. Slag–matte–SiO_2–$P(SO_2)$ = 0.1 atm equilibrium in the Cu–Fe–O–S–Si system at fixed temperature and total pressure of 1 atm. Copper content of slag. Experimental points [373, 375, 377, 380, 381] and calculated lines.

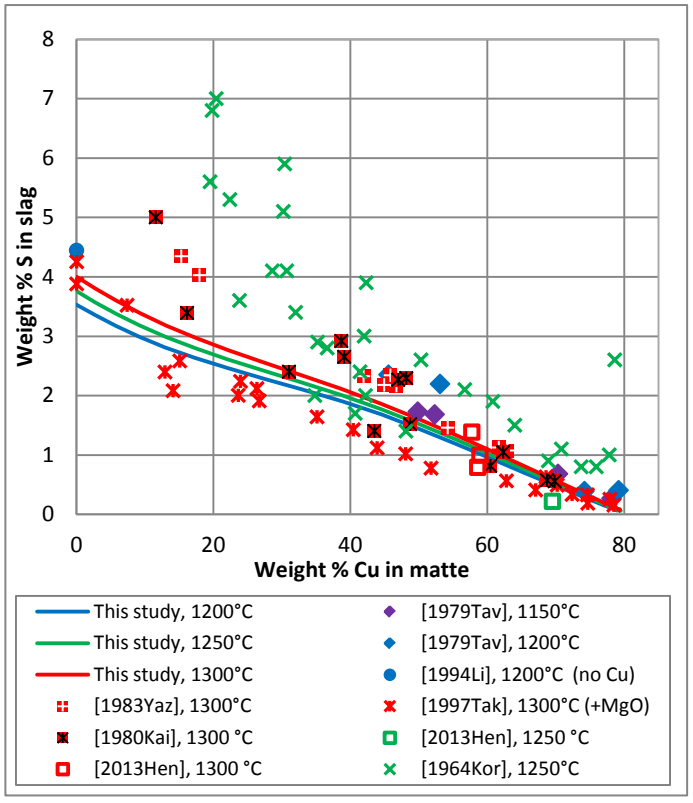

Figure 9.17. Slag–matte–SiO_2–$P(SO_2)$ = 0.1 atm equilibrium in the Cu–Fe–O–S–Si system at fixed temperature and total pressure of 1 atm. Sulfur content of slag. Experimental points [10, 370, 372, 373, 376, 377] and calculated lines.

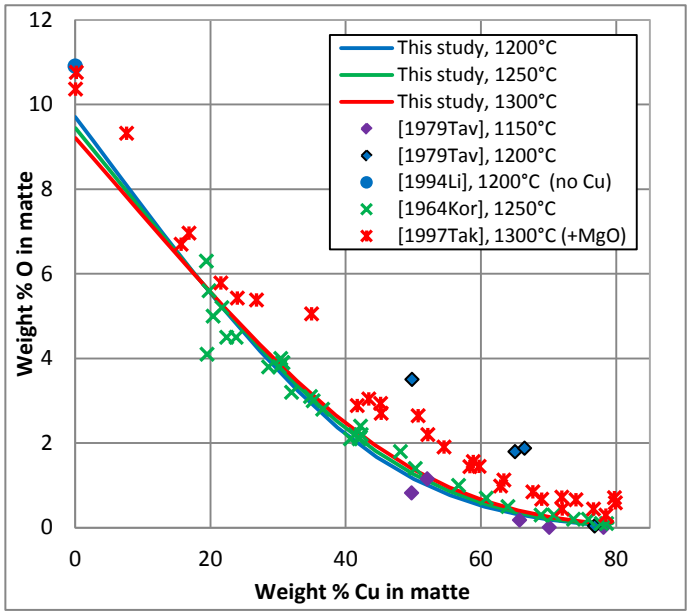

Figure 9.18. Slag–matte–SiO_2–$P(SO_2)$ = 0.1 atm equilibrium in the Cu–Fe–O–S–Si system at fixed temperature and total pressure of 1 atm. Oxygen content of matte. Experimental points [373, 375, 376, 381] and calculated lines.

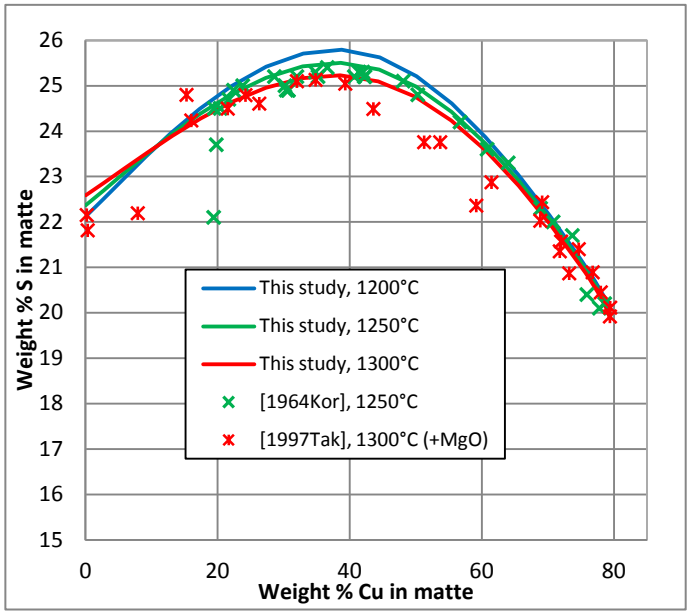

Figure 9.19. Slag–matte–SiO_2–$P(SO_2)$ = 0.1 atm equilibrium in the Cu–Fe–O–S–Si system at fixed temperature and total pressure of 1 atm. Sulfur content of matte. Experimental points [373, 381] and calculated lines.

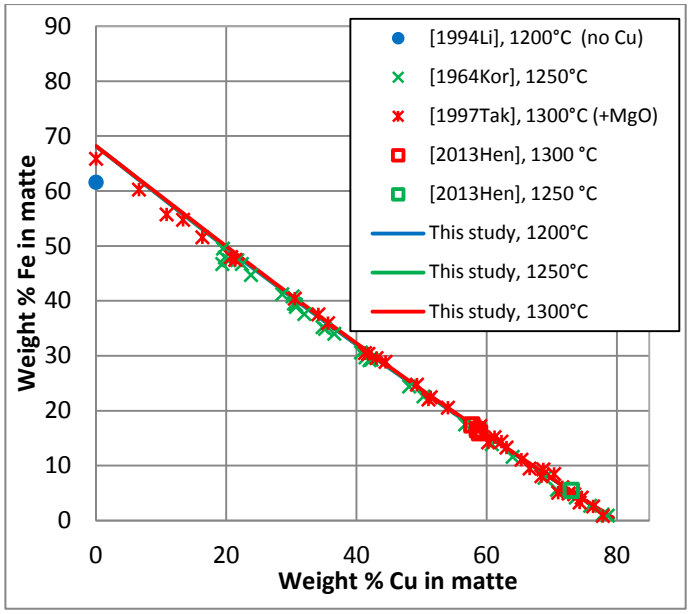

Figure 9.20. Slag–matte–SiO_2–$P(SO_2)$ = 0.1 atm equilibrium in the Cu–Fe–O–S–Si system at fixed temperature and total pressure of 1 atm. Iron content of matte. Experimental points [373, 376, 377, 381] and calculated lines.

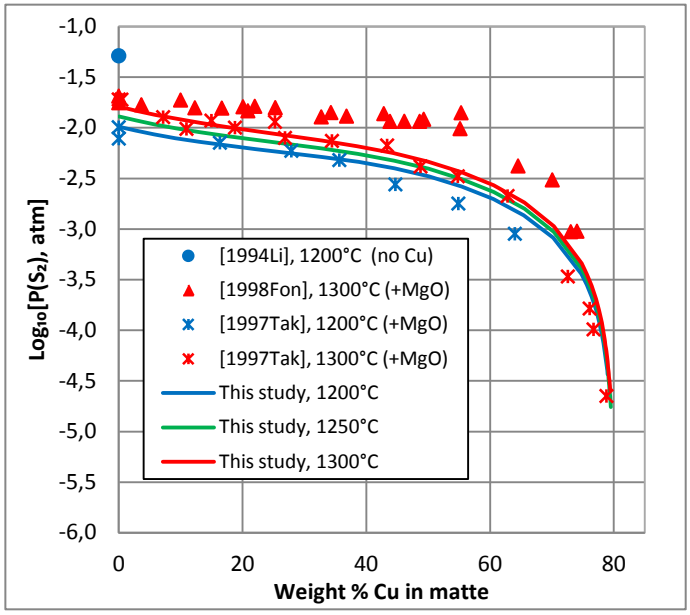

Figure 9.21. Slag–matte–SiO_2–$P(SO_2)$ = 0.1 atm equilibrium in the Cu–Fe–O–S–Si system at fixed temperature and total pressure of 1 atm. Partial pressure of S_2. Experimental points [15, 376, 380] and calculated lines.

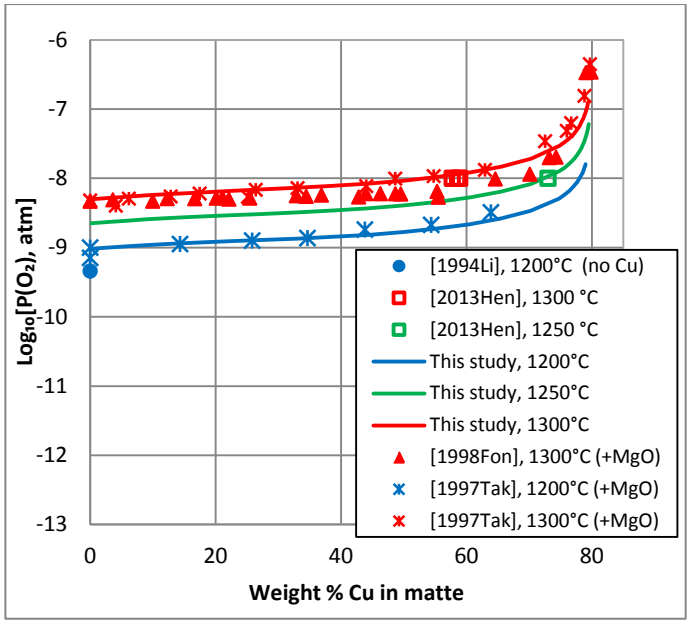

Figure 9.22. Slag–matte–SiO_2–$P(SO_2)$ = 0.1 atm equilibrium in the Cu–Fe–O–S–Si system at fixed temperature and total pressure of 1 atm. Partial pressure of O_2. Experimental points [15, 376, 377, 380] and calculated lines.

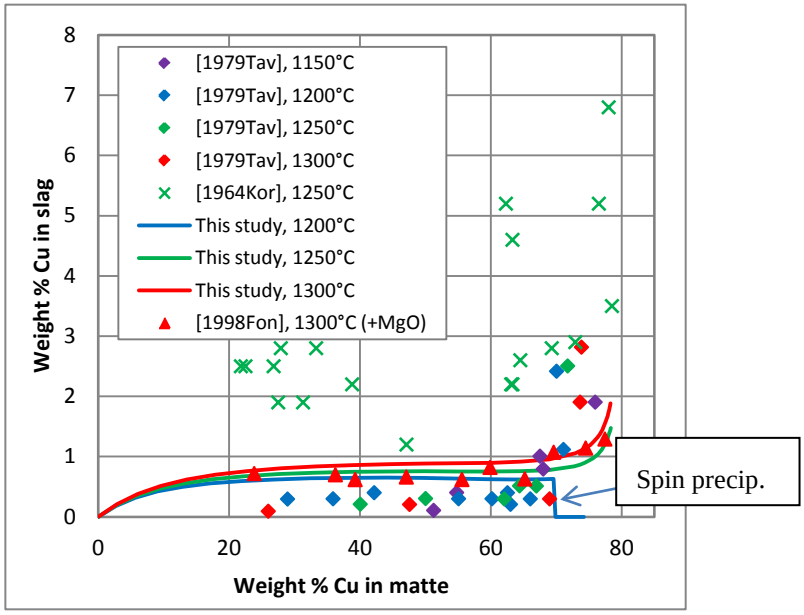

Figure 9.23. Slag–matte–SiO_2–$P(SO_2)$ = 1 atm equilibrium in the Cu–Fe–O–S–Si system at fixed temperature and total pressure of 1 atm. Copper content of slag. Experimental points [373, 375, 380] and calculated lines.

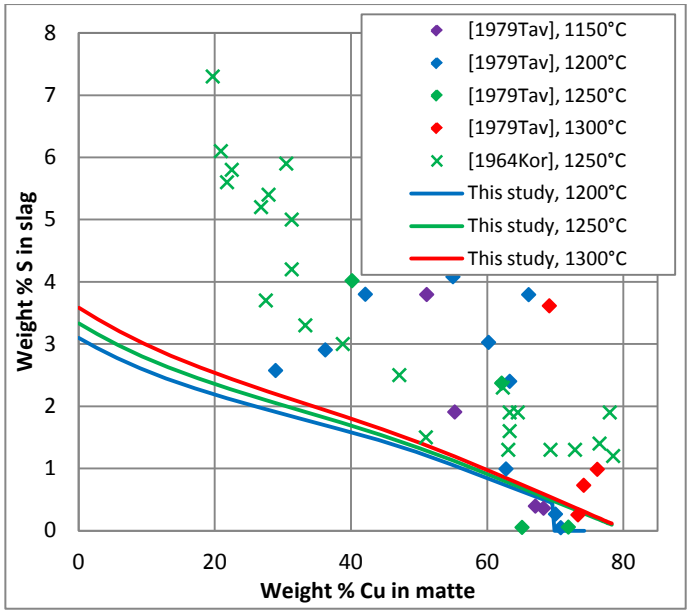

Figure 9.24. Slag–matte–SiO_2–$P(SO_2)$ = 1 atm equilibrium in the Cu–Fe–O–S–Si system at fixed temperature and total pressure of 1 atm. Sulfur content of slag. Experimental points [373, 375, 380] and calculated lines.

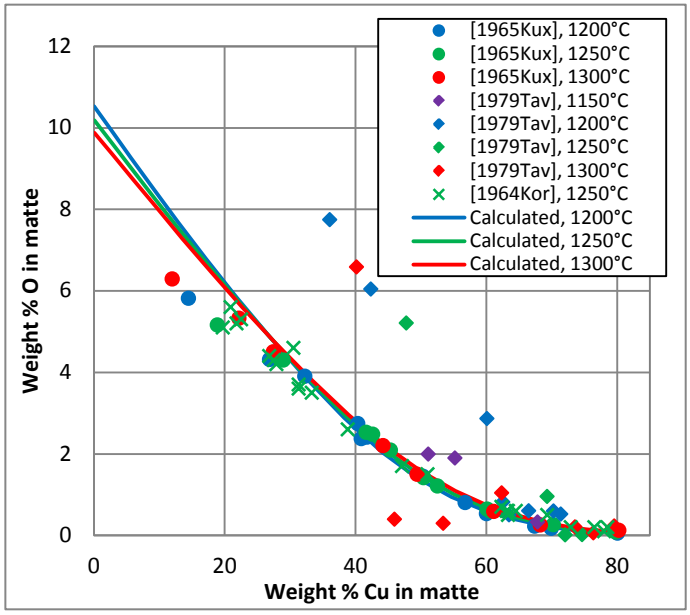

Figure 9.25. Slag–matte–SiO_2–$P(SO_2)$ = 1 atm equilibrium in the Cu–Fe–O–S–Si system at fixed temperature and total pressure of 1 atm. Oxygen content of matte. Experimental points [373-375, 380] and calculated lines.

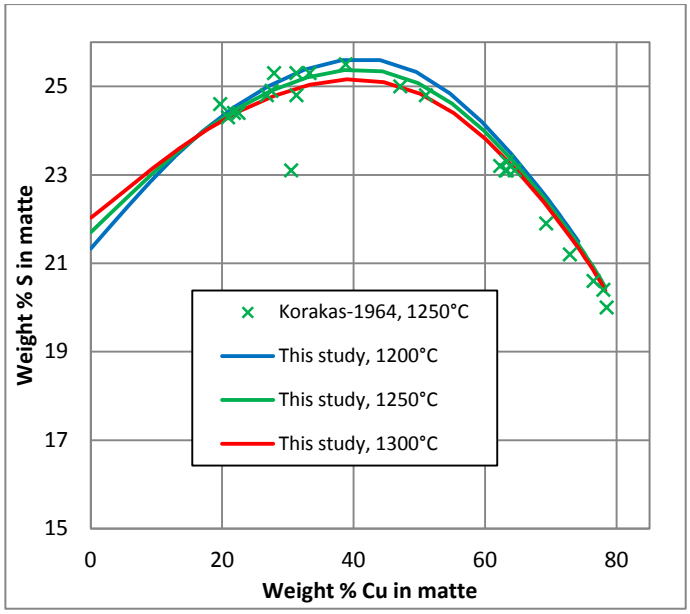

Figure 9.26. Slag–matte–SiO_2–$P(SO_2)$ = 1 atm equilibrium in the Cu–Fe–O–S–Si system at fixed temperature and total pressure of 1 atm. Sulfur content of matte. Experimental points [373, 380] and calculated lines.

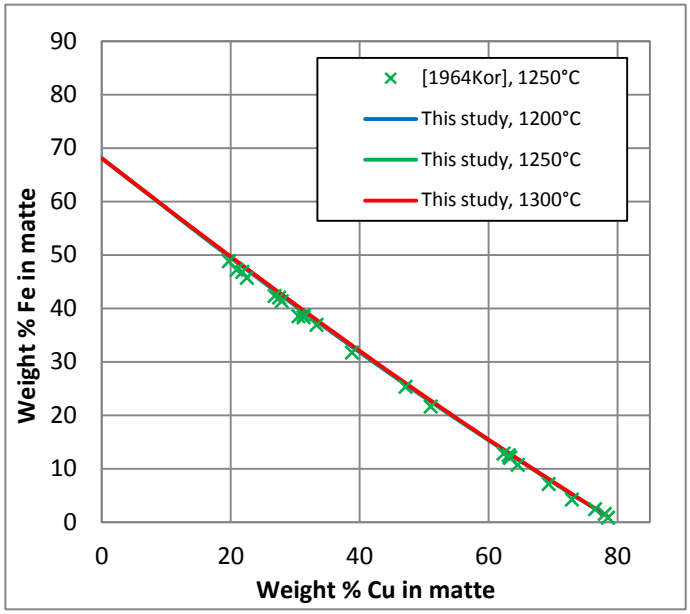

Figure 9.27. Slag–matte–SiO_2–$P(SO_2)$ = 1 atm equilibrium in the Cu–Fe–O–S–Si system at fixed temperature and total pressure of 1 atm. Iron content of matte. Experimental points [373, 380] and calculated lines.

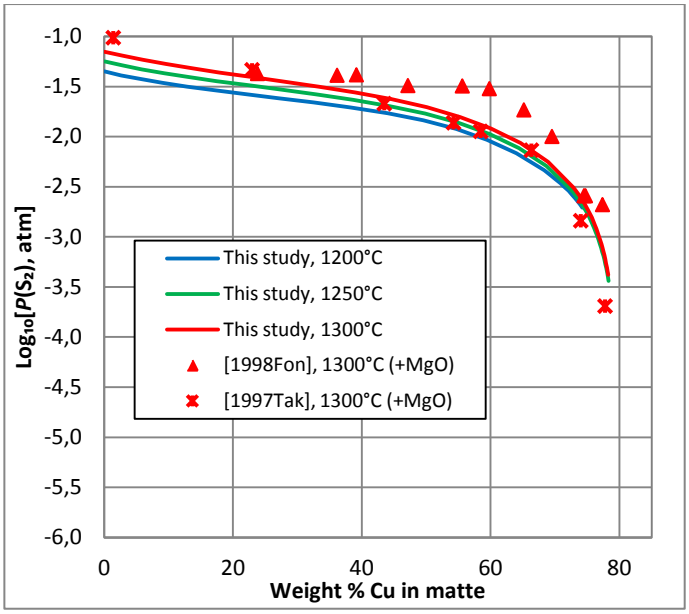

Figure 9.28. Slag–matte–SiO_2–$P(SO_2)$ = 1 atm equilibrium in the Cu–Fe–O–S–Si system at fixed temperature and total pressure of 1 atm. Partial pressure of S_2. Experimental points [15, 380] and calculated lines.

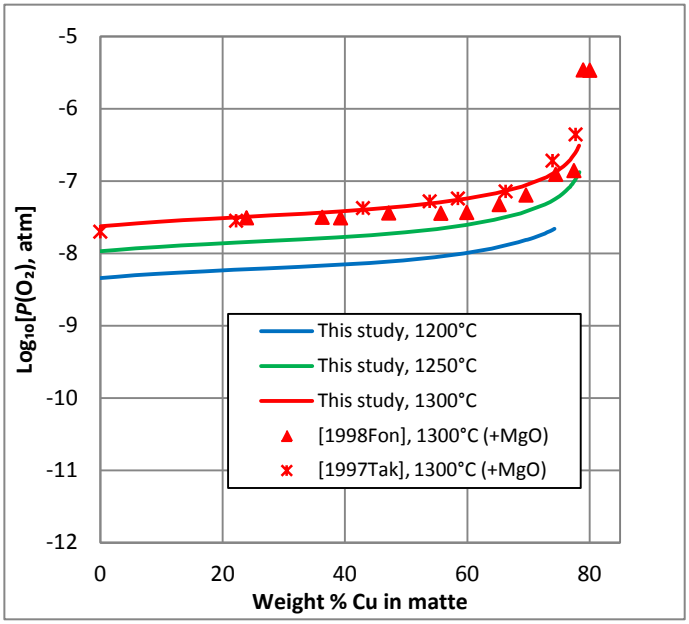

Figure 9.29. Slag–matte–SiO_2–$P(SO_2)$ = 1 atm equilibrium in the Cu–Fe–O–S–Si system at fixed temperature and total pressure of 1 atm. Partial pressure of O_2. Experimental points [15, 380] and calculated lines.

9.3 Optimization of parameters and results

All model parameters for the slag phase in the Cu–Fe–O–Si subsystem were taken from the previous optimizations [1]. Databases for liquid *Matte/Metal* phase and solid compound and

solutions remained unchanged as well. The list of all phases and corresponding references are given in Table 9-1.

According to the Quasichemical formalism in the quadruplet approximation, the introduction of sulfur into the system requires expressions for the Gibbs energies of sulfide end-members: SiS_2, FeS, Fe_2S_3 and Cu_2S.

The Gibbs energy expression for SiS_2 was taken from the sulfide-capacity evaluation of Kang and Pelton [354].

In order to fix the properties of FeS in slag, the results of the Fe–S system optimization were used (see Section 3.1). The Gibbs energy of 0.5Fe + 0.5S liquid was calculated using the *Matte/Metal* solution and these properties were assigned to the FeS end-member in slag.

Completely arbitral thermodynamic properties were assigned to the Fe_2S_3 end-member in the study of Kang and Pelton [354]. It is believed that this sulfide should be stable in liquid under ambient partial pressures of sulfur. In this study, the heat capacity and entropy of Fe_2S_3 were estimated as 2FeS + S, and a large positive enthalpy of formation was assigned to this end-member to prevent its formation in slag.

The thermodynamic properties of Cu_2S were calculated using the results of the optimization of the Cu–S system. The entropy and heat capacity were calculated for 2/3Cu + 1/3S liquid using the *Matte/Metal* database. As a the first approximation, enthalpy was calculated in the same way, but the calculated solubilties of copper and sulfur in slag were too high. Thus, the enthalpy of Cu_2S was one of the adjustable parameters. Hovever, the large positive enthalpy, required to suppress the solubility of Cu_2S in fayalite slag, decreased the solubility of Cu_2S in calcium ferrite slag as well. The latter is going to be discussed in Chapter 10. Instead, a combination of positive enthalpy and a long-range parameter, $\varepsilon_{Cu^+,S}$, was used. More details is given in Section 10.5.1.

The parameter $\Delta g^{\circ}_{Fe^{2+}Fe^{2+}/OS}$ in slag was used to approximately describe the FeO–FeS phase diagram (see Figure 5.12). The parameter $g^{011}_{Fe^{2+}Si/OO(S)}$ was required to decrease the solubility of sulfur in the Fe–O–Si slag to describe the experimental data in Figure 9.5, Figure 9.7 and Figure 9.17.

The thermodynamic modeling coupled with the recent experimental studies of Heano and Jak [377] finally resolved the inconsistencies in the reported copper content of slag (Figure 9.6, Figure 9.16, Figure 9.23). Lower values are always associated with the presence of CaO, MgO or Al_2O_3. In Ca-free slags, the nearly constant content of copper in slag from 30 to 70 wt. % Cu^{Matte} is explained by the balance between oxygen- and sulfur-bounded copper. It is usually referred to as oxidic and sulfidic dissolution of copper in the literature. In the present study, slag is modeled using the Modified Quasichemical Model in quadruplet approximation. So, this effect may be explained in terms of quadruplet formation. Calculated mole fractions of copper containing quadruplets in slag at 1200 °C are plotted in Figure 9.6 (b). Most abundant quadruplets are: Si-Cu^{1+}-O-O, Fe^{2+}-Cu^{1+}-S-S, Fe^{2+}-Cu^{1+}-O-S and Fe^{2+}-Cu^{1+}-O-O. Mole fraction of all quadruplets rises up to 30 wt. % Cu^{Matte}, but then the fall of equilibrium $P(S_2)$ and increase in $P(O_2)$ cause sulfur-containing quadruplets to disappear. Oxygen containing quadruplets continue to rise. These two competing effects cause the total copper content to remain approximately at the same level. The existence of real maximum at 30 wt. % Cu^{Matte} may be further disputed, but to measure it experimentally, the analytical techniques should have the precision higher than 0.1 wt% Cu in slag, which is probably not achievable.

Table 9-1. Optimized properties of stoichiometric compounds and solutions in the Cu–Fe–O–S–Si system

Compounds		**Reference**
CuO, Cu_2O, S, Cu_2S, $CuSO_4$, Cu_2SO_4, $CuO{\cdot}CuSO_4$		[114]
Fe_2O_3, $FeSO_4$, $Fe_2(SO_4)_3$		[227]
FeS, 'Fe_7S_8', Fe_9S_{10}, $Fe_{10}S_{11}$, $Fe_{11}S_{12}$		[26]
$CuFeO_2$		[172]
$CuFeS_2$, $CuFe_2S_3$, Cu_3FeS_4, Cu_3FeS_8, $Cu_4Fe_5S_8$, $Cu_9Fe_8S_{16}$, $Cu_9Fe_9S_{16}$, $Cu_{11}Fe_2S_{13}$		[352]
SiO_2, Fe_2SiO_4		[1]
Solutions	**Temperature range or reference**	**Molar Gibbs energy $g(T)$**
Slag	Modified Quasichemical Formalism (Cu^{1+}, Fe^{2+}, Fe^{3+}, Si^{4+})(O^{2-}, S^{2-})	
$Z^{Fe^{2+}}_{Fe^{2+}Fe^{2+}//OO} = Z^{Fe^{2+}}_{Fe^{2+}Fe^{2+}//SS} = Z^{Fe^{2+}}_{Cu^{1+}Fe^{2+}//OO} = 1.37744375$; $Z^{Fe^{3+}}_{Fe^{3+}Fe^{3+}//OO} = Z^{Fe^{3+}}_{Fe^{3+}Fe^{3+}//SS} = 2.06616563$; $Z^{Fe^{3+}}_{Fe^{3+}Si^{4+}//OO} = 1.37744375$ $Z^{Cu^{1+}}_{Cu^{1+}Cu^{1+}//OO} = Z^{Cu^{1+}}_{Cu^{1+}Cu^{1+}//SS} = Z^{Cu^{1+}}_{Cu^{1+}Si^{4+}//OO} = 0.68872188$; $Z^{Cu^{1+}}_{Cu^{1+}Fe^{2+}//OO} = 1.37744375$ $Z^{Si^{4+}}_{Si^{4+}Si^{4+}//OO} = Z^{Si^{4+}}_{Si^{4+}Si^{4+}//SS} = Z^{Si^{4+}}_{Fe^{3+}Si^{4+}//OO} = Z^{Si^{4+}}_{Cu^{1+}Si^{4+}//OO} = 2.7548875$		
g°_{FeO}, $g^{\circ}_{Fe_2O_3}$, $g^{\circ}_{Cu_2O}$	Table 8–1	
$g^{\circ}_{SiO_2}$	298– 1996 [349]	$-915415.8 + 562.1994T - 83.5136T\ln T + 1227680T^{-1} - 46678699T^{-2} - 1498.77T^{0.5}$
	1996– 3000	$-952208.5 + 564.5491T - 85.7720T\ln T$
$g^{\circ}_{Cu_2S}$	298–1500	$-87753.7 + 375.9011T - 75.2443T\ln T - 0.010213T^2 + 121819T^{-1}$
		$-101721.3 + 520.0975T - 95.1090T\ln T - 0.003250T^2$
g°_{FeS}	298–1500	$-133169.5 + 501.6241T - 80.4969T\ln T - 0.007084T^2 + 391377T^{-1}$
	1500–4000	$-148063.8 + 653.9679T - 101.3996T\ln T$
$g^{\circ}_{SiS_2}$	298–2700	$-283896.9 + 621.8719T - 100.0000T\ln T$
$g^{\circ}_{Fe_2S_3}$	298–1500	$+55230.0 + 1253.1420T - 203.3700T\ln T - 0.010763T^2 + 1132326T^{-1}$
	1500–3000	$+33812.7 + 1481.6272T - 234.7992T\ln T$

Table 9-1. (Continued) Optimized properties of stoichiometric compounds and solutions in the Cu–Fe–O–S–Si system

Cu-Fe-O parameters	Table 8–1	
$\Delta q^{\circ}_{Cu^{+}Si^{4+}/OO}$	[1]	27557.7
$q^{02}_{Cu^{+}Si^{4+}/OO}$	[1]	16500.0
$q^{05}_{Cu^{+}Si^{4+}/OO}$	[1]	255330.8 – 98.0193T
$\omega^{001}_{Si^{4+}Cu^{+}(Fe^{2+})/OO}$	[1]	-82502.0 + 41.0860T
$\omega^{103}_{Si^{4+}Cu^{+}(Fe^{2+})/OO}$	[1]	101390.0
$\omega^{101}_{Si^{4+}Cu^{+}(Fe^{3+})/OO}$	[1]	-12407.4
$\omega^{012}_{Si^{4+}Cu^{+}(Fe^{3+})/OO}$	[1]	-4039.4
$\Delta\omega^{\circ}_{Fe^{2+}Si^{4+}/OO}$	[1]	-30497.2 + 16.8046T
$\omega^{30}_{Fe^{2+}Si^{4+}/OO}$	[1]	16664.9
$\omega^{06}_{Fe^{2+}Si^{4+}/OO}$	[1]	334033.8 – 119.6666T
$\omega^{01}_{Fe^{3+}Si^{4+}/OO}$	[1]	120999.1
$\omega^{07}_{Fe^{3+}Si^{4+}/OO}$	[1]	-25104.0
$\omega^{30}_{Fe^{3+}Si^{4+}/OO}$	[1]	24685.6
$\omega^{101}_{Fe^{2+}Si^{4+}(Fe^{3+})/OO}$	[1]	-47839.9
$\omega^{301}_{Fe^{2+}Si^{4+}(Fe^{3+})/OO}$	[1]	41116.2
$\omega^{012}_{Fe^{2+}Si^{4+}(Fe^{3+})/OO}$	[1]	28451.2
$\omega^{021}_{Fe^{2+}Si^{4+}(Fe^{3+})/OO}$	[1]	73638.4

Table 9-1. (Continued) Optimized properties of stoichiometric compounds and solutions in the Cu–Fe–O–S–Si system

$\Delta g^{\circ}_{Fe^{2+}Fe^{2+}/OS}$		70004.6 – 41.8400*T*
$g^{011}_{Fe^{2+}Si/OO(S)}$		179912
$\varepsilon_{Cu^{+},S}$		-7531.2
Liquid (Metal, Sulfide)	Modified Quasichemical Formalism (Cu^{I}, Cu^{II}, Fe^{II}, Fe^{III}, O, S), Grouping: Cu^{I}, Cu^{II},Fe^{II}, Fe^{III} in group 1; O, S in Group 2	
	[114, 172, 227, 352]	
Fcc , Fe and Cu metals	Bragg-Williams (Cu, Fe, O, S)	
	[114, 172, 227]	
Bcc, solid Fe metal	Bragg-Williams (Cu, Fe, O, S)	
	[172, 227]	
Monoxide, "$Fe_{1-x}O$"-(CuO)	Bragg-Williams (FeO, $FeO_{1.5}$, CuO)	
	[21, 172]	
Spinel, Fe_3O_4-$CuFe_2O_4$	Compound energy formalism: $(Cu^{+2},Fe^{+2},Fe^{+3})^{tetr}[Cu^{+2},Fe^{+2},Fe^{+3},Va]_2^{oct}O_4^{-2}$	
	[21, 172]	
Pyrrhotite, $Fe_{1-x}S$-(CuS), Pyrr	Bragg-Williams (Fe, Cu, Vacancy)S	
	[26, 352]	
MeS_2, FeS_2-(CuS_2), pyrite	Bragg-Williams (FeS_2, CuS_2)	
	[26, 352]	
ISS	Bragg-Williams (Cu_2, Fe, Vacancy)S	
	[352]	
Covellite, CuS-(FeS), Cov	Bragg-Williams (CuS, FeS)	
	[114, 352]	
Digenite-Bornite, Cu_2S-Cu_2FeS_4, DB1 and DB2	Bragg-Williams (Cu_2, Fe, Vacancy)S	
	[114, 352]	

CHAPTER 10 EFFECT OF Ca ON MATTE–SLAG EQUILIBRIA DURING COPPER SMELTING AND CONVERTING

Equation Chapter (Next) Section 1

It was shown previously (Section 9.2.1) that the presence of calcium in fayalite slag has an effect on the solubility of copper and sulfur (Figure 9.6 and Figure 9.7). In this chapter this effect is modeled quantitatively. The thermodynamic model for slag is described in Section 2.3:

$$\left(Ca^{2+}, Cu^{1+}, Fe^{2+}, Fe^{3+}, Si^{4+}\right)\left(O^{2-}, S^{2-}\right) \tag{10.1}$$

The most important parameters affecting the solubility of sulfur are $g^{\circ}_{Cu_2S}$, g°_{FeS} and g°_{CaS}.

10.1 Ca–Fe–O–S and Ca–O–S–Si systems

The Ca–Fe–O and Ca–O–Si systems were assessed previously [1], [348]. The solubility of sulfur in Ca–Fe–O and Ca–O–Si slags was evaluated by Kang and Pelton [354]. The comparison between the sulfide capacity (9.2) calculated in this study, the evaluation of Kang and Pelton [354] and the experimental data is given in Figure 10.1 and Figure 10.2. In the latest article of Piao et al. [19], the solubilities of CaS in $CaO–SiO_2$ slag were measured by a quenching/equilibration/EPMA technique (Figure 10.3). They also presented a model for this slag and described the experimental data using only the Gibbs energy of pure liquid CaS in slag as a parameter. The properties of solid CaS were also adjusted to give the desired results.

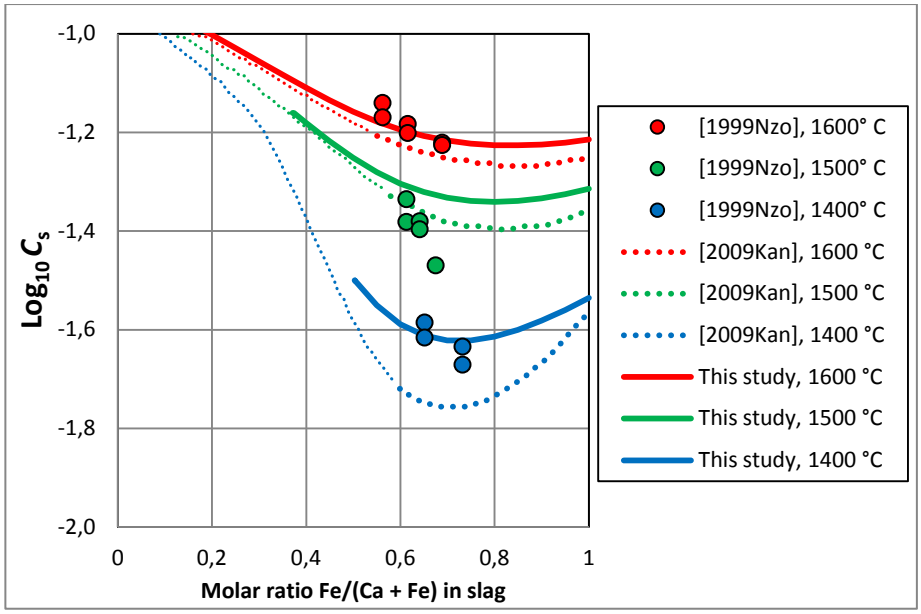

Figure 10.1. Sulfide capacity of slag in the Ca–Fe–O–S system. Experimental points [366]. Calculated lines at 1600 °C correspond to $\log_{10}[P(O_2)$, atm] = -7 and $\log_{10}[P(S_2)$, atm] = -2. Calculated lines at 1400 and 1500 °C correspond to $\log_{10}[P(O_2)$, atm] = -8 and $\log_{10}[P(S_2)$, atm] = -3. Dotted lines – [354], solid lines – this study.

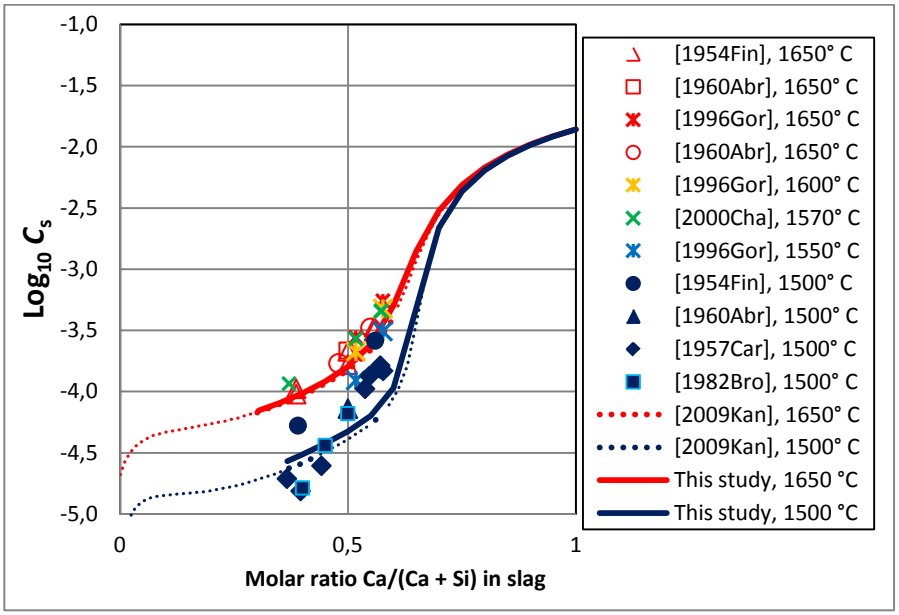

Figure 10.2. Sulfide capacity of slag in the Ca–O–S–Si system. Experimental points [368, 382-386]. Calculated lines correspond to $\log_{10}[P(O_2)$, atm] = -9 and $\log_{10}[P(S_2)$, atm] = -2. Dotted lines – [354], solid lines – this study.

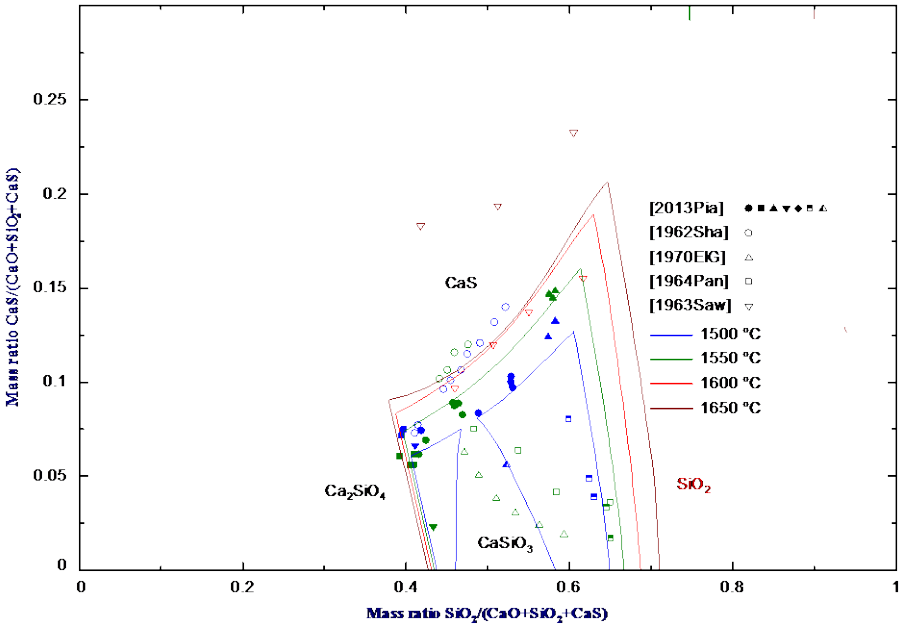

Figure 10.3. Liquidus in the Ca–O–S–Si system. Experimental points [19, 387] and calculated lines.

10.2 Ca–Cu–Fe–O–Si system

The solubility of copper in sulfur-free Ca–Fe–O–Si slags was studied by T. Hidayat [1]. In order to achieve a correct description, the Ca–Fe–O–Si system was re-optimized [1]. The effect of Ca on the activity of $CuO_{0.5}$ in fayalite slag is shown in Figure 10.4. The phase diagram of the Ca–Fe–O–Si system and Ca–Cu–Fe–O–Si system in equilibrium with liquid copper is shown in Figure 10.5. The size of the liquid slag area on these diagrams depends not only on temperature, but on oxygen partial pressure as well. Liquid slag is divided into two areas by the spinel + $\alpha' Ca_2SiO_4$ region. One area originates near the Fe_2SiO_4 composition and is called fayalite slag. The second liquid region appears near $CaFe_2O_4$ and is called calcium ferrite slag. Of course, these two slags have separate fileds up to a certain temperature, at higher temperatures slag forms continuous phase field. The dissolution of copper in slag joins two slags as well. Nevertheless, the thermodynamic and physical properties of these slags are rather different. In particular, they dissolve different amounts of copper and sulfur when equilibrated with matte. The copper and sulfur solubilities in Ca-free fayalite slags were discussed in the previous chapter (Chapter 9). In the next two sections, the solubility of Cu and S in Si-free calcium ferrite slag is presented, as well as the effect of Ca on fayalite slag.

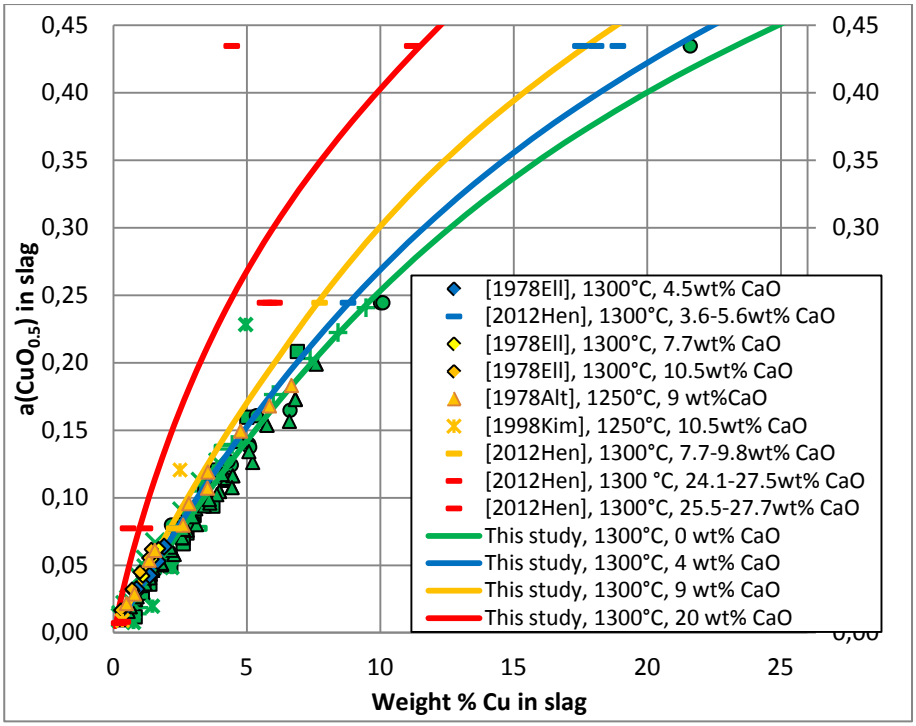

Figure 10.4. Activity of ½(Cu_2O) in slag vs. copper content of silica saturated slag in the Ca–Cu–Fe–O–Si system. Experimental points [360, 362, 363, 388] and calculated lines. Experimental points for Ca-free slags are taken from Figure 9.1.

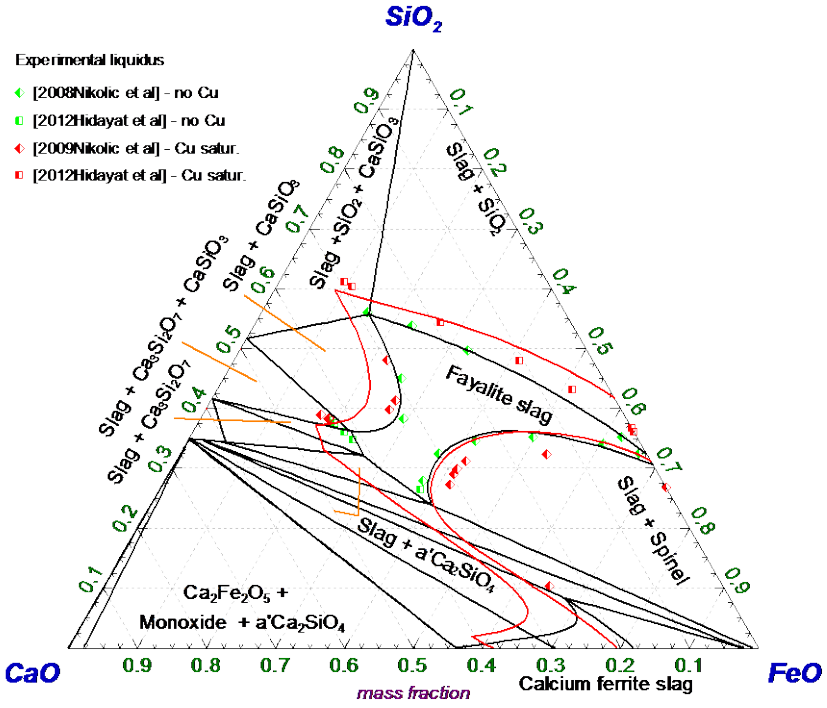

Figure 10.5. Black lines and green symbols [389, 390]: phase diagram of the Ca–Fe–O–Si system at 1300 °C and $P(O_2) = 10^{-6}$ atm. Red lines and symbols [1, 325]: liquid region of the phase diagram of the Ca–Cu–Fe–O–Si system at 1300 °C, $P(O_2) = 10^{-6}$ atm and in equilibrium with copper.

10.3 Ca–Cu–Fe–O–S system

Slag–matte equilibria in the Ca–Cu–Fe–O–S system were studied by Park et al. (1983) [391], Acuna and Yazawa (1986) [392] and by Roghani et al. (1996) [393]. All three works originate from the Tohoku university group. According to the Gibbs phase rule, 7 degrees of freedom must be set in the Ca–Cu–Fe–O–S system in order to fix the equilibrium. In the above mentioned studies, the following degrees of freedom were fixed: temperature, total pressure (1atm), slag, matte, metal copper saturation or fixed $P(SO_2)$, wt% Cu in matte as a measured value. The final degree of freedom can be the Ca/Fe ratio in slag. The authors mentioned that they fixed "mass %Ca in the FeO–CaO feed" – 23% CaO [391], 25% CaO [392], 23% or 10% CaO [393]. During the experiment, the Ca/Fe ratio in slag changed due to the reaction with Cu_2S–FeS matte, so the last degree of freedom was set somewhat ambiguously. The results of the experimental investigations are shown in Figure 10.6-Figure 10.13. The solubility of copper and sulfur in calcium ferrite slag is much higher than in fayalite slag (compare with Figure 9.6 and Figure 9.7). Slag and matte show high mutual solubility, and below 50 wt % of Cu in matte they become one liquid, i.e. the miscibility gap between slag and matte disappears. Calculated lines in Figure 10.6-Figure 10.13 correspond approximately to the conditions of the experiments. In the calculation, the Ca/Fe ratio in slag was varied in such a way, that the total iron content in slag, Fe^{2+} + Fe^{3+}, corresponded to experimentally measured values (Figure 10.8).

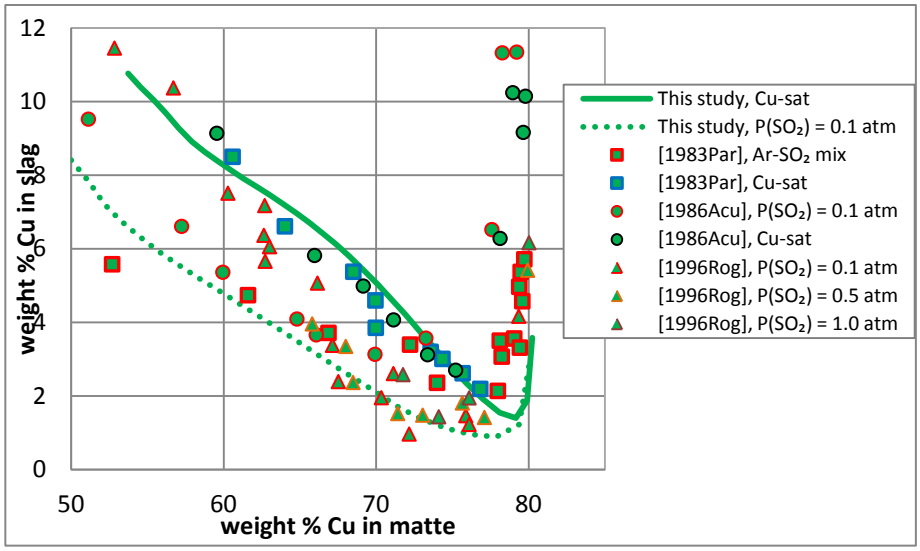

Figure 10.6. Copper content of slag for slag–matte equilibrium in the Ca–Cu–Fe–O–S system at 1250 °C, Cu saturation or fixed $P(SO_2)$, total iron content of slag as in Figure 10.8 and total pressure of 1 atm. Experimental points [391-393] and calculated lines.

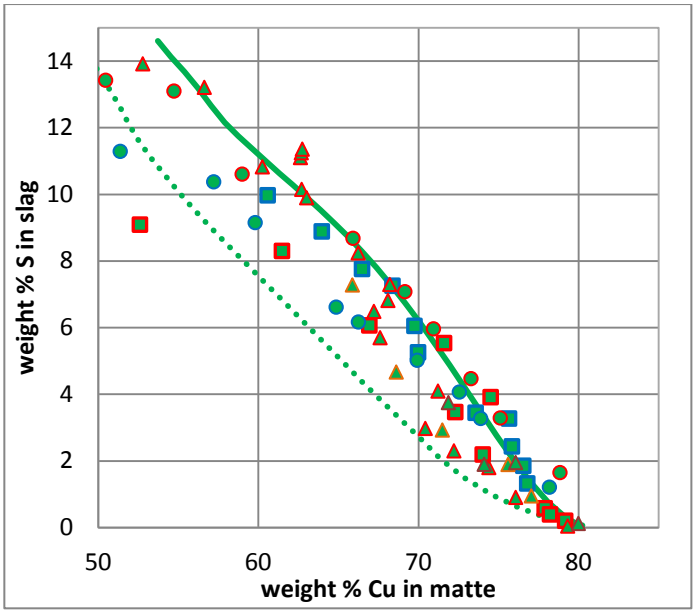

Figure 10.7. Sulfur content of slag for slag–matte equilibrium in the Ca–Cu–Fe–O–S system at 1250 °C, Cu saturation or fixed $P(SO_2)$, total iron content of slag as in Figure 10.8 and total pressure of 1 atm. Experimental points [391-393] and calculated lines. Legend is the same as in Figure 10.6.

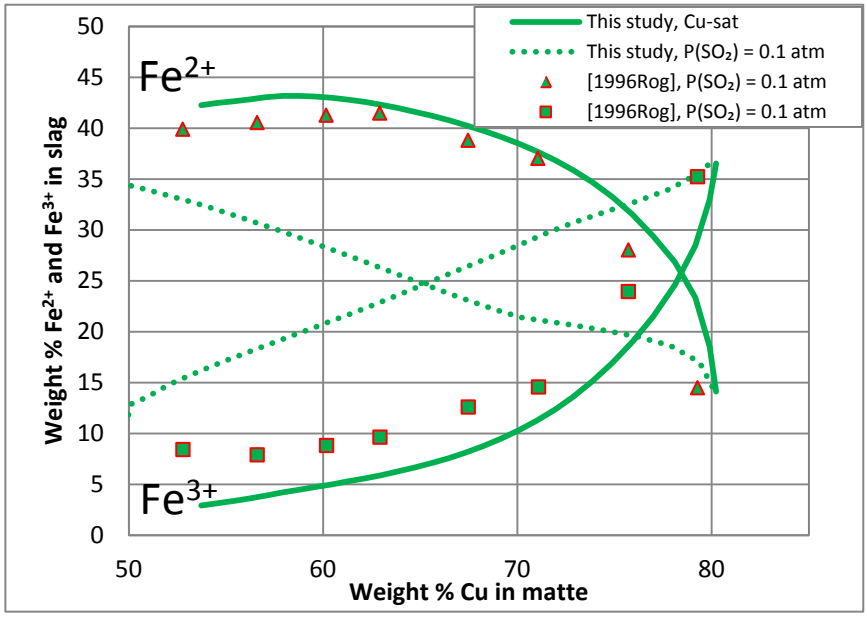

Figure 10.8. Fe^{2+} and Fe^{3+} content of slag for slag–matte equilibrium in the Ca–Cu–Fe–O–S system at 1250 °C, Cu saturation or fixed $P(SO_2)$, total iron content of slag as in Figure 10.8 and total pressure of 1 atm. Experimental points [393] and calculated lines.

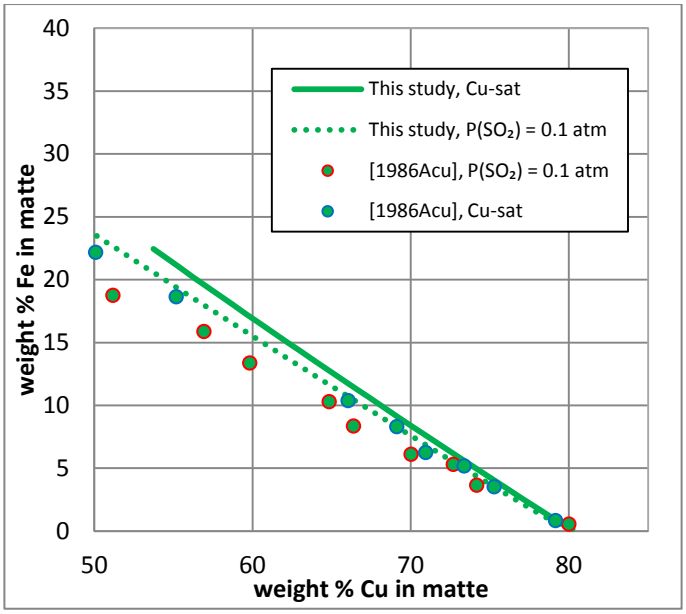

Figure 10.9. Iron content of matte for slag–matte equilibrium in the Ca–Cu–Fe–O–S system at 1250 °C, Cu saturation or fixed $P(SO_2)$, total iron content of slag as in Figure 10.8 and total pressure of 1 atm. Experimental points [392] and calculated lines.

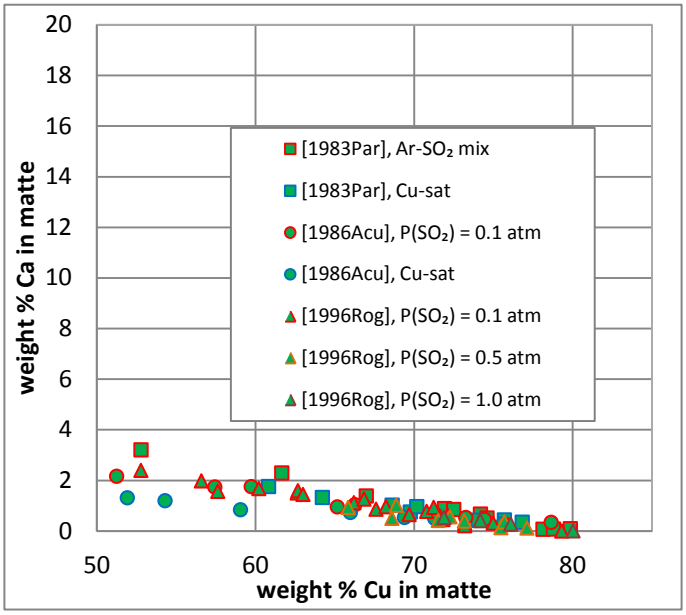

Figure 10.10. Calcium content of matte for slag–matte equilibrium in the Ca–Cu–Fe–O–S system at 1250 °C, Cu saturation or fixed $P(SO_2)$, total iron content of slag as in Figure 10.8 and total pressure of 1 atm. Experimental points [391-393]. The solubility of Ca in matte is neglected in the present study.

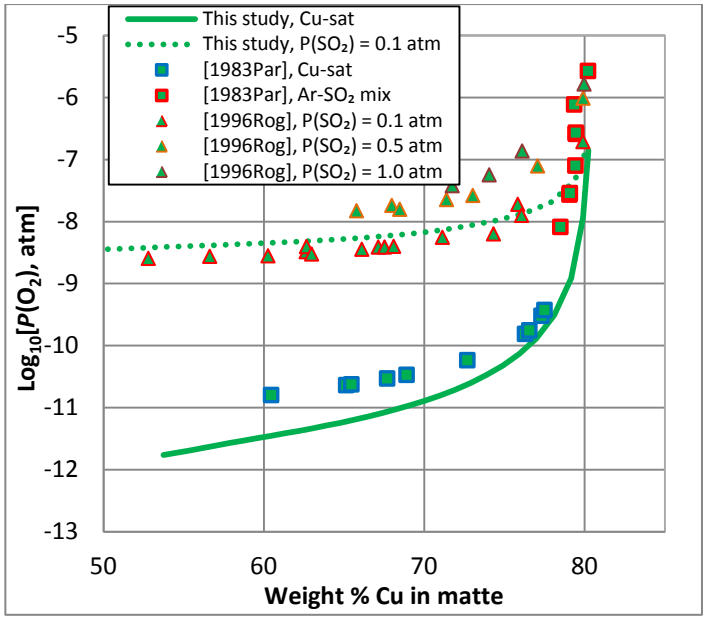

Figure 10.11. Partial pressure of oxygen for slag–matte equilibrium in the Ca–Cu–Fe–O–S system at 1250 °C, Cu saturation or fixed $P(SO_2)$, total iron content of slag as in Figure 10.8 and total pressure of 1 atm. Experimental points [391, 393] and calculated lines.

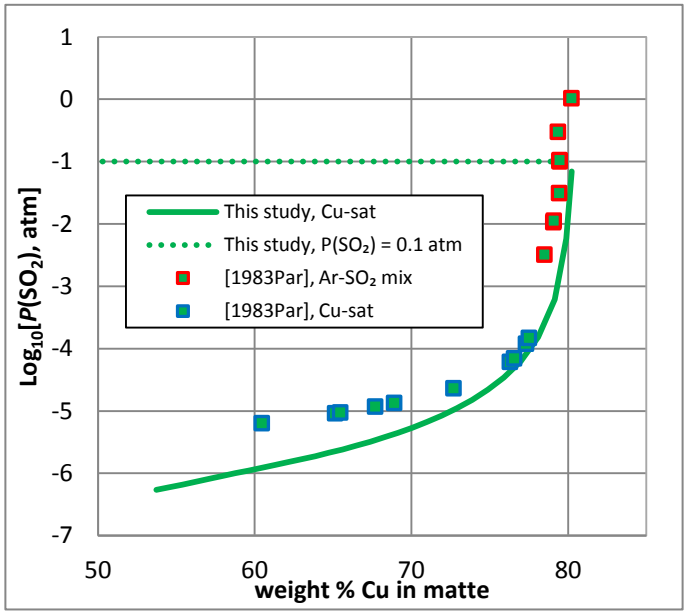

Figure 10.12. Partial pressure of SO_2 for slag–matte equilibrium in the Ca–Cu–Fe–O–S system at 1250 °C, Cu saturation or fixed $P(SO_2)$, total iron content of slag as in Figure 10.8 and total pressure of 1 atm. Experimental points [391] and calculated lines.

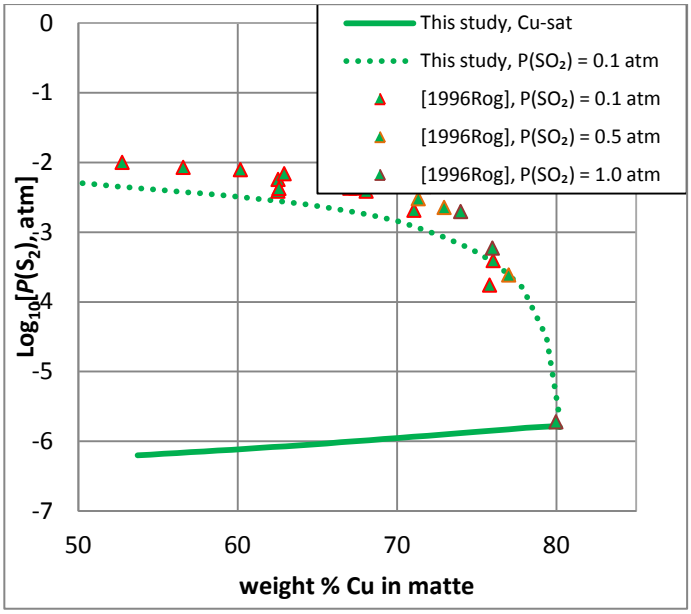

Figure 10.13. Partial pressure of S_2 for slag–matte equilibrium in the Ca–Cu–Fe–O–S system at 1250 °C, Cu saturation or fixed $P(SO_2)$, total iron content of slag as in Figure 10.8 and total pressure of 1 atm. Experimental points [393] and calculated lines.

10.4 Ca–Cu–Fe–O–S–Si system

The effect of calcium on the solubility of copper and sulfur in fayalite slag, equilibrated with matte, SiO_2 and metal (Cu or Fe), was studied by Yazawa et al. (1983) [372] and by Shimpo et al. (1986) [365]. The article of Yazawa et al. [372] summarises the experiemental results for Ca-free slags, slags containing 3 wt% CaO and 11 wt% CaO [378]. It is demonstrated that with the addition of CaO to fayalite slag, the copper and sulfur solubility drops (Figure 10.14 and Figure 10.15). The experimental data of Shimpo et al. [365] confirm this notion – their measured copper and sulfur contents at 8 wt% CaO fall between those, measured at 3 and 11 wt% CaO by Yazawa et al. [372]. It is also shown that calcia replaces iron in slag, not silica (Figure 10.16 and Figure 10.17).

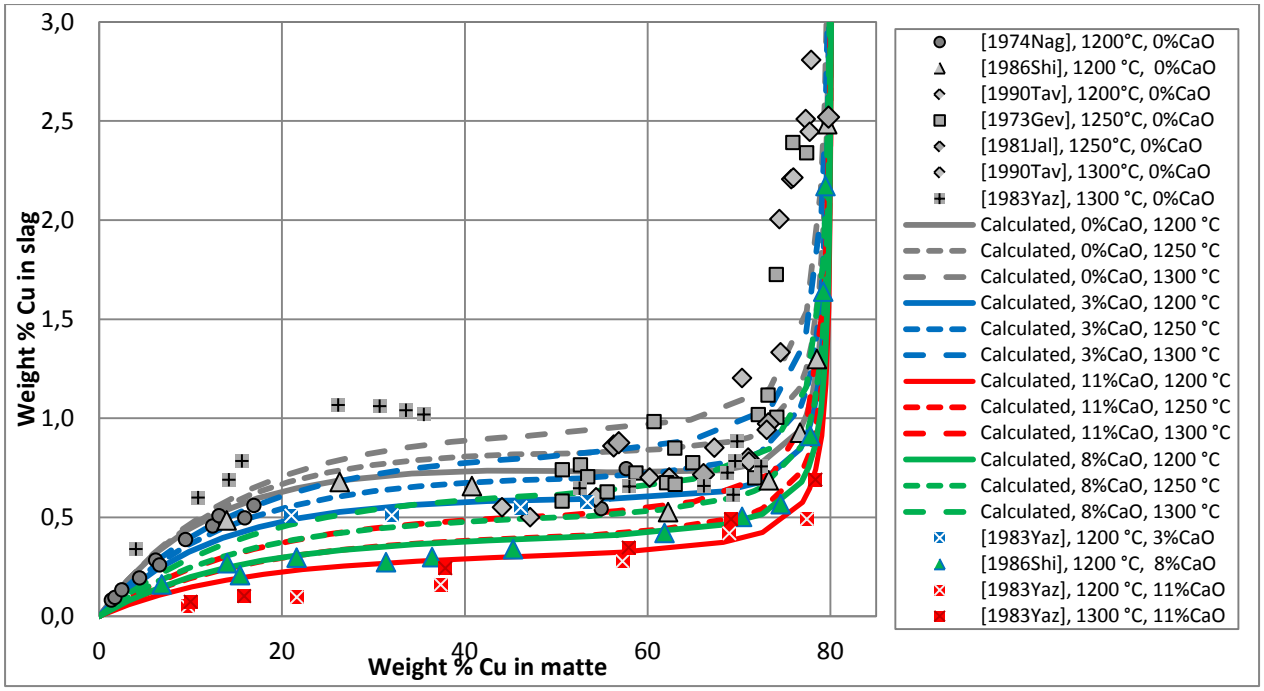

Figure 10.14. Copper content of slag for slag–matte–SiO_2–metal equilibrium in the Ca–Cu–Fe–O–S–Si system at fixed temperature, total pressure of 1 atm and different CaO contents of slag. Experimental points [365, 372] and calculated lines. The experimental points for Ca-free system are taken from Figure 9.6.

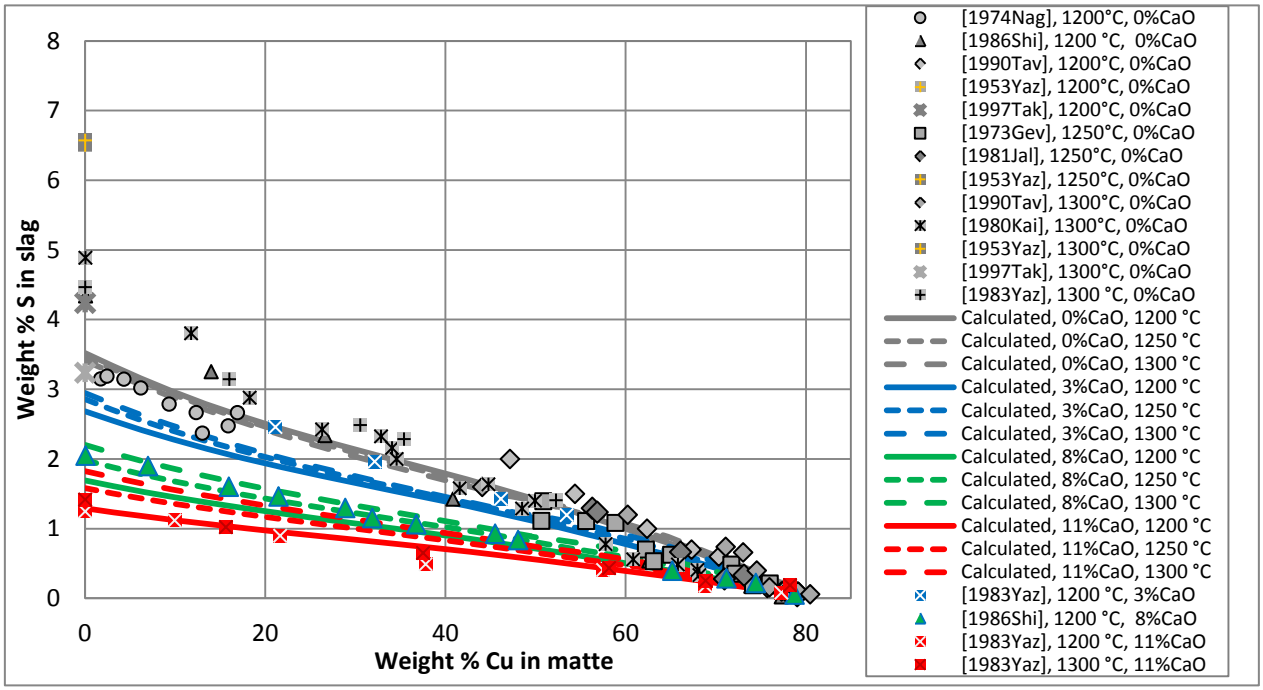

Figure 10.15. Sulfur content of slag for slag–matte–SiO_2–metal equilibrium in the Ca–Cu–Fe–O–S–Si system at fixed temperature, total pressure of 1 atm and different CaO contents of slag. Experimental points [365, 372] and calculated lines. The experimental points for Ca-free system are taken from Figure 9.7.

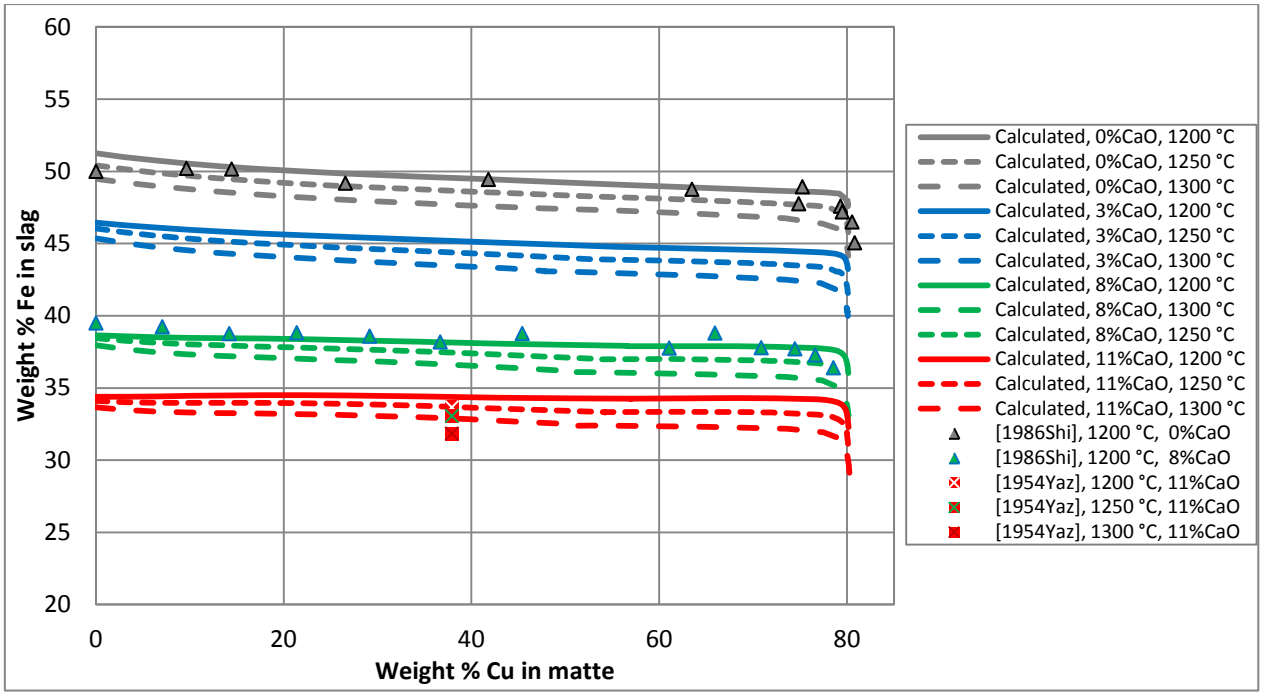

Figure 10.16. Iron content of slag for slag–matte–SiO_2–metal equilibrium in the Ca–Cu–Fe–O–S–Si system at fixed temperature, total pressure of 1 atm and different CaO contents of slag. Experimental points [365, 378] and calculated lines.

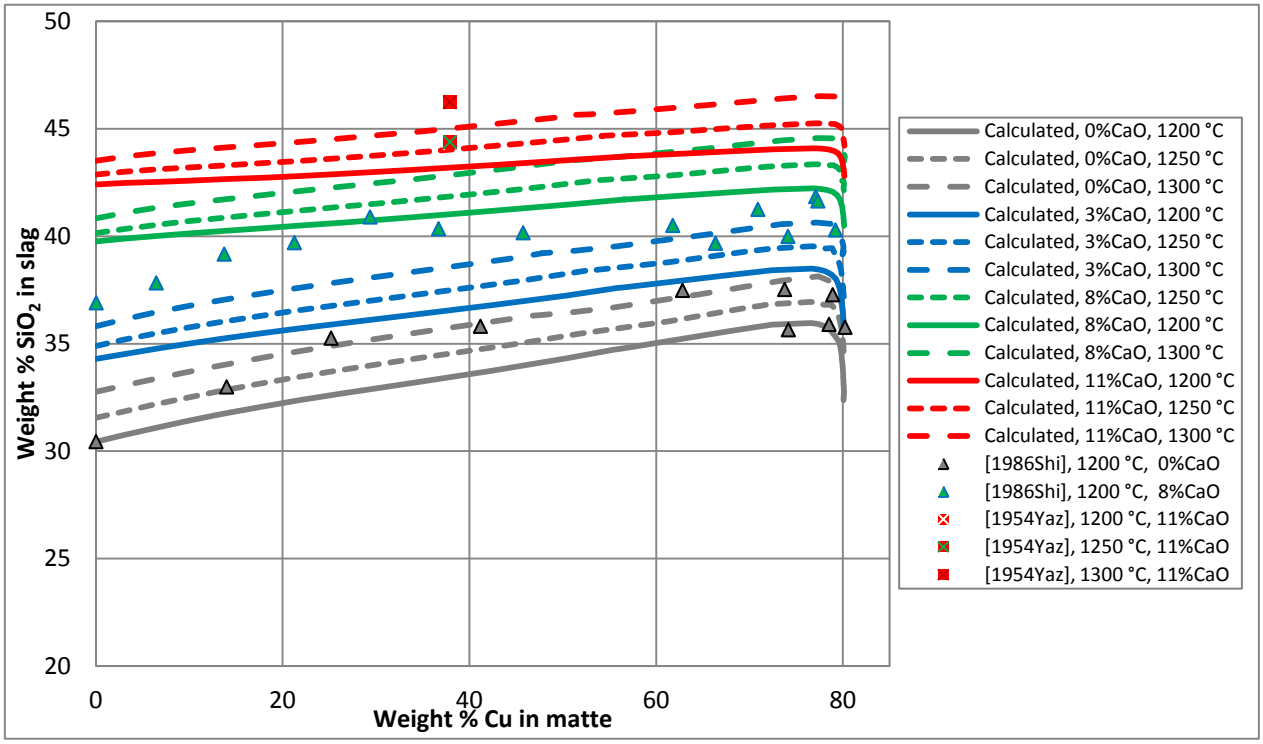

Figure 10.17. Silica content of slag for slag–matte–SiO_2–metal equilibrium in the Ca–Cu–Fe–O–S–Si system at fixed temperature, total pressure of 1 atm and different CaO contents of slag. Experimental points [365, 378] and calculated lines.

10.5 Optimization of parameters and results

The optimized parameters and phases for the Cu–Fe–O–S–Si and Ca–Fe–O–Si systems were adopted from the previous studies (Chapter 9 and Ref. [1]). The Gibbs energies of solid and liquid CaS were taken from the study by Piao et al. [19].

Using the $g^{\circ}_{Cu_2S}$ and g°_{CaS} parameters, equilibria between matte and calcium ferrite slag in the Ca–Cu–Fe–O–S system were calculated at the conditions close to the experiments [391-393]. A good agreement with the experimental results was obtained – the predicted solubility of Cu and S in calcium ferrite slags was much higher than in fayalite slag (Figure 10.6 and Figure 10.7). A disagreement in the Fe^{2+}/Fe^{3+} ratio in calcium ferrite slag at $P(SO_2)$ = 0.1 atm may be explained by the fact that calcium ferrite slags are not viscous enough to be quenched into a glass state. Many reactions that change the Fe^{2+}/Fe^{3+} ratio in slag may occur during the quenching. For instance, our calculations show that under these conditions much of Fe^{3+} in liquid slag forms first nearest neighbor pairs with S^{2-}. However, solid sulfides precipitating from slag contain only Fe^{2+}.

In the present database a small solubility of Ca in matte (Figure 10.10) is neglected. Since slag and matte are modeled as separate solutions, the database cannot predict the disappearance of the miscibility gap between matte and slag below 50 wt % Cu in matte. However, these compositions are far away from the operating conditions, which are commonly used in copper smelting and converting. Calcium ferrite slag is mostly used at the converting stage in systems with large content of copper.

The slag model in the present study is somewhat different from that of Piao et al. [19]. The difference is explained in Section 2.3, in particular, by Equations (2.23) and (2.24). As a result, the solubilities of CaS in the $CaO–SiO_2$ slags (Figure 10.3) at temperatures 1500-1650 °C were not described well enough using the Gibbs energy function g°_{CaS} optimized by Piao et al. [19]. The calculated solubilities were lower than the experimental data. This was corrected by an additional small negative excess parameter, $\Delta g^{011}_{CaSi/OO(S)}$, which gives the effect of sulfur on Reaction (2.19).

As can be seen from Figure 10.14 and Figure 10.15 both copper and sulfur solubility in slag decrease with the addition of CaO. At the same time, the iron content falls and the concentration of SiO_2 rises. The model predicts these effects without any new excess parameters,

but the solubilities of Cu and S in slags fall only half the way down compared to the experimental results. To obtain a good quantitative agreement with the experimental data, we had to assign a large positive value to the parameter, mentioned above, $\Delta g^{011}_{\mathrm{CaSi/OO(S)}}$.

Thus, it was not possible to describe both the solubilities of CaS in $CaO–SiO_2$ slags at 1500-1650 °C and the drop of solubility of Cu and S in fayalite slags at temperatures 1200-1300 °C using a temperature-independent parameter $\Delta g^{011}_{\mathrm{CaSi/OO(S)}}$. To describe both sets of data simultaneously, the parameter was made temperature dependent: $\Delta g^{011}_{\mathrm{CaSi/OO(S)}} = A + BT + CT\ln T$ (Figure 10.18). Even though the coefficients A, B, C have no clear physical meaning, they were optimized to describe all the experimental data up to the temperature of 1650 °C. The difficulties in the optimization may be explained by the uncertainties in the properties of liquid CaS and the complexity of the $\left(Ca^{2+}, Cu^{1+}, Fe^{2+}, Fe^{3+}, Si^{4+}\right)\left(O^{2-}, S^{2-}\right)$ slag. No attempts were found in the literature to describe all experimental data in this six-component system.

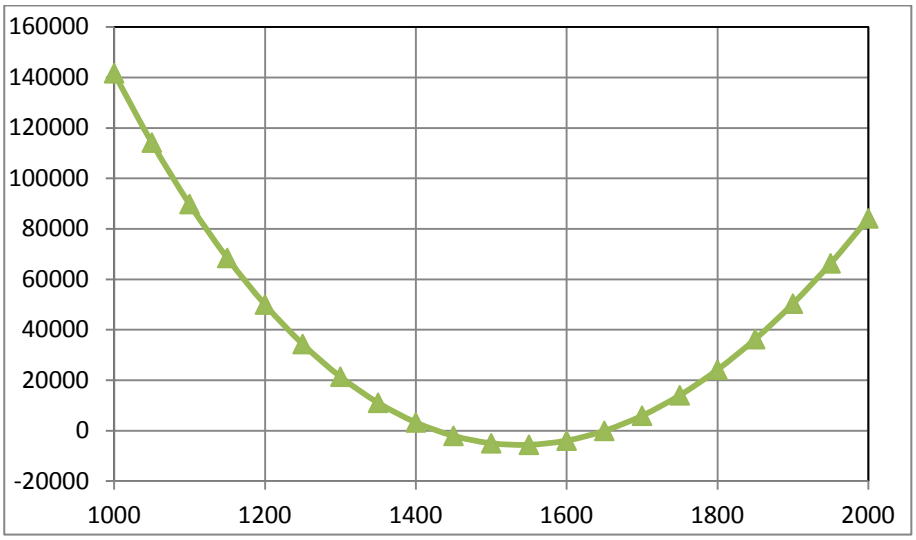

Figure 10.18. Value of the excess parameter $\Delta g^{011}_{\mathrm{CaSi/OO(S)}}$.

10.5.1 Alternative optimization attempts and long range parameter

The solubility of copper in slag is of primary importance for the industry. Three different sets of data were considered simultaneously to optimize models parameters: 1) copper and sulfur contents of SiO_2-saturated fayalite slag in equilibrium with matte in the Cu–Fe–O–S–Si system

(Figures 9.6, 9.7, 9.16, 9.17, 9.23, 9.24); 2) copper and sulfur contents of calcium ferrite slag in equilibrium with matte in the Ca–Cu–Fe–O–S system (Figures 10.6, 10.7); 3) the effect of Ca on the solubility of copper and sulfur in fayalite slag in equilibrium with matte in the Ca–Cu–Fe–O–S–Si system (Figures 10.14, 10.15). The copper and sulfur contents of slag at $\%Cu^{Matte} = 50$ are about 1 and 2 wt. % in set 1) and about 11 and 14 wt% in set 2). At the same time, Ca has a negative effect on the solubilities of Cu and S in SiO_2-saturated fayalite slag: they fall down to 0.25 and 0.7 wt. %, respectively, at 11 wt. % CaO in slag. Without any new parameters, the wt. % Cu and S in slag for set 1) were more than 2 and 3 %, and they were also higher than the experimental data in set 2). Additional model parameters were required to describe the experimental data quantitatively.

The available model parameters, which could be adjusted without changes in the lower-order systems, are: i) the enthalpy of formation of the Cu_2S end-member in slag, $\Delta_f H^\circ(Cu_2S)$; ii) excess parameter between Cu_2S and FeS, $\Delta q^\circ_{Cu^+Fe^{2+}/SS}$, and excess parameter between Cu_2S and CaS, $\Delta q^\circ_{Cu^+Ca^{2+}/SS}$; iii) a long range parameter $\varepsilon_{Cu^+,S}$.

Various combinations of parameters i) and ii) were tried first.

A positive contribution was added to $\Delta_f H^\circ(Cu_2S)$ to describe the data in set 1). As a result, the solubility of Cu and S in set 2) fell too much. A negative $\Delta q^\circ_{Cu^+Ca^{2+}/SS}$ parameter could be added to optimize the data in set 2), but Ca would then have a positive effect on the solubility of Cu and S in set 3), which is against experimental observations.

A positive parameter $\Delta q^\circ_{Cu^+Fe^{2+}/SS}$ could be used to decrease the solubilities of Cu and S in set 1). It had an effect in set 2) as well, decreasing the solubilities. A positive parameter $\Delta q^\circ_{Cu^+Ca^{2+}/SS}$ was necessary to describe the data in set 2), but it was less positive, than $\Delta q^\circ_{Cu^+Fe^{2+}/SS}$. When CaO is added to the fayalite slag, it replaces Fe^{2+} ions by Ca^{2+} ions, So CaO will again have a positive effect on the solubility of Cu and S in set 3), because of the "wrong" balance between $\Delta q^\circ_{Cu^+Fe^{2+}/SS}$ and $\Delta q^\circ_{Cu^+Ca^{2+}/SS}$. Anyway, a positive excess parameter between Cu_2S and FeS is against the experimental evidence in the Cu–Fe–S system (Section 3.3).

Positive interaction parameters between SiO_2 and Cu_2O were previously optimized to describe the experimental data in the Cu–O–Si system [1]. Extensive observations show that it is the positive excess parameter between SiO_2 and Cu_2S that is required as well. It could be used to optimize the solubility of Cu and S in set 1) with no effect on set 2). Then, it becomes possible to introduce a positive parameter $\Delta q^{\circ}_{Cu^{+}Ca^{2+}/SS}$ to describe set 2). Both parameters affect set 3), giving the desired negative effect on the solubility of copper and sulfur. However, in the SiO_2–SiS_2–Cu_2O–Cu_2S reciprocal system, Si^{4+} and S^{2-} form almost no first nearest neighboor pairs. Hence, parameter $\Delta q^{\circ}_{Cu^{+}Si^{4+}/SS}$ has no effect. In the framework of the present model, it is not possible to create an additional positive contribution to the Gibbs energy of mixing between $(SiSi/OO)_{quad}$ and $(CuCu/SS)_{quad}$ quadruplets, and $(CuSi/OS)_{quad}$ is not stable anyway. Hence, no ordinary parameters had the desired effect.

That is why a special "long range parameter" was introduced. The Gibbs energy expression for the SiO_2–SiS_2–Cu_2O–Cu_2S reciprocal system can be written as

$$\begin{aligned} g = {} & (X_{Cu/O}g_{Cu/O} + X_{Cu/S}g_{Cu/S} + X_{Si/O}g_{Si/O} + X_{Si/S}g_{Si/S}) + \\ & \left[(X_{Cu/O} - Y_{Cu}Y_{O})\delta_{Cu,O} + (X_{Cu/S} - Y_{Cu}Y_{S})\delta_{Cu,S} + (X_{Si/O} - Y_{Si}Y_{O})\delta_{Si,O} + (X_{Si/S} - Y_{Si}Y_{S})\delta_{Si,S}\right] \\ & -T\Delta S^{\text{config}} \end{aligned} \qquad (10.2)$$

where $\delta_{i,j} = (g^{\circ}_{ij} - \varepsilon_{ij})$, ε_{ij} is the energy of the first nearest neighbor bond, g°_{ij} is the total lattice energy, Y_i is the equivalent fraction of *i*. The formula (10.2) is written in the pair approximation for the sake of simplicity. The expression in the quadruplet approximation may be derived by analogy. Similar expressions are true for the FeO–FeS–Cu_2O–Cu_2S and CaO–CaS–Cu_2O–Cu_2S reciprocal systems. The parameter $\varepsilon_{Cu^{+},S}$ has the desired effect in data sets 1) and 2). It was possible to describe both of them using the combination of $\varepsilon_{Cu^{+},S}$ and $\Delta_f H^{\circ}(Cu_2S)$. Their values are given in Table 9-1. At the same time, CaO had a qualitatively correct negative effect in data set 3). The parameter $\Delta g^{011}_{CaSi/OO(S)}$ was optimized to obtain the desired quantitative description of data set 3) as described earlier.

Table 10-1. Optimized properties of stoichiometric compounds and model parameters in the Ca-Cu-Fe-O-S-Si system (J mol^{-1} and J mol^{-1}·K^{-1})

Compounds	**Temperature range (K) or reference**	$\Delta H^{o}_{298.15}$ **J·mol^{-1}**	$S^{o}_{298.15}$ **J·mol^{-1}·K^{-1}**	$C_P(T)$ **J·mol^{-1}·K^{-1}**
CaS (solid)	298-1600 [19]	-478230.8	55.7642	$53.5984 + 0.003708T - 177618T^{-2} - 6.1371610^{-7}T^{2} - 2750.145T^{-1}$
	1600-3000 [19]			$52.5376 + 0.003365T - 2579.302T^{-1}$
CaS (liquid)	[19]	-463842.9	40.8170	66.9440
Parameters				
$\Delta g^{011}_{CaSi/OO(S)}$		$12480872 - 58693.2225T + 6903.617445T\ln T$		

CHAPTER 11 SIMULATION OF THE ISASMELT™ FURNACE

Equation Chapter (Next) Section 1

The ISASMELT™ top submerged lance (TSL) bath smelting process was developed in Mount Isa, Australia, by Mount Isa Mines Limited (now a subsidiary of Grlncore Xstrata PLC) during the 1980s [394]. It is now commercialized and has become wide spread in the world (Figure 11.1). By the end of 2011, the total installed capacity of the ISASMELT™ technology exceeded 9,000,000 tons per year of feed materials in copper and lead smelters around the world (Figure 11.2). The technology is equally effective for smelting nickel sulfide concentrates, converting nickel mattes, and producing ferronickel from lateritic ores.

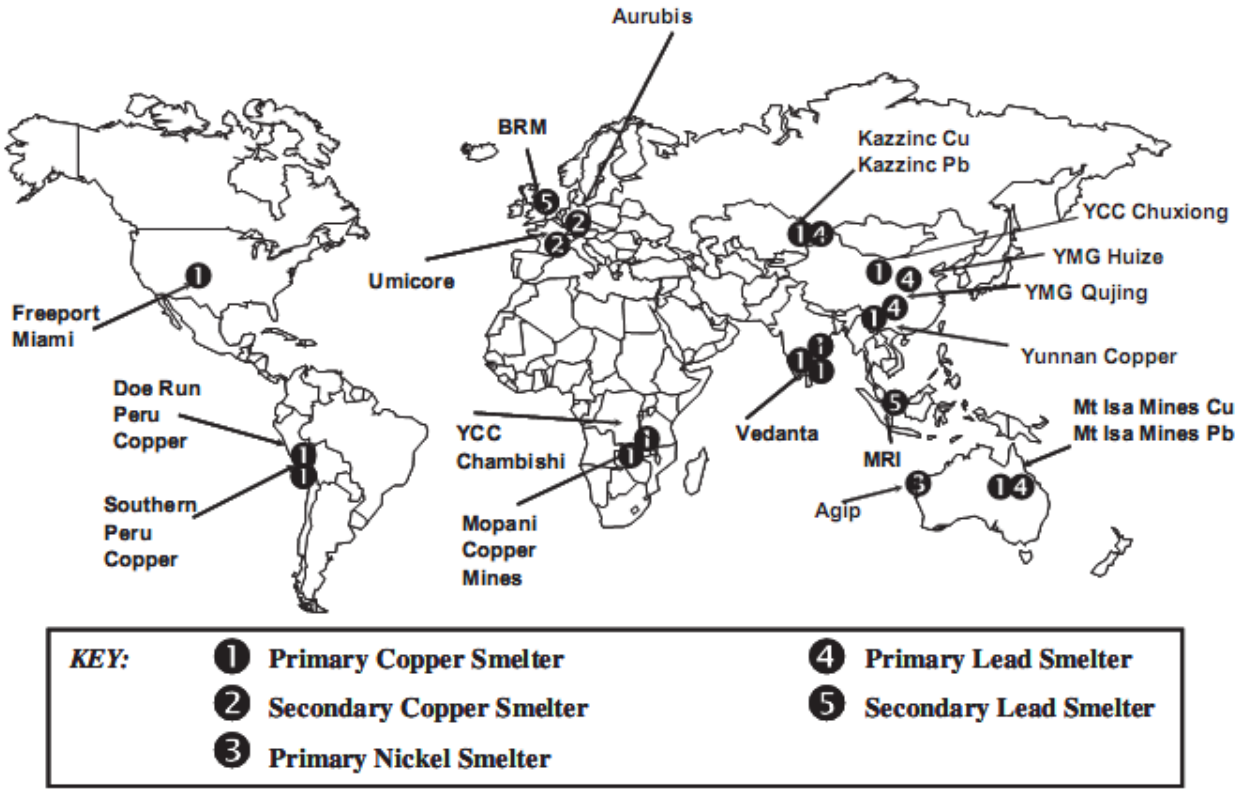

Figure 11.1. Location of ISASMELT™ plants that have been licensed to date [395].

Ten copper smelters were operating the process around the world in 2011. It is the technology of choice for many new smelters and smelter modernization projects, being cost effective for smelting both copper concentrates and secondary materials.

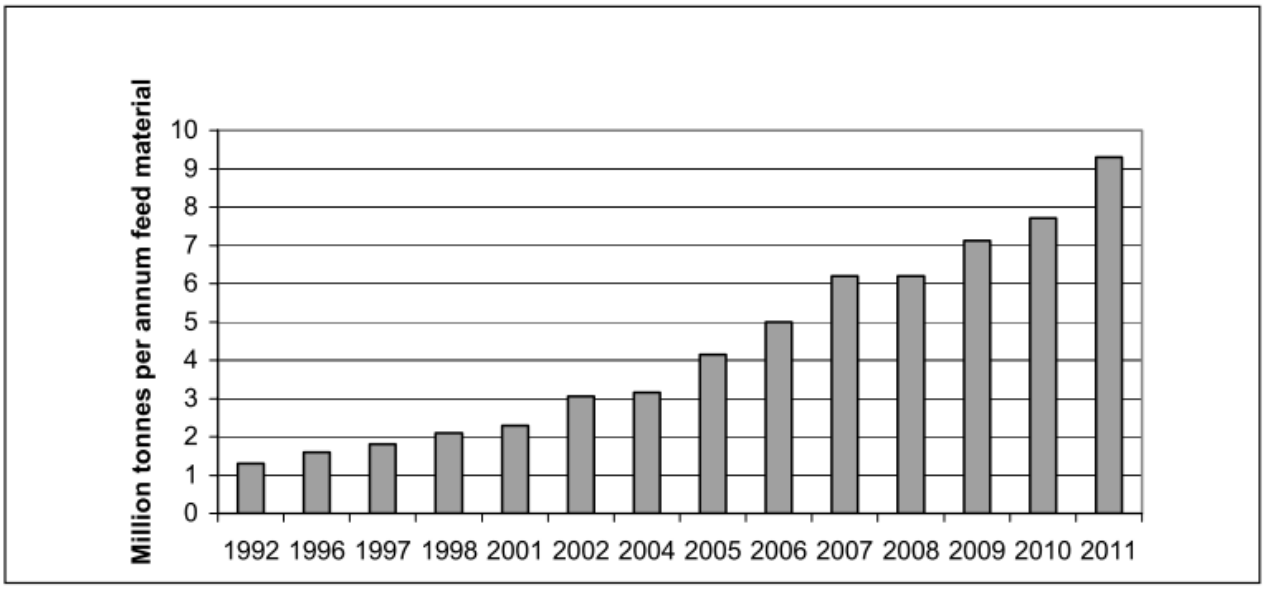

Figure 11.2. Copper ISASMELT™ capacity [394].

Production capacities of more than 330,000 tons per year of copper are being achieved through a single ISASMELT™ furnace with instantaneous feed rates reaching up to 200 t/h. Process development continues on the commercial scale plants at Mount Isa and elsewhere around the world.

It was in 1975 when Mount Isa Mines Limited (MIM) set its sights on a new development occurring at CSIRO in Australia: the Top Submerged Lance (TSL) technology, a new concept for smelting using the Sirosmelt lance. MIM joined forces with CSIRO and participated in lab scale trials of the technology. At that time, MIM was looking for new technologies that could be applied to its lead and copper smelter operations to reduce operating costs while improving the environmental performance. MIM's Mount Isa Lead Smelter used a sinter plant and blast furnace for lead bullion production, while the copper smelter used a fluid-bed roaster and two reverberatory furnaces to produce a copper matte. The matte was then converted to blister copper using Peirce-Smith converters. MIM was seeking alternative smelting processes that would produce off-gases with higher SO_2 content so that the smelter gases could be treated and sulfur captured in an acid plant. MIM also needed to find a process with lower operating costs to remain cost effective with the steady decline in real metal prices.

MIM, jointly with CSIRO, developed the concepts of the Lead ISASMELT™ and Copper ISASMELT™ processes. These were pilot tested on a 250 kg/h test rig in Mount Isa in the early

1980s. Over the years ISASMELT™ has progressed from a 250 kg/h pilot plant scale to industrial facilities that can run up to 200 t/h and treat a variety of materials including nickel, lead and copper concentrates and secondary materials.

During 30 years of developing and operating ISASMELT™ technology on large scale plants, significant technical improvements have occurred in areas such as furnace design, feed preparation systems, offgas handling, operating and process control strategies, refractory management, operator training and commissioning systems. The combination of experience led to the development of the "ISASMELT™ technology package" which is licensed to external clients today. Many of the improvements implemented by plant operators have been passed on to, and adopted by, other licensees. Exchange of ideas and technical improvements occurs through visits to fellow licensee sites and through regular licensee workshops arranged by XT at locations close to the ISASMELT™ installations.

11.1 The ISASMELT™ process

The ISASMELT™ furnace (Figure 11.3) is a vertical steel shell lined with chrome magnesite refractory bricks [396]. The furnace roof and tapping block are made from water-cooled continuous-cast copper cake.

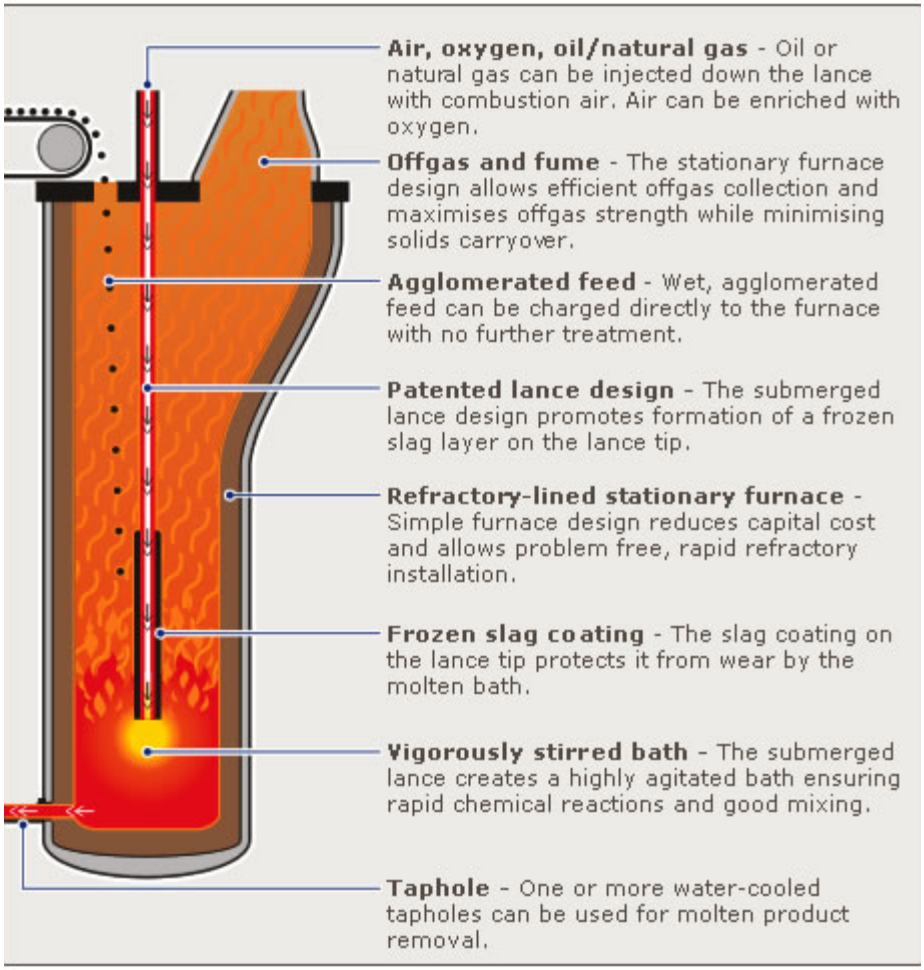

Figure 11.3. The ISASMELT™ concept.

11.1.1 Mount Isa Copper ISASMELT™ Plant

The typical operation conditions are given by Pritchard [396] for Mount Isa Copper ISASMELT™ Plant (built in 1992).

The lance is supported on a dedicated hoist system and can be raised completely clear of the furnace for shutdowns or lance change. It is then lowered through the lance port to its normal operating position below the surface of the bath. The lance position is continuously adjusted as the bath level rises because of extra feed or falls due to tapping, but remains constant under continuous tap conditions. An average lance life is about four days and damaged lances typically require the bottom one or two meters of steel to be replaced before being returned to service. Maintenance on damaged lances is normally carried out on the ground, in the horizontal position. Three or four lances are maintained on standby in a position hanging from the furnace support

structure. Air and oxygen are supplied to the lance from the plant's own centrifugal air-blower and dedicated 525 t/d oxygen plant, respectively.

Auxiliary oil fuel for the furnace is also added through the lance, to give fine control of temperature, and during process stoppages the furnace temperature is maintained by a standby oil-fired burner which is lowered through the feed port. At oxygen-enrichment levels greater than 50 per cent, no oil is used in the lance.

Mount Isa chalcopyrite concentrate is pumped as slurry from the concentrator to a storage thickener. The thickened concentrate is pumped to three hyperbaric (pressure) filters, which produce dried feed (8 wt.% H_2O), which is either stockpiled and reclaimed through the dry concentrate feed-tats or fed direct to the ISASMELT™ process pelletizer, where it is mixed with lump coal (fuel) and fluxes (silica and limestone). The pellet quality is not critical but if the pellets are too small then excessive fines carryover (more than 1 wt. %) can occur into the furnace gas off-take. The pellets are conveyed to the furnace feed floor and dropped down the feed port into the slag bath, which is highly agitated by the air/oxygen from the furnace lance. The furnace is operated at 1170°C and about 90% of the heat load is supplied by burning the concentrate sulfur at an oxygen-enrichment level of about 50 per cent. The balance of heat is supplied by coal which is mixed in the pellets, or a minimal oil-feed down the lance.

The molten bath is controlled at a matte grade of about 58 wt. % copper by adjusting the oxygen/concentrate ratio and flux addition, as required. Higher target matte grades (up to 65 wt. % copper) have been used to suit overall plant production. A typical operating variability is about ±1 wt. %.

The furnace products are tapped through a water-cooled copper block, along a launder into a rotary holding furnace (RHF). The preferred system is a continuous tap operation, but at times when launder repairs are carried out batch tapping is used because there is only one launder. It has been demonstrated that operation of the RHF is easier and gives lower copper losses with continuous tapping because this gives the highest mean settling time.

The RHF is similar in design to a rotary anode furnace, with slag and matte being skimmed on opposite sides. The furnace is heated with oil and oxygen-enriched air. Slag is skimmed from the RHF at a copper grade of 0.5 to 0.8 wt. % into a hot-water slag granulating system. Granulated slag is used for underground mine wet-fill production at Mount Isa. Matte is tapped as

required for the three (two hot) Peirce-Smith converters. The slag granulation system operates with water at about 90°C. The attraction of hot water is the elimination of the need for a cooling-tower/cooling-pond system.

The use of the Rotary Holding Furnace technology to hold, settle and separate copper matte and slag generated in the ISASMELT™ furnace has a number of advantages:

- No electrical energy required: The matte and slag are physically separated in the furnace without the need of electrical energy for reduction. RHF's have been applied for copper matte grades up to about 65% Cu.
- Low copper in slag can be achieved: The slag is slow poured via an automated system to minimize matte carryover to the slag.
- Avoids back-contamination of the matte with minor elements already deported to the slag phase: By avoiding reduction of the slag, the minor element distribution between the slag, matte and gas phase remains unchanged.
- Ability to provide matte to the Peirce-Smith Converters in a very short period of time: By tilting the furnace and pouring through the matte spout a 30 tons matte ladle can be filled in one minute.
- Provision of a surge capacity between the smelting and converting processes.

The off-gas leaving the ISASMELT™ furnace is cooled in an Ahlstrom flux-flow waste-heat boiler. This is designed to quench the off-gas/fume rapidly to about 450°C to minimize SO_3 production and pass through the temperature range where sticky accretion is formed. The particles from the fluid bed actually help to keep the tubes clean. Other attractive features of the boiler are its ease of start-up, low capital cost, and low manpower requirement, which does not require a fully dedicated operator. The flux-flow system comprises three main sections: the mixing chamber, the heat exchanger, and the cyclones. The general arrangement is a typical circulating fluid-bed (CFB) in which the mixing chamber acts as the bottom section of the CFB fluidized by the furnace off-gas. The heat exchanger is a vertical riser containing the boiler tubes, and the cooled gas is de-dusted in cyclones, which return the bed material to the mixing chamber. Most of the solid carryover from the ISASMELT™ is captured with the bed.

Cooled gas from the boiler is further quenched to 150°C in a water-spray gas cooler, and then residual fume is cleaned in an electrostatic precipitator (ESP). The draught at the top of the furnace is controlled at 80 Pa gauge by variable inlet dampers on the induced draught fan at the outlet of the ESP.

The ISASMELT™ furnace is highly instrumented, and controlled through a distributed control system (DCS) from a central control room on the feed floor. The plant is operated by a shift crew of seven: a foreman, control-room operator, feed-preparation operator, tapper, RHF operator, and two general hands.

Matte grade and slag chemistry are monitored by taking a mixed matte and slag sample from the launder at each tap, and allowing the phases to settle out, before sending to the laboratory for XRF assay. Adjustments for matte grade control are normally made only after two or more off-target results, to eliminate possible sampling errors.

In each of the three copper furnaces (Demonstration, CIP, and Cyprus) the ISASMELT™ process has been demonstrated to show a number of major advantages over other copper-smelting processes. The relatively small furnace size means that the capital and operating costs are low, and the small footprint makes it very easy to retrofit an ISASMELT™ into an existing operation without disrupting ongoing production. Yet another bonus from the small size is the relative ease of fume containment, in plant hygiene and environmental control. The high potential for oxygen enrichment of the process air leads to a high sulfur dioxide gas strength suitable for acid production, and the potential for autogenous operation.

The process is very tolerant to variations in feed size and composition and the ability to consume reverts can reduce the load on the converters. Use of pelletized feed reduces solid carryover into the gas stream to about one per cent, and the excellent control of slag chemistry which results from the vigorous mixing means that matte and slag rapidly separate out to leave a discardable slag containing only 0.5 to 0.8 per cent copper.

11.1.2 Southern Peru Ilo Smelter

It was in early 2003, when Southern Peru Copper Corporation (SPCC) was in the process of selecting a new technology that would meet their requirements while keeping capital and operating costs low, when Xtrata Technologies (XT) offered ISASMELT™ as an option for the

modernization of the smelter. At that time, SPCC was facing the challenge of modernizing its installations in order to comply with new environmental regulations defined by the Peruvian government in terms of sulfur capture and particulate material emissions during a period of historically low copper prices. The ISASMELT™ technology package is an integrated assortment of technological research and development, specialist process and mechanical design, proprietary equipment, know-how, training programs, commissioning assistance and on-going technical support and collaboration that combine to ensure successful smelter projects for XT's licensees. The technology transfer includes an arrangement for training operators from new licensees – they learn by operating the full scale production smelter at Mt Isa. After technical and economic evaluation of the conceptual study completed by XT and Fluor, SPCC decided to select the ISASMELT™ and RHF technology package for the modernization of the Ilo smelter in the middle of 2003. SPCC have stated that key criteria for selecting ISASMELT™ were the fact that the ISASMELT™ technology was proven for the planned capacity (1,200,000 tons per year through a single furnace) and the lower capital and operating cost of the ISASMELT™ technology compared with the other competing technologies [397]. Figure 11.4 and Figure 11.5 show flow diagram of Ilo smelter before and after modernization accordingly. Figure 11.6 shows the installation of the ISASMELT™ furnace and Figure 11.7 – installation of RHFs.

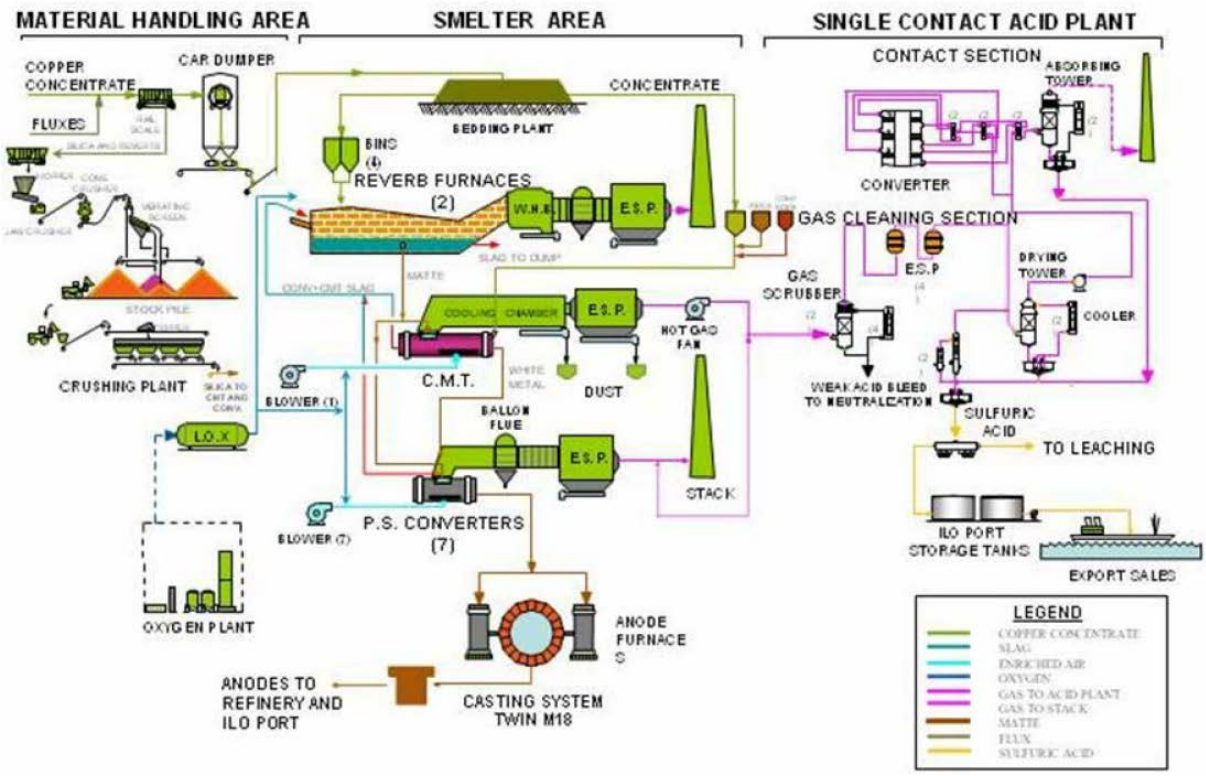

Figure 11.4. ILO smelter – original process flow diagram (before modernization) [398].

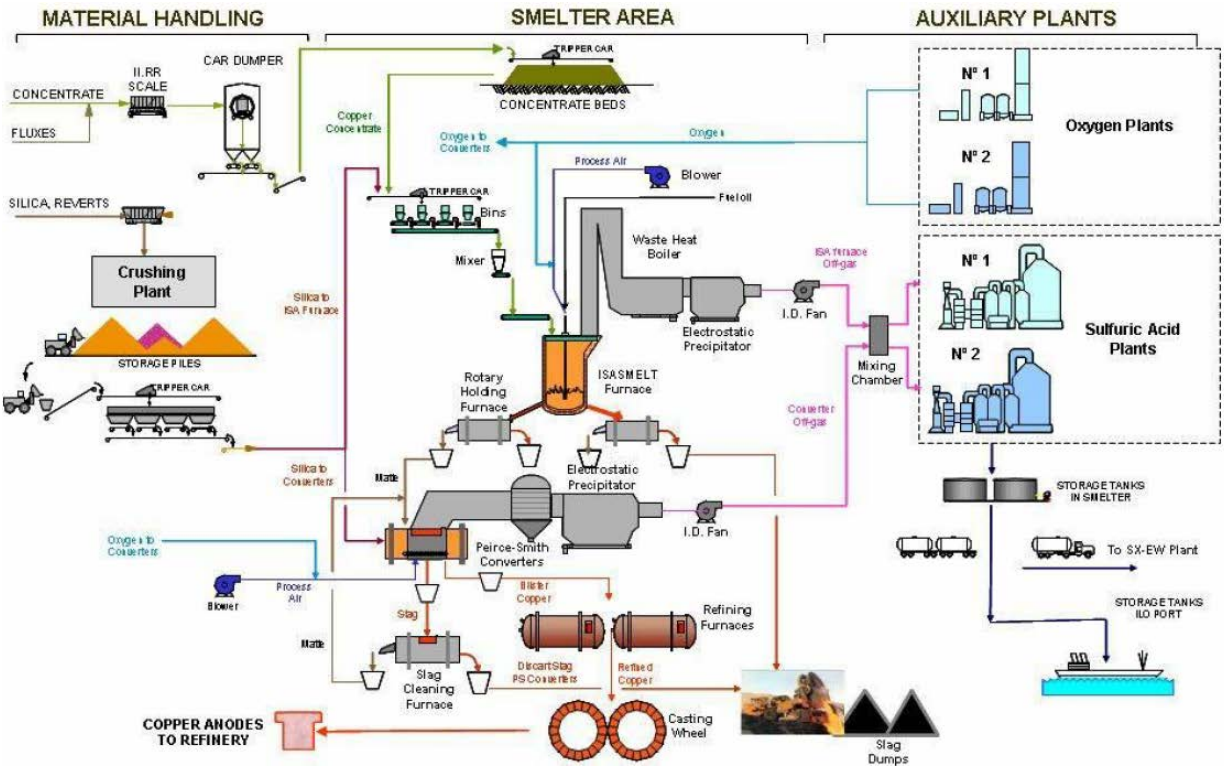

Figure 11.5. Flow diagram of modernized Ilo smelter [398]

Figure 11.6. The ISASMELT™ furnace installation at Ilo copper smelter [398].

Figure 11.7. Rotary holding furnaces at Ilo copper smelter [398].

The Ilo ISASMELT™ plant is similar to the described above Mount Isa Copper ISASMELT™ Plant. The main control variables are: SiO_2/Fe and SiO_2/CaO ratios in slag, matte grade and bath temperature. They were fixed by practical experience and considerations of productivity, brick wear and copper loss to slag, by this way:

Matte Grade

The target (61 - 62% Cu) was fixed in order to ensure that the PS Converters can treat all the matte produced by the ISASMELTTM furnace. Matte grade is controlled by adjusting oxygen addition that enters by the lance, considering matte sample assays.

SiO_2/Fe and SiO_2/CaO Ratios in Slag

The SiO_2/Fe ratio should be maintained at 0.80 – 0.82, in order to help the slag - matte phase's separation and obtain a proper slag mass and slag viscosity. On the other hand sea shell is added in the feed to further drop the melting point of slag, the SiO_2/CaO ratio is set around 7.5. These ratios are controlled adjusting the silica and sea shell fluxes additions, considering RHF slag samples assays. In order to get a proper feedback, the RHF slag and the ISASMELT^{TM} matte samples are processed promptly by the on-site x-ray facilities. The chemical assays are provided to the control room operator in less than 25 minutes.

Magnetite Content in Slag

When the slag sample is cooled, magnetite precipitates out, and this is the magnetite content which is measured in the slag samples with a *Satmagan* instrument. *Satmagan* is a magnetic balance in which the sample is weighed in gravitational and magnetic fields. If the field is strong enough to saturate the magnetic material in the sample, the ratio of the two weighings are proportionally linear to the amount of magnetic material in the sample. These magnetite analyses using cooled solid samples have the problem that the amount of precipitated magnetite crystals varies with the cooling rate of the melt. The slower cooling rate of the sample, the more magnetite content is measured, and this cooling rate depends on the slag sampling method.

Copper loss to slag is to be discussed further. The typical rate of brick wear in the Ilo smelter is shown in Figure 11.8.

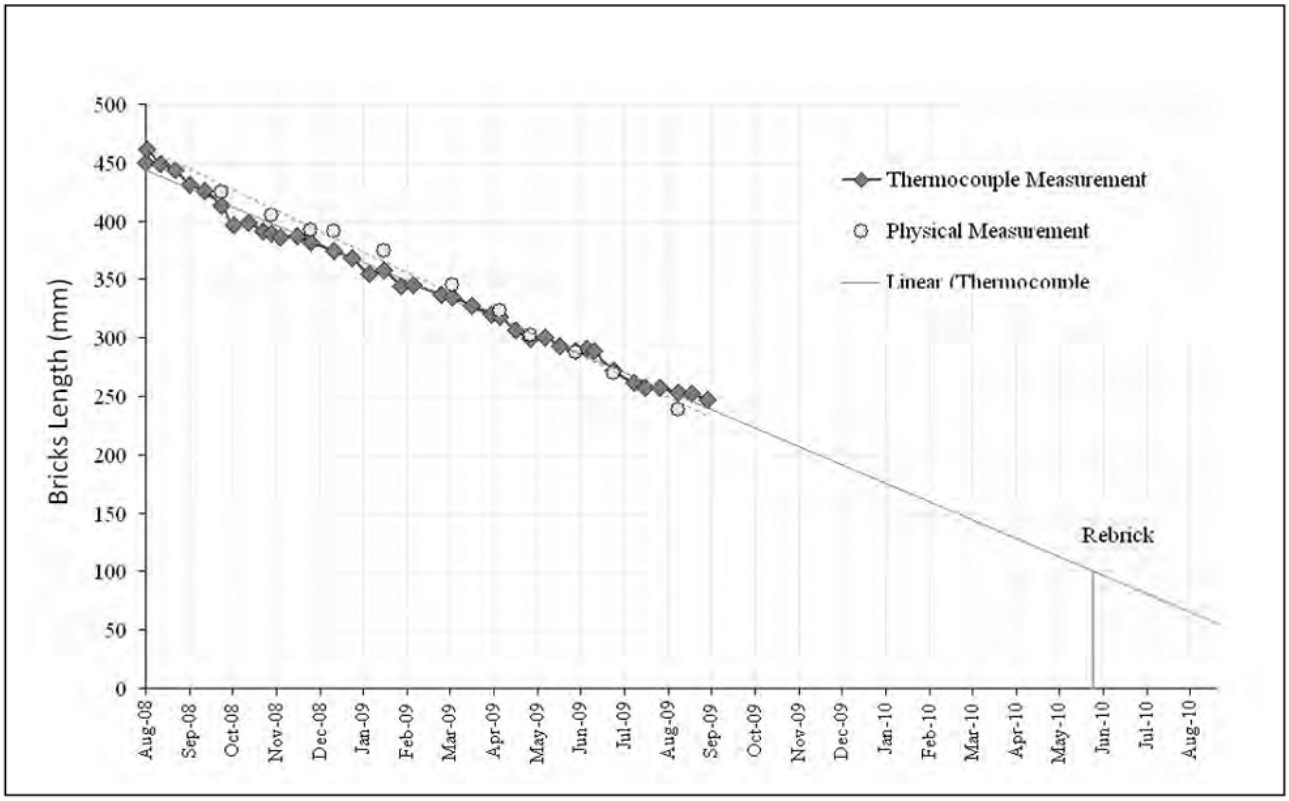

Figure 11.8. ISASMELT™ furnace refractory wear in Ilo smelter [399].

11.1.3 Smelting mechanism

When chalcopyrite ($CuFeS_2$) is heated above 1000 K, as in a wet-charge **reverberatory furnace** smelting, elemental sulfur is liberated according to the decomposition reaction [2]:

$$2CuFeS_2 \rightarrow Cu_2S\ (\text{matte}) + 2FeS\ (\text{matte}) + 0.5S_2 \qquad (11.1)$$

The liberated excess S is oxidized by air outside of the molten baths, and therefore, the partial pressure of SO_2 in the reverberatory furnace atmosphere is not in equilibrium with matte or with slag. In contrast, all the **modern matte smelting** processes aim at a rapid oxidation of chalcopyrite with oxygen-enriched air to produce a high-grade matte by utilizing the excess S as fuel. The simplified smelting reaction may be expressed as

$$\underset{\text{(solid)}}{2CuFeS_2} + \underset{\text{(gas)}}{(1+1.5x)O_2} + \underset{\text{(solid)}}{xSiO_2} \xrightarrow{Fe^{2+} \leftrightarrow Fe^{3+}\text{ in slag}} \underset{\text{(liquid matte)}}{Cu_2S \cdot (FeS)_{2-x}} + \underset{\text{(liquid slag)}}{xFeO \cdot SiO_2} + (1+x)SO_2 \qquad (11.2)$$

where Cu_2S and FeS form matte, and FeO is neutralized with SiO_2 flux to form fayalite slag. Because matte, slag, and gas are produced instantaneously and simultaneously at the oxidizing

reaction site, all three phases are considered to be in equilibrium, where the partial pressure of SO_2 participates fully in matte-slag reactions. In other words, the modern copper smelting is governed by the matte-slag-gas equilibrium, while the reverberatory smelting is governed by the slag-matte equilibrium.

The Copper ISASMELT™ process is a slag reaction process, where fresh feed is digested into the molten slag phase. It is in this phase where the main chemical reactions occur and oxidation of the feed takes place.

The oxygen transfer process is achieved [394] through the controlled oxidation of FeO in slag and subsequent formation of Fe^{3+}. It is the "liquid oxygen" in the form of Fe^{3+} ions in slag that reacts with the concentrate and fluxes to form copper matte, a fayalite slag and SO_2 gas.

Nagamori [2] suggested the Two-Site model for the reaction of coke added to a feed in the ISASMELT™ process. When coal consisting of fine and coarse particles is charged in the furnace, the volatile and fine coal grains burn to help raise the oxidizing reaction temperature for chalcopyrite. The fixed carbon in coarse coal grains survives through the oxidizing reaction to serve later as a reductant for magnetite and copper oxide. The problem of magnetite can become acute when the furnace slag is subsequently treated by settling in an electric or rotary furnace, where not only suspended matte but also solid magnetite may precipitate out. Because the building up of magnetite on the bottom of a settling furnace is a slow process that takes several days, no quick-reducing reaction is needed to prevent the unwanted magnetite precipitation. A gaseous reductant should not be used for reducing magnetite, because such a gas would diffuse freely to the oxidation site where it competes with chalcopyrite for oxygen, thus causing a slower oxidation of chalcopyrite and a corresponding deterioration in furnace throughput. The reaction of solid carbon with slag is slow, yet in practice it can be just fast enough to reduce magnetite, thereby preventing its precipitation. Player [400] reported that the layer of uncombusted coal char was observed on the slag surface at high coal feed rates. He used the data from the Mount Isa copper plant.

11.2 Modeling

11.2.1 Thermodynamic database

The FactSage thermochemical software and databases [4] were used to calculate chemical and phase equilibria for the simulation. The most important phases are slag, matte, gas, spinel, and solid SiO_2. Blister copper is not formed under the conditions of an ISASMELT™ furnace (1150-1200°C, $P(O_2) = 10^{-9}$-10^{-8} atm). The elements found by assays are Al–Cu–Ca–Fe–Mg–Si–O–S–C–(–Pb–Zn–As–Co–Bi–Sb–Au–Ag–Ni–Cd–…) [400], where the elements in brackets are minor elements.

The slag solution was modeled by the Modified Quasichemical Model, MQM [401, 402]. The develpement of the Al–Ca–Cu–Fe–Mg–O–S–Si slag database was reported in this study. The Matte p was modeled by MQM and optimized for the Cu–Fe–O–S system in this study.

The spinel phase was evaluated and optimized in this study for the Al–Ca–Cu–Fe–Mg–O system. The Compound Energy Formalism was used as a model.

Gaseous species and solid SiO_2 from the FactPS (formely FACT53) database [4] were used. Carbon is present in the gaseous species formed by oxidizing of coke, but the solubility of carbon in condensed phases was ignored.

Thus, the Al–C–Cu–Ca–Fe–Mg–Si–O–S system was considered in the present simulation.

11.2.2 Equilibrium approximation

The smelting mechanism is described in a Chapter 11.1.3. The following approximations are used to model the processes in the ISASMELT™ furnace and rotary holding furnaces:

i. **Furnace operates under equilibrium conditions.** It means that all material input fully reacts in one stage. The only adjustable parameter here is the *oxygen utilization*. This parameter shows the portion of input oxygen participating in the chemical reaction. Non-reacted oxygen participates only in heat exchange. The matte grade (wt.% Cu in matte) is used to find the amount of reacted oxygen. If the rate of blow and ingress air is known, oxygen from ingress air is replaced by nitrogen in chemical equilibrium calculations until the correct matte grade is obtained. In this case, nitrogen

does not participate in chemical reactions but still participates in the heat balance and creates a volume necessary for volatile elements to be eliminated. There is a small error in the caclulations due to the difference in C_p between O_2 and N_2

ii. **Every feed flow is equilibrated.** In order to calculate the heat balance, the equilibrium state of input and output flows must be known. The temperature and phase composition of input and output streams should be explicitly set. In this case, the amount of energy required to heat the feed from the initial temperature to the reaction temperature is estimated correctly. The feed analysis is usually given in a form of assays, the bulk composition is known rather than the phase and chemical composition. A reasonable guess was made for the possible phases of input materials and their compositions were calculated. The material balance is not affected by the phase selection in feed flows.

iii. **No reactions occur in rotary holding furnaces.** Even though unreacted carbon is reported by Player (see Chapter 11.1.3) or pig iron is added as a reductant, the content is not mixed. It is possible for reactions to take place on the surface, but the action of reducing agents is compensated by the ingress air trapped while refilling the furnace. The dominant RHF process which must be taken into account is the physical entrainment of matte in slag. It will be shown further that the trapped matte significantly increases copper losses. The *percentage of matte trapped in slag* is the second parameter used in this study. In case some spinel phase was formed, it would be considered entirely trapped by slag.

11.2.3 Operating FactSage streams

To automatize the calculations, the Excel-FactSage-Matlab bundle has been created (Figure 11.9).

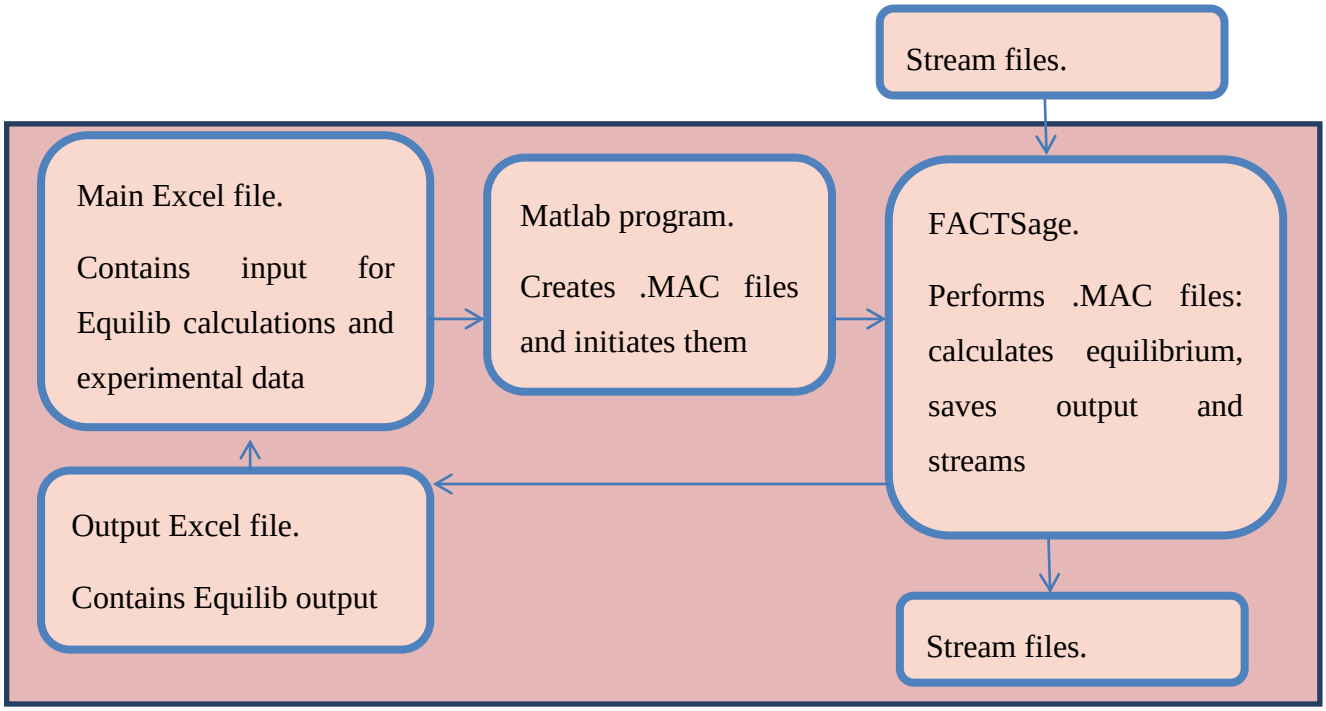

Figure 11.9. The Excel-FactSage-Matlab bundle.

The chemical essays of input flows along with their masses and temperatures are stored in the *Main Excel file*. The *Matlab program* reads this information and creates the .MAC file with the instructions for FactSage. Then the *Matlab program* initiates the .MAC file and EquiSage.exe follows the instructions written there. FactSage opens the Equi*.dat file[3], sets the masses of components and final temperature according to the information written in the *Main Excel file* and calculates the equilibrium. It saves the output streams and exports results to the .xls-output file. The *Main Excel file* is related with the *Output Excel file* so that the calculated data are refreshed. It is easy to manipulate the calculated data and compare it with the experimental assays. The *Stream files* created in this cycle are to be used in the next step. A complex sequence of equilibrated steps, including stream loops, may be created using the described technique.

[3] The Equi*.dat file should be created in advance; the database, phase selection and .xls output data selection are set by the user.

11.3 Discussion

The simulation model consists of the thermodynamic database and the equilibrium approximation described in Chapters 11.2.1 and 11.2.2. To verify the validity of the model the experimental data of Player [400] from the Mount Isa Copper ISASMELT™ Plant were used. The furnace input consisted of 6 flows: concentrate, flux, reverts, coke, blow and ingress air. The bulk composition and flow rates used for simulation are shown in Table 11-1 through Table 11-3.

Table 11-1. Concentrate, Flux and Reverts flows for simulation of the Player [400] results.

	Concentrate		Flux		Reverts	
Weight %	Used	Assay	Used	Assay	Used	Assay
Cu	29.1	27.3	0.5	0.5	38.3	37.4
Fe	28.4	26.7	0.7	0.7	20.6	20.1
S	28.8	27.1	0.2	0.2	7.8	7.6
SiO_2	10.0	9.4	94.0	91.8	11.2	10.9
CaO	0.6	0.6	0.6	0.6	7.5	7.3
Al_2O_3	0.9	0.8	3.6	3.5	0.9	0.9
MgO	1.2	1.1	0.2	0.2	0.6	0.6
Fe_3O_4	0.3	0.3	0.2	0.2	13.2	12.9
PbS	0.2	n/a	0.0	n/a	0.0	n/a
ZnS	0.2	n/a	0.0	n/a	0.0	n/a
NiS	0.2	n/a	0.0	n/a	0.0	n/a
Co_3S_4	0.1	n/a	0.0	n/a	0.0	n/a
Total	100.0	93.3	100.0	97.7	100.0	97.7
T, °C	25.0	n/a	25.0	n/a	25.0	n/a
Mass flow, t/hr.	79.4	79.4	2.7	2.7	9.8	9.8

Table 11-2. Coke flow for simulation of the Player [400] results

Coke		Volatile	Ash
		85.30%	14.70%
Weight%	Used	Assay[1]	Assay[2]
C	74.3	87.1	n/a
H	4.3	5.0	n/a
N	1.7	2.0	n/a
S	1.4	1.6	n/a
O	3.7	4.3	n/a
SiO_2	9.1	n/a	62.0
CaO	0.4	n/a	3.0
Al_2O_3	3.8	n/a	26.0
MgO	0.0	n/a	0.0
Fe_3O_4	1.3	n/a	9.0
Total	100.0	100.0	100.0
T, °C	25.0	n/a	
Mass flow, t/hr.	3.6	3.6	

Table 11-3. Blow and Ingress air* flow for simulation of the Player [400] results

	Ingress air		Blow	
Weight %	Used	Plant data	Used	Plant data
N_2	100%-X	80.2	53.8	53.8
O_2	X	18.8	46.2	46.2
T, °C	25.0	n/a	25.0	n/a
Mass flow, t/hr.	27.0	27.0	52.5	52.5

* - air is considered to be dry, total moisture intake is given in Table 11-4.

Table 11-4. Moisture flow for simulation of the Player [400] results

Moisture		
Weight%	Used	Plant data
H_2O	100	n/a
T, °C	25	n/a
Mass flow, t/hr.	10.38	10.38

It is evident from the tables that assays are not complete (Total < 100%). Moreover, no information is available about the analytical methods used to determine the composition. Compositions of concentrate, flux and reverts were normalized to 100% basis.

Table 11-5. Equilibrium simulation results.

Process parameters:			
X, fraction reacted O_2 from ingress air	0.063	Total oxygen utilization, % (from blow and ingress air)	87.68%
Y, Matte entrained in slag	0.70%		
Equilibrium calculation results			
Temperature, °C	1180		
$Log_{10}[P(O_2)$, atm]	-8.74	$Log_{10}[P(S_2)$, atm]	-2.51
$Log_{10}[P(SO_2)$, atm]	-0.94		
a(Spinel)	1.00	$a(SiO_2)$	0.58
Energy balance, MW	-2.64		

Table 11-6. Material balance: simulation results and plant assays [400].

Slag (+ entrained matte, spinel)	Simulated, wt%	Assay, wt%	Matte	Simulated, wt%	Assay, wt%
Cu	1.0	1.0	Cu	59.3	59.3
Fe	46.3	41.2	Fe	15.6	15.3
Including "Fe_3O_4"*	15.1	10.6	Including "Fe_3O_4"**	2.1	2.4
SiO_2	29.7	30.8	S	23.9	21.8
CaO	3.2	4.8	SiO_2	0.0	0.2
Al_2O_3	2.5	2.8	CaO	0.0	0.0
MgO	2.5	2.5	Al_2O_3	0.0	0.0
S	0.5	0.7	MgO	0.0	0.05
Mass flow, t/hr.	40.6	40.2	Mass flow, t/hr.	44.5	42.4
Gas output	Simulated	Assay			
Mass flow, t/hr.	101.01	104.95			

* All Fe^{3+} in slag accounted for as "Fe_3O_4"

** All oxygen in matte accounted for as "Fe_3O_4"

The results of the simulation are compared with the plant data in Table 11-5 and Table 11-6. The parameter X – effective wt. % of O_2 in ingress air was found to be 0.063. This is equal to

87.68% of all oxygen participated in the reaction. Under these conditions the simulated matte grade is equal to the observed one and energy the balance is described. The heat losses to the environment are calculated to be 2.64 MW. Calculation shows that if the heat loss could be prevented, the adiabatic temperature of the furnace would be 1215 °C. It must be noted that calculated equilibrium $P(O_2)$ does not necessarily correspond to $P(O_2)$ in the output gas, since output gas should carry out the unreacted oxygen from ingress air.

The microstructure of the quenched slag from the Ilo smelter was obtained by the Pyrosearch Center and presented in Figure 11.10. The copper content of matte equilibrated with the slag in the picture is not reported, however it is known that Ilo smelter operates at 61±2 wt.% Cu in matte. Thus the equilibrium $P(O_2)$ should be higher. The iron oxide in Figure 11.10 is most likely the spinel phase present in slag before quenching. Slag also contains droplets of matte, which confirms our model approximation of physical entrainment of matte and spinel in slag. The Cu_2O content in slag measured by an electron probe X-ray microanalyser was found to be □ 0.3 wt.% compared to the bulk 2 wt.%. In the current simulation it is 0.55 and 1.0 respectively.

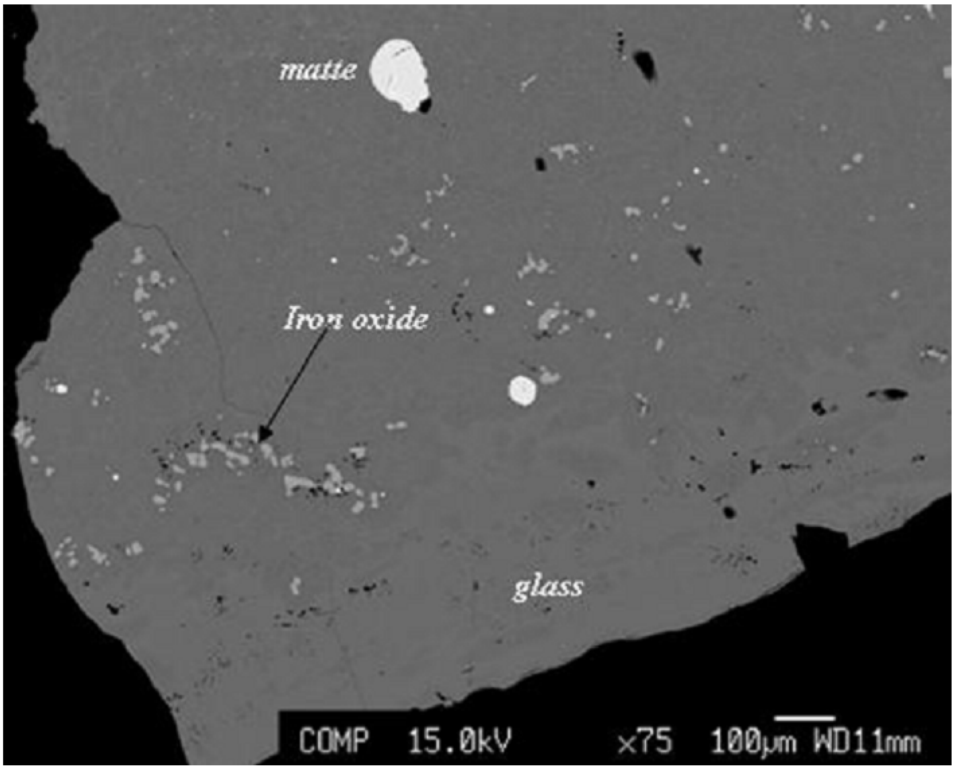

Figure 11.10. Microstructure of the Southern Peru Ilo Smelter slag from rotary holding furnace.

The mass of slag after RHF is increased compared to mass of slag after smelting due to physical entrainment of spinel and matte in slag. The bulk Cu content of slag was the target function to find the entrainment parameter Y. 0.70% of matte was found to be trapped in slag (0.31 t/hr. of matte is trapped in 40.59 t/hr. of slag). Figure 11.11 shows the presence of matte (the white substance) in the discarded slag.

Figure 11.11. Presence of matte in the RHF slag dam site.

To compare slag and matte compositions, the FACTSage output was re-calculated to the assay format used by Player [400]: Cu–Fe–SiO_2–CaO–Al_2O_3–MgO–S and "Fe_3O_4". In was assumed that in slag, all Fe_2O_3 and Fe_2S_3 end-members formed "Fe_3O_4", and in matte all oxygen was bound as "Fe_3O_4". This rough approximation is based on the assumption that the magnetite content found by a magnetic balance depends only on the Fe^{3+} content in slag. In reality, it depends on many factors including the rate of slag cooling. In the simulation, Ca, Mg and Al almost entirely stayed in slag, so the smaller contents of these elements in slag compared to assays is considered to be an error in the input and output assays.

The seemingly higher simulated mass flow of matte and the lower flow of gas may arise from the dust carryover, which was not accounted for by the model. The overall mass balance reported by Player [400] does not sum up exacltly as well: 185.40 t/h input and 188.76 t/h output, though this level of agreement is very good for industrial assays.

The largest inconsistency between the simulation and the assay data reported by Player [400] concerns the SiO_2/Fe ratio in slag (with entrained spinel and matte). The calculated value is 0.64 while the reported one is 0.75. The total iron input (concentrate, reverts, flux and coke) as reported by Player [400] was 25.8 t/h, but the total output (slag, matte) was 22.9. The balance for SiO_2 was 11.9 t/h (input) and 12.4 t/h (output). The difference between the calculated and reported SiO_2/Fe ratio in slag may be explained by the inconsistencies in the plant assay data. On this example, it is demonstrated how the thermodynamic modeling can help in the evaluation of the plant assay data. As the SiO_2/Fe ratio in the output slag is easier to measure, than amounts and compositions of all input streams, it likely that slag assay was correct. To reproduce the plant assay results using model calculation, more reliable information on inputs is required.

11.4 Summary of results

The ISASMELT™ technology is a relatively new, but an already established method of copper smelting. The furnace operates close to the equilibrium conditions. It has been shown in this work that the process may be thermodynamically modeled with only two parameters – the utilization of oxygen and the amount of matte physically entrained in slag. The calculations are performed using the FactSage thermodynamic software and databases. The modeling has demonstrated that some copper losses are due to physical entrainment of matte in slag rather due to the equilibrium solubility of Cu in slag. This fact agrees with the experimental observations.

GENERAL DISCUSSIONS AND CONCLUSIONS

A thermodynamic database for copper smelting and converting was developed. It includes all the important phases in the Al–Ca–Cu–Fe–Mg–O–S–Si chemical system. The solid sulfide, oxide and metal phases are consistent with each other, liquid slag, liquid matte/metal and the gas phase. The suggested thermodynamic models for the slag, matte and spinel are based on the structures of the corresponding phases.

The newly optimized model parameters for phases have been incorporated into the FactSage databases.

The phases, which were extended, and the chemical systems evaluated and optimized in the present study are summarized below.

Phases :

Liquid matte/metal : $\left(Cu^{I},\ Cu^{II},\ Fe^{II},\ Fe^{III},\ O,\ S\right)$

Liquid slag : $\left(Al^{3+}, Ca^{2+}, Cu^{1+},\ Fe^{2+},\ Fe^{3+},\ Mg^{2+}, Si^{4+}\right)\left(O^{2-},\ S^{2-}\right)$

Spinel : $(Al^{+3},Cu^{+2},Fe^{+2},Fe^{+3}, Mg^{+2})^{tetr}[Al^{+3},Ca^{+2},Cu^{+2},Fe^{+2},Fe^{+3},Mg^{+2},Va]_2^{oct}O_4^{-2}$

Monoxide : ($AlO_{1.5}$, CaO, CuO, FeO, $FeO_{1.5}$, MgO)

Stoichiometric compounds : $CuSO_4$, Cu_2SO_4, (CuO)($CuSO_4$), $CuFeO_2$, $FeSO_4$, $Fe_2(SO_4)_3$, $CaFe_2O_4$, $Ca_2Fe_2O_5$, $CaFe_3O_5$, $CaFe_4O_7$, $CaFe_5O_7$, $Ca_4Fe_9O_{17}$, $Ca_4Fe_{17}O_{29}$, $CuAlO_2$.

Limitations:

Liquid matte/metal and liquid slag are modeled using two separate solutions. The mutual solubility of these liquids under the conditions of pyrometallurgical copper production is well described by the model. However, under certain conditions, which are rather far from industrial, the miscibility gap between these liquids may completely disappear. This is shown on the example of the Fe–O–S–Si system (Section 9.1) and the Ca–Cu–Fe–O–S system (Section 10.3). The model suggested in this study is not able to reproduce the disappearance of the miscibility gap between matte and slag.

The solubilities of Al, Ca, Mg and Si in the liquid matte/metal phase are ignored, which is a very good approximation. These solubilities may become important under the conditions, which again far from those during copper smelting and converting (Section 10.3).

The formation of SO_4^{2-} anions in slag and matte phases is not modeled. This can be important in the processes where both $P(O_2)$ and $P(S_2)$ are very high. Even though this is not the case in the copper processing, such conditions may exist during special glass treatments.

Liquid matte/metal and slag databases have a common subsystem, which is Cu–Fe–O. If the concentrations of Al, Ca, Si, Mg and S are very low, the Gibbs energy functions of these two databases become close, which may cause confusion in the Gibbs energy minimization procedure. Thus, certain caution is required when analyzing the results of such calculations. In Al-, Ca-, Si-, Mg-free systems it is possible to prevent this problem by selecting only liquid matte/metal database in the calculation.

In the spinel phase, copper may exist in at least two oxidation states, Cu^{+1} and Cu^{+2}. Unfortunately, no reliable experimental data exist on the Cu^{+1}/Cu^{2+} ratio in spinels. In the present study, only Cu^{2+} was introduced into the model for spinel, however, the effect of Cu^{+1} on the thermodynamic properties was taken into account indirectly, by introducing the excess Gibbs energy of mixing.

Systems:

(1) Cu–O–S system (Chapter 4)

A complete critical evaluation and optimization of the Cu–O and Cu–O–S systems has been performed. A model for the liquid phase has been developed within the framework of the quasichemical formalism. This model describes simultaneously metallic liquid, sulfide liquid (matte) and oxide liquid. For the Cu–O system, the model reflects the existence of two ranges of maximum short-range ordering at approximately the Cu_2O and CuO compositions. All available thermodynamic and phase equilibrium data have been critically evaluated to obtain one set of optimized model parameters for the Gibbs energies of all phases that can reproduce the experimental data within experimental error limits.

(2) Fe–O–S system (Chapter 5)

A complete critical evaluation and optimization of the Fe–O and Fe–O–S systems have been performed. A model for the liquid phase has been developed within the framework of the quasichemical formalism. This model describes simultaneously metallic liquid, sulfide liquid (matte) and oxide liquid. For the Fe–O system, the model reflects the existence of two ranges of maximum short-range ordering at approximately the FeO and Fe_2O_3 compositions. All available thermodynamic and phase equilibrium data have been critically evaluated to obtain one set of optimized model parameters for the Gibbs energies of all phases that can reproduce a majority of the experimental data within experimental error limits. The Fe–S–O miscibility gap between metallic and oxysulfide phases at high temperatures is described semi-quantitatively.

(3) Cu–Fe–O system (Chapter 6)

A complete critical evaluation of all available phase diagram and thermodynamic data for the Cu–Fe–O system at a total pressure of 1 atm has been made, and parameters of thermodynamic models have been optimized to reproduce all experimental data within experimental error limits.

A model for the liquid phase has been developed within the framework of the Quasichemical Formalism. It is applicable over the whole composition range from metallic to oxide liquid. The model for spinel has been developed within the framework of the Compound Energy Formalism. The formation of Cu^{+1} by electron hopping due to the reaction $Cu^{+2} + Fe^{+2} \rightarrow Cu^{+1} + Fe^{+3}$ was taken into account indirectly by introducing an excess model parameter.

(4) Cu–Fe–O–S system (Chapter 7)

The thermodynamic database, combined from the earlier obtained Cu–O–S, Fe–O–S, Cu–Fe–O and Cu–Fe–S databases, proved to be capable of predicting chemical and phase equilibria in the Cu–Fe–O–S system. The ternary parameter $q^{001}_{Fe^{III}Cu^{I}(S)}$ was optimized to describe better the experimental data in the Cu–Fe–O–S system. This parameter could not be obtained from the data in ternary Cu–Fe–S system and have no influence on it.

(5) Ca–Fe–O, Ca–Cu–Fe–O, Al–Cu–O, Al–Cu–Fe–O, Al–Ca–Fe–O, Ca–Fe–Mg–O systems (Chapter 8)

The spinel solution was extended by the addition of Ca and Cu. In the model, Ca^{+2} cations occupy only the octahedral sublattice, while Cu^{+2} cations occupy both the tetrahedral and octahedral sublattices. The spinel database was combined with previously optimized solid and liquid phases in the system. The calculations were made using the combined database and compared with available experimental data. A very good agreement was demonstrated.

(6) Fe–O–S–Si and Cu–Fe–O–S–Si systems (Chapter 9)

A complete critical evaluation of all available phase diagram and thermodynamic data for the Fe–O–S–Si and Cu–Fe–O–S–Si systems at a total pressure of 1 atm has been made. A model for the slag phase has been developed within the framework of the Quasichemical Formalism in the quadruplet approximation. The slag database was combined with the previously obtained databases for solid and liquid phases in the system and used to predict the slag – matte equilibria at conditions close to the pyrometallurgical production of copper. A very good agreement with the experimental data was obtained, particularly in the solubility of copper in the slag phase. This is of primary importance for the copper industry, which tries to prevent copper losses to slag.

(7) Ca–Fe–O–S, Ca–O–S–Si, Ca–Cu–Fe–O–S–Si systems (Chapter 10)

The effect of calcium on the solubility of copper and sulfur in slag is evaluated. Model parameters are optimized to describe quantitatively the solubility of sulfur and copper during the slag–matte–metal equilibrium and sulfide capacities in Cu-free slags.

Application of the database is illustrated in Chapter 11. The Isasmelt^{TM} copper smelting process is simulated, using only two process parameters. The calculated energy and material balance, as well as the distribution of elements between outputs of the smelting furnace, are in good agreement with the plant data.

Further development of the thermodynamic database presented in this study will include the addition of Ni, Co, Pb and Zn, which are minor but important elements during the pyrometallurgical copper extraction. The resulting database for the Al–Ca–Co–Cu–Fe–Mg–Ni–O–Pb–S–Si–Zn chemical system will be also applicable for the simulation of nickel, lead and zinc production processes. Many of the subsystems of this large system have already been optimized, so the future work will consist in closing the gaps.

LIST OF REFERENCES

[1] T. Hidayat, "Equilibria Study of Complex Silicate-based Slag in the Copper Production," Ph.D. thesis, The University of Queensland, 2013.

[2] M. Nagamori, W. J. Errington, P. J. Mackey, and D. Poggi, "Thermodynamic Simulation Model of the Isasmelt Process for Copper Matte," *Metall. Mater. Trans. B,* vol. 25B, pp. 839-853, 1994.

[3] S. A. Degterov and A. D. Pelton, "A Thermodynamic Database for Copper Smelting and Converting," *Metall. Mater. Trans. B,* vol. 30B, pp. 661-669, 1999.

[4] C. W. Bale, *et al.*, "FactSage thermochemical software and databases - recent developments," *Calphad,* vol. 33, pp. 295-311, 2009.

[5] W. G. I. Davenport, M. King, M. Schlesinger, and A. K. Biswas, *Extractive metallurgy of copper, 4th edition*: Pergamon, 2002.

[6] N. Kemori, Y. Shibata, and K. Fukushima, "Thermodynamic Consideration for Oxygen Pressure in a Copper Flash Smelting Furnace at Toyo Smelter," *JOM,* vol. 37, pp. 24-29, 1985.

[7] M.-A. van Ende, Y.-M. Kim, M.-K. Cho, J. Choi, and I.-H. Jung, "A Kinetic Model for the Ruhrstahl Heraeus (RH) Degassing Process," *Metall Mater Trans B,* vol. 42, pp. 477-489, 2011.

[8] M. Hillert and M. Jarl, "A Model for Alloying Effects in Ferromagnetic Metals," *Calphad,* vol. 2, pp. 227-238, 1978.

[9] A. D. Pelton, "A General "Geometric" Thermodynamic Model for Multicomponent Solutions," *Calphad,* vol. 25, pp. 319-328, 2001.

[10] F. J. Tavera and E. Bedolla, "Distribution of copper, sulfur, oxygen and minor elements between silica-saturated slag, matte and copper - experimental measurements," *Int. J. Miner. Process.,* vol. 29, pp. 289-309, 1990.

[11] M. Kameda and A. Yazawa, "The Oxygen Content of Copper Mattes," in *Physical Chemistry of Process Metallurgy, part 2*, vol. 8, 1961, pp. 963-988.

[12] F. Y. Bor and P. Tarassoff, "Solubility of Oxygen in Copper Mattes," *Can. Metall. Q.,* vol. 10, pp. 267-271, 1971.

[13] A. Geveci and T. Rosenqvist, "Equilibrium Relations between Liquid Copper, Iron-Copper Matte, and Iron Silicate Slag at 1250°," *Trans. Inst. Min. Metall.,* vol. 82, pp. C193-C201, 1973.

[14] A. Yazawa and M. Kameda, "Fundamental Studies on Copper Smelting. I. Partial Liquidus Diagram. for FeS-FeO-SiO_2 System," *The Technology Reports of the Tohoku Univ.,* vol. 18, pp. 40-58, 1953.

[15] Y. Takeda, "Oxygen potential measurement of iron silicate slag-copper-matte system," in *Proc. Int. Conf. Molten Slags, Fluxes Salts '97, 5th*, 1997, pp. 735-743.

[16] A. D. Pelton, S. A. Decterov, G. Eriksson, C. Robelin, and Y. Dessureault, "The Modified Quasichemical Model. I - Binary Solutions," *Metall. Mater. Trans. B,* vol. 31B, pp. 651-659, 2000.

[17] A. D. Pelton and P. Chartrand, "The Modified Quasichemical Model. II - Multicomponent Solutions," *Metall. Mater. Trans. A,* vol. 32A, pp. 1355-1360, 2001.

[18] A. D. Pelton, P. Chartrand, and G. Eriksson, "The modified Quasichemical Model. IV - Two Sublattice Quadruplet Approximation," *Metall. Mater. Trans. A,* vol. 32A, pp. 1409-1415, 2001.

[19] R. Piao, H.-G. Lee, and Y.-B. Kang, "Experimental investigation of phase equilibria and thermodynamic modeling of the CaO-Al_2O_3-CaS and the CaO-SiO_2-CaS oxysulfide systems," *Acta Mater.,* vol. 61, pp. 683-696, 2013.

[20] G. Lambotte, "Approche thermodynamique de la corrosion des réfractaires aluminosiliceux par le bain cryolithique : modélisation thermodynamique du système quaternaire réciproque AlF_3-NaF-SiF_4-Al_2O_3-Na_2O-SiO_2," Ph. D thesis, Université de Montréal, École Polytechnique de Montréal, 2012.

[21] S. A. Decterov, E. Jak, P. C. Hayes, and A. D. Pelton, "Experimental Study and Thermodynamic Optimization of the Fe-Zn-O System," *Metall. Mater. Trans. B,* vol. 32 B, pp. 643-657, 2001.

[22] M. Hillert and L.-I. Staffansson, "The Regular Solution Model for Stoichiometric Phases and Ionic Melts," *Acta Chem. Scand.,* vol. 24, pp. 3618-3626, 1970.

[23] M. Hillert, B. Jansson, and B. Sundman, "Application of the Compound-Energy Model to Oxide Systems," *Z. Metallkd.,* vol. 79, pp. 81-87, 1988.

[24] I.-H. Jung, "Critical Evaluation and Thermodynamic Modeling of Phase Equilibria in Multicomponent Oxide Systems," Ph. D. Thesis Université de Montréal, École Polytechnique de Montréal, Université de Montréal, 2003.

[25] V. Prostakova, "Development of a thermodynamic database for nickel containing oxide systems for simulation of nickel extraction from laterite ores," Ph. D. thesis, Ecole Polytechnique of Montreal, 2013.

[26] P. Waldner and A. D. Pelton, "Thermodynamic modeling of the Fe-S system," *J. Phase Equilib. Diff.,* vol. 26, pp. 23-28, 2005.

[27] S. Hayashi and T. Uno, "Activities of Sulfur and Oxygen in Liquid Iron," *Tetsu to Hagane,* vol. 68, pp. 1728-1736, 1982.

[28] H. Nakazawa and N. Morimoto, "Phase relations and superstructures of pyrrhotite, $Fe_{1-x}S$," *Mater. Res. Bull.,* vol. 6, pp. 345-357, 1971.

[29] K. Friedrich, "Note upon the Melting Diagram of the System: Ferrous Sulfide, Iron," *Metallurgie (Halle),* vol. 7, pp. 257-261, 1911.

[30] K. Miyazaki, "The equilibrium diagram of the iron and iron sulfide system," *Sci. Rep. Tohoku Imp. Univ., Ser. 1,* vol. 17, pp. 877-882, 1928.

[31] R. Loebe and E. Becker, "The System: Iron-Iron Sulfide," *Z. Anorg. Chem.,* vol. 77, pp. 301-319, 1913.

[32] E. Jensen, "Pyrrhotite; melting relations and compositions," *Am. J. Sci.*, vol. 240, pp. 695-709, 1942.

[33] W. Burgmann, G. Urbain, and M. G. Frohberg, "Iron-sulfur system in the iron monosulfide (pyrrhotite) region," *Mem. Sci. Rev. Met.*, vol. 65, pp. 567-578, 1968.

[34] M. Nagamori, "Compositions and free enthalpies of metal-saturated silver sulfide and ferrous sulfide," *Can. Met. Quart.*, vol. 9, pp. 531-533, 1970.

[35] M. Nagamori, T. Hatakeyama, and M. Kameda, "Thermodynamics of Fe-S Melts between 1100 and 1300°C," *Trans. Jpn. Inst. Met.*, vol. 11, pp. 190-194, 1970.

[36] C. W. Bale and J. M. Toguri, "Thermodynamics of the Copper-Sulfur, Iron-Sulfur and Copper-Iron-Sulfur Systems," *Can. Metall. Q.*, vol. 15, pp. 305-318, 1976.

[37] L. V. Gurvich, I. V. Veyts, and C. B. Alcock, in *Thermodynamic Properties of Individual Substances, 4th edition*, ed: Hemisphere Publishing Corporation, New York, 1989, pp. 265-316.

[38] Y. Y. Chuang, "The thermodynamics and phase relationships of the Cu-Ni-Fe-S quaternary system and its subsystems," Ph.D. Thesis, University of Wisconsin-Madison, Michigan, 1983.

[39] E. T. Allen, J. L. Crenshaw, and J. Johnston, "Iron-Sulfur Minerals," *Z. Anorg. Chem.*, vol. 76, pp. 201-273, 1912.

[40] G. Hagg and I. Sucksdorff, "The crystal structure of troilite and pyrrhotite," *Z. Physik. Chem.*, vol. B22, pp. 444-452, 1933.

[41] H. E. Merwin and R. H. Lombard, "The system Cu-Fe-S," *Econ. Geol. Bull. Soc. Econ. Geol.*, vol. 32, pp. 203-284, 1937.

[42] H. S. Roberts, "Polymorphism in the iron sulfide-sulfur solid solutions. I. Thermal study," *J. Am. Chem. Soc.*, vol. 57, pp. 1034-1038, 1935.

[43] F. Gronvold and H. Haraldsen, "The phase relations of synthetic and natural pyrrhotites ($Fe_{1-x}S$)," *Acta Chem. Scand.*, vol. 6, pp. 1452-1469, 1952.

[44] R. G. Arnold, "Equilibrium relations between pyrrhotite and pyrite from 325 to 743°," *Econ. Geol. Bull. Soc. Econ. Geol.*, vol. 57, pp. 72-90, 1962.

[45] R. G. Arnold, "Pyrrhotite-pyrite equilibrium relations between 325° and 743°," Princeton Univ., Princeton, NJ 1958.

[46] G. Kullerud, "Two-liquid field in the Fe-S system," *Year Book - Carnegie Inst. Washington*, vol. 60, pp. 174-176, 1961.

[47] P. Toulmin, III and P. B. Barton, Jr., "Thermodynamic study of pyrite and pyrrhotite," *Geochim. Cosmochim. Acta*, vol. 28, pp. 641-671, 1964.

[48] G. Kullerud and H. S. Yoder, "Pyrite stability relations in the Fe-S system," *Econ. Geol. Bull. Soc. Econ. Geol.*, vol. 54, pp. 533-572, 1959.

[49] G. H. Moh and G. Kullerud, "The Fe-S system," *Year Book - Carnegie Inst. Washington*, vol. 63, pp. 207-208, 1964.

[50] R. G. Arnold, "Evidence for liquid immiscibility in the system iron sulfide-sulfur," *Econ. Geol.,* vol. 66, pp. 1121-1130, 1971.

[51] M. W. Chase, *et al.*, "JANAF, Thermochemical Tables," *J. Phys. Chem. Ref. Data,* vol. 14 Suppl. 1, pp. 1774-1777, 1985.

[52] H. Rau, "Energetics of defect formation and interaction in pyrrhotite ($Fe_{1-x}S$) and its homogeneity range," *J. Phys. Chem. Solids,* vol. 37, pp. 425-429, 1976.

[53] A. V. Ditman and I. N. Vechko, "Dissociation of iron sulfide at high temperatures measured by the dew point method," *Inorg. Mater.,* vol. 1, pp. 1394-1399, 1965.

[54] E. Schurmann and H. J. Henke, "Investigation of the sulfuric vapor saturation of the binary system of iron-sulfur within the temperature range from 1200° to 1600°C under atmospheric pressure," *Giessereiforschung,* vol. 23, pp. 165-168, 1971.

[55] C. W. Sherman, H. I. Elvander, and J. Chipman, "Thermodynamic properties of sulfur in molten iron-sulfur alloys," *J. Met.,* vol. 188, pp. 334-340, 1950.

[56] S. Banya and J. Chipman, "Sulfur in liquid iron alloys. I. Binary iron-sulfur," *Trans. Met. Soc. AIME (Amer. Inst. Mining, Met., Petrol. Eng.),* vol. 242, pp. 940-946, 1968.

[57] F. Ishii and T. Fuwa, "Activity of sulfur in liquid iron," *Tetsu to Hagane,* vol. 67, pp. 736-745, 1981.

[58] O. A. Kapustin and V. A. Byrukvin, "Determination of sulfur vapor pressure above sulfide melts," *Russ. Metall.,* pp. 37-41, 1988.

[59] S. Bog and T. Rosenqvist, "Thermodynamics of metal sulfides. I. A thermodynamic study of the iron sulfide-iron oxide melts," *Norges Tek.-Naturvitenskapelige Forskiningsrad Met. Kom. Meddel,* vol. No. 12, pp. 1-20, 1958.

[60] J. Koh and A. Yazawa, "Thermodynamic properties of the copper-sulfur, iron-sulfur and copper-iron-sulfur systems," *Tohoku Daigaku Senko Seiren Kenkyusho Iho,* vol. 38, pp. 107-118, 1982.

[61] C. B. Alcock and L. L. Cheng, "A thermodynamic study of dilute solutions of sulfur in liquid iron, cobalt, and nickel, and binary alloys between these metals," *J. Iron Steel Inst., London,* vol. 195, pp. 169-173, 1960.

[62] S. Hayashi and T. Uno, "The activity of sulfur in liquid iron," *Nagoya Kogyo Daigaku Gakuho,* vol. 33, pp. 261-268, 1982.

[63] M. R. Baren and N. A. Gokcen, "Thermodynamic properties of sulfur in iron, cobalt, nickel, and their binary alloys," in *Proceedings of the 1983 International sulphide Smelting Symposium,* vol. 1, 1983, pp. 41-56.

[64] S. E. Vaisburd, V. G. Dyubanov, I. N. Zedina, A. Y. Stomakhin, and A. F. Filippov, "Enthalpies of sulfur dissolution in iron and nickel," *Izv. Vyssh. Ucheb. Zaved., Chern. Met.,* pp. 53-55, 1972.

[65] Y. Iguchi, Y. Tozaki, M. Kakizaki, T. Fuwa, and S. Ban-Ya, "A calorimetric study of heats of mixing of liquid iron alloys," *Tetsu to Hagane,* vol. 67, pp. 925-932, 1981.

[66] V. S. Sudavtsova, N. O. Sharkina, and V. G. Kudin, "Thermodynamic properties of liquid alloys of Fe-S and Fe-S-metal systems," *Russ. J. Phys. Chem.,* vol. 75, pp. 1061-1064, 2001.

[67] M. Kanda, N. Hasegawa, K. Itagaki, and A. Yazawa, "Thermodynamic study of the liquid iron-sulfur system by use of a drop calorimeter," *Thermochim. Acta,* vol. 109, pp. 275-284, 1986.

[68] A. M. Barloga, K. R. Bock, and N. Parlee, "Iron-carbon-sulfur system from 1149 to 1427°," *Trans. Am. Inst. Min., Metall. Pet. Eng.,* vol. 221, pp. 173-179, 1961.

[69] T. Rosenqvist and B. L. Dunicz, "Solid solubility of sulfur in iron," *J. Met.,* vol. 4, pp. 604-608, 1952.

[70] E. T. Turkdogan, S. Ignatowicz, and J. Pearson, "The solubility of sulfur in iron and iron-manganese alloys," *J. Iron Steel Inst., London,* vol. 180, pp. 349-354, 1955.

[71] W. H. Herrnstein, III, F. H. Beck, and M. G. Fontana, "Solubility and permeability of sulfur in α iron," *Trans. Met. Soc. AIME (Amer. Inst. Mining, Met., Petrol. Eng.),* vol. 242, pp. 1049-1056, 1968.

[72] M. Fischer and K. Schwerdtfeger, "Thermodynamics of the system iron-manganese-sulfur. Part II. Solubility of sulfur and manganese in γ-iron coexisting with sulfide in the temperature range 1100 to 1300°C," *Metall. Trans., B,* vol. 9B, pp. 631-634, 1978.

[73] E. Margot, B. Venard, N. Barbouth, and J. Oudar, "Solubility of sulfur in γ-iron," *C. R. Acad. Sci., Ser. C,* vol. 272, pp. 373-376, 1971.

[74] T. Rosenqvist, "A Thermodynamic Study of Iron, Cobalt, and Nickel Sulfides," *J. Iron Steel Inst.,* vol. 176, pp. 37-57, 1954.

[75] E. T. Turkdogan, "Iron-sulfur system. I. Growth rate of ferrous sulfide on iron and diffusivities of iron in ferrous sulfide," *Trans. Met. Soc. AIME (Amer. Inst. Mining, Met., Petrol. Eng.),* vol. 242, pp. 1665-1672, 1968.

[76] K. Sudo, "Fundamental researches on smelting of sulfide ores. II. The equilibrium in the reduction of solid ferrous sulfide by hydrogen gas," *Science Repts. Research Insts. Tohoku Univ.,* vol. 2, pp. 312-317, 1950.

[77] D. Ferro, V. Piacente, and P. Scardala, "Decomposition enthalpies of iron sulfides," *J. Chem. Thermodyn.,* vol. 21, pp. 483-494, 1989.

[78] P. Waldner, "Thermodynamic modeling of the Cu-S system," Ecole Polytechnique de Montreal, Montreal, QC, Canada, Internal Report, 2005. (FTmisc in C. W. Bale, et al., "FactSage thermochemical software and databases - recent developments," Calphad, vol. 33, pp. 295-311, 2009.)

[79] V.-P. Judin and M. Eerola, "Thermodynamics of Metallic Impurities in Copper-Saturated Copper Sulphide Melts," *Scand. J. Metall.,* vol. 8, pp. 128-132, 1979.

[80] R. Schuhmann and O. W. Moles, "Sulfur Activities in Liquid Copper Sulfides," *J. Metals,* vol. 191, pp. 235-241, 1951.

[81] S. Sudo, "Fundamental Researches on Smelting of Sulphide Ores. On Molten Copper Sulphide," *Bull. Res. Inst. Mineral Dressing Met. (Jpn.),* vol. 10, pp. 45-56, 1954.

[82] M. Moulki and J. Osterwald, "The Miscibility Gap Between Liquid Cu and Liquid Cu_2S," *Z. Metallk.,* vol. 70, pp. 808-810, 1979.

[83] D. J. Chakrabarti and D. E. Laughlin, "Cu-S (Copper-Sulfur)," in *Binary Alloy Phase Diagrams, 2nd edition*. vol. 2, T. B. Massalski, Ed., ed: ASM, Metals Park, 1990, pp. 1467-1471.

[84] V. M. Glazov, S. G. Kim, and G. K. Mambeterzina, "Acoustic Study of Phase Separation in Cu-S Melts," *Russ. J. Phys. Chem.,* vol. 66, pp. 1349-1352, 1992.

[85] J. Niemela and P. Taskinen, "Activities and phase equilibria in copper-sulfur melts by EMF techniques," *Scand. J. Metall.,* vol. 13, pp. 382-390, 1984.

[86] W. R. Cook, "Phase Changes in Cu_2S as a Function of Temperature," National Bureau of Standards (U. S.), U. S. Dept of Commerce, Washington, Special Publication No. 364, 1972.

[87] E. H. Roseboom, "An Investigation of the System Cu-S and Some Natural Copper Sulfides at 25-700 °C," *Econ. Geol.,* vol. 61, pp. 641-672, 1966.

[88] R. W. Potter, "An Electrochemical Investigation of the System Cu-S," *Econ. Geol.,* vol. 72, pp. 1524-1542, 1977.

[89] V. Wehefritz, "Investigation of the System Cu-S," *Z. Phys. Chem. (Neue Folge),* vol. 26, pp. 339-358, 1960.

[90] F. Johannsen and H. Vollmer, "The System Cu-CuS," *Z. Erzbergbau Metallhüttenwes.,* vol. 13, pp. 313-322, 1960.

[91] E. Jensen, "Melting Relations of Chalcocite," Akad. Oslo. I. Mat.-Naturv. Kl., I Kommisjon Hos Jacob Dybwad, Oslo, Avhandl. Norske Videnskaps, No. 6, 1947.

[92] P. Waldner and A. D. Pelton, "Thermodynamic modeling of the Cu-Fe-S system," CRCT, Ecole Polytechnique of Montreal, Internal report, 2006. (FTmisc in C. W. Bale, et al., "FactSage thermochemical software and databases - recent developments," Calphad, vol. 33, pp. 295-311, 2009.)

[93] K. Sudo, "Fundamental Researches on Smelting of Sulphide Ores. VII : On the Equilibrium in the Reduction of Copper Sulphide in Molten Copper by Hydrogen Gas," *Science reports of the Research Institutes, Tohoku University. Ser. A, Physics, chemistry and metallurgy,* vol. 2, pp. 519-530, 1950.

[94] C. W. Bale and J. M. Toguri, "A Thermogravimetric Technique for Continuous Quantitative Sulphur Analysis at Elevated Temperatures," *J. Thermal Anal.,* vol. 3, pp. 153-167, 1971.

[95] J. S. J. Smart and A. A. J. Smith, "Effect of phosphorus, arsenic, sulfur, and selenium on some properties of high-purity copper," *Trans. AIME,* vol. 166, pp. 144-155, 1945.

[96] J. Oudar, "Solubility of Sulfur in Copper at 600-1000 ^{o}C," *Compt. Rend. Hebd. Seances Acad. Sci.,* vol. 249, pp. 259-261, 1959.

[97] H. Schlegel and A. Schuller, "The System Copper-Iron-Sulfur," *Z. Metallkd.,* vol. 43, pp. 421-428, 1952.

[98] J. E. Dutrizac, "Reactions in cubanite and chalcopyrite," *Can. Mineral.*, vol. 14, Pt. 2, pp. 172-181, 1976.

[99] G. Kullerud, "The Cu-Fe-S system," *Year Book - Carnegie Inst. Washington,* vol. 63, pp. 200-202, 1964.

[100] A. Yazawa and M. Kameda, "Fundamental Studies on Copper Smelting. III. Partial Liquidus Diagram for Cu_2S-FeS-FeO System," *The Technology Reports of the Tohoku Univ.*, vol. 19, pp. 239-250, 1955.

[101] T. Rosenqvist and A. Hofseth, "Phase relations and thermodynamics of the copper-iron-sulfur-oxygen system at 700-1000 °C," *Scand. J. Metall.*, vol. 9, pp. 129-138, 1980.

[102] W. A. Krivsky and R. Schuhmann, "Thermodynamics of the Copper-Iron-Sulfur System at Matte Smelting Temperatures," *Trans. AIME / J. Metals,* vol. 209, pp. 981-988, 1957.

[103] P. B. Barton, Jr., "Solid solutions in the system copper-iron-sulfur. I. Copper-sulfur and copper-iron-sulfur joins," *Econ. Geol.,* vol. 68, pp. 455-465, 1973.

[104] T. Ueno, A. Kitakaze, and A. Sugaki, "Phase relations in the copper iron sulfide ($CuFeS_2$)-iron sulfide (FeS) join," *Sci. Rep. Tohoku Univ., Ser. 3,* vol. 14, pp. 283-93, 1980.

[105] D. S. Ebel and A. J. Naldrett, "Fractional crystallization of sulfide ore liquids at high temperature," *Econ. Geol.*, vol. 91, pp. 607-621, 1996.

[106] N. I. Kopylov and S. S. Novoselov, "System Cu_2S-FeS-Na_2S," *Russ. J. Inorg. Chem.*, vol. 9, pp. 1038-1043, 1964.

[107] J. W. Greig, E. Jensen, and H. E. Merwin, "The System Cu-Fe-S," *Year Book - Carnegie Inst. Washington,* pp. 129-134, 1955.

[108] G. Kullerud, R. A. Yund, and G. H. Moh, "Phase relations in the copper-iron-sulfur, copper-nickel-sulfur, and iron-nickel-sulfur systems," in *Magmatic Ore Deposits*, H. D. B. Wilson, Ed., ed Lancaster, Pennsylvania: Economic Geology Publishing Co., 1969, pp. 323-343.

[109] R. A. Yund and G. Kullerud, "Thermal stability of assemblages in the copper-iron-sulfur system," *J. Petrol.*, vol. 7, pp. 454-488, 1966.

[110] D. G. Mendoza, M. Hino, and K. Itagaki, "Phase relations and activity of arsenic in Cu-Fe-S-As system at 1473 K," *Mater. Trans.*, vol. 42, pp. 2427-2433, 2001.

[111] M. Nagamori, T. Azakami, and A. Yazawa, "Activities in the copper-iron-sulfur mattes at 1473 K," *Metall. Rev. MMIJ,* vol. 6, pp. 112-127, 1989.

[112] L. J. Cabri, "New data on phase relations in the copper-iron-sulfur system," *Econ. Geol.*, vol. 68, pp. 443-454, 1973.

[113] P. R. Brett, "The Cu-Fe-S system," *Washington Year Book,* vol. 1962, pp. 193-196, 1963.

[114] D. Shishin and S. A. Decterov, "Critical assessment and thermodynamic modeling of Cu-O and Cu-O-S systems," *Calphad,* vol. 38, pp. 59-70, 2012.

[115] F. Kongoli, Y. Dessureault, and A. D. Pelton, "Thermodynamic Modeling of Liquid Fe-Ni-Cu-Co-S Mattes," *Metall. Mater. Trans. B,* vol. 29B, pp. 591-601, 1998.

[116] R. Schmid, "A Thermodynamic Analysis of the Cu-O System with an Associated Solution Model," *Metall. Trans. B*, vol. 14B, pp. 473-481, 1983.

[117] M. T. Clavaguera-Mora, J. L. Touron, J. Rodriguez-Viejo, and N. Clavaguera, "Thermodynamic description of the Cu-O system," *J. Alloys Compd.*, vol. 377, pp. 8-16, 2004.

[118] B. Hallstedt, D. Risold, and L. J. Gauckler, "Thermodynamic Assessment of the Copper-Oxygen System," *J. Phase Equilib.*, vol. 15, pp. 483-499, 1994.

[119] B. Hallstedt and L. J. Gauckler, "Revision of the Thermodynamic Descriptions of the Cu-O, Ag-O, Ag-Cu-O, Bi-Sr-O, Bi-Ca-O, Bi-Cu-O, Sr-Cu-O, Ca-Cu-O and Sr-Ca-Cu-O Systems," *Calphad*, vol. 27, pp. 177-191, 2003.

[120] L. Schramm, G. Behr, W. Loeser, and K. Wetzig, "Thermodynamic Reassessment of the Cu-O Phase Diagram," *J. Phase Equilib. Diff.*, vol. 26, pp. 605-612, 2005.

[121] E. Heyn, "Copper and oxygen," *Zeit. anorg. Chem.*, vol. 39, pp. 1-23, 1904.

[122] H. Rickert and R. Steiner, "Electrochemical measurements of oxygen diffusion in metals at high temperatures," *Z. Phys. Chem. (Muenchen, Ger.)*, vol. 49, pp. 127-137, 1966.

[123] H. Rickert and H. Wagner, "Electrochemical determination of the activity of oxygen in liquid copper," *Electrochim. Acta*, vol. 11, pp. 87-91, 1966.

[124] J. Osterwald, "Electromotive force measurements on liquid copper in equilibrium with solid or liquid copper(I) oxide," *Z. Phys. Chem. (Muenchen, Ger.)*, vol. 49, pp. 138-146, 1966.

[125] P. Taskinen, "Liquidus Equilibria and Solution Thermodynamics in Copper rich, Copper-Nickel-Oxygen Alloys," *Acta Polytechnica Scand., Chemistry Including Metallurgy Series*, vol. 145, p. 43 pp., 1981.

[126] U. Kuxmann and K. Kurre, "Miscibility Gap in the System Copper-Oxygen and its Alteration by the Oxides CaO, SiO_2, Al_2O_3, $MgO{\cdot}Al_2O_3$, and ZrO_2," *Erzmetall.*, vol. 21, pp. 199-209, 1968.

[127] S. H. Sadat-Darbandi, "Determination of Equilibrium and Transport properties of the Liquid Phases of the System Copper-Oxygen," Dr.-Ing. Dissertation T.U. Berlin, Berlin, 1977.

[128] J. Gerlach, J. Osterwald, and W. Stichel, "Coulometric determination of the miscibility gap between liquid copper and copper(I) oxide," *Z. Metallk.*, vol. 59, pp. 576-579, 1968.

[129] N. Kemori, I. Katayama, and Z. Kozuka, "Thermodynamic study of oxygen in liquid copper," *Trans. Jpn. Inst. Met.*, vol. 21, pp. 275-284, 1980.

[130] Y. Kayahara, K. Ono, T. Oishi, and J. Moriyama, "Thermodynamic Study of the Liquid Cu-O System," *Trans. Jpn. Inst. Met.*, vol. 22, pp. 493-500, 1981.

[131] T. Oishi, Y. Kondo, and O. K., "A Thermodynamic Study of Copper(I) Oxide-Calcium Oxide Melts in Equilibrium with Liquid Copper," *Trans. Jpn. Inst. Metals*, vol. 27, pp. 976-980, 1986.

[132] P. Taskinen, "Thermodynamics of liquid copper-oxygen alloys at 1065-1450 DegC," *Scand. J. Metall.*, vol. 13, pp. 75-82, 1984.

[133] A. Boudene, K. Hack, A. Mohammad, D. Neuschutz, and E. Zimmermann, "Experimental investigation and thermochemical assessment of the system copper-oxygen," *Z. Metallkd.*, vol. 83, pp. 663-668, 1992.

[134] R. Vogel and W. Pocher, "The system: copper-oxygen," *Z. Metallkd.*, vol. 21, pp. 333-337, 1929.

[135] H. S. Roberts and F. H. Smith, "The system copper : cupric oxide : oxygen," *J. Am. Chem. Soc.*, vol. 43, pp. 1061-1070, 1921.

[136] A. V. Kosenko and G. A. Emel'chenko, "Equilibrium Phase Relationships in the system Cu-O under High Oxygen Pressure," *J. Phase Equilib.*, vol. 22, pp. 12-19, 2001.

[137] J. Osterwald, "Phase diagram of the copper-oxygen system in the liquid-phase temperature range," *Z. Metallk.*, vol. 59, pp. 573-576, 1968.

[138] A. M. M. Gadalla, W. F. Ford, and J. White, "Equilibrium Relations in the System CuO-Cu_2O-SiO_2," *Trans. Brit. Ceram. Soc.*, vol. 62, pp. 45-66, 1963.

[139] Z. Moser and K. Fitzner, "The emf measurements involving solid electrolytes in the copper-oxygen system," *Bull. Acad. Pol. Sci., Ser. Sci. Tech.*, vol. 24, pp. 215-220, 1976.

[140] T. Oishi and Z. M. J. Kozuka, "Thermodynamic Properties of Oxygen in Molten Copper and the Effects of Tin and Nickel on These Properties," *Trans. Jpn. Inst. Met.*, vol. 12, pp. 410-416, 1971.

[141] S. Otsuka and Z. Kozuka, "Activities of Oxygen in Liquid Copper and Silver from Electrochemical Measurements," *Metall. Trans. B*, vol. 12B, pp. 501-507, 1981.

[142] A. D. Mah, L. B. Pankratz, W. W. Weller, and E. G. King, "Thermodynamic data for cuprous and cupric oxides," U. S. Dept. of the Interior, Bureau of Mines, 1967.

[143] L. Wohler and N. Jockum, "Thermal chemical measurements of the oxides of copper, rhodium, palladium and indium," *Z. physik. Chem.*, vol. A167, pp. 169-179, 1933.

[144] W. Stichel, Dr.-Ing. Dissertation, T.U. Berlin, 1967.

[145] A. T. Dinsdale, "SGTE Data for Pure Elements," *Calphad*, vol. 15, pp. 317-425, 1991.

[146] R. B. Stewart, J. G. Hust, and R. D. McCarty, "Interim Thermodynamic Properties for Gaseous and Liquid Oxygen at Temperatures from 55 to 300 ° K and Pressures to 300 atm," Boulder, Colorado, 1963. (U. S. Nat. Bur. Stand. Report (NBS Report 7922))

[147] B. Hammer, D. Lenz, P. Reimers, T. Dudzus, and B. F. Schmitt, "Solubility of oxygen in high-purity copper," *Metall (Berlin)*, vol. 38, pp. 41-45, 1984.

[148] M. L. Narula, V. B. Tare, and W. L. Worrell, "Diffusivity and Solubility of oxygen in Solid Copper Using Potentiostatic and Potentiometric Techniques," *Metall. Trans. B*, vol. 14B, pp. 673-677, 1983.

[149] V. M. Horrigan, "The solubility of oxygen in solid copper," *Metall. Trans., A*, vol. 8A, pp. 785-787, 1977.

[150] R. L. Pastorek and R. A. Rapp, "Solubility and diffusivity of oxygen in solid copper from electrochemical measurements," *Trans. AIME*, vol. 245, pp. 1711-1720, 1969.

[151] Q. Zhang and W. W. Smeltzer, "Diffusivity and solubility of oxygen in crystal solid copper," *Youse Jinshu,* vol. 39, pp. 57-61, 1987.

[152] T. Wada, K. Fueki, and T. Mukaibo, "Determination of the solubility of oxygen in copper by the coulometric method," *Bull. Chem. Soc. Jpn.,* vol. 49, pp. 3317-3318, 1976.

[153] F. Bouillon and J. Orszagh, "Oxygen solubility in single-crystalline copper," *J. Phys. Chem. Solids,* vol. 33, pp. 1533-1539, 1972.

[154] A. Phillips and E. N. Skinner, "Solubility of oxygen in high-purity copper," *Trans. AIME,* vol. 143, pp. 301-308, 1941.

[155] J. Schmiedl, V. Repèák, and I. Cempa, "Equilibrium Sudies in the System Cu-S-O," *Trans. Inst. Mining Metall. C,* vol. 86, pp. C88-C91, 1977.

[156] U. Kuxmann and T. Benecke, "Solubility of O in Fused Cu Sulfide," *Erzmetall.,* vol. 19, pp. 215-221, 1966.

[157] H. Jalkanen and M. H. Tikkanen, "Equilibrium Studies on High-Copper Mattes. II. Sulphur-Oxygen Equilibria in the System Cu-S-O along the Liquid Immiscibility Field," *Scand. J. Metall.,* vol. 8, pp. 64-66, 1979.

[158] H. Jalkanen and M. H. Tikkanen, "Equilibrium Studies on High-Copper Mattes. I. A Method for Equilibrating Molten Sulphide-Oxide Systems," *Scand. J. Metall.,* vol. 8, pp. 34-38, 1979.

[159] W. Oelsen, "Deoxidation of smelted copper with iron, phosphorus, and sulfur," *Giesserei,* pp. 383-387, 1952.

[160] W. Lange, *Die thermodynamischen Eigenschaften der Metalloxyde*: Springer-Verlag, Berlin, 1949.

[161] W. Reinders and F. Goudriaan, "Physico-chemical observations of the roasting process II Copper roasting Equilibria in the system Cu-S-O," *Z. Anorg. Allg. Chem.,* vol. 126, pp. 85-103, 1923.

[162] J. Schmiedl, V. Repcak, and M. Stofko, "A contribution on thermodynamics of copper mattes," *Zb. Ved. Pr. Vys. Sk. Tech. Kosiciach,* pp. 301-314, 1977.

[163] E. A. Trofimov and G. G. Mikhailov, "Analysis of phase equilibriums in the Cu-S-O system at 1100-1300 °C," *Izv. Vyssh. Uchebn. Zaved., Tsvetn. Metall.,* pp. 4-9, 2005.

[164] F. Johannsen and U. Kuxmann, "Equilibrium between oxygen and sulfur in molten copper at 1150 Deg," *Z. Erzbergbau Metallhuettenwes.,* vol. 8, pp. 45-58, 1955.

[165] T. Oishi, Y. Tobiyama, Y. Fujiwara, and K. Ono, "Thermodynamic studies of the liquid copper-sulfur-oxygen system," *Trans. Jpn. Inst. Met.,* vol. 28, pp. 971-976, 1987.

[166] K. Sano and H. Sakao, "Physico-Chemical Investigation on Copper Smelting. III. Study of Equilibria between Liquid Copper and Carbon Monoxide-Carbon Dioxide-Sulfur Dioxide Gas Mixtures," *J. Japan Inst. Metals,* vol. 19, pp. 504-508, 1955.

[167] S. Otsuka, Y. A. Chang, and Y. Austin, "Activity Coefficient of Oxygen in Copper-Sulfur Melts," in *Advances in Sulfide Smelting, Proc. Int. Sulfide Smelting Symp. Extr. Process Metall. Meet. Metall. Soc. AIME,* 1983, pp. 33-39.

[168] D. Janke and W. A. Fischer, "Thermodynamic relations for the solution behavior of oxygen in copper-base melts," *Metall (Berlin),* vol. 29, pp. 1189-1193, 1975.

[169] M. W. Chase, *et al.*, "JANAF, Thermochemical Tables," *J. Phys. Chem. Ref. Data,* vol. 14 Suppl. 1, 1985.

[170] I. Barin, O. Knacke, and Kubaschewski, *Thermodynamic Properties of Inorganic Sunstances* vol. 279 (10). Berlin: Springer-Verlag, 1977.

[171] N. Jacinto, S. N. Sinha, M. Nagamori, and H. Y. Sohn, "An equilibrium study of the hydrogen reduction of copper sulfates," *Metall. Trans. B,* vol. 14B, pp. 136-139, 1983.

[172] D. Shishin, T. Hidayat, E. Jak, and S. Decterov, "Critical assessment and thermodynamic modeling of Cu-Fe-O system," *Calphad,* vol. 41, pp. 160-179, 2013.

[173] B. Sundman, "An Assessment of the Fe-O System," *J. Phase Equilib.,* vol. 12, pp. 127-140, 1991.

[174] M. Selleby and B. Sundman, "A Reassessment of the Ca-Fe-O System," *Calphad,* vol. 20, pp. 381-392, 1996.

[175] L. Kjellqvist and M. Selleby, "Thermodynamic Assessment of the Fe-Mn-O System," *J. Phase Equilib. Diffus.,* vol. 31, pp. 113-134, 2010.

[176] L. Kjellqvist, M. Selleby, and B. Sundman, "Thermodynamic modelling of the Cr-Fe-Ni-O system," *Calphad,* vol. 32, pp. 577-592, 2008.

[177] A. V. Khvan, O. Fabrichnaya, G. Savinykh, R. Adam, and H. J. Seifert, "Thermodynamic Assessment of the Cu-Fe-O System," *J. Phase Equilib. Diff.,* vol. 32, pp. 498-511, 2011.

[178] M. Kowalski and P. J. Spencer, "Thermodynamic reevaluation of the Cr-O, Fe-O and Ni-O systems: remodelling of the liquid, bcc and fcc phases," *Calphad,* vol. 19, pp. 229-243, 1995.

[179] R. Luoma, "A thermodynamic analysis of the system Fe-Cr-Ni-C-O," *Acta Polytech. Scand., Chem. Technol. Ser.,* vol. 292, pp. 1-91, 2002.

[180] I.-H. Jung, S. A. Decterov, and A. D. Pelton, "A Thermodynamic Model for Deoxidation Equilibria in Steel," *Metall. Mater. Trans. B,* vol. 35B, pp. 493-507, 2004.

[181] S. A. Decterov, *et al.*, "Oxide Database Development for FactSage," in *Calphad XXX, 27 May 1 June 2001,* 2001, p. 82.

[182] S. A. Decterov, *et al.*, "Thermodynamic Modeling of the Al_2O_3-CaO-CoO-CrO-Cr_2O_3-FeO-Fe_2O_3-MgO-MnO-NiO-SiO_2-S System and Applications in Ferrous Process Metallurgy," in *SAIMM Symposium Series S36 (VII Int. Conf. on Molten Slags, Fluxes & Salts),* 2004, pp. 839-850.

[183] I.-H. Jung, S. A. Decterov, and A. D. Pelton, "Critical Thermodynamic Evaluation and Optimization of the FeO-Fe_2O_3-MgO-SiO_2 System," *Metall. Mater. Trans. B,* vol. 38B, pp. 877-889, 2004.

[184] E. Jak, P. Hayes, A. Pelton, and S. Decterov, "Thermodynamic optimisation of the FeO-Fe_2O_3-SiO_2 (Fe-O-Si) system with FactSage," *Int. J. Mater. Res.,* vol. 98, pp. 847-854, 2007.

[185] I.-H. Jung, S. A. Decterov, and A. D. Pelton, "Thermodynamic modeling of the CoO-SiO_2 and CoO-FeO-Fe_2O_3-SiO_2 systems," *Int. J. Mater. Res.*, vol. 98, pp. 816-825, 2007.

[186] R. Vogel and W. Fulling, "The system iron-iron sulfide (FeS)-wustite (FeO)," *Festskr. J. Arvid Hedvall*, pp. 597-610, 1948.

[187] E. Ohtani and A. E. Ringwood, "Composition of the core, I Solubility of oxygen in molten iron at high temperatures," *Earth Planet. Sci. Lett.*, vol. 71, pp. 85-93, 1984.

[188] L. S. Darken and R. W. Gurry, "The System Iron-Oxygen. II. Equilibrium and Thermodynamics of Liquid Oxide And Other Phases," *J. Am. Chem. Soc.*, vol. 68, pp. 798-816, 1946.

[189] P. A. Distin, S. G. Whiteway, and C. R. Masson, "Solubility of oxygen in liquid iron from 1785° to 1960°C. A new technique for the study of slag-metal equilibria," *Can. Metall. Q.*, vol. 10, pp. 13-18, 1971.

[190] W. A. Fischer and J. F. Schumacher, "The saturation solubility of oxygen in pure iron from the melting point to 2046 DegC, determined using the levitation melting method," *Arch. Eisenhuettenwes.*, vol. 49, pp. 431-435, 1978.

[191] C. R. Taylor and J. Chipman, *Trans. AIME*, vol. 154, pp. 228-247, 1943.

[192] M. N. Dastur and J. Chipman, "Equilibrium in the reaction of hydrogen with oxygen in liquid iron," *Trans. Am. Inst. Min., Metall. Pet. Eng.*, vol. 1, pp. 441-445, 1949.

[193] S. K., "Measurement of Oxygen Activity in iron, Iron-Silicon, Manganese, and Iron-Manganese Melts Using Solid Electrolyte Galvanic Cells," *Trans. Met. Soc. AIME.*, vol. 239, pp. 1276-1281, 1967.

[194] C. Gatellier and M. Olette, "Determination of the free enthalpy of dissolution of oxygen in liquid iron at 1600 ° by using an electrochemical cell with a solid electrolyte," *C. R. Acad. Sci., Paris, Ser. C*, vol. 266, pp. 1133-1135, 1968.

[195] E. S. Tankins, N. A. Gokcen, and G. R. Belton, "The activity and solubility of oxygen in liquid Fe, Ni, and Co," *Trans. Am. Inst. Min., Metall. Pet. Eng.*, vol. 230, pp. 820-7, 1964.

[196] T. P. Floridis and J. Chipman, "Activity of Oxygen in Liquid Iron Alloys," *Trans. AIME*, vol. 212, pp. 549-553, 1958.

[197] N. A. Gokcen, "Equilibria in Reactions of Hydrogen, and Carbon Monoxide With Dissolved Oxygen in Liquid Iron; Equilibrium in Reduction of Ferrous Oxide With Hydrogen, and Solubility of Oxygen in Liquid Iron," *J. Metals*, vol. 206, pp. 1558-1567, 1956.

[198] H. Sakao and K. Sano, "Determination of the equilibrium constant of the reaction of H with O in liquid iron," *Nippon Kinzoku Gakkaishi*, vol. 23, pp. 671-674, 1959.

[199] *Steelmaking Data Sourcebook*: Japan Society for the Promotion of Science, 19th Comm. On Steelmaking, Gordon & Breach Science, New York, NY, 1988.

[200] M. T. Hepworth, R. P. Smith, and E. T. Turkdogan, "Permeability, solubility, and diffusivity of oxygen in b.c.c. iron," *Trans. Metall. Soc. AIME*, vol. 236, pp. 1278-1283, 1966.

[201] J. H. Swisher and E. T. Turkdogan, "Solubility, permeability, and diffusivity of oxygen in solid iron," *Trans. Metall. Soc. AIME,* vol. 239, pp. 426-431, 1967.

[202] J. M. Skeaff and A. W. Espelund, "Electromotive force method for the determination of sulfate-oxide equilibria results for the magnesium, manganese, iron, nickel, copper and zinc systems," *Can. Metall. Q.,* vol. 12, pp. 445-454, 1973.

[203] K. C. Hsieh and Y. A. Chang, "A solid-state emf study of ternary nickel-sulfur-oxygen, iron-sulfur-oxygen, and quaternary iron-nickel-sulfur-oxygen," *Metall. Trans. B,* vol. 17B, pp. 133-146, 1986.

[204] O. A. Musbah and Y. A. Chang, "A Solid-State EMF Study of the Fe-S-O and Co-S-O Ternary Systems," *Oxid. Met.,* vol. 30, pp. 329-342, 1988.

[205] S. C. Schaefer, "Electrochemical determination of Gibbs energies of formation of manganese sulfide and iron sulfide($Fe_{0.9}S$)," RI 8486, 1980.

[206] A. W. Espelund and H. Jynge, "The zinc-iron-sulfur-oxygen system Equilibriums between sphalerite or wurtzite, pyrrhotite, spinel, zinc oxide and a gas phase," *Scand. J. Metall.,* vol. 6, pp. 256-262, 1977.

[207] T. Rosenqvist and P. H. Hynne, "The reaction between iron sulfide and sulfur dioxide," *Tidsskr. Kjemi, Bergves. Metall.,* vol. 13, pp. 196-200, 1953.

[208] D. C. Hilty and W. Crafts, "Liquidus Surface of the Iron-Sulfur-Oxygen System," *J. Metals,* vol. 194, pp. 1307-1312, 1952.

[209] E. T. Turkdogan, G. J. W. Kor, L. S. Darken, and R. W. Gurry, "Sulfides and Oxides in Iron-Manganese Alloys. I. Phase Relations in Iron-Manganese-Sulfur-Oxygen System," *Metall. Trans.,* vol. 2, pp. 1561-1570, 1971.

[210] T. Rosenqvist and T. Hartvig, "The Thermodynamics of Fe-Cu Mattes, and Their Equilibrium with Magnetite," *Norges Tek.-Naturvitenskapelige Forskiningsrud Met. Kom. Meddel,* pp. 21-52, 1958.

[211] S. Bog and T. Rosenqvist, "A Thermodynamic Study of Iron Sulphide-Iron Oxide Melts," in *Nat. Phys. Lab. Symp. No. 9,* vol. 2, 1959, pp. 6B.2-6B.7.

[212] A. J. Naldrett, "A portion of the system Fe-S-O between 900° and 1080°C and its application to sulfide ore magmas," *J. Petrology,* vol. 10, pp. 171-201, 1969.

[213] S. Ueda, K. Yamaguchi, and Y. Takeda, "Phase equilibrium and activities of Fe-S-O melts," *Mater. Trans.,* vol. 49, pp. 572-578, 2008.

[214] H. Johto, H. M. Henao, E. Jak, and P. Taskinen, "Experimental study on the phase diagram of the Fe-O-S system," *submitted to Metallurgical and Materials Transactions B,* April 2, 2013.

[215] E. W. Dewing and F. D. Richardson, "Thermodynamics of Mixtures of Ferrous Sulphide and Oxide," *J. Iron Steel Inst.,* vol. 194, pp. 446-450, 1960.

[216] M. Nagamori and M. Kameda, "Equilibriums between the Fe-S-O System Melts and CO-CO_2-SO_2 Gas Mixtures at 1200°," *Trans. Inst. Metals (Jap.),* vol. 6, pp. 21-30, 1965.

[217] M. Kameda and A. Yazawa, "Effects of Partial Pressures of Oxygen and Sulfur on the Oxygen Content in Copper Matte," in *Studies in Met. (Commemoration for Prof. Matoba), Tohoku Univ.*, 1970, pp. 159-166.

[218] M. Stofko, J. Schmiedl, and T. Rosenqvist, "Thermodynamics of Iron-Sulfur-Oxygen Melts at 1200°," *Scand. J. Metall.*, vol. 3, pp. 113-118, 1974.

[219] V. P. Mintsis, A. G. Ryabko, L. S. Tsemekhman, G. P. Grodinskii, and Y. V. Fisher, "Equilibrium in the iron-sulfur-oxygen system," *Izv. Akad. Nauk SSSR, Met.*, pp. 28-32, 1988.

[220] I. A. Blatov, B. P. Burylev, L. S. Tsemekhman, and S. L. Litvinov, "Thermodynamics of the Interaction of Components of the Fe-S-O System in Equilibrium with the CO-CO_2-SO_2 Gas Phase at 1300 ^{o}C," *Metally*, pp. 34-36, 1997.

[221] M. Nagamori and A. Yazawa, "Thermodynamic observations of the molten FeS-FeO system and its vicinity at 1473 K," *Metall. Mater. Trans. B*, vol. 32B, pp. 831-837, 2001.

[222] L. A. Rose and J. M. Brenan, "Wetting properties of Fe-Ni-Co-Cu-O-S melts against olivine: implications for sulfide melt mobility," *Econ. Geol.*, vol. 96, pp. 145-157, 2001.

[223] R. O. C. Fonseca, I. H. Campbell, H. S. C. O'Neill, and J. D. Fitzgerald, "Oxygen solubility and speciation in sulphide-rich mattes," *Geochim. Cosmochim. Acta*, vol. 72, pp. 2619-2635, 2008.

[224] H. Schenck and H. Hinze, "Equilibriums of the iron-carbon-oxygen system in the temperature and concentration range of molten steel and the effect of phosphorus, manganese, and sulfur," *Arch. Eisenhuettenwes.*, vol. 37, pp. 545-553, 1966.

[225] I. Ansara and Å. Jansson, "Assesment of the copper-iron system," Materials Research Center, The Royal Institute of Technology, Stockholm, Sweden., Trita-Mac-0533, 1993.

[226] S. Nikolic, P. C. Hayes, and E. Jak, "Experimental Techniques for Investigating Calcium Ferrite Slags at Metallic Copper Saturation and Application to the Systems "Cu_2O"-"Fe_2O_3" and "Cu_2O"-CaO at Metallic Copper Saturation," *Metall. Mater. Trans. B*, vol. 40B, pp. 892-899, 2009.

[227] D. Shishin, "Critical assessment and thermodynamic modeling of Fe-O and Fe-O-S systems," *Chapter 5 of this thesis*, 2013.

[228] L. J. Swartzendruber, "Cu-Fe (Copper-Iron)," in *Binary Alloy Phase Diagrams, 2d edition*, T. B. Massalski, Ed., ed: Amer. Soc. Metals, OH, USA, 1996.

[229] T. Inoue and S. Iida, "Specific heat of copper ferrite," *J. Phys. Soc. Jpn.*, vol. 13, p. 656, 1958.

[230] L. A. Reznitskii and S. E. Filippova, "Effect of heat treatment on the heat capacity and heat of phase transformations of lithium and copper ferrites. Determination of the activation energy of diffusion of hardened defects from calorimetric data," in *Fiz. Khim. Ferritov*, 1973, pp. 291-303.

[231] A. E. Katkov and A. A. Lykasov, "Wustite solid solutions in the Fe-Cu-O system," *Inorg. Mater.*, vol. 35, pp. 706-708, 1999.

[232] P. Perrot, S. Amout, J. Vrestal, and M. Materials Science International Team, "Copper - Iron - Oxygen," G. Effenberg and S. Ilyenko, Eds., ed: SpringerMaterials - The Landolt-Börnstein Database, Springer-Verlag Berlin Heidelberg, 2008.

[233] H. V. Kiran, K. Seshan, and D. K. Chakrabarty, "The influence of nickel(2+) ions on the distribution of magnesium(2+) and copper(2+) ions in spinel ferrites," *J. Solid State Chem.,* vol. 41, pp. 63-66, 1982.

[234] S. R. Sawant and R. N. Patil, "Magnetization and structural studies on copper ferrite," *Indian J. Pure Appl. Phys.,* vol. 21, pp. 145-147, 1983.

[235] S. R. Sawant and R. N. Patil, "Cation Distribution Magnetization and Electrical Switching in the Copper-Zinc Ferrite ($Cu_xZn_{1-x}Fe_2O_4$) System," *Indian J. Phys., [PartA],* vol. 56A, pp. 233-238, 1982.

[236] G. A. Petrakovskii, K. A. Sablina, and E. M. Smokotin, "Magnetic properties of copper ferrite single crystals," *Fiz. Tverd. Tela,* vol. 10, pp. 2544-2545, 1968.

[237] M. U. Rana, M. U. Islam, and T. Abbas, "Cation Distribution and Magnetic Interactions in Zn-Substrituted $CuFe_2O_4$ Ferrites," *Mater. Chem. Phys.,* vol. 65, pp. 345-349, 2000.

[238] C. B. Kolekar, P. N. Kamble, and A. S. Vaingankar, "X-ray for IR characterization and susceptibility study of Gd^{3+} substituted copper-cadmium ferrites," *Indian J. Phys., A,* vol. 68A, pp. 529-537, 1994.

[239] B. L. Patil, S. A. Patil, S. R. Sawant, A. S. Jambhale, and R. N. Patil, "Effect of Zr^{4+} substitution of the magnetic properties of Cu-ferrite," *Indian J. Pure Appl. Phys.,* vol. 32, pp. 98-100, 1994.

[240] S. Roy and J. Ghose, "Superparamagnetic nanocrystalline $CuFe_2O_4$," *J. Appl. Phys.,* vol. 87, pp. 6226-6228, 2000.

[241] V. R. Kulkarni, M. M. Todkar, and A. S. Vaingankar, "Electrical resistivity and cation distribution in copper cadmium ferrite ($Cu_xCd_{1-x}Fe_2O_4$) system," *Indian J. Pure Appl. Phys.,* vol. 24, pp. 294-296, 1986.

[242] A. B. Liberman, L. L. Zakirov, F. G. Vagizov, R. A. Nazipov, and E. K. Sadykov, "Mossbauer studies of the effect of the sintering temperature on structural and magnetic properties of CuO-Fe_2O_3-system compounds," *Izv. Akad. Nauk, Ser. Fiz.,* vol. 63, pp. 1411-1415, 1999.

[243] R. G. Kulkarni, B. S. Trivedi, H. H. Joshi, and G. J. Baldha, "Magnetic properties of copper ferrite aluminates," *J. Magn. Magn. Mater.,* vol. 159, pp. 375-380, 1996.

[244] S. H. Lee, K. P. Chae, K. S. Oh, and Y. B. Lee, "Moessbauer study of the spinel system iron sesquioxide-copper monoxide-aluminum oxide, (x = 0.0, 0.4)," *J. Korean Phys. Soc.,* vol. 22, pp. 455-459, 1989.

[245] S. R. Sawant and R. N. Patil, "Electrical resistivity of copper zinc iron oxide ($Cu_xZn_{1-x}Fe_2O_4$) system," *Indian J. Pure Appl. Phys.,* vol. 20, pp. 353-355, 1982.

[246] S. R. Sawant, S. A. Patil, and R. N. Patil, "Cation distribution from Curie temperatures in copper zinc ferrite ($Cu_xZn_{1-x}Fe_2O_4$) system," *Indian J. Pure Appl. Phys.,* vol. 19, pp. 1212-1213, 1981.

[247] S. R. Sawant and R. N. Patil, "Structural and lattice parameter changes in the slow cooled and quenched copper zinc ferrite ($Cu_xZn_{1-x}Fe_2O_4$) samples," *J. Mater. Sci.*, vol. 16, pp. 3496-3499, 1981.

[248] E. Y. Sapozhnikova, *et al.*, "Degree of oxidation of cations in a series of solid solutions of the $CuFe_2O_4$-$Cu_{0.5}Fe_{2.5}O_4$-Fe_3O_4 system," *Russ. J. Inorg. Chem.*, vol. 26, pp. 945-947, 1981.

[249] S. S. Lisnyak, Y. A. Kesler, and Y. D. Tret'yakov, "Interatomic spacings and the evolution of spinel solid solutions for ferrites in the system iron-copper-oxygen," *Dokl. Akad. Nauk SSSR [Phys. Chem.]*, vol. 297, pp. 1421-1424, 1987.

[250] E. Kitzinger and Z. Simsa, "Constitution of $Cu_{0.5}Fe_{2.5}O_4$," *Czech. J. Phys.*, vol. 18, pp. 955-957, 1968.

[251] Z. Simsa, "Distribution of cations and phase transition in ferrite $Cu_{0.5}Fe_{2.5}O_4$," *IEEE Trans. Magn.*, vol. 5, pp. 592-595, 1969.

[252] S. E. Tsitsenovskaya, "Neutron-diffraction study of spinel ferrite $Cu_{0.5}Fe_{2.5}O_{4+gamma}$," *Latv. PSR Zinat. Akad. Vestis, Fiz. Teh. Zinat. Ser.*, pp. 64-8, 1972.

[253] A. D'Huysser, B. Lerebours-Hannoyer, M. Lenglet, and J. P. Bonnelle, "XPS study and the distribution of copper(2+) and copper(+) in copper ferrites," *J. Solid State Chem.*, vol. 39, pp. 246-256, 1981.

[254] E. Kester and B. Gillot, "Cation distribution, thermodynamic and kinetics considerations in nanoscaled copper ferrite spinels. new experimental approach by XPS and new results both in the bulk and on th grain boundary," *J. Phys. Chem. Solids*, vol. 59, pp. 1259-1269, 1998.

[255] A. Nagarajan and A. H. Agajanian, "Magneto-Moessbauer study of $Cu_{0.5}Fe_{2.5}O_4$," *J. Appl. Phys.*, vol. 41, pp. 1642-1647, 1970.

[256] K. E. Kuehn, D. Sriram, S. S. Bayya, J. J. Simmins, and R. L. Snyder, "Synthesis of copper and lithium copper ferrites as high magnetization materials," *J. Mater. Res.*, vol. 15, pp. 1635-1641, 2000.

[257] J. Mexmain, "Cuprous ferrite and its solid solutions with cupric ferrite," *Ann. Chim. (Paris)*, vol. 6, pp. 297-308, 1971.

[258] X. X. Tang, A. Manthiram, and J. B. Goodenough, "Copper Ferrite Revisited," *J. Solid State Chem.*, vol. 79, pp. 250-262, 1989.

[259] Z. Simsa and P. Holba, "Phase transition in $Cu_{0.5}Fe_{2.5}O_4$ investigated by DTA [differential thermal analysis]," *J. Therm. Anal.*, vol. 3, pp. 17-23, 1971.

[260] Y. D. Tret'yakov, V. F. Komarov, N. A. Prosvirnina, and I. B. Kutsenok, "Nonstoichiometry and defect structures in copper oxides and ferrites," *J. Solid State Chem.*, vol. 5, pp. 157-167, 1972.

[261] R. A. Yund and G. Kullerud, "The System Cu- Fe-O," *Carnegie Inst. Washington Yearb. (1961)*, vol. No. 1363, pp. 181-182, 1961.

[262] R. A. Yund and G. Kullerud, "Stable Mineral Assemblages of Anhydrous Copper and Iron Oxides," *Am. Mineral.*, vol. 49, pp. 689-696, 1964.

[263] G. Kullerud, "Review and evaluation of recent research on geologically significant sulfide-type systems," *Fortschr. Mineral.,* vol. 41, pp. 221-70, 1964.

[264] M. Fredriksson and E. Rosen, "Thermodynamic studies of high temperature equilibriums. XIV. On phase relations and equilibrium oxygen pressures in the system copper-copper ferrate-iron(III) oxide-iron(II, III) oxide at temperatures 1100-1300 K," *Chem. Scr.,* vol. 9, pp. 118-121, 1976.

[265] N. G. Schmahl and F. Muller, "Equilibriums in the System Copper-Iron-Oxygen," *Arch. Eisenhuettenwes.,* vol. 35, pp. 527-532, 1964.

[266] S. C. Schaefer, G. L. Hundley, F. E. Block, R. A. McCune, and R. V. Mrazek, "Phase equilibriums and x-ray diffraction investigation of the system copper-iron-oxygen," *Metall. Trans.,* pp. 2557-2563, 1970.

[267] K. T. Jacob, K. Fitzner, and C. B. Alcock, "Activities in the spinel solid solution, phase equilibriums and thermodynamic properties of ternary phases in the system copper-iron-oxygen," *Metall. Trans. B,* vol. 8B, pp. 451-460, 1977.

[268] H. A. Wriedt, "The Fe-O (Iron-Oxygen) System," *Journal of Phase Equilibria,* vol. 12, pp. 170-200, 1991.

[269] R. Barany, L. B. Pankratz, and W. W. Weller, "Thermodynamic properties of cuprous and cupric ferrites," *Bureau of Mines Report of Investigations,* vol. 6513, p. 19 pp., 1964.

[270] T. Yamaguchi and T. Shiraishi, "Eutectoid decomposition of $CuFe_2O_4$-Fe_3O_4 spinel solid solution," in *Ferrites, Proc. Int. Conf.*, 1971, pp. 148-151.

[271] A. E. Katkov and A. A. Lykasov, "Spinel phase relations in the Fe_3O_4-$CuFe_2O_4$ system," *Inorg. Mater.,* vol. 39, pp. 171-174, 2003.

[272] X. G. Liu, "Experimental Phase Equilibria Studies in Oxide Systems for Copper Smelting Slags," Master of Philosophy, School of Chemical Engineering, University of Queensland, Australia, Brisbane, 2012.

[273] H. Paulsson, E. Rosen, and R. Tegman, "Thermodynamic studies of high temperature equilibria. XIII. Potentiometric determination of the stability of copper iron oxide ($CuFeO_2$) using a galvanic cell involving stabilized zirconium oxide as solid electrolyte," *Chem. Scr.,* vol. 8, pp. 193-196, 1975.

[274] A. G. Zalazinskii, V. F. Balakirev, N. M. Chebotaev, and G. I. Chufarov, "Thermodynamic analysis of the reduction, dissociation, and formation of copper aluminate, copper chromate(III), and copper ferrate(II) from the free elements and oxides," *Zh. Neorg. Khim.,* vol. 14, pp. 624-626, 1969.

[275] J. M. Floyd and G. M. Willis, "Phase Relations and Oxygen Dissociation Pressures in the System Cu-Fe-O," in *Research in Chemical and Extraction Metallurgy,* vol. Monograph Series No. 2, 1967, pp. 61-64.

[276] G. Eriksson and R. Tegman, "Thermodynamic studies of high temperature equilibriums. XVII. Determination of the stability of copper ferrate ($CuFe_2O_4$) by emf measurements using stabilized zirconium as solid electrolyte," *Chem. Scr.,* vol. 10, pp. 145-148, 1976.

[277] M. A. Zinovik, "Conditions for the existence of copper-nickel ferrospinels and phase equilibriums during their reduction," *Zh. Neorg. Khim.,* vol. 33, pp. 738-742, 1988.

[278] K. Ono, Y. Imamura, A. Yamaguchi, and J. Moriyama, "Equilibrium phase diagram of the iron - copper - oxygen system," *Nippon Kinzoku Gakkaishi,* vol. 36, pp. 701-704, 1972.

[279] A. G. Zalazinskii, V. F. Balakirev, and G. I. Chufarov, ""Oxygen pressure-composition" diagram in a copper-iron-oxygen system at 1000.deg," *Zh. Fiz. Khim.,* vol. 43, pp. 1636-1637, 1969.

[280] T. Hidayat, "Studies of $P(O_2)$ over the spinel phase in the Cu-Fe-O system," University of Queensland, Brisbane, Australia, Personal communication, 2012.

[281] J. Acuna, M. Sanchez, and A. Luraschi, "Metal-slag and slag-gas equilibria in the copper-iron-oxygen system," in *Alloy Theory Phase Equilib., Pap. Inter Am. Workshop,* 1986, pp. 91-95.

[282] T. Oishi, K. Nakagawa, and K. Ono, "Phase diagram and thermodynamics of the molten copper - iron - oxygen system at 1773 K," *Nippon Kinzoku Gakkaishi,* vol. 53, pp. 692-697, 1989.

[283] Y. Takeda, "Phase diagram of CaO-FeO-Cu_2O slag under copper saturation," in *Metall. Mater. Process.: Princ. Technol., Yazawa Int. Symp.,* vol. 1, 2003, pp. 211-225.

[284] A. Ilyushechkin, P. C. Hayes, and E. Jak, "Liquidus temperatures in calcium ferrite slags in equilibrium with molten copper," *Metall. Mater. Trans. B,* vol. 35B, pp. 203-215, 2004.

[285] I.-H. Jung, S. A. Decterov, and A. D. Pelton, "Critical Thermodynamic Evaluation and Optimization of the Fe-Mg-O System," *J. Phys. Chem. Solids,* vol. 65, pp. 1683-1695, 2004.

[286] A. Yazawa and M. Eguchi, "Equilibrium Studies on Copper Slags used in Continuous Converting," in *Extractive Metallurgy of Copper,* vol. 1, 1976, pp. 3-20.

[287] T. Yamaguchi, "Phase relations in the ferrite region of the system copper-iron-oxygen in air," *Proc. Fujihara Mem. Fac. Eng., Keio Univ. (Tokyo),* vol. 19, pp. 192-198, 1966.

[288] D. S. Buist, A. M. M. Gadalla, and J. White, "Delafossite and the System Cu-Fe-O," *Mineral. Mag.,* vol. 35, pp. 731-741, 1966.

[289] M. A. Zinovik and A. G. Davidovich, "Chemical transformations during synthesis of copper iron oxide ($CuFeO_2$)," *Inorg. Mater.,* vol. 17, pp. 1093-1096, 1981.

[290] M. A. Zinovik, P. V. Lipatov, V. F. Balakirev, and G. I. Chufarov, "A method of constructing the composition-temperature diagrams for copper-containing spinel systems," *Dokl. Akad. Nauk SSSR,* vol. 275, pp. 397-400, 1984.

[291] M. A. Zinovik, "Phase equilibrium diagram in the copper monoxide-cuprous oxide-ferric oxide-iron oxide (Fe_3O_4) system," *Zh. Neorg. Khim.,* vol. 33, pp. 2689-91, 1988.

[292] M. Ristic, B. Hannoyer, S. Popovic, S. Music, and N. Bajraktaraj, "Ferritization of copper ions in the Cu-Fe-O system," *Mater. Sci. Eng., B,* vol. B77, pp. 73-82, 2000.

[293] F. Kenfack and H. Langbein, "Influence of the temperature and the oxygen partial pressure on the phase formation in the system Cu-Fe-O," *Cryst. Res. Technol.,* vol. 39, pp. 1070-1079, 2004.

[294] N. Nanba and S. Kobayashi, "Semiconductive properties and cation distribution of copper ferrites ($Cu_{1-delta}Fe_{2+delta}O_4$)," *Jpn. J. Appl. Phys.*, vol. 17, pp. 1819-1823, 1978.

[295] I. Katayama, T. Matsuda, and Z. Kozuka, "Thermodynamic study on iron oxide (Fe_3O_4)-copper ferrite ($CuFe_2O_4$) system by emf method," *Technol. Rep. Osaka Univ.*, vol. 30, pp. 385-390, 1980.

[296] A. M. M. Gadalla and J. White, "Equilibrium relationships in the system Cu-Fe-O," *Trans. Brit. Ceram. Soc.*, vol. 65, pp. 1-17, 1966.

[297] W. A. Fischer, D. Janke, and W. Ackermann, "Thermodynamics of the dissolution of oxygen in iron-cobalt, iron-nickel, iron-copper, and cobalt-nickel," *Arch. Eisenhuttenwes.*, vol. 41, pp. 361-367, 1970.

[298] E. S. Tankins, "Activity of oxygen in copper-gold, copper-silver, copper-platinum, copper-nickel, copper-cobalt, and copper-iron alloys," *Can. Met. Q.*, vol. 9, pp. 353-7, 1970.

[299] E. S. Tankins, "Activity of oxygen in liquid iron-copper alloys," *Met. Trans.*, vol. 1, pp. 538-40, 1970.

[300] E. S. Tankins, "Thermodynamic properties of dissolved oxygen in liquid iron-copper alloys," *Can. Met. Q.*, vol. 10, pp. 21-3, 1971.

[301] A. K. Biswas and H. P. Seow, "The Thermodynamic Properties of Oxygen in Liquid Copper-Iron Alloys," *Can. Metall. Q.*, vol. 12, pp. 257-64, 1973.

[302] A. H. J. Muir, R. W. Grant, and H. Wiedersich, "Moessbauer investigation of magnetic structures in $CuFeO_2$ [delafossite]," in *Proc. Conf. Appl. Moessbauer Eff.*, Akad. Kiado, Budapest, Hung., 1971, pp. 557-571.

[303] M. Mekata, N. Yaguchi, T. Takagi, S. Mitsuda, and H. Yoshizawa, "Magnetic ordering in delafossite ($CuFeO_2$)," *J. Magn. Magn. Mater.*, vol. 104-107, pp. 823-824, 1992.

[304] H. Ohnishi, T. Teranishi, and S. Miyahara, "The Transition Temperature of Copper Ferrite," *J. Phys. Soc. Japan*, vol. 14, p. 106, 1959.

[305] J. Mexmain, "Copper(II) ferrite," *Ann. Chim. (Paris)*, vol. 4, pp. 429-440, 1969.

[306] E. G. King and K. K. Kelley, "Low-Temperature Heat Capacities of Copper Ferrites(With a Summary of Entropies at 298.15K. of Spinel Minerals.)," *Bureau of Mines Rept. of Investigations*, vol. 5502, p. 6, 1959.

[307] A. B. Naik, S. R. Sawant, S. A. Patil, and J. I. Powar, "On the variation of a.c. susceptibility with temperature for some copper-lithium ferrites," *Bull. Mater. Sci.*, vol. 11, pp. 315-318, 1988.

[308] R. V. Upadhyay and R. G. Kulkarni, "Magnetic properties of the copper titanium ferrite ($Cu_{1+x}Ti_xFe_{2-2x}O_4$) system," *J. Magn. Magn. Mater.*, vol. 74, pp. 327-9, 1988.

[309] A. Navrotsky and O. J. Kleppa, "Thermodynamics of Formation of Simple Spinels," *J. Inorg. Nucl. Chem.*, vol. 30, pp. 479-498, 1968.

[310] T. Rosenqvist, "Phase Equilibria in the Pyrometallurgy of Sulfide Ores," *Metall. Trans. B*, vol. 9B, pp. 337-351, 1978.

[311] H. Schlegel and A. Schuller, "The Fusion and Crystallization Equilibria in the System, Copper-Iron-Sulfur, and their Significance in the Production of Copper," *Freiberger Forsch. B,* vol. 2, p. 32 pp., 1952.

[312] A. Luraschi and J. F. Elliott, "Thermodynamic Behavior of Oxygen and Sulfur in Copper-Iron-Sulfur-Oxygen Mattes at 1200°C," *Trans. Instn Min. Metall. (Section C: Mineral processing & Extractive Metallurgy),* vol. 89, pp. C14-25, 1980.

[313] D. L. Kaiser and J. F. Elliott, "Solubility of Oxygen and Sulfur in Copper-Iron Mattes," *Metall. Trans. B,* vol. 17B, pp. 147-157, 1986.

[314] C. Somsiri and D. R. Gaskell, "The activities of sulfide and oxide components and the solubility of oxygen in copper-iron-sulfur-oxygen mattes at 1300 DegC," *Metall. Mater. Trans. B,* vol. 26B, pp. 1157-64, 1995.

[315] M. Nagamori and A. Yazawa, "The Quaternary Gibbs-Duhem Integration for Molten Cu-Fe-S-O Matters at 1473 K," *Can. Metall. Q.,* vol. 41, pp. 175-192, 2002.

[316] D. L. Kaiser and J. F. Elliott, "Saturation of copper-iron mattes with solid magnetite," *Metall. Trans. B,* vol. 19B, pp. 935-941, 1988.

[317] F. Johannsen and H. Knahl, "Solubility of Oxygen in Copper Matte," *Z. Erzbergbau Metallhuettenwes.,* vol. 16, pp. 611-621, 1963.

[318] H. N. Lander, S. D. Thesis, Mass. Inst. Technol., 1954.

[319] M. Hillert, "The Compound Energy Formalism," *J. Alloys Compd.,* vol. 320, pp. 161-176, 2001.

[320] Y. Takeda, S. Nakazawa, and A. Yazawa, "Thermodynamics of Calcium Ferrite Slags at 1200°C and 1300°C," *Can. Metall. Q.,* vol. 19, pp. 297-305, 1980.

[321] B. Phillips and A. Muan, "Phase Equilibria in the System CaO-Iron Oxide in Air and at 1 atm O_2 Pressure," *J. Am. Ceram. Soc.,* vol. 41, pp. 445-454, 1958.

[322] R. Scheel, "Investigation into the System Lime-Iron-Oxygen," *Arch. Eisenhuttenwes.,* vol. 45, pp. 751-756, 1974.

[323] S. Hara, T. Araki, and K. Ogino, "Metall.Slags Fluxes," in *Int. Symp. Proc. 2nd, 1984,* 1984, pp. 441-451.

[324] M. Timucin and A. E. Morris, "Phase Equilibria and Thermodynamic Studies in the System CaO-FeO-Fe_2O_3-SiO_2," *Metall. Trans.,* vol. 1, pp. 3193-3201, 1970.

[325] S. Nikolic, P. C. Hayes, and E. Jak, "Liquidus Temperatures in the "Cu_2O"-FeO-Fe_2O_3-CaO-SiO_2 System at Metallic Copper Saturation, at Fixed Oxygen Partial Pressures, and in Equilibrium with Spinel or Dicalcium Ferrite at 1200°C and 1250°C," *Metall. Mater. Trans. B,* vol. 40B, pp. 910-919, 2009.

[326] B. Zhao, E. Jak, and P. Hayes, "EPMA studies of the Cu_2O-Fe_3O_4-CaO system in equilibrium with copper," Pyrosearch, The University of Queensland., Personal communication, 2012.

[327] J. S. Diez Vinuela, C. O. Arean, and F. S. Stone, "Synthesis and structural characterization of copper aluminate-cadmium aluminate spinel solid solutions," *J. Chem. Soc., Faraday Trans. 1,* vol. 79, pp. 1191-1198, 1983.

[328] H. S. C. O'Neill, M. James, W. A. Dollase, and S. A. T. Redfern, "Temperature dependence of the cation distribution in $CuAl_2O_4$ spinel," *Eur. J. Mineral.*, vol. 17, pp. 581-586, 2005.

[329] C. O. Arean and J. S. Diez Vinuela, "Structural Study of Copper-Nickel Aluminate ($Cu_xNi_{1-x}Al_2O_4$) Spinels," *J. Solid State Chem.*, vol. 60, pp. 1-5, 1985.

[330] R. F. Cooley and J. S. Reed, "Equilibrium Cation Distribution in Nickel Aluminate, Copper Aluminate, and Zinc Aluminate Spinels," *J. Am. Ceram. Soc.*, vol. 55, pp. 395-398, 1972.

[331] C. Otero Arean, J. S. Diez Vinuela, J. M. Rubio Gonzalez, and A. Mata Arjona, "Crystal chemistry of copper zinc aluminum oxide ($Cu_xZn_{1-x}Al_2O_4$) spinels," *Mater. Chem.*, vol. 6, pp. 165-173, 1981.

[332] P. Porta and A. Mazzarano, "Cation Distribution in Oxidic Spinel Solid Solutions," *Mater. Sci. Monogr.*, vol. 28B(React. Solids, Pt. B), pp. 1053-1054, 1985.

[333] L. A. Fenner, A. S. Wills, S. T. Bramwell, M. Dahlberg, and P. Schiffer, "Zero-point entropy of the spinel spin glasses $CuGa_2O_4$ and $CuAl_2O_4$," *J. Phys.: Conf. Ser.*, vol. 145, pp. 1-4, 2009.

[334] K. T. Jacob and C. B. Alcock, "Thermodynamics of copper aluminates ($CuAlO_2$ and $CuAl_2O_4$) and phase equilibriums in the copper(I) oxide-copper(II) oxide-aluminum oxide system," *J. Am. Ceram. Soc.*, vol. 58, pp. 192-195, 1975.

[335] A. M. M. Gadalla and J. White, "Equilibrium relation in the system Cu_2O-CuO-Al_2O_3," *Trans. Brit. Ceram. Soc.*, vol. 63, pp. 39-62, 1964.

[336] A. F. Bessonov, A. A. Slobodyanyuk, and Y. D. Tret'yakov, "High-temperature study of cupric oxide-aluminum oxide and cuprous oxide-aluminum oxide systems," *Izv. Akad. Nauk SSSR, Neorg. Mater.*, vol. 8, pp. 1270-1274, 1972.

[337] H. Schmalzried, "Measurement of the free enthalpy of reaction in the formation of spinel phases from the single oxides by aid of solid galvanic couples," *Z. Phys. Chem. (Muenchen, Ger.)*, vol. 25, pp. 178-192, 1960.

[338] S. K. Misra and A. C. D. Chaklader, "System Copper Oxide-Alumina," *J. Am. Ceram. Soc.*, vol. 46, p. 509, 1963.

[339] T. Tsuchida, R. Furuichi, T. Sukegawa, M. Furudate, and T. Ishii, "Thermoanalytical study on the reaction of the copper(II) oxide-aluminum oxide (eta, gamma and alpha) systems," *Thermochim. Acta*, vol. 78, pp. 71-80, 1984.

[340] M. Guedes, J. M. F. Ferreira, and A. C. Ferro, "A study on CuO-Al_2O_3 reaction paths," in *Adv. Powder Metall. Part. Mater.*, 2008, pp. 5/1-5/13.

[341] J. Gerlach, P. Kartenbeck, and F. Pawlek, "Affecting the oxygen content of metallic copper by various oxide additions to copper oxide slags," *Z. Erzbergbau Metallhuettenwes.*, vol. 17, pp. 550-553, 1964.

[342] R. H. J. von Wartenberg H., "Melting diagrams of highly refractory oxides: IV, Aluminum oxide," *Z. Anorg. Allg. Chem.*, vol. 207, pp. 1-20, 1932.

[343] T. Oishi, T. Ohba, and K. Ono, "A thermodynamic study of the alumina-saturated copper oxide (Cu_2O)-silicon dioxide melts in equilibrium with liquid copper," in *Proc. Int. Symp. Molten Salt Chem. Technol., 1st*, 1983, pp. 213-216.

[344] A. G. Zalazinskii, G. M. Pis'menskaya, V. F. Balakirev, and G. I. Chufarov, "Phase equilibriums during quasistatic reduction of copper iron aluminum oxide ($CuFe_{1.75}Al_{0.25}O_4$). Communication I," *Khimiya i Tekhnol. Oksid. Magnit. Materialov,* pp. 95-100, 1977.

[345] R. E. Johnson and A. Muan, "Phase Equilibria in the System CaO-MgO-Iron Oxide at 1500°C," *J. Am. Ceram. Soc.*, vol. 48, pp. 359-364, 1965.

[346] R. Fusenig, U. Limbert, and E. Woermann, "Schmelzgleichgewichte im System MgO-Ca_2SiO_4-$Ca_2Fe_2O_5$-$MgFe_2O_4$ und ihr Einfluss auf die Eigenschaften von basischen, feuerfesten Stoffen.," *TIZ-Fachberichte,* vol. 108, pp. 515-23, 1984.

[347] P. Wu, G. Eriksson, and A. D. Pelton, "Critical Evaluation and Optimization of the Thermodynamic Properties and Phase Diagrams of the Calcia-Iron(II) Oxide, Calcia-Magnesia, Calcia-Manganese(II) Oxide, Iron(II) Oxide-Magnesia, Iron(II) Oxide-Manganese(II) Oxide, and Magnesia-Manganese(II) Oxide Systems," *J. Am. Ceram. Soc.*, vol. 76, pp. 2065-2075, 1993.

[348] G. Eriksson, P. Wu, M. Blander, and A. D. Pelton, "Critical Evaluation and Optimisation of the Thermodynamic Properties and Phase Diagrams of the MnO-SiO2 and CaO-SiO2 Systems," *Can. Metall. Q.,* vol. 33, pp. 13-21, 1994.

[349] G. Eriksson and A. D. Pelton, "Critical Evaluation and Optimization of the Thermodynamic Properties and Phase Diagrams of the CaO-Al_2O_3, Al_2O_3-SiO_2, and CaO-Al_2O_3-SiO_2 Systems," *Metall. Trans.*, vol. 24B, pp. 807-816, 1993.

[350] I.-H. Jung, S. A. Decterov, and A. D. Pelton, "Critical Thermodynamic Evaluation and Optimization of the MgO-Al_2O_3, CaO-MgO-Al_2O_3 and MgO-Al_2O_3-SiO_2 Systems," *J. Phase Equilib.*, vol. 25, pp. 329-345, 2004.

[351] P. Chartrand and A. D. Pelton, "The Modified Quasichemical Model. III - Two Sublattices," *Metall. Mater. Trans. A,* vol. 32A, pp. 1397-1407, 2001.

[352] D. Shishin, "Equilibria in the Cu-Fe-O-S system," *Chapter 7 of this thesis*, 2013.

[353] A. D. Pelton, G. Eriksson, and A. Romero-Serrano, "Calculation of Sulfide Capacities of Multicomponent Slags," *Metall. Trans. B,* vol. 24B, pp. 817-825, 1993.

[354] Y.-B. Kang and A. Pelton, "Thermodynamic Model and Database for Sulfides Dissolved in Molten Oxide Slags," *Metall. Mater. Trans. B,* vol. 40, pp. 979-994, 2009.

[355] Y. Takeda, "Oxidic and Sulfidic Dissolution of Copper in Matte Smelting Slag," in *Proc. 4th Int. Conf. of Molten Slags and Fluxes, ISIJ*, 1992, pp. 584-589.

[356] P. B. Mihalop, "The Solubility of Copper in Smelting Slags," Ph.D thesis, University of Birmingham, 1968.

[357] R. W. Ruddle, B. Taylor, and A. P. Bates, "The Solubility of Copper in Iron Silicate Slag," *Trans. Instn Min. Metall. (Section C: Mineral processing & Extractive Metallurgy),* vol. 75, pp. C1-C12, 1966.

[358] R. Altman and H. H. Kellogg, "Solubility of Copper in Silica-Saturated Iron Silicate Slag," *Trans. Instn Min. Metall.,* vol. 81, pp. C163-C175, 1972.

[359] J. R. Taylor and J. H. E. Jeffes, "Slag-Metal Equilibriums between Liquid Nickel-Copper Alloys and Iron Silicate Slags of Varying Composition," *Inst. Min. Metall., Trans., Sect. C,* vol. 84, pp. C136-C148, 1975.

[360] B. J. Elliot, J. B. See, and W. J. Rankin, "Effect of Slag Composition on Copper Losses to Silica-Saturated Iron Silicate Slags," *Trans. Inst. Min. Metall. (Section C: Mineral processing & Extractive Metallurgy),* vol. 87, pp. C204-211, 1978.

[361] T. Oishi, M. Kamuo, K. Ono, and J. Moriyama, "A Thermodynamic Study of Silica-Saturated Iron Silicate Slags in Equilibrium with Liquid Copper," *Metall. Trans. B,* vol. 14B, pp. 101-104, 1983.

[362] H. G. Kim and H. Y. Sohn, "Effects of CaO, Al_2O_3, and MgO Additions on the Copper Solubility, Ferric/Ferrous Ratio, and Minor-Element Behavior of Iron-Silicate Slags," *Metall. Mater. Trans. B,* vol. 29B, pp. 583-590, 1998.

[363] H. M. Henao, P. C. Hayes, and E. Jak, "Phase equilibria of "Cu_2O"-"FeO"-SiO_2-CaO slags at PO_2 at 10^{-8} atm in equilibrium with metallic copper," in *Ninth International Conference on Molten Slags, Fluxes and Salts (MOLTEN12)*, 2012.

[364] W. H. MacLean, "Liquid Phase Relations in the FeS-FeO-Fe_3O_4-SiO_2 System, and their Application in Geology," *Econ. Geol.,* vol. 64, pp. 865-884, 1969.

[365] R. Shimpo, S. Goto, O. Ogawa, and I. Asakura, "A Study on the Equilibrium between Copper Matte and Slag," *Can. Metall. Q.,* vol. 25, pp. 113-121, 1986.

[366] M. M. Nzotta, D. Sichen, and S. Seetharaman, "Sulfide capacities of FeO-SiO_2, CaO-FeO, and FeO-MnO slags," *ISIJ Int.,* vol. 39, pp. 657-663, 1999.

[367] S. R. Simeonov, R. Sridhar, and J. M. Toguri, "Sulfide Capacities of Fayalite-Base Slags," *Metall. Trans. B.,* vol. 26B, pp. 325-334, 1995.

[368] C. J. B. Fincham and F. D. Richardson, "The Behaviour of Sulphur in Silicate and Aluminate Melts," *Proc. Roy. Soc. (London),* vol. 223, pp. 40-62, 1954.

[369] M. Nagamori, "Metal Loss to Slag: Part I. Sulfidic and Oxidic Dissolution of Copper in Fayalite Slag from Low Grade Matte," *Metall. Trans. B,* vol. 5B, pp. 531-538, 1974.

[370] G. H. Kaiura, K. Watanebe, and A. Yazawa, "The Behavior of Lead in Silica-Saturated Copper Smelting Systems," *Can. Metall. Q.,* vol. 19, pp. 191-200, 1980.

[371] H. Jalkanen, "Copper and Sulfur Solubilities in Silica-Saturated Iron Silicate Slags from Copper Mattes," *Scand. J. Metall.,* vol. 10, pp. 177-184, 1981.

[372] A. Yazawa, S. Nakazawa, and Y. Takeda, "Distribution Behavior of Various Elements in Copper Smelting Systems," in *Adv. Sulfide Smelting,* vol. 1, 1983, pp. 99-117.

[373] N. Korakas, "Etude thermodynamic de l'équilibre entre scories ferro-siliceuses et mattes de cuivre. Application aux problèmes posés par la formation de magnetite lors du traitement des minerais sulfurés de cuivre," Ph.D. thesis, Univirsité de Liège, 1964.

[374] U. Kuxmann and F. Y. Bor, "Studies on the Solubility of Oxygen in Copper Mattes under Ferric Oxide Slags Saturated with Silica," *Erzmetall.,* vol. 18, pp. 441-450, 1965.

[375] F. J. Tavera and W. G. Davenport, "Equilibrations of Copper Matte and Fayalite Slag under Controlled Partial Pressures of Sulfur Dioxide," *Metall. Trans. B,* vol. 10B, pp. 237-241, 1979.

[376] H. Li and W. J. Rankin, "Thermodynamics and Phase Relations of the Fe-O-S-SiO_2(sat) System at 1200°C and the Effect of Copper," *Metall. Trans. B,* vol. 25B, pp. 79-89, 1994.

[377] H. M. Henao and E. Jak, "Experimental study of slag-matte equilibria in the Ca-Cu-Fe-O-S-Si system at fixed $P(SO_2)$ and $P(O_2)$," ed: Private Communication: Pyrosearch, University of Queensland 2013.

[378] A. Yazawa and M. Kameda, "Copper Smelting. II. Solubilities of Constituents of Mat in Slag," *The Technology Reports of the Tohoku Univ.,* vol. 19, pp. 1-22, 1954.

[379] A. Yazawa and M. Kameda, "Fundamental Studies on Copper Smelting. IV. Solubility of FeO in Copper Matte from SiO_2-saturated FeO-SiO_2 Slag," *The Technology Reports of the Tohoku Univ.,* vol. 19, pp. 251-261, 1955.

[380] J. M. Font, G. Roghani, M. Hino, and K. Itagaki, "Solubility of copper or nickel in iron-silicate base slag equilibrated with Cu_2S-FeS or Ni_3S_2-FeS matte under high partial pressures of SO_2," *Metall. Rev. MMIJ,* vol. 15, pp. 75-86, 1998.

[381] Y. Takeda, "Copper solubility in matte smelting slag," in *Proc. Int. Conf. Molten Slags, Fluxes Salts '97, 5th*, 1997, pp. 329-339.

[382] K. P. Abraham, M. W. Davies, and F. D. Richardson, "Sulfide Capacities of Silicate Melts. Part I," *J. Iron Steel Inst.,* vol. 196, pp. 309-312, 1960.

[383] P. T. Carter and T. G. Macfarlane, "Thermodynamics of Slag Systems, Part I, The Thermodynamic Properties of CaO-Al_2O_3 Slags. Part II, The Thermodynamic Properties of CaO-SiO_2 Slags," *Journal of The Iron and Steel Institute (London),* vol. 185, pp. 54-66, 1957.

[384] S. D. Brown, R. J. Roxburgh, I. Ghita, and H. B. Bell, "Sulphide Capacity of Titania-Containing Slags," *Ironmaking Steelmaking,* vol. 9, pp. 163-167, 1982.

[385] M. Gornerup and O. Wijk, "Liquidus Relationships in The CaO-Corner of the Ternary System CaO-Al_2O_3-SiO_2," *ISIJ Int.,* vol. 36, pp. 1465-1470, 1996.

[386] M. Chapman, O. Ostrovski, G. Tranell, and S. Jahanshahi, "Sulfide Capacity of Titania-Containing Slags," *Elektrometallurgiya,* vol. 3, pp. 34-39, 2000.

[387] R. A. Sharma and F. D. Richardson, *J. Iron Steel Inst. (London),* vol. 200, pp. 373-379?, 1962.

[388] R. Altman, "Influence of Aluminum Oxide and Calcium Oxide on Solubility of Copper in Silica-Saturated Iron Silicate Slag," *Trans. Instn Min. Metall,* vol. 87, pp. C23-C28, 1978.

[389] S. Nikolic, P. C. Hayes, and E. Jak, "Phase Equilibria in Ferrous Calcium Silicate Slags: Part IV. Liquidus Temperatures and Solubility of Copper in "Cu2O"-FeO-Fe2O3-CaO-SiO2 Slags at 1250 ° C and 1300 ° C at an Oxygen Partial Pressure of 10-6 atm," *Metall. Trans. B,* vol. 39B, pp. 210-217, 2008.

[390] T. Hidayat, P. C. Hayes, and E. Jak, "Experimental Study of Ferrous Calcium Silicate Slags: Phase Equilibria at Between 10^{-5} atm and 10^{-7} atm," *Metall. Mater. Trans. B,* vol. 43, pp. 14-26, 2012.

[391] M. G. Park, Y. Takeda, and A. Yazawa, "Equilibrium relations between liquid copper, matte and calcium ferrite slag at 1250°C," *Tohoku Daigaku Senko Seiren Kenkyusho Iho,* vol. 39, pp. 115-122, 1983.

[392] C. Acuna and A. Yazawa, "Mutual dissolution between matte and ferrite slags," *Trans. Jpn. Inst. Met.,* vol. 27, pp. 881-889, 1986.

[393] G. Roghani, M. Hino, and K. Itagaki, "Phase equilibrium between calcium ferrite slag and copper matte at 1523 K under high partial pressures of SO_2," *Mater. Trans., JIM,* vol. 37, pp. 1431-1437, 1996.

[394] G. R. Alvear, P. Aurthur, and P. Partington, "Feasibility to Profitability with Copper ISASMELT™ " in *Copper*, Hamburg, Germany, vol. 2, 2010, pp. 615-630.

[395] M. L. Bakker, S. Nikolic, and P. J. Mackey, "ISASMELT(TM) TSL - Applications for nickel," *Minerals Engineering,* vol. In Press, Corrected Proof.

[396] J. Pritchard and R. Hollis, "The Isasmelt copper-smelting process," *Int. Min. Metal. Technol. (Hannover),* vol. 1, pp. 125-128, 1994.

[397] S. L. Mariscal and P. W. Torres, "Modernization and start-up of the SPCC Ilo smelter," presented at the Cu2007 - The Carlos Diaz Symposium on Pyrometallurgy, Toronto, Canada, 2007.

[398] C. Carlos Lama, "ILO Smelter," in *V Congresso Brasileiro de Ácido Sulfúrico*, Salvador, 2007.

[399] E. Herrera and L. Mariscal, "Changes in the ISASMELTTM Slag Chemistry at Southern Peru Ilo Smelter," in *Copper 2010*, GDMB, vol. 2, 2010, pp. 749-759.

[400] R. L. Player, "Copper Isasmelt-process investigations," *Howard Worner Int. Symp. Injection Pyrometall.*, pp. 439-446, 1996.

[401] A. D. Pelton and P. Chartrand, "The modified quasi-chemical model: Part II. Multicomponent solutions," *Metallurgical and Materials Transactions A: Physical Metallurgy and Materials Science,* vol. 32, pp. 1355-1360, 2001.

[402] A. D. Pelton, S. A. Degterov, G. Eriksson, C. Robelin, and Y. Dessureault, "The modified quasichemical model. I. Binary solutions," in *Milton Blander Symposium on Thermodynamic Predictions and Applications at the TMS Annual Meeting, 1-2 March 1999*, USA, vol. 31B, 2000, pp. 651-9.